Julius M. Guccione
Ghassan S. Kassab
Mark B. Ratcliffe
Editors

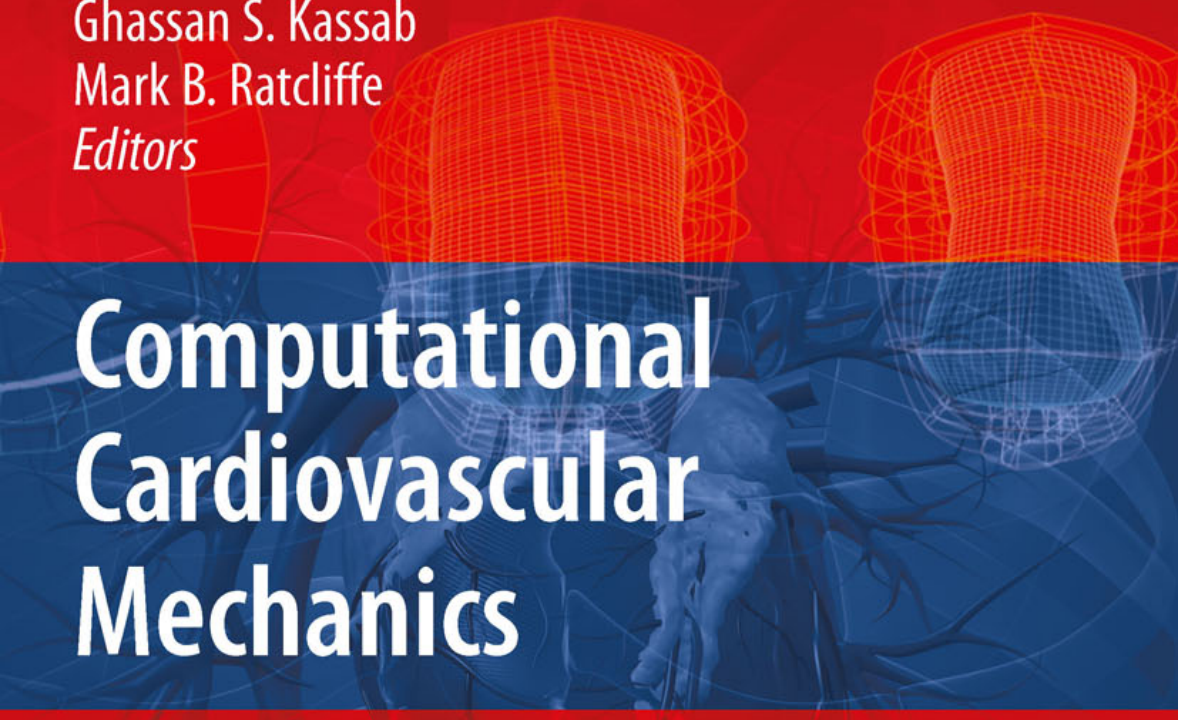

Computational Cardiovascular Mechanics

Modeling and Applications in Heart Failure

Springer

Computational Cardiovascular Mechanics

Julius M. Guccione · Ghassan S. Kassab ·
Mark B. Ratcliffe
Editors

Computational Cardiovascular Mechanics

Modeling and Applications in Heart Failure

Springer

Editors
Julius M. Guccione
Department of Surgery
University of California San Francisco &
the San Francisco VA Medical Center
San Francisco, CA
guccionej@surgery.ucsf.edu

Ghassan S. Kassab
Department of Biomedical Engineering
Indiana University-Purdue University
Indianapolis
Indianapolis, IN, USA
gkassab@iupui.edu

Mark B. Ratcliffe
Department of Surgery
University of California San Francisco &
the San Francisco VA Medical Center
San Francisco, CA
mratcliffe@hotmail.com

ISBN 978-1-4419-0729-5 e-ISBN 978-1-4419-0730-1
DOI 10.1007/978-1-4419-0730-1
Springer New York Dordrecht Heidelberg London

Library of Congress Control Number: 2009937460

Preface

The ultimate aspiration of this book is to promote the application of computational cardiovascular mechanics models to clinical medicine. Patient-specific computational models can aid medical diagnosis and help design optimal treatment for cardiovascular disease. At present, however, most computational biomechanics modeling is still in the research and development stage. Further, the progress that has been made remains largely unrecognized in the clinic.

The objective of this book is, therefore, to present a comprehensive perspective on computational modeling of cardiovascular mechanics from both solid mechanics and fluid dynamics points of view. Since clinical translation of these models is the ultimate objective, we focus on applications in heart failure as this is an area that can particularly benefit from mechanical modeling. With our limited objective, this book does not claim to be a compendium or handbook of current information on the selected topics nor a review of literature; rather, it is largely works of the editors and their associates with a balanced point of view. A comprehensive bibliography is not provided; the list of references is limited to items quoted in the text.

We wish to express our thanks to all authors and publishers who permitted us to quote their publications and reproduce their figures and data in this book. We wish to especially thank Professor Yuan-Cheng Fung for his mentorship. Special thanks should also go to L. Henry Edmunds and Dan Bogen who mentored and continue to mentor Dr. Ratcliffe. Much of the work presented here is the work of our colleagues, fellows, and former students. We wish to thank Drs. Andrew McCulloch, Lewis Waldman, Iraj Motabarzadeh, Vincent de Laborderie, George Zahahak, Ruth Okamoto, Michael Moulton, Sarah Peterson, Michael Pasque, Scott Moonly, Ali Salahieh, Alan Dang, Joseph Walker, Peng Zhang, Joseph Gorman, Robert Gorman, David Saloner, Kevin Healy, Arthur Wallace, Amy Schatz, Carmel Rider, Edith Pallencaoe, Kha Le, Daniel Lin, Jimmy Zhou, Sabee Molloi, Xiaomei Guo, Xiao Lu, Susy Choy, Benny Kaimovitz, Yoram Lanir, and many others who contributed much of the material presented here. To all of them we are thankful.

Finally, we wish to thank the editorial and production staffs of Springer for their professional help and cooperation in producing this book.

San Francisco, California — Julius Guccione
Indianapolis, Indiana — Ghassan Kassab
San Francisco, California — Mark Ratcliffe

Contents

Contributors

Edward J. Berbari Department of Biomedical Engineering, IUPUI, Indianapolis, IN, USA

Mike Burger XYZ Scientific Applications Inc., Livermore, CA, USA

Henry Y. Chen Weldon School of Biomedical Engineering, Purdue University, West Lafayette; Department of Cellular and Integrative Physiology, IUPUI, Indianapolis, IN 46202, USA

Leok Poh Chua School of Mechanical and Aerospace Engineering, Nanyang Technological University, Singapore

Terrace Chua Department of Cardiology, National Heart Centre Singapore, Singapore

William Combs Department of Biomedical Engineering, IUPUI, Indianapolis, IN, USA

Laura R. Croft Department of Bioengineering, University of California, Berkeley, CA, USA

Dan Einstein Biological Monitoring and Modeling, Pacific Northwest National Laboratory, Olympia, WA, USA

Daniel R. Einstein Pacific Northwest National Laboratory, Richland, WA, USA

Liang Ge Department of Surgery, University of California and San Francisco VA Medical Center, San Francisco, CA, USA

Dhanjoo N. Ghista Parkway College, Singapore 150168, d.ghista@gmail.com

Julius M. Guccione Department of Surgery, University of California at San Francisco and San Francisco VA Medical Center, San Francisco, CA, USA, guccionej@surgery.ucsf.edu

Namrata Gundiah Department of Mechanical Engineering, Indian Institute of Science, Bangalore, India

Lindsey J. Healy Department of Bioengineering, University of Utah, Salt Lake City, UT, USA

Edward W. Hsu Department of Bioengineering, University of Utah, Salt Lake City, UT, USA, u0492505@umail.utah.edu

Yunlong Huo Department of Biomedical Engineering, Surgery, and Cellular and Integrative Physiology, IUPUI, Indianapolis, IN 46202, USA

Choon-Sik Jhun Department of Surgery, University of California at San Francisco and San Francisco VA Medical Center, San Francisco, CA, USA, csjhun@gmail.com

Xiangmin Jiao Department of Applied Mathematics and Statistics, Stony Brook University, Stony Brook, NY, USA

Mohammad R. Kaazempur Mofrad Department of Bioengineering, University of California, Berkeley, CA, USA, mofrad@berkeley.edu

Ghassan S. Kassab Weldon School of Biomedical Engineering, Purdue University, West Lafayette; Department of Biomedical Engineering; Department of Surgery; Department of Cellular and Integrative Physiology; Indiana Center for Vascular Biology and Medicine, IUPUI, Indianapolis, IN 46202, USA, gkassab@iupui.edu

Roy C.P. Kerckhoffs Department of Bioengineering, University of California San Diego, La Jolla, CA, USA, roy@bioeng.ucsd.edu

Tian Hai Koh Department of Cardiology, National Heart Centre Singapore, Singapore

Andrew P. Kuprat Pacific Northwest National Laboratory, Richland, WA, USA

Yi Liu Department of Biomedical Engineering, IUPUI, Indianapolis, IN 46202, USA

Karen May-Newman Bioengineering Program, Department of Mechanical Engineering, San Diego State University, San Diego, CA, USA, kmn@kahuna.sdsu.edu

Lawrence J. Mulligan Therapy Delivery Systems/Leads Research, Medtronic, Inc., Mounds View, MN, USA

Mark B. Ratcliffe Department of Surgery, University of California at San Francisco and San Francisco VA Medical Center, San Francisco, CA, USA

Hani N. Sabbah Henry Ford Hospital, Detroit, MI, USA

Meena Sankaranarayanan Mathematics, Department of Science and Humanities, Hindustan University, Padur, Kelambakkam, Chennai, India, meenasankaranarayanan@rediffmail.com

Tan Yong Seng Tan Yong Seng Heart, Lung & Vascular Surgery Pet Ltd, Mount Elizabeth Hospital, Singapore

Nielen Stander Livermore Software Technology Corporation, Livermore, CA, USA

Yi Su Institute of High Performance Computing, Agency for Science, Technology and Research, Singapore

Kay Sun Department of Surgery, University of California at San Francisco and San Francisco VA Medical Center, San Francisco, CA, USA

Kannan Sundaravadivelu Mechatronics and Recording Channel Division, Data Storage Institute, Singapore

Mark Svendsen Weldon School of Biomedical Engineering, Purdue University, West Lafayette, IN, USA

Ru San Tan Department of Cardiology, National Heart Centre Singapore, Singapore

Elaine E. Tseng Department of Surgery, University of California at San Francisco and San Francisco VA Medical Center, San Francisco, CA, USA

Samuel T. Wall Department of Surgery, University of California at San Francisco and San Francisco VA Medical Center, San Francisco, CA, USA

Jonathan F. Wenk Department of Surgery, University of California at San Francisco and San Francisco VA Medical Center, San Francisco, CA, USA
e-mail: jwenk1@gmail.com

Thomas Wischgoll Department of Computer Science and Engineering, Wright State University, Dayton, OH, USA

Si Yong Yeo School of Engineering, University of Swansea, UK

Zhihong Zhang Department of Surgery, University of California at San Francisco and San Francisco VA Medical Center, San Francisco, CA, USA

Liang Zhong Department of Cardiology, National Heart Centre Singapore, Singapore; College of Life Science and Engineering, Huazhong University of Science and Technology, China

Luoding Zhu Department of Mathematical Sciences, IUPUI, Indianapolis, IN 46202, USA

Introduction

Mark B. Ratcliffe, Julius M. Guccione, and Ghassan S. Kassab

Abstract Heart failure (HF) is a huge health and economic problem in the United States. As a consequence, a number of innovative device-based and surgical HF therapies have been introduced in the last 10 years. Examples include the total artificial heart, ventricular assist device, surgical ventricular remodeling, passive constraint, and resynchronization therapy. In general these therapies aim to either increase cardiac output or reverse left ventricular remodeling. However, a number of problems remain unsolved including the effect of therapy on left ventricular stress and function and intraventricular and intra-device flow and thrombus formation.

Mathematical modeling of the cardiovascular system using the finite element (FE) method has become both more powerful and easy to use. FE models of the heart now incorporate constitutive laws based on myocardial architecture that mimic the passive anisotropic nonlinear nature of the myocardium that can simulate active contraction. Inverse solutions now allow the calculation of myocardial material properties and stress. Computational fluid dynamics (CFD) studies can calculate endothelial shear stress and predict thrombosis and hemolysis. The FE method will play an increasing role in the understanding of cardiovascular pathology and in the design of therapies for HF.

The significance of HF as an economic and clinical problem will be discussed. Current device therapy will be discussed with an emphasis on problems that remain to be solved. Next, the chapter outlines the four basic biomechanics modeling steps. We conclude by introducing the chapters to follow.

J.M. Guccione (✉)
Department of Surgery, University of California at San Francisco and San Francisco VA Medical Center, San Francisco, CA, USA
e-mail: guccionej@surgery.ucsf.edu

1 Heart Failure

Heart failure (HF) is an increasing health and economic problem in the United States. For instance, one in eight deaths has HF mentioned on the death certificate. The number of "total mention" deaths from HF was 284,365 in 2004 with HF listed as the underlying cause in 57,120 [58]. Patients with HF use an increasing amount of health care resources. From 1979 to 2005, hospital discharges for HF rose from 400,000 to 1,084,000 [58]. The estimated direct and indirect cost of HF in the United States for 2008 is $34.8 billion [58].

HF is either caused by decreased left ventricular (LV) end-systolic elastance (systolic HF) or decreased diastolic compliance (diastolic HF) [1]. The most common cause of systolic HF is myocardial infarction (MI) secondary to coronary artery disease (~two-thirds of all HF). The annual incidence of MI is 920,000 [58]. Most current therapies, and all those discussed in this book, are designed to treat systolic HF.

The consequences of significant post-MI ventricular remodeling are substantial [2]. An increase in LV size after MI is one of the most important adverse prognostic findings [3–5, 55], and relatively small changes (25 cc) in end-systolic volume are associated with exponential increases in mortality [6]. Although the current incidence of LV aneurysm is unknown, Visner reported an incidence of 22% in 1986 [7] and Benediktsson reported an incidence of 5.3% in 1991 [8]. The percentage of patients with LV aneurysm who develop congestive heart failure (CHF) is 29% [9].

2 Cardiac Surgery

The last 50 years have seen an explosion of device- and engineering-related progress in cardiac surgery and the treatment of HF. Fig. 1 shows some of the landmark events and publications [10] that have occurred since the initial use of cardiopulmonary bypass by Gibbon in 1953 [11].

The number of routine cardiac surgical and interventional cardiology procedures has increased dramatically over the last 50 years. For instance, there were 699,000 open heart operations performed in 2005 [58]. An estimated 1,265,000 percutaneous coronary interventions (PCI) and 469,000 coronary bypass (CABG) procedures were performed in the United States in 2005 [58]. Finally, 106,000 valve prostheses were implanted in 2005 [58].

Survival after cardiac transplantation has gradually increased since the first human cardiac transplant by Barnard in 1967. In 2001, time to 50% survival after heart transplantation in an adult had increased to 10.3 years [12]. However, the need for surgical therapy for HF has outstripped demand. It is estimated that 40,000 people aged 65 or older may benefit from cardiac transplantation. Of those awaiting transplantation, 59% have a non-ischemic cardiomyopathy while 41% have an ischemic cardiomyopathy [57]. Although heart transplantation is increasing in

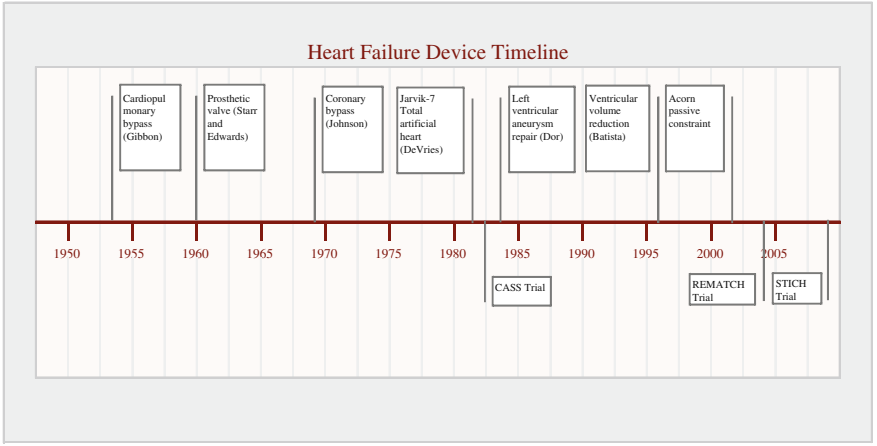

Fig. 1

frequency, scarcity of donors limited the number of heart transplants performed in the US to 2,192 [58]. In 2001, 8.5% of those on the transplant waiting list died awaiting transplant [57].

3 New Devices and Operations

As a consequence, a number of innovative device-based and surgical HF therapies have been introduced, many in the last 10 years. Examples include mechanical circulatory support (total artificial heart, ventricular assist device (VAD)), surgical ventricular remodeling, passive constraint, and resynchronization therapy. In general these therapies aim to either increase cardiac output or reverse LV remodeling.

3.1 Mechanical Circulatory Support

In 1969, Cooley used an artificial heart as a bridge to transplantation but the patient died shortly after second operation [13]. In 1982, DeVries implanted a Jarvik-7 total artificial heart developed at the University of Utah by Jarvik, Kolff, and colleagues [14]. The patient lived for 112 days. Since those early days, there has been tremendous progress. In 2004, the REMATCH trial showed that treatment of end-stage HF with a VAD was a viable therapy [15]. Currently, a large number of VADs and artificial heart devices are under development for use as bridge to transplant, bridge to recovery, or destination therapy. Recent innovations include continuous flow VAD (Fig. 2) and VADs with hydraulic and magnetic rotor suspension.

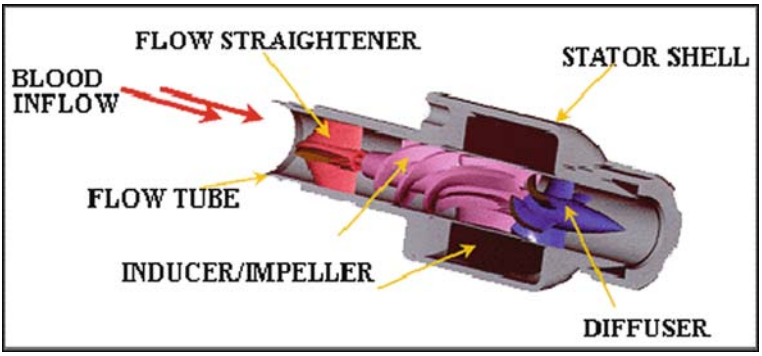

Fig. 2 Micromed axial flow pump

3.2 Surgical Remodeling

A number of surgical procedures have been proposed to stop or reverse ventricular remodeling. In general, these procedures are designed to either decrease stress on the myocardium or to constrain the heart so that further enlargement cannot occur.

Although previously described by Cooley [16] and others, in 1984, Dor popularized the use of an endoventricular circular patch plasty ("Dor procedure") to restore LV size and shape by excluding the infarcted anterior LV wall and interventricular septum in patients with ischemic cardiomyopathy and either akinetic or dyskinetic anterior wall (Fig. 3) [17].

In 2009, the NIH sponsored Surgical Treatment for Ischemic Heart failure (STICH) trial found no survival benefit for surgical ventricular remodeling [18]. The STICH report noted that there may be specific subgroups of patients who might benefit from the combined procedure. However, at this time, the future of the Dor procedure and other surgical remodeling operations is unclear.

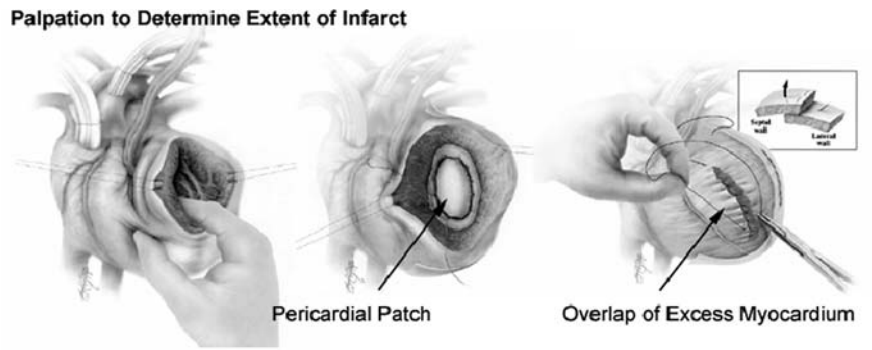

Fig. 3 Surgical Anterior Ventricular Restoration (SAVER). From Athanasthuleas et al, J Am Coll Cardiol 37: 1199, 2001

Also worth noting was the description in 1996 by Batista of a new surgical therapy for HF in patients with dilated cardiomyopathy (DCM) and end-stage CHF in which a viable "slice" of lateral LV wall was resected [19]. Because of problems with diastolic dysfunction and ventricular arrhythmias the Batista operation has largely been abandoned.

3.3 Passive Constraint

Passive LV constraint devices made of woven polyester fabric (Acorn Corcap TM Cardiac Support Device (CSD)) [20, 21] or nitinol (Paracor) [22] have been designed to prevent further ventricular remodeling. Passive LV restraint with Acorn and Paracor is arguably the least invasive and most likely to be applied to patients with ventricular remodeling and/or heart failure after myocardial infarction. Acorn and Paracor devices have not to date received FDA approval (Fig. 4).

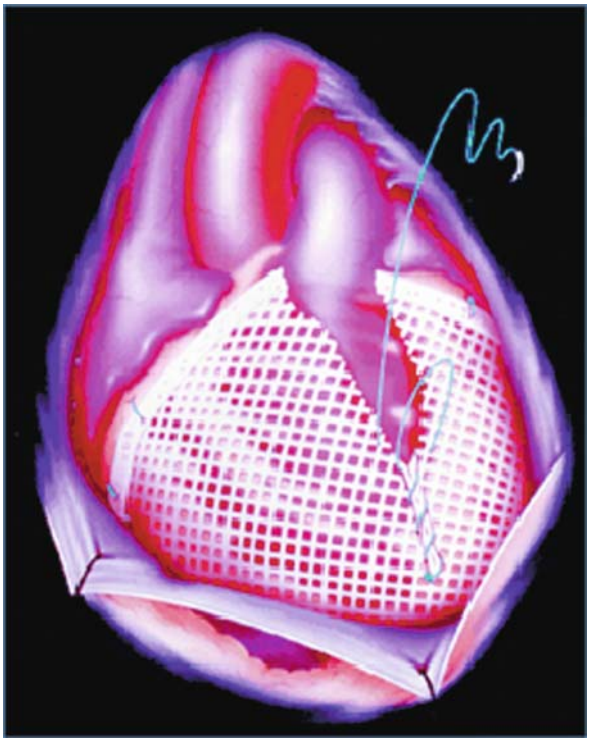

Fig. 4 Acorn cardiac support device (Jacket)

4 Remaining Problems

There are a number of problems that prevent mechanical support, surgical ventricular remodeling operations, and passive constraint devices discussed above from achieving full potential.

4.1 Emboli from Intravascular Devices

First, emboli from mechanical valves and from assist devices remain a major problem. For instance, embolism (1.18%/patient-year) and anticoagulant-related bleeding (2.24%/patient-year) are the dominant complications associated with standard St. Jude prosthesis in the aortic position [23]. Also, 16% of patients in the VAD arm of the REMATCH trial had frank stroke [24].

4.2 The Effect of Device Therapy on Ventricular Function

Next, valve replacement for regurgitant aortic and mitral valves and surgical remodeling procedures are thought to work because they reduce the stress on the myocardium. Stress reduction is important since myocardial stress determines regional coronary blood flow, [25] myocardial oxygen consumption, hypertrophy [26], and remodeling. However, the measurement of myocardial stress is problematic. Huisman previously showed that it is impossible to directly measure regional in vivo myocardial stress because of tethering from surrounding myocardium [27, 28]. Also, the use of force balance equations such as Laplace's law is limited for a thick-walled heart.

Finally, the effect of HF operations on regional and global ventricular function is often difficult to predict. For instance, surgical ventricular remodeling and passive constraint devices may unintentionally create diastolic dysfunction [29].

5 Cardiovascular Applications of the Finite Element Method

Mathematical modeling of the cardiovascular system using the finite element (FE) method has become both more powerful and easier to use. As a consequence, we believe that the FE method will play an increasing role in the understanding of cardiovascular pathology and in the design of therapies for HF.

5.1 A Brief History

As early as 1906, researchers first began suggesting the solution of continuum mechanics problems by modeling the body with a lattice of elastic bars and employing frame analysis methods (see Cook, [30]). In 1941, Courant recognized piecewise

polynomial interpolation over triangular subregions as a Rayleigh–Ritz solution of a variational problem. Since there were no computers at the time, neither approach was practical and Courant's work was largely forgotten until engineers had independently developed it. By 1953, structural engineers were solving matrix stiffness equations with digital computers. The widespread use of FE methods in engineering began with the classic papers by Turner and colleagues [31] Argyris and Kelsey [32]. The name "finite element" was coined in 1960, and the method began to be recognized as mathematically rigorous by 1963.

Solid models of the heart. Many FE models of the LV have been proposed, although most did not include the nonlinear kinematic terms associated with large deformations because iterative solution of the nonlinear governing equations at each load step is required. The importance of adopting nonlinear finite deformation theory for the analysis was demonstrated by Janz and colleagues [33].

The work of Bogen and colleagues deserves mention [34]. Although the FE model used by Bogen was a sphere composed of membrane elements, to our knowledge, Bogen was the first to simulate cardiac contraction and the first to simulate the effect of myocardial infarction [34].

CMISS/Continuity. The FE method that was developed by Drs. Hunter, McCulloch, Guccione, and colleagues specifically for continuum analysis of the heart (CMISS/Continuity) includes several features that are uncommon to conventional FE methods. We and others using Continuity have been exclusively modeling the ventricles as non-homogeneous and anisotropic for nearly 20 years [35–37]. Moreover, these models have been based directly on measured 3D fiber angle and sheet angle distributions (using a variety of measurement techniques). Furthermore, these models have been validated experimentally under a wide range of conditions. More recent models (see, for example, Saucerman et al. 38) now also include the transmural heterogeneity of cellular excitation–contraction coupling mechanisms.

A few FE modeling studies of the LV have validated stress calculations by showing good agreement with myocardial strain measured with implanted markers [39–42]. However, this is invasive and is limited to few simultaneous LV locations. With advancements in MRI, myocardial strain can be quantified noninvasively throughout the LV with tagged MRI [43, 44]. In a pioneering study, Moulton et al. [45] used tagged MRI to determine isotropic, diastolic material properties in a 2D FE analysis of beating canine hearts. Using a more realistic material law, Okamoto et al. [46] determined anisotropic myocardial material properties in a 3D FE model using tagged MRI. The experimental preparation and loading conditions were not physiological, however, to create significant transverse shear strain. Since then, Guccione et al. [47] have successfully modeled end-isovolumic systole in an ovine model of myocardial infarction and determined material parameters that reproduced circumferential stretching (as measured with 2D tagged MRI) in the infarcted border zone. This FE study successfully revealed that the mechanism of circumferential stretching in the infarct border zone during isovolumic systole related to impaired contractile function in that region.

Inverse calculation of myocardial material properties. As an alternative or complementary approach to biaxial mechanical testing, Moulton and colleagues [48]

have suggested the nonlinear material properties of passive, diastolic myocardium could be determined using MRI tissue-tagging, FE analysis, and nonlinear optimization. Material parameters for a proposed exponential strain energy function were determined by minimizing the least squares difference between FE model-predicted and MRI-measured diastolic strain. Six mongrel dogs underwent MRI imaging with radiofrequency (RF) tissue-tagging. Two-dimensional diastolic strains were measured from the deformations of the MRI tag lines. FE models were constructed from early diastolic images and were loaded with the mean early-to-late LV and right ventricular diastolic change in pressure measured at the time of imaging. A nonlinear optimization algorithm was employed to solve the least squares objective function for the material parameters. Although they modeled the myocardium inappropriately as an isotropic material, they suggested that their parameter estimation algorithm provides the necessary framework for estimating the nonlinear, anisotropic, and non-homogeneous material properties of passive myocardium in health and disease in the in vivo beating heart.

6 Computational Fluid Dynamics

Computational fluid dynamics (CFD) is a branch of fluid mechanics that uses numerical methods to solve problems that involve fluid flows in complex geometries. The CFD method is used in conjunction with inlet waveforms (as boundary conditions) to predict the flow field (velocity, streamlines, shear stress, vorticity, etc.) in the region of interest. The CFD method is a numerical model to treat a continuous fluid in a discretized fashion. The fundamental basis of the model in a single-phase blood flow is the partial differential equations or integro-differential equations of continuity and Navier–Stokes. These equations can be simplified by ignoring the viscosity term to yield the Euler equations. Additional simplification, by removing terms describing vorticity, yields the full potential equations. Finally, these equations can be linearized to yield the linearized potential equations.

The Navier–Stokes equations can be discretized at specific locations in space and time, approximated by a system of algebraic equations, and then solved on a computer. Computers are used to perform the millions of calculations required to simulate the interaction of fluids in complex geometries. In many cases, only approximate solutions can be achieved even with high-speed supercomputers. Ongoing research, however, may produce software that improves the accuracy and speed of complex simulation such as in turbulent flows.

6.1 A Brief History

Methods were first developed to solve the linearized potential equations. Two-dimensional methods, using conformal transformations of flow around a cylinder

to the flow around an airfoil were developed in the 1930s. The increase in computational power enabled development of 3D CFD methods. The first solution of a 3D linearized potential equation appeared in the 1960s. Much of the early developments in CFD were made in conjunction with aeronautical applications. A number of commercial and free packages (Commercial Software: ANASYS, FLUENT, ADINA, NASA COSMIC, etc. and Free Codes: FEAT, Free CFD, OpenFlower, OpenFOAM, etc.) for the solution of full 3D Navier–Stokes equations are now available, with NASA being a major early contributor. A brief history on the developments of blood flow solutions has been beautifully articulated in Fung's books (e.g., 49).

6.2 Applications to Cardiovascular System

The CFD method has become a popular approach to understand blood flows in the cardiovascular system. A PubMed Search under "Computational fluid dynamics" found 1,256 reports. For "Computational fluid dynamics andcardiovascular", PubMed lists 441 entries. The earliest study on Pubmed lists Peskin and colleague's paper on CFD of mitral valve [50]. A number of CFD applications are subsequently listed focusing on issues ranging from hemolytic and thromboembolic analysis of Starr–Edwards valve prostheses [51] to analysis of blood flow in arterial bifurcations [52], to analysis of LV ejection [53], to wall shear stress distribution on the endothelium [54], and others.

7 Our Method of Approach

In the introductory chapter of Y.C. Fung's classic monograph *Biomechanics: Mechanical Properties of Living Tissues*, the "Father of Biomechanics" [55] explains how biomechanics is mechanics applied to biology [49]. Here, we consider cardiovascular mechanics as mechanics applied to the diagnosis and treatment of cardiovascular disease. Mechanics is the study of the motion or deformation of particles or solid bodies (kinematics) and the forces or moments responsible for their motion or deformation (kinetics). When we teach undergraduate and graduate courses in cardiovascular mechanics, we point out Y.C. Fung's method of approach in our first lecture. When applied to the cardiovascular system, it consists of the following steps:

(1) Study the anatomy of the heart and vessels, histology of the cardiovascular tissue (blood, ventricular walls, valves, and coronary blood vessels), and the structure and ultrastructure of tissue constituents (blood cells, endothelial cells, myocytes, collagen fibers) in order to know the *geometric configurations* of the heart (end of filling phase or the cardiac cycle or end-diastole, end of ejection phase or end-systole). The unloaded configuration, which probably is not stress-free, is the most difficult configuration of all to determine clinically.

(2) Determine the *mechanical properties* of the cardiovascular tissue. As Y.C. Fung warns, this step is often very difficult because (1) we cannot isolate the tissue for testing, (2) the size of available tissue specimens is too small, or (3) it is difficult to keep the tissue in the normal living condition. Furthermore, cardiovascular tissues are subjected to large deformations, and the stress–strain relationships are anisotropic and nonlinear. The nonlinearity of the constitutive equation makes its determination a challenging task. Despite these challenges, however, one can estimate the mathematical form of the constitutive equation of the cardiovascular tissue and determine (or even optimize) numerical values for the material parameters using physiological experimental data.
(3) Based on the conservation laws of physics and continuum mechanics (conservation of mass, momentum, energy) and the constitutive equations of the cardiovascular tissue, derive the *governing* (partial differential or integral) *equations*.
(4) Understand the heart's *boundary conditions*. These include the pressures on the surfaces of the endocardium, epicardium, valves, and endothelial and adventitial surfaces of coronary blood vessels. These pressures can be measured quite readily in animal models of cardiovascular disease using micromanometer-tipped catheters, but they need to be estimated in human volunteers and patients using noninvasive measurements. The LV heart chamber, for example, can be modeled in isolation using a free body diagram, but then displacement boundary conditions just below the valves must be specified.

This approach produces well-posed boundary value problems which can be solved using various mathematical and typically computational algorithms. The models must then be validated using various experimental approaches which are largely imaging-based for patients. When there is agreement between the computational models and experimental results, one gains confidence in the theory. The model can then be used to predict the behavior of the physiological/pathophysiological system under different conditions. If there is disagreement between the models and experiments, then it is necessary to examine the cause of the discrepancy (i.e., determine whether any of the hypotheses made in the four-step approach need to be re-examined). In the process, one may wish to improve the experiment, or the theory, or both. With the improved theory and experiment, the process is repeated. The iterative process ensues until there is acceptable agreement between theory and experiment. This second alternative is typically what happens and provides real opportunity for discovering new hypotheses.

8 Introduction to Book Chapters

The philosophy of the Fung four-step approach is the theme of the present book and is weaved throughout the various chapters. The chapters are organized into two major sections. The first is focused on modeling of cardiovascular mechanics both

the solid as well as the fluid mechanics. The solid mechanics is focused largely on the heart. For example, the LV mechanics, Chapter 1, is primarily concerned with the unloaded LV geometric configuration. Quantifying this configuration in vivo is quite challenging yet necessary for clinical applications. Chapter 3 is primarily concerned with the mechanical properties of LV myocardium. Because mechanical testing and our computational models in conjunction with experimental strain measurements have shown that even passive myocardium is anisotropic with respect to the local muscle fiber direction, Chapter 3 is preceded by a chapter (Chapter 2) concerned with myofiber architecture. The solid mechanics chapters do not go into details about governing equations because UCSF's Cardiac Biomechanics Laboratory is developing and validating easy-to-use software tools that can be downloaded and used by cardiovascular disease researchers. This user-friendly approach to dealing with governing equations and LV boundary conditions are discussed briefly at the end of Chapter 1. Since models have to be validated using physiological data, Chapter 3 provides a number of examples of model validation. Finally, Chapter 4 is primarily concerned with the optimization of material parameters in constitutive equations for passive and active myocardium using measurements of myocardial strain and LV pressure. The objective of Chapter 5 is to provide an overview of the history, theory, and clinical use of electrical heart models with applications to heart failure.

The next group of chapters in the first section is focused on computational fluid dynamics. The anatomy/geometry of the vascular system is fundamental to the formulation of any boundary value problem. Hence, Chapter 6 introduces the general geometrical features of the vascular system and their geometric scaling while Chapter 7 introduces tools for quantitative reconstruction of the vascular anatomy from medical images (segmentation algorithms) and mesh generation for creation of geometric computational models. The field equations (conservation laws) are then outlined in Chapter 8 along with a number of numerical approaches. Some example applications in the coronary arteries are provided. Since the motion of the fluid is coupled with the motion of the vessel wall, the fluid–structure interaction is considered in Chapter 9 with some illustrative examples. Finally, an overview of the general topic of turbulence in the cardiovascular system is presented in Chapter 10 along with the example of turbulent flows in large aneurysms. In all these chapters, an attempt is made to link the biofluid mechanics of blood with the biology of the vessel wall.

The second major section provides applications of the theory to heart failure from solid and fluid mechanics points of views. For the former, both diagnostics (i.e., local and global indices of contractility, Chapter 11) as well as therapeutic approaches (surgical ventricular restoration, restrain devices, biomaterial implants, and cardiac resynchronization therapy in Chapters 12, 13, 14, and 15, respectively) are discussed. For the latter, the fluid mechanics of heart valves is simulated in Chapter 16 along with simulations of surgical procedures and HF-related devices in the form of CABG (Chapter 17) and VADs (Chapter 18). These chapters provide examples of the utility of the physics-based computational approach in understanding devices and surgical procedures. They highlight the major theme that the

principles of simulation-driven optimization that have revolutionized engineering can be successfully applied to biomedical diagnosis and therapy.

9 Future Directions

It is our hope that the FE methods described in this book will transition from the development phase into research and clinical tools that can be used not only by expert investigators but also by non-experts. To make the software user friendly, this will require the addition of a spontaneous graphic user interface that can guide the user through all phases of the process from image segmentation to mesh generation and then to the FE solution.

Another issue is the hardware required to run the simulations. If a small Linux cluster is necessary to solve problems in a reasonable period of time, it is unlikely that these methods will achieve widespread use. However, the computational horse power of stand-alone computers is constantly increasing and the use of graphics processors for matrix algebra will make stand-alone machines faster still.

During the inaugural BISTIC (Biomedical Information Science and Technology Consortium) Symposium in November 2003, one of the concurrent sessions was dedicated to IMAG's (Interagency Modeling and Analysis Group) interests in multiscale modeling. Subsequently, IMAG focused on the development of the Interagency Opportunities in Multi-Scale Modeling in Biomedical, Biological, and Behavioral Systems Solicitation. IMAG recognized that the modeling community is on the forefront of thinking across the biological continuum, rather than single scale or one level of resolution. In addition, IMAG identified a strong desire among modelers to form multi-disciplinary partnerships across varied research communities.

Finally, computer graphics based animation is becoming increasingly powerful and teaching animations have been developed. Physics-based libraries such as PhysBam [56] have been added although the rationale seems largely to make animations more visually realistic rather than mechanically correct. It is necessary to couple teaching simulators to the FE solvers in which material properties and constitutive relationships are accurate.

Acknowledgments This work was supported by National Institutes of Health grants HL077921 (Dr. Guccione), HL086400, (Dr. Guccione), HL084529 (Dr. Kassab), HL087235 (Dr. Kassab), HL063348 (Dr. Ratcliffe), and HL084431 (Dr. Ratcliffe). This support is gratefully acknowledged.

References

1. Zile MR, Baicu CF, Gaasch WH. Diastolic heart failure–abnormalities in active relaxation and passive stiffness of the left ventricle. *N Engl J Med*. 2004;350:1953–9.
2. Pfeffer MA, Braunwald E, Moye LA, Basta L, Brown EJ Jr, Cuddy TE, Davis BR, Geltman EM, Goldman S, Flaker GC et al. Effect of captopril on mortality and morbidity in patients with left ventricular dysfunction after myocardial infarction. Results of the survival and

ventricular enlargement trial. The SAVE Investigators [see comments]. *N Engl J Med*. 1992;327:669–77.
3. Hammermeister KE, DeRouen TA, Dodge HT. Variables predictive of survival in patients with coronary disease. Selection by univariate and multivariate analyses from the clinical, electrocardiographic, exercise, arteriographic, and quantitative angiographic evaluations. *Circulation*. 1979;59:421–30.
4. Kostuk WJ, Kazamias TM, Gander MP, Simon AL, Ross J Jr. Left ventricular size after acute myocardial infarction. Serial changes and their prognostic significance. *Circulation*. 1973;47:1174–9.
5. Shanoff HM, Little JA, Csima A, Yano R. Heart size and ten-year survival after uncomplicated myocardial infarction. *Am Heart J*. 1969;78:608–14.
6. White HD, Norris RM, Brown MA, Brandt PW, Whitlock RM, and Wild CJ. Left ventricular end-systolic volume as the major determinant of survival after recovery from myocardial infarction. *Circulation*. 1987;76:44–51.
7. Visser CA, Kan G, Meltzer RS, Koolen JJ, Dunning AJ. Incidence, timing and prognostic value of left ventricular aneurysm formation after myocardial infarction: a prospective, serial echocardiographic study of 158 patients. *Am J Cardiol*. 1986;57:729–32.
8. Benediktsson R, Eyjolfsson O, Thorgeirsson G. Natural history of chronic left ventricular aneurysm; a population based cohort study. *J Clin Epidemiol*. 1991;44:1131–9.
9. Nicolosi AC, Spotnitz HM. Quantitative analysis of regional systolic function with left ventricular aneurysm. *Curr Surg*. 1988;45:387–9.
10. Stephenson L. History of cardiac surgery. In: Cohn L Ed. Cardiac surgery in the adult. New York: McGraw Hill, 2008, pp. 3–28.
11. Gibbon JJ. Application of a mechanical heart and lung apparatus to cardiac surgery. *Minn Med*. 1954;37:171.
12. Hunt SA. Taking heart–cardiac transplantation past, present, and future. *N Engl J Med*. 2006;355:231–5.
13. Cooley DA, Liotta D, HallmanGL, Bloodwell RD, Leachman RD, Milam JD. Orthotopic cardiac prosthesis for two-staged cardiac replacement. *Am J Cardiol*. 1969;24:723–30.
14. DeVries WC, Anderson JL, Joyce LD, Anderson FL, Hammond EH, Jarvik RK, Kolff WJ. Clinical use of the total artificial heart. *N Engl J Med*. 1984;310:273–8.
15. Rose EA, Gelijns AC, Moskowitz AJ, Heitjan DF, Stevenson LW, Dembitsky W, Long JW, Ascheim DD, Tierney AR, Levitan RG, Watson JT, Meier P, Ronan NS, Shapiro PA, Lazar RM, Miller LW, Gupta L, Frazier OH, Desvigne-Nickens P, Oz MC, Poirier VL. Long-term mechanical left ventricular assistance for end-stage heart failure. *N Engl J Med*. 2001;345:1435–43.
16. Cooley DA. Ventricular endoaneurysmorrhaphy: a simplified repair for extensive postinfarction aneurysm. *J Card Surg*. 1989;4:200–5.
17. Dor V, Saab M, Coste P, Kornaszewska M, Montiglio F. Left ventricular aneurysm: a new surgical approach. *Thorac Cardiovasc Surg*. 1989;37:11–9.
18. Jones RH, Velazquez EJ, Michler RE, Sopko G, Oh JK, O'Connor CM, Hill JA, Menicanti L, Sadowski Z, Desvigne-Nickens P, Rouleau J-L, Lee KL, the STICH Hypothesis 2 Investigators. Coronary bypass surgery with or without surgical ventricular reconstruction. *N Engl J Med*, 2009;360:1705–17, NEJMoa0900559.
19. Batista RJV, Santos JLV, Takeshita N, Bocchino L, Lima PN, Cunha MA. Partial left ventriculectomy to improve left ventricular function in end-stage heart disease. *J Cardiovasc Surg*. 1996;11:96–7.
20. Blom AS, Mukherjee R, Pilla JJ, Lowry AS, Yarbrough WM, Mingoia JT, Hendrick JW, Stroud RE, McLean JE, Affuso J, Gorman RC, Gorman JH 3rd, Acker MA, Spinale FG. Cardiac support device modifies left ventricular geometry and myocardial structure after myocardial infarction. *Circulation*. 2005;112:1274–83.
21. Pilla JJ, Blom AS, Brockman DJ, Bowen F, Yuan Q, Giammarco J, Ferrari VA, Gorman JH 3rd, Gorman RC, Acker MA. Ventricular constraint using the acorn cardiac support

device reduces myocardial akinetic area in an ovine model of acute infarction. *Circulation*. 2002;106:I207–11.
22. Magovern JA. Experimental and clinical studies with the paracor cardiac restraint device. *Semin Thorac Cardiovasc Surg*. 2005;17:364–8.
23. Lund O, Nielsen SL, Arildsen H, Ilkjaer LB, Pilegaard HK. Standard aortic St. Jude valve at 18 years: performance profile and determinants of outcome. *Ann Thorac Surg*. 2000;69:1459–65.
24. Lazar RM, Shapiro PA, Jaski BE, Parides MK, Bourge RC, Watson JT, Damme L, Dembitsky W, Hosenpud JD, Gupta L, Tierney A, Kraus T, Naka Y. Neurological events during long-term mechanical circulatory support for heart failure: the Randomized Evaluation of Mechanical Assistance for the Treatment of Congestive Heart Failure (REMATCH) experience. *Circulation*. 2004;109:2423–7.
25. Jan KM. Distribution of myocardial stress and its influence on coronary blood flow. *J Biomech*. 1985;18:815–20.
26. Grossman W. Cardiac hypertrophy: useful adaptation or pathologic process? *Am J Med*. 1980;69:576–84.
27. Huisman RM, Elzinga G, Westerhof N, SipkemaP. Measurement of left ventricular wall stress. *Cardiovasc Res*. 1980;14:142–53.
28. Yin FCP. Ventricular wall stress. *Circ Res*. 1986;49:829–842.
29. Ratcliffe MB, Guy TS. The effect of preoperative diastolic dysfunction on outcome after surgical ventricular remodeling. *J Thorac Cardiovasc Surg*. 2007;134:280–3.
30. Cook RD. Concepts and applications of finite elements analysis. New York: John Wiley & Sons, 1981.
31. Turner MJ, Clough RW, Matin HC, Topp LJ. Stiffness and deflection analysis of complex structures. *J Aero Sci*. 1956;9:805–823.
32. Argyris JH, Kelsey S. Energy theorems and structural analysis. London: Butterworths, 1960.
33. Janz RF, Kubert BR, Moriarty TF, Grimm AF. Deformation of the diastolic left ventricle–II. Nonlinear geometric effects. *J Biomech*. 1974;7:509–16.
34. Bogen DK, Rabinowitz SA, Needleman A, McMahon TA Abelmann WH. An analysis of the mechanical disadvantage of myocardial infarction in the canine left ventricle. *Circ Res*. 1980;47:728–41.
35. Guccione JM, McCulloch AD. Mechanics of active contraction in cardiac muscle: Part I–Constitutive relations for fiber stress that describe deactivation. *J Biomech Eng*. 1993;115: 72–81.
36. Guccione JM, McCulloch AD, Waldman LK. Passive material properties of intact ventricular myocardium determined from a cylindrical model [see comments]. *J Biomech Eng*. 1991;113:42–55.
37. McCulloch A, Waldman L, Rogers J, Guccione J. Large-scale finite element analysis of the beating heart. *Crit Rev Biomed Eng*. 1992;20:427–49.
38. Saucerman JJ, Brunton LL, Michailova AP, McCulloch AD. Modeling beta-adrenergic control of cardiac myocyte contractility in silico. *J Biol Chem*. 2003;278:47997–8003.
39. Bovendeerd PH, Arts T, Delhaas T, Huyghe JM, van Campen DH, Reneman RS. Regional wall mechanics in the ischemic left ventricle: numerical modeling and dog experiments. *Am J Physiol*. 1996;270:H398–410.
40. Omens JH, MacKenna DA, McCulloch AD. Measurement of strain and analysis of stress in resting rat left ventricular myocardium. *J Biomech*. 1993;26:665–76.
41. Usyk TP, Mazhari R, McCulloch AD. Effect of laminar orthotopic myofiber architecture on regional stress and strain in the canine left ventricle. *J Elasticity*. 2000;61:143–164.
42. Vetter FJ, McCulloch AD. Three-dimensional stress and strain in passive rabbit left ventricle: a model study. *Ann Biomed Eng*. 2000;28:781–92.
43. Denney TS Jr, Gerber BL, Yan L. Unsupervised reconstruction of a three-dimensional left ventricular strain from parallel tagged cardiac images. *Magn Reson Med*. 2003;49:743–54.
44. Ozturk C, McVeigh ER. Four-dimensional B-spline based motion analysis of tagged MR images: introduction and in vivo validation. *Phys Med Biol*. 2000;45:1683–702.

45. Moulton MJ, Creswell LL, Downing SW, Actis RL, Szabo BA, Pasque MK. Myocardial material property determination in the in vivo heart using magnetic resonance imaging. *Int J Card Imaging*. 1996;12:153–67.
46. Okamoto RJ, Moulton MJ, Peterson SJ, Li D, Pasque MK, Guccione JM. Epicardial suction: a new approach to mechanical testing of the passive ventricular wall. *J Biomech Eng*. 2000;122:479–87.
47. Guccione JM, Moonly SM, Moustakidis P, Costa KD, Moulton MJRatcliffe MB, Pasque MK. Mechanism underlying mechanical dysfunction in the border zone of left ventricular aneurysm: a finite element model study. *Ann Thorac Surg*. 2001;71:654–62.
48. Moulton MJ, Creswell LL, Actis RL, Myers KW, Vannier MW, SzabóBA, Pasque MK. An inverse approach to determining myocardial material properties. *JBiomech*. 1995;28:935–48.
49. Fung YC. Biomechanics: mechanical properties of living tissues. New York: Springer-Verlag, 1981.
50. McQueen DM, Peskin CS, Yellin EL. Fluid dynamics of the mitral valve: physiological aspects of a mathematical model. *Am J Physiol*. 1982;242:H1095–110.
51. Tansley GD, Mazumdar J, Noye BJ, Craig IH, Thalassoudis K. Assessment of haemolytic and thromboembolic potentials–from CFD studies of Starr–Edwards cardiac valve prostheses. *Australas Phys Eng Sci Med*. 1989;12:121–7.
52. Xu XY, Collins MW. A review of the numerical analysis of blood flow in arterial bifurcations. *Proc Inst Mech Eng [H]*. 1990;204:205–16.
53. Georgiadis JG, Wang M, Pasipoularides A. Computational fluid dynamics of left ventricular ejection. *Ann Biomed Eng*. 1992;20:81–97.
54. Satcher RL Jr, Bussolari SR, Gimbrone MA Jr, Dewey CF Jr. The distribution of fluid forces on model arterial endothelium using computational fluid dynamics. *J Biomech Eng*. 1992;114:309–16.
55. Kassab GS. Y.C. "Bert" fung: the father of modern biomechanics. *Mech Chem Biosyst*. 2004;1:5–22.
56. Fedkiw R. PhysBam: physics based modeling. 2009.
57. UNOS. 2002 Annual Report of the U.S. Organ Procurement and Transplantation Network and the Scientific Registry of Transplant Recipients: Transplant Data 1992–2001, United Network for Organ Sharing. 2002.
58. American Heart Association. Heart disease and stroke statistics: 2008 update, American Heart Association, 2008.

Part I
Computational Modeling of Cardiovascular Mechanics

Chapter 1
In Vivo Left Ventricular Geometry and Boundary Conditions

Jonathan F. Wenk, Choon-Sik Jhun, Zhihong Zhang, Kay Sun, Mike Burger, Dan Einstein, Mark Ratcliffe, and Julius M. Guccione

Abstract The first basic biomechanics modeling step outlined in the introductory chapter is to define the geometric configuration. In Chapters 12 and 14 we demonstrate the application of either simple (i.e., axisymmetric truncated ellipsoid) or complex (i.e., fully 3-D) left ventricular (LV) geometric models or finite element (FE) meshes. This chapter is primarily concerned with an instructive review of the methodology we have used to create both types of FE meshes, which relies on the "parametric" meshing software TrueGrid®. Since TrueGrid is rather expensive, Section 1.6 describes the use of free software executables available from the Pacific Northwest National Laboratory. The second basic biomechanics modeling step (determine mechanical properties) is addressed in the next three chapters. The third and fourth basic biomechanics modeling steps (governing equations and boundary conditions) are discussed briefly at the end of this chapter.

1.1 Introduction

The least complex realistic geometric model for regional left ventricular (LV) mechanics is a truncated ellipsoid or prolate spheroid. When stress and strain in a thick-walled pressure vessel vary in more than one direction (e.g., longitudinally and transmurally), the solution of partial differential equations of equilibrium or motion is required. The finite element (FE) method is the most versatile mathematical technique for solving partial differential equations. There are several FE mesh generation programs available. TrueGrid® (XYZ Scientific Applications, Inc., Livermore, CA) is a general-purpose mesh generation program with sophisticated relaxation and parameterization capabilities. In other words, it is possible to use TrueGrid® to generate an FE mesh, the characteristics of which can then

J.M. Guccione (✉)
Department of Surgery, University of California at San Francisco and San Francisco VA Medical Center, San Francisco, CA, USA
e-mail: guccionej@surgery.ucsf.edu

J.M. Guccione, et al. (eds.), *Computational Cardiovascular Mechanics*,
DOI 10.1007/978-1-4419-0730-1_1,

be controlled by a few key parameters. TrueGrid® has been optimized to produce high quality, structured, multi-block hexahedral meshes or grids, and serves as a preprocessor to over 30 of today's most popular analysis codes.

1.2 Anatomy of a Good Grid

Efficiently generating semi-structured meshes, from imaging derived geometries, in a way that is tuned to the physics of the problem remains challenging. Selection of the geometry to be discretized and the approach for grid generation is application dependent. However, for computational cardiac analysis there are some common criteria. Finite computational resources dictate that the grid must be optimally adapted to the geometry in order to minimize both computational cost and discretization error. At the same time, the grid should be organized both by scale and by intrinsic properties. The wall of the heart, for example, is a laminated muscle consisting of three separate layers, each with a separate family of fiber and myocyte orientations. Thus, a grid of the heart muscle must be similarly layered.

In addition, elements must be of high quality. Different quality metrics exist for different elements. For hexahedra, the *scaled-Jacobian* is the most common measure of quality, and measures the degree to which the three edges depart from being mutually orthogonal [1]. For prisms – midway in desirability between hexahedra and tetrahedra – the *scaled aspect ratio* [2], which combines the measures of triangle shapes and edge orthogonality, is an appropriate measure. For tetrahedra, the *aspect ratio*, which is proportional to the ratio of the inscribed radius to the length of the longest edge, is typically reported.

Whether to adopt hexahedra, prisms, tetrahedra, or a hybrid of these elements also depends strongly on application. Automatic, unstructured grid generation with hexahedra remains an active research area in computational geometry for all but the simplest geometries. As geometries become more complex and more detailed, grid generation with layered tetrahedra or a hybrid of layered tetrahedra and prisms becomes the only viable option. Consider, for example, that the layering of the myocardium persists at the smaller scale of the heart geometry, where, for example, the musculature transitions into the connective tissue of the cardiac valves, or at an even smaller scale where the heart muscle involutes to become a network of coronary arteries. These geometries can only be approached with tetrahedra. In the case of fluid–structure interaction problems, different needs arise, since fluids are not generally layered but they do experience large gradients at the wall.

At a minimum, a computational grid of the myocardial wall should be layered in order to account for the layered orientation of myofibers. The approaches to grid generation that are presented in this chapter all meet this criterion. In addition, the elements should be mostly orthogonal to the epicardial and endocardial surfaces. The degrees to which these criteria are met vary according to the approach. Deliberate structured paving of the myocardium with hexahedra is perhaps the most computationally efficient, but is only possible with the simplest geometries. Topological projection of hexahedra, which is the method used in TrueGrid, is

capable of handling more complex geometries than purely structured paving, but the organization of the hexahedra at the intersection of the "butterfly" does not correspond to any physical feature of the geometry, and can result in highly skewed hexahedra, unless handled carefully. Layered tetrahedra meet this later criterion fully, but in general tetrahedra – linear or otherwise – are less desirable than hexahedra or prisms, even though historic problems of volumetric and shear locking long associated with tetrahedra have since been overcome [3, 4]. All else being equal a good tetrahedra is better than a bad brick, though a good brick is almost certainly best.

1.3 Mesh Generation of an Axisymmetric Truncated Ellipsoid Using TrueGrid®

The FE mesh of a globally dilated canine LV was created by TrueGrid® using solid 3-D elements. Figure 1.1 shows an unloaded dilated canine LV modeled as a thick-walled, axisymmetric, truncated, prolate spheroid [5]. Streeter and Hanna [5] suggested the following empirical equation to acquire dimensions on semi-major (a_{endo}, a_{epi}) and semi-minor (b_{endo}, b_{epi}) axes:

$$v = \frac{\pi(2 + 3f_b - f_b^3)}{3} ab^2, \tag{1.1}$$

where V, f_b, a, and b are volume, truncation factor (i.e., $p/a_{\text{epi}} = 0.5$), major radius, and minor radius, respectively. We used a confocal nest of ellipses, i.e., the focal length is given by $d = (a_{\text{endo}}^2 - b_{\text{endo}}^2)^{1/2} = (a_{\text{epi}}^2 - b_{\text{epi}}^2)^{1/2}$. For a canine LV geometry, we used $d = 3.75$ cm, suggested by Streeter and Hanna [5]. However,

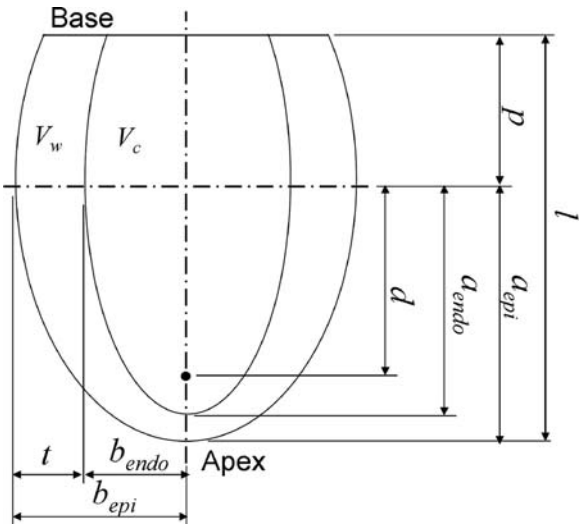

Fig. 1.1 A confocal mathematical geometry of the LV modeled as a thick-walled, axisymmetric, truncated, prolate spheroid. V_{w} = ventricular wall volume, V_{c} = ventricular cavity volume, l = LV length, a_{epi} = major radius of epicardial ellipsoid, a_{endo} = major radius of endocardial ellipsoid, b_{epi} = minor radius of epicardial ellipsoid, b_{endo} = minor radius of endocardial ellipsoid, and t = equatorial wall thickness

one can also use a LV (end-diastolic or end-systolic) cavity long-axis to short-axis ratio (i.e., $3a_{endo}/4b_{endo}$).

Upon acquiring the dimensions (i.e., a_{endo}, b_{endo}, a_{epi}, and b_{epi}) for a mathematical LV geometry, those values are fed into TrueGrid® to generate a solid 3-D FE mesh. The procedure for generating a mathematical LV mesh is given below:

(i) A single block part is created (command: *BLOCK*) so that each of the six faces can be projected to a different surface to form the mathematical LV geometry (Fig. 1.2).
(ii) The four corners need to be deleted to form the butterfly topology (command: *DEI*) (Figs. 1.3 and 1.4).
(iii) Two ellipsoidal surfaces, which represent the endocardial and epicardial surfaces, and one plane surface, which is the basal plane, are defined as the projection surfaces for the block part (commands: *SD*, *SFI*) (Fig. 1.5).
(iv) Loading conditions and boundary conditions are also defined during the mesh generation (commands: *PR*, *NSETI*).
(v) Upon completing all projections, a coarse mathematical LV mesh is generated (command: *ENDPART*) (Fig. 1.6).

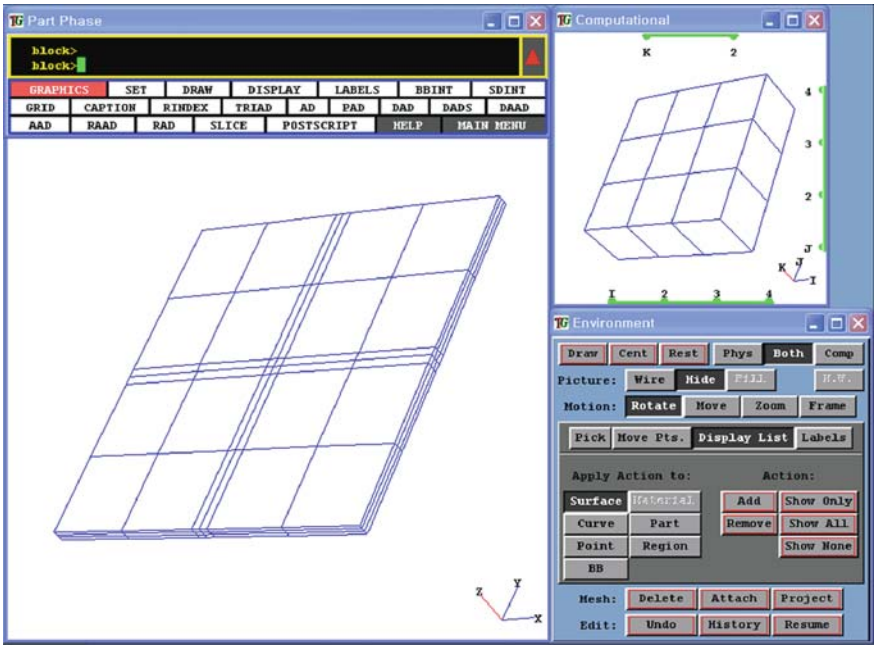

Fig. 1.2 A single block part is created. Each of the six faces will be projected to a different surface to form a mathematical LV geometry

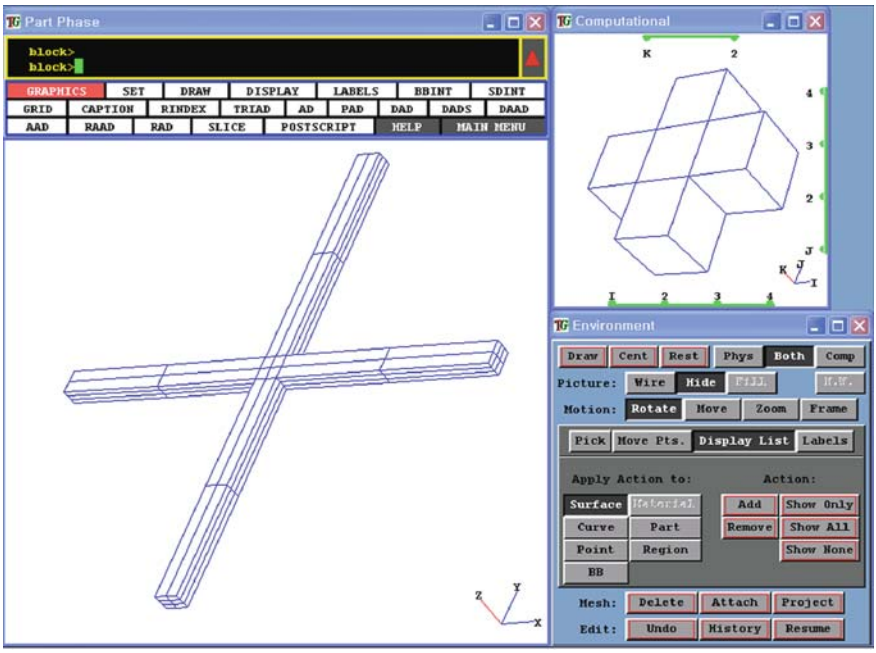

Fig. 1.3 Four corners need to be deleted to form the butterfly topology

(vi) Mesh refinement can be performed at any time after finishing the initial mesh generation (command: *MSEQ*) (Fig. 1.7).
(vii) Finally, the keyword file for a commercial implicit/explicit solver, LS-DYNA (LSTC, Inc., Livermore, CA), is generated (commands: *LSDYNA KEYWORD*, *WRITE*).

The user's manual for TrueGrid® can be found at (http://www.truegrid.com).

The muscle fiber direction throughout the LV is presumed to vary linearly in the transmural direction. In the case of a canine model, the fiber direction is 60° from the circumferential direction at the endocardium and –60° from the circumferential direction at the epicardium [6]. The myocardial wall was refined into three layers: inner wall, mid-wall, and outer wall. The muscle fiber directions are assigned to each layer by a custom Matlab code, referred to as Closer. The total number of elements in our mathematical LV mesh is 1539. One can increase the number of myocardial layers by refining the mesh in the transmural direction. For example, the Acorn CorCap™ Cardiac Support Device (CSD) (see Chapter 13), which is attached to the epicardium of the LV, can be modeled by refining the mesh transmurally and assigning the appropriate material properties to that layer of elements.

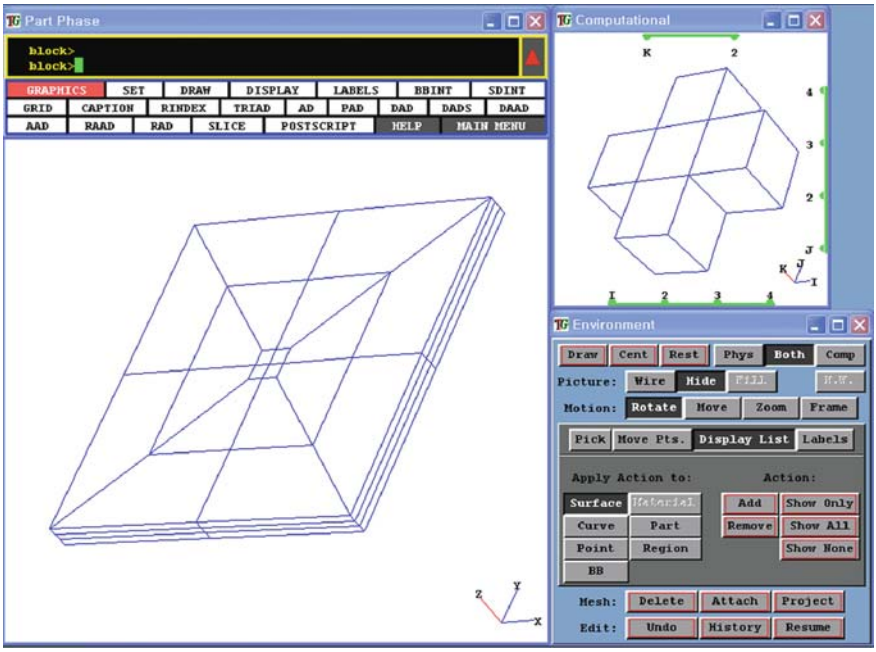

Fig. 1.4 Schema of a standard butterfly topology to wrap up (or project onto) the endocardial and epicardial ellipsoids

1.4 Mesh Generation of an Axisymmetric Truncated Ellipsoid with Polymeric Injections Using TrueGrid®

The FE model depicted in Fig. 1.8 shows a dilated LV with a specific pattern of polymeric injections. The myocardium is shown as a "wire" mesh, the polymeric inclusions are the spheres, and the "airbag" endocardium is shown as the inner shell surface. The airbag has no structural function, but allows the calculation of the volume in the ventricular cavity. The basic geometry of the LV is generated as an axisymmetric model, where the epicardium and endocardium are generated as ellipsoidal surfaces and the base is generated by the truncation of these surfaces, using the procedure described in the previous section. By adjusting the axes lengths of the ellipsoids, the wall thickness and volume of the LV can be adjusted.

The pattern of inclusions is added systematically using the following approach. The location of the first inclusion is typically placed near mid-ventricle, and at mid-wall. The local region around the inclusion, which is represented by a sector ($\sim$24°) of the LV wall, is thickened by perturbing the radius of the endocardium to compensate for the volume displaced by the inclusion, as shown in Fig. 1.9a. To simplify the modeling process, the inclusion and local region are replicated and translated/rotated to generate the desired injection pattern. The pattern is built up one circumferential row at a time, as shown in Fig. 1.9b, until the number of

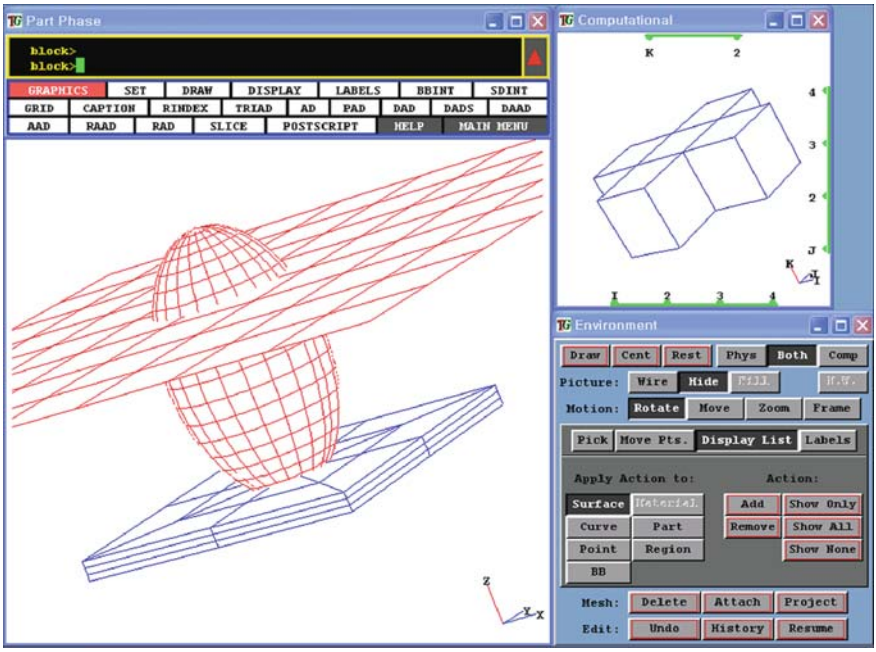

Fig. 1.5 Two ellipsoidal surfaces and one plane surface are needed for a mathematical LV geometry. Top face (to be an endocardial surface) and bottom face (to be an epicardial surface) of the block part are projected to the inner and outer ellipsoidal surfaces, respectively. Four sides of the block part are projected to the plane surface (to be a basal plane)

longitudinal injections is achieved. Once the pattern is generated, the remainder of each circumferential row is filled with sectors that do not contain inclusions.

One of the extremely useful features of TrueGrid® is the ability to parameterize the model. For example, the current model is parameterized such that the following can be modified during an optimization scheme: inclusion radius, dimensions of the local region around each inclusion, number of inclusions in the longitudinal direction, number of inclusions in the circumferential direction, and perturbed radius of the endocardial surface. Once the geometry has been specified, a regular hexahedral mesh is generated within all regions of the model, except for the endocardium, which is lined with quadrilateral shell elements. A smoothing operation is used to improve mesh quality and ensure maximum orthogonality between elements, which decreases the time to convergence during simulation.

The myofiber orientations, which are implemented by the custom Matlab program, Closer, can only be assigned to a model with a continuous set of transmural elements, such as that described in the previous section. Thus, the mapping of myofiber orientations to a model with inclusions needs to be done in two stages. In Stage 1, the orthotropic fiber directions for the myocardial material must be transferred from a reference model, Fig. 1.10a, to the model with small inclusions, Fig. 1.10b. This is done using a subroutine in the software (LS-OPT). Because these

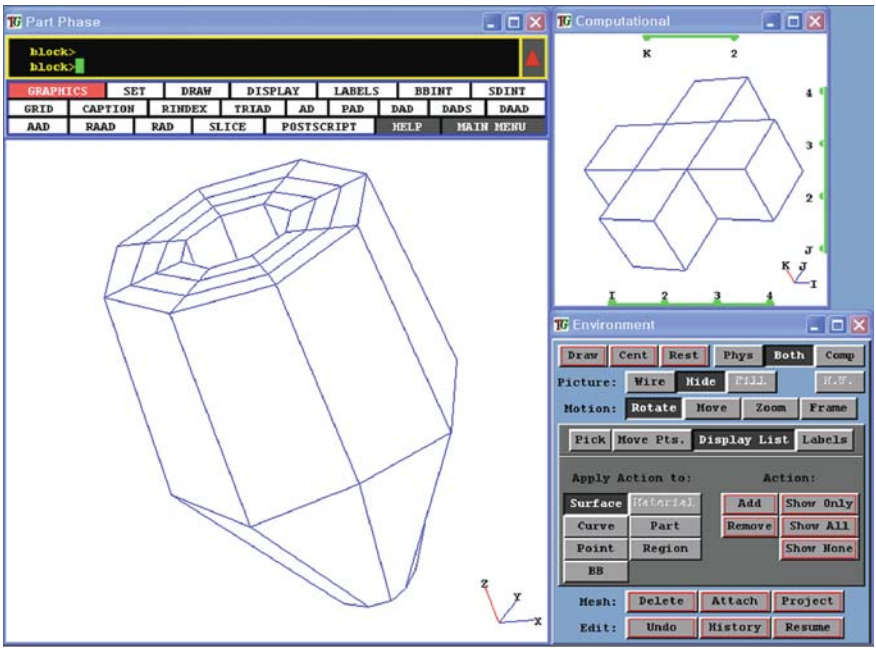

Fig. 1.6 Upon completing all projections, a coarse mathematical LV mesh is generated. Mesh refinement can be performed at any time after finishing the initial mesh generation

two models have different topologies, mapping must be done on a geometric basis, i.e., the fiber orientations associated with a particular coordinate must be transferred from the reference model to the closest coordinate in the new model. In Stage 2, the inclusions are enlarged, Fig. 1.10c, with compensation for volume preservation, while the elements keep the properties assigned in the first stage.

1.5 Mesh Generation of a Full 3-D Non-axisymmetric LV Using TrueGrid®

The following section outlines the steps necessary to create a full 3-D FE mesh that replicates in vivo geometry at end-isovolumic relaxation using both long- and short-axis slice magnetic resonance (MR) images.

1.5.1 Contouring the Epicardium and Endocardium of the Left Ventricle

Typically, 10–15 short-axis slice tagged MR images, taken from apex to base in 5-mm increments, and 6 long-axis slice MR images, taken in 30° increments, are

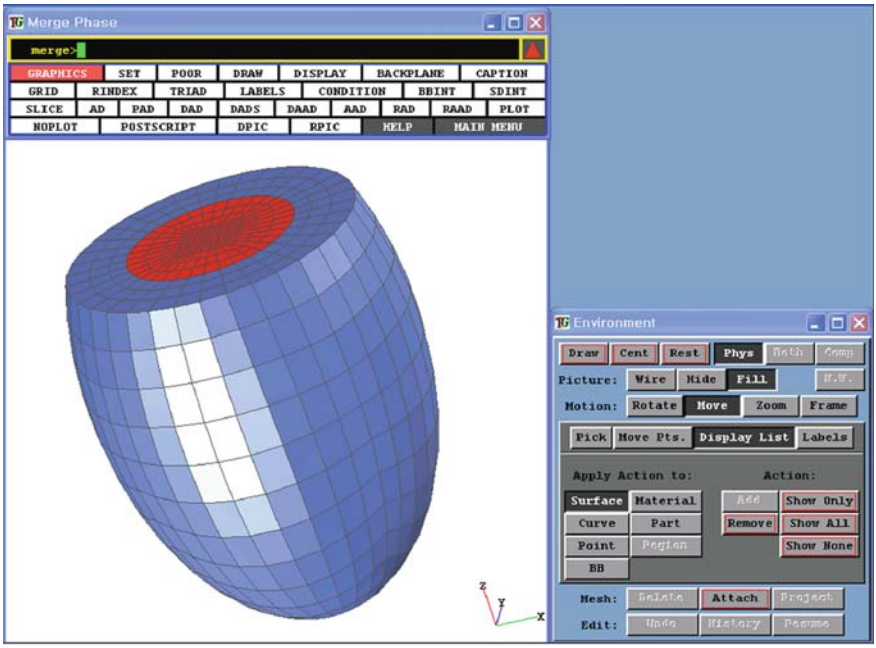

Fig. 1.7 A confocal mathematical LV mesh: a thick-walled, axisymmetric, truncated, prolate spheroid. LV cavity is covered by shell elements to generate an airbag and calculate a cavity volume

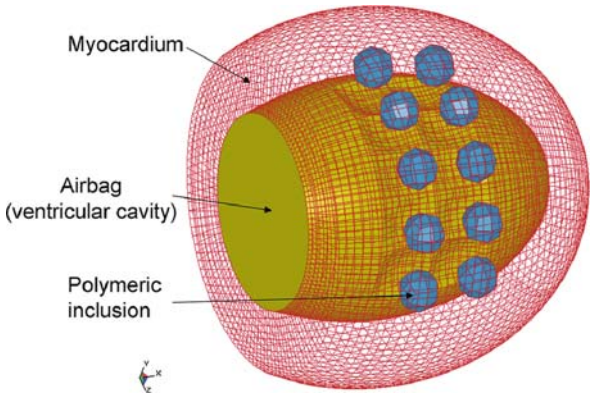

Fig. 1.8 FE model with an injection pattern of two longitudinal inclusions by five circumferential inclusions

obtained using a Symphony MRI scanner (Siemens Medical System). The image processing software Fintags (Laboratory of Cardiac Energetics, National Institutes of Health, Bethesda, MD) was written specifically for processing tagged MR images of the LV [7]. It involves two processes: (1) contouring the epicardium and endocardium, and (2) segmenting out the tags that are used for calculating the strain of the LV. An example of the short- and long-axis contours is shown in Fig. 1.11.

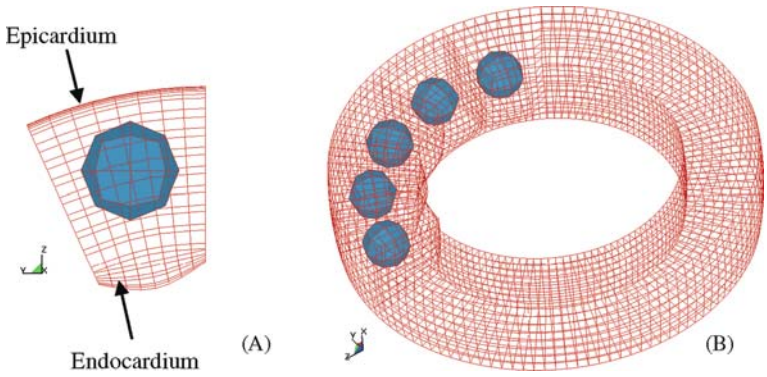

Fig. 1.9 (**a**) Single inclusion surrounded by local sector region, (**b**) single circumferential row of five inclusions

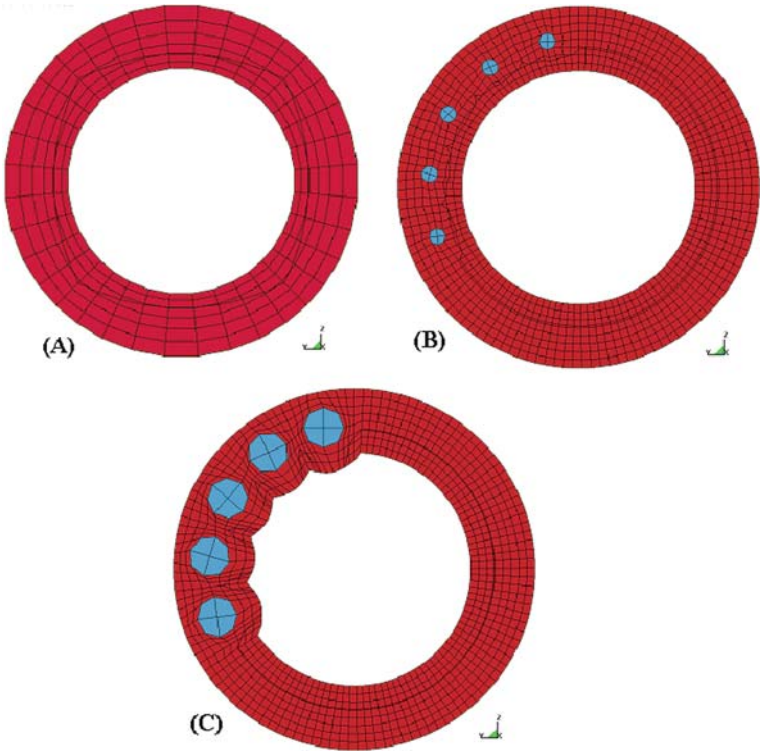

Fig. 1.10 Cross-sections through inclusions used to explain two-stage mapping. (**a**) Cross-section of reference model, (**b**) model produced with partially injected inclusions of radius = 0.1788 cm, $V = 0.02394$ cm^3, (**c**) model with enlarged inclusions produced with fully injected inclusions of radius = 0.35 cm, $V = 0.18$ cm^3

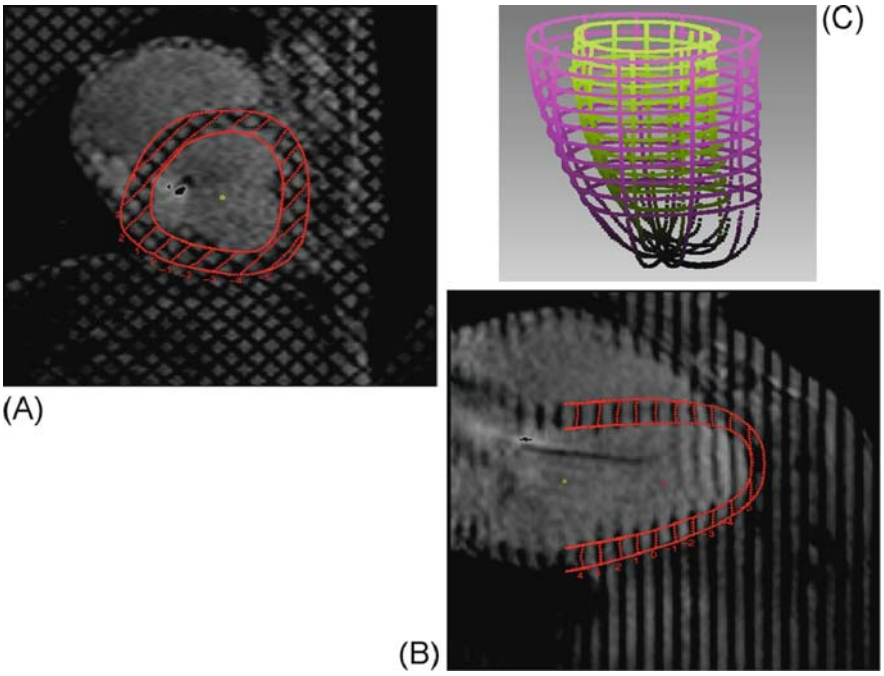

Fig. 1.11 Endocardial and epicardial contours as well as segmented tag-lines were traced from (**a**) short- and (**b**) long-axis MR images to create (**c**) a 3-D geometry. Contours in (**a**) and (**b**) are from Findtags software

The 2-D contours are generated at various times in the cardiac cycle to create the unloaded reference state, end-diastole, and end-systole. The FE model is created using early diastole as the initial unloaded reference state, since the LV pressure is lowest at this point and therefore stress is at a minimum. The end-diastolic and end-systolic data are used to calculate LV volume and compute strain.

1.5.2 Defining Aneurysm, Border Zone and Remote Regions, and Converting 2-D Contour Data to 3-D Data

Aneurysm, border zone, and remote regions are determined from the LV wall thickness. Specifically, the border zone region is defined as the steep transition in wall thickness between remote and aneurysm regions [8]. The software tool FindContours, which was developed by Cardiac Biomechanics lab director Mark Ratcliffe, MD, and lab member Zhihong Zhang, MS (SFVA San Francisco, CA; http://cbl.surgery.ucsf.edu/), is used to determine the aneurysm, border zone, and remote regions, and then to convert the 2-D contour data from Findtags (Fig. 1.11a and b) into 3-D data.

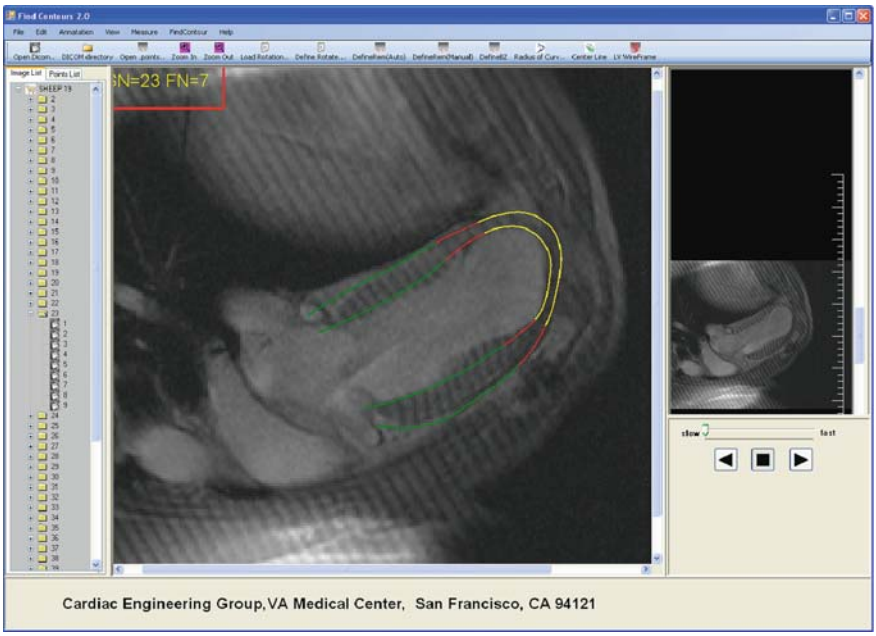

Fig. 1.12 Long-axis contours from Findtags are used to define aneurysm, border zone, and remote region. The remote region extends from the base to the border zone (dark lines), the border zone is seen at the transition in wall thickness, and the aneurysm is seen as the thin wall outlined in light lines.

FindContours requires input files that consist of the Dicom images from MRI scans and the 2-D contour point files from Findtags. The output files are 3-D contour point files for creating endocardial and epicardial IGES surfaces, and 3-D border zone point data for creating the IGES curves of the border zone boundaries.

Six long-axis contours are used to define the three different regions. The points where the border zone region and remote region meet are based on 70% of the thickness of the LV wall. An example of a long axis contour is shown in Fig. 1.12. FindContours calculates these points and then displays the remote region in green. The points where the border zone region and aneurysm region meet are selected manually. The border zone region is displayed in red and the aneurysm in yellow.

1.5.3 Generating IGES Curves for Different Material Areas and IGES Surface for Endocardium and Epicardium

Surface meshes are created from the LV 3-D contour points to replicate the in vivo geometry by using the program Rapidform (INUS Technology, Inc., Sunnyvale, CA). An example of a 3-D surface mesh, generated from Rapidform, is shown in Fig. 1.13. The required input files include the cloud of points that represent the 3-D

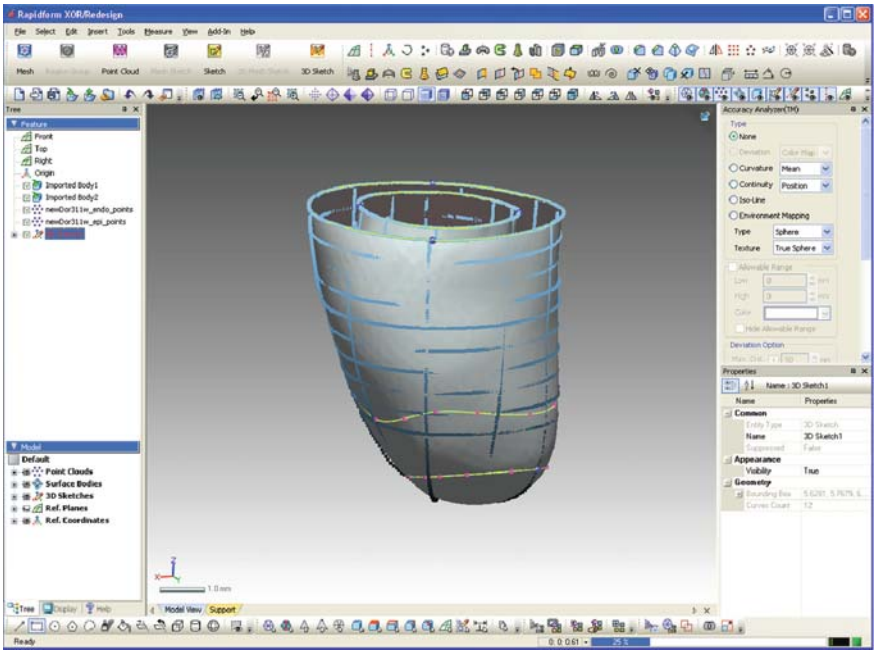

Fig. 1.13 Epicardium and endocardium IGES surfaces are displayed in Rapidform, INUS Technology Inc., Sunnyvale, CA. The *light colored* curve nearby the apex are border zone's boundaries. The *cloud points* are 3-D contours from images

contours of the epicardium and endocardium, and the points that represent the border zone. The output files are epicardium, endocardium, and base IGES surfaces, as well as border zone and remote boundary IGES curves. The steps for creating IGES surfaces are: (1) input cloud points, (2) create polygon mesh, and (3) output IGES surface. For creating border zone boundary IGES curves, the steps are: (1) input points of border zone boundary, (2) create 3D spline curves, (3) project the curves to the polygon mesh, and (4) output the IGES curves.

1.5.4 Creation of FE Mesh Using TrueGrid® and Closer

The epicardium, endocardium, and base IGES surfaces, as well as the border zone and remote boundary IGES curves, are imported into TrueGrid®. The space between the endocardial and epicardial surfaces are filled with eight-node trilinear brick elements (2496 elements total), which generate a volumetric mesh that is three elements thick in the transmural direction, as shown in Fig. 1.14. Upon completion of the mesh, TrueGrid writes an input deck for the FE solver LS-DYNA (LSTC, Livermore, CA). Each region, remote, border zone, and aneurysm, are assigned different material properties. The endocardium is lined with a layer of shell elements

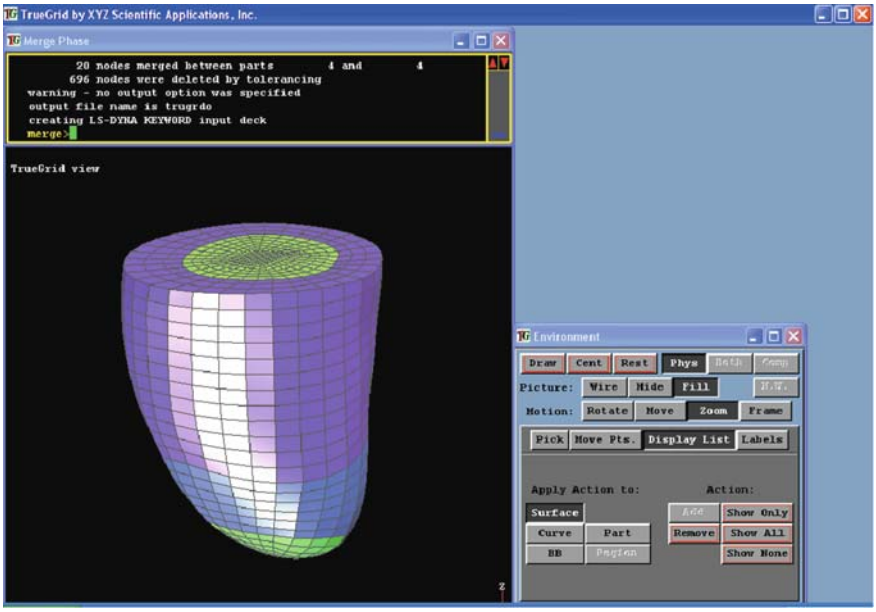

Fig. 1.14 The volumetric mesh is displayed in TrueGrid. The mesh is three elements thick transmurally and has three different material regions (the remote, border zone, and infarct). A layer of shell elements line the endocardial surface and cap off the top of the LV to form a closed volume for LV volume measurements

that extend over the LV base cavity to form an enclosed volume for LV volume measurements. The shell elements are modeled as an extremely soft linearly elastic material (Young's modulus of 1×10^{-10} kPa and Poisson's ratio of 0.3) that offers no mechanical response.

For an ovine LV, myofiber directions of –37°, 23°, and 83° (with respect to the circumferential direction) are assigned at the epicardium, mid-wall, and endocardium, respectively, in the remote and border zone regions [9] by the custom Matlab code Closer, which was developed by UCSF's Cardiac Biomechanics Laboratory (http://cbl.surgery.ucsf.edu/). At the aneurysm region, fiber angles are set to 0° in order to use experimentally determined aneurysm material parameters with respect to this direction [10]. A much more detailed description of ventricular myofiber orientation is provided in the next chapter.

1.6 Create FEA Mesh Using LaGriT-PNNL and MeshMAGIC

LaGriT-PNNL (Pacific Northwest National Laboratory) is a freeware hybrid-grid generator, with particular emphasis on tetrahedra. It is an outgrowth of the original LaGriT (http://lagrit.lanl.gov/) developed at Los Alamos National Laboratory, whose development over the last 6 years has been focused on quality layered

tetrahedral and hybrid prism/tetrahedral grid generation for complex biomedical geometries [2, 11]. MeshMagic is a developing project founded on compiled MATLAB/OCTAVE code, whose philosophy is to hide the complexity of computer programming from the user, enabling the customization of grid generation projects, by calling on sophisticated computational geometry functions. Many of the biomedical-related functions of LaGriT are slowly being ported to MeshMAGIC.

These codes are research, command-line-driven codes, with little documentation. They accept as input one or multiple closed surfaces. On the other hand, the biomedical algorithms begin with an extensive analysis of that surface geometry, which enables them to be fully automatic, once two geometric parameters with physical meaning have been specified. A sketch of that analysis and an introduction to the theory on which these codes rest is presented in Chapter 7.

The input surfaces for LaGriT may derive from CAD, such as illustrated in Fig. 1.13, contours, or from popular isosurfacing algorithms, such as Marching Cubes, available in ITK (www.itk.org) and VTK (www.vtk.org). These surfaces are read into LaGriT-PNNL and processed to generate a high-quality layered tetrahedral grid. Supported surface formats are shown in Table 1.1. Figure 1.15 illustrates a generic input file for the layered tetrahedra shown in Fig. 1.16. User input is encapsulated by « » and explained below. The important user parameters are the element anisotropy and the number of layers. The latter is self-explanatory. The anisotropy parameter is relative to the gradient-limited local feature size, as explained in Chapter 7.

Figure 1.16 illustrates the results of applying the input shown in Fig. 1.15 and the application in MATLAB of the boundary prism algorithm described in [2]. The original surface was provided by the NYU Medical Center and Zhang et al. [12]. The result is a multi-material fluid–structure-interaction-ready boundary layer mesh of a human heart, consisting of heart tissue, blood boundary layer, and blood domains. Panels A and B show the feature size field (defined in Chapter 7) on the outer surface of the heart tissue domain and the blood domain, respectively. Panel B shows the feature size field on the outer surface of the blood domain. Panel C shows a cut through the heart muscle tessellated with layered tetrahedra, where the orientation of the cut plane is indicated in Panel A. Panel D shows the detail of the layered

Table 1.1 Supported formats in LaGrit-PNNL

Read format	Binary	Write format	Binary
LaGriT	Yes	Yes	Yes
STL	Yes	Yes	No
LS-DYNA	No	Yes	No
AVS-UCD	No	Yes	No
GMV	Yes	Yes	Yes
CGNS	Yes	Yes	Yes
GO-CAD	No	No	No
DXF	No	No	No
TECPLOT	No	Yes	Yes
VTK	No	Yes	No

```
read <<format>> <<filename>> 2dmesh

featuresize 2dmesh 0.001/1.0/<<anisotropy>>
massage //// 1 0 0 fspri=fsize fssec=fsiz_out
mmvcsmooth 2dmesh 5 0.5
curvature 2dmesh
featuresize 2dmesh 0.0001/1.0/<<anisotropy>>
massage //// 1 0 0 fspri=fsize fssec=fsiz_out
mmvcsmooth 2dmesh 5 0.5
dump <<format>> <<new_surface_filname>>

autopts 3dmesh 2dmesh <<number_of_layers>>
pset inter1 zq layer 1 0 0 1 ge
filter/pset get inter1/0.000841
rmpoint/compress
connect noadd
erode
rmmat 21 element
rmpoint compress
detectnbd
assign///ivoronoi/-3
recon; recon; recon
detectnbd
assign///ivoronoi/-4
recon; recon; recon
crush_thin_tets
rmpoint element
rmpoint compress
.
.
.
detectnbd

dump <<format>> <<3dmesh_filename>>

finish
```

Fig. 1.15 Typical input for generating layered tetrahedra in LaGriT-PNNL. User parameters and input are shown in between «»

tetrahedral mesh of the heart tissue. Panels E and F are zoomed-in views on the regions of the cardiac valves, showing the prismatic boundary layer alone. Panels G, H, and I show the prismatic boundary layer at about 25% of GLFS of the blood domain, sandwiched between the layered tetrahedra of the tissue and the Delaunay tetrahedra of the blood. Mesh quality statistics are shown in Fig. 1.17.

1.7 A Brief Discussion of Governing Equations and Boundary Conditions

In this book, we do not go into details about the third basic biomechanics modeling step outlined in the introductory chapter: governing equations. This is because UCSF's Cardiac Biomechanics Laboratory (http://cbl.surgery.ucsf.edu/) was awarded a grant from the NIH (HL077921) to develop and validate an easy-to-use software tool for determining myocardial material properties from

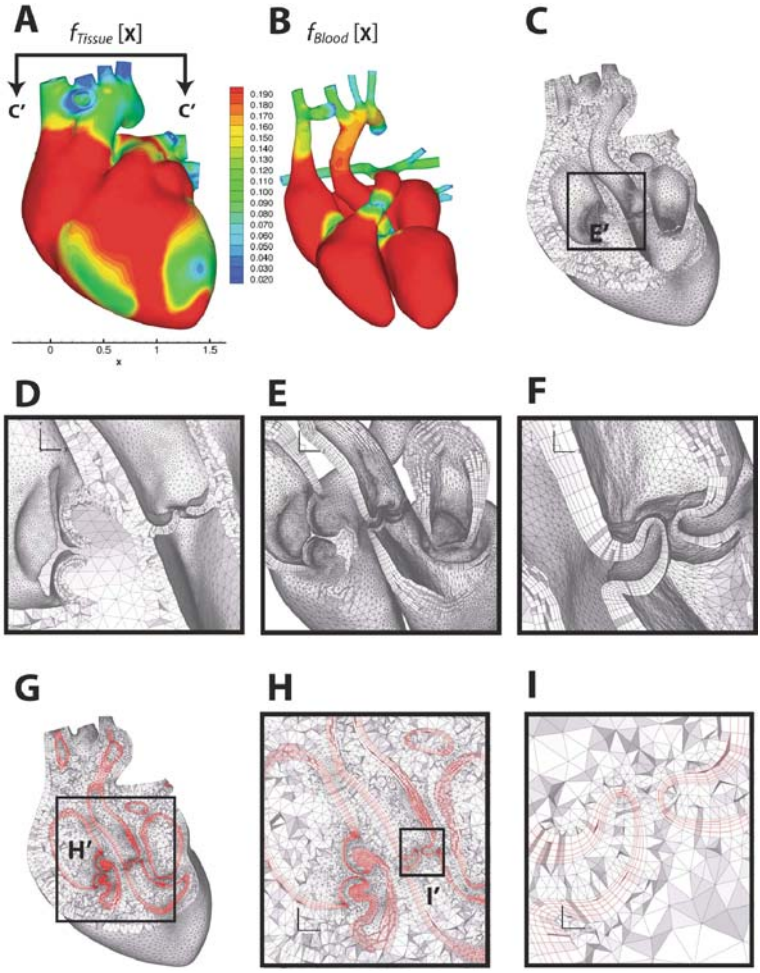

Fig. 1.16 Multi-material boundary layer mesh of a human heart, consisting of heart tissue created in LaGriT-PNNL and MeshMAGIC blood boundary layer (MeshMAGIC). **a** and **b**: Feature size field on the outer surface of the heart tissue domain and the blood domain, respectively. **c**: Orientation of the cut plane indicated in **a**. **d**: Detail of layered tetrahedra generated by input in Fig. 1.15. **e** and **f**: Details of cardiac valves, showing prismatic boundary layer. **g–i**: Prismatic boundary layer sandwiched between layered tetrahedra tissue and blood

magnetic resonance imaging and LV pressure measurements. This software can be downloaded from cmblab.surgery.ucsf.edu. Basically, we use the FE software LS-DYNA to solve the governing equations, thus easing the mathematical burden off the user. These governing equations are based on the principle of virtual work. In our example of the infarcted ovine LV, this principle basically states that the work done by the pressure applied to the endocardial surface is balanced

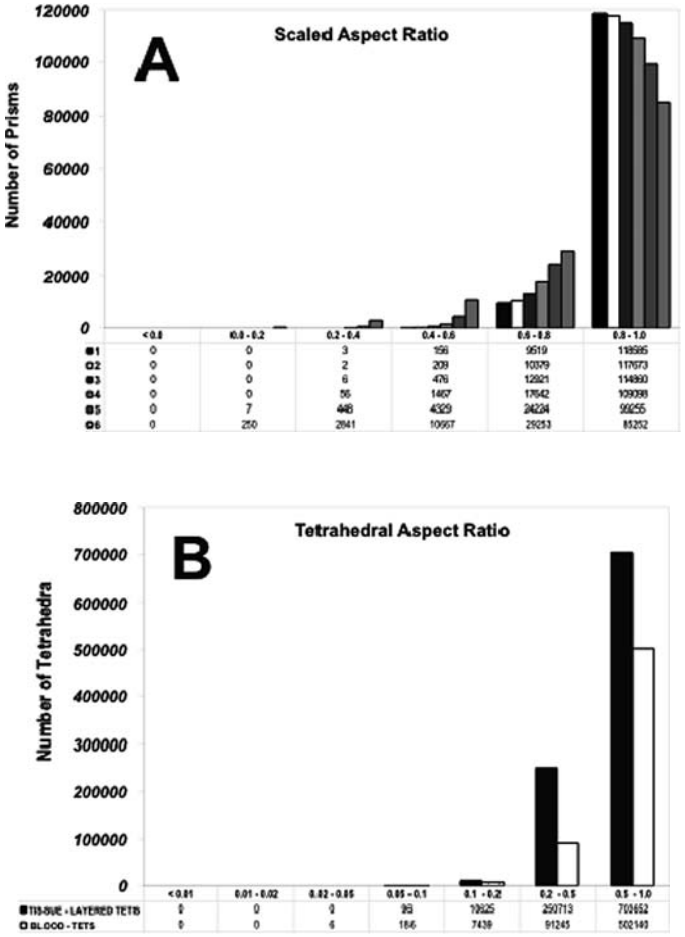

Fig. 1.17 Mesh quality statistics for the computational grid shown in Fig. 1.16

by the potential or strain energy stored in the LV wall. This is easiest to imagine during diastolic filling when an increase in LV pressure causes an increase in LV volume. The balance is more complicated during systole when LV volume can decrease, as LV pressure remains high, because the contraction of the myocardium develops forces internal to the ventricular surfaces. This additional internal energy is what causes the LV wall to thicken despite higher external pressure loading.

The principle of virtual work gets its name because it introduces virtual displacements into the balance of linear momentum, which is the fundamental equation of FE simulations. Virtual displacements are unknowns for which LS-DYNA must solve in areas of the LV where pressure or stress boundary conditions are specified. Specifically, the measured in vivo end-diastolic and end-systolic LV pressures

are used to load the endocardial LV surface. In our example of the infarcted ovine LV, we construct a model of the LV below the aortic and mitral valves. We cannot measure the influence of these valves on the LV in terms of stress, so we instead prescribe displacement boundary conditions that best represent the motion of the LV in this region. Specifically, nodes at the LV base are restricted to displace horizontally, and at the basal epicardial nodes the displacements are constrained in the circumferential direction. These boundary conditions are employed in all of the LV models featured in this book.

Acknowledgments This research was supported by National Institutes of Health grants 5R01 HL077921 (Dr. Guccione) and 5R01 HL063348 (Dr. Ratcliffe), and by CardioPolymers, Inc. (Drs. Guccione and Wenk).

References

1. Knupp PM. Achieving finite element mesh quality via optimization of the Jacobian matrix norm and associated quantities. Part II – A framework for volume mesh optimization. *Int J Numer Methods Eng.* 2000;48:1165–85.
2. Dyedov V, Einstein DR, Jiao X, Kuprat AP, Carson JP, del Pin F. Variational generation of prismatic boundary-layer meshes for biomedical computing. *Int J Numer Methods Eng*. 2009, to appear
3. Taylor RL. A mixed-enhanced formulation for tetrahedral finite elements. *Int J Numer Methods Eng*. 2000;47:205–27.
4. Cisloiub R, Lovell M, Wang J. A stabilized mixed formulation for finite strain deformation for low-order tetrahedral solid elements. *Finite Elem Anal Des.* 2008;44: 472–82.
5. Streeter DD Jr, Hanna WT. Engineering mechanics for successive states in canine left ventricular myocardium. I. Cavity and wall geometry. *Circ Res.* 1973a;33:639–55.
6. Streeter DD Jr, Hanna WT. Engineering mechanics for successive states in canine left ventricular myocardium. II. Fiber angle and sarcomere length. *Circ Res.* 1973b;33: 656–64.
7. Guttman MA, Zerhouni EA, McVeigh ER. Analysis and visualization of cardiac function from MR images. *IEEE Comp Graph Appl.* 1997;17(1):30–8.
8. Moustakidis P, Maniar HS, Cupps BP, Absi T, Zheng J, Guccione JM, Sundt TM and Pasque MK. Altered left ventricular geometry changes the border zone temporal distribution of stress in an experimental model of left ventricular aneurysm: a finite element model study. *Circulation*. 2002;106:I168–75.
9. Omens JH, May KD, McCulloch AD. Transmural distribution of three-dimensional strain in the isolated arrested canine left ventricle. *Am J Physiol.* 1991;261:H918–28.
10. Moonly S. Experimental and computational analysis of left ventricular aneurysm mechanics. In Department of Bioengineering, Vol. Ph.D. Berkeley, San Francisco, CA: University of California, San Francisco with University of California, 2003.
11. Kuprat AP, Einstein DR. An anisotropic scale-invariant un-structured mesh generator suitable for volumetric imaging data. *J Comput Phys*. 2009;228:619–40.
12. Zhang Y, Bajaj C, Sohn B-S. 3D finite element meshing from imaging data. *Comput Methods Appl Mech Eng*. 2005;194:5083–106.

Chapter 2
Imaging-Based Assessment and Modeling of the Structures of the Myocardium

Edward W. Hsu, Lindsey J. Healy, Daniel R. Einstein, and Andrew P. Kuprat

Abstract A precise knowledge of the microstructures of the myocardium such as myocyte organization and myofiber orientation is necessary to better understand material and functional properties of the tissue. By characterizing the diffusion of water exerted by its molecular environment, magnetic resonance diffusion tensor imaging has emerged as a viable alternative to conventional histology for mapping tissue fibers and offers advantages of being nondestructive, relatively convenient, and inherently 3D. This chapter presents assessments and modeling of myocardial structures via diffusion tensor imaging, including their principles, validation, applications, and potential directions for future development.

2.1 Introduction

The hierarchical structure of the myocardium plays a deterministic role in its material properties and functional behaviors. For example, the myocardial fiber orientation is closely linked to the anisotropy in both biomechanical stress [1] and electrophysiological conductivity tensors [2]. Therefore, a precise knowledge of the underlying tissue structure is essential to better interpret as well as model functions of the heart, especially in patient- or subject-specific studies of the organ. Conventional methods to characterize tissue structures are largely based on histology, which often necessitates preservation via fixation, sectioning, mounting, and microscopic examination of the tissue. Although histology-based studies have contributed significantly to our current knowledge of the myocardial structure – for example, the classic counterclockwise epicardial-to-endocardial rotation of myocardial fibers [3] – the approach is methodologically hampered by its labor

E.W. Hsu (✉)
Department of Bioengineering, University of Utah, Salt Lake City, UT, USA
e-mail: edward.hsu@utah.edu

J.M. Guccione, et al. (eds.), *Computational Cardiovascular Mechanics*,
DOI 10.1007/978-1-4419-0730-1_2,

intensiveness, destructive nature, and proneness to processing artifacts. An alternative modality that provides equivalent information but circumvents the limitations of histology is thus highly desirable.

The ideal alternative would be one that not only allows noninvasive examination of the heart at reasonable spatial resolution, but also offers high sensitivity to the tissue microstructure. Magnetic resonance imaging (MRI), which in essence maps the concentration and molecular motion of tissue water, is the natural choice. MR diffusion tensor imaging (MR-DTI or DTI for short) [4], a subset of MRI that measures the anisotropy of water diffusion induced when tissues have an ordered organization, has been used with great success in assessing the brain white matter architecture, and shown to be extremely promising for characterizing structures of the myocardium. This chapter presents the general principles, validation, applications, and potential areas of future development of DTI for characterizing and modeling the myocardial structure.

2.2 Principles of MR Diffusion Tensor Imaging

2.2.1 Basis of Diffusion Encoding in MRI

The MR image intensity is sensitive to the molecular dynamics of tissue water. Whereas the random rotational motion of water molecules gives rise to the intrinsic "relaxation" properties relating to the rate by which the excitable MRI signal recovers (referred to as T1) or the excited signal decays (T2), the translational motion, or diffusion, can cause additional signal loss in the presence of spatially-varying magnetic fields. The latter phenomenon can be described by observing that the MRI signal consists of magnetic moments (or spins) represented as individual vectors spinning at frequencies proportional to the local magnetic field strength. As such, when the field strength is made a linear function of space with slope $\mathbf{G}$ (by the action of the so-called "gradient" coils) for a short duration δ, a spin at location $\mathbf{r}$ would precess at a relative frequency ω (with respect to spins located at the origin) given by

$$\omega = -\gamma(\mathbf{G} \cdot \mathbf{r}) \tag{2.1}$$

and acquire a relative phase angle ϕ:

$$\phi = -\gamma(\mathbf{G} \cdot \mathbf{r})\delta \tag{2.2}$$

where γ is the gyromagnetic ratio for water (specifically the protons of its hydrogen atoms). Suppose at one instant the spin is located at location $\mathbf{r}_1$, and at time Δ later, the spin moves via diffusion to $\mathbf{r}_2$, when the same gradient but opposite polarity is applied. The spin would be imparted with a cumulative phase $\Delta\phi$ proportional to its net displacement ($\mathbf{r}_2$–$\mathbf{r}_1$),

$$\Delta\phi = -\gamma \mathbf{G} \cdot (\mathbf{r}_2 - \mathbf{r}_1)\delta. \tag{2.3}$$

Since the displacement for individual spins is a random process, the effect on the MRI signal, in complex exponential notation, can be obtained by solving for the expected value of the phase dispersion according to

$$I = I_0 \int \exp(-i\Delta\phi) P(\mathbf{r}_2 \mid \mathbf{r}_1) d\phi, \tag{2.4}$$

where I_0 is the diffusion-independent intensity, and P is the conditional probability density function, which for unrestricted diffusion is the normal distribution with standard deviation specified by the Einstein equation $\sqrt{2D\Delta}$.

It follows that when diffusion is encoded by a pair of gradient pulses with $G = |\mathbf{G}|$, the signal intensity can be predicted via the classic Stejskal-Tanner expression [5]

$$I = I_0 \exp(-\gamma^2 G^2 \delta^2 (\Delta - \delta/3) D) \text{ or} \tag{2.5}$$

$$I = I_0 \exp(-bD) \text{ for } b = \gamma^2 G^2 \delta^2 (\Delta - \delta/3). \tag{2.6}$$

Extending to the general case when an arbitrary, time-varying diffusion-encoding gradient $G(t)$ is employed, it can be shown that the diffusion-encoding factor b is given by [6]

$$b = \int_0^{TE} \left(\gamma \int_0^t G(t') \mathrm{d}t' \right)^2 \mathrm{d}t. \tag{2.7}$$

2.2.2 Anisotropic Diffusion Measurements by MRI

The molecular diffusion of water follows closely its microscopic environment, and when tissues have orientation-dependent organization, diffusion becomes anisotropic. If a tissue consists predominantly of packed array of parallel fibers, intuitively diffusion would be faster along than across the fibers. Without delving into the biophysical mechanisms such as restriction and compartmentation that underlie the diffusion anisotropy, the formalism for relating anisotropic diffusion to the MRI signal can be empirically explained by considering a special orthotropic system in which the spins exhibit diffusivities of D_1, D_2, and D_3 along the three orthogonal principal directions of motion encoded by the gradients G_1, G_2, and G_3. Suppose the individual gradients are identical in timing, the unit vector $\mathbf{u} = [u_1 \;\; u_2 \;\; u_3]^T$ specifying the direction of the combined gradient $\mathbf{G}(t)$ can be factored out from the magnitude term G(t), or

$$\mathbf{G}(t) = \begin{bmatrix} G_1(t) \\ G_2(t) \\ G_3(t) \end{bmatrix} = \begin{bmatrix} u_1 \\ u_2 \\ u_3 \end{bmatrix} |\mathbf{G}(t)| = \mathbf{u} \cdot G(t). \tag{2.8}$$

Following the notation of Eq. (2.6), the MRI signal satisfies,

$$I = I_0 \exp\left(-b\mathbf{u}^T \cdot \begin{bmatrix} D_1 & 0 & 0 \\ 0 & D_2 & 0 \\ 0 & 0 & D_3 \end{bmatrix} \cdot \mathbf{u} \right) = I_0 \exp(- b\mathbf{u}^T \cdot \mathbf{D}_\Lambda \cdot \mathbf{u}). \tag{2.9}$$

Comparing to Eq. (2.6), an effective diffusivity, which is a scalar quantity, can be defined as $D_{\text{eff}} = \mathbf{u}^T \cdot \mathbf{D}_\Lambda \cdot \mathbf{u}$..

To extend to the general case when the principal diffusion and laboratory gradient direction $\mathbf{g}$ do not coincide, the latter can by transformed to the local diffusion coordinate system via an appropriate orthonormal rotation matrix, or $\mathbf{u} = \mathbf{Rg}$. Equation (2.9) then becomes

$$I = I_0 \exp\left(-b\mathbf{g}^T\mathbf{R}^T \cdot \mathbf{D}_\Lambda \cdot \mathbf{Rg}\right) = I_0 \exp\left(-b\mathbf{g}^T \cdot \mathbf{D} \cdot \mathbf{g}\right) \tag{2.10}$$

where $\mathbf{D} = \mathbf{R}^T \cdot \mathbf{D}_\Lambda \cdot \mathbf{R}$ corresponds to the diffusion tensor. For 3D space, $\mathbf{D}$ is a symmetric, rank-2 tensor, containing six independent parameters, three for describing the magnitudes and another three for the orientations of diffusion. The relationships between the observed diffusivity and the encoding gradient directions for the cases of isotropic, orthotropic, and generalized anisotropic diffusion are illustrated in Fig. 2.1.

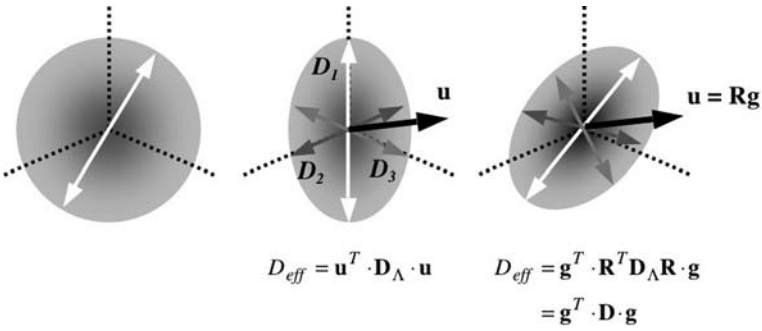

Fig. 2.1 Relationships between diffusivity and MRI encoding direction. Spherical or ellipsoidal surface of probability density function is drawn to correspond cases of isotropic (*left*), orthotropic (*center*), and generalized anisotropic diffusion (*right*). Measured diffusivity for isotropic diffusion is independent of the encoding direction $\mathbf{u}$, whereas it is a product of $\mathbf{u}$ and the diagonal diffusivity matrix $\mathbf{D}_\Lambda$. For generalized anisotropic diffusion, the diffusivity can be obtained by transforming the laboratory gradient direction $\mathbf{g}$ to the orthotropic coordinate system

2.2.3 Strategies and Practical Considerations of DTI

The essence of DTI is to acquire the so-called diffusion-weighted MR images (by inserting the pair of diffusion-sensitizing gradient pulses into the imaging pulse sequence), using the diffusion encoding gradient directions **g** to selectively probe the elements of **D** as described in Eq. (2.10). Because **D** is symmetric, the minimum DTI experiment consists of seven scans, including one in each of six non-collinear diffusion encoding directions to uniquely determine **D**, plus an additional non-weighted "b_0" (for $b = 0$) scan to estimate I_0.

From the image intensities, on a pixel-by-pixel basis, the elements of **D** can be solved either analytically, provided that diffusion is encoded in a certain predetermined set of directions [7], or more often, via multivariate numerical approximation (i.e., curve fitting). Subsequently, the diffusion tensor is diagonalized into its eigenvalues and eigenvectors which, according to Eq. (2.10), correspond to the magnitudes and orientations of the local principal axes of diffusion, respectively. For convenience, rather than comparing the three eigenvalues at the same time, scalar indices are often computed to represent the degree of diffusion anisotropy. A commonly used such index is the fractional anisotropy (FA) [8], which is akin to the normalized standard deviation of the eigenvalues and is defined as

$$FA = \sqrt{\frac{3[(D_1 - D_{\text{av}})^2 + (D_2 - D_{\text{av}})^2 + (D_3 - D_{\text{av}})^2]}{2[D_1^2 + D_2^2 + D_3^2]}}, \tag{2.11}$$

where $D_{\text{av}} = (D_1 + D_2 + D_3)/3$ is the mean diffusivity.

While the above formalism provides a basis to infer tissue structures such as the fiber orientation from characterizations of anisotropic diffusion, in practice, several issues need to be considered to ensure accuracy and quality of the measurements. The greatest technical challenge for DTI is its low signal-to-noise ratio (SNR), due to both the nature of diffusion encoding (i.e., via intensity attenuation) and the large dataset size (minimum of seven scans). Consequently, the minimum DTI experiment likely provides only unacceptable accuracy. To improve SNR, it is often necessary to trade off the spatial resolution, scan time (e.g., averaging of repeated acquisitions), or a combination of both.

Given the above constraints, several studies have investigated ways such as choices of encoding gradient directions for conducting DTI to maximize its accuracy in the presence of image noise. As a rule of thumb, when image averaging is used, it is preferable to do so in the form of image acquisitions in additional gradient directions rather than repeated scans in the same directions [9, 10]. Moreover, for a given number of gradient directions, the directions should be evenly and maximally spread out, as determined by, for example, tessellation of the icosahedron or repulsion of charges on a unit sphere. In terms of the diffusion encoding b factor, either excessively high or low values should be avoided, for they cause too much intensity attenuation resulting in measuring mostly noise or too little intensity dynamic range for good curve fitting. The optimal b value should be one that yields $bD_{\text{av}} \approx 1$ or $\exp(-bD_{\text{av}}) \approx 0.37$.

Besides optimizing the encoding schemes prior to image acquisition, the quality of DTI can also benefit from post-processing enhancements. Noise removal techniques such as partial differential equation (PDE) filtering, which reduces image noise but without the undesirable blurring effects common to most low-pass filters, has been applied to DTI [11]. Importantly, because of the high demands placed on the gradient subsystem during acquisition, instrumentation imperfections (e.g., eddy currents that manifest as residual gradients after they have been switched off) can cause encoding direction-dependent image distortions, which are particularly notorious in echo-planar imaging (EPI). If uncorrected, the distortions would lead to erroneous diffusion tensor estimates at borders and loss of fine structures in the DTI images. Effective retrospective registration techniques based on mutual information (MI), which is useful for matching images of dissimilar contrast, has been developed to correct for these DTI distortions [12].

In summary, an elegant formalism exists that relates anisotropic diffusion to the MRI signal, and serves as the basis for inferring structures of ordered tissues such as the brain white matter and myocardium via DTI. There also exist several technical challenges that may present potential limitations, and need to be considered in the design, implementation, and practical application of DTI.

2.3 DTI Assessments of Myocardial Structures

2.3.1 Prior Developments

Several important works have preceded and contributed either directly or indirectly to the advent of DTI and its applications in myocardial structural characterization. The dependence of the nuclear magnetic resonance (NMR) signal on anisotropic diffusion was recognized and the exact effect was formulated [13] long before the introduction of the MRI scanner. The dependency of diffusion on the measurement gradient direction (i.e., anisotropy) was first observed in muscles using NMR techniques on the rat tibialis anterior [14]. Compared to relaxation-based (T1, T2) imaging, diffusion (non-anisotropic) MRI became widely used much later, after the discovery that it was perhaps the most sensitive imaging technique for detecting acute stroke [15]. A decade later, the tensor-based formalism of anisotropic diffusion was incorporated into MRI (i.e., DTI as we currently know it) [7] which paved the way for quantifying tissue structures such as the fiber orientation in a spatially resolved manner. The first application of DTI for assessing the myocardium was reported soon after, in the perfused rat heart [16].

2.3.2 Histological Validation of DTI Measurements of Myocardial Fiber Orientation

A fundamental premise in the DTI characterization of myocardial fiber structure is that the direction of fastest observed water diffusion (i.e., the eigenvector

of the largest sorted diffusion tensor eigenvalue) coincides with the fiber orientation. Histological validation of the DTI measurements was first reported for freshly excised canine myocardium [17] and later for perfused [18] as well as formaldehyde-fixed rabbit hearts [19]. (In all these studies, DTI was performed and fixation was done before histology.) Overall, excellent correlations between DTI and histological measurements of myocardial fiber orientation were found, not only for point-by-point direct comparison but also in the rate of transmural rotation of the fiber angle (see Fig. 2.2). Barring any differences between animal species, these studies imply that the processes of perfusion and fixation, despite potential effects such as vascular contribution or shrinkage due to dehydration, respectively, have little or no impact on DTI measurements of the myocardial fiber orientation.

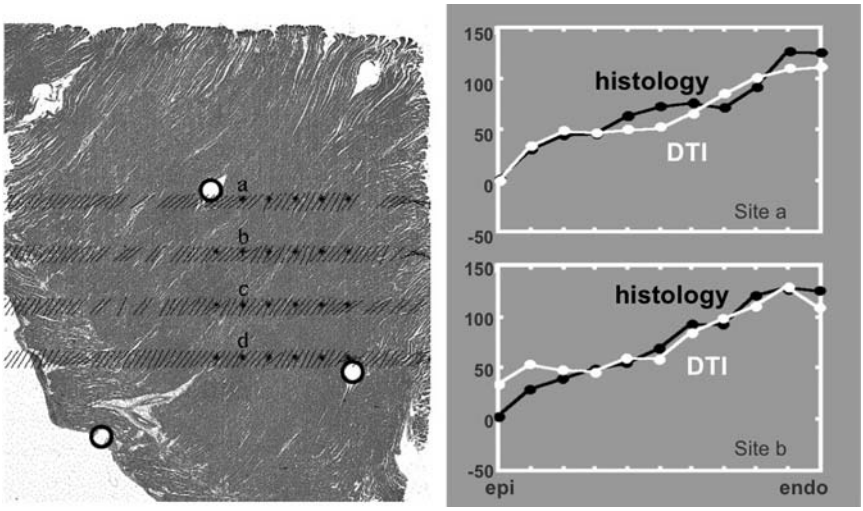

Fig. 2.2 Histological validation of DTI measurements of myocardial fiber orientation. DTI-observed fiber orientations were overlaid onto the corresponding histological section of the myocardium (*left*). Fiber angles at selected sites plotted as functions of transmural depth reveal their distinctive transmural counterclockwise rotation (*right*). Reproduced with permission from [17]

2.3.3 DTI of Normal Hearts

DTI so far has been used to study hearts of a variety of animal species (e.g., dog, sheep, pig, rabbit, rat, and mouse) in various preparations (in vitro arrested under perfusion, freshly excised, or fixed) [17, 20, 21–28]. It has also been performed on (beating) human hearts in vivo [29]. Invariably, most of these first DTI studies have been on normal hearts or myocardial specimens for technical research purposes, including feasibility demonstration, methodological development, and histological validation. For visualization, the dimensionality of parameters in the diffusion tensor is often reduced, and the residual information is shown as grayscale or color-coded

functions of space. The most commonly employed technique for displaying myocardial DTI data is to show only the fiber orientation helix angle (equivalent to the angle of inclination of the primary eigenvector from the cylindrical cardiac short axis plane) in a color-coded map.

One area that was a major impetus for the development of cardiac DTI, and where the technique has been soon applied, is in the so-called "morphologically-accurate" or specimen-specific modeling of myocardial physiology, including biomechanics [30] and electrophysiology [31]. These studies typically involve the generation of finite element structural models of the myocardium from DTI data, followed by computational simulations of physiological responses under various theoretical assumptions and experimental conditions. Many times the same functional responses were measured in situ (prior to DTI), and excellent qualitative correspondence has been found between the empirical measurements and computational "predictions".

Although structural and structure–function studies have confirmed largely what is already known in general (e.g., the counterclockwise rotation of myofibers from the epicardium to endocardium), they underscore DTI as a viable, if not more advantageous, alternative to conventional histology for quantitatively characterizing myocardial structures. To appreciate the technical advancement, consider that most DTI studies of myocardial structures reported to date have employed "multislice" (i.e., series of 2D slices) MRI acquisitions. Compared to the in-plane pixel dimensions, the relatively large slice thickness used can complicate reconstruction of the 3D myocardial fiber structure. On the other hand, 3D DTI, particularly a high-resolution scan, has been hampered by the prolonged acquisition time that is often measured not in hours but days!

The practical utility of 3D DTI was dramatically improved by the so-called reduced encoding DTI [32], where the scan time was significantly shortened without compromising the measurement accuracy by combining undersampling of the data (taking advantage of the high degree of image-to-image similarity) and sophisticated constrained reconstruction of the diffusion images. The methodology was instrumental in the successful demonstration of 3D DTI of the whole-fixed mouse heart, at 100-μm isotropic spatial resolution (in-plane and slice thickness), as shown in Fig.2.3 [20]. To date, the work remains the highest-resolution DTI of the myocardium ever performed and is the first to directly show that the mouse myofibers are not organized in layers of discrete orientations but instead undergo continuous rotation across the ventricular wall.

2.3.4 DTI and the Myocardial Laminar Structure

The existence of myocardial laminar structure has important implications for biomechanical modeling of the tissue [33], but is subject to some controversy, since artifacts (i.e., tissue dehydration and shrinkage during fixation and physical disruption during sectioning) of the histological techniques used in the first reports cannot

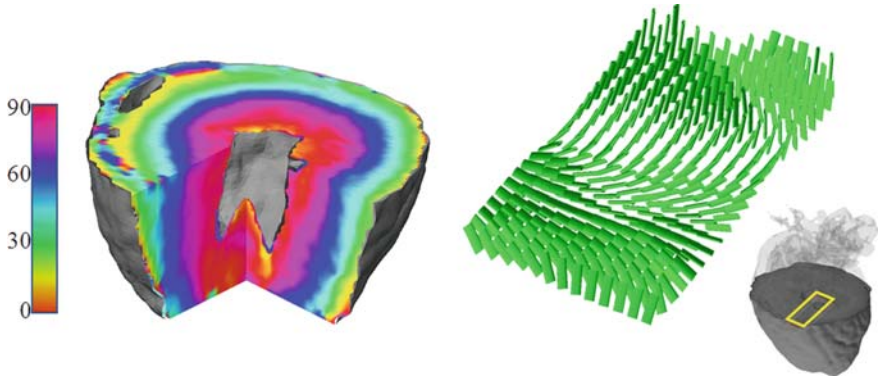

Fig. 2.3 DTI assessment of the 3D fixed mouse heart. Color-coded myocardial fiber helix angles measured at 100 μm intervals are shown for the truncated ventricular volume (*left*). Diffusion tensor fields in the specified area are also shown as flattened cylinders with edges corresponding to directions of fastest and second fastest diffusion (*right*). Note the smooth transitioning transmural fiber orientations in the helix angle map and the organization of the flattened cylinders that may indicate the existence of myocardial laminar structure. Reproduced with permission from [20]

be ruled out. Because of the inherently 3D nature of the tensor description, DTI is a natural alternative for detecting and characterizing the laminar structure. DTI parameters can be linked to the myocardial laminar structure in either one of two ways. First, just as the direction of fastest diffusion (or the primary diffusion tensor eigenvector) is taken as the local myocardial fiber orientation, the plane spanned by the directions of first two fastest diffusion dimensions (or the primary and secondary eigenvectors) can be taken as the laminar plane. Second, the direction of slowest diffusion (or the tertiary eigenvector) can be taken as the axis normal to the laminar structure.

Although direct histological validation has yet to be performed, largely due to limitations of histology, studies of the secondary and tertiary diffusion tensor eigenvectors in the myocardium are consistent with descriptions of the myocardial laminar structure [17, 23, 34]. The organized appearance of the secondary (or tertiary) eigenvector fields in the myocardium (see Fig. 2.3) lends credibility that they are not mere statistical sorting artifacts resulting from noise in the DTI measurements. Moreover, that similar organized pattern of diffusion tensor fields were observed in unfixed (both freshly excised and perfused) myocardium diminishes the likelihood that the laminar structures are related to fixation and sectioning artifacts of histology.

2.3.5 Scalar DTI Measurements and Myocardial Structure

Most DTI studies of the myocardium conducted to date have focused on the directional aspects of the structural measurements such as the fiber and even laminar orientations. Scalar DTI quantities such as the FA can be significant in two ways.

First, because of its spatial resolution (typically in the order of 1 mm), each DTI measurement necessarily reflects the diffusion behavior averaged over multiple myocytes (and extracellular space) contained within the pixel volume. Therefore, the FA can be a correlate for the micrscopic myofiber disarray often associated with myocardial diseases. Indeed, several studies [35, 36] have already found detectable FA changes in diseases such as myocardial infarction and hypertrophic cardiomyopathy.

Second, it is known that even in the normal myocardium there exist transmural differences in the myocyte size and density, and that diffusion MRI is highly sensitive to these cellular structural parameters. A recent study [25] has noted that the FA is constant only in the epicardium, but decreases progressively toward the endocardium. The decrease of diffusion anisotropy is attributed to an increase in the transverse diffusivities (i.e., second and third eigenvalues) while the longitudinal diffusivity (first eigenvalue) remains unchanged, which is consistent with the larger myocyte size and lower density known for the endocardium. Although the exact relationship between the DTI scalar quantities and the underlying tissue cellular structures remains to be established, these findings suggest that measurable quantities of DTI other than fiber and laminar orientations may also provide useful structural information of the tissue.

2.3.6 DTI of Diseased Hearts

A natural extension in the applications of cardiac DTI is to study alterations of the myocardial structures caused by diseases and possibly their therapeutic interventions. Disease-induced changes in the myocardial structure can manifest in several ways. Microscopically (i.e., in the scale comparable to the spatial resolution of DTI), the fiber disarray common to many myocardial diseases can be seen as decreased FA due to reduced degree of diffusion anisotropy. Regional fiber disarray can also appear as increased deviation of myocardial fiber orientation among neighboring image pixels. These changes in diffusion anisotropy attributed to pathological fiber disarray have been reported in recent DTI studies of myocardial infarction [35] and hypertrophic cardiomyopathy [36].

More macroscopically, due to the continual remodeling of the myocardial structures to, for example, compensate for the changing biomechanical loading, it was expected that myocardial diseases would result in DTI-detectable changes of the gross myocardial fiber orientations. However, contrary to expectation, no significant change in the myocardial fiber orientation was found in myocardial infarction in one study [24]. Another study, on dyssynchronous failing hearts [37], also failed to detect significant alterations in the fiber orientation despite significant changes in the wall thickness due to chamber dilation. One potential limitation of these studies is that DTI was performed on groups of individual hearts, rather than longitudinally on the same hearts. Consequently, the results may have been complicated by

issues related to inter-specimen registration and statistics of non-scalar quantities, the technical difficulty of which should by no means be underestimated.

2.3.7 In Vivo DTI of the Beating Heart

A key advantage of MRI is its noninvasiveness, which makes it suited for in vivo imaging applications. Without exception, DTI is the same and has been employed to characterize myocardial structures in the beating heart. Besides the SNR limitations common to all DTI experiments, DTI of the beating heart faces the additional technical challenge of imaging and measuring diffusion in an organ that is subject to periodic but large (compared to the diffusion length scale) displacements. Because the diffusion-induced spin phase shift is a function of the spatial coordinate, motion or tissue strain during diffusion encoding creates a path-dependent "memory effect" on the signal of the image pixel, which, if remain uncorrected, would lead to erroneous characterizations of diffusion and myocardial structure.

The effect of motion on diffusion in DTI of the beating heart can be eliminated by either measuring separately the tissue strain [38], which requires additional scans, or encoding diffusion at precisely the cardiac cycle "sweet spot", where the positive and negative contributions of strain over the entire cycle cancel each other [39]. Using either technique, DTI has been applied on human hearts for studying the normal myocardial biomechanics [38], myocardial infarction [40], and hypertrophic cardiomyopathy [36]. Although obviously the spatial resolution and quality of DTI of beating hearts currently do not compare to those obtainable on specimen hearts, their developments to date and initial applications are very encouraging and pave the way for longitudinal studies in humans as well as experimental animal models.

2.4 Applications of MR Diffusion Tensor Imaging

2.4.1 Image-to-Grid Mapping of MR-DTI Data

From a computational perspective, diffusion tensor data are piecewise constant fields. For example, fiber angles are three fields of direction cosines; fractional anisotropy is a material field that is associated with local myofiber dispersion; and "apparent diffusion" is a field associated with myofiber integrity. These fields are piecewise constant because there is a single value associated with each voxel. Though this data is inherently 3D, it exists on a voxelated Cartesian grid, rather than the typically unstructured hexahedral, tetrahedral, or hybrid grid of finite element models. This raises the issue of how to "associate" or map these quantities to unstructured computational grid. Once mapped, these quantities can serve the role of initializing a computational analysis or validating computational predictions. The fiber angle, for example, must be assigned for each computational cell in order to prescribe local material anisotropy.

The approach to mapping is presented as geometric relationship between a source Cartesian imaging grid and an arbitrary target unstructured grid. It is assumed that source and target grids occupy approximately the same geometry within a certain tolerance, such as would be the case if DTI data and computational grid were either both based on ex vivo data or both based on in vivo data. The tolerance is necessary because geometry in an image is implicit, while the geometry of a computational grid is explicit. Furthermore, operations of smoothing and surface adaptivity typical of grid generation imply some deformation of the geometry. The algorithms presented are embodied in the code I2G, available from the Pacific Northwest National Laboratory.

The approach consists of computing a sparse matrix of intersection volumes V_{ij} between the jth voxel of the image and the ith element of the computational mesh in $O(N\ log(N))$ time, where N is the number of nonzero V_{ij}. To efficiently find corresponding local neighborhoods of intersecting cells a coordinated walk is performed on source and target grids, which is an $O(N)$ process. Subsequently, all V_{ij} are reordered such that they can be packed into a sparse matrix. This need only be done once, and then a sparse matrix-vector multiply can be rapidly performed once for each field (Fig. 2.4). It is important to note that the algorithm requires no a priori mapping between the image and the grid. With a geometry as complex as that of the heart and associated structures, such an a priori mapping would be clearly impossible.

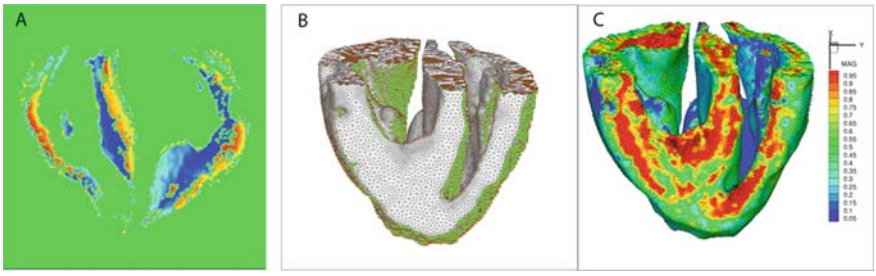

Fig. 2.4 Automatic mapping of cell fields from imaging data to arbitrary unstructured grids in n log(n) time. (**a**) DTI data; (**b**) overlap between DTI data and unstructured grid; (**c**) myofiber angles mapped to the computational grid

In terms of interpolation, there are two weighting schemes. The first is a conservative scheme that enforces equality between the weak form of the integrals of the image and finite element fields over the domain. This would be appropriate for fields relating to mass or energy that must be conserved. The second instead conserves minima and maxima, and is the more appropriate for direction cosines.

V_{ij} can be computed exactly for any arbitrary unstructured grid consisting of convex planar polyhedra. In other words, for linear finite elements, or all finite volume cells. Cases where not all faces are planar, as for example with trilinear hexahedra having bilinear faces, require special treatment to be computationally efficient. These special cases are also addressed in I2G.

One obvious limitation of this approach is that it assumes that the image and grid cohabit the same geometry. Regions of the image outside of the finite element domain are easily masked. Efficient computation of that mask is accomplished by applying a directed point inclusion query on the centroids of the voxels of the image [41], in order to locate which voxels are inside the surface of the finite element domain and which are outside. This mask is automatically calculated by I2G, and is necessary to preserve efficiency in the coordinated walk that finds voxel element intersections. In cases were image and grid do not refer to the same geometry, such as where one refers to an ex vivo geometry and the other to an in vivo geometry, the image may be registered to the binary mask of the unstructured grid. This registration is not part of I2G, but must be performed as a preprocessing step.

Registration typically has two stages. In the first, a global affine transformation is applied to the finite element grid. This is acceptable since affine transformations are reversible, and thus after mapping, the grid may be returned to its original configuration. The mask is then computed from this deformed grid, and a nonlinear warp based on MI is computed between the image and the mask. The image is then transformed into the space of deformed grid and the mapping is performed. Thereafter, the grid is returned to its original configuration.

2.4.2 Anatomical and Pathological Variations in Fiber Organization

Global and local alterations of ventricular geometry and fiber structure can follow pathological remodeling [42]. For example, mitral valve regurgitation can lead to volume overloading, resulting in myocardial hypertrophy, affecting the entire ventricular wall. These geometric changes can be accompanied by tissue changes, such as wall thickening or thinning [43]. Moreover, these tissue changes carry over to the associated fiber structure in cases of ischemia-induced heart disease, which is characterized by local scarring. An understanding of these changes is therefore important to understanding cardiac mechanics in both health and disease.

However, quantifying fiber variation and remodeling across a population or treatment is complicated by sometimes profound disease-induced variations on top of "normal" anatomical variations. Recent efforts in cardiac computational anatomy [44] attempt to normalize these differences by establishing a "normative" geometry to which samples from the population can be deformed. This atlas-based approach seeks to establish a common coordinate system to which each heart is transformed, by solving a series of linear and nonlinear registration problems for each geometry [44]. The "normative" geometry therefore acts as a standard against which all others are compared. By computing a nonlinear transformation between sample hearts and the standard, it is possible to compute a deformation field, which highlights local areas of remodeling. In addition, since the nonlinear transformation is voxel-based, it applies to the diffusion tensor data as well, permitting eigenvalues and eigenvectors to be mapped onto the template. In this manner, it is possible to quantitatively

compare the principal fiber directions, as well as the fractional anisotropy [44]. It is important to note that to make these transformations tractable, and in order to preserve the diastolic conformation, it is generally necessary to inject polymer into each of the four chambers [44].

In one study, five dyssynchronous volume overloaded canine hearts were compared to a normative heart [44]. Local and global remodeling was evidenced by ventricular volume reduction as well as regional decreases in septal, anterior, and posterior wall thickness [44]. The primary fiber structure, however, did not differ greatly when compared to normal hearts, consistent with earlier observations [45, 46]. There were differences in the third eigenvector of the diffusion tensor which was correlated with the myocardial sheet direction. Indeed, there was shown to be significant regional differences in sheet structure remodeling. Specifically, a decrease in the sheet normal angle was found in an early-activated septum but no change was found in the late-activated lateral wall [44].

2.5 Future Directions

Despite some practical limitations, DTI has already emerged as a viable alternative to histology, if not the method of choice, for assessing the structures of the myocardium. In addition to structural characterization, the inherently 3D and digital natures of the data make DTI well suited for computational analyses of cardiac functions such as biomechanics and electrophysiology. Early DTI studies of myocardial structures and functions included in this chapter have demonstrated the potential, as well as point out some possible areas for future developments of the methodology.

Perhaps the greatest challenge, or opportunity, in the acquisition methodology of DTI has been, and will likely continue to be, the low spatial resolution and long scan times imposed by the low SNR. Although the introduction of fast imaging techniques such as EPI [47] and "parallel imaging" [48] has helped speed up the acquisition, they require even greater sacrifice on the spatial resolution to maintain the SNR. Because the images that make up a DTI dataset share a high degree of similarity (e.g., the size and shape of the imaged organs remain essentially the same, and contrast changes generated by anisotropic diffusion encoding of the tissue structure are of low spatial frequency in nature), an alternative or adjunct to fast imaging is to employ reduced encoding imaging to eliminate redundancy in the image acquisition. The validity of the concept has already been demonstrated [32], and further developments will likely allow DTI to be performed in significantly shorter scan time, better accuracy be achieved in the same scan time, or a combination of both.

A second area of needed future developments is in the statistics of DTI data, which will benefit studies requiring group (e.g., comparing diseased to normal hearts) or longitudinal (comparing the same hearts at different time points) analysis. These studies invariably require some form of image registration to identify anatomically equivalent points of the organ among the images, followed by the application of statistics. Although much has been developed in the fields of image registration and computation anatomy, the nature of the DTI data, which are tensors or vectors

and not simply scalars in nature, can present an additional level of complication. For example, it is easy to see that DTI registration requires the step of tensor transformation in addition to traditional image registration [49]. However, the formalism for tensor transformation, especially when image registration requires non-rigid warping of the coordinate system, either remains unclear or awaits validation.

DTI has had a great start in its methodological developments and applications. Further developments, either in terms of acquisition or post-analysis, will undoubtedly add to the practical utility of the already powerful tool for studying the structures and structure–function relationships of the myocardium [50].

References

1. Guccione JM, McCulloch, AD, Waldman LK. Passive material properties of intact ventricular myocardium determined from a cylindrical model. *J Biomech Eng*. 1991;113(1):42–55.
2. Taccardi B, Macchi E, Lux RL, Ershler PR, Spaggiari S, Baruffi S, Vyhmeister Y. Effect of myocardial fiber direction on epicardial potentials. *Circulation*. 1994;90(6):3076–3090.
3. Streeter DD, Jr., Spotnitz HM, Patel DP, Ross J Jr., Sonnenblick EH. Fiber orientation in the canine left ventricle during diastole and systole. *Circ Res*. 1969;24(3):339–347.
4. Basser PJ. Inferring microstructural features and the physiological state of tissues from diffusion-weighted images. *NMR Biomed.* 1995;8(7–8):333–344.
5. Stejskal EO, Tanner JE. Spin diffusion measurements: spin echoes in the presence of a time-dependent field gradient. *J Chem Phys.* 1965;42:288.
6. Mattiello J., Basser, PJ, Le Bihan D.. Analytical expressions for the b matrix in NMR diffusion imaging and spectroscopy. *J Magn Reson A.* 1994;108(2):121–141.
7. Basser PJ, Mattiello, J., LeBihan D.. Estimation of the effective self-diffusion tensor from the NMR spin echo. *J Magn Reson B.* 1994;103(3):247–254.
8. Pierpaoli C., Basser PJ. Toward a quantitative assessment of diffusion anisotropy. *Magn Reson Med.* 1996;36:893–906.
9. Jones DK, Horsfield, MA, Simmons A.. Optimal strategies for measuring diffusion in anisotropic systems by magnetic resonance imaging. *Magn Reson Med.* 1999;42(3):515–525.
10. Papadakis NG, Xing D., Huang CL, Hall, LD, Carpenter TA. A comparative study of acquisition schemes for diffusion tensor imaging using MRI. *J Magn Reson*. 1999;137(1):67–82.
11. Mistry NN, Hsu EW. Retrospective distortion correction for 3D MR diffusion tensor microscopy using mutual information and Fourier deformations. *Magn Reson Med*. 2006;56(2):310–316.
12. Rohde GK, Barnett AS, Basser PJ, Marenco, S., Pierpaoli C.. Comprehensive approach for correction of motion and distortion in diffusion-weighted MRI. *Magn Reson Med*. 2004;51(1):103–114.
13. Stejskal EO. Use of spin echoes in a pulsed magnetic-field gradient to study aniosotropic, restricted diffusion and flow. *J Chem Phys*. 1965;43(10):2597–3603.
14. Cleveland GG, Chang DC, Hazlewood, CF, Rorschach HE. Nuclear magnetic resonance measurement of skeletal muscle: anisotropy of the diffusion coefficient of the intracellular water. *Biophys J*. 1976;16(9):1043–1053.
15. Warach S., Mosley M, Sorensen, AG, Koroshetz W.. Time course of diffusion imaging abnormalities in human stroke. *Stroke.* 1996;27(7):1254–1256.
16. Garrido L., Wedeen VJ, Kwong KK, Spencer, UM, Kantor HL. Anisotropy of water diffusion in the myocardium of the rat. *Circ Res*. 1994;74(5):789–793.
17. Hsu EW, Muzikant AL, Matulevicius SA, Penland, RC, Henriquez CS. Magnetic resonance myocardial fiber-orientation mapping with direct histological correlation. *Am J Physiol*. 1998;274(5 Pt 2):H1627–34.

18. Scollan DF, Holmes A, Winslow, R, Forder J.. Histological validation of myocardial microstructure obtained from diffusion tensor magnetic resonance imaging. *Am J Physiol.* 1998;275(6 Pt 2):H2308–18.
19. Holmes AA, Scollan, DF, Winslow RL. Direct histological validation of diffusion tensor MRI in formaldehyde-fixed myocardium. *Magn Reson Med*. 2000;44(1):157–161.
20. Jiang Y, Pandya K, Smithies O, Hsu EW. Three-dimensional diffusion tensor microscopy of fixed mouse hearts. *Magn Reson Med*. 2004;52(3):453–460.
21. Hsu EW, Buckley DL, Bui JD, Blackband, SJ, Forder JR. Two-component diffusion tensor MRI of isolated perfused hearts. *Magn Reson Med*. 2001;45(6):1039–1045.
22. Schmid P, Jaermann T, Boesiger P, Niederer PF, Lunkenheimer PP, Cryer, CW, Anderson RH. Ventricular myocardial architecture as visualised in postmortem swine hearts using magnetic resonance diffusion tensor imaging. *Eur J Cardiothorac Surg*. 2005;27(3): 468–472.
23. Helm PA, Tseng HJ, Younes L, McVeigh, ER, Winslow RL. Ex vivo 3D diffusion tensor imaging and quantification of cardiac laminar structure. *Magn Reson Med*. 2005;54(4): 850–859.
24. Walker JC, Guccione JM, Jiang Y, Zhang P, Wallace AW, Hsu EW, Ratcliffe MB. Helical myofiber orientation after myocardial infarction and left ventricular surgical restoration in sheep. *J Thorac Cardiovasc Surg*. 2005;129(2):382–390.
25. Jiang Y, Guccione JM, Ratcliffe MB, Hsu EW. Transmural heterogeneity of diffusion anisotropy in the sheep myocardium characterized by MR diffusion tensor imaging. *Am J Physiol Heart Circ Physiol*. 2007;293(4):H2377–H2384.
26. Scollan DF, Holmes A, Zhang, J, Winslow RL. Reconstruction of cardiac ventricular geometry and fiber orientation using magnetic resonance imaging. *Ann Biomed Eng*. 2000;28(8): 934–944.
27. Haber I., Friehs I., Jiang Y., Del Nido, PJ, Hsu E. Diffusion tensor imaging of left ventricular hypertrophy. in *International Society of Magnetic Resonance Thirteenth Scientific Meeting*. 2005, Miami Beach, FL.
28. Chen J, Liu W, Zhang H, Lacy L, Yang X, Song SK, Wickline, SA, Yu X.. Regional ventricular wall thickening reflects changes in cardiac fiber and sheet structure during contraction: quantification with diffusion tensor MRI. *Am J Physiol Heart Circ Physiol.* 2005;289(5):H1898–H18907.
29. Reese TG, Weisskoff RM, Smith RN, Rosen BR, Dinsmore, RE, Wedeen VJ. Imaging myocardial fiber architecture in vivo with magnetic resonance. *Magn Reson Med*. 1995;34(6):786–791.
30. Guccione JM, Costa, KD, McCulloch AD. Finite element stress analysis of left ventricular mechanics in the beating dog heart. *J Biomech.* 1995;28(10):1167–1177.
31. Tranquillo JV, Hlavacek, J, Henriquez CS. An integrative model of mouse cardiac electrophysiology from cell to torso. *Europace.* 2005;7 Suppl 2:56–70.
32. Hsu EW, Henriquez CS. Myocardial fiber orientation mapping using reduced encoding diffusion tensor imaging. *J Cardiovasc Magn Reson.* 2001;3(4):339–347.
33. LeGrice IJ, Smaill BH, Chai LZ, Edgar SG, Gavin, JB, Hunter PJ. Laminar structure of the heart: ventricular myocyte arrangement and connective tissue architecture in the dog. *Am J Physiol.* 1995;269(2 Pt 2):H571–H582.
34. Helm P, Beg MF, Miller, MI, Winslow RL. Measuring and mapping cardiac fiber and laminar architecture using diffusion tensor MR imaging. *Ann N Y Acad Sci.* 2005;1047: 296–307.
35. Chen J, Song SK, Liu W, McLean M, Allen JS, Tan J, Wickline, SA, Yu X.. Remodeling of cardiac fiber structure after infarction in rats quantified with diffusion tensor MRI. *Am J Physiol Heart Circ Physiol.* 2003;285(3):H946–H954.
36. Tseng WY, Dou J, Reese, TG, Wedeen VJ. Imaging myocardial fiber disarray and intramural strain hypokinesis in hypertrophic cardiomyopathy with MRI. *J Magn Reson Imaging.* 2006;23(1):1–8.

37. Helm PA, Younes L, Beg MF, Ennis DB, Leclercq C, Faris OP, McVeigh E, Kass D, Miller MI, Winslow RL. Evidence of structural remodeling in the dyssynchronous failing heart. *Circ Res.* 2006;98(1):125–132.
38. Dou J, Tseng WY, Reese, TG, Wedeen VJ. Combined diffusion and strain MRI reveals structure and function of human myocardial laminar sheets in vivo. *Magn Reson Med.* 2003;50(1):107–113.
39. Dou J, Reese TG, Tseng, WY, Wedeen VJ. Cardiac diffusion MRI without motion effects. *Magn Reson Med.* 2002;48(1):105–114.
40. Wu M, Tseng W, Su M, Liu C, Chiou K, Wedeen V, Reese T, Yang C.. Diffusion tensor magnetic resonance imaging mapping the fiber architecture remodeling in human myocardium after infarction: correlation with viability and wall motion. *Circulation.* 2006;114:1036–1045.
41. Khamayseh AK, Kuprat AP. Deterministic point inclusion methods for computational applications with complex geometry. *Comput Sci Discov.* Volume, 22 pp
42. Anderson KP, Walker R, Urie P, Ershler PR, Lux RL, Karwandee SV. Myocardial electrical propagation in patients with idiopathic dilated cardiomyopathy. *J Clin Invest.* 1993;92(1):122–140.
43. Prinzen FW, Cheriex EC, Delhaas T, van Oosterhout MF, Arts T, Wellens, HJ, Reneman RS. Asymmetric thickness of the left ventricular wall resulting from asynchronous electric activation: a study in dogs with ventricular pacing and in patients with left bundle branch block. *Am Heart J.* 1995;130(5):1045–1053.
44. Helm P.. *A novel technique for quantifying variability of cardiac anatomy: application to the dyssynchronous failing heart*. John Hopkins University, Baltimore, MD, 2005.
45. Ashikaga H, Criscione JC, Omens JH, Covell, JW, Ingels NB Jr.. Transmural left ventricular mechanics underlying torsional recoil during relaxation. *Am J Physiol Heart Circ Physiol.* 2004;286(2):H640–H647.
46. Omens JH, Covell JW. Transmural distribution of myocardial tissue growth induced by volume-overload hypertrophy in the dog. *Circulation.* 1991;84(3):1235–1245.
47. Mansfield P.. Multi-planar image formation using NMR spin echoes. *J Phys C: Solid State Phys.* 1977;10:L55–L58.
48. Pruessmann KP, Weiger M, Scheidegger, MB, Boesiger P.. SENSE: sensitivity encoding for fast MRI. *Magn Reson Med.* 1999;42(5):952–962.
49. Alexander DC, Pierpaoli C, Basser, PJ, Gee JC. Spatial transformations of diffusion tensor magnetic resonance images. *IEEE Trans Med Imaging.* 2001;20(11):1131–1139.
50. Kuprat AP, Mosso SJ. *Efficient algorithms for mapping cell quantities between overlapped 3D unstructured meshes*. Los Alamos National Laboratory Report LA-UR-05-5084, 2005.

Chapter 3
Constitutive Equations and Model Validation

Choon-Sik Jhun, Jonathan F. Wenk, Kay Sun, and Julius M. Guccione

Abstract Of the four basic biomechanics modeling steps outlined in the Introduction, determining the constitutive equations for cardiovascular tissue is often the most difficult step, especially when the tissue properties vary with time and sarcomere length history, as is the case with contracting myocardium. Using a cylindrical model to study transmural variations in stress and strain rather than a finite element model of the entire left ventricle allows for the implementation of a time- and sarcomere length history-dependent constitutive equation. The cylindrical model simulations can then be repeated with progressively simpler constitutive equations and the resulting transmural stress and strain distributions compared to determine under what conditions the most computationally efficient constitutive equations are valid. This chapter is primarily concerned with an instructive review of the constitutive equations we have implemented in cylindrical and finite element models of the passive and beating left ventricle, including that of diseased and surgically treated hearts. The last section of this chapter is concerned with experimental measurements that we have used to validate these models.

3.1 Introduction

To understand the path that we took in developing a constitutive equation for actively contracting myocardium, that became a standard feature in commercial finite element software (LS-DYNA, Livermore Software Technology Corporation, Livermore, CA; academic license, $500/year), it is instructive to start with the first biomechanics textbook ever written, *Biomechanics: Mechanical Properties of Living Tissues*, by Fung [1]. Our method of approach (outlined in the Introduction

J.M. Guccione (✉)
Department of Surgery, University of California at San Francisco and San Francisco VA Medical Center, San Francisco, CA, USA
e-mail: guccionej@surgery.ucsf.edu

J.M. Guccione, et al. (eds.), *Computational Cardiovascular Mechanics*,
DOI 10.1007/978-1-4419-0730-1_3,

of this book and mentioned in the abstract of this chapter) is described in Chapter 1 of Biomechanics (Introduction: A Sketch of the History and Scope of the Field). Introductions to the engineering concepts of stress, strain, and the constitutive equation for the Hookean elastic solid (Hooke's law) are given in Chapter 2 of Biomechanics (The Meaning of the Constitutive Equation). Basically, stress is force per unit area, strain is change in length normalized by undeformed length, and the Hookean elastic solid has a linear relationship between stress and strain; it returns to its original shape upon removal of external loads (i.e., no permanent or plastic deformation occurs). However, not until near the end of Chapter 7 of Biomechanics (Bioviscoelastic Solids) is there a constitutive equation that is appropriate for non-contracting or passive myocardium. In Section 7.12.1 of Biomechanics (Other Examples), a pseudo-strain-energy function, W, was proposed in the form of

$$W = 0.5\alpha_{ijkl}E_{ij}E_{kl} + (\beta_0 + \beta_{mnpq}E_{mn}E_{pq}) \exp\left(\gamma_{ij}E_{ij} + \kappa_{mnpq}E_{mn}E_{pq} + \cdots\right) \quad (3.1)$$

where α_{ijkl}, β_0, β_{mnpq}, γ_{ij}, and κ_{mnpq} are constants to be determined empirically, E_{ij} are 3-D (Green's) strain tensor components and the indices $i, j, k \ldots$ range over 1, 2, 3." We will revisit Eq. (3.1) in the next section.

3.2 Passive Material Properties of Intact Ventricular Myocardium Determined from a Cylindrical Model

In LS-DYNA, Material_128 uses the following pseudo-strain-energy function to describe the regional mechanics of passive myocardium:

$$W = 0.5C \exp\left[b_f E_{11}E_{11} + b_t(E_{22}E_{22} + E_{33}E_{33} + E_{23}E_{23} + E_{32}E_{32}) + b_{fs}(E_{12}E_{12} + E_{21}E_{21} + E_{13}E_{13} + E_{31}E_{31})\right] \quad (3.2)$$

where C, b_f, b_t, and b_{fs} are constants (as opposed to tensors, but, in general, they can vary spatially) and an orthogonal "fiber" coordinate system has been defined (with the subscript "1" denoting the muscle fiber direction, "2" denoting the cross-fiber direction, and "3" denoting the radial or transmural direction). In other words, E_{11} is myofiber strain, E_{22} is cross-fiber (in-plane) strain, E_{33} is radial strain, $E_{23} = E_{32}$ is shear strain in the plane perpendicular or transverse to the myofiber direction, $E_{12} = E_{21}$ is shear strain in the plane transverse to the radial direction, and $E_{13} = E_{31}$ is shear strain in the plane transverse to the cross-fiber direction. Equation (3.2) is a major simplification of Eq. (3.1). For example (assuming homogeneous material properties), Eq. (3.2) has only four unknown material parameters to be determined from experimental measurements, whereas Eq. (3.1) has, in general, (81 + 1 + 81 + 9 + 81 =) 253 unknown material parameters. How did we go from 253 to only 4 material parameters? The answer: material symmetry. We could

go all the way down to only two material parameters if passive myocardium was isotropic ($b_f = b_t = b_{fs}$). However, we know that it is instead anisotropic, with passive stiffness in the myofiber direction about three times greater than that in the plane transverse to the myofiber direction. It is interesting to note that this 3:1 fiber:transverse ratio holds for the propagation of electricity and diffusion of water molecules in ventricular myocardium as well. Based on a number of our cylindrical and finite element modeling studies that used a range of different myofiber orientation distributions, we recommend for a normal canine heart the following values for the material constants in Eq. (3.2): $C = 0.88$ kPa, $b_f = 18.5$, $b_t = 3.56$, and $b_{fs} = 1.63$.

3.3 Mechanics of Active Contraction in Cardiac Muscle

What about the mechanics of active contraction in cardiac muscle? Can we find values for C, b_f, b_t, and b_{fs} in Eq. (3.2) that would allow us to model the regional mechanics of a beating left ventricle (LV)? The answer: not without changing the unloaded or strain-reference configuration. Otherwise, the volume at the end of ejection would never decrease below the unloaded volume, which is not physiological. We believe a better approach follows from experimental measurements of the force, length, velocity of shortening and calcium concentration relationship for cardiac muscle (Section 10.5 of Biomechanics [1]). Cardiac muscle physiologists, especially those trained to use the laser diffraction techniques championed by Dr. Henk ter Keurs, are interested in measuring the active component of myofiber stress and relating it to the entire sarcomere length time course. For example, in the study of tension development and sarcomere length in rat cardiac trabeculae by [2] passive stress and peak total stress during a twitch was measured over the full range of sarcomere lengths believed to occur in the heart (1.6–2.4 μm). They found that the shape of the relationship between peak active stress (peak total stress minus passive stress) and sarcomere length depended on calcium concentration ([Ca]) in the muscle bath (linear relationship at [Ca] = 0.5 mM; concave up at [Ca] < 0.5 mM; concave down at [Ca] > 0.5 mM) (Fig. 3.1). How can we generalize this finding to a 3-D constitutive equation for intact ventricular myocardium? The answer: define total 3-D myocardial stress as the sum of passive 3-D myocardial stress (derived from Eq. 3.2) and an active uniaxial stress component in the (local) myofiber direction that is a function of *time*, *sarcomere length,* and *intracellular calcium concentration*.

The effect of sarcomere length on the time course of isometric tension development is shown in Fig. 3.2. The time courses of predicted active tension (dashed lines) are very similar to those of measured active force (solid lines). Time-to-peak tension depends on the rise in free calcium whereas the decay of force is determined by decline in actin activation and slowing of cross-bridge cycling rates.

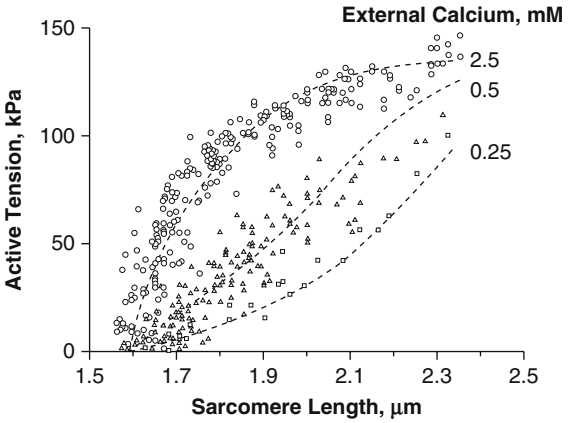

Fig. 3.1 The effect of external calcium on the peak active tension–sarcomere length relation. The relation between peak active tension predicted by the model (*dashed lines*) and sarcomere length is in good agreement with measurements at external calcium concentrations of 0.25 mM (*squares*), 0.5 mM (*triangles*), and 2.5 mM (*circles*). The experimental relation at 2.5 mM external calcium was used to determine the length-dependence of the model calcium affinity. Lowering peak free calcium from 4.35 μM to 2 μM shifted this relation to that at 0.5 mM external calcium. This information was used to predict the peak tension–sarcomere length relation at an external calcium concentration of 0.25 mM (1.194 μM free calcium) (From Guccione and McCulloch [8], with permission from ASME)

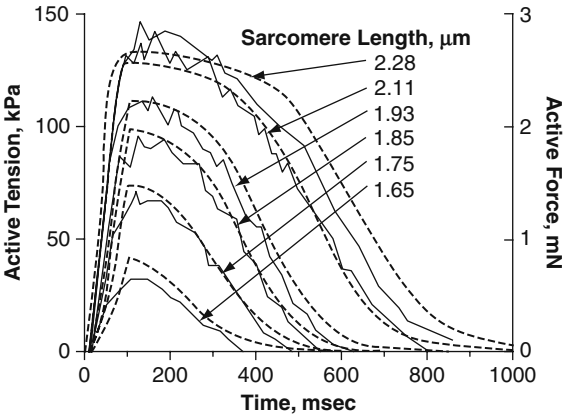

Fig. 3.2 The effect of sarcomere length on the time course of isometric tension development. The time courses of predicted active tension (*dashed lines*) are very similar to those of measured active force (*solid lines*) (From Guccione and McCulloch [8], with permission from ASME)

3.4 Constitutive Relations for Fiber Stress That Describe Deactivation

One very interesting phenomenon that has been observed in isolated cardiac muscle but is not shown in Section 10.5 of Biomechanics [1] is deactivation. A rapid change of length applied during isometric contraction of skeletal or cardiac muscle

may result in redeveloped tension less than appropriate for the new length because of "deactivation" of the contractile system. The amount of shortening deactivation is directly related to both the time during the contraction when the length change occurs and to the extent of muscle shortening (Fig. 3.3). If the muscle is permitted to shorten early in the contraction, the redeveloped tension will be appropriate to the new length as predicted from the classic Frank–Starling relationship. However, the same length change, which is imposed later in the contraction, results in a redeveloped tension that is less than predicted. Furthermore, a greater change in length results in less tension being redeveloped than if a smaller length decrement is applied at the same time during the contraction. It has been demonstrated that the reduced tension during active muscle shortening is associated with reduced affinity of troponin C for Ca^{2+}. The free Ca^{2+} is then picked up by the sarcoplasmic reticulum (SR), with less Ca^{2+} available for tension development until the subsequent contraction [3].

The distribution moment (DM) model [4] has simulated experimental data on skeletal muscle, but it has not been used previously to study the mechanics of active contraction in cardiac muscle. In contrast to previous models of striated muscle contraction, all parameters have physical meaning, and assumptions concerning biophysical events within the cell are consistent with available data. In order to simulate cardiac muscle deactivation using the DM model it was necessary to make the cross-bridge detachment rates large for large displacements from the neutral equilibrium position of a cross-bridge. To examine the effect of cooperativity on cardiac muscle contraction, we used the DM model's tight coupling scheme with binding of one or two calcium sites regulating contraction. As observed experimentally, our model predicted a reduction of isometric tension development following rapid shortening lengthening transients when contraction is regulated by either one or two calcium binding sites. The predicted deactivating effect increased if the transient was applied late in the twitch when contraction is regulated by two calcium binding sites, but not when it is regulated by one site (Fig. 3.4). This is the first study in which deactivation has been simulated without making any provisions for length-dependent calcium troponin dissociation [5].

3.5 Cylindrical Models of the Systolic Left Ventricle

In the study of Guccione and associates [6], models of contracting ventricular myocardium were used to study the effects of different assumptions concerning active tension development on the distributions of stress and strain in the equatorial region of the intact LV during systole. Three models of cardiac muscle contraction were incorporated (Fig. 3.5) in a cylindrical model for passive left ventricular mechanics developed previously [7]. Systolic sarcomere length and fiber stresses predicted by a general "deactivation" model of cardiac contraction [8] were compared with those computed using two less complex models of active fiber stress. In a time-varying "elastance" model (Eq. 3.3), isometric tension development was

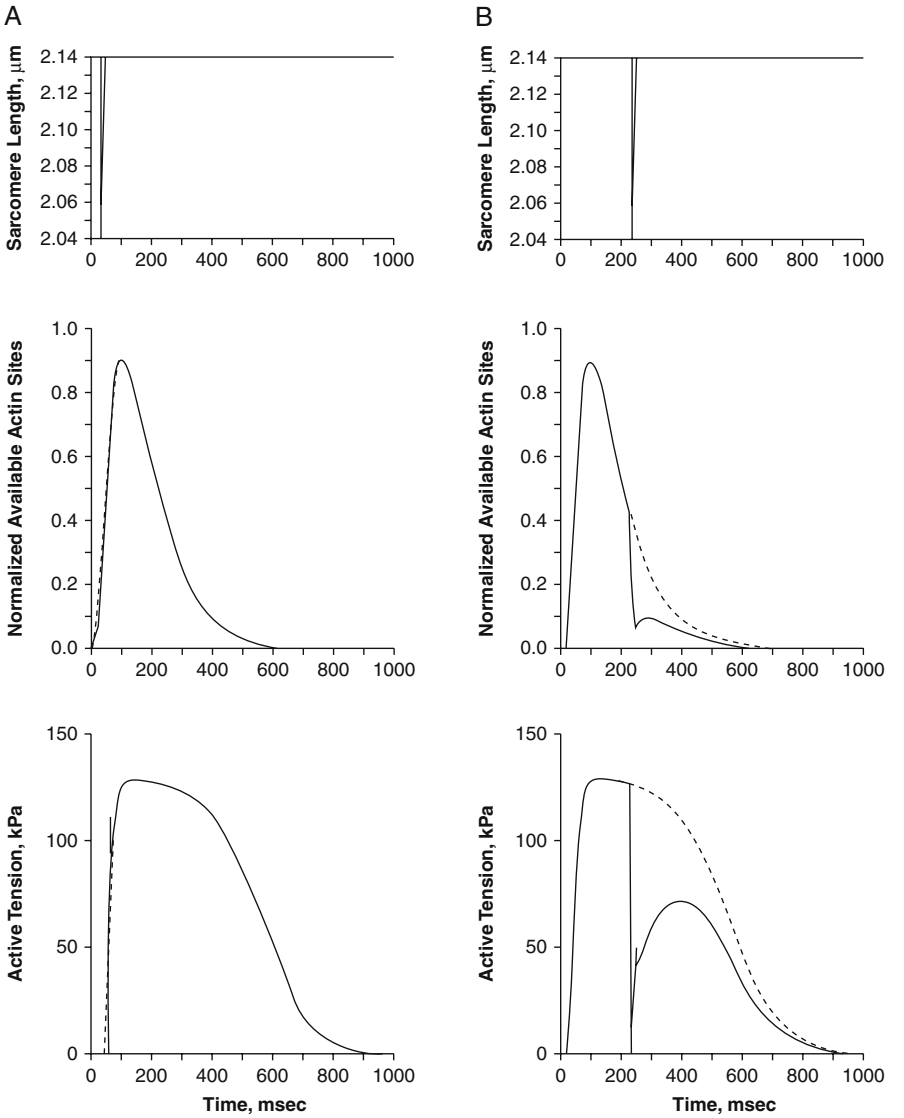

Fig. 3.3 The effect of shortening transients applied at different times during an isometric twitch on predicted tension redevelopment. Transients imposed before time-to-peak tension have little effect on tension redevelopment (**a**), but those applied during relaxation produce deactivation (**b**). During the transient of 20 ms duration, shortening and lengthening velocities are 10 μm/s. A control contraction (*dashed line*) was predicted at a constant sarcomere length of 2.14 μm. In **a**, the shortening impulse was applied 20 ms after onset of contraction. Afterwards, redeveloped actin binding sites and twitch tension (*solid lines*) attained control levels for the remainder of the contraction since free calcium was still rising. In **b**, the shortening impulse was applied 220 ms after onset of contraction. Afterwards, redeveloped actin binding sites and twitch tension (*solid line*) never reach control levels because free calcium was less than 25% of maximum (From Guccione and McCulloch [8], with permission from ASME)

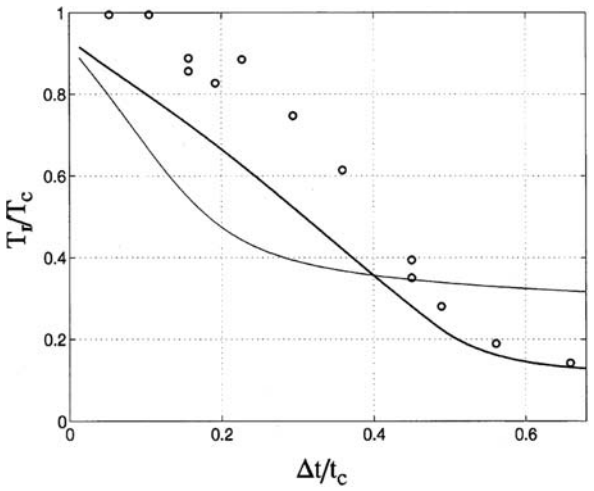

Fig. 3.4 The predicted deactivating effect increases if the shortening transient is applied late in the twitch when contraction is regulated by two calcium binding sites (*thick line*), but not when it is regulated by one site (*thin lines*). Peak redeveloped tension (T_r) divided by control tension (T_c) at that time is plotted against the interval between contraction onset and the end of the length transient (Δt) divided by control contraction duration (t_c). The experimental data (*circles*) of [23] are shown for comparison (From Guccione et al. [5], with permission from Elsevier)

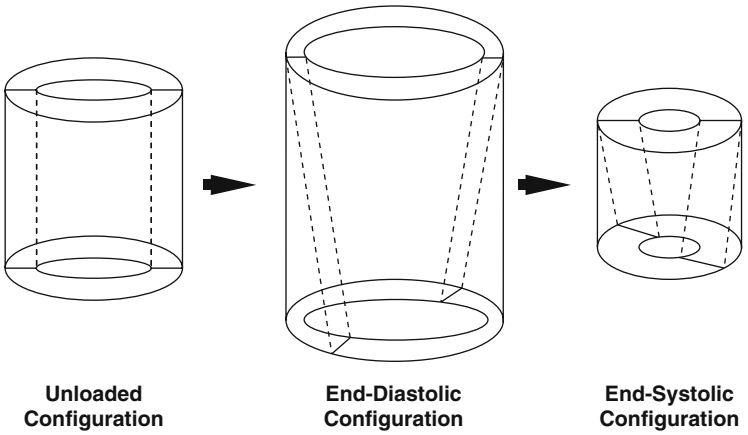

Fig. 3.5 Passive and active left ventricular deformation modeled by inflation, stretch, and twist of a cylinder (From Guccione et al. [6], with permission from ASME)

computed from a function of peak intracellular calcium concentration, time after contraction onset, and sarcomere length; a "Hill" model was formulated by scaling this isometric tension using the force–velocity relation derived from the deactivation model.

For the same calcium ion concentration, the sarcomeres in the deactivation model shortened approximately 0.1 μm less throughout the wall at end-systole than those in the other models. Thus, muscle fibers in the intact ventricle are subjected to rapid length changes that cause deactivation during the ejection phase of a normal cardiac cycle.

In Material_128 of LS-DYNA, the active fiber directional stress component is defined by a time-varying elastance model, which at end-systole is reduced to [9, 10],

$$T_0 = \frac{1}{2} T_{\max} \frac{\mathrm{Ca}_0^2}{\mathrm{Ca}_0^2 + E\mathrm{Ca}_{50}^2} \left(1 - \cos\left(\frac{0.25}{m l_R \sqrt{2E_{11}+1} + b} + 1\right)\pi\right), \tag{3.3}$$

with m and b as constants, and the length-dependent calcium sensitivity, $E\mathrm{Ca}_{50}$, is given by

$$E\mathrm{Ca}_{50} = \frac{(\mathrm{Ca}_0)_{\max}}{\sqrt{\exp[B(l_R\sqrt{2E_{11}+1} - l_0)] - 1}}, \tag{3.4}$$

where B is a constant, $(\mathrm{Ca}_0)_{\max}$ is the maximum peak intracellular calcium concentration, l_0 is the sarcomere length at which no active tension develops, and l_R is the stress-free sarcomere length. The material constants for active contraction were found to be [11]: $\mathrm{Ca}_0 = 4.35$ μmol/L, $(\mathrm{Ca}_0)_{\max} = 4.35$ μmol/L, $B = 4.75$ μm^{-1}, $l_0 = 1.58$ μm, $m = 1.0489$ s μm^{-1}, $b = -1.429$ s, and l_R was set at 1.85 mm. Figure 3.6 shows isometric twitches predicted by the Deactivation model, Hill model, and Elastance model at three different sarcomere lengths

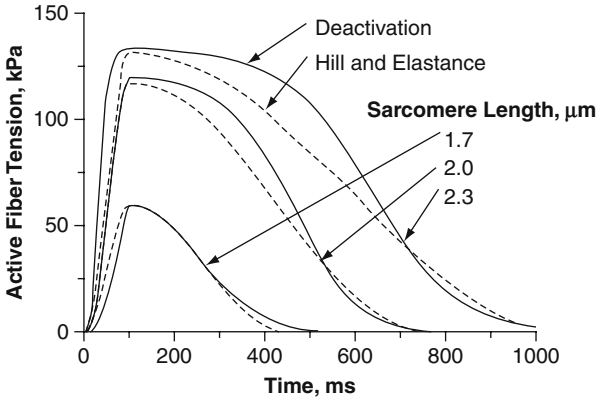

Fig. 3.6 Comparison of isometric twitches predicted by the "Deactivation" model, "Hill" model, and "Elastance" model at a range of sarcomere lengths. Twitches computed by the different models are similar except for the relaxation phase at long lengths. However, this difference does not affect the conclusions drawn from the ventricular models (From Guccione et al. [6], with permission from ASME)

ranging from 1.7 to 2.3 μm. The largest difference in the two sets of predicted tension time courses occurred during relaxation. The transmural sarcomere length distribution predicted at end-diastole increased from 2.17 μm at the endocardium to a maximum of 2.23 μm at the subendocardium and then decreased to 2.16 μm at the epicardium as shown in Fig. 3.7. In Fig. 3.8,

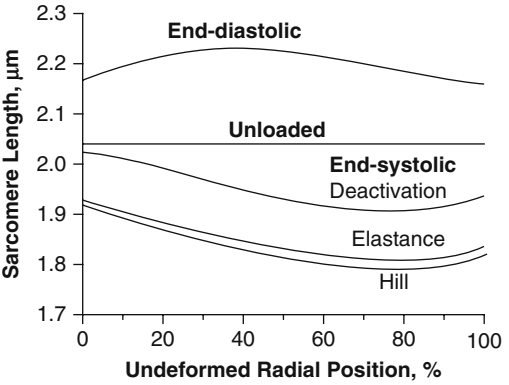

Fig. 3.7 Transmural sarcomere length distributions predicted by the three models in the unloaded reference state, at end-diastole and at end-systole. The end-diastolic distribution has a maxima at 37% of the wall thickness from the endocardium. Sarcomeres in the deactivation model shorten much less than those in the other models at all transmural locations. Therefore, deactivation occurs during the ejection phase of a normal cardiac cycle. Note that the three end-systolic distributions are of identical shape (From Guccione et al. [6], with permission from ASME)

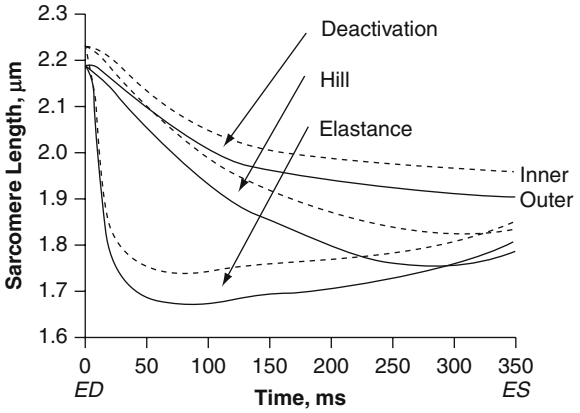

Fig. 3.8 Predicted sarcomere lengths at two transmural locations in the left ventricular wall plotted as a function of time from end-diastole to end-systole. Inner, 34.6% of wall thickness from endocardium; Outer, 78.2%. Note differences between sarcomeres in deactivation and Hill models increase with time from 100 ms to 300 ms after end-diastole, and peak sarcomere shortening is slightly less and occurs much later in Hill model than in elastance model (From Guccione et al. [6], with permission from ASME)

sarcomere lengths at two transmural locations in all three models are plotted as a function of time from end-diastole. The "Inner" and "Outer" sarcomeres are located at positions 34.6% and 78.2%, respectively, across the wall thickness from the endocardium. Differences between sarcomere lengths in the deactivation and Hill models increase with time between 100 ms and 300 ms after onset of contraction where free calcium decreases rapidly in the former model.

Based on the biaxial stretching experiments of [12] and FE analyses of [13, 14], it has been found that cross-fiber, in-plane stress equivalent to 40% of that along the myocardial fiber direction should be incorporated into models of active contraction. It should be noted that when the cross-fiber, in-plane stress component is implemented, Ca_0 should be less than the $(Ca_0)_{max}$ reported above, in order to reproduce the results found in [11]. The results reported in works before 2005 could be replicated with the 40% cross-fiber, in-plane stress and a Ca_0 that is less than $(Ca_0)_{max}$, but the conclusions of those papers would be unaltered.

3.6 The Effects of Cross-Fiber Deformation on Axial Fiber Stress in Myocardium

We incorporated a 3-D generalization of the Huxley cross-bridge theory in a finite element model of ventricular mechanics to examine the effect of nonaxial deformations on active stress in myocardium [15]. According to this new theory, which assumes that macroscopic tissue deformations are transmitted to the myofilament lattice, lateral myofilament spacing affects the axial fiber stress (Fig. 3.9). We calculated stresses by Eq. (3.5) and deformations at end-systole under the assumption of strictly isometric conditions. Equation (3.5) describes the normalized twitch force assuming that $\alpha(1) = 1$ (full overlap), as $F(1) = 1$ by definition of F. The maximum axial twitch tension, $\sigma_{ua}^{(a)}$, for uniaxial is measured as a function of sarcomere length, the conditions of isotropic transverse deformation ($\lambda_x = \lambda_y = \lambda_r = \rho$), and incompressibility ($\lambda_y^2 \lambda_z = 1$).

$$\frac{\sigma_{ua}^{(a)}}{(\sigma_{ua}^{(a)})_{\lambda_{z=1}}} = \lambda_z \alpha(\lambda_z) \frac{\left[1 + \frac{1}{\beta^*}\left\{\frac{1}{\Phi(1)F(\lambda_z^{-1/2})} - 1\right\}\right]^{-1}}{\left[1 + \frac{1}{\beta^*}\left\{\frac{1}{\Phi(1)} - 1\right\}\right]^{-1}} \tag{3.5}$$

Estimates for the overlap function $\alpha(\lambda_z)$ were calculated geometrically from the myofilament dimensions [16]. In this work, F(1), a constant scaling factor was equal to 4/5. This leaves only β^* (i.e., the value of the activation factor at twitch peak) unknown on the right-hand side of Eq. (3.5), whereas the left-hand side is known from experiment as a function of the sarcomere length, or equivalently, of

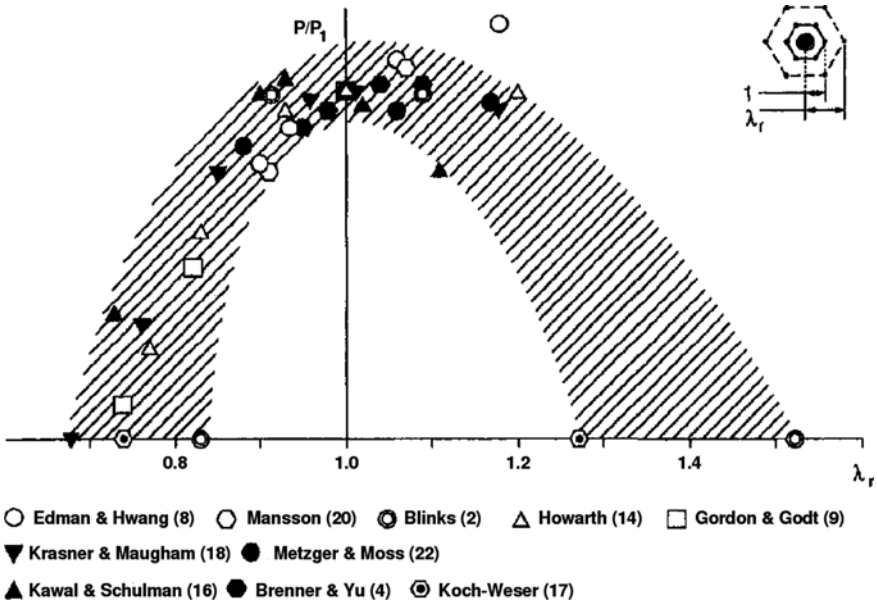

Fig. 3.9 Relation between isometric force and lateral myofilament spacing estimated from several published experiments involving osmotic perturbations of intact and skinned fibers. Closed symbols are for skinned fibers and open symbols are for intact fibers. $\lambda_r = 1$ corresponds to the lattice spacing under isotonic conditions at optimal sarcomere length (where maximum axial tetanic stress is generated). The shaded "arch" indicates the authors' subjective impression of the trend and range of the available data (From Zahalak et al. [15], with permission from ASME)

λ_z. This calculation yielded a value of β^* that varied little with λ_z, so in subsequent analysis β^* was given the constant value 0.4, and this reproduced the isometric twitch-tension curve reasonably well.

Figure 3.10 shows a schematic diagram of a section of myocardium in the undeformed state and the deformed state. Figure 3.11 shows computed passive, end-systolic fiber, and total Cauchy stresses, plotted as a function of sarcomere length, for the case of uniform extension in the fiber direction when $I_R = 1.85\ \mu$m. Our results suggest that at the end of ejection, nonaxial deformations may significantly reduce active axial fiber stress in the inner half of the wall of the normal LV (18–35% at endocardium, depending on location with respect to apex and base). Moreover, this effect is greater in the case of a compliant ischemic region produced by occlusion of the left anterior descending or circumflex coronary artery (26–54% at endocardium). On the other hand, stiffening of the remote and ischemic regions (in the case of a 2-week-old infarct) lessens the effect of nonaxial deformation on active stress at all locations (9–32% endocardial reductions). These calculated effects are sufficiently large to suggest that the influence of nonaxial deformation on active fiber stress may be an important consideration in cardiac mechanics.

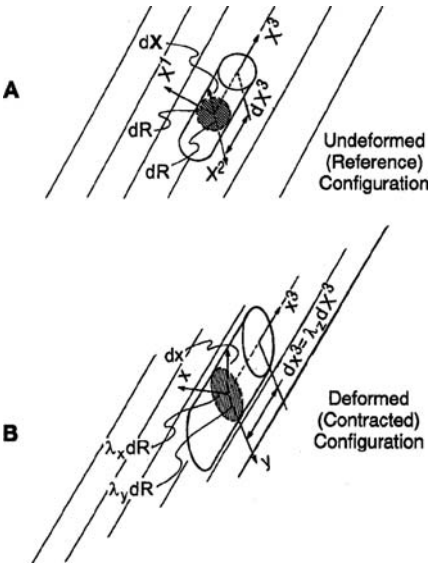

Fig. 3.10 Schematic diagram of a section of myocardium in the undeformed state, showing the general material coordinates (X^1, X^2, X^3), and the deformed state, showing the special spatial coordinates (x, y, x^3). Note the deformation of a material circular cylinder into a spatial elliptic cylinder, with the principal axes of the cross-section lying along the x and y directions (From Zahalak et al. [15], with permission from ASME)

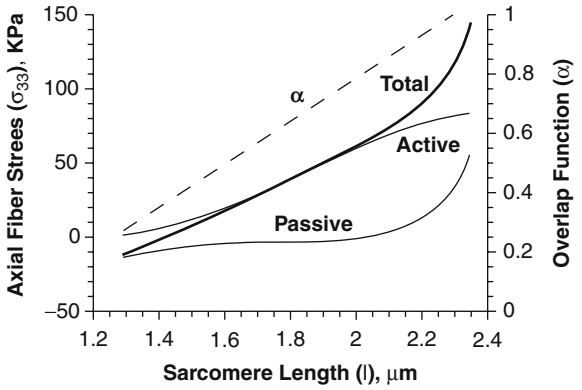

Fig. 3.11 Computed passive, end-systolic fiber and total Cauchy stresses, plotted as a function of sarcomere length, for the case of uniform extension in the fiber direction when $I_R = 1.85$ μm. The active stress shown is a graph of Eq. (3.5), with $(\sigma_{ua}^{(a)})_{\lambda_z=1} = (\sigma/2)/[1 + \{\Phi(1)^{-1} - 1\}/\beta^*]$. The parameter values are F(1) = 0.8, $\beta^* = 0.4$, and $\sigma_0 = 272$ kPa. The passive stress is computed from Eq. (3.2), with the parameter values of $C = 0.88$ kPa, $b_f = 18.48$, $b_t = 3.58$, and $b_{fs} = 1.63$. The computed overlap function, a, is also shown as a function of sarcomere length and was computed from the geometric model of Landesberg and Sideman [16]. In the unloaded reference model configuration, I_R varies linearly across the wall from 1.78 μm (endocardium) to 1.91 μm (epicardium). The reference sarcomere length for calculation of λ_z is 2.36 μm (From Zahalak et al. [15], with permission from ASME)

3.7 Experimental Measurements Used to Validate Regional Ventricular Mechanics Models

By "regional" ventricular mechanics models we mean mathematical models based on the conservation laws of continuum mechanics that can compute at least transmural distributions of left ventricular wall stress and strain. These distributions are statically indeterminant, which means they cannot be determined by statics or a force balance between left ventricular pressure and average stress across the wall or the Law of LaPlace, which ignores myocardial material properties. To date, there is no experimental methodology available to validate such models with direct measurements of forces or stress in an intact LV. As an alternative, we have used experimental measurements of 2-D and 3-D myocardial strain and left ventricular pressures and volumes to validate our regional ventricular mechanics models.

The following are examples concerning our models of normal regional ventricular mechanics. The epicardial strain measurements by [6] using bi-plane video imaging of epicardial markers during passive inflation of the LV in isolated arrested canine hearts were used to validate the cylindrical and finite element models of [7, 17]. The transmural 3-D end-systolic strain measurements by [18, 19] using bi-plane X-ray of radiopaque markers implanted in beating canine hearts were used to validate the cylindrical and finite element models of [6, 11, 15]. The transmural 3-D passive strain measurements by [20] using bi-plane X-ray of radiopaque markers implanted in isolated arrested canine hearts were also used to validate the finite element model of [11]. In one of our studies of normal regional ventricular mechanics, active myocardial stress was actually measured rather than computed. However, this was a very novel study in which twitching cardiac trabeculae from the rat right ventricle were subjected to sarcomere length time courses that we measured in anterior and posterior LV regions of beating canine hearts using bi-plane X-ray of implanted radiopaque markers and ex vivo histological study [21, 22].

Acknowledgments This work was supported by National Institutes of Health grant 5R01 HL077921 (Dr. Guccione). This support is gratefully acknowledged.

References

1 Fung YC. Biomechanics: mechanical properties of living tissues. New York: Springer-Verlag, 1993.
2 ter Keurs HE, Rijnsburger WH, van Heuningen R, Nagelsmit MJ. Tension development and sarcomere length in rat cardiac trabeculae. Evidence of length-dependent activation. *Circ Res*. 1980b;46:703–14.
3 Leach JK, Priola DV, Grimes LA, Skipper BJ. Shortening deactivation of cardiac muscle: physiological mechanisms and clinical implications. *J Investig Med*. 1999;47:369–77.
4 Zahalak GI, Ma SP. Muscle activation and contraction: constitutive relations based directly on cross-bridge kinetics. *J Biomech Eng*. 1990;112:52–62.
5 Guccione JM, Motabarzadeh I, Zahalak GI. A distribution-moment model of deactivation in cardiac muscle. *J Biomech*. 1998;31:1069–73.

6 Guccione JM, Waldman LK, McCulloch AD. Mechanics of active contraction in cardiac muscle: Part II – Cylindrical models of the systolic left ventricle. *J Biomech Eng*. 1993;115:82–90.
7 Guccione JM, McCulloch AD, Waldman LK. Passive material properties of intact ventricular myocardium determined from a cylindrical model. *J Biomech Eng*. 1991;113:42–55.
8 Guccione JM, McCulloch AD. Mechanics of active contraction in cardiac muscle: Part I – Constitutive relations for fiber stress that describe deactivation. *J Biomech Eng*. 1993;115: 72–81.
9 Tozeren A. Constitutive equations of skeletal muscle based on cross-bridge mechanism. *Biophys J*. 1985a;47:225–36.
10 Tozeren A. Continuum rheology of muscle contraction and its application to cardiac contractility. *Biophys J*. 1985b;47:303–9.
11 Guccione JM, Costa KD, McCulloch AD. Finite element stress analysis of left ventricular mechanics in the beating dog heart. *J Biomech*. 1995;28:1167–77.
12 Lin DH, Yin FC. A multiaxial constitutive law for mammalian left ventricular myocardium in steady-state barium contracture or tetanus. *J Biomech Eng*. 1998;120:504–17.
13 Usyk TP, Mazhari R, McCulloch AD. Effect of laminar orthotropic myofiber architecture on regional stress and strain in the canine left ventricle. *J Elasticity*. 2000;61:143–64.
14 Walker JC, Ratcliffe MB, Zhang P, Wallace AW, Fata B, Hsu EW, Saloner D, Guccione JM. MRI-based finite-element analysis of left ventricular aneurysm. *Am J Physiol Heart Circ Physiol*. 2005;289:H692–700.
15 Zahalak GI, de Laborderie V, Guccione JM. The effects of cross-fiber deformation on axial fiber stress in myocardium. *J Biomech Eng*. 1999;121:376–85.
16 Landesberg A, Sideman S. Mechanical regulation of cardiac muscle by coupling calcium kinetics with cross-bridge cycling: a dynamic model. *Am J Physiol*. 1994;267:H779–95.
17 Guccione JM, McCulloch AD. Finite element modeling of ventricular mechanics. In: Theory of heart: biomechanics, biophysics, and nonlinear dynamics of cardiac function, edited by Glass L, Hunter PJ, McCulloch AD, New York: Springer-Verlag, 1991, p. xvii, 611p, pp. 121–44.
18 Waldman LK, Fung YC, Covell JW. Transmural myocardial deformation in the canine left ventricle. Normal in vivo three-dimensional finite strains. *Circ Res*. 1985;57:152–63.
19 Waldman LK, Nosan D, Villarreal F, Covell JW. Relation between transmural deformation and local myofiber direction in canine left ventricle. *Circ Res*. 1988;63:550–62.
20 Omens JH, May KD, McCulloch AD. Transmural distribution of three-dimensional strain in the isolated arrested canine left ventricle. *Am J Physiol*. 1991;261:H918–28.
21 Guccione JM, Le Prell GS, de Tombe PP, Hunter WC (1997a) Measurements of active myocardial tension under a wide range of physiological loading conditions. *J Biomech* 30, 189–92.
22 Guccione JM, O'Dell WG, McCulloch AD, Hunter WC. Anterior and posterior left ventricular sarcomere lengths behave similarly during ejection. *Am J Physiol*. 1997b;272:H469–77.
23 ter Keurs HE, Rijnsburger WH, van Heuningen R. Restoring forces and relaxation of rat cardiac muscle. *Eur Heart J*. 1980a;Suppl A:67–80.

Chapter 4
Determination of Myocardial Material Properties by Optimization

Jonathan F. Wenk, Choon-Sik Jhun, Kay Sun, Nielen Stander, and Julius M. Guccione

Abstract The previous chapter includes a computationally efficient strain energy function for describing the three-dimensional relationship between stress and strain in passive myocardial material properties, the material parameters of which were formally optimized using left ventricular pressure and epicardial strain measurements in a cylindrical model. Results from such a model are confined at best to the equatorial region of the left ventricle. A finite element model of the entire left ventricle is required to determine regional variations in myocardial material properties. The most important or at least interesting finding from such a study is that myocardial contractility in the (border zone) region adjacent to a myocardial infarction is much less than (typically only half) that in regions remote from the myocardial infarction. This finding has been confirmed with active stress measurements in skinned muscle fibers dissected from these regions. This chapter is concerned with brief descriptions of the studies from our laboratory that have led up to our current knowledge concerning regional variations of myocardial contractility in infarcted left ventricles.

4.1 Introduction

Prior to the advent of tagged MRI, finite element (FE) studies of the left ventricle (LV) have validated stress calculations by showing good agreement with myocardial deformations (strains) measured with implanted markers [1, 2, 3, 4, 5]. However, this is invasive and is limited to only a few simultaneous LV locations (usually only 2). With advancements in MRI, myocardial deformation can be quantified noninvasively throughout the LV with tagged MRI [6, 7]. In a pioneering study, Moulton et al. [8] used tagged MRI to determine isotropic, diastolic material properties in

J.M. Guccione (✉)
Department of Surgery, University of California at San Francisco and San Francisco VA Medical Center, San Francisco, CA, USA
e-mail: guccionej@surgery.ucsf.edu

J.M. Guccione, et al. (eds.), *Computational Cardiovascular Mechanics*,
DOI 10.1007/978-1-4419-0730-1_4,

a two-dimensional (2-D) FE analysis of beating canine hearts. We have followed Dr. Michael Pasque's lead by using tagged MRI to measure regional myocardial strain in an ovine model of left ventricular aneurysm. The overall philosophy of our lab, however, is while it is possible for us to measure a significant effect of a novel surgical procedure or medical device on three-dimensional (3-D) myocardial strain distributions, a realistic 3-D FE model is required to interpret these strain distributions based on computed distributions of myocardial material properties and stress. Imagine how unsafe it would be to travel in an airplane designed only on the basis of the deflection of or strain within the wing (kinematics) and not also on the basis of the stresses on the materials that compose the wing (kinetics).

4.2 Epicardial Suction: An Approach to Mechanical Testing of the Passive Ventricular Wall

Mathematical models are needed to provide a sound basis for interpreting the non-homogeneous changes in cardiac mechanical function that occur in regional pathological disorders, such as ischemic heart disease, in terms of changes in the local properties of the heart muscle. Previous in vitro experiments used to estimate parameters in 3-D constitutive relations, such as biaxial testing of excised myocardial sheets or passive inflation of the isolated arrested heart, have not included significant transverse shear deformation or in-plane compression, which can occur in vivo. Therefore, the purpose of this study was to use an approach, termed epicardial suction, to quantify the material properties of intact canine left ventricular wall, especially those related to transverse shear [9].

A suction cup with a square orifice approximately 2.5×2.5 cm was positioned on the lateral free wall of the LV. The suction cup was attached to the epicardium by vacuum pressure (12 kPa) and applied continuously in the narrow channel surrounding the cup. The square suction orifice allowed the boundaries of the cup to be easily represented in our FE model. The suction cup was then attached to a holding fixture, and the suction cup and heart were then lowered into an acrylic cylinder filled with a mixture of cold saline and cardioplegic solution.

The amount of deformation during the application of epicardial suction was measured with a grid of magnetically ''tagged'' planes using a technique known as double delays alternating with nutations for tailored excitation (DANTE). On the image plane, the magnetically tagged planes appear as tag lines and their intersections as tag intersection points. As epicardial suction is applied, the heart wall deforms and images acquired at later time delays show the deformed location of the tag intersection points. These points are used to measure displacements at numerous locations.

A detailed description of the FE method we used is given in Costa et al. [10]. The Galerkin FE equations for 3-D finite elasticity were derived in prolate spheroidal coordinates, allowing the ventricular geometry and boundary conditions to be modeled with fewer low-order elements. A 3-D solid mathematical representation of the

LV was developed for each experiment from MR images of the heart. Each model had a total of 500 nodes and 360 isoparametric FEs with trilinear Lagrange basis functions for each of the prolate spheroidal coordinates. Nodes on the epicardium at the edges of the suction cup were fully constrained. The epicardial element surfaces within the suction cup boundaries were loaded with the experimentally measured pressure for each deformed configuration.

Although this method can be applied with many types of constitutive relations, for this analysis we modeled the ventricular wall as pseudoelastic and having an exponential strain energy function. The wall was modeled as either (1) a homogeneous, exponential, transversely isotropic material or (2) an exponential, transversely isotropic myocardium covered by a thin, isotropic epicardium. Following the approach in Guccione et al. [11], the passive, intact ventricular wall was modeled using the strain energy function derived in Chapter 3.

We followed an approach similar to that of Moulton et al. [12] to determine regional myocardial material properties from an FE model and a set of MR-tagged image data. However, we formulated our optimization objective function with respect to measured displacements rather than strain. We minimized the sum of the squared differences between the FE model predicted and experimental in-plane displacement components, at three suction pressures. It should be noted that for all experiments, the mean displacement error is slightly less for the model with a separate isotropic epicardium.

The complex deformation caused by the epicardial suction can be seen in short- and long-axis MR-tagged images in Fig. 4.1. At the center of the suction cup, the heart wall undergoes a bending deformation. This can be seen by the radial thickening, with circumferential and longitudinal compression near the endocardium, and radial thinning, with circumferential and longitudinal stretching near the epicardium. Away from the center of the suction cup, the initially square regions formed by adjacent tag intersection points are distorted into trapezoidal regions, which indicate significant transverse shearing. In the short-axis images, circumferential-radial shearing is seen, while longitudinal-radial shearing is seen in the long-axis images.

The deformed shape and transmural strain distributions were determined from the FE model solution using the optimized material parameters. The FE model is able to reproduce the experimental deformation pattern as shown by short- and long-axis deformed shape plots through the center of the suction cup for a representative experiment, shown in Fig. 4.2. The transmural distributions of 3-D strain components, referred to by the cardiac coordinates, are shown in Fig. 4.3a and b for the center of the suction cup at a suction pressure of 3.2 kPa. Notice that longitudinal strain is negative near the endocardium and positive near the epicardium, whereas radial strain (RS) is positive near the endocardium and negative close to the epicardium. These strain patterns correspond to the bending mode of deformation evident in Fig. 4.1. While the shear strain components are generally small at the center of the suction cup, due to the symmetry of the loading, the transverse shears, referred to by the cardiac coordinates, are larger away from the center of the cup, as shown in Fig. 4.3c and d.

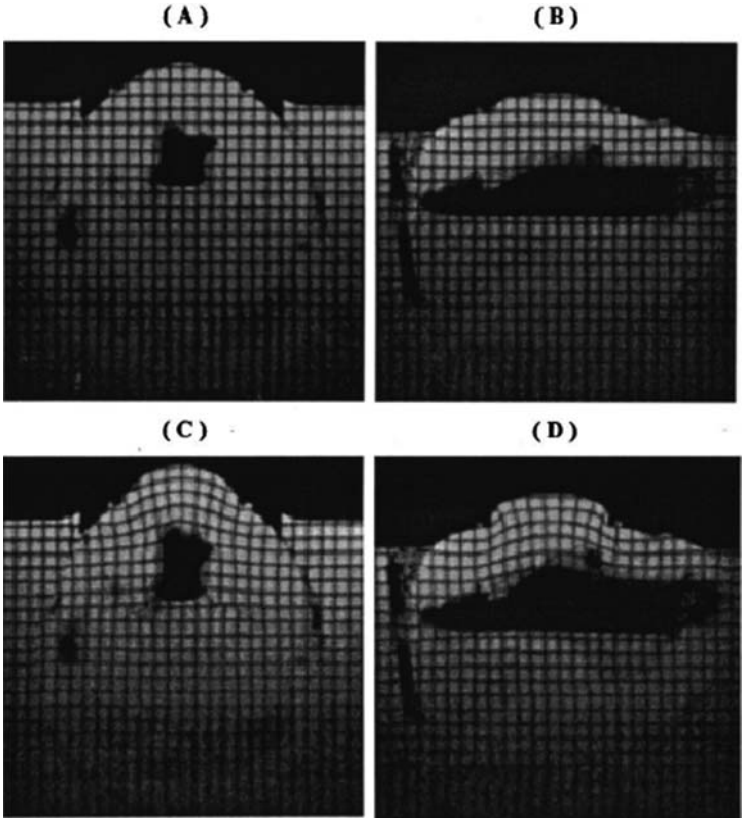

Fig. 4.1 MR-tagged images through center of suction cup for experiment 6. (**a**) and (**b**): Undeformed short- and long-axis images. (**c**) and (**d**): Images acquired at $t = 105$ ms, suction pressure $= 3.2$ kPa. (From Okamoto et al. [9], with permission from ASME.)

In this study, we developed an approach for the mechanical testing of the ventricular wall and made the first estimates of material properties for passive myocardium under significant transverse shear. This study is also the first, to our knowledge, to determine anisotropic myocardial material properties from MR tagging using a 3-D FE model. In agreement with previous studies [2], the myocardial material parameter values we obtained for both the homogeneous model and the model with separate epicardium demonstrated that myocardium is nonlinear and anisotropic with greater stiffness in the fiber direction. Our results also suggest that the epicardium plays a significant role in passive ventricular mechanics.

4.3 Akinetic Myocardial Infarcts Must Contain Contracting Myocytes, Material Parameter Estimation

Infarcted segments of myocardium demonstrate functional impairment ranging in severity from hypokinesis to dyskinesis. We sought to better define the

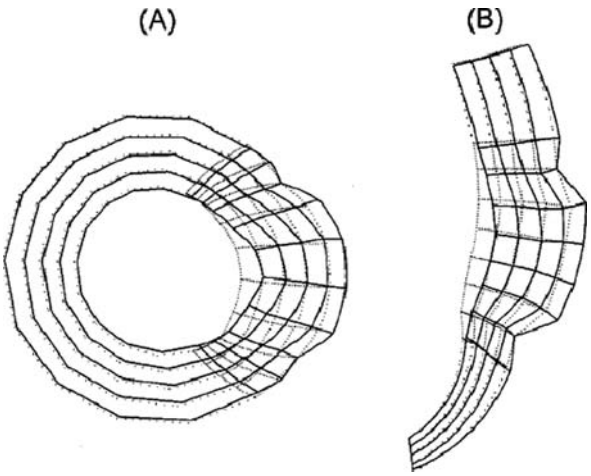

Fig. 4.2 Deformed shape plots of FE solution (Exp. 6) with optimized homogeneous material parameters at suction pressure of 3.2 kPa, corresponding to Fig. 4.1a and b. (**a**) Short-axis view through center of suction cup and (**b**) long-axis view through center of suction cup. (From Okamoto et al. [9], with permission from ASME.)

contributions of passive material properties (stiffness) and active properties (contracting myocytes) to infarct thickening. Using an FE model, we tested the hypothesis that infarcted myocardium must contain contracting myocytes to be akinetic and not dyskinetic [13]. We previously simulated [14] the border zone (BZ) of an ovine anteroapical infarct with a large deformation FE model of the LV incorporating nonlinear diastolic and systolic material properties linked to myocyte fiber architecture. Although BZ systolic function was thought to be normal and altered BZ systolic motion, the result of high stress [15], we were able to show that BZ systolic function must be reduced by 50% for the BZ to stretch during isovolumic systole [14]. Given that such FE simulations can calculate regional deformation and stress from the unloaded structural geometry (LV at early diastolic filling), external loads (LV cavity pressure), and material properties, the FE method is inherently suited to determine the contribution of contracting myocytes in akinetic vs. dyskinetic segments.

A single sheep from a group previously reported by Bowen [16] underwent anteroapical ischemia and reperfusion after 1 h. Subdiaphragmatic, 2-D long-axis echocardiographs were obtained through a sterile midline laparotomy (1.8–4.2 MHz probe, SONOS 5500; Agilent Technologies, Andover, MA) 12 weeks post-infarction and videotaped at 30 Hz. The animal model displayed significant LV remodeling at 12 weeks (infarct thickness 5.1 ± 0.3 mm; LV volume at end-systole 33 ± 6 mL) [16]. Echocardiographs at early diastolic filling (Fig. 4.4), end-diastole, and end-systole were selected, digitized, and analyzed (Findtags; Medical Imaging Lab, Johns Hopkins University, Baltimore, MD). Guided by the video echocardiogram, epicardial and endocardial contours were hand-traced, and the border between akinetic and kinetic regions identified.

Thirty two cardiac contour points were used to construct a 2-D mesh of the LV in prolate spheroidal coordinates, shown in Fig. 4.5a. Using a focal length of 25.0 mm,

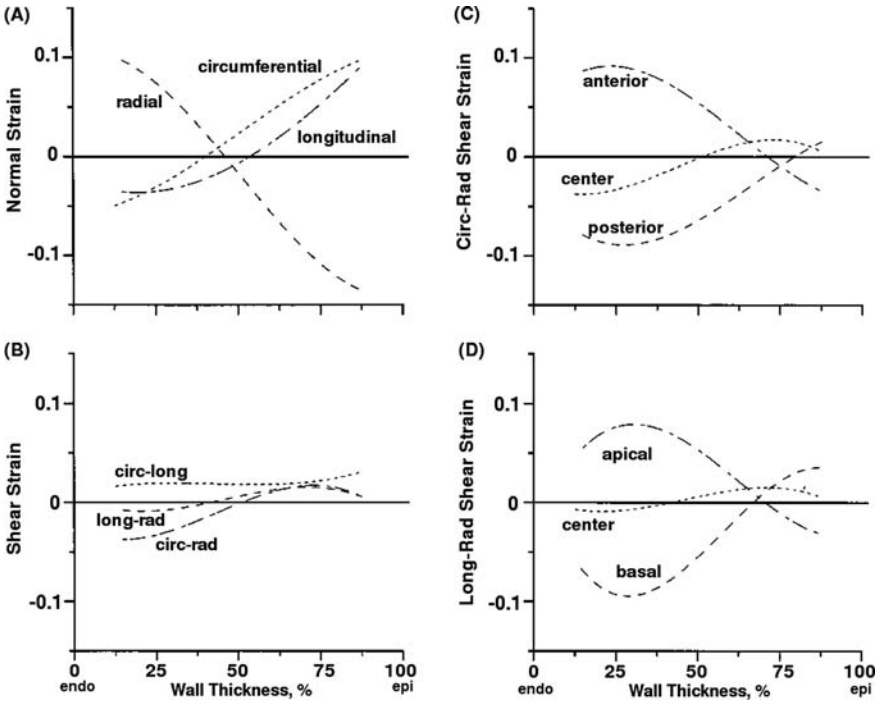

Fig. 4.3 Normal (**a**) and shear (**b**) strain components as a function of transmural position in FE elements through center of suction cup. (**c**) Radial-circumferential shear strains in elements through the center of suction cup and to the anterior and posterior of center elements. (**d**) Radial-longitudinal shear strains in elements through the center of suction cup, and in elements toward the apex and base. All values were predicted from the FE model for experiment 6 using optimized material parameters at experimental pressure of 3.2 kPa. (From Okamoto et al. [9], with permission from ASME.)

the FE software (Continuity; Cardiac Mechanics Research Group, University of California, San Diego, CA) interpolated a 3-D model composed of 16 elements. The FE mesh was subdivided into eight elements circumferentially and three elements transmurally producing the 192-element model of the end-diastolic LV, shown in Fig. 4.5b. This subdivision allowed regional, non-axisymmetric variation of the ventricular wall.

Diastolic and systolic material properties were defined using Eqs. (3.2), (3.3), and (3.4). A sharp boundary was assumed between the infarcted and uninfarcted regions, and diastolic and end-systolic material properties of the remote uninfarcted myocardium were assumed to be normal ($C = 0.876$ kPa, $T_{max} = 135.7$ kPa). Scaling the parameter T_{max} by a "percentage of contracting myocytes" between 100% and 0% reduced the ability of the infarcted region to develop active stress. This approach (as opposed to altering $(Ca_0)_{max}$) [2] does not change the shape of the relationship between active stress and sarcomere length. Of note, T_{max} represents the

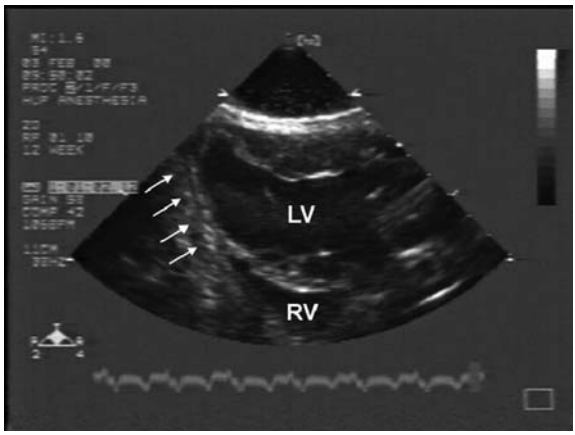

Fig. 4.4 Transesophageal echocardiogram of an ovine heart model of ischemic cardiomyopathy showing a long-axis image at the beginning of diastolic filling [13]

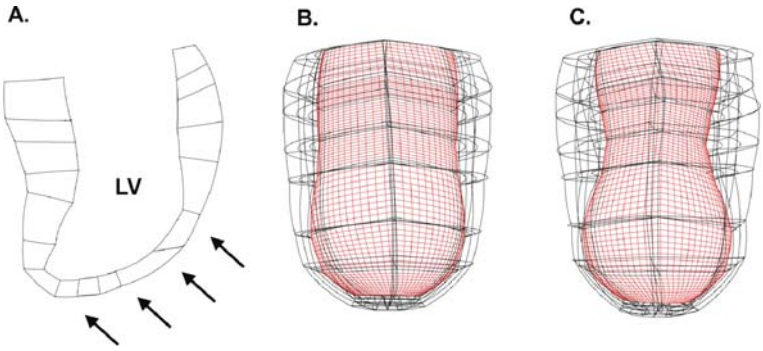

Fig. 4.5 (**a**) Two-dimensional prolate-spheroidal finite element mesh of the LV produced by tracing the endocardial and epicardial contours of the ovine echocardium. *Arrows* denote akinetic elements. (**b**) Model configuration obtained for an end-diastolic LV chamber pressure of 2.67 kPa (20 mmHg) and diastolic stiffness of 0.876 kPa. (**c**) Model configuration obtained for an end-systolic LV chamber pressure of 13.33 kPa (100 mmHg), diastolic stiffness of 0.876 kPa, and akinetic segments

percentage of surviving infarct myocytes; all are assumed to have normal contractility. In each case the end-systolic elastance (E_{ES}) is obtained by (1) incrementally increasing T_{max} in both the remote and infarct regions and load to 120 mmHg, and then (2) reducing load to 0 mmHg.

The change in wall thickness between end-diastole and end-systole was measured with the average RS, which describes the fractional change of wall thickness. Negative RS indicates thinning of the myocardial wall during systole (dyskinesis). Positive values indicate wall thickening (contraction). RS was measured at 24 locations distributed throughout the akinetic region. These represent all the locations where RS can be directly calculated in our model. Akinesis was defined as an average RS between –0.01 and 0.01. At a given diastolic stiffness, the percentage of

surviving myocytes was modified until akinesia was observed. T_{max} was increased when the RS indicated a dyskinetic heart and decreased when the result was hypokinesis until akinesis was obtained. Finally, to determine the amount of diastolic stiffness required for akinesis in a region with no contracting myocytes, we ran an initial simulation with normal diastolic stiffness and no contractility. These conditions produced a dyskinetic LV. Subsequent simulations increased diastolic stiffness in the abnormal region until akinesis was reached.

When the infarct was assigned a normal diastolic stiffness, 20% of the myocytes (T_{max} = 27.1 kPa) needed to contract in order to produce akinesis (average RS = 0.0033). Reducing the number of contracting myocytes to 10% (T_{max} = 13.6 kPa) produced a dyskinetic infarct (average RS = –0.0381) and a hypokinetic infarct (average RS = 0.0787) at 35% (T_{max} = 47.5 kPa). The difference in RS between groups (hypokinetic vs. akinetic vs. dyskinetic) was statistically significant ($P < 0.0001$). Figure 4.6 shows the RS of these models plotted against the position of the infarct. Notably, the region of the infarct closest to the BZ had the greatest variability in RS. In the akinetic and dyskinetic model, there is an increase in RS, whereas the hypokinetic model has reduced RS at the region closest to the BZ. The statistically significant difference in RS between groups ($P < 0.0001$) and pattern of akinesis flanked by dyskinesis and hypokinesis was seen in all diastolic stiffness parameters tested.

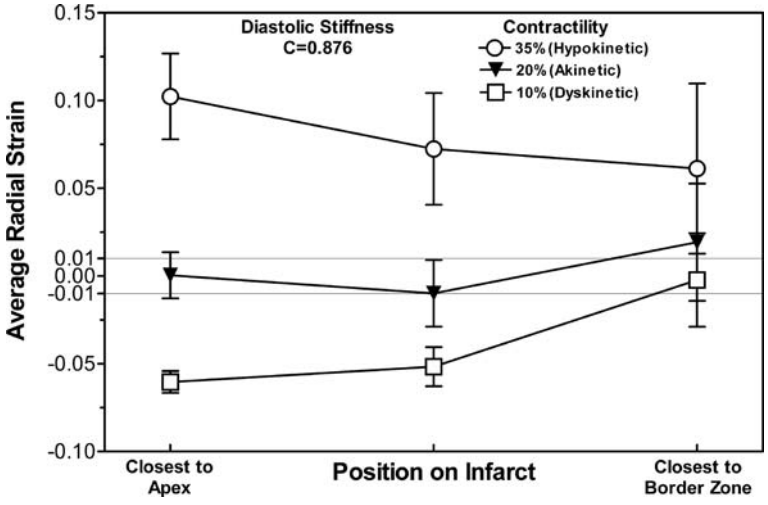

Fig. 4.6 Plot of average radial strain against location on the infarct for a heart with a diastolic stiffness (*C*) of 0.876 kPa. In the region of the infarct closest to the border zone in the akinetic and dyskinetic heart, there is an increase in radial strain, likely due to a tethering effect from the adjacent normal tissue [13]

Our simulations demonstrated that akinesis in a region void of contracting myocytes must be 285 times stiffer than normal myocardium. For instance, increasing diastolic stiffness to 100 or even 200 was insufficient for akinesia (average

RS of –0.0233 and –0.0121, respectively), i.e., the LV remained dyskinetic. In the physiological stiffness range of 0.876–10 kPa, the models with no contractility demonstrated significant dyskinesia, with average RS ranging from –0.08 to –0.07. Thus, if infarct stiffness is <285 times normal, contracting myocytes are required to prevent dyskinetic infarct wall motion. It is not merely possible for normal myocytes to survive in a region of akinesis: contracting myocytes are obligatory.

4.4 Informal Optimization of Regional Myocardial Contractility in a Sheep with Left Ventricular Aneurysm

Building on previous work [14, 13], the present study uses tagged MRI to validate nonlinear, anisotropic, 3-D FE models in four sheep with myocardial infarction (MI), in order to determine systolic material parameters in 3-D stress–strain relationships [17]. Moreover, this study incorporates ovine aneurysm material properties measured with biaxial stretching [18] and detailed helix angle measurements made with magnetic resonance diffusion tensor imaging (MR-DTI) in each heart [19].

After development of a large ventricular aneurysm (22.5 ± 1.5 weeks post-MI), systolic strains were measured with tagged MRI as described in detail previously [20]. Tagged MR images were transferred to a Silicon Graphics workstation (Mountain View, CA), where the endocardium and epicardium were contoured and tags were tracked semi-automatically. Systolic myocardial strains were calculated from tag-line deformation using the 4-D B-spline method [7] relative to cardiac coordinates (i.e., circumferential, longitudinal, and radial) at the midwall and around the circumference in each short-axis slice.

Three-dimensional FE models were created to replicate in vivo geometry at end-isovolumic relaxation by using both long- and short-axis slices. LV volume was calculated for each time frame throughout systole. The minimum LV volume was taken to be end-isovolumic relaxation, and passive material laws were assumed to hold from this point. Endocardial and epicardial surfaces, as described above, were discretized into a FE mesh containing 18 elements longitudinally, 12 elements circumferentially, and 1 element transmurally with trilinear elements in prolate spheroidal coordinates; the focal length was set to two-thirds of the distance from the base to the lowest endocardial point. Comparable to the method employed by Moustakidis et al. [21], aneurysm, remote, and BZ regions of the model were determined by ventricular wall thickness; the BZ region was defined at the steep transition in wall thickness between remote and aneurysm regions, shown in Fig. 4.7. Cardiac myofiber orientations from each heart were incorporated into the model, based on MR-DTI data. Fiber angles in the aneurysm were set to 0° to use experimentally determined aneurysm material parameters with respect to this direction [18].

Boundary constraints were applied in the same manner as described in previous models [22]. End-systolic pressure (ESP) and end-diastolic pressure (EDP) measured from the LV pressure catheter were offset by the minimum LV pressure

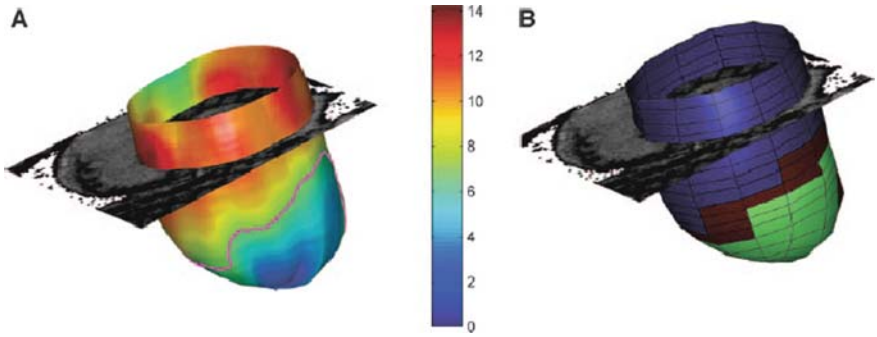

Fig. 4.7 Illustration of the border zone. (**a**) Border zone was defined at the steep transition of wall thickness between normal and aneurysm regions; color scale units are in mm. (**b**) Elements in the FE model incorporating the remote, border zone, and aneurysm regions, with the border zone at the transition [17]

and applied to the endocardium of the FE model. The diastolic and systolic material response was defined using the nonlinear, anisotropic strain energy function in Chapter 3. Previously published passive parameters for normal myocardium were used as initial values for the remote myocardium [9, 2]. Material parameters determined from biaxial stretching experiments were used in the aneurysm [18]. Because of a lack of experimental data of aneurysm tissue under shear loading, b_{fs} was kept constant across all regions. In accordance with biaxial stretching experiments of Lin and Yin [23] and FE modeling results from Usyk et al. [4], simulations were also performed with an in-plane, cross-fiber stress equal to 40% of that along the muscle fiber direction.

An iterative approach was taken to determine appropriate material parameters that reproduce the measured in vivo ventricular volumes and myocardial strains, and is summarized in [17]. Briefly, the FE model was inflated to the measured offset EDP, while the passive material parameter C was scaled independently in the aneurysm and non-aneurysm regions to get the correct end-diastolic volume (EDV). Upon convergence, the model was further inflated to the measured offset ESP, and systolic contraction was simulated in the remote region, while in the BZ, T_{max} was reduced by 50% [14]. T_{max} was then scaled until the end-systolic volume (ESV) converged. Then, midwall systolic strains were compared between tagged MRI measurements and the nearest central integration points from each element in the end-diastolic configuration, using root mean square (RMS) error. After each iteration, the strain component with the highest RMS error was addressed by scaling its corresponding passive material parameter. The entire process was manually iterated until overall RMS error improved only slightly between iterations.

Strain comparisons were very good and spanned all functional (remote, BZ, and aneurysm) and circumferential regions (anterior, posterior, lateral, and septal walls; 11 ± 3 short-axis slices, 630 ± 187 strain comparisons/animal). Figure 4.8 illustrates excellent agreement between circumferential strains measured with tagged MRI and those calculated with FE modeling in one animal (RMS error $= 0.039$).

Notice the model agrees well with the measured experimental strains around the circumference and in the aneurysm, BZ, and remote regions, shown in Fig. 8a–c. Figure 4.9 illustrates RMS error between measured strains from tagged MRI and those predicted by the FE model. The addition of in-plane, active cross-fiber stress equal to 40% of that in the fiber direction improved strain agreement in every strain component. Compared with modeling myocyte contraction only in the direction of the muscle fibers, overall RMS error decreased by 27% (0.074 ± 0.016 to 0.054 ± 0.011, $P < 0.05$) when active cross - fibre stress is included. It should be noted that stress increased from the remote region to the BZ and was highest in the aneurysm. Fiber stress increased by 24% in the BZ relative to remote regions (24.2 ± 2.7 to 29.9 ± 2.4 kPa, $P < 0.01$). Cross-fiber stress showed even greater regional anisotropy, increasing by 115% in the BZ (5.5 ± 0.7 to 11.7 ± 1.3 kPa, $P = 0.02$). Radial stress was similar in all regions.

The study outlined in this section details significant advancements in rigorously validated FE models of the LV after MI. This study includes four unique FE models customized with (1) detailed helical fiber angles measured with MR-DTI; (2) in vivo geometry measured with MRI; (3) aneurysm material properties measured with biaxial stretching; (4) in vivo volumes reproduced at measured, in vivo pressures; and (5) agreement to in vivo strains measured with tagged MRI throughout the LV. No previous biomechanical models of MI have been so rigorously validated: 630 ± 187 strain comparisons were made per animal, compared with 2 in the previous study [14]. FE model strains show significantly better agreement with experimental measurements when active cross-fiber stress is added, equal to 40% of that in the fiber direction. These biomechanical findings represent a fundamental change in modeling active myocardial contraction. Before these studies were performed, myocyte contraction was modeled only in the direction of the muscle fiber.

4.5 A Computationally Efficient Formal Optimization of Regional Myocardial Contractility in a Sheep with Left Ventricular Aneurysm

Recently, our laboratory developed a very efficient and fast method to formally optimize regional myocardial contractility from tagged MR images and cardiac catheterization pressures [24]. Our approach was demonstrated with data from sheep, 14 weeks after anteroapical myocardial infarction. The proposed method involves performing FE simulations using the customized commercial FE solver (LS-DYNA) that was programmed with the passive and active myocardial material laws described in Chapter 3. The forward FE solutions are fed into the optimization software (LS-OPT), which was customized to determine the systolic myocardial material parameters ($T_{\max}$) using the successive response surface method (SRSM) approach by targeting the in vivo systolic strains and LV volumes. The in vivo systolic strains and LV volumes were determined from tagged MRI, which also provided the LV endocardial and

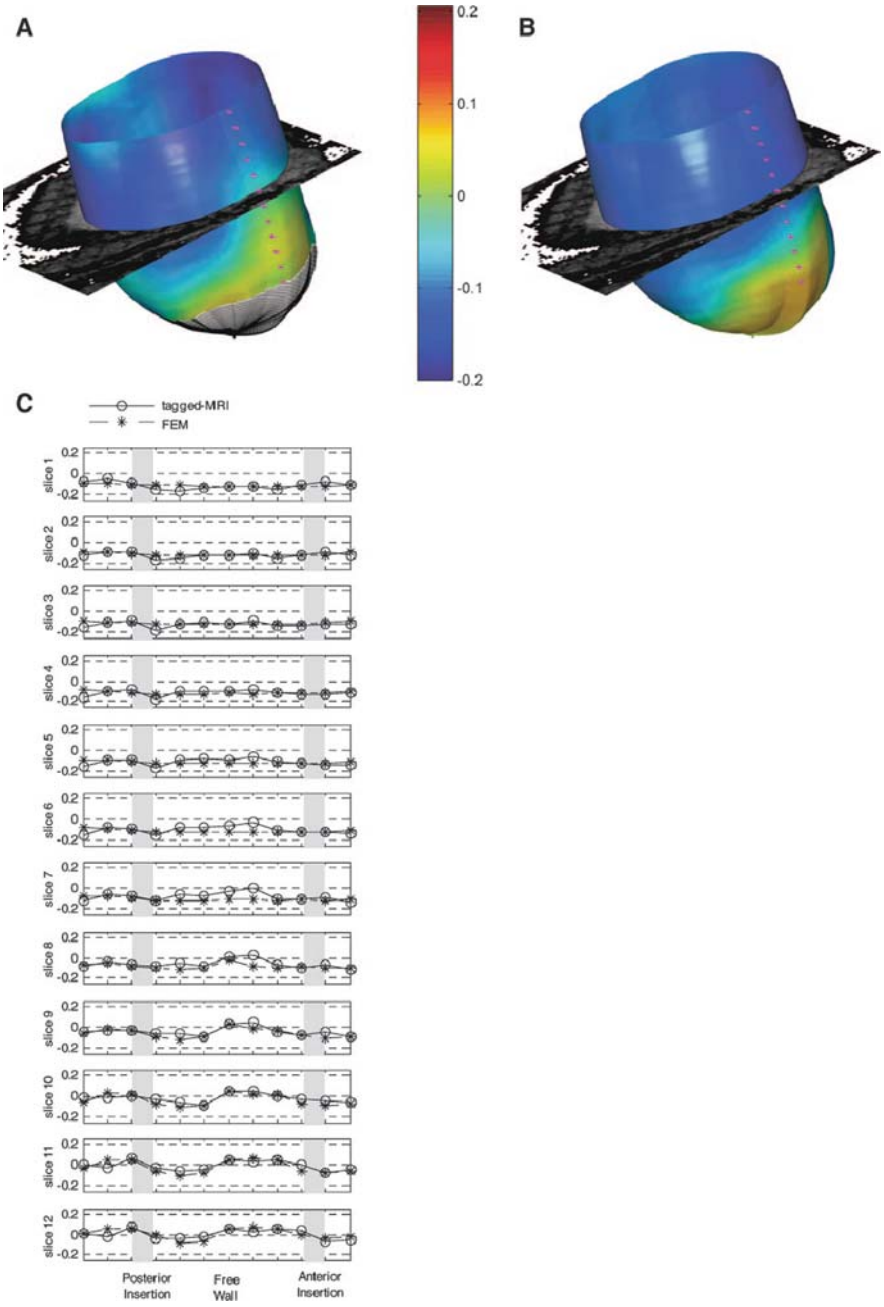

Fig. 4.8 Circumferential strains for tagged MRI (**a**) and finite element calculations (**b**). (**c**) Detailed point-by-point comparison. Slice locations in (**c**) are indicated with magenta lines in (**a**) and (**b**), with slice 1 being the most basal [17]

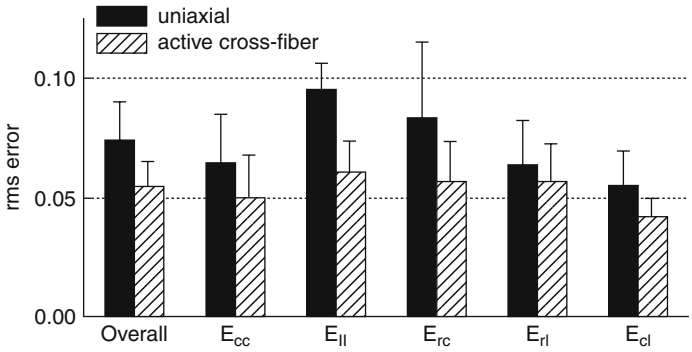

Fig. 4.9 RMS error between end-systolic strain measurements from tagged MRI and strain predictions from FE modeling. Error decreased in all strain components after the addition of active cross-fiber stress. E_{cc}, circumferential strain; E_{ll}, longitudinal strain; E_{rc}, E_{rl}, and E_{cl}, shear strains [17]

epicardial contours that were used to generate the FE model. The FE model loading conditions were obtained from cardiac catheterization measurements of LV pressures. Figure 4.10 summarizes the optimization methodology.

Data collected from adult sheep [25] were used to demonstrate the methodology and accuracy of the FE optimization tool. Briefly, the sheep underwent anteroapical myocardial infarct following the procedures described in Markovitz et al. [26]. At 14 weeks post-myocardial infarction, a series of orthogonal short- and long-axis tagged MR images were acquired as described previously [25]. The end-diastolic and end-systolic LV pressures were measured with a non-ferromagnetic transducer-tipped pressure catheter (model SPC-320; Millar Instruments, Houston, TX) inserted into the LV via sterile neck incisions [25] and used to define the endocardial boundary conditions of the FE model.

A customized version of the MR image tagging post-processing software, FindTags (Laboratory of Cardiac Energetics, National Institutes of Health, Bethesda, MD) was used to contour the endocardial and epicardial LV surfaces and also to segment the systolic tags for each image slice [27]. Systolic myocardial strains (six Lagrangian Green's strain tensor components in cylindrical coordinates; circumferential, longitudinal, and radial) at midwall and around the circumference in each short-axis slice were calculated from tag-line deformation using the 4-D B-spline-based motion tracking technique [7], as shown in Fig. 4.11.

An FE model was created using early diastole as the initial unloaded reference state since the LV pressure is lowest at this point and therefore stress is at a minimum. From the LV contours at early diastole, aneurysm, remote, and BZ regions were determined based on the ventricular wall thickness. Specifically, the BZ region is defined as the steep transition in wall thickness between remote and aneurysm regions [21]. Surface meshes were then created from the LV contours to replicate the in vivo geometry, as well as measure EDV and ESV (Rapidform, INUS

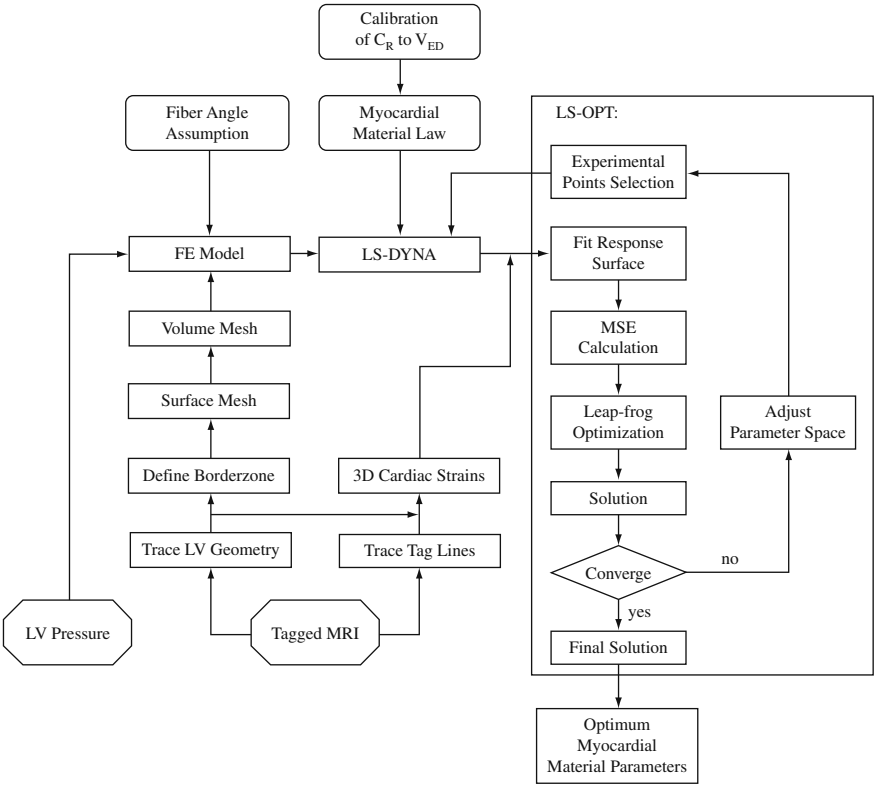

Fig. 4.10 A flowchart illustrating the process involved in determining the optimum myocardial material parameters from tagged MR images and LV pressures from cardiac catheterization

Technology, Inc., Sunnyvale, CA). The spaces between the endocardium and epicardium surfaces were filled with eight-node trilinear brick elements with a single integration point, for computational efficiency, to generate a volumetric mesh that is refined into three elements transmurally (TrueGrid, XYZ Scientific Applications, Inc., Livermore, CA). Each zone, remote, BZ, and infarct, was assigned different material properties. The inner endocardial surface was lined with a layer of soft non-structural shell elements to form an enclosed volume for LV volume measurements. A mesh convergence study determined that 2496 elements are required and further mesh refinement only results in a 1% change in strain predictions. An example of the endocardial and epicardial surfaces, as well as the 3-D mesh, is shown in Fig. 4.12.

Cardiac myofiber angles of –37°, 23°, and 83° were assigned at the epicardium, midwall, and endocardium, respectively, in the remote and BZ regions [28]. Cross-fiber, in-plane stress, equivalent to 40% of that along the myocardial fiber direction, was added [17]. At the aneurysm region, fiber angles were set to 0° in order to use

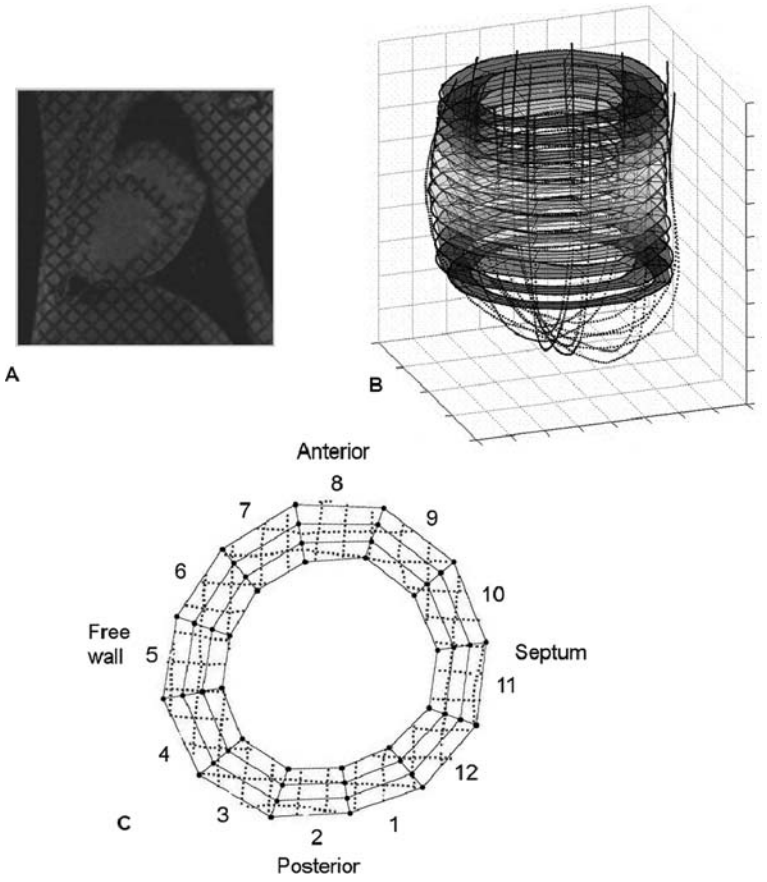

Fig. 4.11 Three-dimensional cardiac strain analysis from in vivo tagged MR images. Endocardial and epicardial contours as well as segmented tag-lines were traced from (**a**) short-axis, as well as long-axis, MR images to create (**b**) a 3-D geometry. (**c**) Each short-axis slice was divided into 12 sectors and a 4-D B-spline-based motion tracking technique was applied to the tag-line (*dotted lines*) deformations in order to calculate the Lagrangian Green's strains in cylindrical coordinates. For each sector of each short-axis slice, longitudinal, radial, circumferential, and shear strains throughout systole were determined

experimentally determined aneurysm material parameters with respect to this direction [18]. In other words, the constitutive equation for the aneurysm is in terms of strain components that are referred to in cardiac (i.e., circumferential and longitudinal) coordinates instead of fiber coordinates. Nodes at the LV base were restricted to displace horizontally, and circumferential displacements were constrained at the basal epicardial nodes. The inner endocardium wall was loaded to the measured in vivo end-diastolic and end-systolic LV pressures.

The minimum of the objective function, consisting of 960 strain and 2 LV volume data points, was reached in ten iterations. The optimized $T_{\max\_R}$ and $T_{\max\_B}$

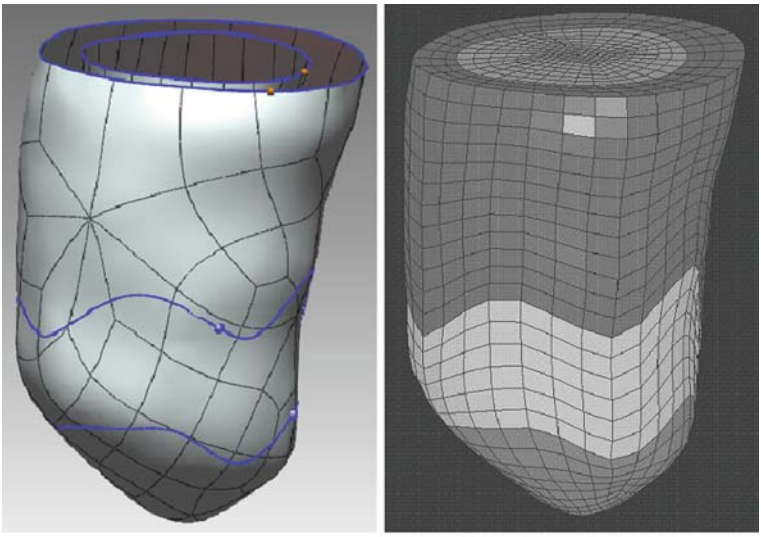

Fig. 4.12 Creation of the FE model of the LV using geometry from in vivo tagged MR images. Endocardial and epicardial contours extracted from short- and long-axis MR images were used to generate (**a**) a surface mesh with three distinct LV regions (remote, BZ, and aneurysm). The surface meshes provide projection surfaces for (**b**) the volumetric mesh, which is refined into three elements transmurally. A layer of shell elements line the endocardial surface and cap off the top of the LV to form a closed volume for LV volume measurements

(remote and BZ) for this sheep are 190.1 and 60.3 kPa, respectively, with 90% confidence intervals at 14.9% and 16.9%, respectively. This represents a decrease in BZ contractility that is 3.15 times less than the remote region. V_{SD} was accurately predicted at 110.8 mL, only 4.9% higher than the measured value of 105.6 mL. The predicted systolic strains, using the optimized material parameters, were generally in decent agreement with the in vivo measured strains. The insertion points of the right ventricle (RV) to the LV showed the largest difference between the measured and predicted strains since the RV was not included in the model. The RMS error for the circumferential strain component between the 137 pairs of measured and predicted strains in the remote zone was 0.048, and in the BZ the RMS error was 0.070 using 55 pairs of strain points. Unfortunately, there were no strain measurements in the infarct zone as short-axis MR images were not acquired in that area. The significant depression in optimized T_{max_B} relative to T_{max_R} was confirmed by direct ex vivo force measurements from skinned fiber preparations. In addition, the optimized values of T_{max_B} and T_{max_R} were not overly sensitive to the passive material parameters specified. The computation time of less than 5 hours associated with our proposed method for estimating regional myocardial contractility in vivo makes it a potentially very useful clinical tool.

4.6 Future Directions

In summary, a software tool was developed that can determine the in vivo myocardial material properties using minimally invasive measurements, namely tagged MR images and cardiac catheterization. This tool can assess the regional mechanical function of the myocardium in vivo without excising tissue for mechanical testing nor having to interpret functionality based on deformation and global cardiac performance. Changes in myocardial material properties of the same heart as it remodels over time can be tracked using this tool. In addition, it can be used to evaluate the efficacy of surgical interventions on the LV, such as infarct plication, Dor procedure SAVER procedure, and medical devices, like the Myosplint device and biomaterial injection therapy, by comparing the material properties before and after treatment.

Acknowledgments This research was supported by a grant from the Whitaker Foundation (Dr. Guccione) and National Institutes of Health grant 5R01 HL077921 (Dr. Guccione).

References

1. Bovendeerd PH, Arts T, Delhaas T, Huyghe JM, van Campen DH, Reneman RS. Regional wall mechanics in the ischemic left ventricle: numerical modeling and dog experiments. *Am J Physiol Heart Circ Physiol*. 1996;270:H398–H410.
2. Guccione JM, McCulloch AD, Waldman LK. Passive material properties of intact ventricular myocardium determined from a cylindrical model. *ASME J Biomech Eng*. 1991;113:42–55.
3. Omens JH, MacKenna DA, McCulloch AD. Measurement of strain and analysis of stress in resting rat left ventricular myocardium. *J Biomech*. 1993;26:665–676.
4. Usyk TP, Mazhari R, McCulloch AD. Effect of laminar orthotropic myofiber architecture on regional stress and strain in the canine left ventricle. *J Elasticity*. 2000;61:143–164.
5. Vetter FJ, McCulloch AD. Three-dimensional stress and strain in passive rabbit left ventricle: a model study. *Ann Biomed Eng*. 2000;28:781–792.
6. Denney TS Jr, Gerber BL, Yan L. Unsupervised reconstruction of a three-dimensional left ventricular strain from parallel tagged cardiac images. *Magn Reson Med*. 2003;49:743–754.
7. Ozturk C, McVeigh ER. Four-dimensional B-spline based motion analysis of tagged MR images: introduction and in vivo validation. *Phys Med Biol*. 2000;45(6):1683–1702.
8. Moulton MJ, Creswell LL, Downing SW, Actis RL, Szabo BA, Pasque MK. Myocardial material property determination in the in vivo heart using magnetic resonance imaging. *Int J Card Imaging*. 1996;12:153–167.
9. Okamoto RJ, Moulton MJ, Peterson SJ, Li D, Pasque MK, Guccione JM. Epicardial suction: a new approach to mechanical testing of the passive ventricular wall. *J Biomech Eng*. 2000 Oct;122(5):479–487.
10. Costa KD, Hunter PJ, Rogers JR, Guccione JM, Waldman LK, McCulloch AD. A three-dimensional finite element method for large elastic deformations of ventricular myocardium: Part I—Cylindrical and spherical coordinates. *ASME J Biomech Eng*. 1996;118: 452–463.
11. Guccione JM, Costa KD, McCulloch AD. Finite element stress analysis of left ventricular mechanics in the beating dog heart. *J Biomech*. 1995;28:1167–1177.
12. Moulton MJ, Creswell LL, Actis RL, Myers KW, Vannier MW, Szabo BA, Pasque MK. An inverse approach to determining myocardial material properties. *J Biomech*. 1995;28: 935–948.
13. Dang AB, Guccione JM, Mishell JM, Zhang P, Wallace AW, Gorman RC, Gorman JH 3rd, Ratcliffe MB. Akinetic myocardial infarcts must contain contracting myocytes: finite-element model study. *Am J Physiol Heart Circ Physiol*. 2005 Apr;288(4):H1844–H1850.

14. Guccione JM, Moonly SM, Moustakidis P, Costa KD, Moulton MJ, Ratcliffe MB, Pasque MK. Mechanism underlying mechanical dysfunction in the border zone of left ventricular aneurysm: a finite element model study. *Ann Thorac Surg*. 2001 Feb;71(2):654–662.
15. Moulton MJ, Downing SW, Creswell LL, Fishman DS, Amsterdam DM, Szabo BA, Cox JL, Pasque MK. Mechanical dysfunction in the border zone of an ovine model of left ventricular aneurysm. *Ann Thorac Surg*. 1995;60:986–997.
16. Bowen FW, Hattori T, Narula N, Salgo IS, Plappert T, Sutton MG, Edmunds LH Jr. Reappearance of myocytes in ovine infarcts produced by six hours of complete ischemia followed by reperfusion. *Ann Thorac Surg*. 2001;71:1845–1855.
17. Walker JC, Ratcliffe MB, Zhang P, Wallace AW, Fata B, Hsu EW, Saloner D, Guccione JM. MRI-based finite-element analysis of left ventricular aneurysm. *Am J Physiol Heart Circ Physiol*. 2005 Aug;289(2):H692–H700.
18. Moonly SM. Experimental and computational analysis of left ventricular aneurysm mechanics (PhD thesis). San Francisco, CA: University of California, San Francisco with University of California, Berkeley, 2003.
19. Walker JC, Guccione JM, Jiang Y, Zhang P, Wallace AW, Hsu EW, Ratcliffe MB. Helical myofiber orientation after myocardial infarction and left ventricular surgical restoration in sheep. *J Thorac Cardiovasc Surg*. 2005;129:382–390.
20. Guccione JM, Beitler JR, Moonly SM, Walker JC, Zhang P, Wallace AW, Saloner DA, Ratcliffe MB. The effect of LV aneurysm plication on end-systolic strain in the sheep: a 3-D MR tagging study. Biomedical Engineering Society Annual Fall Meeting. Nashville, TN, 2003.
21. Moustakidis P, Maniar HS, Cupps BP, Absi T, Zheng J, Guccione JM, Sundt TM, Pasque MK. Altered left ventricular geometry changes the border zone temporal distribution of stress in an experimental model of left ventricular aneurysm: a finite element model study. *Circulation*. 2002;106:I168–I175.
22. Costa KD, Hunter PJ, Wayne JS, Waldman LK, Guccione JM, McCulloch AD. A three-dimensional finite element method for large elastic deformations of ventricular myocardium. II. Prolate spheroidal coordinates. *J Biomech Eng*. 1996;118:464–472.
23. Lin DH, Yin FC. A multiaxial constitutive law for mammalian left ventricular myocardium in steady-state barium contracture or tetanus. *J Biomech Eng*. 1998;120:504–517.
24. Sun K, Stander N, Jhun C-S, Zhang Z, Suzuki T, Wallace AW, Saloner DA, Einstein DR, Ratcliffe MB, Guccione JM. A computationally efficient formal optimization method for estimating regional variations of in-vivo myocardial contractility in infarcted left ventricles. *J Biomech Eng.* 2009; 131:111001.
25. Guccione JM, Walker JC, Beitler JR, Moonly SM, Zhang P, Guttman MA, Ozturk C, McVeigh ER, Wallace AW, Saloner DA, Ratcliffe MB. The effect of anteroapical aneurysm plication on end-systolic three-dimensional strain in the sheep: a magnetic resonance imaging tagging study. *J Thorac Cardiovasc Surg*. 2006;131(3):579–586, e3.
26. Markovitz LJ, Savage EB, Ratcliffe MB, Bavaria JE, Kreiner G, Iozzo RV, Hargrove WC 3rd, Bogen DK, Edmunds LH Jr. Large animal model of left ventricular aneurysm. *Ann Thorac Surg*. 1989;48(6):838–845.
27. Guttman MA, Zerhouni EA, McVeigh ER. Analysis and visualization of cardiac function from MR images. *IEEE Comp Graph Appl*. 1997;17(1):30–38.
28. Omens JH, May KD, McCulloch AD. Transmural distribution of three-dimensional strain in the isolated arrested canine left ventricle. *Am J Physiol*. 1991;261(3 Pt 2):H918–H928.

Chapter 5
Computational Models of Cardiac Electrical Activation

Mark Svendsen, William Combs, Edward J. Berbari, and Ghassan Kassab

Abstract Models of cardiac electrical activation have been proposed for over 100 years. While the major components of the cardiac source and volume conductor models have not changed over the years, they have become increasingly complex and more robust. Although modeling of body surface potentials (forward model) and cardiac potentials (inverse model) has been a major topic of research, the clinical utility has yet to be fully realized. Integrated cardiac models with electrical, mechanical, neural, metabolic, circulatory, and genetic inputs are currently being developed. These integrated models are likely to provide new insights into cardiac electrical activation during heart failure and generate new hypotheses about multisystem coupling in the heart. The objective of this chapter is to provide an overview of the history, theory, and clinical use of electrical heart models with applications to heart failure.

5.1 Introduction

For over a century, the electrical activation in the heart has been a major area of clinical and experimental research. Even during the early stages of electrocardiography, models were developed to help understand the electrical and physical basis of the electrocardiogram (ECG). Early analytical methods utilized basic descriptors of the cardiac source(s) and the body surface and laid a foundation for the highly detailed computational models of today.

Computational modeling of cardiac activation plays an important role in the advancement of cardiac electrophysiology (EP). Models allow clinicians and researchers to test hypotheses about the spatial, temporal, and physiological characteristics involved in electrical activation that are not easily testable in vivo. Although much effort is needed to create these models, once developed they represent an

M. Svendsen (✉)
Weldon School of Biomedical Engineering, Purdue University, West Lafayette, IN, USA
e-mail: msvendse@iupui.edu

J.M. Guccione, et al. (eds.), *Computational Cardiovascular Mechanics*,
DOI 10.1007/978-1-4419-0730-1_5,

efficient approach for simulating normal and heart failure (HF) conditions. Most computational models are based on in vivo measurements and provide results which uncover new hypotheses that can be validated experimentally, thus creating an iterative cycle that improves both experimental and computational research to advance the field.

This chapter focuses on whole heart models of electrical activation. A detailed review of electrical modeling at a cellular and tissue level can be found in previous works [1, 2]. Here, we will provide a brief history of EP mathematical models and their utility. The strengths, weaknesses, and current status of the two major areas of modeling research, the forward and the inverse problems, are described along with current clinical applications related to HF. Finally, some future directions are highlighted.

5.2 Modeling History

Willem Einthoven, "the father of electrocardiography", developed the first model of cardiac electrical activation [3]. Einthoven's cardiac source consisted of a single 2D cardiac dipole with variable magnitude and direction. The source was situated in an electrically homogeneous medium from which the resulting ECG could be reconstructed. The ECG recording sites of the right arm, left arm, and left leg, formed the well-known Einthoven equilateral triangle in which the cardiac source was assumed to be situated statically in the center. Despite the simplicity of Einthoven's description of cardiac activation, single dipole models were surprisingly accurate in describing resultant body surface potentials and a clinical application, called vectorcardiography, emerged from this premise. Further improvements in accuracy were made by using multiple static sources as well as single and multiple moving sources [4–10]. Although these models provided reliable results on the body surface, they were not clinically useful because these sources had no physiological basis.

In 1931 Wilson, MacLeod, and Barker presented a source model with physiological relevance [11]. They described the cardiac sources as multiple dipoles situated on a "wave of excitation" that propagated throughout the myocardium. The relevance of this model was established by correlating the dipole moment of the sources and the spatial gradient of the transmembrane action potential of the cardiomyocytes along the wavefront of activation. This correlation was verified experimentally by Spach and his colleagues in canine hearts [12–14] and later theoretically predicted by Miller and Geselowitz [15, 16]. A detailed description of the full ventricular activation sequence in human hearts was described by Durrer and his colleagues in 1970 [17]. The isochrones of activation provided by Durrer coupled with the theory provided by Wilson gave researchers the necessary tools to model normal and disrupted activation using physiologically relevant data [15, 16, 18, 19].

Although these tools created more realistic anatomical and physiological cardiac models, more accurate methods were still needed to elucidate the relationship between ECG recordings and physiology and pathophysiology. In addition, models

were needed to explain complex arrhythmias, express finer details of the conduction pathway system, and describe the interaction between electrical activation and mechanical, metabolic, and neurological influences. As computational and imaging technology advanced, clinicians and researchers have been able to construct more detailed and integrated methods of exploring these complex interactions. Currently, there are several groups that are continuing to develop and refine highly integrated cardiac models for the study of HF [20–26]. A graphical description of the historical progression of these models is shown in Fig. 5.1.

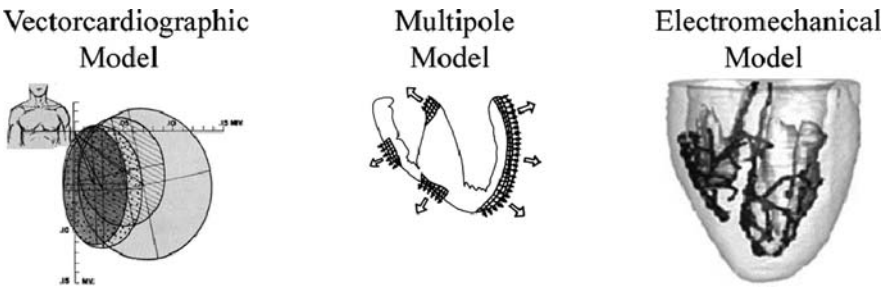

Fig. 5.1 Progression of electrical heart models from the single source vectrocardiographic models to multiple dipole models based on isochrones of activation, and finally to integrated electromechanical models with high levels of detail including the Purkinje fiber network [67, 9, 26]

5.3 Major Components of Electrical Models

Traditionally, a complete description of whole heart electrical activation requires the cardiac source model and the volume conductor model (Fig. 5.2). The cardiac source model simulates the electrical sources generated in the heart, while the volume conductor model simulates the resulting body surface potentials.

A comprehensive model must include an accurate and detailed anatomical/geometric description of the heart and volume conductor. Anatomical models are usually obtained through CT or MR scans, which provide excellent detail of the tissue surfaces in both animal and human subjects. The NIH and the National Library of Medicine have provided CT and MR data for the entire male and female body (The Visible Human Dataset) [27]. These open source datasets, as well as custom-made animal and human datasets, have been used by several researchers to create realistic heart and torso models [24, 28–31]. Another method for obtaining a realistic heart and torso geometry is through the use of ultrasonic imaging. This method has been used by the Auckland research group [32] and is an accurate way of providing patient-specific heart and torso geometries that may be useful for EP or HF procedures such as cardiac ablations and cardiac resynchronization therapy (CRT), respectively.

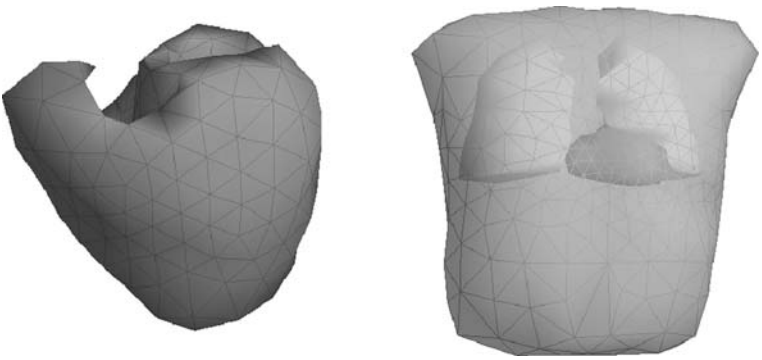

Fig. 5.2 The ECGSIM heart and torso model. The heart model is a boundary element model with 576 nodes that allows for regional control of depolarization and repolarization times. The torso model consists of boundary elements of the body surface and lungs (ECGSIM, used by permission [68])

The data obtained from the anatomical imaging is used to create a geometric heart and torso model in the form of a finite element (FE) or boundary element (BE) model. If only the surface of the heart or body is required, then BE methods may be adequate and a computationally less expensive method compared to FE methods. BEs are often used for the outer torso surface in forward models and the epicardium in inverse models, while FEs are generally used to incorporate anisotropy and detailed fiber orientation [21, 26].

5.3.1 The Cardiac Source Model

The cardiac source model is generally characterized by the magnitude, temporal course, and spatial location of the electric signals in a realistic heart geometry. The magnitude, timing, and location of the cardiac sources have been established using methods such as direct cardiac mapping of isochrones of activation [15, 16]. Some approaches provide detailed anatomy of the conduction system, including the AV node, the His and bundle branches, and/or the Purkinje fibers [21, 24, 26], while others omit the conduction system [33]. More realistic cardiac representations generally provide greater accuracy and more information, while other models only necessitate a moderate level of anatomical or physiological detail. The models that neglect the conduction pathways have relied on experimentally derived activation times taken from animal or human studies, while models that include components of the conduction system often require detailed anatomical structure generated through histological reconstruction of the conduction pathways. Several groups are now incorporating these finer details of cardiac activation which produce a more accurate description of electrical function [21, 24, 26].

5.3.2 The Volume Conductor Model

Volume conductor models describe the electrical signals seen throughout the body as a result of the sources generated in the heart. Typically, the volume conductor model only includes the torso and does not include the arms or legs since the potentials of interest are similar at the proximal and distal ends of the limbs. Depending on the detail in the model, components such as the lungs, ribs, fat, muscle, blood, and skin are included. For the forward model, the blood in the ventricles, the lungs, and the body surface are important features. For the inverse problem, the relative affect of the tissues in the torso have not been quantified. For models requiring several different tissue types, the use of CT and MR is the standard. The use of BEs is preferred over more computationally expensive FEs because the potentials of interest are on the body surface and not inside the tissue volume.

5.3.3 Model Assumptions

There are several assumptions that are crucial for the cardiac source and volume conductor model formulation. The heart can be represented as static or dynamic. The static assumption during cardiac activation is not unreasonable considering that both aortic valve opening and ventricular ejection normally occur after the completion of the QRS complex. In source models that include repolarization, however, the assumption of a static heart is unjustified since myocardial contraction generally occurs around the time of the T wave.

In the volume conductor, the individual tissues are assumed to be passive conductors of the electrical signal. Due to the cut-off frequencies used in a typical ECG, capacitive and inductive components can be ignored and the flow of current through these tissues can be represented as current through a simple resistor. Depending on the model complexity, the conductivity within a given tissue will be either isotropic or anisotropic. The outer boundary of the volume conductor is assumed to be bounded and insulated, which enforces a zero current flux boundary condition at the skin/air interface [11]. This assumption is valid since the conductivity of air is much less than that of the skin [34]. The quasi-static assumption implies that the potentials seen in the volume conductor are directly related to the instantaneous electrical signals generated by the cardiac sources and are not related to any previous electrical activity. Finally, the linearity assumption implies that a given potential in the volume conductor that results from multiple sources is equivalent to the sum of the potentials of each source.

5.3.4 Model Theory

The majority of the source models are firmly based on the bidomain theory, which expresses the heart as two regions, the intracellular and the extracellular space.

These two regions are assumed to be separated by a single continuous layer, yet both regions are assumed to interpenetrate each other throughout the cardiac volume. Since the heart volume acts much like a syncytium and electrical signals are transmitted from neighboring cardiomyocytes via gap junctions, the bidomain representation is fairly accurate in its description of the heart. A theoretical description of the cardiac sources in relation to the bidomain theory is necessary for understanding the strengths and weaknesses of the model assumptions. A brief description of the bidomain theory with a direct application to the transmembrane potential is described here [35, 36].

At any point in the model, the total current density (J) can be described in terms of a source current arising from the region (J_s) plus any conductance currents that are being propagated through the region as

$$\overline{J} = \overline{J_s} - \sigma \nabla \Phi, \tag{5.1}$$

where σ is the conductivity and Φ is the potential. This general expression can be directly applied to the heart as

$$\overline{J}_{\text{heart}} = \overline{J_s} - \sigma \nabla \Phi. \tag{5.2}$$

The source current term drops out of this expression for non-cardiac regions since the surrounding tissue does not generate electric signals themselves. Thus, a modification of the equation can be applied to the torso region as

$$\overline{J}_{\text{torso}} = -\sigma \nabla \Phi. \tag{5.3}$$

The total current density relationship in the heart can be reformulated based on the bidomain theory in terms of the intracellular (i) and extracellular (e) domains to yield

$$\overline{J}_{\text{heart}} = -\sigma_i \nabla \Phi_i - \sigma_e \nabla \Phi_e. \tag{5.4}$$

The difference between the intracellular and extracellular potentials is defined as the transmembrane potential by

$$\Phi_m = \Phi_i - \Phi_e. \tag{5.5}$$

This term can be used to transform the total current density equation into a new expression given by

$$\overline{J}_{\text{heart}} = -\sigma_i \nabla \Phi_m - (\sigma_i + \sigma_e) \nabla \Phi_e. \tag{5.6}$$

The continuity equation, which states that the divergence of the total current density is equal to the time derivative of the charge density (ρ), applies to both the cardiac source and volume conductor models as

$$\nabla \cdot \bar{J} + \frac{\partial \rho}{\partial t} = 0. \tag{5.7}$$

This implies that the total current entering and leaving a given volume in the heart or torso is equal to the rate of change of the charge density. Because of the quasi-static nature of the models, the divergence of the total current density is equal to zero as expressed by

$$\nabla \cdot \bar{J} = 0. \tag{5.8}$$

After taking the divergence of the total density equation and applying the quasi-static condition, a new expression for the heart has the form

$$\nabla \cdot (\sigma_{\mathrm{i}} + \sigma_{\mathrm{e}}) \nabla \Phi_{\mathrm{e}} = -\nabla \cdot \sigma_{\mathrm{i}} \nabla \Phi_{\mathrm{m}}. \tag{5.9}$$

Equation (5.9) for the heart volume relates the extracellular potential at any point to its transmembrane potential. This expression is important because it establishes a relationship between the epicardial/endocardial recordings and the transmembrane potential. The former can be determined fairly easily while the latter is much more difficult to obtain in vivo, but is more physiologically relevant. A similar expression can also be applied to the torso region which does not contain any transmembrane component as

$$\nabla \cdot \sigma_e \nabla \Phi_e = 0. \tag{5.10}$$

A further simplification of the bidomain theory which forces the intracellular potential to be equal to the transmembrane potential leads to the mono-domain formulation which is also commonly used in cardiac source models. These equations provide the basic formulation in which FE and BE models are based. Readers interested in how these equations are applied to FE and BE model formulation are referred to other works [1, 37].

5.4 Forward Models of Electrocardiography

Forward models of electrocardiography are used to determine the body surface potentials that arise from a given cardiac activation sequence (Fig. 5.3). The solutions to forward problems have been determined for over a century and applied to studies of myocardial ischemia and infarction, ventricular hypertrophy, and conduction disorders in the form of Wolf Parkinson White (WPW) syndrome, left bundle branch block (LBBB), late potentials, and abnormal intra-QRS potentials (AIQPs) [9, 10, 15, 19, 38].

The application of the bidomain theory to the forward problem requires the use of lead fields. Lead fields provide a transfer function that relates the cardiac sources to the potentials seen in the torso. Specifically, a single lead field vector is defined as the potential created in the heart when a unit current is passed from one pole of

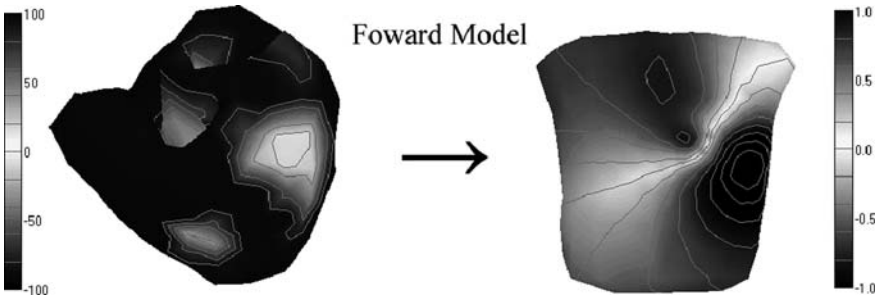

Fig. 5.3 The forward model of electrocardiography. Forward models utilize the known sources in the heart to solve for the potentials seen in the torso and on the body surface (ECGSIM, used by permission [68])

the lead to the other [39]. For a given source and conductor set, there must be a lead field vector from every heart location to every point of interest in the torso. These lead fields are stored in a stiffness matrix (S). The product of the stiffness matrix and the array of cardiac potentials (Φ_s) results in an array of the resulting body surface potentials (Φ_b) for a given time instant

$$\Phi_b = S\Phi_s. \tag{5.11}$$

Thus, for a quasi-static model there will be a set of cardiac source arrays for each time step that will be individually multiplied by the stiffness matrix to obtain a unique set of body surface potentials.

5.5 The Inverse Problem of Electrocardiography

Each time an ECG is interpreted, a crude attempt is made to solve the inverse problem of electrocardiography. The inverse problem of electrocardiography seeks to determine the electrical sources seen in the heart as a result of a given set of body surface potentials (Fig. 5.4). Even during the early years of body surface recordings, the ECG was clinically useful in determining conduction disorders, myocardial infarction, and ventricular hypertrophy [40, 41]. Since the standard 12-lead ECG is limited in its ability to describe full cardiac activation, large body surface mapping is needed for inverse solutions.

The inverse problem can be solved in a similar manner as the forward model using lead fields. However, the inverse model requires finding the inverse of the stiffness matrix (S^{-1}). The solution of the cardiac potentials can be calculated by multiplying the inverted stiffness matrix by the body surface potentials

$$\Phi_s = S^{-1}\Phi_b. \tag{5.12}$$

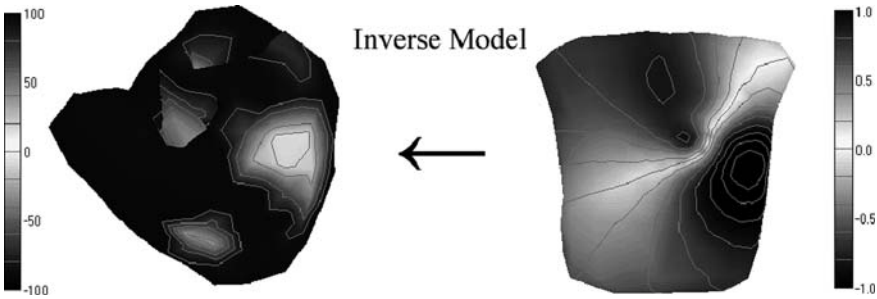

Fig. 5.4 The inverse model of electrocardiography. Inverse models utilize known body surface potentials to solve for the potentials seen inside the heart volume and/or on the heart surfaces (ECGSIM, used by permission [68])

5.6 Limitations of Forward and Inverse Models

Despite the millions of ECGs recorded daily, real time usage of forward and inverse solutions is not integrated into routine clinical practice. Although multiple studies have validated inverse methods and demonstrated their usefulness in cases of arrhythmias, WPW, and CRT for the treatment of HF, these models have yet to become widely used [42–45]. To obtain validation of a forward or inverse model, each patient would require an invasive endocardial and/or epicardial mapping session, a separate CT or MR scan to develop the heart and torso model, and a high-density mapping session to obtain the body surface potentials. Time would then be required to develop the heart and torso models, input the source data, solve the problem, and interpret the results. While all of these procedures are necessary to obtain accurate results, the time and money needed for scanning and mapping procedures may not be feasible in routine cases [46].

While the forward problem is extremely useful in helping researchers understand how a given cardiac activation pattern is represented on the body surface, its clinical utility is limited. This stems from the fact that clinicians are more interested in the sources in the heart rather than those on the body surface. Thus, from a clinical standpoint, if the cardiac sources are already known, as is the case with the forward problem, then the resulting body surface potentials are not needed.

On the other hand, the inverse problem has great clinical relevance, but most models are very difficult to solve. This stems from the fact that while a unique set of body surface potentials result from a single set of cardiac sources in the forward problem, multiple cardiac solutions exist for a single set of body surface potentials in the inverse problem. In order to deal with this issue, constraints must be used to ensure appropriate convergence. These constraints are accomplished for epicardially based solutions through regularization techniques which reduce error and maximize the smoothness of the activation patterns. Constraints are typically applied by assigning a certain location and timing of the points in which activation

breaks through the heart surfaces [47]. Hence, some knowledge of when and where breakthrough occurs is necessary, but often unknown.

In epicardial-based solutions, there is some concern about accuracy since the model is temporally unconstrained. For example, some models may have activation patterns in which there are unphysiological jumps in activation between successive time steps [48]. Methods have been developed to temporally constrain these activation patterns, but they generally require an accurate estimate of some component of the solution a priori, which is not easily determined. Also, some models require knowledge of the true nature of the cardiac sources to constrain or verify results, but this is not clinically accessible.

The inverse problem is also ill-posed, which implies that even small changes to the input body surface potentials or heart/torso geometry can result in large changes/errors in the solution. The ill-posed nature of the model has been demonstrated by numerous studies, which have shown that even slight model parameter changes can produce large variability in the inverse solution [49–52]. Therefore, the activation and geometric models must be extremely precise to be clinically useful.

5.7 Clinical Application of Inverse Models

Despite the limitations seen in inverse methods, they have been used clinically for multiple EP applications. The most useful clinical utilization of inverse methods has been through the model developed by Rudy and colleagues [53]. This model, termed electrocardiographic imaging (ECGI), has overcome several of the limitations that are typically encountered with inverse methods. Through the use of the method of fundamental solutions (MFS) which does not require the generation of finite or BEs, ECGI is a relatively easy and fast method for obtaining inverse solutions for patients [54, 55]. The MFS eliminates several of the ill-natured problems seen in traditional inverse formulations and is efficient since manual correction of errors in heart and torso meshes are unnecessary. In addition, when ECGI has been compared to traditional BE methods, it was shown to provide a more accurate inverse solution [54].

The ECGI formulation requires an ECG-gated CT scanning session for the construction of a patient-specific heart and torso model in addition to a separate body surface potential mapping session using a 250-electrode vest sampled at 1 kHz (Fig. 5.5) [54]. This information provides the input into the ECGI software and the resulting output is an epicardial-based inverse solution. The inverse solution can be seen in several different forms which include epicardial potential maps, isochrones of depolarization and repolarization, and local epicardial electrograms. The major strengths of the ECGI method include the fact that characteristics of activation can be analyzed at any point in the cardiac cycle with fine temporal resolution, atrial as well as ventricular activation patterns can be displayed, and information about the intramural nature of activation is available [56].

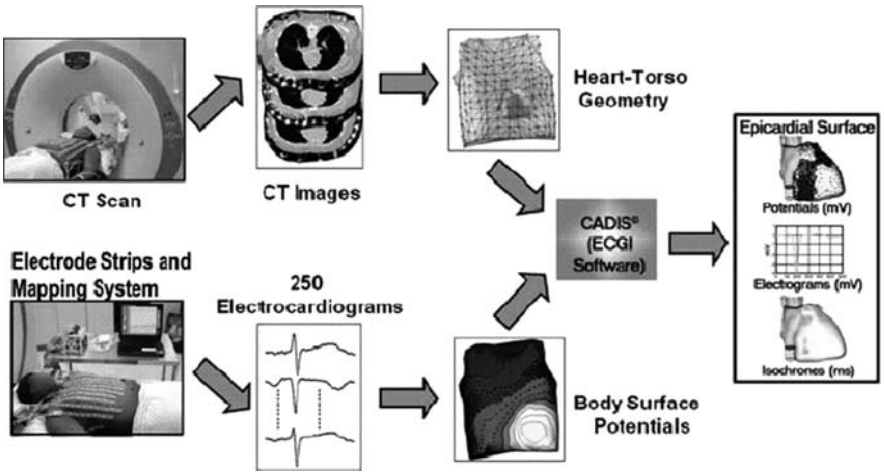

Fig. 5.5 The ECGI inverse method. A CT scan is taken of the subject from which a series of images are used to create a heart and torso geometry. A mapping session is needed to obtain 250 electrocardiogram recordings on the body surface. The geometry and body surface potentials are fed into the ECGI software to obtain epicardial potentials, electrograms, and isochrones of activation and repolarization [62]

ECGI was first validated extensively in several normal and diseased canine hearts placed in torso tanks, which allowed for direct comparisons between the measured and computed activation patterns [53, 56, 57]. In 2004, the first validation of ECGI was shown during normal activation, bundle branch block, and ventricular pacing in humans [58]. Subsequently, ECGI has been used in multiple clinical cases to guide and/or confirm EP therapy for ablations and CRT [42–45, 55, 59–62]. Since invasive EP studies are required before many of these procedures, ECGI may never be the sole method for assessing cardiac activation, but it may be a valuable tool to guide therapy.

5.8 Future Directions for Electrical Modeling

Integrated whole heart models have great promise for providing a comprehensive description of myocardial function. Although electrical activation is affected by such factors as coronary blood flow, mechanical loading, and neurological inputs, the integration of these factors into a single heart model is not an easy task. Despite the large computational cost for any integrated multi-scale model, the limiting factor for its construction is usually a lack of understanding about how the physiological factors interact with each other.

The Cardiome project envisioned by James Bassingthwaighte (Fig. 5.6) is a multi-center, multi-disciplinary project with the goal of developing quantitative integrated models of cardiac function [25, 63]. The Cardiome project is a part of

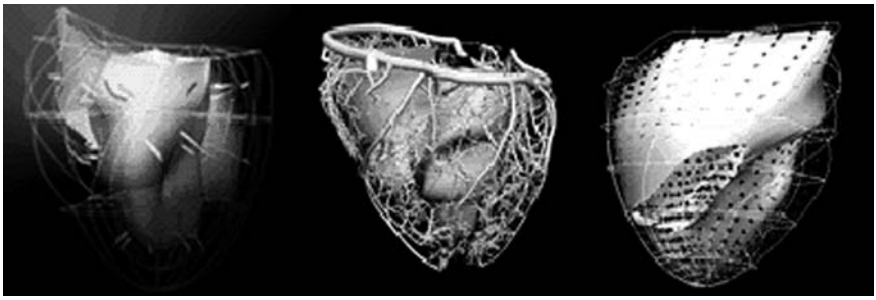

Fig. 5.6 Cardiome integrated heart model. These heart views demonstrate the electrical activation, coronary circulation, and myocardial mechanics aspects of the model (Welcom Trust [69])

the larger Bassingthwaighte Physiome project, which seeks to develop mathematical descriptions of cellular, tissue, organ, and organism function. Over 15 different groups are working together to develop a whole heart model with integrated electrical, mechanical, circulatory, metabolic, neural, genetic, and biomolecular inputs [63]. Because this project is linked to the larger Physiome project, there is great opportunity for the integration of this heart model with other organ groups, including the peripheral circulation, the kidneys, and the lungs. While this project is over a decade old, much work is still needed in every major area (from cellular to whole organ function).

Most of the progress in integrated heart models has come in the area of electrical and mechanical (EM) coupling, which has been incorporated by several groups [20–22, 23, 24, 25, 26]. These have already been useful in the study of HF with application to CRT [21, 22]. Sophisticated EM models include cellular-based excitation–contraction coupling equations that provide physiologically relevant electrical and mechanical activation patterns [23]. They may also be used to elucidate mechanisms related to how mechanical activation affects electrical activation (mechano-electric feedback), which may be important for clinical applications, like CRT.

There is also a desire to integrate information about electromechanical coupling with the circulatory components including blood flow through the cardiac chambers and the coronary circulation. The pressure boundary conditions of the blood in the cardiac chambers have been used to simulate preload and afterload conditions using a Windkessel model [21], but no whole heart model has truly integrated the flow of blood through the chambers or the coronary circulation with electrical and mechanical activation. Extensive models of the entire coronary vascular system have been developed and characterized in swine [64–66] which provide a morphometric framework for anatomically based models of coronary circulation. The integration of local metabolic coronary blood supply with electromechancial models may have enormous utility in understanding physiological and pathophysiological mechanisms.

There remains a fundamental need for further improvements in cardiac electrical models. Developments in the area of cellular-based activation coupled with further improvements in computational power are important for addressing some of the current limitations. Recently, the ability to store and manipulate large amounts of data coupled with the use of segmented and parallel processing has made cellular-based modeling a possibility. Since the estimates for the number of cells is in the billions, the number of elements will be extremely large. As further biology and physiology is added to these models, they will become increasingly more complex and will require more computational memory and speed. Thus, there is a continued need to further increase computational power and efficiency. There is also a need for further reductionism to understand the components of the heart and its conductivity system more systematically to enable models well rooted in realism. Finally, validation of the predictions through integrative studies is always a must to gain confidence in the model and to expand the range of utility. To make these models more clinically relevant, it will take efforts from clinicians, physiologists, and engineers working in unison.

5.9 Conclusion

Cardiac models of electrical activation continue to be useful in HF research and clinical practice. The development of increasingly more biologically and physiologically realistic integrated models will be critical to tailoring patient-specific therapies through CRT and future approaches to management of HF patients.

Acknowledgments This research was funded in part by NIH HL055554-11 and HL-084529.

References

1. Pullan AJ, Buist ML, Cheng LK. Mathematical modelling the electrical activity of the heart: from cell to body surface and back again. Hackensack, NJ: World Scientific Publishing Co., 2005.
2. Austin TM, Hooks DA, Hunter PJ, Nickerson DP, Pullan AJ, Sands GB, Smaill BH, Trew ML. Modeling cardiac electrical activity at the cell and tissue levels. *Ann NY Acad Sci*. 2006;1080:334–7.
3. Einthoven W. Die galvanometrische Registrirung des menschlichen Elektrokardiogramms, zugleich eine Beurtheilung der Anwendung des Capilar-Elektrometers in der Physiologie. *Pfluegers Arch*. 1903;99:472–80.
4. Burger HC, Van Milaan JB. Heart-vector and leads. *Br Heart J*. 1946;8:157–61.
5. Frank E. Determination of the electrical center of ventricular depolarization in the human heart. *Am Heart J*. 1955;49:670–92.
6. McFee R, Parungao A. An orthogonal lead system for clinical electrocardiography. *Am Heart J*. 1961;62:93–100.
7. Taccardi B. Distribution of heart potentials on the thoracic surface of normal human subjects. *Circ Res*. 1963;12:341–52.
8. Selvester RH, Solomon JC, Gillespie TL. Digital computer model of a total body electrocardiographic surface map. An adult male-torso simulation with lungs. *Circulation*. 1968;38:684–90.

9. Holt JH, Barnard ACL, Lynn MS, Svendsen P. A study of the human heart as a multiple dipole electrical source: I. Normal Adult male subjects. *Circulation*. 1969a;40:687–96.
10. Holt JH, Barnard ACL, Lynn MS. A study of the human heart as a multiple dipole electrical source. II. Diagnosis and quantitation of left ventricular hypertrophy. *Circulation*. 1969b;40:697–710.
11. Wilson FN, Macleod AG, Barker PS. The distribution of the currents of action and of injury displayed by heart muscle and other excitable tissues. In: The distribution of the currents of action and of injury displayed by heart muscle and other excitable tissues. Ann Arbor, MI: University of Michigan Press, 1931.
12. Spach MS, Barr RC, Serwer GA, Kootsey JM, Johnson EA. Extracellular potentials related to intracellular action potentials in the dog Purkinje system. *Circ Res*. 1972;30:509–19.
13. Spach MS, Barr RC. Origin of epicardial ST-T wave potentials in the intact dog. *Circ Res*. 1976;39:475–87.
14. Spach MS, Barr RC, Serwer GA, Kootsey JM, Johnson EA. Extracellular potentials related to intracellular action potentials in the dog Purkinje system. *Circ Res*. 1979;45:188–204.
15. Miller WT, Geselowitz DB. Simulation studies of the electrocardiogram. I. The normal heart. *Circ Res*. 1978a;43:301–15.
16. Miller WT, Geselowitz DB. Simulation studies of the electrocardiogram. II. Ischemia and infarction. *Circ Res*. 1978b;43:315–23.
17. Durrer D, van Dam RT, Freud GE, Janse MJ, Meijler FL, Arzbaecher RC. Total excitation of the isolated human heart. *Circulation*. 1970;41:899–912.
18. Salu Y, Marcus ML. Computer simulation of the precordial QRS complex: effects of simulated changes in ventricular wall thickness and volume. *Am Heart J*. 1976;92:758–66.
19. Lorange M, Gulrajani RM. Computer simulation of the Wolff-Parkinson-White preexcitation syndrome with a modified Miller-Geselowtiz heart model. *IEEE Trans Biomed Eng*. 1986;33:862–73.
20. Simelius K, Nenonen J, Horacek M. Modeling cardiac ventricular activation. *Int J Bioelectromagnetism*. 2001;3:51–8.
21. Usyk TP, Le Grice IJ, McCulloch A. Computational model of three-dimensional cardiac electromechanics. *Comput Vis Sci*. 2002;4:249–57.
22. Xia L, Huo M, Liu F, He B, Crozier S. Motion analysis of right ventricular wall based on an electromechanical biventricular model. *Conf Proc IEEE Eng Med Biol Soc*. 2004;2: 898–901.
23. Nickerson D, Niederer S, Stevens C, Nash M, Hunter P. A computational model of cardiac electromechanics. *Conf Proc IEEE Eng Med Biol Soc*. 2006:5311–14.
24. Sermesant M, Delingette H, Ayache N. An electromechanical model of the heart for image analysis and simulation. *IEEE Trans Med Imaging*. 2006;25:612–25.
25. Bassingthwaighte J, Hunter P, Noble D. The cardiac physiome: perspectives for the future. *Exp Physiol*. 2009;94:597–605.
26. Dou J, Xia L, Zhang Y, Shou G, Wei Q, Liu F, Crozier S. Mechanical analysis of congestive heart failure caused by bundle branch block based on an electromechanical canine heart model. *Phys Med Biol*. 2009;54:353–71.
27. National Library of Medicine (U.S.) Board of Regents (1990) Electronic imaging: Report of the Board of Regents (1990). U.S. Department of Health and Human Services, Public Health Service, National Institutes of Health. NIH Publication 90-2197.
28. Johnson CR, Macleod RS, Ershler PR. A computer model for the study of electrical current flow in the human thorax. *Comput Biol Med*. 1992;22:305–23.
29. Weixue L, Ling X. Three-dimensional simulation of epicardial potentials using a microcomputer-based heart-torso model. *Med Eng Phys*. 1996;17:625–32.
30. Pullan AJ, Cheng LK, Nash M, Bradley CP, Paterson DJ. Noninvasive electrical imaging of the heart: theory and model development. *Ann Biomed Eng*. 2001;29:817–36.
31. Seemann G, Hoper C, Sachse FB, Dossel O, Holden AV, Zhang H. Heterogeneous three-dimensional anatomical and electrophysiological model of human atria. *Philos Transact A Math Phys Eng Sci*. 2006;364:1465–81.

32. Cheng LK, Sands GB, French RL, Withy SJ, Wong SP, Legget ME, Smith WM, Pullan AJ. Rapid construction of a patient-specific torso model from 3D ultrasound for non-invasive imaging of cardiac electrophysiology. *Med Biol Eng Comput*. 2005;43:325–30.
33. van Oosterom A, Oostendorp TF. ECGSIM: an interactive tool for studying the genesis of QRST waveforms. *Heart*. 2004;90:165–68.
34. Klepfer RN, Johnson CR, Macleod RS. The effects of inhomogeneities and anisotropies on electrocardiographic fields: a three-dimensional finite element study. *IEEE Trans Biomed Eng*. 1997;44:706–19.
35. Leon LJ, Horacek BM. Computer model of excitation and recovery in the anisotropic myocardium. *J Electrocardiol*. 1991;24:1–15.
36. Geselowitz DB, Miller WT, 3rd. A bidomain model for anisotropic cardiac muscle. *Ann Biomed Eng*. 1983;11:191–206.
37. Pullan A. A high-order coupled finite element/boundary element torso model. *IEEE Trans Biomed Eng*. 1996;43:292–8.
38. Svendsen MC, Oostendorp TF, Berbari EJ. Evaluation of auto-regressive modeling procedures for the detection of abnormal intra-QRS potentials using a boundary element electrocardiographic model. *Comput Cardiol*, *September 30–October 3, 2007, Durham, North Carolina*. 2007.
39. Malmivuo J, Plonsey R. Bioelectromagnetism: principles and applications of bioelectric and biomagnetic fields. New York: Oxford University Press, 1995.
40. Einthoven W. Le telecardiogramme. *Arch Int de Physiol*. 1906;4:132–64.
41. Pardee HEB. An electrocardiographic sign of coronary artery obstruction. *Arch Intern Med*. 1920;26:244–57.
42. Jia P, Ramanathan C, Ghanem RN, Ryu K, Varma N, Rudy Y. Electrocardiographic imaging of cardiac resynchronization therapy in heart failure: observation of variable electrophysiologic responses. *Heart Rhythm*. 2006;3:296–310.
43. Varma N, Jia P, Rudy Y. Electrocardiographic imaging of patients with heart failure with left bundle branch block and response to cardiac resynchronization therapy. *J Electrocardiol*. 2007;40:S174–8.
44. Wang Y, Cuculich PS, Woodard PK, Lindsay BD, Rudy Y. Focal atrial tachycardia after pulmonary vein isolation: noninvasive mapping with electrocardiographic imaging (ECGI). *Heart Rhythm*. 2007a;4:1081–4.
45. Wang Y, Schuessler RB, Damiano RJ, Woodard PK, Rudy Y. Noninvasive electrocardiographic imaging (ECGI) of scar-related atypical atrial flutter. *Heart Rhythm*. 2007b;4:1565–7.
46. Huiskamp G, van Oosterom A. Tailored versus realistic geometry in the inverse problem of electrocardiography. *IEEE Trans Biomed Eng*. 1989;36:827–35.
47. Huiskamp G, Greensite F. A new method for myocardial activation imaging. *IEEE Trans Biomed Eng*. 1997;44:433–46.
48. Macleod RS, Brooks DH. Recent progress in inverse problems in electrocardiology. *IEEE Eng Med Biol Mag*. 1998;17:73–83.
49. van Oosterom A, Huiskamp G. The effect of torso inhomogeneities on body surface potentials quantified using "tailored" geometry. *J Electrocardiol*. 1989;22:53–72.
50. Cuppen JJ, van Oosterom A. Model studies with the inversely calculated isochrones of ventricular depolarization. *IEEE Trans Biomed Eng*. 1984;31:652–59.
51. Johnston PR, Kilpatrick D. The inverse problem of electrocardiology: the performance of inversion techniques as a function of patient anatomy. *Math Biosci*. 1995;126:124–45.
52. Cheng LK, Bodley JM, Pullan AJ. Effects of experimental and modeling errors on electrocardiographic inverse formulations. *IEEE Trans Bio Eng*. 2003;50:23–32.
53. Oster HS, Taccardi B, Lux RL, Ershler PR, Rudy Y. Noninvasive electrocardiographic imaging: reconstruction of epicardial potentials, electrograms, and isochrones and localization of single and multiple electrocardiac events. *Circulation*. 1997;96:1012–24.
54. Wang Y, Rudy Y. Application of the method of fundamental solutions to potential-based inverse electrocardiography. *Ann Biomed Eng*. 2006;34:1272–88.

55. Ghosh S, Avari JN, Rhee EK, Woodard PK, Rudy Y. Noninvasive electrocardiographic imaging (ECGI) of epicardial activation before and after catheter ablation of the accessory pathway in a patient with Ebstein anomaly. *Heart Rhythm*. 2008a;5:857–60.
56. Oster HS, Taccardi B, Lux RL, Ershler PR, Rudy Y. Electrocardiographic imaging: noninvasive characterization of intramural myocardial activation from inverse-reconstructed epicardial potentials and electrograms. *Circulation*. 1998;97:1496–507.
57. Burnes JE, Taccardi B, Rudy Y. A noninvasive imaging modality for cardiac arrhythmias. *Circulation*. 2000;102:2152–8.
58. Ramanathan C, Ghanem RN, Jia P, Ryu K, Rudy Y. Noninvasive electrocardiographic imaging for cardiac electrophysiology and arrhythmia. *Nat Med*. 2004;10:422–8.
59. Intini A, Goldstein RN, Jia P, Ramanathan C, Ryu K, Giannattasio B, Gilkeson R, Stambler BS, Brugada P, Stevenson WG, Rudy Y, Waldo AL. Electrocardiographic imaging (ECGI), a novel diagnostic modality used for mapping of focal left ventricular tachycardia in a young athlete. *Heart Rhythm*. 2005;2:1250–2.
60. Ghosh S, Avari JN, Rhee EK, Woodard PK, Rudy Y. Hypertrophic cardiomyopathy with preexcitation: insights from noninvasive electrocardiographic imaging (ECGI) and catheter mapping. *J Cardiovasc Electrophysiol*. 2008a;19:1215–7.
61. Ghosh S, Avari JN, Rhee EK, Woodard PK, Rudy Y. Noninvasive electrocardiographic imaging (ECGI) of a univentricular heart with Wolff-Parkinson-White syndrome. *Heart Rhythm*. 2008b;5:605–8.
62. Ghosh S, Rhee EK, Avari JN, Woodard PK, Rudy Y. Cardiac memory in patients with Wolff-Parkinson-White syndrome. Noninvasive imaging of activation and repolarization before and after catheter ablation. *Circulation*. 2008c;118:907–15.
63. Bassingthwaighte J. Design and strategy for the cardionome project. *Adv Exp Med Biol*. 1997;430:325–39.
64. Kassab GS, Rider CA, Tang NJ, Fung YC. Morphometry of pig coronary arterial trees. *Am J Physiol*. 1993;265:H350–65.
65. Kassab GS, Fung YC. Topology and dimensions of pig coronary capillary network. *Am J Physiol*. 1994a;267:H319–25.
66. Kassab GS, Lin DH, Fung YC. Morphometry of pig coronary venous system. *Am J Physiol*. 1994b;6 (Pt 2):H2100–13.
67. Haywood LJ, Selvester RH. Analysis of right and left atrial vectorcardiograms. Timed records of 100 normal persons. *Circulation*. 1966;33:577–87.
68. ECGSIM 1.3 beta. Department of Medical Physics, University of Nijmegen, The Netherlands. 10 August 2006. <www.ecgsim.org/download.html>.
69. Welcom Trust Heart Physiome Project. 15 March 2009. <http://heart.physiomeproject.org/projects_whole_heart_modelling.html>

Chapter 6
Geometrical Features of the Vascular System

Ghassan S. Kassab

Abstract Biomechanics relates the function of a physiological system to its structure. The objective of biomechanics is to deduce the function of a system from its geometry, material properties, and boundary conditions based on the balance laws of mechanics. Geometry clearly plays a major role in formulation of boundary value problems in biomechanics and is intimately related to function and physiology. Here, we shall provide an overview of the geometric features of the vascular system with special emphasis on the vascular system of the heart (coronary circulation).

6.1 Introduction

The vascular system consists of aorta (elastic artery) which branches into smaller elastic vessels and eventually muscular arteries. These conduit arteries branch further and give rise to the microcirculation consisting of arterioles, capillaries, and venules. The venules collect into larger veins and eventually converge to the venae cavae. The geometry of the various vessels reflects an adaptation to function. The aorta (higher pressures) is thicker and more elastic to serve a Windkessel function [1]. The smaller arteries have tone to auto-regulate blood flow and organ perfusion. The capillaries are smallest and thinnest of vessels to promote transport of oxygen and nutrients and remove waste products. The veins have significant capacitance to collect blood and are thin-walled due to the low pressures and interconnectedness.

The geometric (morphological) features (diameter, lengths, vessel wall thickness, etc.) of the vasculature (arteries, capillaries, and veins) are necessary to understand the circulation, to predict the pressure–flow relationship, to determine the longitudinal pressure and flow distribution, to understand the distensibility of the blood

G.S. Kassab (✉)
Department of Biomedical Engineering, Surgery, and Cellular and Integrative Physiology, IUPUI, Indianapolis, IN, USA
email: gkassab@iupui.edu

J.M. Guccione, et al. (eds.), *Computational Cardiovascular Mechanics*,
DOI 10.1007/978-1-4419-0730-1_6,

vessels, to study atherogenesis or restenosis, and to determine the effect of hypertension, hypertrophy, flow-overload, and tissue remodeling on the circulation. This is analogous to the need to know the structure of the circuitry as well as the distribution of the resistors, capacitors, and inductors in an electric circuit if one wishes to analyze an electric instrument. Trying to understand the circulation without the morphometric data is like exploring a continent without a map. Specifically, in a network analysis of blood flow, the circuit must agree with the anatomical data on the branching pattern and geometry of the vasculature, and the basic hemodynamic equations and boundary conditions must be satisfied.

In this chapter, we will provide an overview of the role of vessel geometry in hemodynamics. We will use the coronary vasculature to illustrate how the morphometry of the vascular system can be determined through a reductionist approach and subsequently reconstructed through an integrationist approach. We will then relate the structure to function analytically through a set of scaling laws based on physical principles. The clinical translatability of these approaches and concepts will be discussed.

6.2 Significance of Vessel Geometry

The prescription of geometry or morphometry (measurement of form or shape) is necessary for the formulation of any BVP. Since a BVP is a problem which has values assigned on the physical boundary of the domain in which the problem is specified, the importance of geometry or form is obvious. Specifically, there are several reasons for specifications of geometry: (1) A mathematical model of the vasculature must obey geometric similarity which requires knowledge of the diameter and length of every vessel segment. (2) A mathematical analysis of a blood vessel must also obey the rule of dynamic similarity which reduces to the simulation of two dimensionless parameters, the Reynolds number, N_R (N_R=<I>ρUD</I>/<I>μ</I> where U is the mean flow velocity, D is the lumen diameter of vessel, and <I>ρ</I> and <I>μ</I> are the density and viscosity of blood, respectively), and Womersley number, N_W (N_W=D/2(<I>ρω</I>/<I>μ</I>)$^{1/2}$, where <I>ω</I> is the circular frequency of pulsatile flow). (3) For a steady laminar flow, Poiseuille's formula states that the flow rate (volume/time) is directly proportional to the product of the fourth power of the diameter and the pressure drop and is inversely proportional to the first power of the vessel length. (4) In an unsteady flow, the characteristic impedance is the ratio <I>ρc</I>/A, where <I>ρ</I> is the density of blood, c is the speed of flexural waves in the blood vessel, and A is the cross-sectional area (CSA) (proportional to the square of diameter) of the vessel. (5) The mean circumferential Cauchy stress, <I>σ </I>(force per deformed area), in a cylindrical vessel wall is given by $\sigma = \frac{PD}{2h}$, where P is the blood pressure and h is the wall thickness. Hence, it is clear that the geometry of a blood vessel (e.g., diameter, length, wall thickness, and curvature) must be accurately quantified for a realistic biomechanical analysis of vessel function.

6.3 Coronary Vasculature

The heart muscle is nourished by a complex system of blood vessels that make up the coronary circulation. The function of the coronary circulation is to continually supply blood to meet the continuous requirements of cardiac tissue that is critical to the health of the heart. The coronary arterial system consists of large epicardial coronary arteries (EPCA) that span the surface of the heart and give rise to intramyocardial coronary arteries (IMCA) that penetrate into the inner layers of the heart. The asymmetric branching pattern of the coronary arterial tree is rather complex [2] and gives rise to millions of capillary blood vessels that nourish the myocardium.

6.3.1 Reduction of Coronary Morphology

The reduction–integration approach was used to first dissect apart the coronary vasculature to quantify the geometry of individual vessels, followed by a mathematical reconstruction to integrate the system. Kassab [3] has reviewed the methodologies used to dissect apart the entire coronary vasculature and quantitatively describe its morphology. Briefly, silicone elastomer was used to prepare casts of the vasodilated vasculature in a diastolic-arrested porcine heart [4, 5]. For vessels 50 μm in diameter, morphometric measurements of segment diameter, length, and connectivity were made from casts of the vasculature after digestion of myocardial tissue. Data on coronary vessels <50 μm (arterioles, capillaries, and venules) were obtained from optical reconstructions of histological sections removed from the left and right ventricular wall [4, 6, 5].

The branching pattern of the coronary arteries is largely tree-like with few collaterals in the swine model [4]. The venous system, on the other hand, has significant intra- and inter-venous connections [5]. The cross-section of a coronary artery or arteriole is circular while that of veins and venules is elliptical in diastole [7, 5]. These features of the geometry (morphometry) were quantitatively characterized based on a vessel ordering scheme [7, 5].

To facilitate the mathematical description of the vasculature, Kassab and colleagues have added four new innovations to morphometry [4, 5, 8]: the diameter-defined Strahler ordering system for assigning the order numbers of the vessels, the distinction between series and parallel vessel segments, the connectivity matrix to describe the asymmetric branching pattern of vessels, and the longitudinal position matrix to describe the longitudinal position of daughter vessels along the length of their parent vessels. These innovations were used to study the entire anatomy of the coronary vasculature in the pig and have yielded the *first complete* set of morphometric data on the coronary arteries [4, 8], capillaries [6], and veins [5] in health as well as that of arterial remodeling in right ventricular hypertrophy [7]. Once the porcine coronary morphometric database was complete, some of the numerous applications to understanding the structure–function relation in normal and disease coronary circulation have been demonstrated [9–16, 2, 17–27].

6.3.2 Integration of Coronary Vasculature

A large-scale stochastic reconstruction of the asymmetric coronary arterial trees (right coronary artery, RCA; left anterior descending, LAD; and left circumflex, LCx) of the porcine heart has been carried out as shown in Fig. 6.1 [16]. The model spans the entire coronary arterial tree down to the capillary vessels. The 3-D tree structure was reconstructed initially in rectangular slab geometry by means of global geometrical optimization using parallel simulated annealing (SA) algorithm. The SA optimization was subject to constraints prescribed by measured morphometric features of the coronary arterial trees. Subsequently, the reconstructed trees were mapped onto a prolate spheroid geometry of the heart. The transformed geometry was determined through least squares minimization of the related changes in both segments lengths and their angular characteristics. Vessel diameters were assigned based on a novel representation of diameter asymmetry along bifurcations. The reconstructed RCA, LAD, and LCx arterial trees show qualitative resemblance to native coronary networks, and their morphological statistics are consistent with the measured data. This model constitutes the first most extensive reconstruction of the entire coronary arterial system which can serve as a geometric foundation for studies of flow in an anatomically accurate 3-D coronary vascular model.

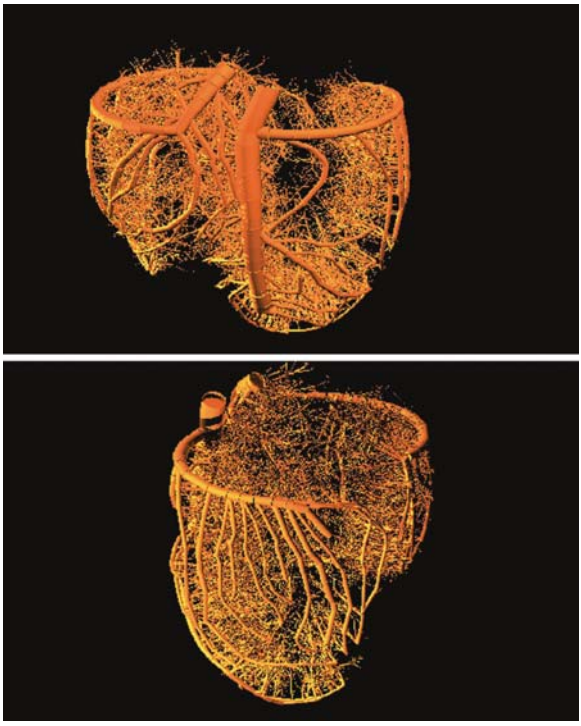

Fig. 6.1 A reconstructed coronary arterial tree including the RCA, LAD, and LCx arteries: (**a**) lateral left and (**b**) posterolateral oblique left views [16]

6.4 Structure–Function Relation

Although the morphogenesis of the vascular tree is likely to be determined by a preprogrammed genetic algorithm, a number of physical, chemical, and biological factors related to the functional needs of a particular tissue determine the subsequent growth and remodeling during postnatal development. The detailed form of tree structures reflects the changes brought about by natural selection and adaptation to the environment which reflects a survival value of the structure. The design determinants of structure are undoubtedly multi-factorial and an analysis of their effects on structure and function is often non-trivial.

Since biological trees are used to conduct fluids, energy expenditure is required because of frictional losses. The frictional losses are reduced when the vessel branches have larger diameters. This comes with a cost, however, for the metabolic construction and maintenance of the larger volume of the structure. Eighty years ago, Murray [28] proposed a compromise between the frictional and metabolic cost expressed as a cost function. Murray only considered the metabolic cost of blood but Liu and Kassab [25] extended the metabolic cost to blood and vessel wall. The formulation of the minimum energy hypothesis led to the well-known Murray's law which can be expressed as $Q=kD^3$, where Q and D are the volumetric flow rate and diameter of a vessel segment, respectively, and k is a proportionality constant [28]. Murray's law predicts a universal exponent of 3.0 for all trees whose internal flows obey laminar conditions. Fifty years later, Uylings [29] argued that the exponent can vary in the range of 2.33–3.0 depending on whether the flow is turbulent (2.33) or laminar (3.0). Numerous papers have been published in the past 80 years on Murray's law and on the validation of the exponent. The studies show support but with significant scatter. In review of the literature, Sherman [30] concluded that Murray's law is not obeyed in the most proximal bifurcations of aorta, the pulmonary trunk, the venae cavae, and the pulmonary veins.

Both Murray's formulation and Uylings' modification are focused on a particular vessel segment. The flow rate through a vessel branch, however, depends not only on the resistance of that branch but also on the total resistance of the tree distal to that branch. Hence, the formulation of an optimization principle requires the treatment of a tree structure as an integrated whole. Zhou et al. [31] (ZKM model) generalized the "minimum energy hypothesis" to an entire coronary arterial tree. In the process, a vessel segment was defined as a stem and the entire tree distal to the stem was defined as a crown [32]. Obviously, the entire tree consists of many stem-crown units down to the capillary vessels as shown in Fig. 6.2. At each bifurcation, there is a unique stem-crown unit which continues down to the smallest unit: an arteriole with two capillaries for an arterial tree or a venule and two capillaries for a venous tree. Functionally, each stem supplies or collects blood from the crown for an arterial or venous tree, respectively. The details of the capillary network (non-tree structure) beyond the first bifurcation were excluded from the analysis. Hence, the analysis applies strictly to a tree (arterial or venous) structure down to the first capillary bifurcation.

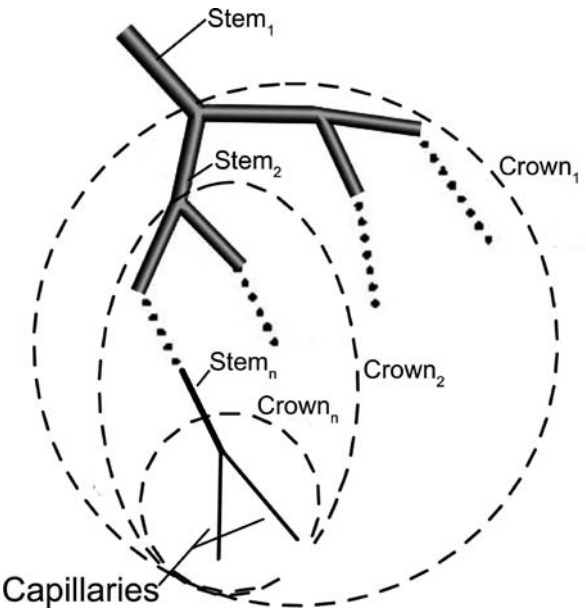

Fig. 6.2 A schematic illustration of the definition of stem-crown unit. Three stem-crown units are shown successively with the smallest unit corresponding to an arteriole-capillary or venule-capillary unit [18]

If A and Q represent the mean CSA and blood flow rate of a stem, respectively, and V and L represent the cumulative arterial volume and length of a crown, respectively, the ZKM model predicts the following relationships: $V/V_{\max} = (L/L_{\max})^{\beta}$, $(D/D_{\max}) = (L/L_{\max})^{\chi}$, and $Q/Q_{\max} = (D/D_{\max})^{\delta}$, where $D_{\max}$, $Q_{\max}$, $V_{\max}$, and $L_{\max}$ correspond to the diameter and flow rate of the most proximal stem, the volume of the entire crown, and the cumulative arterial length of the crown (Fig. 6.3). The exponents β ($\sim$1.4), χ ($\sim$0.46), and δ ($\sim$2.1) relate to the crown flow resistance and are determined from the experimental data [19]. The last exponent is not equal to 3.0 as predicted by Murray's law [28]. These generalized scaling laws clearly show the significance of vessel geometry and flow (function).

These relationships have been determined and validated for the coronary arterial trees in the following three ways: (1) A hemodynamic analysis of coronary arterial blood flow based on detailed anatomical data yields these relationships over the entire arterial network [18, 19], (2) a generalization of Murray's cost function and conservation of energy predict the same result over the entire coronary arterial tree [31], and (3) in vivo data on coronary stem flow rate, crown length, and volume using digital subtraction angiography [33] verified the relationships for vessels proximal to about 0.5 mm in diameter as observed in an angiogram.

In addition to the coronary vasculature, it was shown that the scaling laws apply to all vascular trees for which there exists morphometric data (e.g., pulmonary; vessels of various skeletal muscles, mesentery, omentum, and conjunctiva) which verifies the hypothesis that the cost of construction of the tree structure and operation of fluid conduction are minimized [18]. This reveals the similarity of nature's

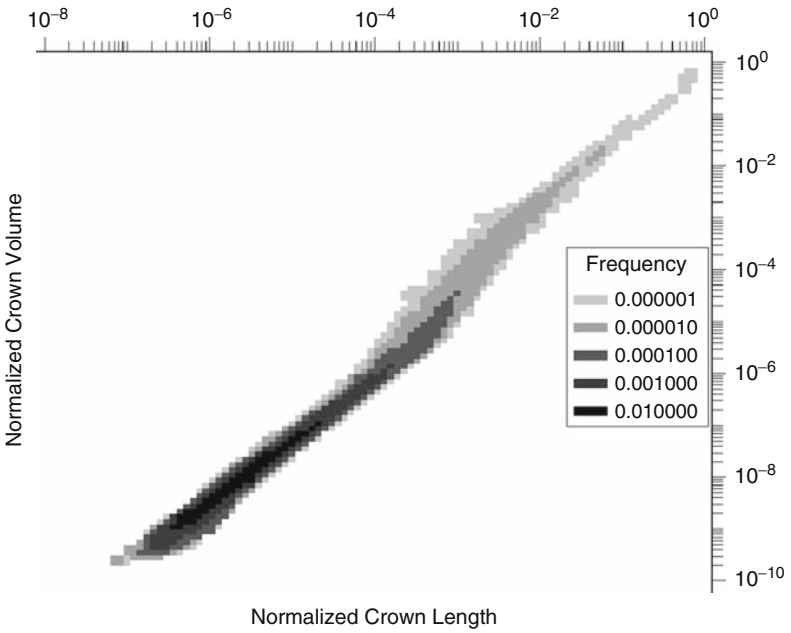

Fig. 6.3 An iso-density plot between crown volume and length of crown for the RCA. The total number of data points shown is 858,353 [19]

scaling laws that dictate the design of various vascular trees and the underlying physical and physiological principles.

6.4.1 Volume Scaling

An additional volume scaling relation of the form: $V_c = K_v D_s^{2/3} L_c$ has been recently proposed based on allometric scaling, where V_c and L_c are cumulative vessel volume and length in the tree, respectively, and D_s is the diameter of vessel segment [24]. The scaling relation was validated in vascular trees of various organs including the heart, lung, mesentery, muscle, and eye of different species. Based on the "Minimum Energy Hypothesis" and volume scaling relation, the structure–function scaling relations were predicted including the volume–length, diameter–length, and flow–diameter relations with exponent values of $1\frac{2}{7}(1.3)$, $\frac{3}{7}(0.43)$, and $2\frac{1}{3}(2.3)$, respectively. These exponents are similar to those derived based on minimization of cost function which provide further validation for the volume scaling relation.

6.4.2 Resistance Scaling

A novel resistance scaling law for a vascular tree (i.e., the resistance of a vessel segment scales with the equivalent resistance of the corresponding distal tree) was

also recently proposed [51]. The formulation can be written as $\frac{R_s}{R_c} \propto \frac{L_s}{L_c}$ (R_s and L_s are the resistance and length of a vessel segment, respectively; R_c and L_c are the equivalent resistance and total length of the corresponding distal tree) which was validated for the coronary vascular systems of the heart, lung, mesentery, muscle, eye, and others. The novel resistance scaling law, coupled with the $^3/_4$-power scaling law for metabolic rates (allometric scaling), can predict the same structure–function relations discussed earlier.

The resistance scaling law provides a theoretical and physical basis for understanding the hemodynamic resistance of the entire tree (or a subtree). The resistance scaling can also be expressed as $R_c = K_c \frac{L_c}{D_s^4}$, where L_c is the crown length that is defined as the sum of the lengths of each vessel in the crown, D_s is the diameter of the stem vessel proximal to the crown, and K_c is a constant that depends on the branching ratio, diameter ratio, total number of tree generations, and viscosity in the crown [23]. The scaling law illustrates the relationship between the structure (tree) and function (resistance), in which the crown resistance is proportional to the crown length and inversely proportional to the fourth power of stem diameterD_s^4. The small crown resistance corresponds to a small crown length, thus matching the transport efficiency of the crown. An increase of stem diameter can decrease the resistance, which may contribute to the self-scaling of a biological transport system [34–36]. The resistance scaling law provides an integration between a single vascular unit and the whole (millions of vessels) and imparts a rationale for diagnosis of disease processes as well as assessment of therapeutics as described below.

6.5 Functional Hierarchy

The question of functional design of the coronary arterial system has been the subject of numerous investigations [37, 38, 18, 39–41]. Zamir and colleagues have suggested that the arterial system can be classified into “distributing” vessels that remain on the surface of distinct zones of the heart and give rise to “delivering” vessels that penetrate those zones to implement the delivery of blood [39, 40]. As a basis for this classification, Zamir and Silver [39] showed that the distributing vessels have a lower branching rate than delivering vessels. The delivering vessels were found to divide more profusely and terminate more rapidly than the distributing vessels. Additional evidence for the differences in the branching pattern of EPCA and IMCA came from X-ray studies of Tanaka et al. [42]. They found that the self-similar branching pattern of coronary arteries was discrete at the connection between the EPCA and IMCA [42]. Finally, Ritman and colleagues found a similar discontinuity between EPCA and IMCA vessels using micro-CT [37, 38].

Kassab showed that there not only exists a characteristic variation in CSA or diameter that distinguishes EPCA from IMCA (Fig. 6.4a) but also a similar characteristic pattern of blood flow as shown in Fig. 6.4b [17]. These results suggest functional differences between the two types of vessels. Kassab also showed the existence of a functional difference between large and small IMCA that demarcates a possible transition from vessels involved in conduction to those vessels involved

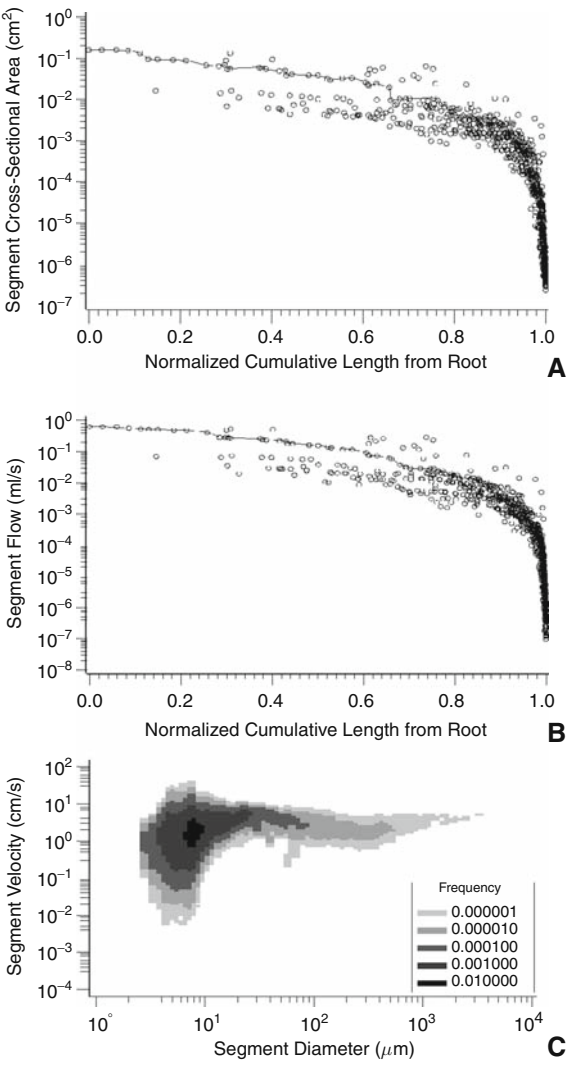

Fig. 6.4 The relationship between the (**a**) segment CSA and (**b**) segment flow and the normalized cumulative length of the segment from the root of the trunk and the primary branches of LAD arterial tree. The *solid line* denotes the main trunk. (**c**) An iso-density plot showing five layers of frequency between the velocity in a vessel segment and the corresponding diameter of the vessel for the LAD arterial tree. The total number of data points shown are 859 (Fig. 6.4a and b) and 1,872,027 (Fig. 6.4c) [17]

in transport based on the behavior of flow velocity (Fig. 6.4c). Proximal to these vessels the velocity is fairly uniform but drops significantly distal to those vessels towards the capillary branches. This finding suggests functional differences between large and small IMCA. Collectively, these observations suggest a functional hierarchy of the coronary vascular tree and provide direct evidence of a structure–function relation. Clearly, the role of the vessel CSA or diameter is central to the transition of flow or velocity.

Although the structure–function relation is one of the oldest paradigms in biology and medicine, this was the first direct evidence of the structure–function relation in the coronary circulation. The transition from EPCA to IMCA is evident in the CSA

(structure) and flow (function) curves (Fig. 6.4a and b, respectively). The structure of the EPCA vessels is suited for distribution of blood flow to various regions of myocardium without significant diminishment of blood flow. Furthermore, the transition from conductive to transportive flow further demarcates the functional hierarchy of the IMCA (Fig. 6.4c). The proximal portion of the IMCA, whose role is flow delivery, maintains a constant velocity of conduction while the distal vessels significantly reduce the velocity to ensure ample transit time for transport of oxygen and nutrients. Collectively, these observations lead to a functional hierarchal model of the coronary arterial tree in normal hearts. This functional model may serve as a reference state for understanding coronary circulatory dysfunction. Clearly, coronary artery disease will affect both the CSA and flow patterns and hence cardiac function. Hence, the present CSA, flow, and velocity profiles may represent the signatures of normal coronary circulation and deviations from these patterns may indicate perfusion abnormalities.

In summary, it appears that globally the coronary vasculature minimizes the energy of construction and operation while locally it serves the specific function of the heart in relation to distribution, conduction, and transport. Hence, the functional hierarchy obeys the minimum energy hypothesis and the resulting scaling laws which dictate the vessel geometry.

6.5.1 Possible Mechanisms for the Functional Hierarchy

Metzger and Kasnow [43] proposed a common genetic mechanism for all branching structures, including blood vessels independent of organ region. Furthermore, since EPCA and IMCA are formed from the same extra-cardiac source of endothelial cells, it is unlikely that the differences are embryological [44]. A possible explanation for the differences in EPCA and IMCA is dictated by local demand. In the inner layers of the heart, angiogenesis is stimulated as the local tissue oxygen gradient increases during postnatal growth of myocardium. The EPCA, on the other hand, only grow in diameter or CSA in response to increased flow or wall shear stress [45]. There is evidence that capillary density and the number of small arterioles increase during the postnatal period [46, 47]. The larger vessels, however, only increase in CSA and segment length [48]. Similar observations (increase in diameter and length of larger vessels and increase in number of smaller vessels) were made in a swine model of flow-overload-induced remodeling of the right ventricular branches in right ventricular hypertrophy [7].

6.6 Potential Clinical Applications

Since a detailed biomechanical analysis requires data on the geometry of an organ (e.g., the shape of the heart and the size of the blood vessels), developments in biomechanics overlap with advances in anatomy and imaging. Structural imaging

is necessary for quantifying organs, tissues, and cellular and molecular structures which serve as a basis for the construction of biomechanical and integrative models. Imaging modalities include magnetic resonance imaging, computerized tomography (CT), positron emission tomography, and ultrasound at the organ level; micro-CT and optical coherence tomography at the tissue level; confocal and interference microscopy, multi-photon microscopy, and electron tomography at the cellular level; and X-ray crystallography at the molecular level.

Clearly, patient-specific anatomy of the coronary arteries can be determined from CT scans to enable analysis and diagnosis. Specifically, the scaling laws can predict the crown volume from the stem diameter and crown length in the vasculature obtained by conventional imaging (e.g., CT scans or angiography). With the rapid developments in whole-body CT scanning, the utility of the scaling laws becomes apparent. The geometry (diameters and lengths) of the vasculature for an organ system or entire organism can be determined for the larger vessels (within resolution of imaging). The utility of such data for measurement of vessel geometry can lead to establishment of scaling parameters for normal population of patients. The scatter of data and degree of accuracy to evaluate the sensitivity of such approach remains to be determined.

An additional utility of the scaling law relates to computational modeling for determination of local blood fluid mechanics. The scaling laws can be used to determine appropriate boundary conditions for the computational software that has both basic and clinical significance [49]. The computational software, coupled with the noninvasive imaging techniques, can provide quantitative information (e.g., 3-D visualization of pressure and velocity fields at any points inside the lumen), which may help clinicians select appropriate treatment.

Finally, the integrative quantitative model of coronary vasculature can not only be used to test hypotheses and address basic issues in cardiology but may also serve as a valuable educational tool. Indeed, the model has a strong visual component and will be set up in an interactive, user-friendly mode [26]. It can become a valuable tool for cardiovascular scientists, physiologists, and students. The emergence of the World Wide Web provides an excellent environment for shared retrieval, display, and execution of the model together with the meta-information that contains the model context.

6.7 The Cardiome Project: Integration of Cardiac Structure and Function

The Cardiome is the description, in quantitative, testable form, of the functioning of the normal heart and its responses to intervention [50]. One of the central goals of the Cardiome Project is to implement a 3-D dynamic model of the beating heart that integrates the coronary vasculature and circulation, blood-tissue transport, mechano-energetics and metabolism, cardiac tissue mechanics, and electrophysiology. The modeling of the 3-D coronary vasculature is imperative since it strongly

influences the regional mechanics, energetics, and electrophysiology of the beating heart. The implementation of the Cardiome project is an important direction for future research in cardiology.

6.8 Summary and Conclusions

The geometry of the coronary vasculature is fundamental to the formulation of any boundary value problem of coronary circulation. Here, we presented the reductionist/integrationist approach for the faithful reconstruction of the coronary vasculature. The quantitative models of the vasculature yielded quantitative relations that link structure to function, i.e., scaling laws of coronary vasculature. The scaling laws imply that the geometry of the coronary vasculature is not random or arbitrary but obeys the minimum energy hypothesis, i.e., principle of efficiency. A functional hierarchy also emerged to reflect the local requirements of a 3-D organ. These features add significantly to our understanding of vascular design as well as provide potential tools for diagnosis and treatment to restore homeostasis of organ function.

Acknowledgments This research was funded in part by NIH HL055554-11, HL-084529, and HL087235.

References

1. Guo X, Kassab GS. The variation of mechanical properties along the length of the aorta in the C57BL/6 mouse. *Am J Physiol*. 2003;285(6):H2614–22.
2. Kaimovitz B, Huo Y, Lanir Y, Kassab GS. Diameter asymmetry of porcine coronary vasculature: structural and functional implications. *Am J Physiol*. 2008;294(2):H714–23.
3. Kassab GS. The coronary vasculature and its reconstruction. *Ann Biomed Eng*. 2000;28: 903–15.
4. Kassab GS, Rider CA, Tang NJ, Fung YC. Morphometry of pig coronary arterial trees. *Am J Physiol* (*Heart Circ Physiol* 34). 1993a;265: H350–65.
5. Kassab, GS, Fung YC. Topology and dimensions of the pig coronary capillary network. *Am J Physiol* (*Heart Circ Physiol*). 1994b;36:H319–25.
6. Kassab GS, Lin D, Fung YC. Morphometry of the pig coronary venous system. *Am J Physiol* (*Heart Circ Physiol* 36). 1994a;267:H2100–13.
7. Kassab GS, Imoto K, White FC, Rider CA, Fung YC, Bloor CM. Coronary arterial tree remodeling in right ventricular hypertrophy. *Am J Physiol* (*Heart Circ Physiol* 34). 1993;265:H366–75.
8. Kassab GS, Pallencaoe E, Schatz A, Fung YC. The longitudinal position matrix of the pig coronary vasculature and its hemodynamic implications. *Am J Physiol* (*Heart Circ Physiol*). 1997a;42:H2832–42.
9. Kassab GS, Fung YC. The pattern of coronary arteriolar bifurcations and the uniform shear hypothesis. *Ann Biomed Eng*. 1995;23:13–20.
10. Kassab GS, Berkley J, Fung YC. Analysis of pig's coronary arterial blood flow with detailed anatomical data. *Ann Biomed Eng*. 1997b;25:204–17.
11. Kassab GS, Lee KN, Fung YC. A hemodynamic analysis of coronary capillary blood flow based on detailed anatomical and distensibility data. *Am J Physiol* (*Heart Circ Physiol*). 1999;277(6):H2158–66.

12. Kassab GS, Schatz A, Imoto K, Fung YC. Remodeling of the bifurcation asymmetry of right ventricular branches in hypertrophy. *Ann Biomed Eng*. 2000;28:424–30.
13. Smith NP, Kassab GS. Analysis of coronary blood flow interaction with myocardial mechanics based on anatomical models. *Phil Trans R Soc Lond A*. 2001;359:1251–63.
14. Mittal N, Zhou Y, Linares C, Ung S, Kaimovitz, B, Molloi S, Kassab GS. Analysis of blood flow in the entire coronary arterial tree. *Am J Physiol* (*Heart Circ Physiol*). 2005a;289: H439–46.
15. Mittal N, Zhou Y, Ung S, Linares C, Molloi S, Kassab GS. A computer reconstruction of the entire coronary arterial tree based on detailed morphometric data. *Ann Biomed Eng*. 2005b;33(8):1015–26.
16. Kaimovitz B, Lanir Y, Kassab GS. Large-scale reconstruction of the porcine coronary arterial vasculature based on detailed anatomical data. *Ann Biomed Eng*. 2005;33(11):1517–35.
17. Kassab GS. A functional hierarchy of coronary circulation: Direct evidence of a structure–function relation. *Am J Physiol*. 2005;289:H2559–65.
18. Kassab GS. Scaling laws of vascular trees: of form and function. *Am J Physiol*. 2006;290:H894–903.
19. Kassa GS. Design of coronary circulation: The minimum energy hypothesis. *Compt Methods Appl Mech Eng*. 2007;196:3033–42.
20. Huo Y, Kassab GS. Pulsatile blood flow in the entire coronary arterial tree: theory and experiment. *Am J Physiol*. 2006;291(3):H1074–87.
21. Huo Y, Kassab GS. A hybrid one-dimensional/Womersley model of pulsatile blood flow in the entire coronary arterial tree. *Am J Physiol Heart Circ Physiol*. 2007;292(6): H2623–33.
22. Huo Y, Linares CO, Kassab GS. Capillary perfusion and wall shear stress are restored in the coronary circulation of hypertrophic right ventricle. *Circ Res*. 2007;100(2):273–83.
23. Huo Y, Kassab GS. Scaling of flow resistance: from single branch to entire distal tree. *Biophys J*. 2009a;96:339–46.
24. Huo Y, Kassab GS. A scaling law of vascular volume. *Biophys J*. 2009b;96:347–53.
25. Liu, Y, Kassab GS. Metabolic dissipation in vascular trees. *Am J Physiol*. 2007;292(3):H1336–9.
26. Wischgoll T, Meyer J, Kaimovitz B, Lanir Y, Kassab GS. A novel method for visualization of entire coronary arterial tree. *Ann Biomed Eng*. 2007a;35(5):694–710.
27. Wischgoll T, Choy JS, Ritman EL, Kassab GS. Validation of image-based extraction method for morphometry of coronary arteries. *Ann Biomed Eng*. 2007b;35(5):694–710.
28. Murray CD. The physiological principle of minimum work. I. The vascular system and the cost of blood volume. *Proc Nat Acad Sci USA*. 1926;12:207–14.
29. Uylings HBM. Optimization of diameter and bifurcation angles in lung and vascular tree structures. *Bull Math Biol*. 1977;39:509–19.
30. Sherman TF. On connecting large vessels to small: the meaning of Murray's Law. *J Gen Physiol*. 1981;78:431–53.
31. Zhou Y, Kassab GS, Molloi S. On the design of the coronary arterial tree: A generalization of Murray's law. *Phys Med Bio*. 1999;44:2929–45.
32. Wahle A, Wellnhofer E, Mugaragu I, Sauer HU, Oswald H, Fleck E. Quantitative volume analysis of coronary vessel systems by 3-D reconstruction from biplane angiograms. *IEEE Med Imaging Conf*. 1993;2, 1217–21.
33. Zhou Y, Kassab GS, Molloi S. In vivo validation of the design rules of the coronary arteries and their application in the assessment of diffuse disease. *Phys Med Bio*. 2002;47:977–93.
34. Clark ER. Studies on growth of blood vessels in the tail of the frog larvae, by observation and experiment on the living animal. *Am J Anat*. 1918;23:37–88
35. Hudlicka O, Tyler KR. *Angiogenesis: the growth of the vascular system*. London: Academic Press, 1986, 221.
36. Zweifach BW. The microcirculation in experimental hypertension: State-of-the-art review. *Hypertension*. 1983;5:I10–6.

37. Beighley PE, Thomas PJ, Jorgensen SM, Ritman EL. Maturation of arterial branching geometry – A micro-CT-based analysis. *Ann Biomed Eng*. 1996;24 (Supl 1):S37.
38. Beighley PE, Britton SL, Gerard-Koch L, Ritman EL. LV myocardial microcirculation in rats selectively bred for running endurance. *FASEB J*. 2004;18(4):A257.
39. Zamir M, Silver MD. Morpho-functional anatomy of the human coronary arteries with reference to myocardial ischemia. *Can J Cardiol*. 1985;1:363–72.
40. Zamir M. Distributing and delivering vessels of the human heart. *J Gen Physiol*. 1988;91: 725–35.
41. Zamir M. Flow strategy and functional design of the coronary network. In Kajiya, F, Klassen GA, Spaan JAE and Hoffman JIE (Eds.) *Coronary Circulation: Basic Mechanism and Clinical Relevance*, 1990.
42. Tanaka A, Mori H, Tanaka E, Mohammed MU, Tanaka Y, Sekka T, Ito K, Shinozaki Y, Hyodo K, Ando M, Umetani K, Tanioka K, Kubota M, Abe S, Handa S, Nakazawa H. Branching patterns of intramural coronary vessels determined by microangiography using synchrotron radiation. *Am J Physiol* (*Heart Circ Physiol* 45). 1999;276:H2262–7.
43. Metzger RJ, Kasnow MA. Genetic control of branching morphogenesis. *Science*. 1999;284:1635–39.
44. Baldwin HS. Early embryonic vascular development. *Cardiovasc Res*. 1996;31:E34–5.
45. Kassab GS, Gregersen H, Nielsen SL, Liu X, Tanko L, Falk E. Remodeling of the coronary arteries in supra-valvular aortic stenosis. *J. Hypertension*. 2002;20(12):2429–37.
46. Mayrovitz HN, Tuma RF, Wiedeman MP. Relationship between microvascular blood velocity and pressure distribution. *Am J Physiol*. 1977;232(4):H400–05.
47. Rakusan K, Turek Z. Protamine inhibits capillary formation in growing rat hearts. *Circ Res*. 1985;57:393–8.
48. Tomanek RJ. Formation of the coronary vasculature: a brief review. *Cardiovasc Res*. 1996;31:E46–51.
49. Huo Y, Choy JS, Svendsen M, Sinha A, Kassab GS. Effects of vessel compliance on flow pattern in the porcine epicardial right coronary arterial tree. *J Biomech*. 2009c;26;42(5): 594–602.
50. Bassingthwaighte JB. Design and strategy for the Cardionome Project. *Adv Exp Med Biol*. 1997;430:325–39.
51. Huo Y, Kassab GS. Scaling of flow resistance: from single branch to entire distal tree. *Biophysical J*. 2009;96:339–346.

Chapter 7
Vascular Geometry Reconstruction and Grid Generation

Thomas Wischgoll, Daniel R. Einstein, Andrew P. Kuprat, Xiangmin Jiao, and Ghassan S. Kassab

Abstract The geometry of vascular system is an important determinant of blood flow in health and disease. There is a strong geometric component to atherosclerosis in coronary heart disease since lesions are preferentially located at bifurcation points and regions of high curvature. The influence of these local structures on recirculation and deleterious shear stresses and their role in plaque development is widely accepted. Over time, researchers have turned to MR, CT, or biplane images of vascular trees to faithfully capture these features in the flow simulations. Historically, this has taken the form of labor-intensive manual reconstructions from morphometric measurements based on the centerline, whereby small idealized subsets of vascular trees are developed into computational grids. With improved imaging, image processing, and geometric reconstruction algorithms, researchers have begun to develop geometrically accurate computational models directly from the medical images. This chapter provides an overview of contemporary methods for image processing, centerline detection, boundary condition definition, and grid generation of both clinical and research images of cardiovascular structures.

7.1 Introduction

Computational fluid dynamics (CFD) has become an increasingly important component of integration and discovery in cardiovascular research. Although fluid and tissue stresses are not easily measured, they can be predicted through physics-based simulations. This is critical for cardiovascular research because vessel wall shear stress profiles can endothelial function, thrombus formation, and rupture, as well as the growth of aneurysms and atherosclerotic plaque. These and other cardiovascular

T. Wischgoll (✉)
Department of Computer Science and Engineering, Wright State University, Dayton, OH, USA
e-mail: thomas.wischgoll@wright.edu

J.M. Guccione, et al. (eds.), *Computational Cardiovascular Mechanics*,
DOI 10.1007/978-1-4419-0730-1_7,

issues are generally coupled multiphysics problems with a strong geometric component. These geometries are increasingly derived from imaging modalities such as magnetic resonance imaging (MRI) or computed tomography (CT), and are complex and articulated across multiple scales.

Efficient visualization, analysis, and unstructured mesh generation of these multiple geometries in a way that is tuned to the physics of the problem remains challenging. Finite computational resources dictate that computational geometry algorithms must be efficient and that the grids must be optimally adapted to the geometry in order to minimize both computational cost and discretization error. At the same time, cardiovascular biophysical simulations require that the grid be organized both by scale and by intrinsic properties. The arterial wall, for example, is a laminated tissue consisting of three separate layers, each with a separate family of collagen and elastin fibers and smooth muscles. Thus, a grid of the vessel wall must be similarly layered. That same layering persists at all scales of a vascular network. These transitions of scale are mirrored in the blood. The lumen of a coronary arteriole, for example, may be several orders of magnitude smaller than the thickness of a ventricle, and thus there is a need to manage error over a range of meaningful scales. Although the issue of scale clearly exists in both the fluid and the solid domains of physiological problems, an optimal discretization of the fluid and solid will be quite different due to the very different physics that dominate each domain. The most notable difference is that fluid problems tend to have strong gradients at the boundary.

Here, we survey some recent developments for computational grids for vascular CFD or fluid–solid interaction simulations. Specifically, we focus on image processing, centerline detection, and grid generation. Image processing, and particularly image segmentation, is a necessary first step for both centerline detection and grid generation. Given a centerline, some researchers have defined idealized grids based on subsets of arterial trees, wherein each segment of the centerline is associated with a diameter and length, and assembled into a network of tapered tubes. Although these types of grids have yielded valuable insights into cardiovascular flow, our focus is to develop grids directly from the medical image. Nevertheless, the centerline remains an important data structure for morphometric analysis and thus has an important role in the determination of physiological multiscale boundary conditions. Specifically, the centerlines allow for the computation of various quantitative measurements, such as vessel length, vessel radius, and bifurcation angles.

7.2 Image Processing

In order to identify the geometry of the vasculature, typically MRI or CT is used resulting in a volumetric image. A volumetric image consists of voxels aligned along a regular 3-D grid. It is generally not likely that the boundary of the vessels is exactly located at these voxels. A better precision can be achieved by finding the exact location in between a set of voxels. Since an accurate representation of

the object boundary is crucial to any further processing of the data, improvement of the precision is an essential step. Different approaches are available depending on the need of the algorithm used to further process the result. Some algorithms for computing the centerline only require an accurate representation of individual points. On the other hand, grid generating algorithms typically require a surface representation of the boundary; i.e., the points need to be connected by some geometric primitive. The following subsections provide examples of both types of algorithms.

7.2.1 Segmentation of the Vessel Boundary

The method described here uses similar techniques as described by Canny's non-maxima suppression [1] but extended to three dimensions. First, the image gradient is computed for every voxel. Using an experimentally determined threshold, all voxels with a gradient length below this threshold are neglected. The advantage of this gradient-based thresholding is that it is less sensitive to the selected threshold compared to intensity-based segmentation algorithms. This is particularly important for smaller vessels (1 voxel in diameter or less) that can be missed due to partial volume effects when using intensity segmentation.

In order to achieve sub-voxel precision, the gradients of the voxels exceeding the threshold are compared to their neighbors to identify local maxima along the gradient. In 3-D, the direct neighborhood of a single voxel generally consists of 26 voxels forming a cube that surrounds the current voxel. In order to find the local maximum along the current gradient, the gradients of the neighboring voxels in positive and negative directions have to be determined. When using 2-D images, nearest-neighbor interpolation of these gradients [2] may work but yield incorrect results in a 3-D volumetric image. Therefore, the gradients on the boundary of the cube formed by the neighboring voxels are interpolated linearly to determine a better approximation of the desired gradients.

Once the neighboring gradients in positive and negative direction of the current gradient are computed, they are compared to find the local maxima. Thus, if the length of the current gradient is larger than the length of both of its neighbors, the local maximum can be calculated similar to the 2-D case. When interpolated quadratically, the three gradients together form a parabolic curve along the direction of the current gradient. In general, the current gradient is larger than the interpolated neighbors since only local maxima are considered in this step. Hence, the local maximum can be identified by determining the zero of the first derivative of the parabolic curve. The determination of all local maxima within the volumetric image in this fashion then results in a more accurate and smoother approximation of the object boundary with sub-voxel precision. Once all points on the boundary are extracted from the volumetric image using this gradient approach with sub-voxel precision, the resulting point cloud can be further processed to identify the centerlines.

7.2.2 Segmentation Under Topological Control

In order to create a volume grid that is faithful to the medical image, it is necessary to produce a triangulated isosurface from a segmentation of the data. An important consideration is to produce such an isosurface while preserving correct vessel topology. From a topological point of view, an arterial tree (excluding the capillary bed) is homeomorphic with a sphere. Due to finite resolution, isosurfacing algorithms such as Marching Cubes [3] are unable to determine whether voxels that connect only by a corner or by an edge should truly be connected. This ambiguity can give rise to multiple handles that corrupt segmentations. Therefore segmentations must be performed under topological control [4].

To segment the data, a fuzzy connected-threshold algorithm is applied to the image in order to convert the series of grayscale images into a binary volume. Connectedness is restricted to face connectivity to prevent ambiguous representations of the surface between vessels and background. Face connectivity is accomplished both by restricting the region growing algorithm to faces and by a post-segmentation connectivity check that reassigns voxels found to possess vertex or edge connectivity.

Subsequently, loops are removed to bring the face-connected segmentation into proper topology using an automated approach based on skeletonization, loop detection, loop cutting, and clean-up. A breadth-first search of branches in the skeleton is applied, starting at the top of the coronary ostia. To find the optimal cutting location within the loop, a test cut is performed separately for each skeleton voxel belonging to the loop. Cuts are then affected at the region of minimum cross-sectional area and maximum path length from the ostia.

To extract the isosurface from the segmented image, we apply the Marching Tetrahedra variant of the popular Marching Cubes algorithm (Fig. 7.1). This produces a closed triangulated surface, devoid of boundary patches at the inlets and outlets and whose surface density is a function of resolution of the underlying data.

7.3 Centerline Detection

Numerous algorithms for extracting centerlines from volumetric data sets are available. An overview of the various techniques can be found in the paper by Cornea et al. [5]. Some methods begin with all voxels of a volumetric image and use a thinning technique to shrink down the object to a single line [6, 7, 8, 9, 10, 11–13, 14]. Ideally, the topology of the object should be preserved as proposed by Lobregt et al. [15] which is the basic technique used in commercial software systems, such as Analyze^{TM}. Luboz et al. [3] used a thinning-based technique to determine vessel radii and lengths from a CT scan. A smoothing filter was employed to eliminate the jaggedness of the thinning process and the results were validated using a silicon phantom. A standard deviation of 0.4 mm between the computed and the actual

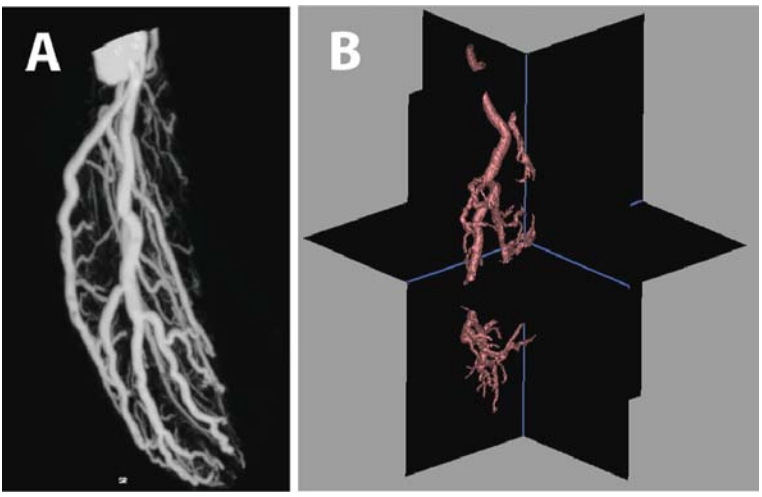

Fig. 7.1 Maximum intensity projection of mouse coronary vasculature (**a**). Segmentation and isosurface extraction (**b**)

measurements was reported for a scan with a resolution of 0.6 mm. The disadvantage of thinning algorithms is that they can only be applied to volumetric data sets and the centerlines are described at voxel-precision resulting in somewhat jagged lines, which do not allow accurate measurements of branch angles.

Other approaches use the distance transform or distance field in order to obtain centerlines. For example, fast marching methods [16, 17] can be employed to compute the distance field. Voxels representing the centerlines of the object are identified by finding ridges in the distance field. The resulting candidates must then be pruned first. The resulting values are connected using a path connection or minimum span tree algorithm [18, 19, 20]. The distance field can also be combined with a distance-from-source field to compute a skeleton [21]. Similar to thinning approaches, these methods are voxel-based and tend to generate the same jagged centerlines. This implies that a centerline can deviate from its original location by up to half a voxel due to the numerical representation.

A more recent method by Cornea et al. [31] computes the distance field based on a potential similar to an electrical charge and then uses a 3-D topological analysis to determine the centerlines. Typically, this approach is very accurate. The computations of the centerlines for a CT-scanned volumetric image of a typical size, such as $512\times512\times200$, would take several months, however, which renders it impractical.

Techniques based on Voronoi diagrams [22, 23] define a medial axis using the Voronoi points. Since this approach usually does not result in a single line but rather a surface-shaped object, the points need to be clustered and connected in order to obtain centerlines. Voronoi-based methods can be applied to volumetric images as well as point sets. These methods usually tend to extract medial surfaces rather than single centerlines. Hence, clustering of the resulting points is required which may introduce numerical errors.

For extracting centerlines from volumetric images, geometry-based approaches are preferable over voxel-based approaches. Due to the discrete nature of a voxel of the volumetric image, the location of the centerline can have an error of half a voxel. Geometry-based methods do not have this shortcoming. Nordsletten et al. [24] determined normal vectors based on an iso-surface computed using the volumetric image. These normal vectors are projected inward. The resulting point cloud is then collected and connected by a snake algorithm.

The method described in the following subsections follows an algorithm developed by Wischgoll et al. [20]. The major advantage of this approach lies in the demonstrated accuracy based on actual validations between computed vessel diameters and optical measurements for porcine hearts. This algorithm consists of several steps. Since the object is given as a volumetric CT-scanned image, the object boundary is extracted as previously described. A vector field is then computed that is orthogonal to the object boundary surface. Once the vector field is computed, the centerlines can be determined by applying a topological analysis to this vector field. As a last step, gaps between segments of the centerlines can be closed automatically and vessel diameters can be computed. The following subsections explain these steps in detail.

7.3.1 Vector Field

The proposed method computes the centerlines by applying a topological analysis to a vector field that is determined based on the geometric configuration of the object of which the centerlines are to be determined. The vector field is computed at the identified points on the vessel boundary in such a way that the vectors are orthogonal to the vessel boundary surface. Based on these vectors, the vector field inside the vessels is computed using linear interpolation.

Since the vasculature is given as a volumetric data set, the image gradients can be used to define these vectors on the boundary surface. These image gradients are previously determined as they are needed for extracting the boundary. Since the points are only moved along the direction of the image gradient when determining the subvoxel precision, this image gradient is still orthogonal to the boundary surface and therefore represents a good approximation for the desired vector field.

7.3.2 Determination of the Centerlines

In order to determine the centerlines of the object, a tetrahedrization of all points on the object boundary is computed first. For this, Si's [18] fast implementation of a Delaunay tetrahedrization algorithm is used. Tetrahedra outside of the vessels are removed based on the gradient vectors. Note that this step also closes small gaps that may exist since tetrahedra covering these gaps will still have vectors attached to the vertices which point inward. Since vectors are known for each vertex

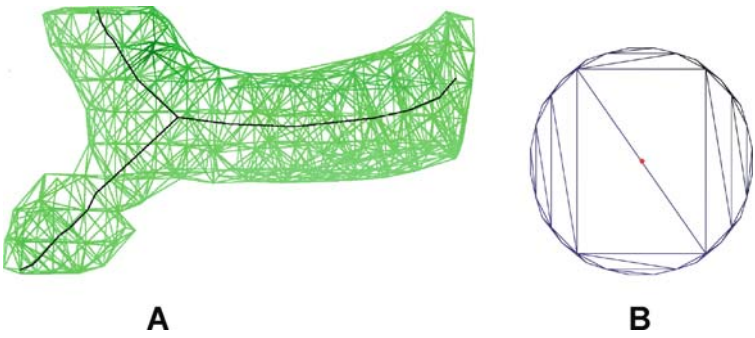

Fig. 7.2 A bifurcation for a small vessel (3 voxels in diameter). The extracted centerline is shown along with the respective tetrahedrization (**a**); Single slice through the tetrahedrization of the phantom data set. The point on the centerline is identified in the center of the image (**b**)

of every tetrahedron, the complete vector field can be computed using this tetrahedrization by linear interpolation within each tetrahedron. This vector field is then used to identify points of the centerlines which are then connected with each other. Figure 7.2a shows an example of the tetrahedrization with outside tetrahedra removed as previously described for a small vessel with a diameter of about 3 voxels. Based on this tetrahedrization and associated vector field, the centerlines can be identified.

In order to perform a topological analysis on the faces of the tetrahedra, the vector field has to be projected onto those faces first. Since tri-linear interpolation is used within the tetrahedra, it is sufficient to project the vectors at the vertices onto each face and then interpolate linearly within the face using these newly computed vectors. Based on the resulting vector field, a topological analysis can be performed on each face of every tetrahedron.

Points on the centerlines can be identified by computing the singularities within the vector field interpolated within every face of the tetrahedrization. For example, for a perfectly cylindrical object, the vector boundary points directly at the center of the cylinder. When examining the resulting vector field at a cross-section of the cylinder, a focus singularity is located at the center of the cylinder within this cross-section. The location of this focus singularity resembles a point on the centerline of the cylinder. Hence, a singularity of type node, focus, or spiral within a face of a tetrahedron indicates a point of the centerline. Since not all objects are cylindrical in shape and given the numerical errors and tolerances, points on the centerlines can be identified from singularities that resemble focus and spiral singularities. Figure 7.2b illustrates an example for a cylindrical object for which a cross-section (a slice perpendicular to the object) is shown. There are two large triangles that connect two opposite sides of the object. Based on these triangles, which resemble faces of tetrahedra of the tetrahedrization, the center point (shown in red) can be identified based on the topological analysis within these triangles.

Obviously, only faces that are close to being a cross-section of the object should be considered to identify points on the centerlines. To determine such cross-sectional faces, the vectors at the vertices can be used. If the vectors at the vertices, which are orthogonal to the object boundary, are approximately coplanar with the face, then this face describes a cross-section of the object. As a test, the scalar product between the normal vector of the face and the vector at all three vertices can be used. If the result is smaller than a user-defined threshold, this face is used to determine points on the centerlines. If we compute the singularity on one of these faces, then we obtain a point which is part of the centerlines. Note that since linear interpolation is used within the face, only a single singularity can be present in each face. In case of bifurcations, there will be two neighboring tetrahedra which contain a singularity, one for each branch. Additionally, this approach disregards boundary points from noise voxels. In order for a set of boundary points to be considered, they need to have gradient vectors that point towards the center from at least three different directions. Hence, boundary points based on noise voxels are automatically neglected.

After computing the center points, vessel diameters are computed for each center point and all points within the vicinity are identified. From this set of points, only the ones that are within the slice of the vessel used to determine the center point are selected to describe the boundary. The radius is then computed as the average of the distances between the center points and the points on the boundary of the vessel slice.

Once individual points of the centerlines (including the corresponding vessel diameters) are computed by identifying the focus and spiral singularities within the faces of the tetrahedra, this set of points must be connected in order to retrieve all centerlines. Since the tetrahedrization describes the topology of the object, the connectivity information of the tetrahedra can be used. Thus, identified points of the centerlines of neighboring tetrahedra are connected with each other forming the centerlines. In some cases, gaps will remain due to the choice of thresholds which can be closed using the method described in the next section.

7.3.3 Geometric Reconstruction

Based on the centerlines extracted from the volumetric image, various measurements can be extracted, such as vessel radius or bifurcation angles. A comparison of the computed radii, which were measured as the distance between centerline and vessel wall, and optical measurements of the radii for the main trunk of five porcine hearts show an excellent accuracy with an average error of 0.7% and rms error of 1.1% of the radii. Using the centerline and radii information, conic cylinders can be formed to represent the individual vessel segment. By representing every segment in this way, the vascular tree can be reconstructed. Figure 7.3 shows an example of such a geometric reconstruction of a porcine heart.

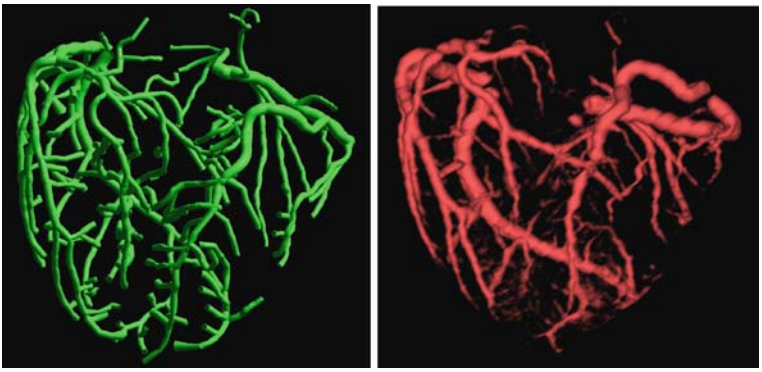

Fig. 7.3 Geometric reconstruction of the vascular tree (*left*) down to the scan resolution based on the centerline and radii information extracted from a CT-scanned porcine heart (*right*). (Wischgoll et al. [20] by permission)

Fig. 7.4 Interactive visualization of vasculature based on the geometric reconstruction showing quantitative measurements

Since the vasculature is represented as geometry, the visualization software not only facilities the gathering of statistical information about the morphometry but it also allows a user to perform various measurements, such as distances or bifurcation angles. By interactively selecting individual vessel segments, for example, the rendering of the geometric reconstruction is overlaid with quantitative measurements, including segment volume and surface area as depicted in Fig. 7.4.

7.4 Grid Generation

With surfaces derived from imaging data, the organization and density of the original surface triangles depend on the resolution of the digital data. The characteristic dimension of the surface triangles is on the order of 1 voxel. Simply generating a volume grid from the original surface could result in grossly under-resolving the computed field where the surface density is close to that of the local feature size

or conversely over-resolving the computed field where the surface density is much finer than that of the local feature size. These issues lead to a consideration of the local feature size as an important criterion for sizing and gradation control of the surface that is complementary to criteria that attempt to preserve surface features, topology, and curvature. Moreover, the local feature size in vessel geometry is related to the local diameter. Thus, a measure of the local feature size can also provide a guide for organizing elements radially in layers. This approach has the advantage of creating elements that are mostly parallel to the wall, which reduces discretization error in flows that are predominately axial. At the same time, it essentially decouples strategies for controlling grid density in the normal and tangential directions. It also directly embeds a local understanding of scale into the grid, since the local diameter is related to the local scale.

A robust and computationally efficient metric for local scale is the so-called gradient-limited feature size (GLFS) [25]. Unlike other measures of the local feature size, the GLFS (see Fig. 7.5) can be defined directly on a triangulated surface mesh without a background grid and without referencing the medial axis. Thus, determination of the GLFS is not only computationally efficient, but also robust in the sense that it is Lipchitz continuous and does not change unreasonably under perturbation of the surface mesh. Grids that are organized according to GLFS, such that roughly the same number of layers of elements can be found at all resolved scales, are said to be *scale-invariant*. Scale-invariance is critical in grids of vascular trees because it assures that discretization error at the smallest scale does not unduly affect solution error at the highest scale. In other words, the discretization error is equilibrated at all resolved scales. Combined with the GLFS, the idea of scale-invariance enables the automatic generation of quality anisotropic unstructured grids, while keeping the overall computational cost of the problem tractable. This approach has been adopted in two complementary scale-invariant gridding algorithms for quality layered tetrahedra [25] and quality hybrid prismatic-tetrahedral grids [8]. These algorithms have been implemented in two software frameworks, Lagrit-PNNL and MeshMagic. The defined GLFS in these two algorithms serves three functions: (1) as a field for tangential adaptation of the surface grid, (2) as a metric for creating layered tetrahedra, and (3) as a speed function for construction of a prismatic boundary layer by application of the Generalized Huygens' Principle [26]. Below we define the GLFS and outline these algorithms with examples.

7.4.1 Definition of GLFS

Let *S* be an oriented closed triangulated surface, which is derived from the isosurface of imaging data by the Marching Cubes algorithm. For a vascular tree, *S* will consists of a single connected component with genus 0. However, this is not an intrinsic limitation of the approach. As illustrated in Fig. 7.6, we modify *S* to produce a high-quality surface mesh *S'* by performing the operations of smoothing, refinement, and de-refinement while limiting perturbations to a small fraction of a voxel.

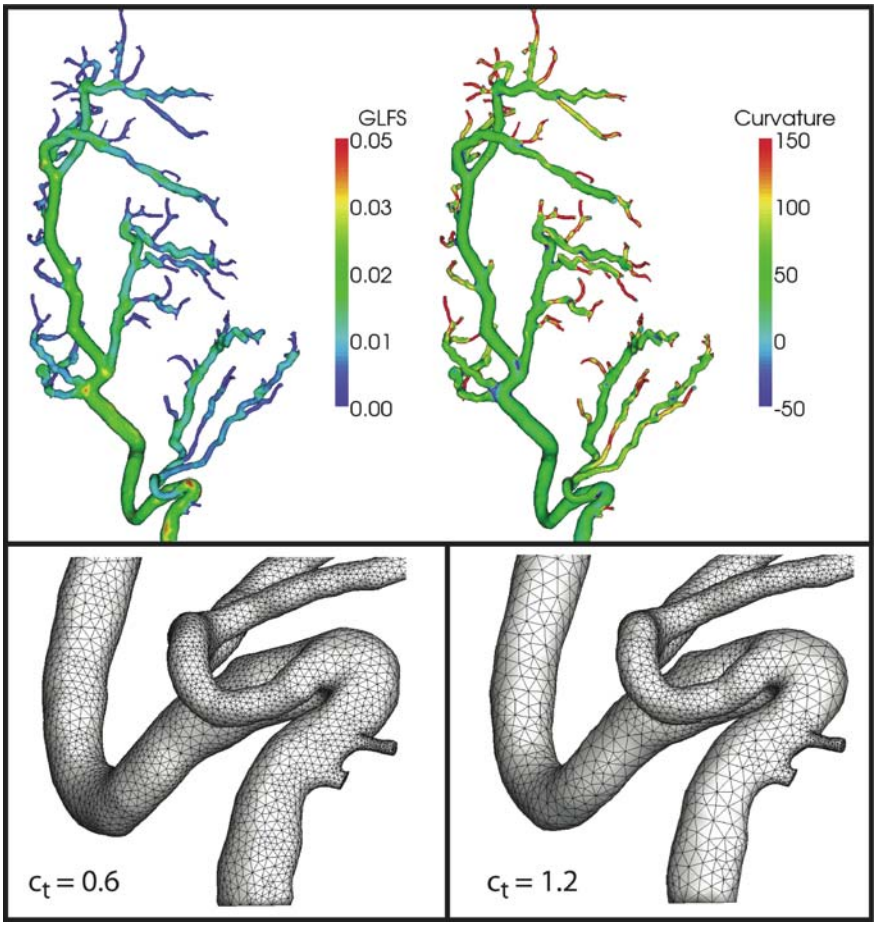

Fig. 7.5 GLFS and first principal curvature (*top panel*) defined on a mouse coronary arterial tree from computed tomography. Efficient computation of these sizing fields was performed in less than 5 s for this geometry on a laptop. Based on the GLFS modulated by the curvature, the original surface mesh from Marching Cubes is selectively refined and de-refined. The bottom panel shows the tangential adaption of the triangulated surface mesh for c_t values of 0.6 (152282 triangles) and 1.2 (129366 triangles). The curvature field for linear values of c_t prevents further de-refinement of the surface grid. For certain applications, it may make sense to convolve the GLFS with a non-linear function that weights higher or lower scales. These operations are supported in Lagrit-PNNL and MeshMagic

For any point $\boldsymbol{x}$ of S, we define *the raw feature size* or *local diameter* $F[\boldsymbol{x}]$ as the length of the line segment formed by first shooting a ray from $\boldsymbol{x}$ in the direction of $\hat{\mathbf{n}}[\mathbf{x}]$, the inward normal at $\boldsymbol{x}$, and then truncating the ray at its first intersection with S; that is

$$F[\mathbf{x}] \equiv \min\left\{\lambda > 0 \left| x + \lambda \hat{\mathbf{n}}[\mathbf{x}] \right| \in S\right\}. \tag{7.1}$$

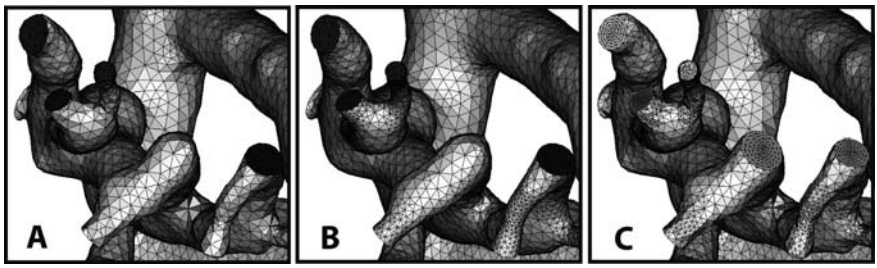

Fig. 7.6 Elaboration of closed surface mesh. Truncation produces valid triangulations and optimally orthogonal planes (**a**). Those triangulations may then be adapted to the physics of the problem (**b**) in order to produce a quality layered tetrahedral [25] grid (**c**)

Since S is closed, with a robust normal $\hat{\mathbf{n}}$ [1] the ray proceeding from $\mathbf{x}$ in the direction $\hat{\mathbf{n}}$ will intersect S at least once, and hence $F[\boldsymbol{x}]$ is well-defined. Similarly, we also perform an outward interrogation of the geometry to compute another raw feature size field F_{out} using $\hat{\mathbf{n}}_{\text{out}} = -\hat{\mathbf{n}}_{\text{in}}$. This outwards value is finite in some areas (e.g., at concave parts of S) and is applied only to the adaptation of surface meshes, where it is necessary to respect a minimum sampling frequency for Delaunay methods.

The raw feature size computed by ray tracing is bounded, but it is sensitive to abrupt changes in the geometry. To address this, we first impose user-specified lower and upper bound to the feature size, denoted by $L_{\min}$ and $L_{\max}$, respectively. Thereafter, we compute a new feature size $f[\boldsymbol{x}]$ by modifying $F[\boldsymbol{x}]$, so that the spatial gradient is relatively insensitive to these changes in S. We accomplish this by performing a gradient-limiting procedure [25]. First, we initialize $f[\boldsymbol{x}]$ to $F[\boldsymbol{x}]$. Given a bound G on the surface gradient of $f[\boldsymbol{x}]$, the algorithm places the directed edges that violate the gradient limit into a max-priority queue, ranked by the key

$$f[x_1] - (f[x_2] + G|x_1 - x_2|)\,. \tag{7.2}$$

which measures how much the gradient violates the gradient limit for a directed edge x_1x_2 on S. Let x_ix_j be the directed edge with the highest priority in the queue. We relax $f[\boldsymbol{x_i}]$ to satisfy the gradient limit, recompute the gradient violation for the edges incident on $\boldsymbol{x}_i$, and update the priority queue accordingly. The process continues until the queue is empty. For computational efficiency, ray-triangle intersections are queried within an axis-aligned bounding box (AABB) tree [27] that contains at its leaf nodes the bounding box for each triangle. This algorithm has a complexity of $O(N \log N)$, where N is the number of triangles in S. Figure 7.5a shows $f[\boldsymbol{x}]$ for a coronary arterial tree from micro-CT.

7.4.2 Layered Anisotropic Tetrahedra

Once the surface mesh has adapted to some function of the GLFS with edge lengths on the surface equal to about $c_t f[x_i]$, where c_t is a user definable parameter, it is

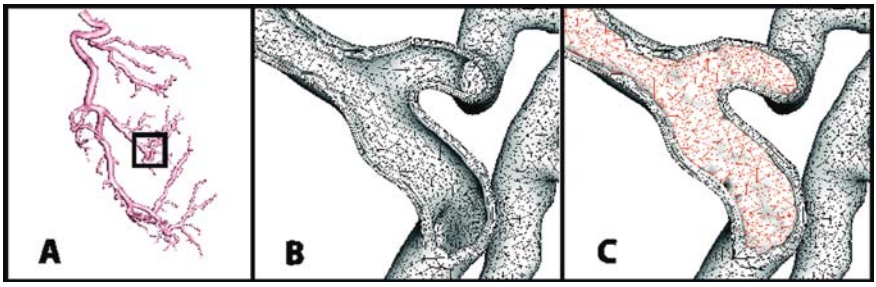

Fig. 7.7 Hybrid prismatic/tetrahedral grid better resolve strong gradients, shear stresses, and particle dynamics at the wall while reducing the overall element count. *Panel A* shows the orientation of the cut-away plane. *Panel B* shows the layer of prisms at the wall. *Panel C* shows the tetrahedra and prisms together

possible to construct either a layered tetrahedral volume grid (Fig. 7.6c) or a layered hybrid prismatic/tetrahedral grid (Fig. 7.7c), depending on the solver.

To create a layered tetrahedral grid, points are cast along "seeding rays" from each point $\mathbf{x}_i$ on the surface S' in the direction $\hat{\mathbf{n}}[\mathbf{x}_i]$. If M is the target number of layers across the cross-section of the geometry, then points $\mathbf{x}_i^m, 0 \leq m \leq \frac{M}{2}$, are distributed – equally or according to some desired ratio spacing – between $\mathbf{x}_i^0 \equiv \mathbf{x}_i$ on the surface and $\mathbf{x}_i + \frac{1}{2} f[\mathbf{x}_i]\hat{\mathbf{n}}[\mathbf{x}_i]$. Due to gradient-limiting, $f[\mathbf{x}_i] \leq F[\mathbf{x}_i]$. In areas where there is greater inequality, extra 'filler' points $\mathbf{x}_i^{M/2+1}, \ldots, \mathbf{x}_i^{m_i}$ are inserted between $\mathbf{x}_i + \frac{1}{2} f[\mathbf{x}_i]\hat{\mathbf{n}}[\mathbf{x}_i]$ and $\mathbf{x}_i + \frac{1}{2} F[\mathbf{x}_i]\hat{\mathbf{n}}[\mathbf{x}_i]$. The presence of these filler points guarantees that points are distributed over the whole geometry [25], but with possible overlap, and possibly undesirable proximity to portions of the surface that are nearly grazed by the seeding rays. Consequently, a filtering operation eliminates duplicate points that lie within a fraction of $L_{\min}$ of each other. Finally a Delaunay algorithm connects these points with the restriction that the filler points are not inserted if Delaunay point insertion would connect them to any point $\mathbf{x}_i$ on S'. Tetrahedra that contain no interior points (points $\mathbf{x}_i^m, m \geq 1$) are removed. Finally, the tetrahedral grid is improved with layer-aware, edge-flipping operations and a "crushing algorithm" that inserts nodes on the opposed diagonals of slivers and then merges them, eliminating the slivers. We note that the surface edge lengths $c_t f[\mathbf{x}_i]$ are independent of layer thicknesses.

7.4.3 Hybrid Prismatic/Tetrahedral Grids

In the case of hybrid prismatic/tetrahedral grids, we similarly begin with an adaption of the surface to $c_t f[\mathbf{x}_i]$. Instead of casting and reconnecting points, however, our method advances a surface layer by solving the Lagrangian evolution equation,

$$\frac{\partial x}{\partial t} = f(\mathbf{x},t)\ \hat{\mathbf{n}}, \tag{7.3}$$

where t denotes time, $\hat{\mathbf{n}}$ denotes the unit surface normal, and $f(\boldsymbol{x}, t)$ denotes the GLFS, as defined above.

Generating a layer of prisms reduces to marching the vertices in time by discretizing Eq. (7.3). To avoid "swallowtails" [28] in strongly concave regions and in regions with large curvatures, we apply the *face offsetting method* in [29], which is based on a geometric construction called the *generalized Huygens' principle* and numerical techniques of least-squares approximation and eigenvalue analysis. A comprehensive exposition of the approach is given in [8]. Here we simply note that unlike previous approaches, which propagate vertices along some vertex normals, this algorithm propagates faces and reconstructs the vertices. Mesh quality is achieved by applying a novel prismatic variational smoothing procedure to improve base triangle shapes and edge orthogonality. Following face-offsetting, we tetrahedralize the interior with a boundary constrained Delaunay method [30].

7.4.4 Element Quality

Discretization error can have two sources: (1) insufficient grid density to resolve computed gradients, and (2) "badly" shaped elements. What exactly constitutes a badly shaped element is somewhat application dependent. It is generally accepted that an isotropic element, i.e. an element with nearly equal internal angles and approximately equal edge lengths, is "good" and a highly skewed element is "bad". However, for certain classes of problems such as CFD, isotropic elements may be neither necessary nor particularly appropriate. Nevertheless, the accuracy or speed of some applications can be compromised by just a few bad elements, so it is important to be able to judge element quality by some standard measure. In Fig. 7.8, we present the quality statistics of the layered tetrahedral grid shown in Fig. 7.6, and the hybrid prism/tet grid shown in Fig. 7.7. For tetrahedra, we report the aspect ratio which is proportional to the ratio of the inscribed radius to the length of the longest edge. For prisms, we report instead the so-called scaled aspect ratio [8], whose definition is somewhat more involved. In effect, the scaled aspect ratio combines the measures of triangle shapes and edge orthogonality. Both quality metrics vary between 0 and 1, where 1 is optimal.

7.5 Summary

There is no doubt that patient-specific treatment requires the tools to quantify standard patient images using conventional imaging (CT, MRI, etc.). This chapter presents validated image segmentation in conjunction with mesh generation algorithms to create mathematical models of patient vasculature. These mathematical models can then be coupled with physics-based simulations to provide the desired diagnostic or prognostic indices. This approach will clearly impact patient

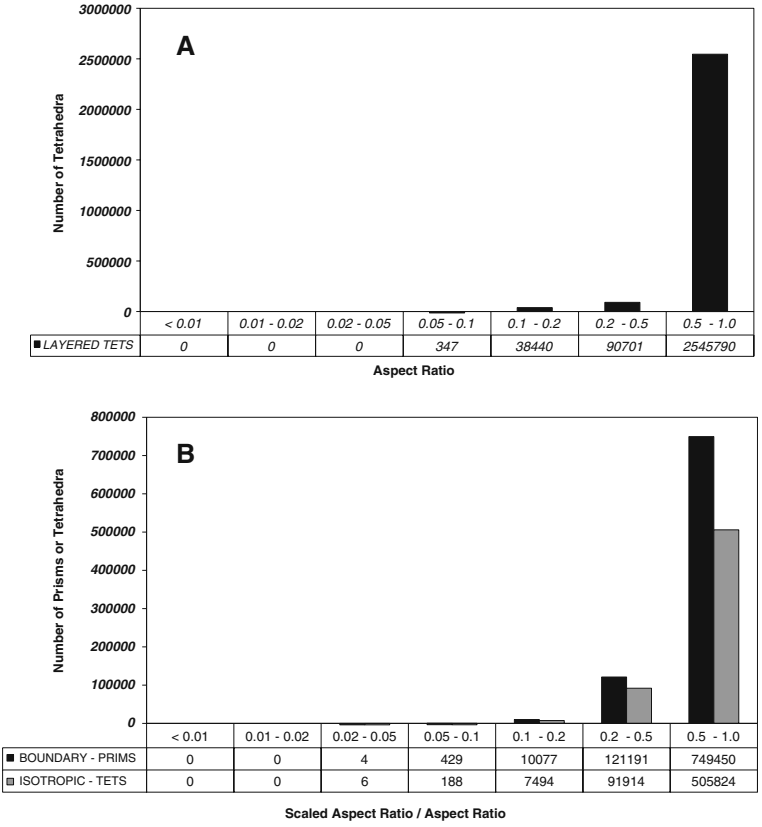

Fig. 7.8 Element quality statistics for a layered tetrahedral grid of the mouse coronary geometry (**a**), and for the hybrid prism/tetrahedral grid (**b**), shown in black and grey bars, respectively. Both grids were produced with $c_t = 0.6$. For grid (**a**) the number of layers M was set to 8

management medically and surgically, particularly for heart failure where interventions affect the vasculature of the heart.

Acknowledgments This research was supported in part by Wright State University; the Ohio Board of Regents; the National Heart and Blood Institute HL055554-11, HL-084529, and HL073598; the National Institute of Environmental Health Sciences P01ES011617; and by the National Science Foundation DMS-0809285.

References

1. Canny JF. A computational approach to edge detection. *IEEE Trans Pattern Anal Mach Intell*. 1986;PAMI-8(6):679–98.
2. Jain R, Kasturi R, Schunck BG. Machine vision. New York: McGraw-Hill, Inc., 1995.
3. Lorensen WE, Cline HE. Marching cubes: a high resolution 3D surface construction algorithm. *Comput Graph*. 1987;21(4).

4. Carson JP, Einstein DR, Minard KR, Fanucchi MV, Wallis CD, Corley RA. Lung airway cast segmentation with proper topology, suitable for computational fluid-dynamic simulations. *Comput Med Imaging Graph.* (submitted).
5. Cornea ND, Silver D, Min P. Curve-skeleton applications. Proceedings of IEEE visualization, 2005, pp. 95–102.
6. Bertrand G, Aktouf Z. A three-dimensional thinning algorithm using subfields. *Vis Geom III*. 1994;2356:113–24.
7. Brunner D, Brunnett G. Mesh segmentation using the object skeleton graph. Proceedings of IASTED international conference on computer graphics and imaging, 2004, pp. 48–55.
8. Dyedov V, Einstein DR, Jiao X, Kuprat AP, Carson JP, del Pin F. Variational generation of prismatic boundary-layer meshes for biomedical computing. *Int J Numer Methods Eng*. 2009;79(8):907–945.
9. Lee T, Kashyap RL, Chu CN. Building skeleton models via 3-D medial surface/axis thinning algorithms. *CVGIP: Graph Model Image Process*. 1994;56(6):462–78.
10. Lohou C, Bertrand G. A 3D 12-subiteration thinning algorithm based on P-simple points. *Discrete Appl Math*. 2004;139:171–95.
11. Palágyi K, Kuba A. Directional 3D thinning using 8 subiterations. Proceedings of discrete geometry for computer imagery, *Lect Notes Comput Sci*. 1999;1568:325–36.
12. Palágyi K, Kuba A. A parallel 3D 12-subiteration thinning algorithm. *Graph Model Image Proc*. 1999;61(4):199–221.
13. Saha PK, Chaudhuri BB, Dutta Majumder D. A new shape preserving parallel thinning algorithm for 3D digital images. *Pattern Recognit*. 1997;30(12):1939–55.
14. Tsao YF, Fu KS. A parallel thinning algorithm for 3-D pictures. *Comput Graph Image Process*. 1981;17:315–31.
15. Lobregt S, Verbeek PW, Groen FCA. Three-dimensional skeletonization: principle and algorithm. *IEEE Trans Pattern Anal Mach Intell*. 1980;2(1):75–7.
16. Sethian JA. Fast marching methods. *SIAM Rev*. 1999;41(2):199–235.
17. Telea A, Vilanova A. A robust level-set algorithm for centerline extraction. Eurographics/IEEE symposium on data visualization, 2003, pp. 185–94.
18. Si H.TetGen. A quality tetrahedral mesh generator and three-dimensional Delaunay triangulator. WIAS Technical Report No. 9, 2004.
19. Wan M, Dachille F, Kaufman A. Distance-field based skeletons for virtual navigation. Proceedings of IEEE visualization, 2001, pp. 239–45.
20. Wischgoll T, Choy JS, Ritman ES, Kassab GS. Validation of image-based extraction method for morphometry of coronary arteries. *Ann Biomed Eng*. 2008;36(3):356–68.
21. Zhou Y, Toga AW. Efficient skeletonization of volumetric objects. *IEEE Trans Vis Comput Graph*. 1999;5(3):196–209.
22. Amenta N, Choi S, Kolluri R.The power crust. Proceedings of 6th ACM symposium on solid modeling, 2001, pp. 249–60.
23. Dey TK, Goswami S. Tight Cocone: a water-tight surface reconstructor. Proceedings of 8th ACM symposium. Solid modeling applications, 127–34. *Journal version in J Comput Inform Sci Eng*. 2003;30:302–7.
24. Nordsletten DA, Blackett S, Bentley MD, Ritman EL, Smith NP. Structural morphology of renal vasculature. *Am J Physiol Heart Circ Physiol*. 2006;291(1):H296–309.
25. Kuprat-AP, Einstein-DR. An anisotropic scale-invariant unstructured mesh generator suitable for volumetric imaging data. *J Comput Phys*. 2009;228:619–40.
26. Jiao X, Zha H. Consistent computation of first- and second-order differential quantities for surface meshes. In ACM solid and physical modeling symposium, 2008.
27. Khamayseh A, Hansen G. Use of the spatial kD-tree in computational physics applications. *Commun Comput Phys*. 2007;2:545–76.
28. Sethian JA. Level set methods and fast marching methods: evolving interfaces in computational geometry, fluid mechanics, computer vision, and materials science. Cambridge: Cambridge University Press, 1999.

29. Jiao X. Face offsetting: a unified approach for explicit moving interfaces. *J Comput Phys*. 2007;220:612–625.
30. Si H. Adaptive tetrahedral mesh generation by constrained Delaunay refinement. *Int J Numer Methods Eng*. 2008;856–80.
31. Cornea ND, Silver D, Yuan X, Balasubramanian R. Computing hierarchical curve-skeletons of 3D objects. *Vis Comput*. 2005;21(11):945–55.
32. Luboz V, Wu X, Krissian K, Westin CF, Kikinis R, Cotin S, Dawson S. A segmentation and reconstruction technique for 3D vascular structures. MICCAI 2005, *Lect Notes Comput Sci*. 2005;3749:43–50.

Chapter 8
Governing Equations of Blood Flow and Respective Numerical Methods

Yunlong Huo and Ghassan S. Kassab

Abstract Coronary heart disease which is a major cause of heart failure in the United States has a focal nature which is due to local hemodynamic disturbances. The computational fluid dynamics (CFD) method has become a powerful approach to understand blood flows in the cardiovascular system and its local features. This chapter outlines the field equations for blood flow and some of the approaches for numerical solutions. Specifically, the text focuses on the finite difference (FD) and finite element (FE) methods with applications to blood flow dynamics in coronary arteries.

8.1 Introduction to Computational Fluid Dynamics

The blood flow in the cardiovascular system is so complicated that it is rarely solvable analytically [1]. Most of the analytical solutions are carried out, based on simplified vascular geometry, such as a cylindrical vessel segment. Experiments are used to measure the temporal spatially averaged blood flow. Computational fluid dynamics (CFD) methods are then used in conjunction with the experimental waveforms (as boundary conditions) to predict blood flow disturbances (e.g., flow separation, secondary flow, stagnation point flow, reversed flow, and/or turbulence) due to convective inertia. Flow disturbances can locally induce abnormal biological response, such as dysfunction of endothelial cells, monocyte deposition, elevated wall permeability to macromolecules, particle migration into the vessel wall, smooth muscle cell proliferation, and microemboli formation. Since the spatial complexities of blood flow in the cardiovascular system cannot be visualized with current imaging methods, theory and computational modeling are a necessity.

Y. Huo (✉)
Department of Biomedical Engineering, Surgery, and Cellular and Integrative Physiology, IUPUI, Indianapolis, IN 46202, USA
e-mail: yhuo@iupui.edu

J.M. Guccione, et al. (eds.), *Computational Cardiovascular Mechanics*,
DOI 10.1007/978-1-4419-0730-1_8,

The CFD method has emerged as a powerful tool to study flow patterns in blood vessels with the development of electronic computers. For example, Perktold et al. [2] compared Newtonian and non-Newtonian unsteady fluid flow in normal carotid arteries. Kleinstreuer and his colleagues [3, 4] studied the relationship between non-uniform hemodynamics at the rabbit aorto-celiac junction. Berger and his associates [5] investigated blood flow with a turbulence model in stenotic vessels. He and Ku [6, 7] solved pulsatile flow in the human coronary arteries. Ramaswamy et al. [8] performed numerical simulation to study the effects of motion of the coronary artery on the unsteady fluid dynamics.

8.2 Governing Equations

The blood flow must obey the conservation laws [9, 10, 11, 12]. The governing equations for blood flow are the mass (continuity) and momentum conservation equations

$$\frac{\partial \rho}{\partial t} + \nabla \cdot (\rho v) = 0, \tag{8.1}$$

$$\begin{aligned} &\frac{\partial (\rho v)}{\partial t} + \nabla \cdot (\rho v v) = \\ &\quad -\nabla p + \nabla \lambda (\mathrm{tr} D) I + \nabla \cdot \mu \left(\nabla v + (\nabla v)^T \right) + \rho f, \end{aligned} \tag{8.2}$$

where v and p are blood velocity and pressure, respectively. tr$D$ is the trace of the strain rate tensor (D) representing a volumetric deformation and I is the unit tensor. ρ and μ are the density and dynamic viscosity, respectively, and f is a body force. In the larger arteries and veins, the blood flow can be assumed to be isotropic, Newtonian, and incompressible fluids [13]. The governing equations can then be simplified to

$$\nabla \cdot v = 0, \tag{8.3}$$

$$\rho \frac{\partial v}{\partial t} + \rho v \cdot \nabla v = -\nabla p + \mu \nabla^2 v + \rho f. \tag{8.4}$$

Equation (8.4) is known as the Navier–Stokes (N–S formulation of the momentum equation).

8.3 General CFD Methods

The CFD method is a numerical model to treat a continuous fluid in a discretized fashion. The fundamental basis of the model in a single-phase blood flow is the partial differential equations (PDE) or integro-differential equations of continuity

and N–S equations, which can be discretized at specific locations in space and time, approximated by a system of algebraic equations, and then solved on a computer. The method of a numerical solution can be summarized as follows:

- Select an appropriate mathematical model and boundary conditions
- Select a suitable discretization method
- Select the correct coordinate system and basis vectors
- Create the numerical grid
- Solve the algebraic equations
- Set the convergence criteria for iterative method

The most important properties of numerical model are consistency, stability, and convergence, as defined below:

- Consistency: A numerical scheme is consistent if its discrete operator becomes exact as the grid spacing ($\Delta x_i \to 0$ and/or $\Delta t \to 0$) tends to zero.
- Stability: A numerical scheme is stable if it does not enlarge the errors that appear in the course of numerical solution process.
- Convergence: A numerical scheme is convergent if the solution of the discretized equations tends to the exact solution of the differential equations as the grid spacing ($\Delta x_i \to 0$ and/or $\Delta t \to 0$) tends to zero.

The numerical model has an approximate solution, which includes several kinds of errors:

- Modeling errors: the difference between the actual blood flow and the exact solution of the mathematical model.
- Iteration errors: the difference between the iterative and exact solutions of the algebraic equations.
- Round-off errors: due to the fact that floating point numbers are represented by finite precision in a computer.
- Truncation errors: a discretization error caused by the fact that a discrete approximation is made to the continuous equations.

The accuracy of numerical solutions depends on the selected discretization method. There are many discretization methods, the most popular approaches of which are finite difference (FD), finite volume (FV), and finite element (FE) methods.

The FD method is the most classical and straightforward approach for numerical solution of PDE in simple geometries. In FD method, the PDE is converted into a set of FD equations at each grid point that can be solved subject to the appropriate boundary conditions. Taylor series expansion or polynomial fitting is generally used to obtain an approximation to the first and second derivatives of the variables with respect to the coordinates. The FD method is very efficient on structured meshes (simple geometry), but difficult to implement in complex geometries.

In comparison with the FD method, the FV method enforces the integral conservation law in small control volumes (CVs) defined by the computational mesh. In the FV method, the variable values are calculated at the central node of each CV. Interpolation is used to express variable values at the CV surface and the appropriate quadrature formulae are used to simulate the surface and volume integrals. The advantage of FV method is that it is suitable for complex geometries but the disadvantage is that the higher-order FV method is more difficult to develop in three-dimensional (3-D) geometries.

The FE method has many common features to FV method. The FE procedure begins with the division of the continuum region into a number of simply shaped regions called elements. Within each element, the variables are interpolated by functions of compatible order, in terms of values to be determined at a set of nodal points. For purpose of developing the equations for these nodal point unknowns, an individual element may be separated from the assembled system. The FE method can address any arbitrary geometry, but it is time-consuming to solve the assembled large sparse matrices. Since the FE method is similar to the FV method, we only describe the FE method in the following subsections and the details of the FV method can be found in standard textbook [14].

8.4 Finite Difference Method

Since the FD method has been given in detail in many textbooks [15, 16, 17], we will only use a hyperbolic example here in the context of blood flow in the coronary arteries. The 1-D continuity and momentum equations were used to solve the blood flow in the entire epicardial coronary arterial tree of a vasodilated, potassium-arrested porcine heart through the FD method [18]. We investigate the left common coronary arterial (LCCA) tree comprising of left anterior descending artery (LAD) and left circumflex artery (LCx), as shown in Fig. 8.1. The 1-D equations were formulated for a Newtonian, incompressible fluid in an elastic tree. The 1-D analysis consists only of larger coronary arteries, every vessel of which is assumed to be cylindrical with impermeable wall. Therefore, the fluid flow in every vessel segment is axisymmetric and laminar with no-slip boundary condition (i.e., the velocity of fluid at the wall equals the velocity of the wall). Various geometrical parameters in a typical vessel can be represented as length L, radius R, cross-sectional area A, surface S, volume V, and wall thickness h, that can vary with time and space. Furthermore, the dynamic parameters are represented as the velocities of fluid flow [$u_r(r, z, t)$, $u_x(r, z, t)$]. The volumetric flow rate and the pressure in the vessel are $q(z, t)$ and $p(z, t)–p_0$ (intravascular pressure minus external pressure which is assumed to be zero in diastole), respectively. A cylindrical coordinate system is used with radial (r) and axial (z) directions; the hemodynamic quantities $u_r(r, z, t)$, $u_z(r, z, t)$, $q(z, t)$, and $p(z, t)$ may be represented as u_r, u_z, q, and p.

In order to derive the 1-D equations, the continuity (mass conversation) and momentum equations for tube flow may be simplified from Eqs. (8.3) and (8.4) to

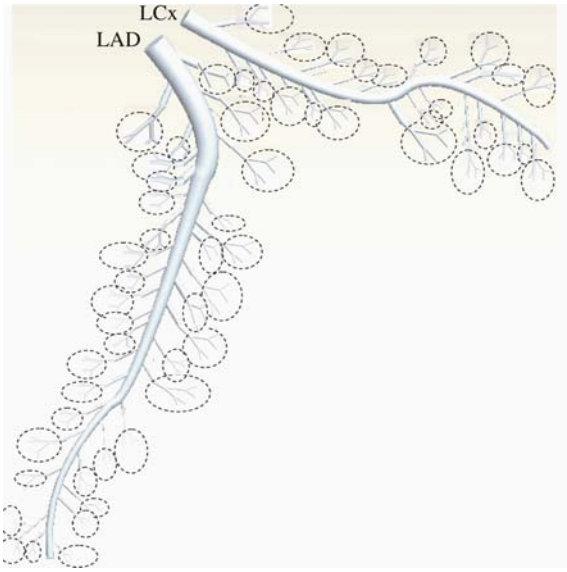

Fig. 8.1 Schematic representation of the computational domains (the main trunk and primary branches) in the LCCA tree which consists of the LAD and LCx arterial trees [18]

$$\frac{\partial u_z}{\partial x} + \frac{1}{r}\frac{\partial (r u_r)}{\partial r} = 0, \tag{8.5}$$

$$\begin{aligned} &\frac{\partial u_z}{\partial t} + u_z \frac{\partial u_z}{\partial z} + u_r \frac{\partial u_z}{\partial r} + \frac{1}{\rho}\frac{\partial p}{\partial z} = \\ &\quad \frac{\nu}{r}\frac{\partial}{\partial r}(r\frac{\partial u_z}{\partial r}) + \nu \frac{\partial^2 u_z}{\partial z^2}, \end{aligned} \tag{8.6}$$

where $\nu = \mu/\rho$ is the kinematic viscosity. After some transformation, Eqs. (8.5) and (8.6) can be written as

$$\frac{\partial A}{\partial t} + \frac{\partial q}{\partial z} = 0, \tag{8.7}$$

$$\frac{\partial q}{\partial t} + \frac{\partial}{\partial z}\left(\frac{4}{3}\frac{q^2}{A}\right) + \frac{A}{\rho}\frac{E_{\text{stat}} h_0}{R_0 A_0}\frac{\partial A}{\partial z} = -8\pi\nu\frac{q}{A} + \nu\frac{\partial^2 q}{\partial z^2}, \tag{8.8}$$

where E_{stat} is the static Young's modulus obtained from measurements [18]. Equations (8.7) and (8.8) are the basic equations, which can be simplified to

$$\begin{aligned} &\frac{\partial A}{\partial t} + \frac{\partial q}{\partial z} = 0, \\ &\frac{\partial q}{\partial t} + a\frac{\partial q}{\partial z} + b\frac{\partial A}{\partial z} = c + d\frac{\partial^2 q}{\partial z^2}, \end{aligned} \tag{8.9}$$

where

$$a = \frac{8}{3}\frac{q}{A}, \quad b = -\frac{4}{3}\left(\frac{q}{A}\right)^2 + \frac{A}{\rho}\frac{E_{\text{stat}}h_0}{R_0A_0}, \quad c = -8\pi\nu\frac{q}{A}, \quad d = \nu.$$

For the large vessels, Eq. (8.9) can be solved by the time-centered implicit (Trapezoidal) FD method. Here, we define $q_{\text{m}}^{\text{n}} = q(m\Delta z,n\Delta t)$ and $A_{\text{m}}^{\text{n}} = A(m\Delta z,n\Delta t)$, where $0<n\leq N$ for the current time step and $0<m\leq M$ expresses the position along a vessel divided into M subintervals. Therefore, the discretization in Eq. (8.9) may be written as follows:

$$(-0.25\,k)q_{m-1}^{n+1} + A_m^{n+1} + (0.25\,k)q_{m+1}^{n+1} = F_1, \tag{8.10}$$

$$\begin{aligned}(-0.25bk)A_{m-1}^{n+1} + (-0.25ak - 0.5\xi d)q_{m-1}^{n+1} + \\ (1+\xi d)q_m^{n+1} + (0.25bk)A_{m+1}^{n+1} + \\ (0.25ak - 0.5\xi d)q_{m+1}^{n+1} = F_2,\end{aligned} \tag{8.11}$$

where

$$k = \frac{\Delta t}{\Delta x} \quad \text{and} \quad \xi = \frac{\Delta t}{\Delta x^2},$$

$$F_1 = (0.25\,k)q_{m-1}^n + A_m^n + (-0.25\,k)q_{m+1}^n,$$

$$\begin{aligned}F_2 = c + (0.25bk)A_{m-1}^n + (0.25ak + 0.5\xi d)q_{m-1}^n + (1-\xi d)q_m^n + \\ (-0.25bk)A_{m+1}^n + (-0.25ak + 0.5\xi d)q_{m+1}^n.\end{aligned}$$

The detailed description of the FD solution can be found in Huo and Kassab [18]. The viscosity (μ) and density (ρ) of the solution were 1.1 cp and 1 g/cm^3, respectively, to mimic the validation experiments using cardioplegic solution in the isolated arrested heart preparation. The coronary wall thickness was obtained from experiments [19]. The static Young's modulus was estimated as $\sim 7.0\times10^6$ (dynes/cm^2) as described in a previous publication [20]. Since the time-centered implicit (Trapezoidal) FD method is stable and second-order in both time and space, the mesh size (Δx) was selected as 0.05 cm and the time step (Δt) was set to 2.0×10^{-3}.

Figure 8.2 shows the calculated flow waves at the inlet of LCCA tree, which are within ± 1SD of the experimental measurement. In comparison with the traditional Womersley method, the 1-D method has slightly better agreement with the experimental measurements. Figure 8.3 shows the flow waves sequentially at different spatial positions along the main trunk starting from the inlet of LAD artery while Fig. 8.4 shows the flow waves at the inlet of various primary branches. The decrease in the amplitude along the main trunk is apparent, but the flow waveform remains relatively unchanged except for a very small phase angle shift in the potassium-arrested heart. This is because the primary branches shunt the flow away from the main trunk. Since primary branches have different CSA, the flow waves at the inlet

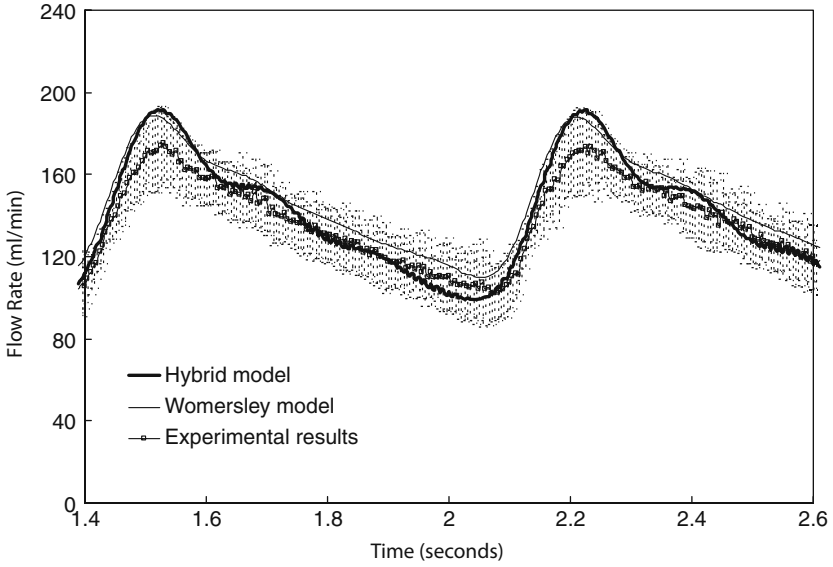

Fig. 8.2 A comparison of pulsatile flow between the hybrid 1-D/Womersley model and full Womersley-type model and experimental results at the inlet of the entire LCCA tree down to the first capillary bifurcation [18]

of primary branches show different amplitudes. When the flow waves are normalized by the time-averaged flow rate, however, it is found that the flow waves tend to scale to a single curve except for a small phase angle difference in the arrested heart, which reflects a structure–function relationship between the mean flow and vessel diameter [21].

8.5 Finite Element Method

The FE method is a computer-aided mathematical technique for obtaining approximate numerical solution of the physical phenomena subject to initial and boundary conditions. The FE method originally arose from applications in solid mechanics (elasticity, plasticity, statics, and dynamics). To date, applications have been expanded to the broad field of engineering sciences such as heat transfer (conduction, convection, and radiation), fluid mechanics (inviscid or viscous, compressible or incompressible), acoustics, and electromagnetics.

There are two types of optimizing routes leading to the FE formulation: (a) methods of weighted residuals (MWR), which are applicable when the governing equations are differential equations, (b) variational method (VM), which is applicable when the governing equations are variational (integral) equations. The MWR seek to minimize the residue in the differential equations. There are four basic types in the MWR route: (a) the collocation method, (b) the subdomain method, (c) the

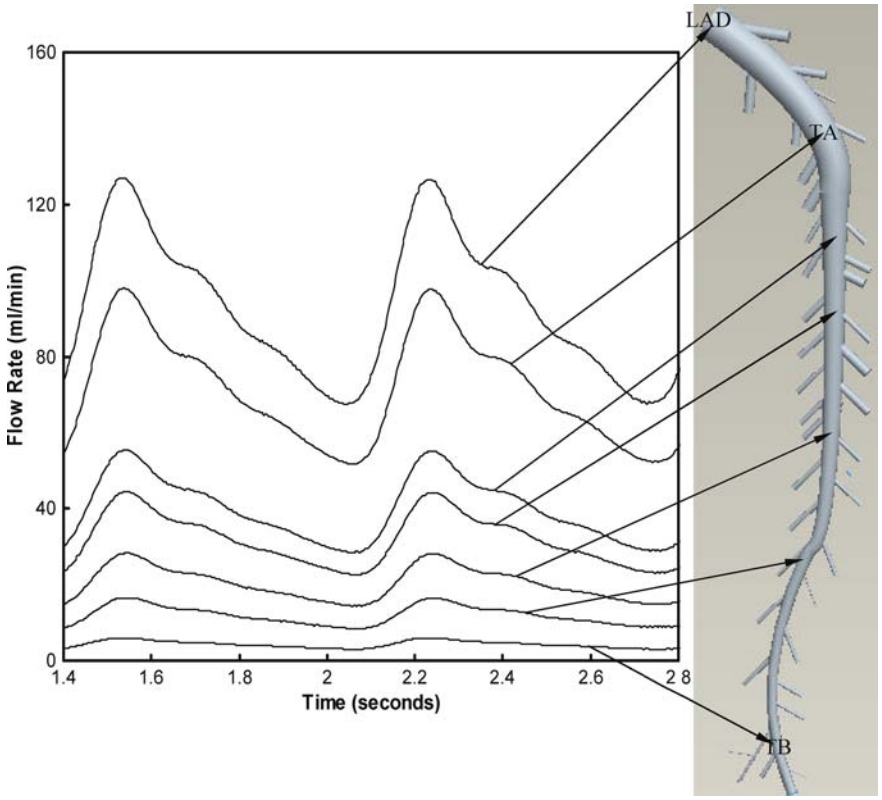

Fig. 8.3 Flow waves sequentially along the main trunk starting from the inlet of LAD artery [18]

least-squares method, (d) the Galerkin method. The variational principles attempt to minimize some physical quantity (e.g., energy).

The basic idea of the FE method is summarized as follows: (a) the domain of the problem is partitioned into smaller regions, called elements, (b) in each element, the governing equations are transformed into algebraic equations called the element equations, (c) the terms in the element equations are numerically evaluated for each element in the mesh, (d) the resulting numbers are assembled into a much larger set of algebraic equations called the system equations, (e) the system equations are solved by using the numerical technique on a computer, (f) the final operation displays the solutions to tabular, graphical, or pictorial form.

The Galerkin form of the MWR begins with the division of the continuum regions of interest into a number of simply shaped regions called elements, as shown in Fig 8.5. An Eulerian description of blood fluid motion was used in the field equations (elements are assumed to be fixed in space). Within each element, the velocity and pressure in Eqs. (8.3) and (8.4) are approximated by

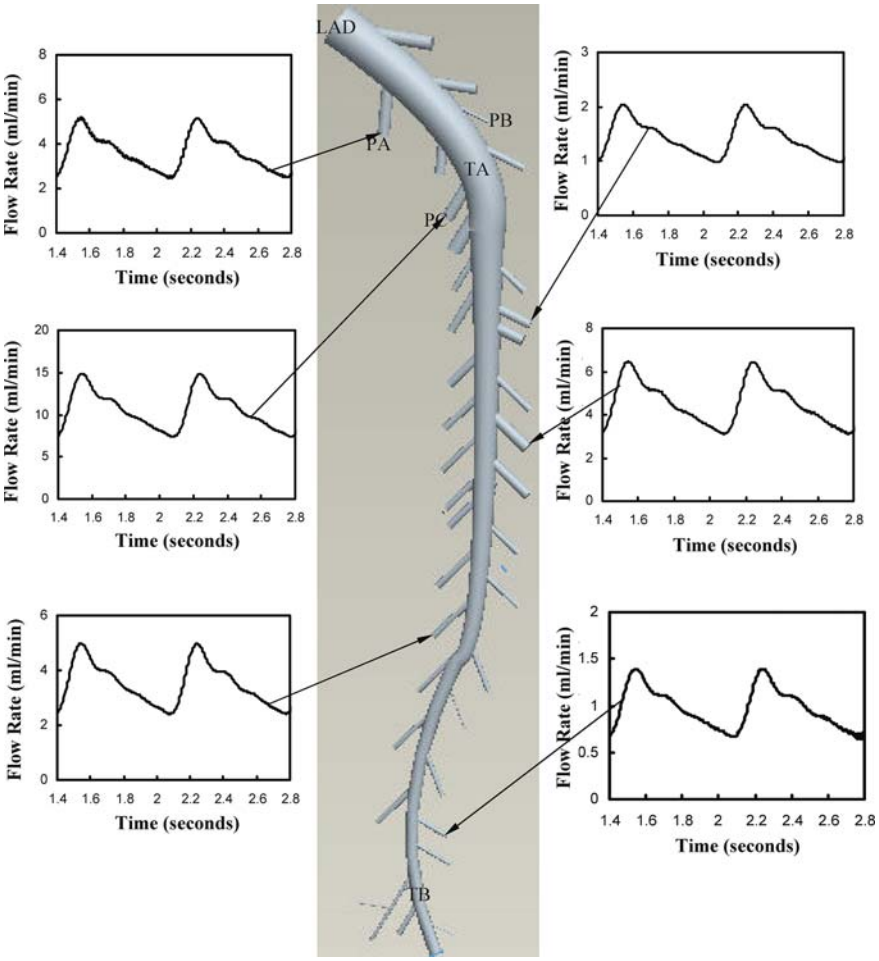

Fig. 8.4 Flow waves of the primary branches of LAD arterial trunk [18]

$$u_i(x_j,t) = \varphi^T(x_j)U_i(t);\ p(x_j,t) = \psi^T(x_j)P(t), \tag{8.12}$$

where x_j ($j = 1,2,3$) or (x, y, z) are the Cartesian coordinates, $U_i(t)$ and $P(t)$ (subscript i denotes the i-th component of velocity vector) are the unknown column vectors at each element nodal point, and $\varphi^T(x_j)$ and $\psi^T(x_j)$ are column vectors of the interpolation functions. Substitution of these approximations into the field equations and boundary conditions yields a set of equations:

$$F_1(\varphi,U_i) = R_1 \quad \text{Mass conservation}, \tag{8.13}$$

$$F_2(\varphi,\psi,U_i,P) = R_2 \quad \text{Momentum conservation}, \tag{8.14}$$

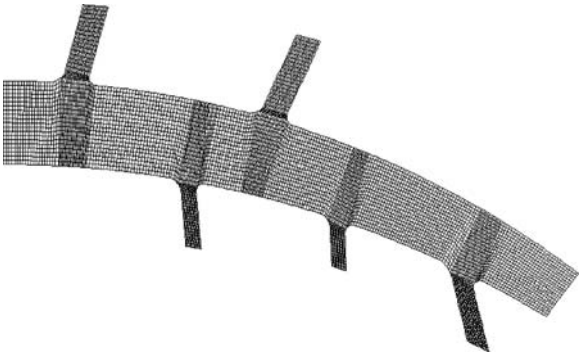

Fig. 8.5 Two-dimensional (2-D) finite element mesh of a branching coronary artery tree

where R_1 and R_2 are the residuals (errors) resulting from the use of the approximations of Eq. (8.12). The Galerkin form of the MWR seeks to reduce these errors to zero, in a weighted sense, by making the residuals orthogonal to the interpolation functions of each element (i.e., φ and ψ). These orthogonal conditions are expressed by

$$\begin{aligned} \int_{V_{CV}} (F_1 \cdot \psi) \mathrm{d}V = \int_{V_{CV}} (R_1 \cdot \psi) \mathrm{d}V = 0; \\ \int_{V_{CV}} (F_2 \cdot \varphi) \mathrm{d}V = \int_{V_{CV}} (R_2 \cdot \varphi) \mathrm{d}V = 0. \end{aligned} \tag{8.15}$$

Using the definition of the Galerkin procedure (Eq. 8.15) and the FE approximations (Eq. 8.12), the following integral equations of continuity and momentum can be written:

$$\left(\int_{V_{CV}} \psi \frac{\partial \varphi^T}{\partial x_i} \mathrm{d}V \right) U_i = 0, \tag{8.16}$$

$$\begin{aligned} &\left(\int_{V_{CV}} \rho \varphi \varphi^T \mathrm{d}V \right) \frac{\mathrm{d}U_i}{\mathrm{d}t} + \left(\int_{V_{CV}} \rho \varphi \mathrm{u}_j \frac{\partial \varphi^T}{\partial x_j} \mathrm{d}V \right) U_i - \\ &\left(\int_{V_{CV}} \frac{\partial \varphi}{\partial x_i} \psi^T \mathrm{d}V \right) P + \left(\int_{V_{CV}} \mu \frac{\partial \varphi}{\partial x_j} \frac{\partial \varphi^T}{\partial x_j} \mathrm{d}V \right) U_i + \\ &\left(\int_{V_{CV}} \mu \frac{\partial \varphi}{\partial x_j} \frac{\partial \varphi^T}{\partial x_i} \mathrm{d}V \right) U_j = \int_{\Gamma_{CV}} \mathrm{T}_i \varphi \mathrm{d}\Gamma + \int_{V_{CV}} \rho f_i \varphi \mathrm{d}V. \end{aligned} \tag{8.17}$$

Here we used the Gauss theorem to reduce the second-order diffusion terms in the momentum equation and pressure term to first-order terms plus a surface integral. The appearance of the surface integrals containing the applied surface stresses (tractions) corresponds to the nature boundary conditions for the problem. The momentum equation can be written as a matrix form:

$$\begin{bmatrix} M & 0 & 0 & 0 \\ 0 & M & 0 & 0 \\ 0 & 0 & M & 0 \\ 0 & 0 & 0 & 0 \end{bmatrix} \begin{bmatrix} \dot{U}_1 \\ \dot{U}_2 \\ \dot{U}_3 \\ \dot{P} \end{bmatrix} + \begin{bmatrix} \sum A_i(U_i) & 0 & 0 & 0 \\ 0 & \sum A_i(U_i) & 0 & 0 \\ 0 & 0 & \sum A_i(U_i) & 0 \\ 0 & 0 & 0 & 0 \end{bmatrix} \begin{bmatrix} U_1 \\ U_2 \\ U_3 \\ P \end{bmatrix} +$$

$$\begin{bmatrix} 2K_{11} + K_{22} + K_{33} & K_{12} & K_{13} & -C_1 \\ K_{21} & K_{11} + 2K_{22} + K_{33} & K_{23} & -C_2 \\ K_{31} & K_{32} & K_{11} + K_{22} + 2K_{33} & -C_3 \\ -C_1^T & -C_2^T & -C_3^T & 0 \end{bmatrix} \begin{bmatrix} U_1 \\ U_2 \\ U_3 \\ P \end{bmatrix} = \begin{bmatrix} F_1 \\ F_2 \\ F_3 \\ 0 \end{bmatrix}, \quad [8.18]$$

where the global matrices M, $\sum A_i(U_i)$, C_i, and K_{ij} are assembled from the following element matrices:

$$M = \int_{V_{CV}} \rho \varphi \varphi^T \mathrm{d}V,$$

$$\sum A_i(U_i) = \int_{V_{CV}} \rho \varphi u_j \frac{\partial \varphi^T}{\partial x_j} \mathrm{d}V,$$

$$C_i = \int_{V_{CV}} \frac{\partial \varphi}{\partial x_i} \psi^T \mathrm{d}V,$$

and

$$K_{ij} = \int_{V_{CV}} \mu \frac{\partial \varphi}{\partial x_j} \frac{\partial \varphi^T}{\partial x_i} \mathrm{d}V.$$

The matrix (Eq. 8.18) focuses on a single FE and the limited portion of the respective continuum. The discrete representation of the entire continuum region of interest is obtained through an assemblage of elements, which is enforced through the appropriate summation of equations for nodes common to the adjacent elements.

8.5.1 Two-Dimensional Flow Patterns in the Epicardial LAD Arterial Tree

In this subsection, we extend the full-scale tree simulation to 2-D FE model in the large epicardial arteries. We use the model to perform a detailed hemodynamic analysis in a LAD epicardial arterial tree including the main trunk and primary branches, based on measured morphometric data. The detailed geometrical parameters (e.g., diameter and length of the vessels) are obtained from measured coronary morphometric data [22]. The optimum branching angles between primary branches and main trunk are computed using the formulations in Huo and Kassab [18]. The continuity and Navier–Stokes equations are solved using the Galerkin FE method

(Eq. 8.18). The spatial and temporal wall shear stress (WSS), WSS spatial gradient (WSSG), and oscillatory shear index (OSI) are calculated based on the detailed flow fields.

The nine-node isoparametric quadrilateral elements are adopted in the FE simulation of LAD epicardial arterial tree. The velocity is approximated using biquadratic interpolation functions and the continuous pressure at the four corner nodes of the element is approximated using a bilinear interpolation. A convergence criterion of 1×10^{-4} is set for relative error associated with determination of velocity and pressure. Different meshes and mesh distributions are also used to check the mesh dependency. The final mesh used for the computations is shown in Fig 8.5 for numerical computation of LAD main trunk and primary branches. It was found that any further refinement of the mesh produces an error smaller than 0.1% (relative to the final mesh). The viscosity (μ) and density (ρ) of the solution were selected as 4 cp and 1.06 g/cm^3, respectively, to mimic the blood flow in large epicardial arteries.

Figure 8.6a shows time-averaged velocity vector fields over one cardiac cycle. The Reynolds, Womersley, and Dean numbers over one cardiac cycle are equal to 141, 4, and 170, respectively, in the main trunk of LAD tree. It is found that the parabolic flow profile is greatly distorted at the bifurcation of main trunk and primary branches. Figure 8.6b, c show the distribution of time-averaged WSS and WSSG over one cardiac cycle, respectively (corresponding to Fig. 8.6a). The primary branches yield high and low WSS near flow divider and opposite to flow divider, respectively, at the bifurcations between main trunk and primary branches.

8.5.2 Three-Dimensional Flow Patterns in the Epicardial LAD Arterial Tree

Similar to the 2-D FE model in the epicardial LAD arterial tree, we investigated the 3-D pulsatile blood flow based on CT scans in Fig. 8.7a [23]. The inlet LAD flow velocity was measured using a Doppler in an anesthetized pig and the outlet pressure boundary condition was estimated based on scaling laws [24, 21]. The continuity and Navier–Stokes equations are solved using the 3-D Galerkin FE method (Eq. 8.18). We use the tetrahedron elements of smart size which provide reasonably shaped elements during automatic mesh generation (e.g., the concentration of mesh is implemented at bifurcations and small vessels). Before the final simulation, a mesh dependency was conducted so that the relative error in two consecutive mesh refinements is smaller than 1% for the maximum velocity for steady-state flow with inlet flow velocity equal to the time-averaged velocity over a cardiac cycle. A total of almost 500,000 FEs were required to accurately mesh the computational domains. The final mesh used for the computations is shown in Fig. 8.7b for the numerical computation of LAD main trunk and primary branches, where the diameter and length of the LAD trunk (down to 2.0 mm in diameter) and primary branches (larger than > 1.0 mm) were selected. The backward method was used for the time integration. A constant time step was employed, where $\Delta t = 0.004$ s with 124 total time step per cardiac cycle. At each time step, convergence criteria of 1×10^{-4} and

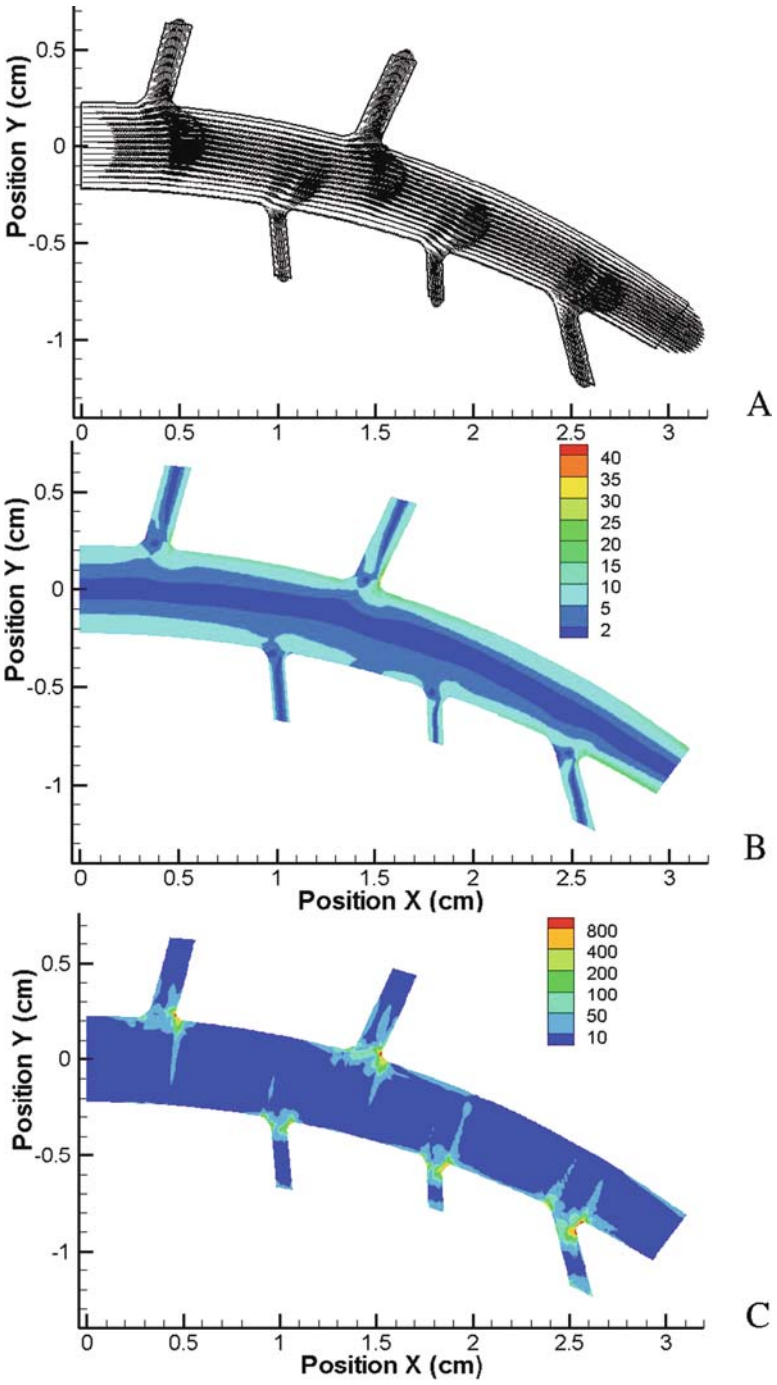

Fig. 8.6 (**a**) Time-averaged velocity vector fields (grid units/magnitude of velocity = 0.008) over one period of cardiac cycle; (**b**) Distribution of time-averaged WSS (unit: dynes · cm^{-2}) over one cardiac cycle; (**c**) Distribution of time-averaged WSSG (unit: dynes · cm^{-3}) over one cardiac cycle

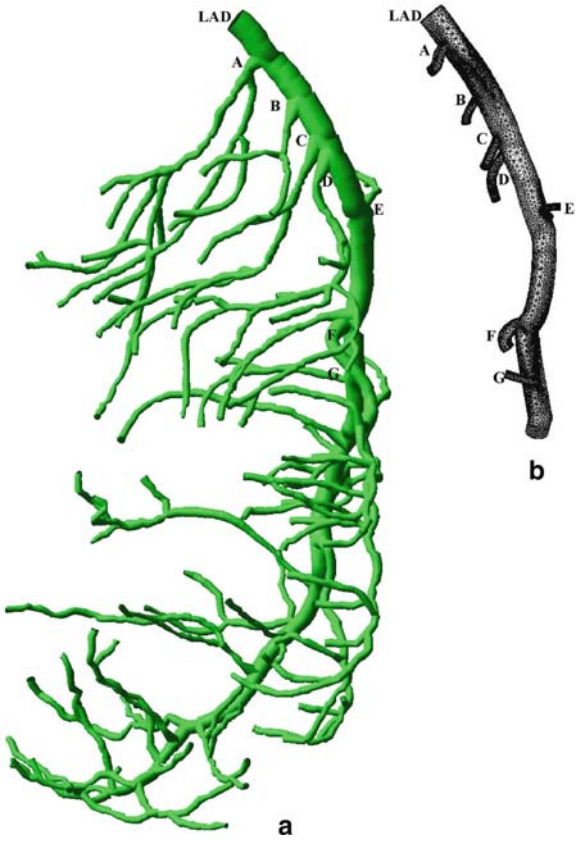

Fig. 8.7 (**a**) CT scan of porcine LAD arterial tree, (**b**) finite element mesh for numerical computation of LAD main trunk ($\geq$2.0 mm in diameter) and primary branches ($\geq$1.0 mm in diameter) [23]

1×10^{-12} were set for relative error associated with determination of velocity and pressure, respectively. Three cardiac cycles were required to achieve convergence for the transient analysis.

Figure 8.8a shows the time-averaged cross-sectional flow velocity vector over a cardiac cycle. Reynolds and Dean numbers averaged over a cardiac cycle and Womersley number are approximately equal to 110, 132, and 3, respectively, in main trunk of LAD artery. It is found that the blunt core velocity profile at the inlet of LAD is developed into a parabolic velocity profile (fully-developed Hagen–Poiseuille velocity profile) at about 2.2 cm from the inlet of LAD. The fully-developed parabolic profile is distorted at the bifurcation of main trunk and primary branches. The mean flow velocity over the cross-sectional area of main trunk remains uniform because relative errors are within $\pm10\%$. Figure 8.8b, c show the distribution of time-averaged WSS and WSSG over a cardiac cycle, respectively. It is found that WSS distribution is complex near bifurcations of main trunk and primary branches. In particular, Fig. 8.8 depicts that the values of WSSG near bifurcations are much higher than those of other sites. The fluid flow in the vicinity of bifurcations is further explored below to understand the complex flow patterns.

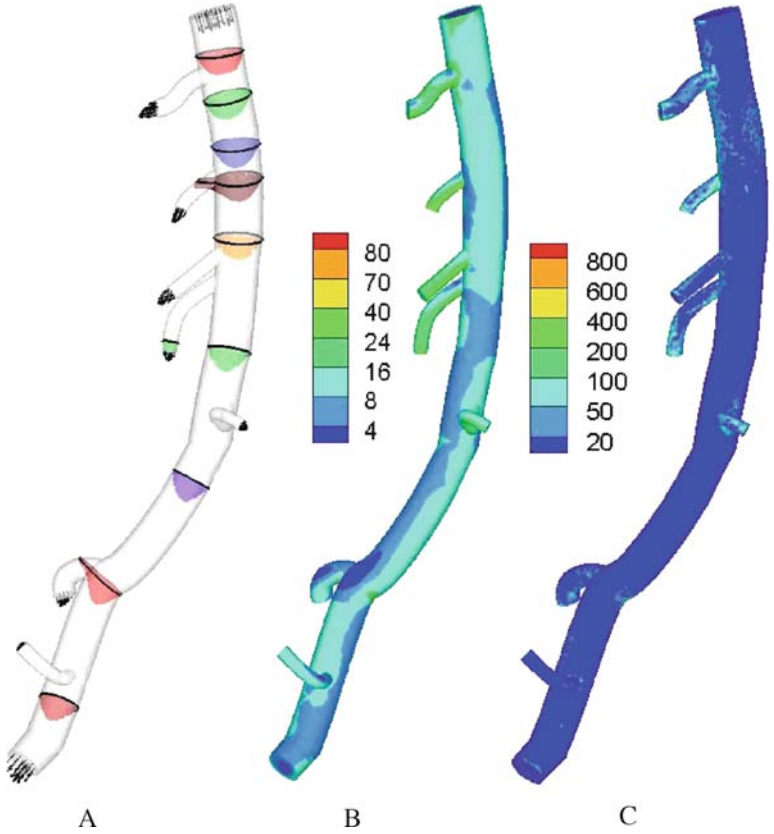

Fig. 8.8 (**a**) Time-averaged velocity vector (grid units/magnitude of velocity = 0.0085), (**b**) WSS (unit: dynes · cm^{-2}), and (**c**) WSSG (unit: dynes · cm^{-3}) fields over a cardiac cycle in anterior view, respectively [23]

Because primary branches A–D in Fig. 8.7b have similar diameter ratio to main trunk (D_{pb}/D_m is approximately equal to 0.33, where D_{pb} and D_m are the diameters of primary branch and mother vessel in main trunk, respectively), branch A was selected for further analysis. In comparison with primary branch A, branch F with larger diameter ratio (D_{pb}/D_m is equal to 0.71) was used to investigate the effect of diameter ratio. Figure 8.9a, b show the time-averaged WSS (unit: dynes · cm^{-2}) distribution at bifurcations (primary branch A and F, respectively, in Fig. 8.7b) over a cardiac cycle. It is found that high (>30 dynes · cm^{-2}) and low time-averaged WSS (less than <6 dynes · cm^{-2}) occur near the flow divider (defined as the anastomosis at the downstream wall of primary branch proximal to main trunk, as shown in Fig. 8.9) and opposite to the flow divider, respectively. There are two areas opposite to the flow divider: one in primary branches and the other in main trunk, as shown in Fig. 8.9a, b. Low WSS is approximately crescent-shaped. There are two important areas with low WSS in the wall of main trunk lateral to the junction orifice of main

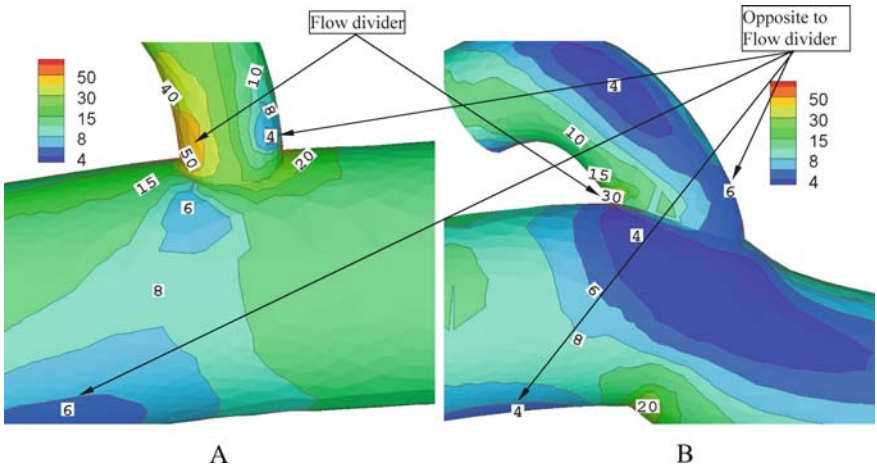

Fig. 8.9 (**a**) Time-averaged WSS (unit: dynes · cm^{-2}) distribution at bifurcation (primary branch *A* in Fig. 8.7b) over a cardiac cycle, (**b**) time-averaged WSS (unit: dynes · cm^{-2}) distribution at bifurcations (primary branch *F* in Fig. 8.7b) over a cardiac cycle. *Dash lines* represent the flow direction in main trunk and primary branches [23]

trunk and primary branches. Comparison of Fig. 8.9a with 8.9b shows that zones of low WSS are enlarged for a larger diameter ratio. It is noted that low WSS is not exactly opposite to flow divider.

In correspondence to Figs. 8.9a, b and 8.10a, b show the respective OSI distribution at bifurcations over a cardiac cycle. It is found that low WSS approximately coincides with high OSI, which approximately obeys a power law. Furthermore, Fig. 8.11a, b show the time-averaged WSSG (unit: dynes · cm^{-3}) distribution at previously cited bifurcations over a cardiac cycle. High time-averaged WSSG is found in region of bifurcations and has relatively large value near the flow divider, which coincides with high WSS zones.

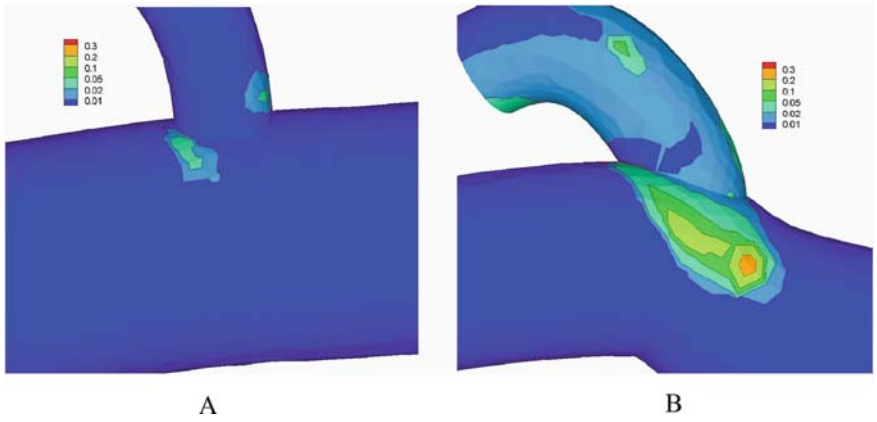

Fig. 8.10 OSI distribution at bifurcations over a cardiac cycle. Figures (**a**, **b**), respectively, correspond to (**a**, **b**) in Fig. 8.9 [13]

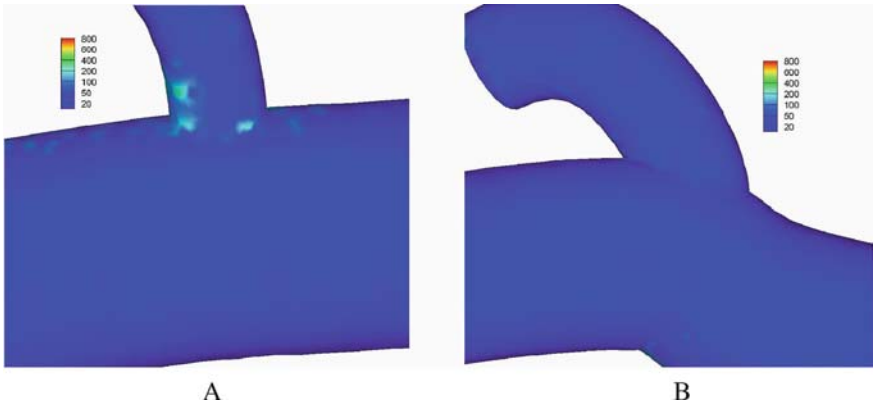

Fig. 8.11 Time-averaged WSSG (unit: dynes · cm^{-3}) at bifurcations over a cardiac cycle. Figures (**a**, **b**), respectively, correspond to (**a**, **b**) in Fig. 8.9 [23]

Figure 8.12a, b show the distribution of flow velocity vectors and streamlines in the sectioned area of bifurcations at diastole. Vortical flow occurs at the flow divider and flow separation and reversal are found opposite to flow divider. Flow separation and stagnation lead to low WSS, flow reversal induces high OSI, and vortical flow is associated with high WSSG. The disturbed flows in Fig. 8.12 illustrate the cause of abnormal hemodynamic parameters in Figs. 8.9, 8.10, and 8.11.

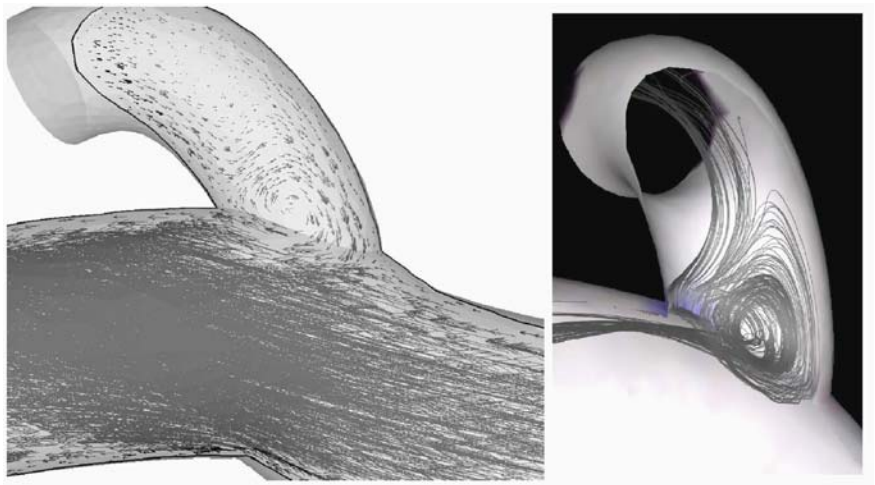

Fig. 8.12 Distribution of (**a**) flow velocity vectors (grid units/magnitude of velocity = 0.05) and (**b**) streamlines in the sectioned area of bifurcation *F* (primary branch *F* in Fig. 8.7b) at diastolic time [23]

The 2-D and 3-D FE models present several major findings including: (1) low time-averaged WSS and high OSI, approximately obeying a power law, coincides with disturbed flows opposite to the flow divider and lateral to the junction orifice; (2) zones of low time-averaged WSS and high OSI amplify at higher flow rates at the inlet of LAD and with larger diameter ratio; and (3) high time-averaged WSSG is found in region of bifurcations with the maximum value at the flow divider.

8.6 Conclusion

The CFD method is a powerful tool to elucidate the local fluid fields which cannot be experimentally measured in vivo. The presence of flow disturbances causes endothelial dysfunction and coronary heart disease. Since heart failure is a heart/vessel problem, it is essential to understand the hemodynamic interplay which can lead to the demise of endothelial function and hence alter cardiac afterload. Clearly, there is a positive feedback mechanism which causes a spiral demise of the heart. An understanding of the interplay between the heart and local hemodynamic effects on the endothelium may help us design therapeutics to stop the vicious cycle of cardiac deterioration. Much effort is still needed to use the CFD models to understand the heart/vessel problem in heart failure.

Acknowledgments These studies were supported in part by the National Institute of Health–National Heart, Lung, and Blood Institute Grants 2 R01 HL055554-11, HL084529, and HL087235 (Kassab, G. S.) and the American Heart Association Scientist Development Grant 0830181 N (Huo, Y.).

References

1. Fung YC. *Biomechanics: circulation*, 4th Ed. New York: Springer-Verlag, 1996.
2. Perktold K, Resch M, Florian H. Pulsatile non-Newtonian flow characteristics in a three-dimensional human carotid bifurcation model. *ASME J Biomech Eng*. 1991;113:464–75.
3. Buchanan JR Jr, Kleinstreuer C, Truskey GA, Lei M. Relation between non-uniform hemodynamics and sites of altered permeability and lesion growth at the rabbit aorto-celiac junction. *Atherosclerosis*. 1999;143:27–40.
4. Kleinstreuer C, Hyun S, Buchanan JR Jr, Longest PW, Archie JP Jr, Truskey GA. Hemodynamic parameters and early intimal thickening in branching blood vessels. *Crit Rev Biomed Eng*. 2001;29:1–64.
5. Berger SA, Jou LD. Flows in stenotic vessels. *Annu Rev Fluid Mech*. 2002;32:347–82.
6. He X, Ku DN. Pulsatile flow in the human left coronary artery bifurcation: average conditions. *ASME J Biomech Eng*. 1996;118:74–82.
7. Ku DN. Blood flow in arteries. *Annu Rev Fluid Mech*. 1997;29:399–434.
8. Ramaswamy SD, Vigmostad SC, Wahle A, Lia YG., Olszewski M.E, Braddy KC, Brennan TMH., Rossen JD, Sonka M., Chandran KB. Fluid dynamics in a human left anterior descending coronary artery with arterial motion. *Ann Biomed Eng*. 2004;32:1628–41.
9. Bird RB, Stewart WE, Lightfoot EN. *Transport phenomena*. New York: John Willey & Sons, 1962.
10. Panton RL. *Incompressible flow*. New York: John Willey & Sons, 1984.

11. Acheson DJ. Elementary Fluid Dynamics. Oxford applied mathematics and computing science series. 1990.
12. Li BQ. *Discontinuous finite elements in fluid dynamics and heat transfer*. London: Springer-Verlag, 2006.
13. Nichols WW. O'Rourke MF. *McDonald's blood flow in arteries: theoretical, experimental and clinical principles*, 4th Ed. New York: Oxford University Press, 1998.
14. Patankar SV. Numerical heat transfer and fluid flow, Hemisphere, 1980.
15. Fletcher CAJ. *Computational techniques for fluid dynamics, Volume I.* Berlin: Springer-Verlag, 1991a.
16. Fletcher CAJ. *Computational techniques for fluid dynamics, Volume II.* Berlin: Springer-Verlag, 1991b.
17. Ferziger JH, Peric M. *Computational methods for fluid dynamics*. New York: Springer-Verlag, 2002.
18. Huo Y, Kassab GS. A hybrid one-dimensional/Womersley model of pulsatile blood flow in the entire coronary arterial tree. *Am J Physiol Heart Circ Physiol*. 2007;292:H2623–33.
19. Guo X, Kassab GS. Distribution of stress and strain along the porcine aorta and coronary arterial tree. *Am J Physiol Heart Circ Physiol*. 2004;286:H2361–8.
20. Huo Y, Kassab GS. Pulsatile blood flow in the entire coronary arterial tree: theory and experiment. *Am J Physiol Heart Circ Physiol*. 2006;291:H1074–87.
21. Huo Y, Kassab GS. A scaling law of vascular volume. *Biophys J*. 2009b;96:347–53.
22. Kassab GS, Rider CA, Tang NJ, Fung YC. Morphometry of pig coronary arterial trees. *Am J Physiol Heart Circ Physiol*. 1993;265:H350–65.
23. Huo Y, Wischgoll T, Kassab GS. Flow patterns in three-dimensional porcine epicardial coronary arterial tree. *Am J Physiol Heart Circ Physiol*. 2007;293:H2959–70.
24. Huo Y, Kassab GS. The scaling of blood flow resistance: from a single vessel to the entire distal tree. *Biophys J*. 2009a;96:339–46.

Chapter 9
Fluid–Structure Interaction (FSI) Modeling in the Cardiovascular System

Henry Y. Chen, Luoding Zhu, Yunlong Huo, Yi Liu, and Ghassan S. Kassab

Abstract The cardiovascular system experiences strong fluid–structure interaction (FSI). This chapter presents the theoretical formulations for two powerful FSI techniques: the arbitrary Lagrangian Eulerian (ALE) and the immersed boundary (IB) methods. Examples of FSI applications to aortic cross-clamping used during surgical treatment of heart failure and valveless pumping are also presented.

9.1 Introduction

Nature has an abundance of fluid–structure interaction (FSI) phenomena. Some examples in the cardiovascular system include valve opening and closure, ventricular ejection, and vessel/myocardial interaction in coronary circulation, and many others. In systolic heart failure, for example, the ventricular ejection of blood is weakened which alters the FSI between the ventricle and blood and hence the passive motion of the heart valves. This change of FSI significantly affects the physiology of the heart and peripheral vasculature and can lead to deterioration of the cardiovascular system.

FSI problems are generally complex because the structures are usually freely moving with large deformation. Typically, the Navier–Stokes equations are formulated in Eulerian coordinates, and the solid motion equations are formulated in Lagrangian. The two sets of partial differential equations are coupled on the moving interfaces which separates the fluid and solid component. The coupling is not known at priori and has to be solved as part of the problem; i.e., the FSI is a free-moving boundary problem. The FSI models have an additional unknown variable (the time-dependent interface position) and are more challenging than a corresponding fixed boundary problem. Thus analytical solutions to FSI problems are rare and a computational approach is usually the only option.

H.Y. Chen (✉)
Weldon School of Biomedical Engineering, Purdue University, West Lafayette, IN 46202, USA
e-mail: hychen@purdue.edu

J.M. Guccione, et al. (eds.), *Computational Cardiovascular Mechanics*,
DOI 10.1007/978-1-4419-0730-1_9,

There are a variety of methods for FSI, including the immersed boundary (IB) [1, 2, 3], the arbitrary Lagrangian Eulerian (ALE) [4, 5, 6], and the fictitious domain methods [41, 42]. The ALE and IB methods have been widely used in computational studies of the cardiovascular system. In this Chapter we shall focus on these two FSI methods for applications to the cardiovascular system.

9.2 The Arbitrary Lagrangian Eulerian (ALE) Method

9.2.1 Governing Equations

The governing equations for the fluid domain are the Navier–Stokes and continuity equations [7]:

$$\frac{\partial \vec{V}}{\partial t} + \vec{V} \cdot \vec{\nabla} \vec{V} + \frac{\vec{\nabla} p}{\rho} - 2\frac{\eta}{\rho} \vec{\nabla} \cdot D = \vec{0},$$

$$\vec{\nabla} \cdot \vec{V} = 0$$

where V is fluid velocity, P is fluid pressure, ρ is fluid mass density, η is fluid dynamic viscosity, and $\vec{\nabla}$ is the gradient operator. D is the fluid rate of deformation tensor.

The governing equations for the solid are the momentum and equilibrium equations [35]:

$$\begin{aligned} &\rho a_i - \sigma_{ij,j} - \rho f_i = 0 \quad \text{in} \quad {}^s\Omega(t), \\ &\sigma_{ij} n_j - t_i = 0 \quad \text{on} \quad {}^s\Gamma(t) \end{aligned}$$

where ${}^s\Omega(t)$ is the structural domain at time t, t_i is surface traction vector, σ_{ij} is stress of the solid, and a_i is the acceleration of the material point along the ith direction.

9.2.2 Material Models

Soft tissues are typically nonlinear pseudo- or hyper-elastic materials [40]. These materials are best described by strain energy functions such as the Fung and Ogden models. The Ogden model expresses the strain energy by principle stretches λ_α, α=1,2,3, instead of using strain invariants:

$$W = \sum_{p=1}^{N} \frac{\mu_p}{\alpha_p} \left(\lambda_1^{\alpha_p} + \lambda_2^{\alpha_p} + \lambda_3^{\alpha_p} - 3 \right),$$

where N, α_p, and μ_p are material constants.

The three principle values of the Cauchy stress can be computed as

$$\sigma_\alpha = p + \lambda_\alpha \frac{\partial W}{\partial \lambda_\alpha} \quad \alpha = 1,2,3,$$

where p is pressure. The principle first and second Piola–Kirchhoff stresses are computed by

$$P_\alpha = \lambda_\alpha^{-1}\sigma_\alpha \quad S_\alpha = \lambda_\alpha^{-2}\sigma_\alpha.$$

In the classical anisotropic Fung model, the strain energy density is expressed as (Fung, 1998)

$$W = \frac{C}{2}[\exp(Q) - 1]$$

and

$$Q = b_1 E_{\theta\theta}^2 + b_2 E_{zz}^2 + b_3 E_{rr}^2 + 2(b_4 E_{\theta\theta} E_{zz} + b_5 E_{zz} E_{rr} + b_6 E_{\theta\theta} E_{rr}),$$
$$+ b_7(E_{\theta z}^2 + E_{z\theta}^2) + b_8(E_{zr}^2 + E_{rz}^2) + b_9(E_{\theta r}^2 + E_{r\theta}^2)$$

where C, $b_{1\text{–}9}$ are material parameters determined experimentally. The various E's are components of the Green–Lagrange strain tensor.

9.2.3 The ALE Formulation for Fluid–Structure Interaction

The ALE is an effective way to treat FSI problems. Instead of using either a single Lagrangian approach or a single Eulerian approach, the ALE describes the motion of fluid in a moving reference frame whose velocity is almost arbitrary with the sole constraint that the velocity on the fluid–solid boundary must equal to that of the boundary. Note that the velocity of the reference frame is usually neither the fluid particle velocity such as in a pure Lagrangian description nor zero in a pure Eulerian description.

After introducing a reference frame which moves with some velocity, the ALE-modified Navier–Stokes equation for a viscous incompressible flow follows as [4, 5]

$$\rho\left(\frac{\partial u_i}{\partial t} + (u_j - \widehat{u}_j)\frac{\partial u_i}{\partial x_j}\right) - \frac{\partial}{\partial x_j}\left(\mu\left(\frac{\partial u_i}{\partial x_j} - \frac{\partial u_j}{\partial x_i}\right)\right) + \frac{\partial p}{\partial x_i} = 0,$$

$$\frac{\partial u_j}{\partial x_j} = 0, \quad i,j = 1,2,3,$$

where u_j, $j = 1, 2, 3$ are the components of the flow velocity; $\widehat{u}_j$, $j = 1, 2, 3$ are the components of the domain velocity; p is the pressure, ρ is the fluid density, and μ is the dynamic viscosity. Note that the reference frame velocity only affects the convection term.

The boundary conditions for the inflow boundaries could be measured experimentally. The boundary condition for the surface traction can be prescribed at the outflow boundaries.

9.2.4 A Numerical Procedure for ALE Solutions

The treatment of the two different flow domains $G(t^n)$ and $G(t^{n+1})$ is a major step of the numerical solution at the time level t^{n+1}. Boukir et al. presented a first-order approximation based on a numerical procedure which consists of the following three steps [8, 43]:

(1) Calculate the domain velocity:

$$\hat{u}_j^n = \frac{x_j^{n+1} - x_j^n}{t_j^{n+1} - t_j^n}, \quad j = 1, 2, 3,$$

where x_j^{n+1}, $j = 1, 2, 3$ and x_j^n, $j = 1, 2, 3$ are the coordinates of the nodes at time levels t^{n+1} and t^n.

(2) Compute the solution, $\overline{u}_j^{n+1}$, $j = 1, 2, 3$ and $\overline{p}^{n+1}$ in the domain $G(t^n)$ by using the domain velocity $\widehat{u}_j^n$, $j = 1, 2, 3$ in the ALE-modified Navier–Stokes equation.

(3) Use a first-order approximation for the velocity u_j^{n+1}, $j = 1, 2, 3$, and the pressure p^{n+1} in $G(t^{n+1})$. Boukir et al. presented that

$$u_j^{n+1}(x^{n+1}) = \overline{u}_j^{n+1}(x^n), \quad j = 1, 2, 3,$$

$$p^{n+1}(\mathbf{x}^{n+1}) = \overline{p}^{n+1}(\mathbf{x}^n), \quad j = 1, 2, 3.$$

9.2.5 Alternative Approach for Treatment of Fluid with Moving Boundary

When the moving wall boundary is considered, the moving wall surface, represented by the equation $S(\mathbf{x},t)=0$, must always remain a surface (kinematic) condition as

$$\frac{\partial S}{\partial t} + \mathbf{v}_{\text{wall}} \cdot \nabla S = 0,$$

where $\mathbf{v}_{\text{wall}}$ is wall surface velocity. The convective term in the Navier–Stokes equation is changed to $\rho(\mathbf{v} + \mathbf{v}_{\text{node}}) \cdot \nabla \mathbf{v}$, where $\mathbf{v}_{\text{node}}$ is the finite element nodal velocity due to the wall motion. The boundary conditions of the flow domain include the

inlet/outlet velocity profile, and moving wall boundary condition on the solid–fluid interface. The inlet and outlet velocity profiles can be obtained experimentally.

9.2.6 Discretization and Numerical Solution of the Discrete Equations

The Navier–Stokes and kinematic condition Equations can be solved using the Galerkin FE method [9, 10]. Briefly, the computational domain of the vessel flow is first divided into small elements. With each element, the dependent variables **v** and P are interpolated by the shape functions, $\phi(\mathbf{x})$ and $\psi(\mathbf{x})$, respectively, as

$$\mathbf{v}^m(\mathbf{x},t) = \phi^T(\mathbf{x})\mathbf{V}^m(t);\ \mathbf{P}(\mathbf{x},t) = \psi^T(\mathbf{x})\mathbf{P}(t),$$

where $\mathbf{V}^m(t)$ and $\mathbf{P}(t)$ (superscript m denotes the mth velocity component) are the unknown column vectors at an element nodal point. The matrix form of the finite element discretized equations may be written as follows:

$$\begin{bmatrix} \mathrm{M} & 0 \\ 0 & 0 \end{bmatrix} \begin{bmatrix} \dot{V} \\ \dot{P} \end{bmatrix} + \begin{bmatrix} \mathrm{A(V)} + \mathrm{K} & -\mathrm{C} \\ -\mathrm{C} & 0 \end{bmatrix} \begin{bmatrix} \mathrm{V} \\ \mathrm{P} \end{bmatrix} = \begin{bmatrix} \mathrm{F}_1 \\ \mathrm{F}_2 \end{bmatrix},$$

where the global matrices **M**, **A**(**V**), **C**, and **K** are assembled from the following element matrices:

$$\mathrm{M}^e = \int_{\Omega^e} \rho\phi\phi^{\mathrm{T}} dV;\ \mathrm{A}^e = \int_{\Omega^e} \rho\phi(\mathrm{v} + \mathrm{v}_{\mathrm{node}}) \cdot \nabla\phi^T;\ (C^e)_j = \int_{\Omega^e} \mathbf{e}_j \cdot \nabla\phi\psi^T dV$$

and

$$(\mathbf{K}^{\mathrm{e}})_{ij} = \left(\int_{\Omega^e} \mu\nabla\phi \cdot \nabla\phi^T \mathrm{d}V \right) \delta_{ij} + \int_{\Omega^e} \mu(\mathbf{e}_i \cdot \nabla\phi)(\mathbf{e}_j \cdot \nabla\phi^T)\mathrm{d}V$$

in which $^{\Omega}{}_{\mathrm{e}}$ is the computational domain of an element, $\mathbf{e}_i$ (i =1, 2, 3) is a unit vector in the ith coordinate direction. The right-hand side of equation, $\mathbf{F}_1$ and $\mathbf{F}_2$, can be obtained from the inlet and outlet conditions, respectively, which is iteratively updated at every time step in the transient computation.

To incorporate the moving wall kinematic boundary condition, the front tracking technique can be applied. By this technique, the nodes along the wall surface are allowed to move such that they remain on the moving surface all the times. Thus, kinematic condition equation can be solved using the weighted residuals method as

$$\int_{\Gamma_f} \zeta \left(\frac{\partial S}{\partial t} + \mathbf{v}_{\mathrm{wall}} \cdot \nabla S \right) = 0$$

where Γ_f and ξ are computational domain and the shape function of the wall surface, respectively. The fluid calculations with moving wall will be solved iteratively with the time differentials approximated by the implicit time differencing scheme.

9.2.7 Formulations for Fluid–Structure Coupling

The Navier–Stoke equations for the fluid and the momentum and equilibrium equations for the solid are coupled on the fluid–solid interface via the kinematic and dynamic conditions as follows:

$$\underline{\mathbf{d}}_f = \underline{\mathbf{d}}_s,$$

$$\mathbf{n}\cdot\underline{\boldsymbol{\tau}}_{\mathrm{f}} = \mathbf{n}\cdot\underline{\boldsymbol{\tau}}_{\mathrm{s}}.$$

where $\mathbf{n}$ denotes the normal vector of the interface. The symbols $\underline{\mathbf{d}}_{\mathrm{f}}$ and $\underline{\mathbf{d}}_{\mathrm{s}}$ denote the fluid and solid displacements. The symbols $\underline{\boldsymbol{\tau}}_{\mathrm{f}}$ and $\underline{\boldsymbol{\tau}}_{\mathrm{s}}$ denote the fluid and solid stresses. The underline indicates the variable is evaluated on the solid–fluid interface.

The solid and fluid models can be coupled by the fluid nodal positions on the FSI interfaces which are determined by the kinematic conditions. The displacements of the other fluid nodes are determined so as to preserve the initial mesh quality. The ALE-modified governing equations for fluid flow are then solved. For the dynamic case, the fluid stresses are integrated along the fluid–solid interface and applied on the corresponding solid nodes.

9.2.8 Finite Element Equations of the Coupled System

Let the fluid equations and the solid equations be represented by $\mathbf{G}_{\mathrm{f}}[\mathbf{f}, \mathbf{f}] = 0$ and $\mathbf{G}_{\mathrm{s}}[\mathbf{d}, \dot{\mathbf{d}}, \ddot{\mathbf{d}}] = 0$, respectively, where $\mathbf{f}$ represents the fluid variables and $\mathbf{d}$ represents the solid displacements. Let the solution vectors of the coupled system be $\mathbf{X} = (\mathbf{X}_{\mathrm{f}}, \mathbf{X}_{\mathrm{s}})$, where $\mathbf{X}_{\mathrm{f}}$ and $\mathbf{X}_{\mathrm{s}}$ are fluid and solid solution vectors defined at the nodes respectively. Thus, $\underline{\mathbf{d}}_{\mathrm{s}} = \underline{\mathbf{d}}_{\mathrm{s}} = (\mathrm{X}_{\mathrm{s}})$ and $\underline{\boldsymbol{\tau}}_{\mathrm{f}} = \underline{\boldsymbol{\tau}}_{\mathrm{f}}(\mathrm{X}_{\mathrm{f}})$. The equations of the coupled system can be expressed as [11, 5]:

$$\mathbf{F}[\mathbf{X}] \equiv \begin{bmatrix} \mathbf{F}_f[\mathbf{X}_f\,, \underline{\mathbf{d}}_s(\mathbf{X}_s)] \\ \mathbf{F}_s[\mathbf{X}_s\,, \underline{\mathbf{d}}_f(\mathbf{X}_f)] \end{bmatrix} = \mathbf{0},$$

where $\mathbf{F}_{\mathrm{f}}$ and $\mathbf{F}_{\mathrm{s}}$ are finite element equations corresponding to equations $\mathbf{G}_{\mathrm{f}}$ and $\mathbf{G}_{\mathrm{s}}$ respectively.

9.2.9 Iterative Computing of Two-Way FSI Coupling

The computational procedure is summarized in Fig. 9.1. For each time step, the fluid model is solved first, with the imposed boundary condition; then the fluid pressure and shear stress fields are passed onto the solid model, and displacements and stresses of the solid are solved; with the solid model updated, onto the next time

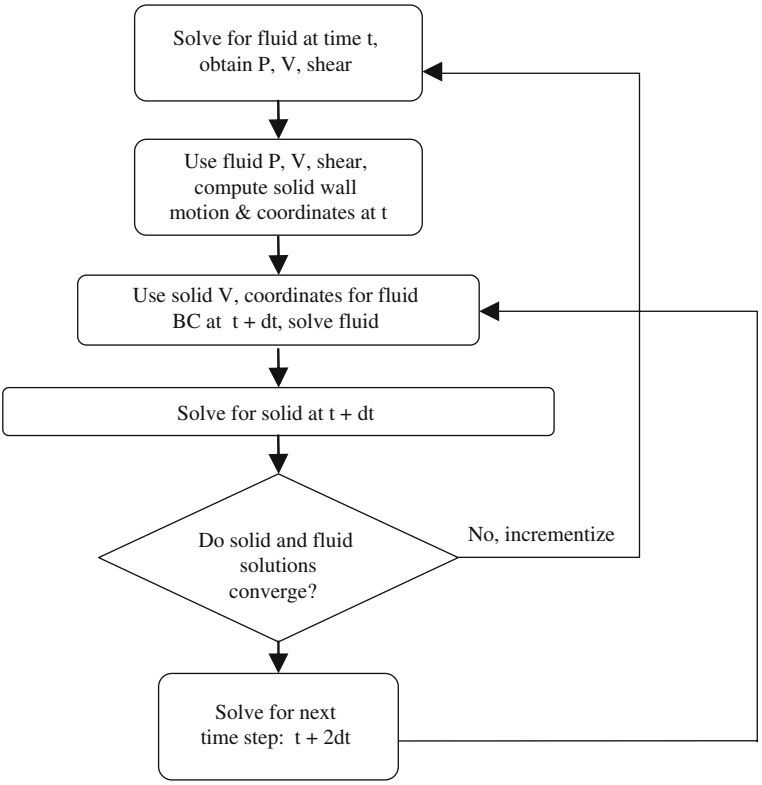

Fig. 9.1 The flow chart for fluid–structure interaction iterative algorithm

step, the fluid variables are solved again. This process continues until the solutions converge [5, 11].

9.3 The Immersed Boundary (IB) Method

9.3.1 Introduction

The IB method is a practical and effective method for mathematically formulating and numerically solving problems involving interactions between an elastic structure and an incompressible viscous fluid. The immersed elastic structure can be either passive (e.g., a flapping flag) or active (e.g., a swimming eel); it can either be neutrally buoyant (e.g., a swimming sperm) or heavier/lighter than the surrounding fluid (e.g., a flying insect).

The IB method was formulated by Charles S. Peskin [1, 2] for studying the flow patterns around human heart valves in the 1970s, and has since become a general method for investigating flexible structure–viscous fluid interaction problems. It has

been applied to both natural and prosthetic cardiac valves [1, 12–14], and to the modeling and simulation of the whole heart [15–17].

There exists a variety of different versions of the IB method [3]. The underlying philosophy is that the entire system (viscous fluid + elastic body) is treated as an incompressible composite material and an Eulerian description is used to describe its dynamics as a whole. In addition, a Lagrangian description is used to depict the motion of the immersed elastic body where the connection between Eulerian and Lagrangian variables are realized by the Dirac delta function. In general, the incompressible viscous Navier–Stokes equations with additional forcing term from the immersed boundary (and variable density resulting from the mass of the immersed body if it is not neutrally buoyant) are used to govern the whole system. The governing equations are discretized on a fixed Eulerian uniform grid while the equations of the elastic structure are discretized on a collection of Lagrangian moving points which do not necessarily coincide with the fixed Eulerian mesh points. It should be noted that the shape and position of the immersed boundary is not known in advance and has to be determined from the solution. Thus, the Navier–Stokes solver does not require the shape and location of the moving elastic body. The influence of the latter is taken into account by spreading the mass and force to the nearby fluid. The motion of IB is updated by the surrounding fluid velocity via interpolation because of the no-slip conditions at the boundary. The interaction between the fluid and the elastic body is mediated by a smoothed approximation to the Dirac delta function which plays an important role in the IB method. This smoothed delta function is used to spread the mass and force of the boundary to the fluid and to compute the new position of the boundary by interpolating its velocity from the surrounding fluid velocity field.

9.3.2 Mathematical Formulation

The mathematical formulation for the IB method reads as follows:

$$\rho\left(\frac{\partial \mathbf{u}}{\partial t} + \mathbf{u}\cdot\nabla\mathbf{u}\right) + \nabla p = \mu\Delta\mathbf{u} + \mathbf{f},$$

$$\nabla\cdot\mathbf{u} = 0,$$

$$\rho(\mathbf{x},t) = \int M(\boldsymbol{\alpha})\delta(\mathbf{x} - \mathbf{X}(\boldsymbol{\alpha},t))d\boldsymbol{\alpha},$$

$$\mathbf{f}(\mathbf{x},t) = \int \mathbf{F}(\boldsymbol{\alpha},t)\delta(\mathbf{x} - \mathbf{X}(\alpha,t))d\boldsymbol{\alpha},$$

$$\begin{aligned}\frac{\partial \mathbf{X}}{\partial t}(\boldsymbol{\alpha},t) &= \mathbf{u}(\mathbf{X}(\boldsymbol{\alpha},t),t)\\ &= \int \mathbf{u}(\mathbf{x},t)\delta(\mathbf{x}-\mathbf{X}(\boldsymbol{\alpha},t))d\mathbf{x},\end{aligned}$$

$$\mathbf{F} = -\frac{\wp E}{\wp \mathbf{X}},$$

where t is the time, $\mathbf{x}$ is a fixed Eulerian coordinate, $\mathbf{u}$ is velocity, p is pressure, ρ is fluid mass density, μ is fluid dynamic viscosity, f is the Eulerian force density applied by the immersed elastic structure to the fluid, M is the mass density of the immersed structure, $\boldsymbol{\alpha}$ is the Lagrangian coordinates associated with the structure, $\mathbf{X}$ is the position of the structure, E is the elastic potential energy of the structure, $\mathbf{F}$ is the Lagrangian force density applied by the structure to the fluid, and $\frac{\wp E}{\wp \mathbf{X}}$ is the variational derivative of E with respect to $\mathbf{X}$.

9.3.3 Discretization and Numerical Methods

The IB formulation is a nonlinear system of integral–differential equations which may be numerically solved by different versions of the IB method among which are the Fast Fourier Transform (FFT) version and the multi-grid version. Typically, a finite difference method is used for the discretization of the above nonlinear system on a spatially periodic computational domain. If the immersed flexible structure is neutrally buoyant in the fluid, the Eulerian mass density is a constant in space and time. The discrete FFT is routinely used to solve the discretized incompressible Navier–Stokes equations [2, 18, 3]. If the immersed structure is not neutrally buoyant, the mass density varies with space and time which precludes the use of FFT. Instead the multi-grid version of the IB method [18, 3, 19] may be used. In the multi-grid IB method, the Chorin's classical projection method [20, 21] extended to the case of variable mass density is used to discretize the integral–differential equation system on a series of non-staggered gradually coarsened grids, and a multi-grid method is used for solving the discrete equations. In both cases, the convection term is linearized and a skew-symmetrical treatment is employed to guarantee the conservation of fluid kinetic energy.

9.4 Applications

9.4.1 Application of the ALE FSI to Surgical Devices

Vascular cross-clamping is applied in many cardiovascular surgeries such as coronary bypass, aorta repair, valve procedures, and surgical ventricular restoration for treatment of heart failure. Although some clamps are marketed as so called "atraumatic", evidence suggests otherwise [22]). Experimental studies have found that clamping causes various degrees of damage to the artery, from endothelium

denudation to severe intima injury as observed by histology [37–39]. Endothelial damage increases platelet uptake and may progress to thrombus formation with the risk of vessel occlusion [23, 22].

Studies by Margovsky et al. found that deposition of platelets was proportional to endothelial damage [36]. Functional studies on vessel reactivity also revealed long-term effects of clamping on vessel function. Intramural stress concentrations in the vessel wall and related injuries have been linked to disease processes such as lipid invasion and calcification via the inflammatory process [24]. The greatest risk in clamping lies in the compression that can break vulnerable plaque in an atherosclerotic aorta. Once released, the plaque may cause vessel occlusion and stroke.

9.4.2 Computational Studies

Since aortic clamping alone is performed in about 500,000 patients per year worldwide particularly for heart failure surgery [25], a safer clamp would benefit many patients. A common design feature of popular atraumatic clamps such as the Cooley clamp involves a protruded clamp area for more gripping and prevents tissue slippage. The vessel deformation and stress analysis can provide valuable insights into the causes of tissue injury [23, 26, 27]. Realistic computational models may lead to significant improvement of vascular clamp design, and are therefore of potential interest to surgeons and clamp manufacturers.

Despite the apparent clinical significance, however, there have been few computational studies of clamping. Gasser et al. [26] and Calvo et al. [27] provided clamp simulations that did not include fluid or FSI. The models were also not able to occlude completely (90% in Gasser and Holzapfel, and 60% in Calvo et al.) and difficulties in achieving convergence when the vessel was highly deformed were cited. Arterial clamping involves large deformations and contact between multiple rigid bodies and soft tissue which are computationally challenging. A model combining such multi-body contact with FSI adds additional challenges.

9.4.3 Possible Injury Mechanisms

Recently, Chen and Kassab implemented clamp simulations including large deformation and FSI. They found that in the case of the cylindrical clamp, the radial compression and axial stresses were of largest magnitude but shear stress was relatively small. Therefore, the injury mechanism is likely to stem from compression and axial stresses caused by the clamps (Fig. 9.2).

The vessel may be more prone to injury by the large compressive stress during closure as aorta normally does not experience significant compression. The high compressive stresses predicted by the model are consistent with vessel injuries from

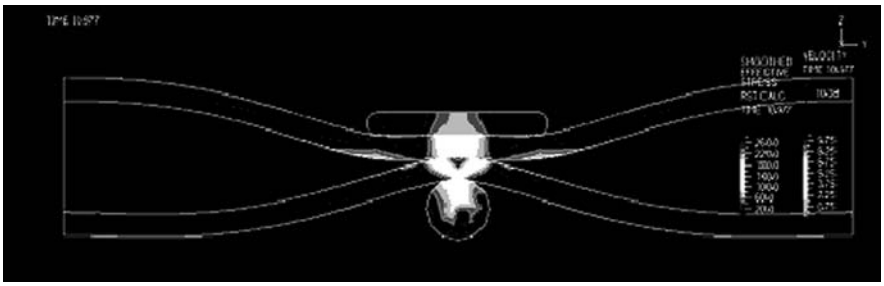

Fig. 9.2 The stress distribution with the cylindrical and plate clamps. The wall stresses caused by the cylindrical clamp were much higher than those of the plate clamp (Chen and Kassab)

clamping as revealed by histological studies. Even stresses that are considered non-destructive may have long-term effects as revealed by experimental studies on vessel function such as the ability to relax or constrict [28].

9.4.4 Fluid Dynamics

Figures 9.3 and 9.4 illustrate the dynamic and highly transient nature of the fluid during the closure process and support the importance of implementing the FSI model (Chen and Kassab). Fluid shear stresses became higher towards the endothelium. It is well known that abnormally low or high WSS have effects on endothelial biology [29].

Although these effects are transient and hence acute, they may cause thrombosis. Experimental studies by Markulsky et al. found that endothelial damage from so-called atraumatic clamps increased platelet uptake and may progress to accumulation of thrombus with the risk of thrombosis. They further found that deposition of platelets on the clamped surface was proportional to the extent of endothelial lesions.

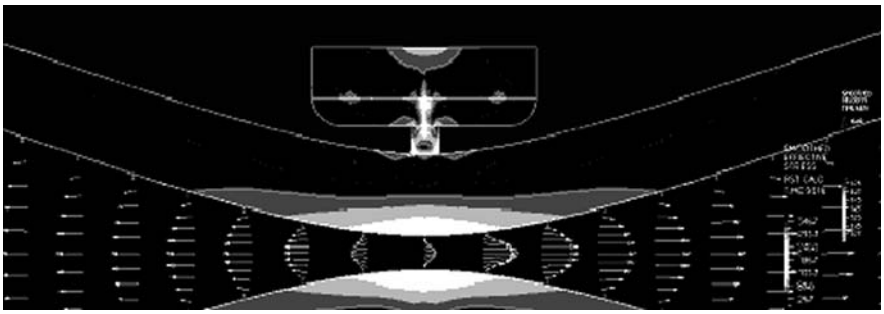

Fig 9.3 Flow reversal profile in the FSI model (Chen and Kassab)

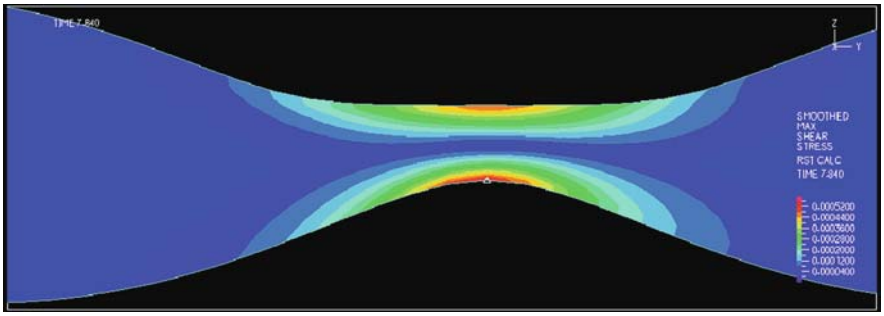

Fig. 9.4 Fluid shear stresses induced by the plate-like and cylindrical clamps (zoom in view) (Chen and Kassab)

Figure 9.3 demonstrates that at about 70% occlusion, flow reversal in the upstream section was observed as indicated by the negative flow. This has important implications as reverse flow can acutely cause endothelium to produce more superoxides which can scavenge nitric oxide [30].

This FSI model simulates an aortic cross-clamping process for heart failure repair with emphasis on closure dynamics of both solid and fluid. Both the fluid and solid mechanics during the closure process are found to be highly transient and dynamic. The utility of the model is to enable optimization of the design of clamps that may cause less trauma to arteries. Furthermore, this model may serve as a basis for virtual clamping where surgeons can examine various surgical scenarios in silico and predict the mechanical stresses in the vessel wall.

9.4.5 Application of the IB Method

The IB method has been successfully applied to numerous problems in computational biofluid dynamics [3]. Here we shall briefly review two applications as illustrations: valveless pumping [31] and closing and opening of a couple of flexible fibers in a flowing viscous fluid [32].

9.4.6 Valveless Pumping

The valveless pump is interesting in that it provides a net flow in the circulatory system at the early stage of the human embryo when the heart valves have not yet developed. The net flow is produced by the beating of the premature heart without the valves. Many researchers have worked on the theory and mechanism of valveless pumping through theoretical studies and laboratory experiments [33]. Jung and Peskin investigated the valveless pumping through numerical simulations using the FFT version of the IB method. They considered a periodic rectangular domain

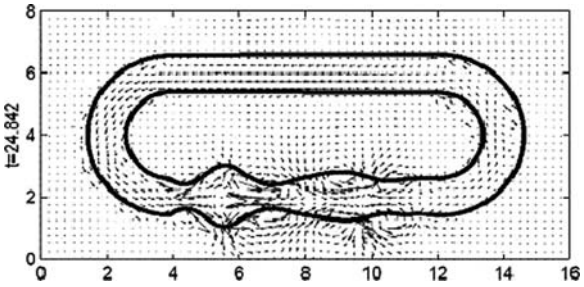

Fig. 9.5 Velocity vector field of an anticlockwise net flow generated by the valveless pumping [31]

filled with a viscous incompressible fluid. A closed loop (in the shape of a racetrack) was immersed in the domain. The loop was rigid except for the flat bottom portion that was flexible. The motions were driven by prescribed sinusoidal oscillations of fraction of the flexible portion of the loop. Figure 9.5 shows a typical simulation result where the dark rectangle is the computational domain and the red curves represent the loop. The blue dots represent fluid markers and the arrows visualize the velocity field. A counterclockwise net flow is produced by valveless pumping.

9.4.7 Flexible Fiber in a Flow Field

Flexible fibers in a viscous flow field represent a number of biological problems including a glycocalyx on the endothelium, a primary cilia on cell surfaces, microvilli in the intestines, and others. Experiments were performed by Zhang et al. [34] on the interaction of a pair of flexible fibers both fixed at the upper tips and separated by a horizontal distance D in a flowing viscous incompressible fluid. The elastic fibers form a valve-like structure. When the distance D is large enough compared to the fiber length L (i.e. $D/L > 0.21$), the valve executes an anti-phase clapping motion resembling the closing and opening of a cardiovascular valve in two dimensions. Zhu and Peskin [32] performed numerical simulations of the 2D valve–fluid system using the multi-grid version of the IB method. The simulation was performed on a rectangular domain with aspect ratio 1:2 (width to height), see Fig. 9.6. A viscous fluid flows from top to bottom. No-slip boundary condition is used for the two side walls, and measured velocity profiles are used at the inlet (top) and outlet (bottom).

The simulation results are shown in Fig. 9.6 for two typical time instants (top panel time $= 11$, bottom panel time $= 11.6$). The left panels plot the instantaneous positions of fluid markers generated in bursts intermittently at the inlet for visualization of fluid particles. The right panels shows vorticity contours for visualization of the vertical field. After a short adjustment period, the system "forgets" its initial conditions, and the two fibers settle into their stable anti-phase clapping state. This motion of closing and opening of the fibers is analogous to that of a heart valve. The

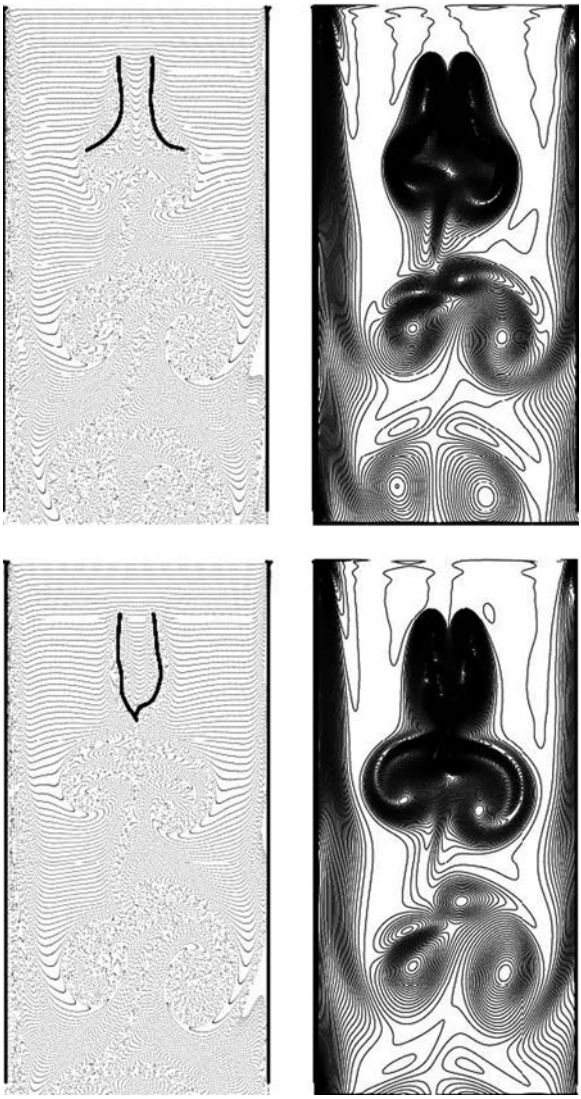

Fig. 9.6 The clapping motions (opening/closing) of two flexible fibers in a flowing viscous fluid. Dimensionless time = 11 (*top*) and 11.6 (*bottom*)

clapping frequency is about 41 Hz. The closing and opening is periodic in time and self-sustaining. In these simulations, the valve formed by the flexible fibers was able to close fully before opening. The FSI involved in the simulation and the actual heart valves share multiple similarities. In both cases, the valves are passive, flexible, and are immersed in a viscous incompressible moving fluid. They interact through the surrounding fluid and execute cyclic closing–opening motion.

9.5 Conclusion

The cardiovascular system is an extremely complex living system which involves complicated interactions of flowing blood and distensible soft vessels. The blood is a non-Newtonian complex fluid consisting of a plasma and numerous suspensions such as deformable cells (e.g., red blood cells, white blood cells, and platelets), enzymes, and hormones. The vessels are typically a multiple-layered structure made of living soft matters which are active, nonlinear, visco-elastic, and whose mechanical properties may be time-dependent. It remains a difficult task to model and simulate the cardiovascular FSI. The utility of the FSI approach to understand heart failure remains a laudable goal for the future.

Acknowledgments This research was supported in part by the National Institute of Health-National Heart, Lung, and Blood Institute Grant HL055554-11, HL084529, and HL087235 (G. Kassab), and U.S. National Science Foundation grant DMS-0713718 (L. Zhu).

References

1. Peskin CS. Flow patterns around heart valves: a digital computer method for solving the equations of motion. (PhD thesis). *Physiol., Albert Einstein Coll. Med, Univ. Microfilms.* 1972;378:72–80.
2. Peskin CS Flow patterns around heart valves: a numerical method. *J Comput Phys.* 1977;25:220.
3. Peskin CS. The immersed boundary method. *Acta Numer.* 2002;11:479.
4. Hughes, TJR, Liu, WK, Zimmermann, TK. Lagrangian Eulerian finite element formulation in incompressible viscous flows. *Comput Methods Appl Mech Eng.* 1981;29:329–49
5. Donea J, Giuliani S, Halleux JP. An arbitrary Lagrangian Eulerian finite element method for transient dynamic fluid structure interactions. *Comput Methods Appl Mech Eng.* 1982;33: 689–723
6. Formaggia L, Nobile F. A stability analysis for the arbitrary Lagrangian Eulerian formulation with finite elements. *EastWest J Numer Math.* 1999;7:105–31.
7. Fefferman C/L. Existence & smoothness of the Navier–Stokes equation. Princeton, NJ: Princeton University, Department of Mathematics. 2000.
8. Boukir K, Nitrosso B, Maury, B. A characteristics-ALE method for variable domain Navier–Stokes equations. In: Wrobel LC, Sarler B, and Brebbia CA, Eds., Computational modeling of free and moving boundary problems III. Boston: Computational Mechanics Publications Southampton, 1995, pp. 57–65.
9. Huo Y, Guo X, Kassab GS. The flow field along the entire length of mouse aorta and primary branches. *Ann Biomed Eng.* 2008 May;36(5):685–99.
10. Tawhai MH, Hunter PJ. Multibreath washout analysis: modeling the influence of conducting airway asymmetry. *Respir Physiol.* 2001 Sep;127(2-3):249–58.
11. Bathe KJ. Finite element procedures. Englewood Cliffs: Prentice-Hall, 1995, 1037 pp.
12. McQueen DM, Peskin CS, Yellin EL. Fluid dynamics of the mitral valve: Physiological aspects of a mathematical model. *Am J Physiol.* 1982;242:H1095–110.
13. McQueen DM, Peskin CS. Computer-assisted design of pivoting-disc prosthetic mitral valves. J *Thorac Cardiovasc Surg.* 1983;86:126–35.
14. McQueen DM, Peskin CS. Computer-assisted design of butterfly bileaflet valves for the mitral position. *Scand J Thorac Cardiovasc Surg.* 1985;19:139–48.
15. McQueen DM, Peskin CS. A three-dimensional computer model of the human heart for studying cardiac fluid dynamics. *Comput Graph.* 2000;34(1):56–60.

16. Kovacs SJ, McQueen DM, Peskin CS. Modelling cardiac fluid dynamics and diastolic function. *Philos Transact A Math Phys Eng Sci.* 2001;359(1783):1299–314
17. Vigmond EJ, Clements C, McQueen DM, Peskin CS. Effect of bundle branch block on cardiac output: A whole heart simulation study. *Prog Biophys Mol Biol.* 2008;97(2–3):520–42.
18. Peskin CS, McQueen DM. Computational biofluid dynamics. *Contemp Math.* 1993:141:161.
19. Zhu L, Peskin CS. Simulation of a flapping flexible filament in a flowing soap film by the immersed boundary method. *J Comput Phys.* 2002;179(2):452–68.
20. Chorin AJ. Numerical solution of the Navier–Stokes equations. *Math Comp.* 1968;22:745.
21. Chorin AJ. On the convergence of discrete approximations to the Navier–Stokes equations. *Math Comp.* 1969;23:341
22. Jackiewicz TA, McGeachie JK, Tennant M. Structural recovery of small arteries following clamp injury: a light and electron microscopic investigation in the rat. *Microsurgery*. 1996;17(12):674–80.
23. Margovsky AI, Chambers AJ, Lord RS. The effect of increasing clamping forces on endothelial and arterial wall damage: an experimental study in the sheep. *Cardiovasc Surg.* 1999;7(4):457–63.
24. Deiwick M, Glasmacher B, Baba HA, Roeder N, Reul H, Bally G, Scheld HH. In vitro testing of bioprostheses: influence of mechanical stresses and lipids on calcification. *Ann Thorac Surg*. 1998;66(6 Suppl):S206–11.
25. STS Adult CV Surgery National Database. (2007) Executive summary. Durham, NC:Duke University Medical Center.
26. Gasser TC, Schulze-Bauer CA, Holzapfel GA. A three-dimensional finite element model for arterial clamping. *J Biomech Eng.* 2002;124(4):355–63.
27. Calvo B, Martínez MA, Peña E, Doblaré M. A directional damage model for fibred biological soft tissues. *Int J Numer Methods Eng.* 2007;69:2036–57.
28. Barone GW, Conerly JM, Farley PC, Flanagan TL, Kron IL. Assessing clamp-related vascular injuries by measurement of associated vascular dysfunction. *Surgery*. 1989;105(4):465–71.
29. Kassab GS, Navia JA, Lu X. Proper orientation of the graft artery is important to ensure physiological flow direction. *Ann Biomed Eng.* 2006;34(6):953–7.
30. Lu X, Kassab GS. Nitric oxide is significantly reduced in ex vivo porcine arteries during reverse flow because of increased superoxide production. *J Physiol.* 2004;561:575–82.
31. Jung E, Peskin CS. 2-D simulation of valveless pumping using the immersed boundary method. *SIAM J Sci Comput.* 2001;23(1):19–45.
32. Zhu L, Peskin CS. Interaction of two flapping filaments in a flowing soap film. *Phys Fluids* 2003;15(7):1954–60.
34. Zhang J, Childress S, Libchaber A, Shelley M. Flexible filaments in a flowing soap film as a model for one-dimensional flags in a two-dimensional wind. *Nature* 2000;408:835.
35. Fung YC. Biomechanics: motion, flow, stress, and growth. Springer-Verlag, New York, 1998.
36. Margovsky AT, Lord RSA, Meek AC, Bobryshev YV. Artery wall damage and platelet uptake from so-called atraumatic arterial clamps: an experimental study. *Cardiovasc Surg.* 1997;5:42–47.
37. Okazaki Y, Takarabe K, Murayama J, Suenaga E, Furukawa K, Rikitake K, Natsuaki M, Itoh T. Coronary endothelial damage during off-pump CABG related to coronary-clamping and gas insufflation. *Eur J Cardiothorac Surg*. 2001;19:834–39.
38. Ross DE.. Chasing the wrong villain. http://www.ctsnet.orgsections/newsandviews/inmyopinion/articles/article-58.html, 2006
39. Slayback JB, Bowen WW, Hinshaw DB. Intimal injury from arterial clamps. *Am J Surg*. 1976;132(2):183–8.
40. Zhang W, Chen HY, Kassab GS. A rate-insensitive linear viscoelastic model for soft tissues. *Biomaterials*. 2007 Aug;28(24):3579–86.
41. Glowinski R, Pan T, Periaux J. A fictitious domain method for external incompressible viscous flow modeled by Navier-Stokes equations. *Comp. Methods in Appl. Mech. and Eng*. 1994;112(1–4):113–148.

42. Glowinski R, Pan T, Hesla T, Joseph D, Periaux J. A fictitious domain approach to the direct numerical simulation of incompressible viscous flow past moving rigid bodies: Application to particulate flow. *J. Comput. Phys*. 2001;169(2):363–426.
43. Prosi M, Perktold K, Schima H. Effect of continuous arterial blood flow in patients with rotary cardiac assist device on the washout of a stenosis wake in the carotid bifurcation: a computer simulation study. *J. Biomech*. 2007;40(10):2236–43.

Chapter 10
Turbulence in the Cardiovascular System: Aortic Aneurysm as an Illustrative Example

Liang Ge and G.S. Kassab

Abstract Turbulence is a fluid regime characterized by chaotic and stochastic changes of flow. The onset of turbulence can occur under disease conditions and is known to have adverse effects on the function of the cardiovascular (CV) system. This chapter outlines the basic features of turbulence in the CV system. As a specific example, simulation of turbulent flow in an abdominal aortic aneurysm (AAA) is presented. The simulated results show that transition to turbulence occurs in large aneurysms with high Reynolds number. Onset of turbulence is seen to drastically change the distribution of wall shear stress and fluid pressure. The general implications are enumerated.

10.1 Introduction

Turbulent flow is a flow status characterized with a large number of chaotic and random eddies or vortices. This includes high-momentum convection, low-momentum diffusion, and rapid fluctuation of pressure and velocity in space and time. Flow that is not turbulent is called laminar flow. The solutions of the Navier–Stokes equations governing fluid motion are unstable at large Reynolds numbers where turbulence occurs. The sensitive dependence of the initial and boundary conditions makes fluid flow stochastic both in time and in space so that a statistical description is warranted.

The dimensionless Reynolds number (ratio of inertial to viscous forces) characterizes whether flow conditions lead to laminar or turbulent flow. For example, for flow in a cylinder or vessel, a Reynolds number > 4000 (2100–4000 is known as transitional flow) will be turbulent. The Reynolds number is defined as $\rho UD/\mu$ where ρ and μ are the fluid density and viscosity of blood and U and D are the mean

L. Ge (✉)
Department of Surgery, University of California and San Francisco VA Medical Center, San Francisco, CA, USA

J.M. Guccione, et al. (eds.), *Computational Cardiovascular Mechanics*,

DOI 10.1007/978-1-4419-0730-1_10,

flow velocity and vessel diameter. At low Reynolds number where the viscous forces dominate the inertial forces, the flow is laminar, i.e., smooth. As the Reynolds number increases (increase in density, speed, or diameter; or decrease of viscosity), the transition to turbulent flow may occur. In turbulent flow, unsteady vortices appear on many scales and interact with each other.

Turbulence causes the formation of eddies of many different length scales. The large-scale structures contain most of the kinetic energy of the turbulent motion. The energy transport from large-scale to smaller-scale structures occurs mainly by an inertial mechanism. This process creates smaller and smaller structures which produce a hierarchy of eddies. Eventually this process creates structures that are small enough that molecular diffusion and hence viscous forces become important. The scale at which this happens is the Kolmogorov length scale.

Turbulence occurs ubiquitously in nature, ranging from rising smoke to industrial flows in a combustion engine. Under normal physiological conditions, the blood flow in the cardiovascular (CV) system is typically laminar or only weakly turbulent (ventricles and large aorta). Strong turbulent flows, however, can occur under disease conditions. For example, implantation of a mechanical heart valve or blood vessel stenosis often leads to flow turbulence [1]. The onset of turbulence in CV flows has tremendous impact on the CV system. It may increase the mechanical energy loss, thus imposing larger work load on the heart. It can also promote disease through an atherogenic response of endothelial cells. Hence, the study of flow turbulence in CV system is of tremendous importance.

Although the exact role of turbulence in the progression of CV disease is not fully understood, it is well known to promote pathogenesis of CV system. For example, turbulent flow causes significantly more blood clots than laminar flow [2]. Such flow-induced platelet-damage and clot formation is believed to be the leading cause of blood clotting in patients with implanted mechanical heart valves. This issue significantly limits the long-term clinical outcome of mechanical heart valves [3]. Turbulent flow can also impact the progression of atherosclerosis through flow-mediated mechanotransduction of endothelial cells. In vitro studies show that endothelial cells subjected to turbulent flows have higher turnover rate than those subjected to laminar flow [4].

To illustrate some of the features of turbulence, we present computational fluid dynamics (CFD) model of flow through an abdominal aortic aneurysm (AAA). AAA is a localized dilation of the infrarenal aorta. Rupture of AAA causes bleeding which is associated with very high mortality and mobility rate. Currently AAA rupture ranks the 11th leading cause of death in the United States. Although the exact mechanism governing the genesis, progression, and eventual rupture remains unknown and somehow controversial [5], it is well appreciated that biomechanical factors, including blood flow shear stress and arterial wall stress, play key roles in the progression of AAA. Here, we illustrate the impact of AAA geometry on turbulence transition and consequently impact the aortic wall shear stress (WSS) through numerical CFD simulations. Transition to turbulence was observed in large aneurysm models. The onset of turbulence was seen to have tremendous impact on WSS and fluid pressure.

10.2 Simulation of Aortic Aneurysm Flow

A simplified AAA geometric model is used as shown in Fig. 10.1. The profile of the curve is described as:

$$y(x) = R\left[1 + \frac{1}{2}(D-1)\left(1 - \cos\left(\frac{2\pi x}{L}\right)\right)\right]. \tag{10.1}$$

The model geometry is characterized with two simple geometrical parameters: the size ratio $D = R_{\max}/R$ and the aspect ratio $L = l/R$ as shown in Fig. 10.1. This construction of the aneurysm geometry allows easy scaling of the aneurysm size which has been previously adopted in a number of experimental studies to investigate the aneurysm flows [6, 7]. Although not physiologically correct, the model geometry has been shown to reproduce some of the important flow features observed in real aneurysm flows.

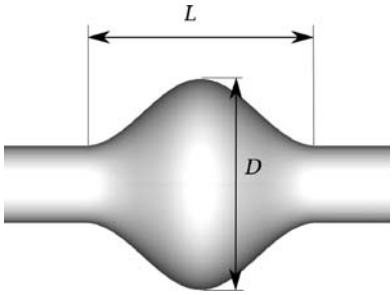

Fig. 10.1 The geometry of the simulated AAA models

The blood was assumed to be an incompressible Newtonian fluid. The aortic wall was assumed to be non-deformable solid walls and hence no fluid–structure interaction (FSI) was considered. Under these assumptions, the pulsatile flow motion through an AAA is governed by the unsteady Navier–Stokes equations, whose dimensionless form reads as

$$\frac{\partial u_i}{\partial x_i} = 0, \tag{10.2}$$

$$\frac{\partial u_i}{\partial t} + \frac{\partial u_i u_j}{\partial x_j} = -\frac{\partial p}{\partial x_i} + \frac{1}{\mathrm{Re}}\nabla u_i, \tag{10.3}$$

where u_i denotes the dimensionless velocity components in space (u_i=u_i/U, U the characteristic velocity), p is the dynamics pressure, and Re=$(\rho UD)/\mu$ is the Reynolds number of the flow.

The governing equations were solved using an in-house CFD solver. The solver was originally developed to investigate the flow turbulence often observed in bileaflet mechanical heart valves. The detail of the flow solver has been presented elsewhere [8]. Briefly, the solver uses a curvilinear grid system to discretize flow

domain. A representative grid used to discretize the aneurysm flow domain is shown in Fig. 10.2. In order to address the well-known odd–even decoupling problem seen in incompressible flow simulations, the flow solver adopts a staggered-grid approach to store the velocity and pressure components. Such an arrangement allows the enforcement of the divergence free condition (Eq. 10.2) up to machine zero. The combination of staggered-grid storage and curvilinear grid system, however, is well-known to lead to complicated discretization of the momentum equation (Eq. 10.3). This issue was addressed by using an innovative hybrid scheme that combines the advantages of staggered-grid (no odd–even decoupling) and non-staggered grid (easy discretization) approaches [8]. The unsteady governing equations are advanced in time using a fractional step approach. The momentum equations are solved using a Newton–Krylov method and the pressure Poisson equation is solved by a multigrid approach. The combination of these numerical schemes leads to a very efficient CFD solver. The CFD solver has second-order accuracy in space and time which has been validated in previous works [1, 8].

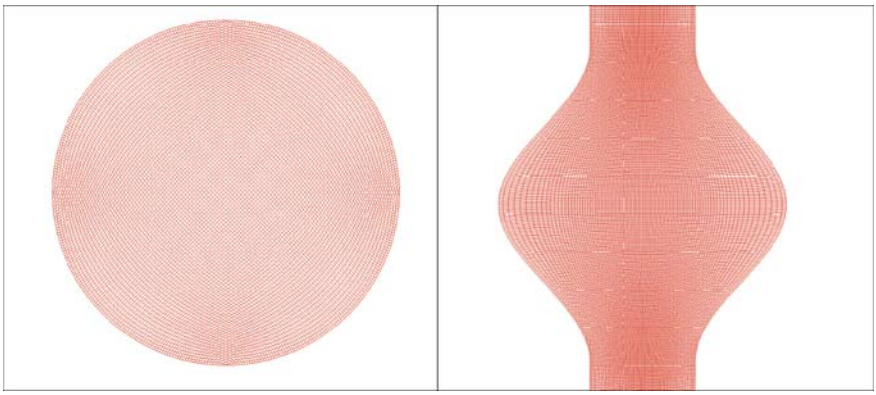

Fig. 10.2 Curvilinear grid used to discretize the AAA geometry

The inlet flow condition was based on the physiological flow waveform measured under resting condition [9]. It is a triphasic waveform (Fig. 10.3), consisting of a large systolic forward flow, followed by a backward flow during early diastole and a second (smaller) diastolic forward flow. The peak Reynolds number is 2300 and the average Reynolds number is approximately 500 (heart rate of 72 beats/min).

Numerical simulations were carried out for three different aneurysm geometries. The diameter of the upstream aorta is 1.8 cm. The aspect ratio L of each model was set to 3. The size ratio, which determines the diameter of the aneurysm, of these models was 1.5, 2.1, and 2.75, respectively. This is equivalent to a 2.7 cm, 3.78 cm, and 4.95 cm aneurysm, respectively.

For each aneurysm model, the inlet and outlet were placed at 5.5 and 7.5 diameter away from the center of the aneurysm. Each aneurysm model is discretized with a curvilinear grid with more than 3 million ($101 \times 101 \times 321$) grid nodes. A plug

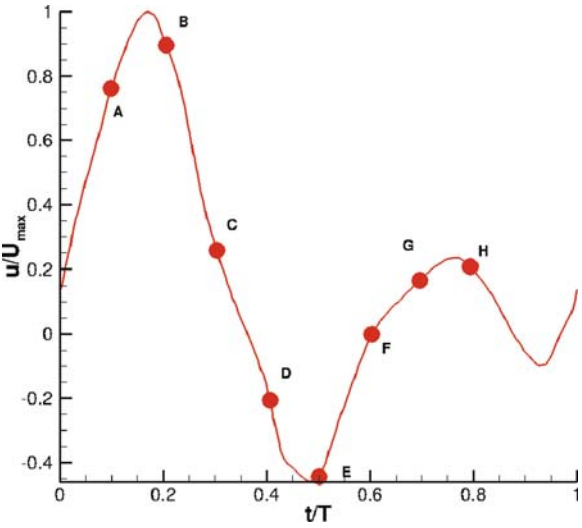

Fig. 10.3 Inlet physiological flow waveform under resting conditions

velocity profile was specified at the inlet of aneurysm. Each cardiac cycle was simulated with 2000 time steps. For each model, the simulations were carried out for at least five cardiac cycles if the flow is laminar or ten cycles if the flow is turbulent.

10.3 Simulation Results

In the three models studied, onset of turbulent flow was observed both in the intermediate and large aneurysm models while only laminar flow was observed in the small aneurysm. Since the majority of flow characteristics are very similar between the two cases with turbulent flows, only results from the large and small aneurysms will be presented below.

10.3.1 Two-Dimensional Instantaneous Flow Field

The 2D flow features of the large aneurysm model at selected time instants through a cardiac cycle are visualized (Fig. 10.4). A characteristic feature of the flow is the initialization, evolution, and eventual rupture of a vortex ring structure. Initially, the onset of upstream forward flow at the early systole forms a thin shear layer near the aortic wall (Fig. 10.4a). This shear layer is initially fully attached to the wall. The continuous growth of incoming flow causes the shear layer to grow. At a later time, the strength of the shear layer is too large to be fully attached to the wall, thus leading to the separation of a small vortex ring structure from the proximal

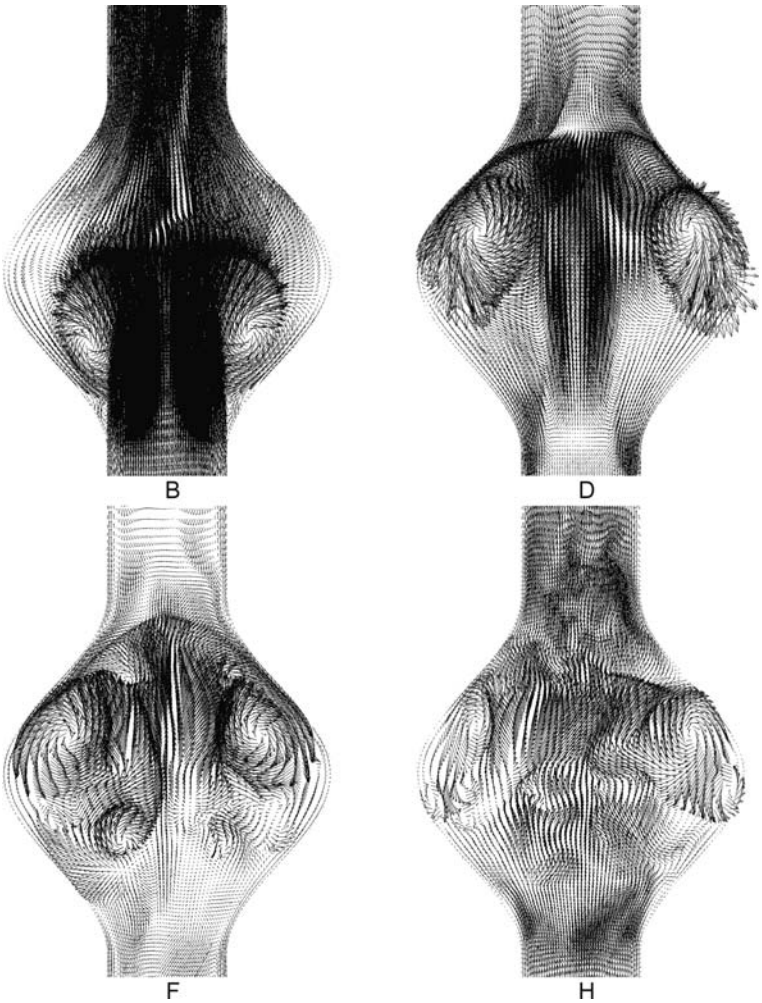

Fig. 10.4 Snapshots of instantaneous 2D flow features of the large aneurysm model visualized on a center plane parallel to the flow direction. The time instants A–H are shown in Fig. 10.3

neck of the aneurysm (Fig. 10.4b). This ring is then transported downstream by the blood flow which increases the strength of the ring. The ring subsequently reaches the distal end of the aneurysm wall and impinges on the wall (Fig. 10.4d). The impinging vortex ring induces a new vortical structure (Fig. 10.4d), which rotates in a direction opposite to that of the impinging vortex ring. Both the impinging vortex ring and the newly formed vortical structure move toward the middle of the aneurysm (Fig. 10.4e) and eventually break into large number of small and chaotic vortices (Fig. 10.4f–h); i.e., onset of the transition to flow turbulence. It

should be noted that the turbulent vortices that appear during the late half of cardiac cycle remain in the intra-aneurysm region and their remnants are visible at early systole.

The flow in the small aneurysm is characteristically different from the large model flow (Fig. 10.5). The initial flow separation and formation of a vortex ring at the proximal end of the aneurysm occur much later into the cardiac cycle. Once formed, the vortex ring also travels toward the distal end. But the distance traveled is much shorter in the small aneurysm (Fig. 10.5c and d) and unlike the large aneurysm flow, the vortex ring does not impinge on the aortic wall. Instead, the strength of the vortex ring decays before the structure reaches the distal end and the remaining strength is not sufficient to induce a large opposite vortex. As a result, the onset of small vortices are not observed in this flow. The well-organized instantaneous flow pattern in this structure indicates that the flow remains laminar in the small aneurysm.

10.3.2 Three-Dimensional Flow Structures

To appreciate the complicated flow structures, we analyzed the coherent vortical structures in these model flows using the Q-criterion approach. The Q-criterion is defined as:

$$q = \frac{1}{2}\left(\|\Omega\|^2 - \|S\|^2\right), \tag{10.4}$$

where S and Ω denote the symmetric and asymmetric part of the velocity gradient tensor, respectively, and $\|\bullet\|$ is the Euclidean matrix norm. Positive q indicates that the rotation rate dominates the strain rate locally. Regions of positive q are therefore occupied by vortical structures [10]. This approach has been previously used to visualize the 3D flow features in blood flows through bileaflet mechanical heart valves [1].

The 3D coherent structures of the large model flow are shown in Fig. 10.8. At the early systole, small vortical structure remaining from the previous cycle is seen in the aneurysm region. The incoming systolic flow washes these small structures downstream, which leads to the formation of a number of elongated longitudinal vortices (Fig. 10.6b). At the proximal side, a well-organized vortex ring is formed due to flow separation (Fig. 10.6b). This ring is advected toward the distal end of the AAA by the intraluminal flow and impinges on the distal wall at a later time instant (Fig. 10.6d). The interaction between the impinging vortex ring and the distal AAA wall induces a secondary vortex ring (Fig. 10.6d), which rotates in the opposite direction to the impinging ring as mentioned earlier. This secondary vortex ring breaks up into a large number of small vortical structures which leads to the onset of turbulence in this region (Fig. 10.6e). At the time of secondary vortex ring breakup, the impinging vortex ring remains coherent as reflected by the ring-like structure in Fig. 10.6e. This indicates that the small vortical structures primarily originate

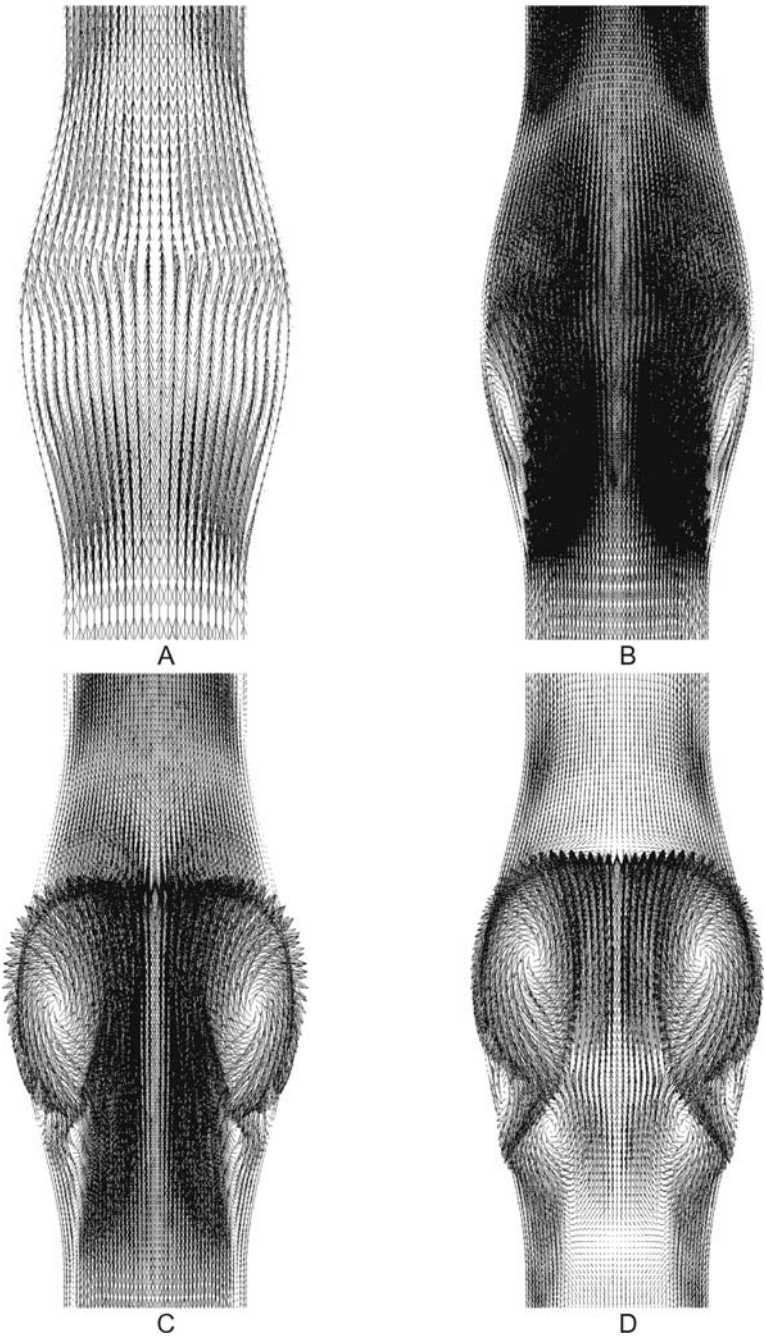

Fig. 10.5 Snapshots of instantaneous 2D flow features of the small aneurysm model visualized on a center plane parallel to the flow direction. The time instants A–H are shown in Fig. 10.3

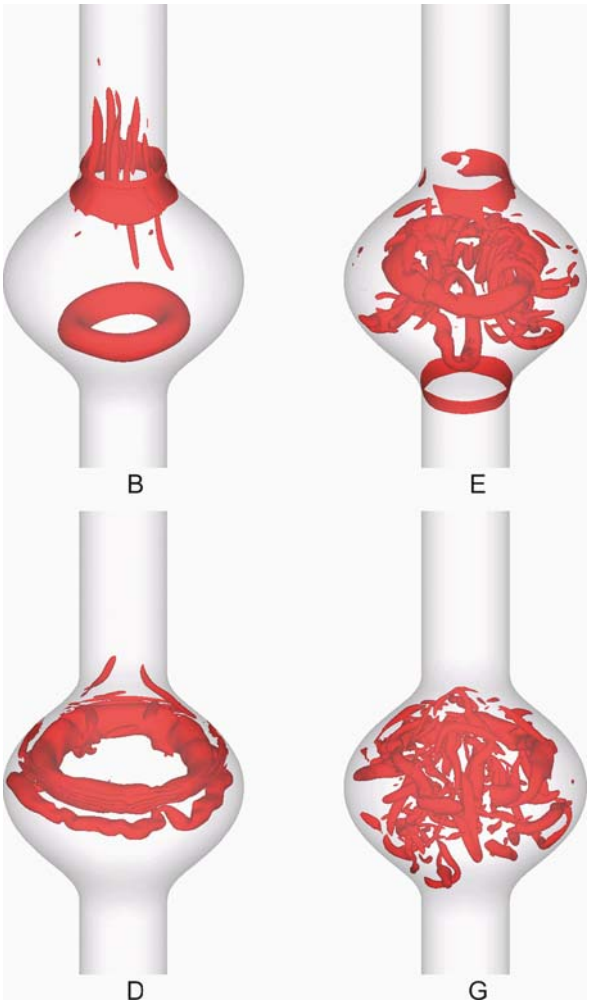

Fig. 10.6 Three-dimensional vortical structure of the large aneurysm model flow visualized with Q-criterion. The time instants A–H are shown in Fig. 10.3

from the secondary vortex ring, not the impinging ring that first emerged from the proximal aneurysm neck. The interaction between the small vortex structures and the impinging ring eventually leads to the break of the coherent ring at a later time instant (Fig. 10.6 g).

The difference between the small and large model flows is once again revealed in Fig. 10.7. Throughout the cycle, the flow in the small model is dominated by a well-organized ring. The strength of the vortex ring diminishes due to the viscous effect of the blood and dissipates before it reaches the distal end of the aortic wall.

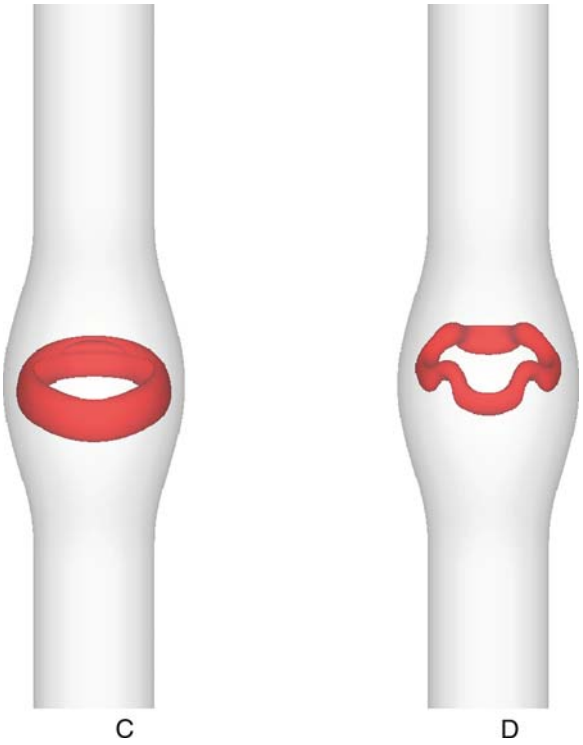

Fig. 10.7 Three-dimensional vortical structure of the small aneurysm model flow visualized with Q-criterion. The time instants A–H are shown in Fig. 10.3

10.3.3 Transition to Turbulence Due to Interaction Between Vortex Ring and Aortic Wall

The difference of the vortex ring dynamics between the two aneurysm models seen in Figs. 10.6 and 10.7 is likely to be the major factor leading to the different turbulent/laminar flow regimes between the two aneurysm models. Ring-like vortical structures are widely seen in nature and have been extensively investigated due to their fundamental fluid mechanics importance [11]. The evolution of the vortex ring in simplified AAA models has been experimentally measured using the particle image velocimetry technique [7]. Vortex ring formation has also been demonstrated in the pulsatile flows through a stenosed aorta [12] and through a bileaflet mechanical heart valve [1]. In both the stenosed aorta and valve flows, the vortex ring was seen to break into a very chaotic web of small eddies and hence the onset of flow turbulence. The current results reveal a slightly different vortex-ring break-up mechanism. The leading vortex ring induces a second vortex ring near the distal aortic wall. This induced vortex breaks up into a chaotic system prior to the leading vortex ring, and subsequently dissolves the leading vortex ring into small and chaotic ones. These small vortices recirculate within the aneurysm until the onset of flow systole at the next cardiac cycle, when they are washed away from the aneurysm.

The different vortex ring dynamics between the small and large aneurysm is caused by the aortic wall. In the case of the small aneurysm, the growth of the leading vortex ring is significantly restricted by the aortic wall which limits the growth of the strength of the ring. The weaker ring in the small aneurysm was seen to not travel as far as the one in the large aneurysm and was not able to extract a second ring from the distal end walls. The lack of this second ring significantly reduces the complexity of the intraluminal flow and likely increases the stability of the flow. As a result, we did not observe a transition to turbulence in the small aneurysm.

The interaction between the vortex ring and aortic wall clearly demonstrates the importance of boundary condition on the vortex ring evolution. The majority of previous vortical ring investigations focus on wall-free vortex rings where the size of vortex ring is relatively small compared with the size of the ambient fluid flow domain. The complicated flow pattern induced by the vortex-ring/wall interaction suggests that the vortex ring dynamics may be very different from wall-free rings. This is a worthwhile direction for further investigations.

10.3.4 Time History of the Instantaneous Velocity Field

Figure 10.8 shows the time histories of streamwise and spanwise velocity components recorded at a center point located near the distal end of the large (Fig. 10.8a) and small aneurysm (Fig. 10.8b). A stark contrast between the two cases is clearly seen in the figures. The time history of the small aneurysm is well-organized throughout the cardiac cycles, revealing the laminar flow nature of this model. The large aneurysm, on the other hand, is dominated with random velocity fluctuations which indicate the existence of flow turbulence in this model.

The instantaneous velocity history for the large aneurysm model shows that the fluctuation of the two spanwise velocity components appears to be more intensive than the streamwise velocity. This may be attributed to the large number of vortical structures observed under turbulence conditions which are aligned longitudinally. The longitudinal vortices create stronger cross-section circular than streamwise fluctuation, thus leading to more dominant velocity fluctuation along the two spanwise directions.

10.3.5 Impact of Turbulence on Shear Stress Distribution in the Flow Domain

By definition, shear stress is a second-order tensor whose values are coordinate dependent. In order to quantitatively evaluate the level of shear stress the concept of local maximum stress was used to analyze the stress distribution. The local maximum stress is defined as the difference between the maximum and minimum principle stress; namely:

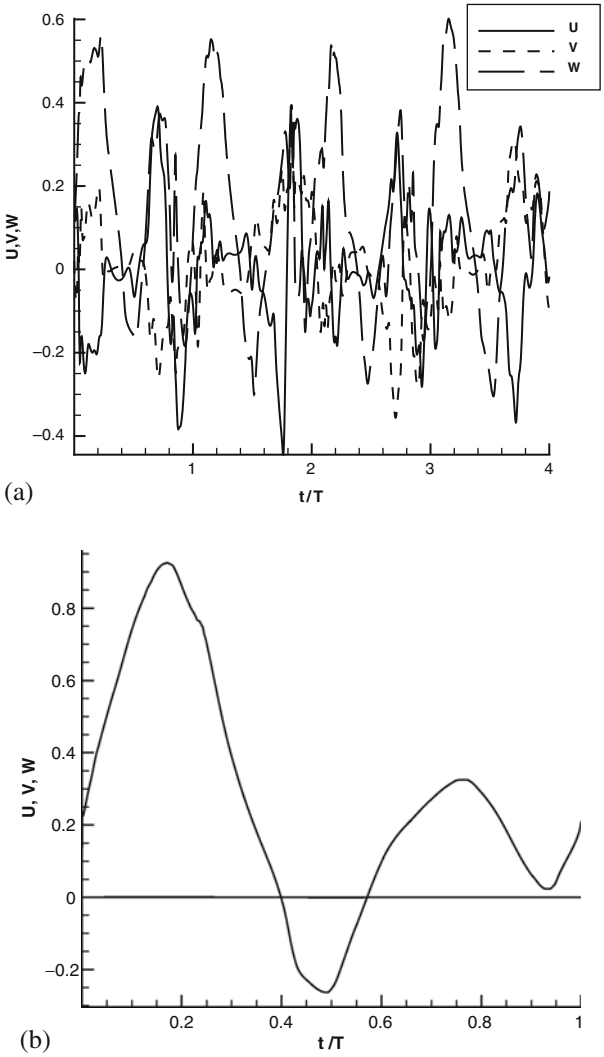

Fig. 10.8 Time history of instantaneous velocity components recorded at a center point near distal end of the aneurysm. (**a**) Large aneurysm model; (**b**) small aneurysm model

$$\tau_{\max} = \frac{1}{2}(\sigma_1 - \sigma_3), \tag{10.5}$$

where σ_1 and σ_3 are the maximum and minimum principle stress of the stress tensor τ_{ij}.

The contours of local maximum stress at the near-peak systolic flow distribution of the large and the small aneurysm models are shown in Fig. 10.9. The peak value of local maximum stress is not significantly different between the small and large

aneurysms. Area of regions of relatively high stress, however, is greater in the large aneurysm case. In the small aneurysm, where flow remains laminar throughout the cycle, the high stress region is only seen in a relatively thin layer attached to the aortic wall. The large aneurysm, however, is seen to have islands of high stress in the middle of aneurysm due to the impact of turbulence transition.

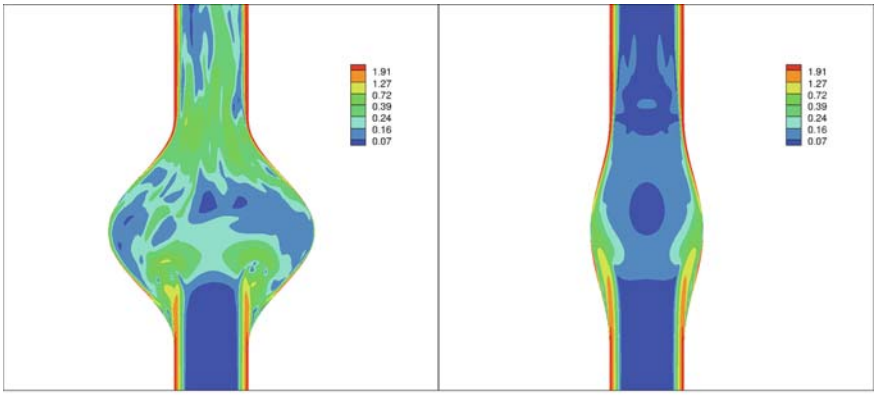

Fig. 10.9 Contours of maximum local shear stress at time instant B (Fig. 10.3) on a center plane parallel to the flow direction. (**a**) Large aneurysm model; (**b**) small aneurysm model

The transition to flow turbulence in the large aneurysm may partly explain the high incidence of intraluminal thrombus observed in large aneurysms [13]. Animal models have shown that turbulent flows promote thrombus formation [2]. Possible mechanisms leading to increased thrombus formation include elevated shear stress level, elongated particle residence time, and increased cell-to-cell interaction [14]. As seen in Fig. 10.9, the peak value of local maximum stress is not significantly different between the small aneurysm (laminar flow) and the large aneurysm (turbulent flow) models. Although the area of high stress regions is seen to be greater in the large aneurysm case, this difference alone is unlikely to cause significantly different shear exposure. The increased recirculation time caused by the chaotic vortical systems (Fig. 10.4) may be more significant in the intraluminal thrombus formation. Quantitative studies on the particle dynamics in these complicated flow fields are currently underway.

10.3.6 Impact of Turbulence on WSS

To quantify the fluid shear stress acting on the aortic wall, a local wall coordinate system consisting of a normal vector and two tangential vectors is defined. The normal vector, $\overline{n}$, is the unit vector perpendicular to the wall surface. The two tangential

vectors, t_1 and t_2, are two unit vectors located on the surface plane. t_2 is defined as $t_2 = \frac{n \times z}{|n \times z|}$ (where z is the unit vector along z-axis) and t_1 is perpendicular to t_2. In order to calculate the stress, the 3D velocity vector at the near-wall nodes was first projected to this local wall coordinate system as $u_n = \vec{u} \cdot \vec{n}$, $u_{t_1} = \vec{u} \cdot \vec{t}_1$ and $u_{t_2} = \vec{u} \cdot \vec{t}_2$.

Two important parameters of the WSS, namely the magnitude and direction, can be calculated as:

$$\tau = \mu \frac{\sqrt{u_{t_1}^2 + u_{t_2}^2}}{d}, \tag{10.6}$$

$$\theta = \arccos\left(\frac{u_{t_1}}{\sqrt{u_{t_1}^2 + u_{t_2}^2}}\right), \tag{10.7}$$

where d is the shortest distance from the near-wall grid node to the wall.

The distribution of WSS magnitude in the large aneurysm model is shown in Fig. 10.10. Similar to the distribution of pressure, the WSS is also inhomogeneous in the circumferential direction and characterized with pockets of high and low WSS regions. The distribution of direction (θ) is more chaotic than the stress magnitude, which indicates the rapid change of near-wall flow direction. The distribution of stress magnitude and direction of the small aneurysm case is axisymmetric (results not shown).

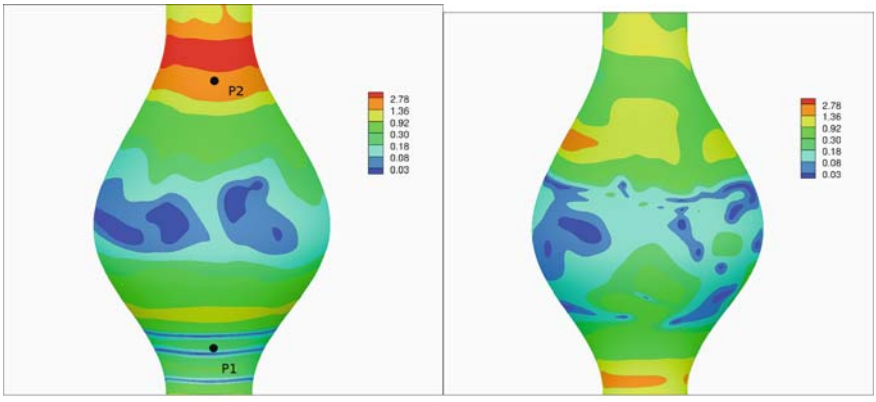

Fig. 10.10 Contours of surface shear stress (large aneurysm model). (**a**): Time instant B; (**b**): time instant E

The time history of stress magnitude and direction was monitored at two points, P_1 (near proximal neck) and P_2 (near distal neck) as indicated in Fig. 10.10 and the results are presented in Fig. 10.11. As expected, the time history is characterized with random fluctuation, especially the direction of the shear stress.

WSS is known to play key role in the remodeling process of aortic wall. The magnitude, the strength of stress oscillation (quantified by an oscillatory shear index

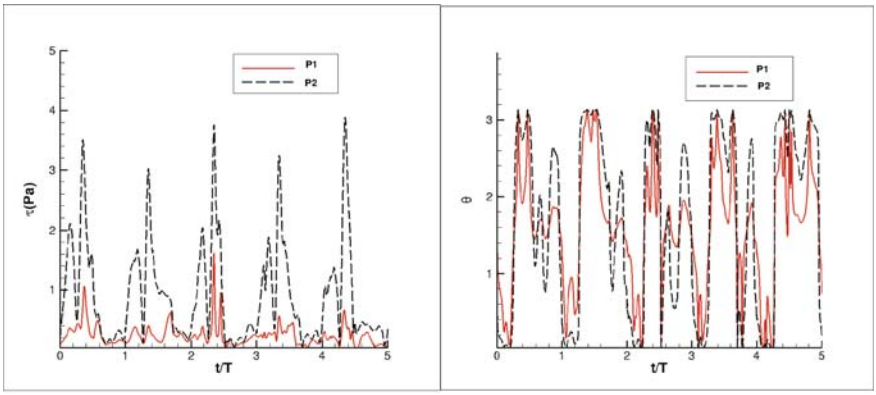

Fig. 10.11 Time history of instantaneous WSS. (**a**): Magnitude; (**b**): angle (θ)

[15], which is defined as OSI $= 1/2(1 - (|\int \tau \mathrm{d}t|/\int |\tau|\mathrm{d}t))$, and the gradient of shear stress have all been suggested to have certain pathological role.

With the onset of flow turbulence, as seen in the large aneurysm models, the shear stress cannot be identified by the above-mentioned parameters. The surface stress was seen to point to all directions and no dominant direction can be identified. The temporal and spatial gradient of WSS is significantly larger than the laminar flow (small aneurysm) case. The biological significance of this turbulent WSS needs to be quantified through in vitro and in vivo cell biology experiments.

10.3.7 Model Limitations

The major limitation of the current model is that it did not consider the FSI effect between the aortic wall and the intraluminal flow. Although it is likely that the FSI would not significantly affect the fundamental fluid mechanical features (such as turbulent flow transition), the wave propagation caused by FSI can change the vortex ring dynamics. Therefore, it is important to include the FSI in future studies. A second limitation is that the simulation only considered symmetric aneurysm models. Recent investigations on the blood flow through stenotic aorta show that asymmetry may promote the transition to turbulence [12]. Since the majority of AAAs have asymmetric geometry, the simulation of a more realistic geometry is a must in future studies.

10.4 Implications

The progression and eventual rupture of AAAs are strongly affected by hemodynamics factors, including blood flow shear stress and blood pressure. Conditions such as low flow shear stress [16] or elevated blood pressure [17] have been shown

to upregulate matrix metalloproteinases (MMPs). MMPs are a family of zinc-dependent proteolysis enzymes that can digest a wide range of extracellular matrix proteins. The flow-induced upregulation of MMPs leads to the degradation of medial elastin, a sentinel characteristic of AAA [18]. In animal AAA models, relatively high flow shear stress is shown to promote endothelial cell and smooth muscle cell proliferation, and suppress the progression of AAA compared with low shear stress level [19]. The shear stress-regulated endothelial cell response, such as MMP-9 [20] and Cathespin L [21], has been suggested as a potential mechanism that limits AAA progression.

Turbulent AAA flows have been observed under both in vivo [22] and in vitro [6, 7] conditions and are anticipated to have major impact on the hemodynamics through AAA. Due to many numerical challenges, the fundamental features of AAA have not been reproduced in numerical simulations even under relatively simple geometrical conditions [23]. Here, we used an advanced CFD solver to simulate the turbulent flows through AAAs. The geometry and flow conditions closely resemble the conditions used in the experimental measurements conducted by Peattie et al. [6]. The observed flow features from current CFD simulations agree well with the experimental results previously reported [6]; namely, laminar flow was observed only in a small aneurysm while the larger aneurysm flows were turbulent. The key components required to reproduce these flow features numerically include high-accuracy numerical schemes as well as high-resolution grid systems. The grid spacing in the aneurysm region was about 0.2–0.3 mm. Such a grid resolution can fully resolve all scales of eddy motions typically seen in this type of flows [14]. Further validations of the numerical results are needed.

It should be noted that no disturbance was specified at the inlet; i.e., perfectly stable and symmetric conditions were used at the inlet. The transition to turbulence observed in the simulation indicates that the turbulence is caused by the nature of flow instability within the aneurysm region. The observed turbulent flows in current simulations, combined with in vitro experimental observations, indicate that turbulent flows may occur naturally for clinically important aneurysms (usually larger than 5 cm), even under resting conditions. It is therefore very important to consider the impact of turbulent flow on AAA's progression.

10.5 Future Studies

The onset of flow turbulence was also shown to drastically change the distribution of pressure field. Since the current study did not consider the FSI effect, we could not quantitatively evaluate the aortic wall stress. It is reasonable to anticipate, however, this may have major impact on the aortic wall stress. Under in vivo conditions, the spatial gradient of pressure is known to propagate as a wave in the CV system [24]. The chaotic flow fluctuation seen in the large aneurysm would clearly change the pressure wave propagation and hence the distribution of wall stress. This indicates the importance of incorporating turbulence simulations into future FSI simulations of AAA hemodynamics.

10.6 Summary and Conclusions

The velocity field in a turbulent flow is stochastic unlike laminar flow which is deterministic. The flow is normally turbulent in the ventricles and ascending aorta where the Reynolds number is sufficiently high. In disease states, however, turbulent flow can extend to other portions of the vasculature and has negative implications on endothelial function. In AAA, the flow may transition to turbulence if the dilatation is sufficiently large. This has important implications for energy losses and interactions with the endothelium that may lead to further deterioration of the aortic wall. A better understanding of the initiation and amplification of turbulence in AAA may lead to improved diagnostics for early detection as well as therapeutics for stabilizing the aortic wall.

References

1. Dasi LP, et al. Vorticity dynamics of a bileaflet mechanical heart valve in an axisymmetric aorta. *Phys Fluids*. 2007;19:067105.
2. Stein P, Sabbah H. Measured turbulence and its effect on thrombus formation. *Circ Res*. 1974;35:608–14.
3. Yoganathan AP, He Z, Jones SC. Fluid mechanics of heart valves. *Ann Rev Biomed Eng*. 2004;6:331–62.
4. Davies PF, et al. Turbulent fluid shear stress induces vascular endothelial cell turnover in vitro. *Proc Natl Acad Sci USA*. 1986;83:2114–7.
5. Wassef M, et al. Challenges and opportunities in abdominal aortic aneurysm research. *J Vasc Surg*. 2007;45:192–8.
6. Peattie RA, Riehle TJ, Bluth EI. Pulsatile flow in fusiform models of abdominal aortic aneurysms: flow fields, velocity patterns and flow-induced wall stresses. *J Biomech Eng*. 2004;126:438.
7. Salsac A, et al. Evolution of the wall shear stresses during the progressive enlargement of symmetric abdominal aortic aneurysms. *J Fluid Mech*. 2006;560:19–51.
8. Ge L, Sotiropoulos F. A numerical method for solving the 3D unsteady incompressible Navier–Stokes equations in curvilinear domains with complex immersed boundaries. *J Comput Phys*. 2007;225:1782–809.
9. Moser UT, Vieli A. Human abdominal aorta: comparative measurements of blood flow with MR imaging and multigated Doppler US. *Radiology*. 1989;171:487–92.
10. Hunt JCR, Wray A, Moin P. Eddies, stream and convergence zones in turbulent flows, Report CTR-S88 1988.
11. Gharib M, Rambod E, Shariff K. A universal time scale for vortex ring formation. *J Fluid Mech*. 1998;360:121–40.
12. Lee SE, et al. Direct numerical simulation of transitional flow in a stenosed carotid bifurcation. *J Biomech.* 2008;41:2551–61.
13. Harter LP. Ultrasonic evaluation of abdominal aortic thrombus. *J Ultrasound Med*. 1982;1:315–8.
14. Ge L, et al. Characterization of hemodynamic forces induced by mechanical heart valves: Reynolds vs. viscous stresses. *Ann Biomed Eng.* doi: 10.1007/s10439-007-9411-x
15. Ku DN, et al. Pulsatile flow and atherosclerosis in the human carotid bifurcation. Positive correlation between plaque location and low oscillating shear stress. *Arterioscler Thromb Vasc Biol*. 1985;5:293–302.

16. Bassiouny HS, et al. Flow regulation of 72-kD collagenase IV (MMP-2) after experimental arterial injury. *Circulation*. 1998;98:157–63.
17. Chesler NC, Ku DN, Galis ZS. Transmural pressure induces matrix-degrading activity in porcine arteries ex vivo. *Am J Physiol Heart Circ Physiol*. 1999;277:2002–9.
18. Campa J, Greenhalgh R, and Powell J. Elastin degradation in abdominal aortic aneurysms. *Atherosclerosis.* 1987;65:13–21.
19. Sho E, et al. Arterial enlargement, tortuosity, and intimal thickening in response to sequential exposure to high and low wall shear stress. *J Vasc Surg*. 2004;39:601–12.
20. Magid R, Murphy TJ, Galis ZS. Expression of matrix metalloproteinase-9 in endothelial cells is differentially regulated by shear stress role of c-Myc*. *J Biol Chem*. 2003;278:32994–9.
21. Platt MO, Ankeny RF, Jo H. Laminar shear stress inhibits cathepsin L activity in endothelial cells. *Arterioscler Thromb Vasc Biol*. 2006;26:1784.
22. Ferguson GG. Turbulence in human intracranial saccular aneurysms. *J Neurosurg*. 1970;33: 485–97.
23. Humphrey JD, Taylor CA. Intracranial and abdominal aortic aneurysms: similarities, differences, and need for a new class of computational models. *Ann Rev Biomed Eng*. 2008;10.
24. Fung YBiomechanics: mechanical properties of living tissues. Berlin: Springer, 1993.

Part II
Applications in Heart Failure

Chapter 11
Noninvasive Assessment of Left Ventricular Remodeling: Geometry, Wall Stress, and Function

Liang Zhong, Ru San Tan, Yi Su, Si Yong Yeo, Terrace Chua, Tian Hai Koh, Dhanjoo Ghista, and Ghassan Kassab

Abstract Left ventricular (LV) remodeling after myocardial infarction (MI) plays an important role in the progression of heart failure (HF). Changes in the shape, size, and function of the LV are caused by altered mechanical properties of the injured myocardium. As the survival rate after MI improves with medical advances, the incidence of HF patients increases. Hence, an accurate depiction of the LV remodeling process facilitates disease surveillance and monitoring of therapeutic efficacy. It may also help determine the choice of treatment, e.g., surgery to remove the infarcted wall segment and reduce the LV cavity size. Traditionally, there are several ways of characterizing LV remodeling: changes in LV diameter, LV volume, ejection fraction, and qualitative or semi-quantitative descriptors of LV shape. In this chapter, we present a new approach to quantify LV shape (in terms of curvedness), wall stress, and function by using computational modeling.

11.1 Introduction

Heart failure (HF) is associated with significant morbidity and mortality due to progressive myocardial dysfunction, accompanied by left ventricular (LV) remodeling. LV remodeling may be defined as a change in shape, size, and function of the LV due to physiological or pathological conditions [1]. Physiological change is a compensatory change in the dimensions and function of the heart in response to physiological stimuli induced by exercise such as an athlete's heart [2]. Pathological changes can be seen in disorders of the ventricles due to ischemic cardiomyopathy [3], hypertension [4], hypertrophy [5], and dilated cardiomyopathy [6].

Relatively small increases in ventricular volume are associated with an independent increase in the risk of death in patients with coronary artery disease, MI, or

L. Zhong (✉)
Department of Cardiology, National Heart Centre Singapore, Singapore
e-mail: zhong.liang@nhc.com.sg

J.M. Guccione, et al. (eds.), *Computational Cardiovascular Mechanics*,
DOI 10.1007/978-1-4419-0730-1_11,

HF [3]. Interventions having favorable impact on LV remodeling process (or on restoration of LV remodeling) have been shown to improve mortality in patients with HF [7]. However, some therapeutic treatments aiming solely at improving cardiac output or blood flow do not slow HF progression or reduce mortality [8]. Therefore, reversal of LV remodeling (through medical or surgical treatment) has been recognized as a therapeutic target in HF of all etiologies.

Measures to assess LV remodeling include heart size, shape and mass, wall stress, and ventricular contractility [1]. Each measure is indicative of a different aspect of the disease state. Understanding the extent of LV remodeling can help assess the prognosis of HF: the greater the extent of the remodeling, the poorer the prognosis.

11.1.1 Left Ventricular Structural Remodeling

LV structural remodeling includes molecular and cellular changes which are manifested clinically as changes in LV size and shape. The cellular rearrangement of the ventricular wall is associated with a significant increase in LV volume and mass.

The LV size and shape changes after MI have been extensively studied in animals, such as rats [9, 3]. Initially, there is thinning and distension of both the infarcted and noninfarcted myocardium, causing increased wall stress. The noninfarcted myocardium subsequently becomes hypertrophied in response to the increased wall stress. Hypertrophy of surviving myocytes occurs in proportion to the infarct size for infarctions involving up to 20% of the ventricle. There is little additional hypertrophy in larger infarctions [9].

During the diastolic phase, the stiffened MI element acts as a stress concentration insert, causing the neighboring noninfarcted myocardium to be highly stressed. During the systolic phase, the MI element does not contract. Hence, the neighboring noninfarcted myocardium will have to contract more strongly (as a compensatory mechanism) in order to raise the intra-LV pressure to eject the blood. In this way, the noninfarcted myocardium is more stressed due to the presence of the MI and hence becomes hypertrophied in response to the increased wall stress.

Progressive LV dilation occurs up to 3–4 months post-infarction and cardiac output begins to fall [3]. The ventricular remodeling that occurs after infarction in animals is similar to what happens in patients [10]. As the heart undergoes remodeling, it becomes less elliptical and more spherical (Fig. 11.1) [11]. There are also changes in ventricular mass and volume – all of which may adversely affect cardiac function.

LV structural remodeling occurs regionally. Yet, efforts to characterize the overall change in LV shape have been made by global LV chamber analysis by the sphericity index (SI), which measures the ratio of either (a) the long-axis to short-axis [12] or (b) end-diastolic (ED) volume to the volume of sphere having the measured long-axis diameter [12]. There is a major limitation in the SI analysis of the entire chamber, since the single plane ratio reflects a linear alteration in the two axes of the entire ventricular chamber. SI does not focus on regional shape abnormalities, as these changes may precede secondary global ventricular dilation.

Parameter	3 weeks	1 year
End-diastolic volume	302 ml	377 ml
End-systolic volume	186 ml	271 ml
Circumference	59.5 cm	62.8 cm
Contractile segment	30.5 cm	33.8 cm
Non-contractile segment	23.7 cm	23.5 cm
Diastolic sphericity index	0.71	0.74
Systolic sphericity index	0.60	0.77

Fig. 11.1 Late ventricular enlargement, or remodeling, resulting from increased circumference and sphericity, produces a marked increase in volume. The increase in circumference is due to lengthening of the contractile tissue rather than due to further expansion of the infarcted, noncontractile segment. The increased sphericity results from a rounding out of the sharp abnormalities in contour at the margins of the infarct. Adopted from Mitchell et al. [25]

Hence, Fourier analysis [13] or radius curvature analysis is used to quantify LV shape [14]. Recently, we have developed a curvedness parameter to describe LV shape by using computational modeling ([6, 15]).

11.1.2 Left Ventricular Functional Remodeling

The initial remodeling phase after a MI results in a necrotic area and scar. Hypertrophy of the noninfarcted myocardium is a compensatory mechanism for maintenance of LV function and cardiac output [5] that may initially result in hyperfunction of the LV. This augmentation has a limit, however, after which the noninfarcted myocardium is unable to compensate. In fact, concomitantly the thinned infarcted wall segment will deform. This is because the infarcted wall segment cannot contract and hence develops increased stiffness. It is hence unable to sustain the intra-LV pressure and may deform into an aneurysm [16].

After a large MI, muscle function in the noninfarcted myocardium is augmented initially and then eventually deteriorates. Data show that at 6 weeks after a large infarction, there was contractile dysfunction with increased muscle stiffness, myocyte hypertrophy, and increased collagen content in the residual noninfarcted myocardium [17]. It is deemed that a mechanical stimulus (e.g., an increase in wall stress) is probably responsible for the progressive deterioration in muscle function [18]. In the rat infarct model, the functional changes are reflected in the mortality data. The 6-month survival for rats with infarcts is generally 50%, but 35% for rats with large infarcts [19]. In clinical studies, it is difficult to separate changes in organ and muscle function. In this regard, the hemodynamic data (of LV pressure and volume) can at best reflect a summation of changes in ventricular–arterial coupling. Changes in the peripheral circulation also affect LV function, because a damaged ventricle is unable to adjust to the demands of peripheral circulation.

Clinically, evaluation of ventricular systolic function often forms the basis for clinical decisions, because it can be assessed by several widely available imaging

techniques with different contractility indices (Table 11.1). The relative ease of determining LV ejection fraction (EF) ensures its ubiquitous use for assessment of cardiac function in both clinical and experimental studies, despite the fact that it is highly dependent upon preload and afterload [20]. Furthermore, EF may lead to misinterpretation of the pathophysiology such as a high EF in severe mitral regurgitation [21] or a low EF with severe aortic stenosis [22]. Hence, much effort has been devoted to developing load-independent indices to measure contractility, the most accurate of which requires continuous acquisition of ventricular pressure and/or volume data during sudden preload change.

Table 11.1 Selected indices and measures of LV contractility

Functional parameters	Preload independence	Afterload independence	Clinical utility
LVEF, % [20]	No	No	Yes
dP/dt_{max}, mmHg/s [23]	No	No	Yes
E_{es}, mmHg/ml [24]	Yes	Yes	No
PAMP, watt/cm^2 [26]	Yes	Yes	No
$E_{a,max}$, mmHg/ml [25]	Yes	Yes	No
$d\sigma^*/dt_{max}$, s^{-1} [27, 15]	Yes	Yes	Yes
Strain, % [29]	No	No	Yes
Strain rate, s^{-1} [29]	No	No	Yes
T_{max}, (Pa) ([30], [31], Walker et al. 2008)	–	–	Yes

From continuous ventricular pressure and/or volume data these LV contractility indices can be determined. These indices include dP/dt_{max} [23], end-systolic (ES) elastances [24], maximal active elastance [25], and preload adjusted maximal power [26]. We have specifically developed the $d\sigma^*/dt_{max}$ index [27] and validated it as being relatively independent of loading conditions in the physiological range. In our studies, its noninvasive determination enhances its utility in the clinical setting like quantifying the effect of surgical ventricular restoration in patients with ischemic dilated cardiomyopathy (IDCM) [28]. In contrast to these global indices, measures of regional LV contractility, in terms of strain and strain-rate (SR) assessment, have recently become feasible in routine clinical echocardiography [29]. However, their acquisition and analysis still present a number of technical challenges and complexities which limits their widespread use. T_{max} is the maximum isometric tension achieved at the longest sarcomere length and maximum intracellular calcium concentration, and represents intrinsic regional myocardial contractility ([30], [31], [45]). MRI-based finite element method for estimating its value confers its potential clinical utility.

11.1.3 Changes in Left Ventricular Wall Stress After MI

Myocardial infarction produces elevated LV ED pressure (due to enhanced LV myocardial stiffness), as well as global and regional alterations in ventricular

geometry and material properties of the myocardium. The net effects of these alterations on the regional distribution of wall stress have not been defined. The effects of chronic MI on the regional diastolic wall stress have been studied in the rat LV using finite element models (FEM) [12]. Heterogeneity in wall stress was shown for infarcted hearts, with higher stresses at the apex and lower wall stresses at the base of all hearts.

LV wall stress has been studied by several biomechanical models [32]. Some approaches are limited by idealized geometric assumptions and are only valid for spherical or ellipsoidal shape (global wall stress). Other approaches are applicable to any arbitrary shape of the LV [33] but they introduce errors in the measurement of the thickness of the LV wall and radius of curvature [34]. The technical limitations of these methods do not permit precise regional measurements of three-dimensional (3D) wall curvature.

In summary, LV remodeling affects the biology of the cardiac myocyte, the LV geometry and architecture, and LV wall stress distribution, all of which affect LV contractile function (Table 11.2). A number of changes that occur during the process of LV remodeling may contribute to worsening of HF. Principal among these changes is the increase in LV wall stress that occurs during LV remodeling. Indeed, one of the first observations of the abnormal geometry of remodeled ventricle was that the remodeled heart was not only larger, but also more spherical in shape [35]. The increase in LV size and resultant change in LV geometry from the normal prolate ellipsoid shape to a more spherical shape creates a number of mechanical burdens for the failing heart, most notably an increase in LV ED wall stress.

Table 11.2 Left ventricular remodeling in shape, size, and mechanical disadvantage

Alterations in left ventricular chamber geometry	1. Wall thinning 2. Spherical shape
Biomechanical disadvantage created by LV remodeling	1. Increased wall stress 2. Increased oxygen utilization 3. Afterload mismatch 4. Worsening hemodynamic overloading 5. Diminished LV contractility 6. Worsening activation of compensatory mechanisms

Since the load on the ventricle at end-diastole contributes significantly to the afterload of the ventricle, it follows that LV dilation itself will increase the work of the ventricle and hence oxygen utilization. In addition to the increase in LV ED volume, LV wall thinning and the increase in afterload created by LV dilation lead to a functional afterload mismatch that may further contribute to a decrease in forward cardiac output [36]. Moreover, the high ED wall stress may lead to episodic hypoperfusion of the subendocardium with resultant worsening of LV function [37] and increased oxidative stress.

In the following sections, we will present (i) LV imaging and 3D reconstruction from magnetic resonance imaging (MRI), (ii) computational 3D surface shape

descriptor, (iii) computational 3D regional systolic wall stress and wall thickening, and (iv) comparison of curvedness and systolic wall stress between normal and patients with IDCM, based on our recent work [6].

11.2 LV Imaging and 3D Reconstruction

Figure 11.2 depicts the MR short- and long-axes planes or images, during ED and ES phases. For this purpose, the MRI data were processed using a semi-automatic technique provided in the CMRtools suite (Cardiovascular Solution, UK). Short- and long-axis images were displayed simultaneously such that segmentation in the two planes proceeded interactively to reduce registration errors. For each phase, every control point on the endomyocardium was constrained to lie on the intersection of the short- and long-axis views.

Additional long-axis planes (which are orthogonal to the short-axis planes) were constructed. These long-axis planes serve as the basis for fitting a series of B-spline curves which represent the contours of the endocardial surface. This allows the addition or manipulation of control points to obtain the desired boundary locations. In so doing, a radial set of long-axis contour planes (orthogonal to the short-axis images) is created which provides a more comprehensive set of contour points for defining the LV geometry.

The set of LV contour points derived from the segmentation process are then triangulated, using our in-house toolkit to produce the reconstructed 3D LV surface. The papillary muscles and trabeculae were not included in the chamber volume to obtain smooth endocardial contours suitable for shape analysis. The 3D reconstructions of a typical IDCM LV and normal LV during ED and ES phases are shown in Fig. 11.3.

From the reconstructed LV, we determined LV volume, mass, stroke volume, and EF. A sixth-order polynomial function was then used to curve-fit the volume–time data to determine the volume rate (dV/dt). The contractility index $d\sigma^*/dt_{max}$ was calculated using the formula $[1.5 \times (dV/dt_{max})/V_m]$, where V_m is myocardial volume at the ED phase, and σ^* is a pressure-normalized wall stress as previously reported [27]. Global LV shape was assessed by calculating the SI in diastole using the formula SI = AP/BA, where BA is measured in four-chamber view from the apex to the mid-point of the mitral valve and AP is measured as the axis that perpendicularly intersects the mid-point of the long axis. SI value of unity suggests a spherical LV.

11.3 Computation of 3D Surface Shape Descriptors

Herein, the intrinsic LV surface properties are computed via an analytical approach, using a surface patch fitting method. Similar surface fitting methods have been used by researchers to investigate the surface curvatures of anatomical structures of the human body and also to define anatomical landmarks for various applications [38, 39].

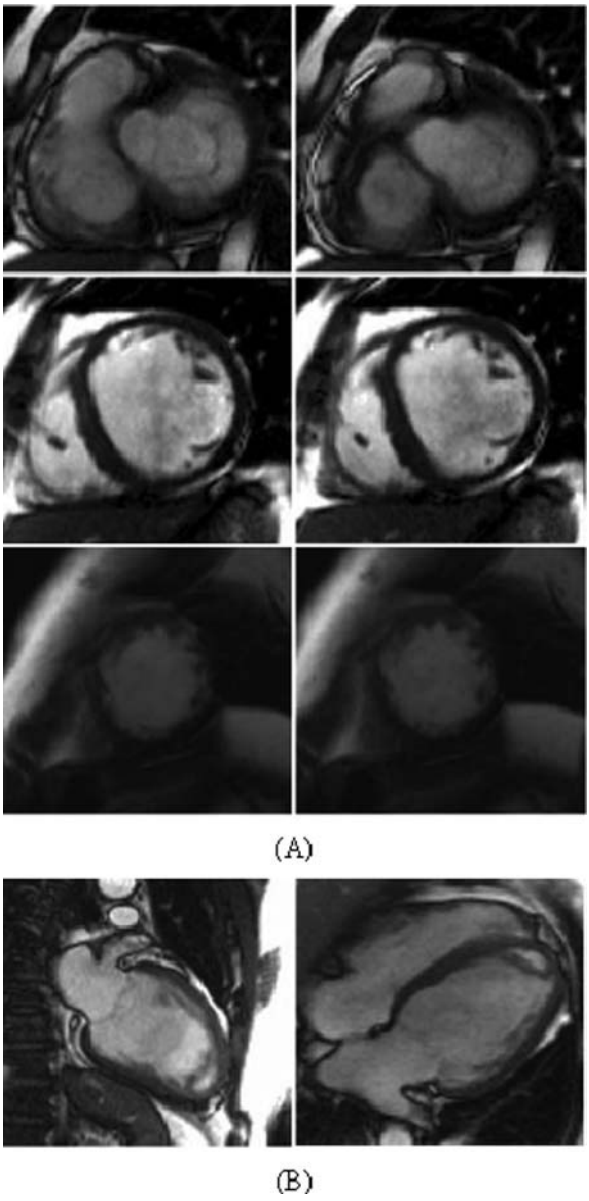

Fig. 11.2 Sample segmented trueFISP 2D cine MR images of (**a**) short-axis slices acquired at the base, middle, and apex (from top to bottom, respectively) and (**b**) long-axis of the left ventricle. The end-diastolic and end-systolic phases are depicted in the left and right columns, respectively

11.3.1 Local Surface Patch Fitting

In the vicinity of a point **x**, the surface can be approximated by an osculating paraboloid which may be represented by a quadratic polynomial with parameters d*u*

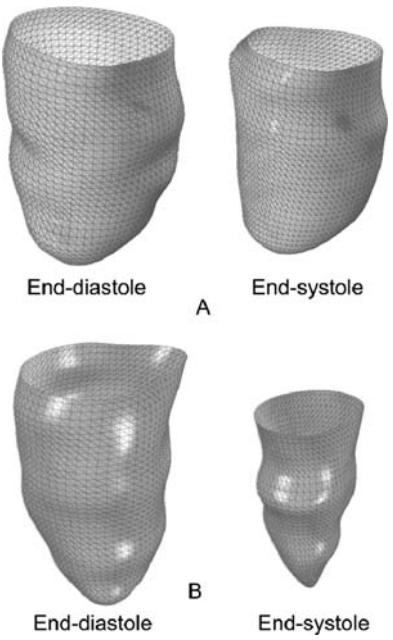

Fig. 11.3 Three-dimensional reconstruction of LV endocardial surface at end-diastole and end-systole for (**a**) IDCM and (**b**) normal

and dv. This polynomial is represented as a Taylor expansion at $\mathbf{x}$ of the paraboloid surface, by omitting the higher-order terms after the quadratic term

$$\mathbf{x}(u + \mathrm{d}u, v + \mathrm{d}v) = \mathbf{x}_{00} + \mathbf{x}_u \mathrm{d}u + \mathbf{x}_v \mathrm{d}v + (\mathbf{x}_{uu}\mathrm{d}u^2 + 2\mathbf{x}_{uv}\mathrm{d}u\mathrm{d}v + x_{vv}\mathrm{d}v^2)/2 \quad (11.1)$$

The coefficients $\mathbf{x}_{00}$, $\mathbf{x}_u$, $\mathbf{x}_v$, $\mathbf{x}_{uu}$, $\mathbf{x}_{uv}$, and $\mathbf{x}_{vv}$ are the zero, first, and second derivatives of $\mathbf{x}$ with respect to u and v at the surface point $\mathbf{x}_{00} = \mathbf{x}(u, v)$. With these six derivatives, the curvatures of the surface can be computed. A function given by $z = f(x, y)$, which is a second-order polynomial of the form

$$z = c_1 + c_2 p + c_3 q + c_4 p^2 + c_5 pq + c_6 q^2 \quad (11.2)$$

is used to fit the approximating surface patch. In Eq. (11.2), $p = x – x_\mathrm{o}$ and $q = y – y_\mathrm{o}$, where x_o and y_o are the x and y coordinates of the center point $\mathbf{x}_\mathrm{o}$ of the surface patch under consideration. The six coefficients of the paraboloid are then obtained by the least-squares solution of an over-determined system of linear equations

$$\begin{Bmatrix} z'_1 \\ z'_2 \\ z'_3 \\ \vdots \\ z'_n \end{Bmatrix} = \begin{bmatrix} 1 & p_1 & q_1 & p_1^2 & p_1 q_1 & q_1^2 \\ 1 & p_2 & q_2 & p_2^2 & p_2 q_2 & q_2^2 \\ 1 & p_3 & q_3 & p_3^2 & p_3 q_3 & q_3^2 \\ \vdots & \vdots & \vdots & \vdots & \vdots & \vdots \\ 1 & p_n & q_n & p_n^2 & p_n q_n & q_n^2 \end{bmatrix} \begin{Bmatrix} c_1 \\ c_2 \\ c_3 \\ c_4 \\ c_5 \\ c_6 \end{Bmatrix} \quad (11.3)$$

where n is the number of points in the neighborhood of a selected surface point, and the coefficients c_i are given by Eq. (11.2).

The coefficients c_1–c_6 are selected such that the differences of the fitted paraboloid and the data points are minimized, which is similar to minimizing the differences between z_n (measured value of z) and Z'_{n} (calculated value of z). The minimization problem is expressed in terms of an error function:

$$E(z) = \sum_{n=1}^{N} G_n(z'_n - z_n)^2 = \sum_{n=1}^{N} G_n(z(p_n, q_n) - z_n)^2, \tag{11.4}$$

where N represents the number of points within the fitted paraboloid, and G is a distance weighting function, such that

$$G_i = f \cdot (e^{(-(p_i^2+q_i^2)/d^2)}),\ i = 1,2,3,\ldots N, \tag{11.5}$$

where f and d are arbitrary constants which can be adjusted accordingly. The error function E will have a minimum when

$$\frac{\partial E}{\partial c_i} = 0,\ i = 1,2,3,4,5,6 \tag{11.6}$$

thus yielding six linear equations required to compute the six coefficients.

The first coefficient c_1 is actually the z value of the center point $\mathbf{x}_{\mathrm{o}}$ on the fitted surface patch. The other coefficients c_2–c_6 can be interpreted as the first and second derivatives of $\mathbf{x}$ with respect to p and q at $\mathbf{x}_{\mathrm{o}}$. With these coefficients, we can easily derive the principal curvatures κ_1 and κ_2, using the theory of differential geometry [40]. Figure 11.4 represents a sample principal curvature analysis on the endocardial

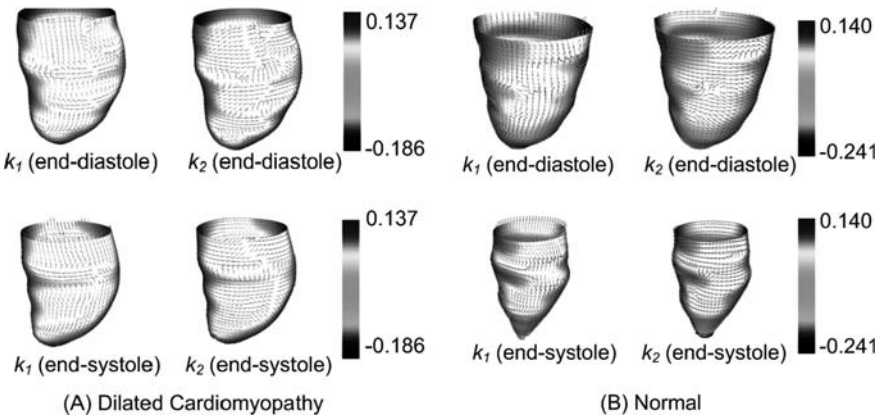

Fig. 11.4 The plots represent principal curvature analysis done on the endocardial wall of the left ventricle. The *arrowheads* represent directions of maximum principal curvature (*left panel*) and minimum principal curvature (*right panel*) of the endocardial surface of (**a**) IDCM and (**b**) normal subjects

wall of the left ventricle in IDCM and normal heart. The arrowheads represent the directions of the principal curvature on the surface of the endocardium.

The local shape descriptor, which is based on the curvedness C as presented by Koenderink and van Doom [41], can then be defined as

$$C = \sqrt{\frac{\kappa_1^2 + \kappa_2^2}{2}}. \tag{11.7}$$

The index C is a positive value, and describes the magnitude of the curvedness at a point, and thus is a measure of how curved a surface is.

11.3.2 Computation of LV Surface Curvatures

As shown in Fig. 11.5, the procedure for determining the LV surface curvatures (κ_1, κ_2, and C) from cardiac MR images can be described as follows:

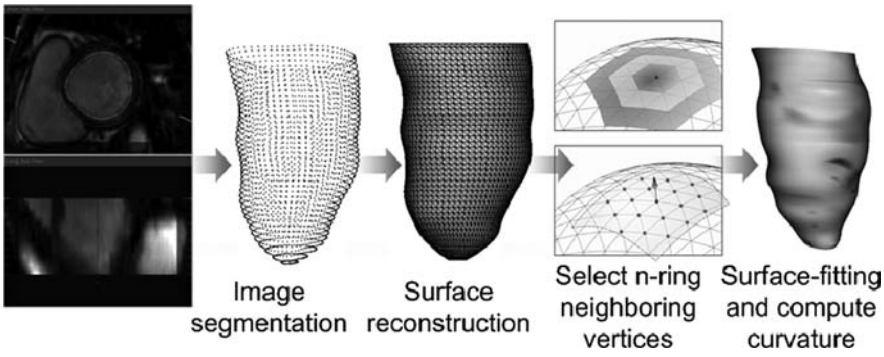

Fig. 11.5 Procedure for acquiring LV surface curvatures from cardiac MR images

1. Interactively segment the LV contours from the cardiac MR images.
2. Reconstruct the LV surface by triangulation of the LV contour points derived from the segmentation process.
3. For each vertex, select the n-ring neighboring vertices.
4. At each selected vertex, perform quadratic surface patch fitting and compute the surface curvature.

The choice of the n-ring neighboring points used for the patch fitting is arbitrary. However, as shown in the previous section, there are six unknowns c_1–c_6 in the quadratic function. Therefore, at least five neighboring points around the selected vertex are required for the local patch fitting, and a one-ring neighborhood may produce errors in regions with insufficient points. On the other hand, selecting a

region with too many points (e.g., a six-ring neighborhood) will cause an "over-smoothing" of the surface patch being considered. Therefore in this work, local surface fitting and curvature computation at each vertex is performed based on a set of five-ring neighboring points.

In order to perform regional analysis of the LV surface shape, the reconstructed LV surface is divided into 16 segments (Fig. 11.6), using the standardized myocardial segmentation and nomenclature described by Cerqueira et al. [42]. In particular, the LV endocardial surface is divided into three different segments (i.e., basal, mid, and apical). The point separating the basal anterior and anteroseptal region is identified from the original MR image, using the intersection of the right ventricular wall and the LV as a reference point. The basal and mid segments are then divided into six equal regions, and the apical segment is divided into four regions. The regional (or mean) curvedness C_{Rgn} for each segment is then defined (in terms of the curvedness C_i of the vertices of the segment) as

$$C_{\mathrm{Rgn}} = \frac{1}{N}\sum_{i}^{N} C_i,\ i = 1,2,3,\ldots N, \tag{11.8}$$

where N denotes the number of vertices within each region and C_i is given by Eq. (11.7).

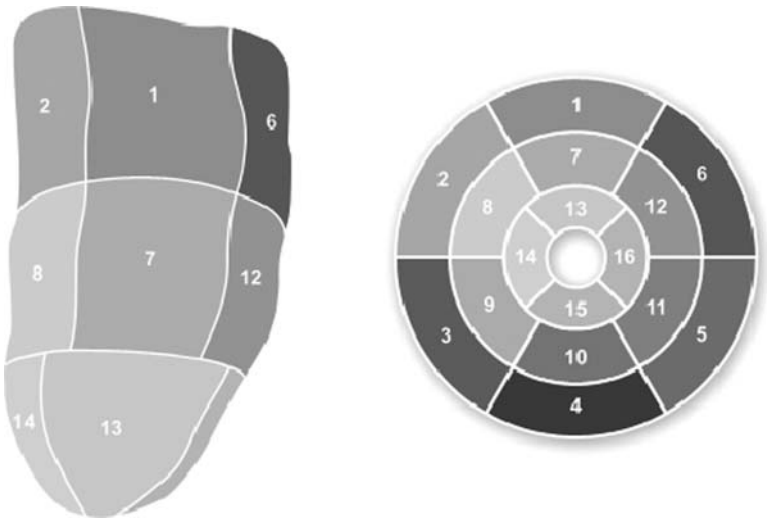

Fig. 11.6 Standardized myocardial segmentation and nomenclature for LV

We then define a normalized index to measure the extent of surface curvedness change at each LV region from ED phase to ES phase, denoted as the percent regional curvedness phase-change ΔC_{Rgn}, given by

$$\Delta C_{\mathrm{Rgn}} = \frac{C_{\mathrm{Rgn,ES}} - C_{\mathrm{Rgn,ED}}}{C_{\mathrm{Rgn,ES}}} \times 100\%, \tag{11.9}$$

where $C_{\mathrm{Rgn,ED}}$ and $C_{\mathrm{Rgn,ES}}$ are regional curvedness computed at ED and ES, respectively. A positive ΔC_{Rgn} indicates that a region becomes more curved from ED to ES, and a negative ΔC_{Rgn} indicates that a region becomes flatter during the systolic phase.

In addition to the evaluation of curvature measures on each point of the surface mesh, the LV radius (R) and wall thickness (T) are deduced from the 3D geometry of the LV. The main steps of the method are summarized in Zhong et al. [6].

11.4 Regional Peak Systolic Wall Stress and Wall Thickening

The wall stress is given by the equilibrium of forces between the LV cavity and the wall. Following Grossman et al. [43], the regional peak systolic wall stress (WS) is determined from the inner radius (R) and wall thickness (T) at end-systole by

$$\mathrm{WS} = 0.133 \times \mathrm{SP} \times \frac{R}{2T \times (1 + (T/2R))}, \tag{11.10}$$

where SP is the peak systolic ventricular blood pressure in millimeters of mercury (mmHg). In this study, SP was assessed by the systolic noninvasive blood pressure [44]. Here, WS was calculated using the radius and wall thickness values derived with our 3D curvature approach.

The wall thickening (WT) is expressed at each segment by means of the following formula:

$$\mathrm{WT} = \frac{\mathrm{EST} - \mathrm{EDT}}{\mathrm{EDT}}, \tag{11.11}$$

where EST and EDT are wall thickness at end-systole and end-diastole, respectively.

11.5 Comparison Between Ischemic Dilated Cardiomyopathy LV and Normal LV

11.5.1 Global LV Function Between IDCM LV and Normal LV

The hemodynamic and volumetric parameters of the subjects are summarized in Table 11.3. In IDCM patients, the cardiac contractility index $\mathrm{d}\sigma^*/\mathrm{d}t_{\max}$ and LV EF were significantly lower than that in the control normal subjects. In addition, the LV ED and ES volumes in IDCM patients were greater than those in control subjects. By visual inspection, the LV in IDCM patients has a broader apex than in normal subjects. The increase in dilated volume in the LV with IDCM was accompanied

Table 11.3 Characteristics of normal control and ischemic dilated cardiomyopathy (IDCM) patients

	Control (n=10)	IDCM (n=10)	p value
Age (years)	39 ± 17	52 ± 9	0.05
Weight (kg)	67 ± 15	71 ± 16	0.57
Height (cm)	169 ± 8	164 ± 8	0.18
Diastolic blood pressure (mmHg)	73 ± 12	70 ± 9	0.54
Systolic blood pressure (mmHg)	122 ± 17	113 ± 12	0.19
Heart rate (beats/min)	70 ± 9	81 ± 18	0.10
Cardiac Index (ml/m^2)	3.3 ± 0.4	2.3 ± 0.4	< 0.001
EDVI (ml/m^2)	73 ± 10	144 ± 27	< 0.001
ESVI (ml/m^2)	26 ± 6	114 ± 32	< 0.001
Ejection fraction (%)	65 ± 5	22 ± 9	< 0.001
Sphericity index, SI	0.52 ± 0.06	0.62 ± 0.08	< 0.05
$d\sigma^*/dt_{max}$ (s^{-1})	5.7 ± 1.3	2.4 ± 0.9	< 0.001

EDVI, end-diastolic volume index; ESVI, end-systolic volume index; $d\sigma^*/dt_{max}$, cardiac contractility index ($=1.5\times(dV/dt_{max})/V_m$), where dV/dt_{max} is maximum volume rate, and V_m is the myocardial volume.

by a corresponding increase in sphericity. Consequently, the LVs with IDCM were significantly more spherical than those in control subjects.

11.5.2 Variation of Curvedness, Peak Systolic Wall Stress, and Wall Thickening from Base to Apex in Normal LV

In general, normal hearts demonstrate the following regional differences: curvedness is highest at the apex, while among the four circumferential zones, the inferior regions have bigger curvedness than the lateral region, especially at ED. In IDCM, the curvedness is highest at the apex, while there is no significant difference among the six circumferential zones. Similar to normal subjects, a gradient from the base to apex was seen (ANOVA, P<0.001) [6].

Wall thickness and radius of the LV cavity were measured in the short-axis plane, long-axis plane (perpendicular to the short-axis) and 3D surface. The wall stress (WS) calculated with these data are shown in Fig. 11.7a (2DSWS), 11.7b (2DLWS), and 11.7c (3DWS). Peak systolic wall stress in endocardium in the short-axis plane (Fig. 11.7a) and long-axis plane (Fig. 11.7b) revealed a significant difference from base to apex (ANOVA, P<0.0001). A short-axis and long-axis analysis showed a 48% ± 17% and 51% ± 14% increase of the circumferential mean of the peak systolic wall stress between basal and apical sections, respectively. When wall thickness and radius of the cavity were calculated in the 3D space, the variation of the wall stress (3DWS) from the

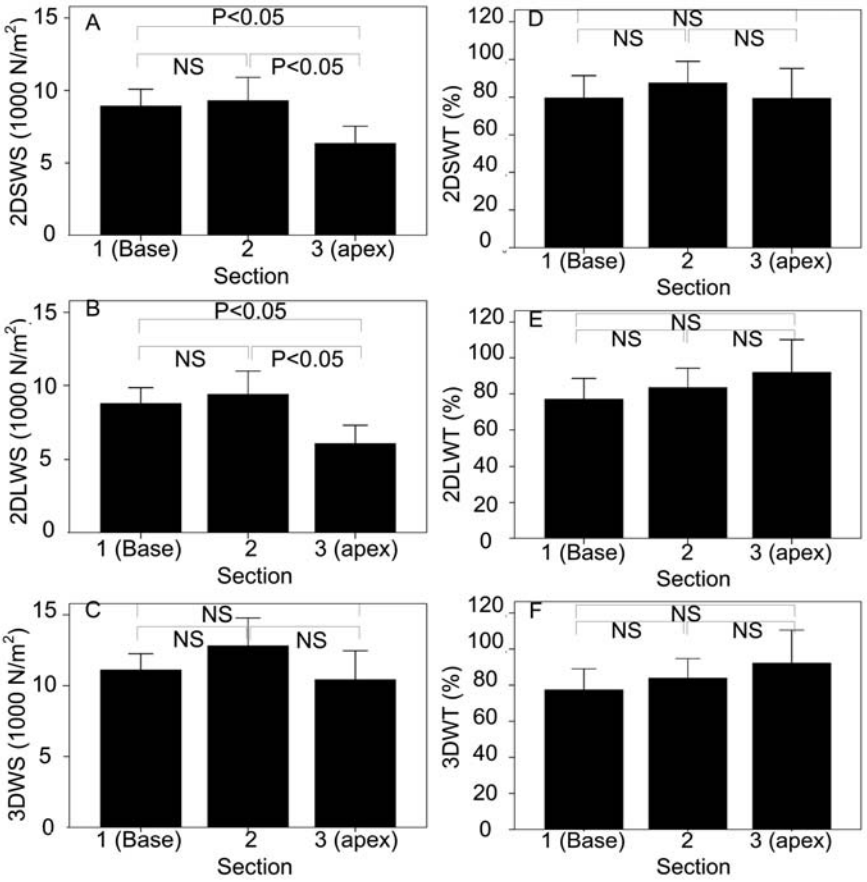

Fig. 11.7 Left ventricular systolic wall stress and wall thickening from base to apex in normal subjects. Estimation of wall stress (**a**) 2DSWS in short-axis direction, (**b**) 2DLWS in long-axis direction, and (**c**) 3DWS by taking 3D wall curvature. Estimation of wall thickening (**d**) 2DSWT in short-axis direction, (**e**) 2dLWT in long-axis direction, (**f**) 3DWT by taking 3D wall curvature. The values are means ± SD. *P*, two-tailed significance of paired differences. N.S., not significant

base to apex was no longer observed (Fig. 11.7c). The differences between 2DSWS and 3DWS, 2DLWS and 3DWS were reduced more at the basal level. The 3DWS values tend to be highest at the anterior and the lowest at the inferior.

The LV wall thickening (WT) values determined in the short-axis plane, long-axis plane, and 3D surface are shown in Fig. 11.7d (2DSWT), 11.7e (2DLWT), and 11.7f (3DWT). There was no significant difference from the base to apex in the wall thickening. The comparison between 3DWT and a 2D assessment of wall thickening (i.e., 2DSWT and 2DLWT) did not reveal significant differences at the basal and mid-zone, anterior, septal, and lateral regions.

11.5.3 Comparison of Curvedness, Peak Systolic Wall Stress, and Wall Thickening in Ischemic Cardiomyopathy LV and Normal LV

Significant differences in ED curvedness, C_{ED}, were noted in all regions, except in base and anterior. Also, significant differences in ES curvedness, C_{ES}, were noted in all regions between normal and IDCM groups [6].

In patients with IDCM, peak systolic 3DWS was significantly increased compared with normal values (Fig. 11.8a). There is a gradient of mean wall stress from the base to apex with 3DWS. It was also observed that 3DWS was highest at the apex in IDCM, and 3DWT was significantly decreased in all regions compared with normal LV values (Fig. 11.8b). In addition, 3DWT is minimal at the inferior segments

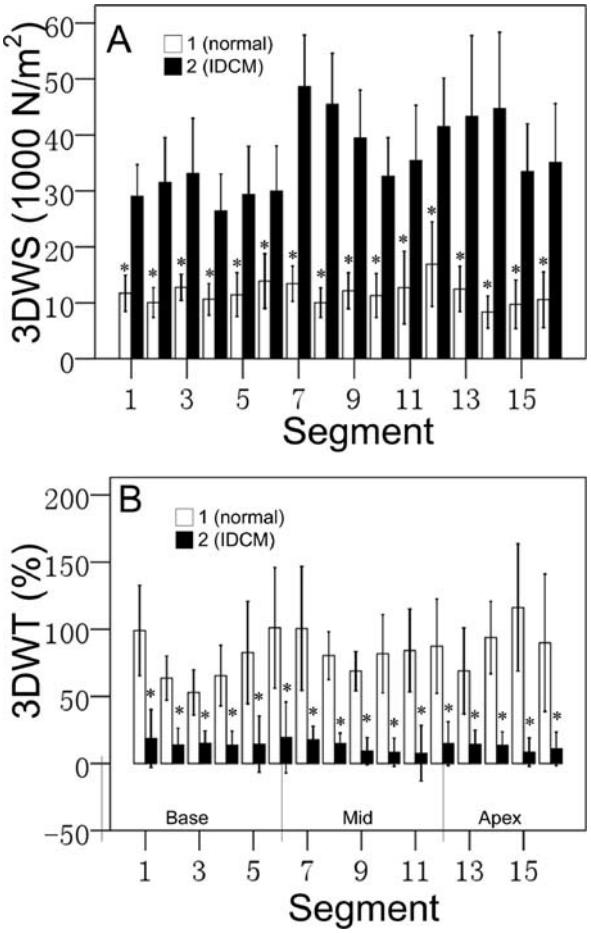

Fig. 11.8 Variation of peak systolic wall stress, 3DWS, of the left ventricle in normal subjects and in patients with ischemic dilated cardiomyopathy (IDCM). (**a**) 3DWS assessment from 3D curvature; (**b**) 3DWT assessment from 3D curvature. Values are depicted as mean ± SD. *Significant difference between ischemic dilated cardiomyopathy vs. normal subjects

and maximal at the anterior segments. There is also significant variation among the four circumferential regions (ANOVA, $P<0.001$) and from base to apex (ANOVA, $P<0.001$).

11.6 Summary

There is no doubt that LV remodeling and its role in HF progression are multimechanistic and complex. A key issue is the characterization of cardiac remodeling generated from clinical imaging must be accurately characterized functionally to ensure that patients receive optimal therapy. The challenge is to develop even more specific measures of LV remodeling that can be incorporated into the clinical management pathway. This will help to improve the choice of suitable treatment and prognosis.

A framework has been developed for the analysis of LV regional curvature, wall stress, and wall thickening as applied to normal subjects and patients with IDCM. The methodology relies on MR anatomical data and local surface fitting techniques to interrogate LV geometry at ED and ES. The 3D approach proposed in this work is found to be better than the 2D approaches for precise evaluation of the regional wall stress. In patients with IDCM, a decrease of ES curvedness and an increase of peak systolic wall stress, and decrease of global contractile functional index are observed compared with normal subjects. This decrease in wall surface curvature, corresponding increase in regional peak systolic wall stress, and associated decrease in global LV contractility index ($d\sigma^*/dt_{max}$) can constitute important functional prognostic indices of LV remodeling.

Acknowledgments This research was supported in part by National Heart Centre Research Grant and the National Institute of Health – National Heart, Lung, and Blood Institute Grant HL84529 and 2R01HL055554-11.

References

1. Cohn JN, Ferrari R, Sharpe N. Cardiac remodeling – concepts and clinical implications: a consensus paper from an international forum on cardiac remodeling. Behalf of an International Forum on Cardiac Remodeling. *J Am Coll Cardiol.* 2000;35:569–382.
2. Maron BJ. Distinguishing hypertrophic cardiomyopathy from athlete's heart: a clinical problem of increasing magnitude and significance. *Heart* 2005;91(11):1380–82.
3. Pfeffer JM, Pfeffer MA, Fletcher PJ, Braunwald E. Progressive ventricular remodeling rat with myocardialinfarction. *Am J Physiol Heart Circ*. 1991;260:H1406–14.
4. Ganau A, Devereux RB, Roman MJ. Patterns of left ventricular hypertrophy and geometric remodeling in essential hypertension. *J Am Coll Cardiol.* 1992;19(7):1559–60.
5. Cohen MV, Yang XM, Neumann T. Favorable remodeling enhances recovery of regional myocardial function in the weeks after infarction in ischemically preconditioned hearts. *Circulation.* 2000;102:579–83.
6. Zhong L, Su Y, Yeo SY, Tan RS, Ghista DN, Kassab GS. Left ventricular regional wall curvedness and wall stress in patients with ischemic dilated cardiomyopathy. *Am J Physiol Heart Circ Physiol.* 2009b;296(3):H573–84.

7. Greenberg B, Quinones MA, Koilpillai C, Limacher M, Shindler D, Benedict C, Shelton B. Effects of long-term enalapril therapy on cardiac structure and function in patients with left ventricular dysfunction. *Circulation.* 1995;91:2573–81.
8. The Digitalis Investigation Group. The effects of digoxin on morality and morbidity in patients with heart failure. *N Engl J Med.* 1997;336:525–33.
9. Rubin SA, Fishbein MC, Swan HJC. Compensatory hypertrophy in the heart after myocardial infarction in the rat. *J Am Coll Cardiol*. 1983;61:1435–41.
10. Gaballa MA, Goldman S. Ventricular remodeling in heart failure. *J Card Fail*. 2002;8: S476–85.
11. Mitchell GF, Lamas GA, Vaughan DE, Pfeffer MA. Left ventricular remodeling in the year after first anterior myocardial infarction: a quantitative analysis of contractile segment lengths and ventricular shape. *J Am Coll Cardiol*. 1992;19:1136–44.
12. Kono T, Sabbah HN, Steain PD, Brymer JF, Khaja F. Left ventricular shape as a determinant of mitral regurgitation in patients with several heart failures secondary to either coronary artery disease or idiopathic dilated cardiomyopathy. *Am J Cardiol.* 1991;68:355–9.
13. Kass DA, Trail TA, Keating M, Altieri PI. Abnormalities of dynamic ventricular shape change in patients with aortic and mitral valvular regurgitation: assessment by Fourier shape analysis and global geometric indexes. *Circ Res*. 1988;62:127–38.
14. Manici GB, DeBoe SF, Anselmo E, Simon SB. Quantitative regional curvature analysis: an application of shape determination of the assessment of segmental left ventricular function in man. *Am Heart J*. 1987;113:326–34.
15. Yeo SY, Zhong L, Su Y, Tan RS, Ghista DN. A curvature-based approach for left ventricular shape analysis from cardiac magnetic resonance imaging. *Med Biol Eng Comput*. 2009;47(3):313–22.
16. Radhakrishnan S, Ghista DN, Jayaraman G. Mechanical analysis of the development of left ventricular aneurysms. *J Biomech*. 1980;13:1031–9.
17. Litwin SE, Litwin CM, Raya TE, Warner A, Goldman S. Contractility and stiffness of non-infarcted myocardium following coronary ligation in rats: effects of chronic angiotensin converting enzyme inhibition. *Circulation.* 1991;83:1028–37.
18. Hirota Y, Shimizu G, Kaku K, Saito T, Kino M, Kawamura K. Mechanisms of compensation and decompensation in dilated cardiomyopathy. *Am J Cardiol.* 1984;54:1033–38.
19. Bing OH, Brooks WW, Conrad CH, Weinstein KB, Spadaro J, Padvany P. Myocardial mechanics of infarcted and hypertrophied non-infarcted myocardium following experimental coronary artery occlusion. In: *International Erwin Riesch Symposium*, 1983, pp. 235–44.
20. Borrow KM, Neumann A, Marcus RH. Effects of simultaneous alterations in preload and afterload on measurements of left ventricular contractility in patients with dilated cardiomyopathy: comparisons of ejection phase, isovolumetric and end-systolic force–velocity indexes. *J Am Coll Cardiol*. 1992;20:787–95.
21. Zile MR, Gaasch WH, Carroll JD. Chronic mitral regurgitation: predictive value of preoperative echocardiographic indexes of left ventricular function and wall stress. *J Am Coll Cardiol.* 1984;3:235–42.
22. Gunther S, Grossman W. Determinants of ventricular function in pressure-overload hypertrophy in man. *Circulation*. 1979;59:679–88.
23. Broughton A., Korner PI. Steady-state effects of preload and afterload on isovolumic indices of contractility in autonomically blocked dogs. *Cardiovasc Res.* 1980;14:245–53.
24. Suga H, Sagawa K, Shoukas AA. Load independence of the instantaneous pressure–volume ratio of the canine left ventricular and effects of epinephrine and heart rate on the ratio. *Circ Res*. 1973;32:314–22.
25. Zhong L, Ghista DN, Ng EY, Lim ST. Passive and active ventricular elastances of the left ventricle. *Biomed Eng Online.* 2005;4(1):14.
26. Kass DA, Beyer R. Evaluation of contractile state by maximal ventricular power divided by the square of end-diastolic volume. *Circulation*. 1991;84:1698–708.

27. Zhong L, Tan RS, Ghista DN, Ng EY, Chua LP, Kassab GS. Validation of a novel noninvasive cardiac index of left ventricular contractility in patients. *Am J Physiol Heart Circ Physiol*. 2007;292(6):H2764–72.
28. Zhong L, Sola S, Tan RS, Ghista DN, Kurra V, Navia JL, Kassab GS. Effects of surgical ventricular restoration on left ventricular contractility assessed by a novel contractility index in patients with ischemic cardiomyopathy. *Am J Cardiol*. 2009a;103:674–79.
29. Voigt JU, Lindenmeier G, Werner D, Flachskampf FA, Nixdorff U, Hatle L, Sutherland GR, Daniel WG. Strain rate imaging for the assessment of preload-dependent changes in regional left ventricular diastolic longitudinal function. *J Am Soc Echocardiogr*. 2002;15(1): 13–19.
30. Walker JC, Ratcliffe MB, Zhang P, Wallace AW, Fata B, Hsu EW, Saloner D, Guccione JM. Magnetic resonance imaging-based finite element stress analysis after linear repair of left ventricular aneurysm. *J Thorac Cardiovasc Surg*. 2005a;135:1094–102.
31. Walker JC, Ratcliffe MB, Zhang P, Wallace AW, Fata B, Hsu EW, Saloner D, Guccione JM. MRI-based finite-element analysis of left ventricular aneurysm. *Am J Physiol Heart Circ Physiol*. 2005b;289:H692–700.
32. Yin FC. Ventricular wall stress. *Circ Res*. 1981;49:829–42.
33. Jana R. Estimation of local myocardial stress. *Am J Physiol Heart Circ Physiol*. 1982;242:H875–81.
34. Beyar R, Shapiro E, Graves W, Guier W, Carey G, Soulen R, Zerhouni E, Weisfeldt M, Weiss J. Quantification and validation of left ventricular wall thickening by a three-dimensional element magnetic resonance imaging approach. *Circulation*. 1990;81:297–307.
35. Linzbach AJ. Heart failure from the point of view of quantitative anatomy. *Am J Cardiol*. 1960;5:370–82.
36. Pouleur H, Rousseau MF, van Eyll C, Meilin J, Youngblood M, Yusuf S. Cardiac mechanics during development of heart failure. SOLVD Investigators. *Circulation.* 1993;87:V14–20.
37. Shannon RP, Komamura K, Shen YT, Bishop SP, Vatner SF. Impaired regional subendocardial coronary flow reserve in conscious dogs with pacing-induced heart failure. *Am J Physiol Heart Circ Physiol*. 1993;265:H801–09.
38. Drerup B, Hierholzer E. Objective determination of anatomical landmarks on the body surface: measurement of the vertebra prominens from surface curvature. *J Biomech*. 1985;18:467–74.
39. Liu X, Kim W, Drerup B, Mahadev A. Tibial torsion measurement by surface curvature. *Clin Biomech*. 2005;20:443–50.
40. Willmore TJ. An introduction to differential geometry. Oxford University Press, Delhi, 1985.
41. Koenderink JJ, van Doom AJ. Surface shape and curvature scales. *Image Vis Comput.* 1992;10:557–65.
42. Cerqueira MD, Weissman NJ, Dilsizian V, Jacobs AK, Kaul S, Laskey WK, Pennell DJ, Rumberger JA, Ryan T, Verani MS. Standardized myocardial segmentation and nomenclature for tomographic imaging of the heart: a statement for healthcare professional from the Cardiac Imaging Committee of the Council on Clinical Cardiology of the American Heart Association. *Circulation.* 2002;105:539–42.
43. Grossman W, Braunwald E, Mann T, McLaurin L, Green L. Contractile state of the left ventricle in man as evaluated from end-systolic pressure–volume relations. *Circulation*. 1977;56:845–52.
44. Reichek N, Wilson J, St. John Sutton M, Plappert, TA, Goldberg S, Hirshfeld JW. Noninvasive determination of left ventricular end-systolic stress: validation of the method and initial application. *Circulation.* 1982;65:99–108.
45. Walker JC, Ratcliffe MB, Zhang P, Wallace AW, Hsu EW, Saloner DA, Guccione JM. Magnetic resonance imaging-based finite element stress analysis after linear repair of left ventricular aneurysm. *J Thorac Cardiovasc Surg*. 2008;35:1094–1102.

Chapter 12
Surgical Left Ventricular Remodeling Procedures

Jonathan F. Wenk, Choon-Sik Jhun, Kay Sun, Mark B. Ratcliffe, and Julius M. Guccione

Abstract Perhaps the most straightforward clinical application of validated regional ventricular mechanics models for diseased hearts is the simulation of a novel surgical procedure or medical device for treating heart failure or ischemic cardiomyopathy. In each study our cardiac biomechanics laboratory uses one of two different approaches: (1) an axisymmetric truncated ellipsoidal model with left ventricular (LV) cavity and wall volumes typical of the failing human heart or animal model of heart failure to determine efficacy of the surgical procedure or device; or (2) an animal- or patient-specific fully 3-D model of the infarcted LV created using echocardiography or MRI to optimize the design of the surgical procedure or device. This chapter is concerned with brief descriptions of the studies from our laboratory that provide the best examples of these two approaches.

12.1 Introduction

Probably without ever knowing it, Dr. Randas Batista, MD, has forever changed the field of cardiac mechanics or at least its application to cardiac surgery. While his novel (if not radical) surgical procedure for treating heart failure probably will never be performed again in the United States, the Batista procedure or ventricular volume reduction surgery (VVRS) appears to have been the primary catalyst for a number of "startup" companies concerned with developing novel devices for treating heart failure. In other words, Dr. Batista's failed attempt to treat heart failure by surgically remodeling the LV must have inspired the inventions of, for example, the Myocor™ Myosplint®, the Acorn Cardiovascular CorCap™ Cardiac Support Device or CSD, and the Paracor Medical HeartNet™ Ventricular Support System or VSS.

J.M. Guccione (✉)
Department of Surgery, University of California at San Francisco and San Francisco VA Medical Center, San Francisco, CA, USA
e-mail: guccionej@surgery.ucsf.edu

J.M. Guccione, et al. (eds.), *Computational Cardiovascular Mechanics*,
DOI 10.1007/978-1-4419-0730-1_12,

12.2 Residual Stress Produced by Ventricular Volume Reduction Surgery Has Little Effect on Ventricular Function and Mechanics

VVRS is a surgical therapy that includes the resection of a viable slice of the lateral left ventricular (LV) wall in patients with dilated cardiomyopathy (DCM) and end-stage congestive heart failure. The primary objective of this therapy is to reduce the size of the LV to restore a more optimal physiologic volume/mass relationship. It has been suggested that VVRS can reconstitute the residual stress–strain state of the LV. To determine the extent to which residual stress is involved, we used a three-dimensional (3-D) finite element model to simulate the effect of VVRS under two different conditions: (1) when the unloaded postoperative configuration is stress free and (2) when the unloaded postoperative configuration is subjected to residual stress. This was done to examine the effects on LV stroke volume (SV)/end-diastolic pressure (Starling) relationships as well as on regional distributions of stress in the local muscle fiber direction (fiber stress) [1].

A finite element model of the dilated poorly contractile LV was developed (Fig. 12.1a). Finite element meshes were created with 3-D solid elements (eight nodes, trilinear nodal displacement interpolation in prolate spheroidal coordinates, and constant hydrostatic pressure within each element). Converged solutions were obtained when the mesh was refined into only 5 elements transmurally and 14 elements longitudinally. The unloaded dilated LV shape is a thick-walled axisymmetric truncated ellipsoid with the same cavity and wall volume as those used in the study of Ratcliffe et al. [2]. Longitudinal displacement of all nodes at the apex and base, and circumferential displacement of the epicardial nodes at the base, were constrained. The model was loaded with a range of physiologic intraventricular pressures with the use of the 3-D method of Costa et al. [3]. The mathematical descriptions for diastolic and systolic myocardial material properties (nonlinear stress–strain relations), which are assumed to be homogeneous and anisotropic

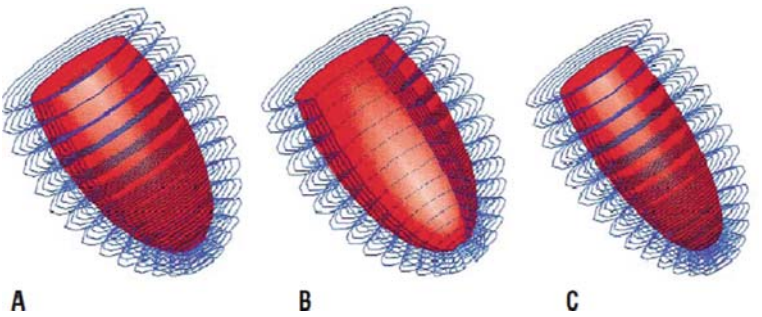

Fig. 12.1 (**a**) Globally dilated, poorly contractile LV model in unpressurized state. LV wall is represented as a wire frame, and endocardial surface (smooth interior) has been rendered. (**b**) Same finite element model as in (**a**) but with 20% of LV wall removed. (**c**) Unpressurized state of model after 20% VVRS. (From Guccione et al. [1, 19], with permission from Elsevier.)

[4], are given in Chapter 3. The muscle fiber orientation throughout the LV was assumed to vary (linearly) in the transmural direction from 60° clockwise from the circumferential direction at the endocardium to 60° counterclockwise from the circumferential direction at the epicardium on the basis of experimental measurements made by Streeter et al. [5] in canine hearts, owing to the absence of these data from patients with DCM.

The effects of VVRS were simulated with the use of the globally dilated heart model. Ten percent and 20% of LV mass was removed from the initial unloaded configuration as slices or wedges subtending angles of 36° and 72°, respectively (Fig. 12.1b). Then new unloaded configurations were obtained by closing up the openings (Fig. 12.1c). Specifically, circumferential displacements of the nodes on the resected surfaces were prescribed, longitudinal displacements of the nodes at the apex and base were constrained, and pressures on the endocardial and epicardial surfaces were set to zero. In one set of simulations, the new unloaded configurations were considered to be stress free. In another set, residual stresses in the new unloaded configurations were taken into account by treating the initial unloaded configurations with the wedges missing as the stress-free reference configurations.

The calculations of the diastolic and systolic pressure–volume relationships as well as the Starling relationship are outlined in Guccione et al. [1]. For each simulation (DCM, and 10% and 20% VVRS with and without residual stress), stress in the local muscle fiber direction was computed throughout the LV wall at end-diastole and end-systole of the initial pressure–volume loop (end-diastolic pressure = 20 mmHg; end-systolic pressure = 100 mmHg). To obtain overall end-diastolic and end-systolic fiber stresses, we calculated the mean values from the centers of the 70 finite elements (where the hydrostatic pressure component of stress is most accurate). It should be noted that these values do not correspond to those calculated by a global force balance (the law of Laplace), which does not take into account the transmural variation in muscle fiber orientation (or myocardial material properties).

The effect of VVRS on the SV/end-diastolic pressure (Starling) relationship is shown in Fig. 12.2. Ten percent and 20% VVRS shift the pre-resection Starling relationship progressively downward. When residual stress is implemented in the model simulation of VVRS, the additional decrease in SV at fixed LV end-diastolic pressure is small (10% VVRS: 2.0% at 1 mmHg and 2.0% at 20 mmHg; 20% VVRS: 2.2% at 1 mmHg and 3.1% at 20 mmHg). It should be noted that SV decreases and ejection fraction increases with VVRS. As in the study of Ratcliffe et al. [2], SV was reduced in all cases because the decrease in diastolic compliance was not sufficiently compensated by the improvements in end-systolic elastance. Again, these results suggest that residual stress produced by VVRS has little effect on LV function.

The effect of VVRS on end-diastolic and end-systolic transmural distributions of fiber stress from a midventricular location of the model is shown in Fig. 12.3. First, notice that VVRS decreases fiber stress progressively at all transmural locations. Second, notice that the residual stress produced by VVRS had very little effect on fiber stress in this case, except perhaps at the epicardium (where it caused a decrease in end-diastolic fiber stress and an increase in end-systolic fiber stress). The effects

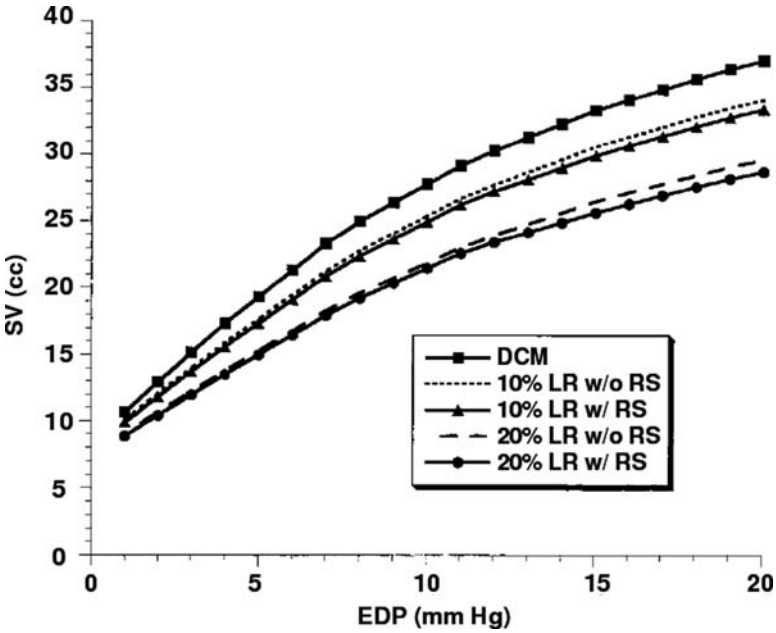

Fig. 12.2 The effect of VVRS on the stroke volume/end-diastolic pressure (Starling law) relationship. Ten percent lateral VVRS without residual stress *(short dashes)*, 10% lateral VVRS with residual stress *(triangles)*, 20% lateral VVRS without residual stress *(long dashes)*, and 20% lateral VVRS with residual stress *(circles)* progressively decrease stroke volume at the same end-diastolic pressure. Note that VVRS has a much greater effect on the LV Starling relationship than does residual stress. *LR*, Lateral VVRS; *RS*, residual stress; *SV*, stroke volume. (From Guccione et al. [1, 19], with permission from Elsevier.)

of the residual stress produced by VVRS on fiber stress at different locations were either so small or variable that the effect on mean fiber stress was negligible.

It is interesting and perhaps surprising that both the finite element model of Ratcliffe et al. [2] and the one used in the present study simulated end-diastolic pressure–volume relationships that shifted more to the left (to lower LV volumes) than the end-systolic pressure–volume relations, especially because the myocardial material properties of these models were quite different (i.e., isotropic vs. anisotropic). Moreover, this was still the case when we repeated our simulations of VVRS with a more ellipsoidal unloaded DCM model. Because the net effect of VVRS was a depression of ventricular function (as measured by the Starling relationship) regardless of the choice of myocardial material properties and baseline ventricular geometry, this suggests that there is something fundamentally wrong with this surgical therapy from a global cardiac mechanics point of view. On the other hand, surgical therapies that both reduce ventricular fiber stress and maintain or increase SV are ideal.

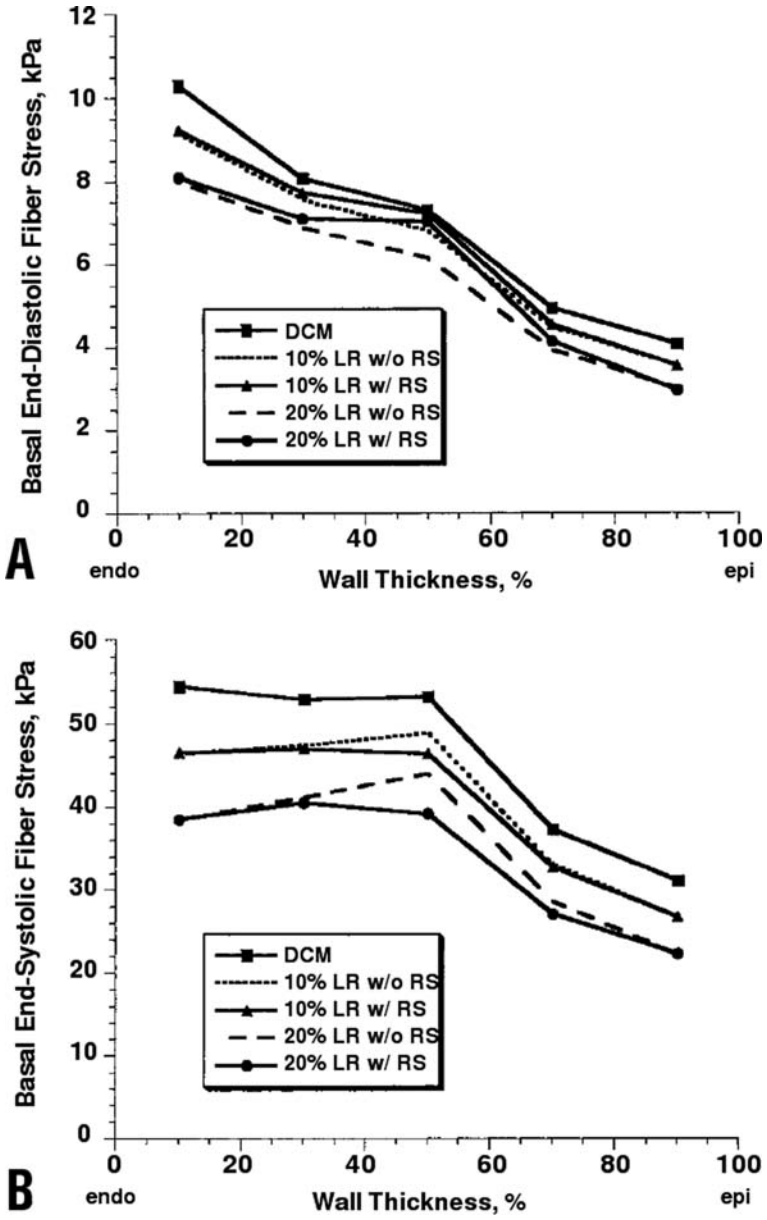

Fig. 12.3 The effect of VVRS on transmural distributions of end-diastolic (**a**) and end-systolic (**b**) fiber stress through a midventricular region. Note that VVRS has a much greater effect on these stresses than residual stress. The primary effect of residual stress in this region is to decrease end-diastolic fiber stress near the epicardium but increase end-systolic fiber stress at the same location. *LR*, Lateral VVRS; *RS*, residual stress; *endo*, endocardium; *epi*, epicardium. (From Guccione et al. [1, 19], with permission from Elsevier.)

12.3 Effect of Ventricular Size and Patch Stiffness in Surgical Anterior Ventricular Restoration

Surgical anterior ventricular restoration (SAVER) has been proposed for dilated ischemic cardiomyopathy with an akinetic distal anterior LV wall [6, 7]. Briefly, the SAVER procedure uses a Fontan purse-string suture and a pericardium patch to reconstruct the LV by reducing the circumference of the aneurysm "neck." After the infarct is incised, the residual akinetic myocardium is closed over the patch in two layers, as shown in the Introduction. Of note, surgical tools designed for use in the SAVER operation including endoventricular mannequins and pre-formed pericardial patches with attached sewing ring are now commercially available [8, 9].

We used our FE model of the LV with an akinetic but contractile anterior LV wall [10] to simulate the SAVER operation. Separate versions of the model with normal and dilated LV sizes were developed and used to simulate the SAVER operation with and without patch of varying stiffness. We hypothesized that SAVER increases SV, reduces mean myofiber stress, and that optimal results are achieved without a patch. The pre SAVER finite element model is shown in Fig. 4.5 of Chapter 4. Details about the boundary conditions, material properties, and mesh generation, which is based on hand-traced ecocardiographs of the epicardial and endocardial surfaces, are given in Dang et al. [11].

Thirty-two cardiac contour points were used to construct a 2-D mesh of the LV in prolate spheroidal coordinates. Using a focal length of 25.0 mm, the FE software Continuity (Cardiac Mechanics Research Group, University of California, San Diego, CA) interpolated a 3-D model composed of 16 elements. The FE mesh was subdivided into eight elements circumferentially and three elements transmurally producing the end-diastolic LV model. This subdivision allowed regional, non-axisymmetric variation of the ventricular wall. To evaluate SAVER on a markedly dilated LV representative of clinical candidates, the focal length of the model was scaled and wall thickness reduced, resulting in a 75% increase in chamber volume at early diastole. Diastolic and systolic material responses are described in Chapter 3. A sharp boundary was assumed between the infarcted and noninfarcted regions. The noninfarcted region was assigned normal diastolic stiffness and systolic material. Reduction of the infarct ability to develop active stress was accomplished by scaling T_{max} by a "percentage of contracting myocytes."

The SAVER operation was simulated by causing a constant volume deformation of the normal myocardium. Specifically, a FE model with infarct elements removed underwent an isochoric (constant volume) deformation by application of an inward force to border zone (BZ) nodes. Partial excision (40% of akinetic area) of the infarct was simulated by manually inputting nodes representing the wall thickness and shape of the infarct. In patch simulations, patches averaging 2-mm thickness lined the chamber wall from the edges of the BZ. In the absence of material property data for surgical materials, diastolic stiffness of 10.0 kPa was considered standard. Owing to software limitations, a stiff patch was simulated as 50.0 kPa in the dilated model and as 100.0 kPa in the normal-sized model. Two-dimensional early diastolic (a), and 3-D end-diastolic (b) and end-systolic (c) FE meshes after SAVER are

shown in Fig. 12.4. The wireframes represent the ventricular wall. In panels b and c, the endocardium is represented by the interior grid.

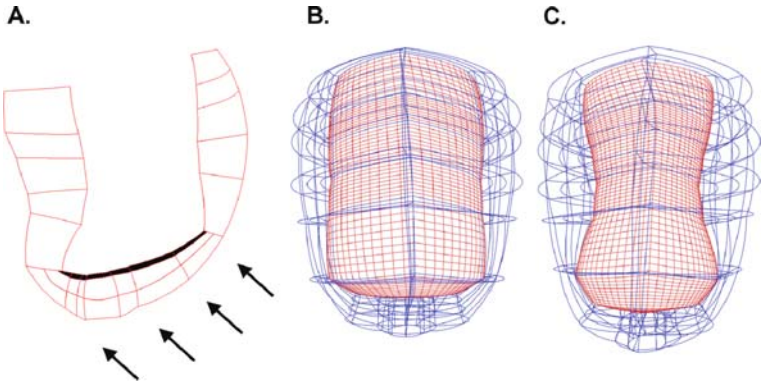

Fig. 12.4 Postoperative 2-D mesh (**a**) and 3-D meshes at end-diastole (**b**) and end-systole (**c**). *Arrows* indicate infracted elements, the *dark region* indicates a patch

Figure 12.5 shows the effect of SAVER on the SV/end-diastolic pressure (Starling) relationship. The SAVER operation shifts the Starling relationship downward and rightward. It should be noted that SAVER was more beneficial in

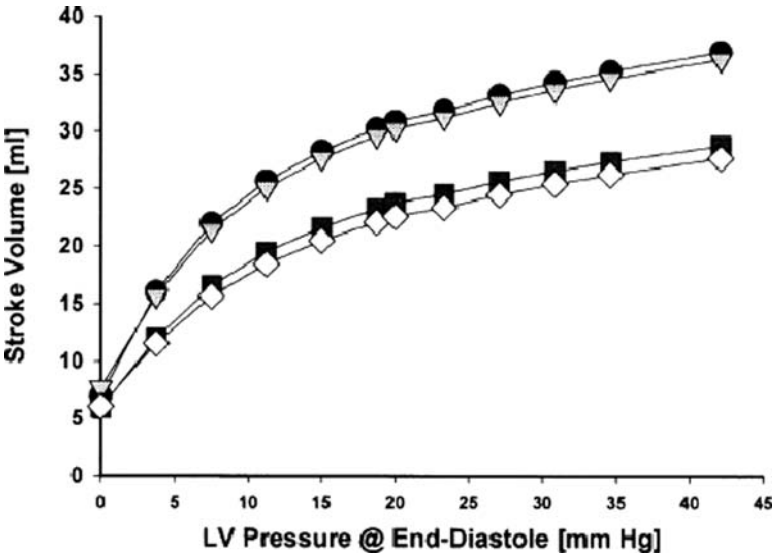

Fig. 12.5 Stroke volume/end-diastolic pressure (Starling law) relationship before and after a simulated surgical anterior ventricle restoration (SAVER) operation on a dilated LV. Circles = preoperative simulation; triangles = SAVER without patch; squares = SAVER with compliant patch; diamonds = SAVER with stiff patch. (From Dang et al. [11], with permission from Elsevier.)

dilated ventricles. The SV reduction after patchless SAVER in the dilated ventricle was minimal. Increasing patch stiffness, *C*, progressively increases the shift. As described by Guccione et al. [1], SV consistently diminished because the decreased diastolic compliance was not sufficiently compensated by the improved end-systolic elastance.

The effect of SAVER on end-diastolic (a) and end-systolic (b) longitudinal distributions of myofiber stress is shown in Fig. 12.6. Preoperative end-diastolic myofiber stress is mildly increased in the BZ but more than doubled in the infarct itself. Preoperative end-systolic myofiber stress is substantially increased in the BZ. The SAVER operation reduces end-diastolic and end-systolic BZ and infarct myofiber stress. This result may prevent further damage and improve contractility over time. Increasing patch stiffness progressively reduces myofiber stress.

In conclusion, the SAVER operation reduces myofiber stress in the akinetic infarct at the expense of a reduction in the Starling relationship. The reduction in SV after SAVER without patch in the dilated ventricle was minimal. Effects of patch stiffness were mixed. A patch made of stiffer material should cause a greater reduction in stress but also has the greatest negative effect on SV. These simulations support the use of SAVER in the dilated heart without a patch.

12.4 MRI-Based Finite Element Stress Analysis of Linear Repair of Left Ventricular Aneurysm

Surgical ventricular remodeling or restoration has been proposed as a way to reduce LV volume and improve long-term mortality after anteroapical myocardial infarction (MI). Linear repair was initially popular; however, results were mixed, and more recently patch aneurysmorrhaphy has been in favor. On the other hand, results are difficult to interpret because objectively evaluating the effect of the repair itself is complicated by concomitant procedures such as valve repair and coronary revascularization. By using the methodology proposed in previous studies [12], the present study used FE analysis to compute mid-wall stress in sheep hearts that have undergone aneurysm plication. Material properties were determined that allowed the FE models to reproduce end-systolic 3-D strain measurements made with tagged MRI. FE models included myocyte fiber angle measurements made for the first time after this procedure [13]. The present study was undertaken to test the hypothesis that end-systolic stress is reduced in all areas of the LV after infarct plication [14].

The infarct procedure performed on the sheep has been described in detail [15]. After development of a ventricular aneurysm, aneurysm plication was performed without cardiopulmonary bypass (13.4 $\pm$ 2.3 weeks post-MI). A partial lower sternotomy was performed under general anesthesia, and pericardial adhesions were divided. The transition between infarcted and noninfarcted myocardium was palpated, and the LV aneurysm was plicated between two strips of Dacron felt. Polypropylene sutures (2-0 Prolene, MH needle, Ethicon Inc, Sommerville, NJ) were passed through the felt, through and through the aneurysm at its border, and

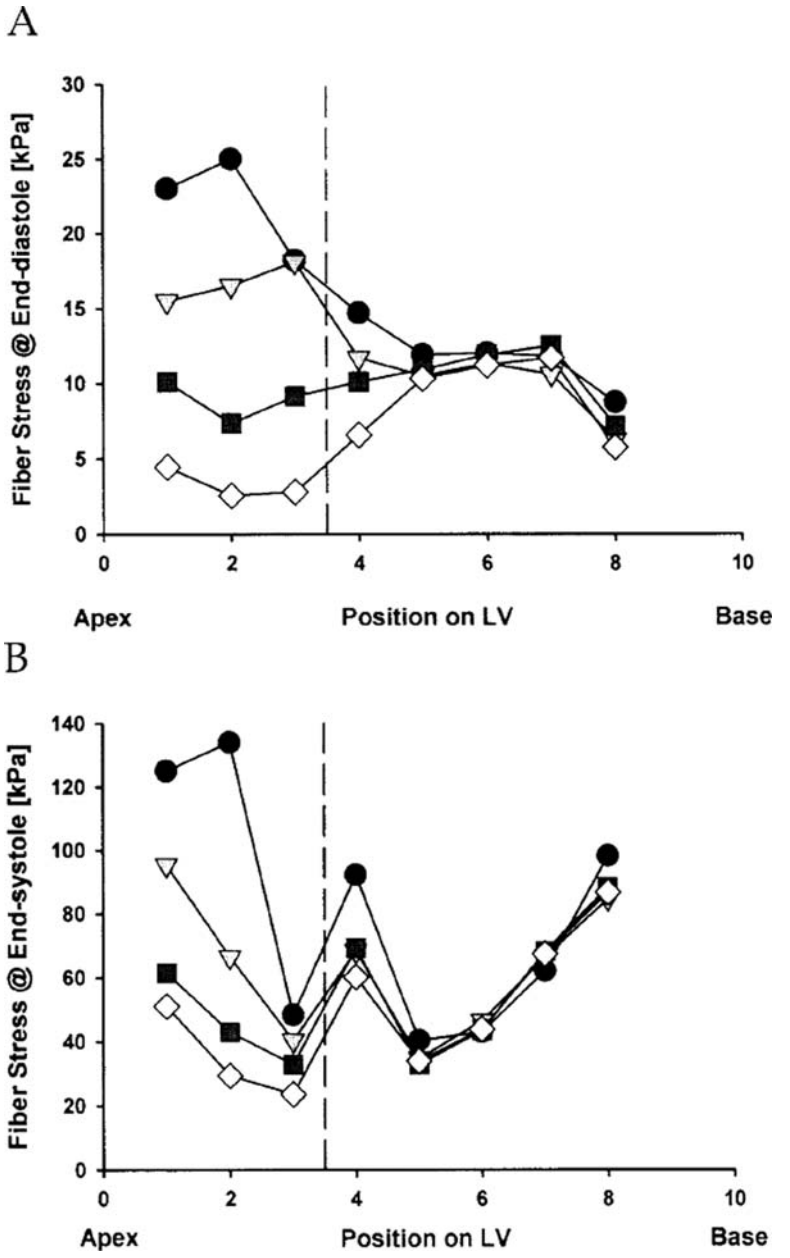

Fig. 12.6 Regional myofiber stress at end-diastole and end-systole for (**a, b**) a dilated LV. Connecting lines only associate simulation groups; particularly in the border zone, linear interpolation is inappropriate. *Dashed line* = infarct versus noninfarct; *solid circles* = preoperative; *open triangles* = SAVER without patch; *solid squares* = SAVER with compliant patch; *diamonds* = SAVER with stiff patch. (From Dang et al. [11], with permission from Elsevier.)

through the opposite strip of felt in a horizontal mattress fashion. The sternotomy was closed, and the sheep recovered from anesthesia. Six weeks after the plication procedure (20.0 ± 2.9 weeks post-MI, 6.6 ± 0.5 weeks post-plication), systolic strains were measured with tagged MRI [16]. Systolic myocardial strains were calculated from tag-line deformation [17] in cardiac coordinates (i.e., circumferential, longitudinal, and radial) at the mid-wall in 12 equally spaced "sectors" around the circumference in each short-axis slice.

Helix angle measurements made using diffusion tensor magnetic resonance imaging (DTMRI) in the same hearts [13] were incorporated into the FE model by aligning geometry from the two data sets and sampling the nearest points from the DTMRI data set [12]. The FE analysis followed the same methodology as described in [12]. The material laws used in the model have been described in Chapter 3. In the septal aneurysm, material parameters determined from biaxial stretching experiments were used [18]. In the BZ, $T_{\max}$ was reduced by 50% in accordance with results from Guccione et al. [19] and Walker et al. [12]. Because of a lack of experimental data of aneurysm tissue under shear loading, b_{fs} was kept constant across all regions. In accordance with biaxial stretching experiments of Lin and Yin [20] and results from our previous study [12], an in-plane, cross-fiber stress was added equal to 40% of that along the muscle fiber direction. By following an iterative approach described previously [12], transversely isotropic material parameters were systematically varied and $T_{\max}$ scaled to reproduce measured ventricular volumes and myocardial strains.

Compared with our previous study on sham-operated animals [12], models of linear repair reproduced tagged MRI measurements equally well (overall RMS error: plication = 0.060 ± 0.009, sham = 0.054 ± 0.011, P =.37; Fig. 12.7). Passive material properties for two of the animals were closer to those determined previously by Okamoto et al. [21] (C = 0.512 kPa, bf = 67.1, bt = 24.2, bfs = 21.6). Values for

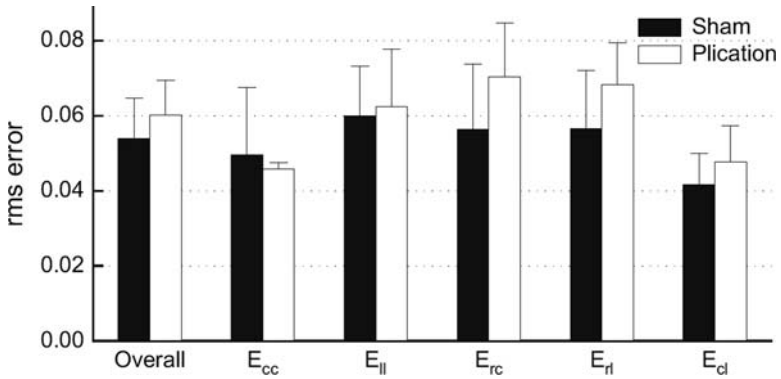

Fig. 12.7 Root mean square error of model predictions relative to strain measurements made with tagged MRI. Root mean square error in the plication models was the same as rms error in the aneurysm models, indicating both FE models reproduced strain measurements with the same certainty. rms, Root mean square. (From Walker et al. [12, 13], with permission from Elsevier.)

four of the animals converged closer to those from Omens et al. [22] ($C = 1.1$ kPa, bf = 9.2, bt = 2, bfs = 3.7).

In general, mid-wall fiber stress after a linear repair was lower than in sham-operated animals (Fig. 12.8). In the retained infarct, fiber stress decreased by 52% (sham = 36.6 ± 5.7 kPa, plication = 17.5 ± 5.3 kPa, $P = .003$). In the BZ, overall fiber stress decreased by 39% (sham = 32.5 ± 2.5 kPa, plication = 19.7 ± 3.6 kPa, $P = .001$); moreover, fiber stress in this region decreased to the level of remote regions after plication. In the septum, however, BZ fiber stress remained high (sham = 31.3 ± 5.4 kPa, plication = 23.8 ± 5.8 kPa, $P = .29$).

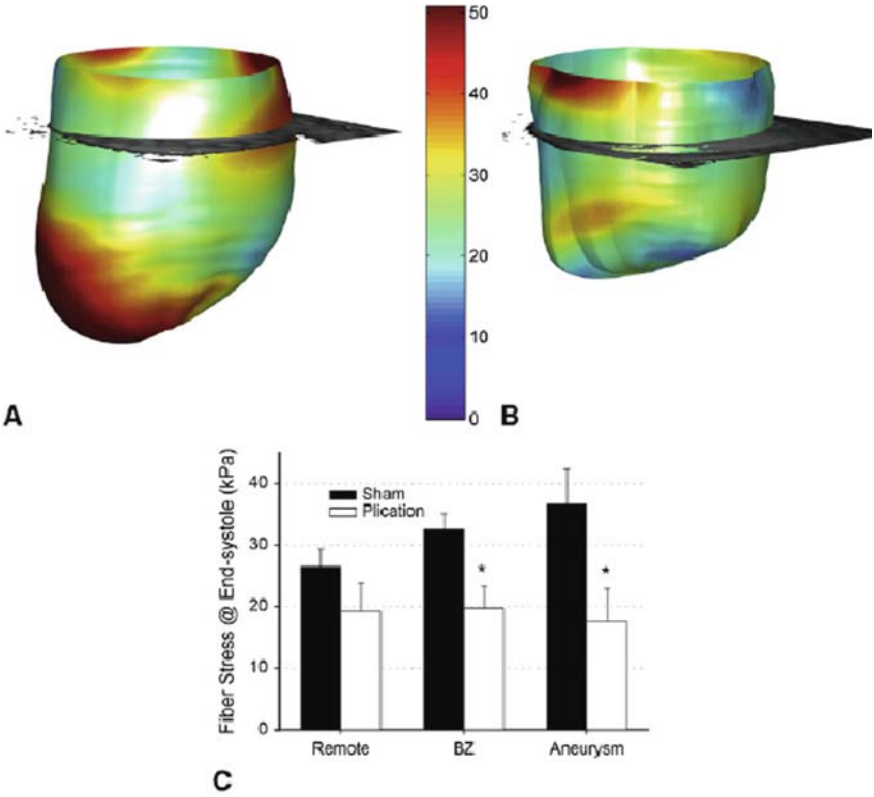

Fig. 12.8 End-systolic midwall fiber stress in a representative aneurysmal heart (**a**) and post-plication heart (**b**), septal-posterior view. Averaged across all models (**c**), fiber stress decreased in the border zone and infarct but did not significantly decrease in remote regions. After plication, border zone stress was at the same level as remote regions. $^*P < 0.05$ plication versus sham. BZ, Border zone (From Walker et al. [12, 13], with permission from Elsevier)

Cross-fiber stress decreased after plication in BZ and infarct regions (Fig. 12.9). Cross-fiber stress decreased by 47% in the retained infarct (sham = 38.7 ± 5.0 kPa, plication = 20.6 ± 7.1 kPa, $P < .01$) and decreased 41% overall in the BZ (sham = 13.0 ± 1.5 kPa, plication = 7.7 ± 2.1 kPa, $P = .01$). However, in the septal

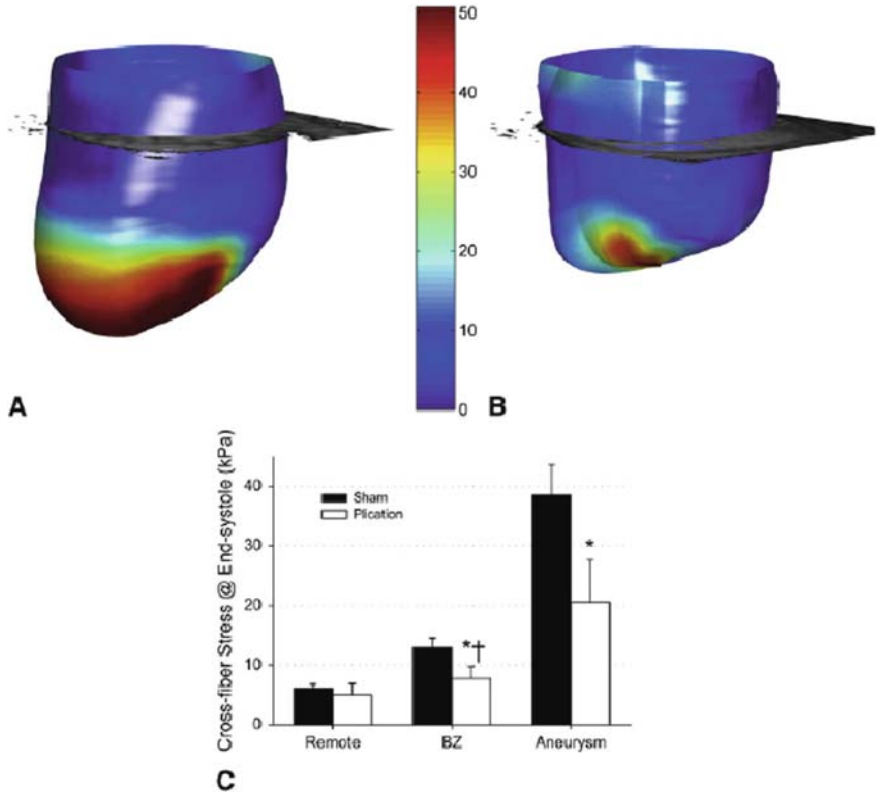

Fig. 12.9 End-systolic midwall cross-fiber stress in a representative aneurismal heart (**a**) and post-plication heart (**b**), septal-posterior view. Cross-fiber stress concentration exists in the infarct of the aneurysmal heart (**a**) and remains in the nonexcluded septal infarct after plication (**b**). Averaged across all models (**c**), cross-fiber stress decreased in the border zone and infarct but not in remote regions. After plication, border zone cross-fiber stress was still significantly elevated above remote regions. $^{*}P < 0.05$ plication versus sham. $\dagger P < 0.05$ plication remote versus border zone. BZ, Border zone. (From Walker et al. [12, 13], with permission from Elsevier.)

BZ the cross-fiber stress was still 75% higher than in remote regions after plication (remote $= 5.9 \pm 1.9$ kPa, BZ $= 10.3 \pm 3.6$ kPa, $P < .01$).

Although there have been several FE studies of MI [19], to our knowledge none have been performed on LV aneurysm plication. Because of the simplifying assumptions made to develop the closed form equation used in other studies [23, 24] and the regional validation to tagged MRI presented in the current study, we expect that our stress calculations are more accurate. FE analysis demonstrates that aneurysm plication decreases fiber stress without depressing SV. On the basis of these results, aneurysm plication should be an effective therapeutic strategy relative to no treatment. However, a high cross-fiber stress remains in the BZ of the retained septal infarct. Surgical remodeling procedures that exclude the septum may decrease stress

in this region and warrant future studies. Future work will also include comparison of our method with analytic and competing FE methods.

Acknowledgments This research was supported by National Institutes of Health grants 5R01 HL077921 and HL086400 (Dr. Guccione) and 5R01 HL063348 (Dr. Ratcliffe).

References

1. Guccione JM, Moonly SM, Wallace AW, Ratcliffe MB. Residual stress produced by ventricular volume reduction surgery has little effect on ventricular function and mechanics: a finite element model study. *J Thorac Cardiovasc Surg*. 2001 Sep;122(3):592–9.
2. Ratcliffe MB, Hong J, Salahieh A, Ruch S, Wallace AW. The effect of ventricular volume reduction surgery in the dilated, poorly contractile left ventricle: a simple finite element analysis. *J Thorac Cardiovasc Surg*. 1998;116:566–77.
3. Costa KD, Hunter PJ, Wayne JS, Waldman LK, Guccione JM, McCulloch AD. A three-dimensional finite element method for large elastic deformations of ventricular myocardium. II. Prolate spheroidal coordinates. *J Biomech Eng.* 1996;118:464–72.
4. Guccione JM, Costa KD, McCulloch AD. Finite element stress analysis of left ventricular mechanics in the beating dog heart. *J. Biomech*.1995;28:1167–77.
5. Streeter DD Jr, Spotnitz HM, Patel DP, Ross J Jr, Sonnenblick EH. Fiber orientation in the canine left ventricle during diastole and systole. *Circ Res*. 1969;24:339–47.
6. Di Donato, M. et al., Akinetic versus dyskinetic postinfarction scar: relation to surgical outcome in patients undergoing endoventricular circular patch plasty repair. *J Am Coll Cardiol.* 1997;29:1569–75.
7. Athanasuleas CL, et al., Surgical anterior ventricular endocardial restoration (SAVER) in the dilated remodeled ventricle after anterior myocardial infarction. RESTORE group. Reconstructive endoventricular surgery, returning torsion original radius elliptical shape to the LV. *J Am Coll Cardiol.* 2001;37(5):1199–209.
8. *The TR^{3}ISVR^{TM} Surgical Ventricular Restoration System*. 2003. Available from: http://www.chasemedical.com/prod_trisvr.htm.
9. *The CorRestore System*. 2003. Available from: http://www.somanetics.com/correstore_system.htm.
10. Dang A, Guccione J, Gorman R, Ratcliffe M. Influence of patch material stiffness on stroke volume with surgical anterior ventricular endocardial restoration in ischemic cardiomyopathy: a finite element model study. Chicago: American College of Cardiology, 2003.
11. Dang AB, Guccione JM, Zhang P, Wallace AW, Gorman RC, Gorman JH 3rd;Ratcliffe MB. Effect of ventricular size and patch stiffness in surgical anterior ventricular restoration: a finite element model study. *Ann Thorac Surg*. 2005 Jan;79(1):185–93.
12. Walker JC, Ratcliffe MB, Zhang P, Wallace AW, Fata B, Hsu EW, Saloner D, Guccione JM. MRI-based finite-element analysis of left ventricular aneurysm. *Am J Physiol Heart Circ Physiol*. 2005 Aug;289(2):H692–700.
13. Walker JC, Guccione JM, Jiang Y, Zhang P, Wallace AW, Hsu EW, Ratcliffe MB. Helical myofiber orientation after myocardial infarction and left ventricular surgical restoration in sheep. *J Thorac Cardiovasc Surg.* 2005;129:382–90.
14. Walker JC, Ratcliffe MB, Zhang P, Wallace AW, Hsu EW, Saloner DA, Guccione JM. Magnetic resonance imaging-based finite element stress analysis after linear repair of left ventricular aneurysm. *J Thorac Cardiovasc Surg*. 2008 May;135(5):1094–102, 1102.e1-2.
15. Markovitz LJ, Savage EB, Ratcliffe MB, Bavaria JE, Kreiner G, Iozzo RV, Hargrove WC 3rd;Bogen DK, Edmunds LH Jr. Large animal model of left ventricular aneurysm. *Ann Thorac Surg*. 1989;48(6):838–45.
16. Guccione JM, Walker JC, Beitler JR, Moonly SM, Zhang P, Guttman MA;, et al. The effect of anteroapical aneurysm plication on end-systolic three-dimensional strain in the sheep: a magnetic resonance imaging tagging study. *J Thorac Cardiovasc Surg*. 2006;131:579–86. e3.

17. Ozturk C, McVeigh ER. Four-dimensional B-spline based motion analysis of tagged MR images: introduction and in vivo validation. *Phys Med Biol*. 2000;45(6):1683–702.
18. Moonly SM. Experimental and computational analysis of left ventricular aneurysm mechanics (PhD thesis). San Francisco, CA: University of California, San Francisco with University of California, Berkeley, 2003.
19. Guccione JM, Moonly SM, Moustakidis P, Costa KD, Moulton MJ, Ratcliffe MB, Pasque MK. Mechanism underlying mechanical dysfunction in the border zone of left ventricular aneurysm: a finite element model study. *Ann Thorac Surg*. 2001 Feb;71(2):654–62.
20. Lin DH, Yin FC. A multiaxial constitutive law for mammalian left ventricular myocardium in steady-state barium contracture or tetanus. *J Biomech Eng*. 1998;120:504–17.
21. Okamoto RJ, Moulton MJ, Peterson SJ, Li D, Pasque MK, Guccione JM. Epicardial suction: a new approach to mechanical testing of the passive ventricular wall. *J Biomech Eng*. 2000 Oct;122(5):479–87.
22. Omens JH, May KD, McCulloch AD. Transmural distribution of three-dimensional strain in the isolated arrested canine left ventricle. *Am J Physiol*. 1991;261(3 Pt 2): H918–28.
23. Taniguchi K, Sakurai M, Takahashi T, Imagawa H, Mitsuno M, Nakano S, et al. Postinfarction left-ventricular aneurysm: regional stress, function, and remodeling after aneurysmectomy. *J Thorac Cardiovasc Surg*. 1998;46:253–9.
24. Savage EB, Downing SW, Ratcliffe MB, Fallert M, Gupta KB, Tyson GS, et al. Repair of left ventricular aneurysm. Changes in ventricular mechanics, hemodynamics, and oxygen consumption. *J Thorac Cardiovasc Surg*. 1992;104:752–62.

Chapter 13
Passive Left Ventricular Constraint Devices

Choon-Sik Jhun, Namrata Gundiah, Kay Sun, Hani N. Sabbah, E. Elaine Tseng, Mark B. Ratcliffe, and Julius M. Guccione

Abstract Both myocardial infarction and volume overloading associated with regurgitant valve lesions lead to eccentric left ventricular (LV) hypertrophy. The mechanism is presumed to be positive feedback between diastolic LV wall stress and eccentric LV hypertrophy. Further, in each case, an increase in LV size is an important adverse prognostic finding. The experience with skeletal muscle cardiomyoplasty led to the hypothesis that passive constraint of LV enlargement would interrupt the diastolic stress and eccentric hypertrophy cycle, in addition to halting and possibly reversing the adverse LV remodeling. A number of passive constraint devices such as the Acorn CorCap^{TM} Cardiac Support Device (CSD), Paracor Medical HeartNet^{TM} Ventricular Support System (VSS), and Myocor^{TM} Myosplint® have been used. Most recently, an Adjustable Fluid Filled Balloon CSD was proposed by Ghanta and colleagues. In this chapter we model the effect of passive constraint devices, with the exception of the Paracor Medical HeartNet^{TM} VSS, on the LV stroke volume/end-diastolic pressure (Starling) relationship and regional distributions of stress in the local muscle fiber direction.

13.1 Introduction

An increase in left ventricular (LV) size after myocardial infarction (MI) [1–4] is the most important adverse prognostic finding. For instance, relatively small changes (25 cc) in end-systolic volume (ESV) after MI are associated with exponential increases in mortality [4]. An increase in LV size in patients with non-ischemic cardiomyopathy is also associated with increased mortality [5]. The underlying mechanism is assumed to be positive feedback between diastolic LV wall stress and

J.M. Guccione (✉)
Department of Surgery, University of California at San Francisco and San Francisco VA Medical Center, San Francisco, CA, USA
e-mail: guccionej@surgery.ucsf.edu

J.M. Guccione, et al. (eds.), *Computational Cardiovascular Mechanics*,
DOI 10.1007/978-1-4419-0730-1_13,

eccentric LV hypertrophy [6]. Several studies of cardiomyoplasty [7–9] have suggested that passive diastolic constraint can improve the mechanical and functional performance of the LV by preventing its further dilation.

The Acorn CorCap™ Cardiac Support Device (CSD) (Acorn Cardiovascular, Inc., St. Paul, MN) is an ellipsoidal "sock" of loosely woven PET-polyester fabric that, when placed over the left and right ventricles, prevents LV distention (Fig. 13.1a). The underlying hypothesis is that the CSD and other passive constraint devices will reduce the strain and stress associated with progressive ventricular dilation and, therefore, halt progressive cardiac remodeling, improve cardiac function, and encourage reverse ventricular remodeling. Because of concern that the CSD would produce ventricular constriction, the CSD is loosely sized to the epicardial, end-diastolic size of the combined left and right ventricles. The Acorn device has been shown to reduce the end-diastolic volume (EDV) [10,11], shear strain [11], and infarct area [12] when applied early after MI. Histological investigation also showed reduced myocyte hypertrophy and attenuation of interstitial fibrosis [13]. A randomized clinical trial of 300 patients with heart failure, with and without mitral regurgitation, is now complete. The composite endpoint favored the Acorn device (p=0.024) although there was no difference in mortality [14]. In addition, patients treated with the Acorn device had lower EDV and ESV over 3 years of follow-up [15].

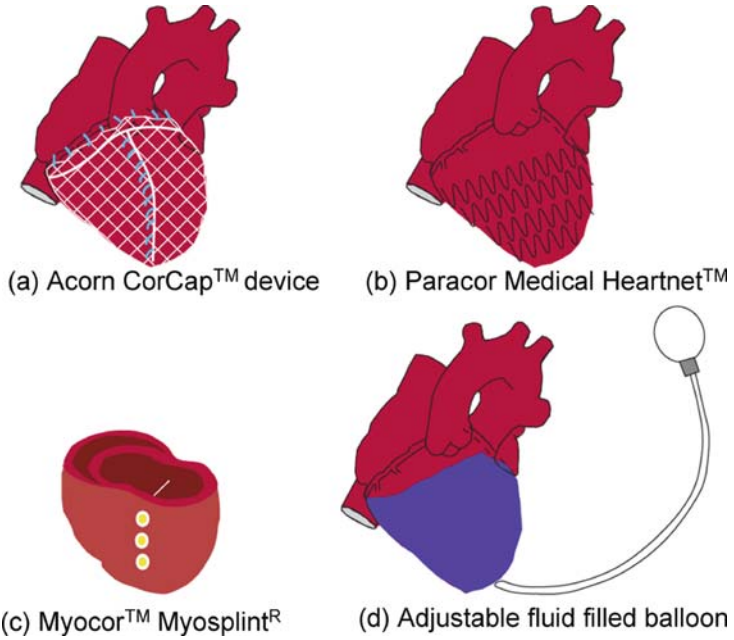

Fig. 13.1 (**a**) Cartoon showing the Acorn Cardiac Support Device (Jacket) placed around the left and right ventricles. (**b**) The Paracor Medical Heartnet™ Ventricular Support System. (**c**) A section through the ventricles with the three Myocor™ Myosplint® rods in the LV. (**d**) Adjustable fluid-filled balloon

The Paracor Medical HeartNet™ Ventricular Support System (VSS) is a passive constraint device made of silicone-coated nitinol wire (Fig. 13.1b). In addition to its "shape memory" properties, nitinol can undergo large strain at relatively constant stress (super-elastic) [16]. As a consequence, the compliance of the Paracor device is flat over a large range of volume. Presumably, this allows the Paracor device to apply epicardial pressure at end-diastole and at end-systole, and to continue to apply pressure as the LV becomes smaller [17, 18]. The Paracor device has been placed on dogs after serial intracoronary microsphere injection [19] and volume loops obtained 2 weeks after Paracor device implantation show significant reduction in both EDV and ESV. Similar results were obtained by Magovern, who placed Paracor devices in sheep immediately after anteroapical MI [17].

The Myocor™ Myosplint® (Myocor, Inc., Maple Grove, MN) is a transcavitary tensioning device (Fig. 13.1c) designed to change LV shape and reduce wall stress [20]. Typically, three Myosplints, each consisting of two epicardial pads connected by a tension member, are placed along the long axis of the LV. This draws the opposing anterior and posterior walls of the LV together and creates a bilobular cross-section with decreased chamber radius [16]. Recently, the adjustable fluid-filled balloon CSD (Fig. 13.1d) was developed by Ghanta and colleagues [21]. They suggested an optimized ventricular restraint as 3 mmHg to prevent and reverse pathological LV dilatation.

In this chapter, we quantify the effect of these passive constraint devices, with the exception of the Paracor Medical Heartnet™, on the LV stroke volume/end-diastolic pressure (EDP) (Starling) relationship and regional distributions of stress in the local muscle fiber direction.

13.2 Acorn CorCap™ Cardiac Support Device on the Failing Left Ventricle: Original Polyester Mesh Fabric Design

By using a 3-D finite element (FE) model, we tested the hypothesis that the CSD reduces end-diastolic wall stress with minimal depression of pump function at the time of implantation. The Acorn CorCap™ CSD is composed of a fabric with an open mesh structure, which greatly complicates mechanical engineering analysis of the CSD. To use the principles of continuum mechanics to model the CSD fabric, we obtained CSD fabric samples, embedded them in a silicone gel, and performed biaxial mechanical testing on the composite material (CSD fabric + silicone) [22]. The CSD composites and silicone controls (no CSD fabric) underwent biaxial testing and the results were separately fit to the passive myocardial material law, described in Eq. (3.2) in Section 3.2 in Chapter 3. Here Section 3.2 refers to "Passive Material Properties of Intact Ventricular Myocardium Determined From a Cylindrical Model" in Chapter 3. The two sets of material parameters were subtracted from each other leaving the parameters of the CSD alone (Table 13.1). From biaxial stress–strain relationships obtained in the composite material and in the silicone gel alone, we were able to derive a constitutive (stress/strain) equation that

Table 13.1 Passive material properties of Acorn fabric-silicone composite and pure silicone were obtained by planar biaxial mechanical testing

	b_f	b_t	b_{fs}	C (kPa)	RMS
Acorn CSD/silicone composites	4.48	7.18	0.00	450.22	21.88
Silicone controls	3.16	2.66	0.00	369.73	6.15
Acorn CSD	1.33	4.51	0.00	80.50	

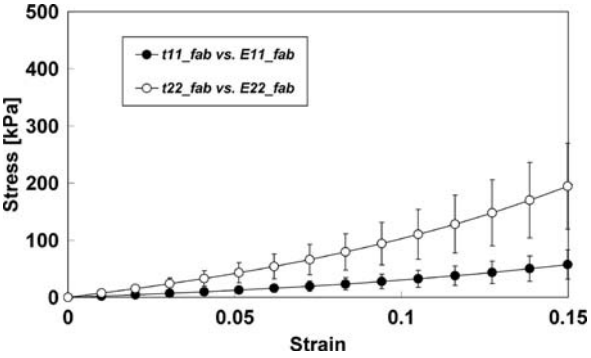

Fig. 13.2 The biaxial mechanical properties of the Acorn CSD fabric were extracted simply by subtracting the material properties of the silicone controls from those of the composites (i.e., Acorn CSD + silicone) (• = fitted stress vs. strain in x-direction, ○ = fitted stress vs. strain in y-direction)

describes the mechanical properties of the CSD for any orientations of the primary and secondary fabric populations (Fig. 13.2). A FE model of a globally dilated canine LV was created (see Section 1.3 in Chapter 1). Because the Acorn CSD is attached onto the epicardium, we assume that the implant acts as a layer added to the myocardium. The CSD was modeled using two thin layers, with one layer having fibers at 90° and one layer at 18° (Fig. 13.3).

We utilized a hyperelastic model describing the diastolic myocardial material properties [23, 24] to model the CSD. In contrast, the myocardium was modeled to have active and passive properties that were given by Walker and colleagues [25]. The generated stress/strain curves were fitted to the hyperelastic model in order to obtain the diastolic material constants of the CSD fabric (*C, bf, bt, bfs*), which were subsequently used as inputs to a 3-D FE model. An end-systolic pressure (ESP) of 90 mmHg and EDP of 17 mmHg, empirically observed, were applied to the model. The CSD was not pre-stretched in the simulation. Our results showed that the CSD greatly reduced end-diastolic wall stress by more than 40% (Fig. 13.4). Diastolic stiffness was increased by the CSD, but no notable alteration of end-systolic pressure–volume relationship was found (Fig. 13.5). The Starling relationship was depressed ∼12% at a given physiologic pre-load by the CSD

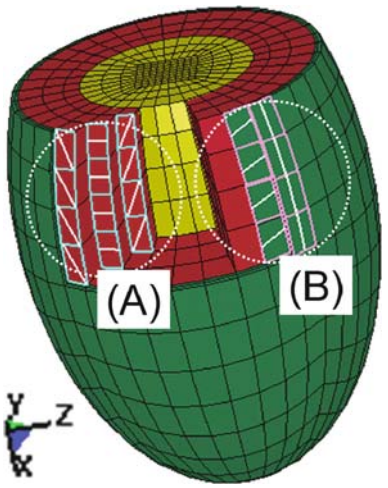

Fig. 13.3 Schematics of structural mesh of canine left ventricle with the Acorn CSD; the muscle fiber orientation of left ventricle (60°/0°/–60° for inner wall, mid-wall, and outer wall, respectively) is shown in *circled area A*. The fabric orientation of the Acorn CSD (primary angle of 90° and secondary angle of 18°) is shown in *circled area B*

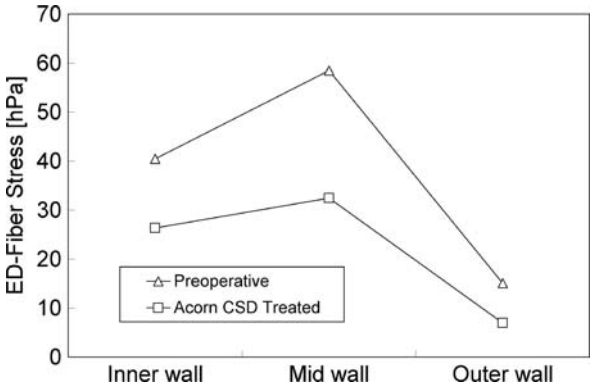

Fig. 13.4 End-diastolic (ED) fiber stress of preoperative (Δ) and the Acorn CSD treated (□) (10 hPa = 1 kPa)

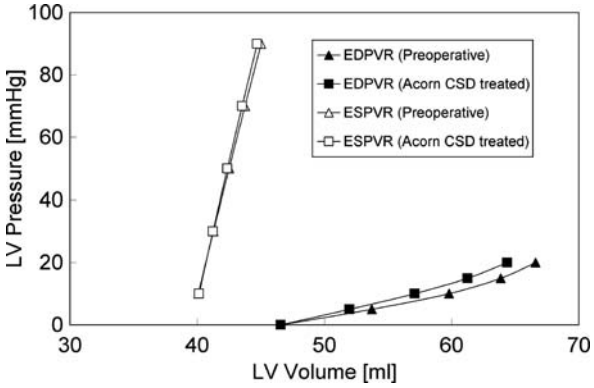

Fig. 13.5 End-systolic pressure–volume relationship (ESPVR) and end-diastolic pressure–volume relationship (EDPVR)

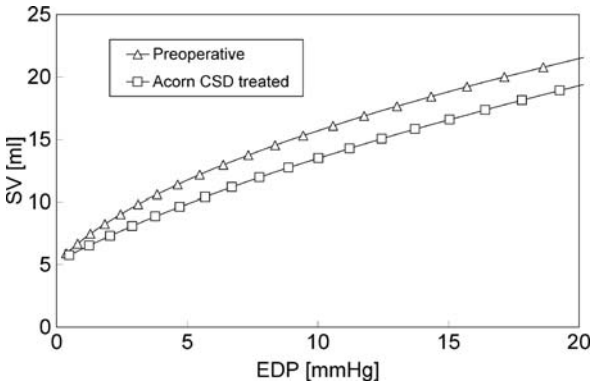

Fig. 13.6 Stroke volume (SV)/End-diastolic pressure (Starling) relationship (△: preoperative, □: Acorn CSD treated)

(Fig. 13.6). In conclusion, the CSD greatly reduces end-diastolic wall stress with some depression of pump function at the time of implant. This finding suggests that the optimal wrap tightness may be very important at the time of implant as well.

13.3 Acorn CorCap^{TM} Cardiac Support Device on the Failing Left Ventricle: Modified Polyester Mesh Fabric Design

The geometric profile of the Acorn CSD before application is approximately a hemi-ellipse. At the time of application, a matching Acorn CSD size is selected and placed over the diseased heart. Excess fabric is loosely gathered into a custom clamp and then excised [26]. Cheng and associates [11] noticed that the Acorn CSD can cause significant fabric reorientation during the sizing, resulting in alteration of initial anisotropic compliance characteristics [27]. However, no study on the Acorn CSD has reported on the effect of variations in fabric orientation despite the potential variability of ventricular function and myocardial properties caused by the alteration of initial fabric design. To quantify if the Acorn CSD design is optimal as far as regional LV mechanics and pump function are concerned, we used the mathematical model that we derived for the Acorn CSD and re-ran the simulations performed in the previous section after modifying the orientation of the fabric weave. We tested the hypothesis that an alteration of structural and mechanical anisotropy of the Acorn CSD induced by the fabric reorientation has little or no effect on end-diastolic myofiber stress distributions and pump function.

Two cases of fabric orientations were simulated: (i) both the primary and secondary fabric populations were reoriented from the original fabric design and (ii) only the secondary fabric population was reoriented. Both the primary and secondary fabric populations were rotated by 15°, 30°, and 45° from the initial fabric orientation (i.e., 90° and 18° from the circumferential direction for the primary and

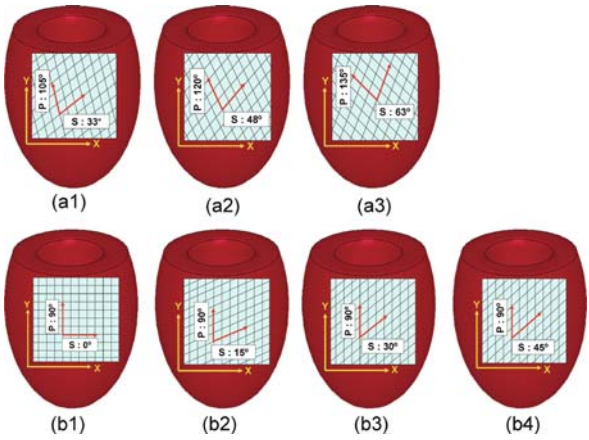

Fig. 13.7 (**a**) Both the primary and secondary fabric populations were rotated by 15°, 30°, and 45° from the initial fabric orientation, thus the fabric structures that we simulated were (a1) 105°/33°, (a2) 120°/48°, and (a3) 135°/63°, where 90° and 18° are initial fabric orientations for the primary and secondary fabric populations, respectively. (**b**) Rather than rotating the secondary fabric population from the initial secondary fabric orientation of 18°, the secondary fabric population was set to (b1) 0°, (b2) 15°, (b3) 30°, and (b4) 45° while the orientation of the primary fabric population was held constant as 90°

secondary fabric populations, respectively). Thus the fabric structures that we simulated for this case were 105°/33° (= 90°/18° + 15°), 120°/48° (= 90°/18° + 30°), and 135°/63° (= 90°/18° + 45°). Figure 13.7 (a1–a3) shows the Acorn CSD fabrics with the LV that represent the primary/secondary fabric orientations. Next, keeping the orientation of the primary fabric population constant at 90°, only the secondary fabric population was reoriented. The orientation of the secondary fabric population was set to 0, 15, 30, and 45°. Thus the fabric structures that we simulated for this case were 90°/0°, 90°/15°, 90°/30°, and 90°/45°. Figure 13.7 (b1–b4) shows the Acorn CSD fabrics with LV that represent the secondary fabric orientations. By using the mathematical model that describes the mechanical properties of the CSD for any orientations of the primary and secondary fabric populations,

$$\begin{aligned} T_{11} &= 2w_{iso}\psi_1(\lambda_1^2 - \lambda_3^2) + 2w_{aniso}\,\lambda_1^2\left[\psi_4 \cos^2\alpha + \psi_6 \cos^2\alpha'\right] \\ T_{22} &= 2w_{iso}\psi_1(\lambda_1^2 - \lambda_3^2) + 2w_{aniso}\,\lambda_1^2\left[\psi_4 \sin^2\alpha + \psi_6 \sin^2\alpha'\right] \end{aligned} \tag{13.1}$$

the stress/strain curves corresponding to each fabric orientation were generated shown in Eq. (13.1) (Fig. 13.8). In our previous modeling study with an initial fabric structure of the Acorn CSD, we assumed that since the Acorn CSD is attached onto the epicardium, the implant can be interpreted to act as an extra myocardial layer. As such, we utilized the same hyperelastic model that describes diastolic myocardial material properties [23, 24] to model the CSD. For all seven fabric reorientations, the generated stress/strain curves were fitted to the hyperelastic model in order to

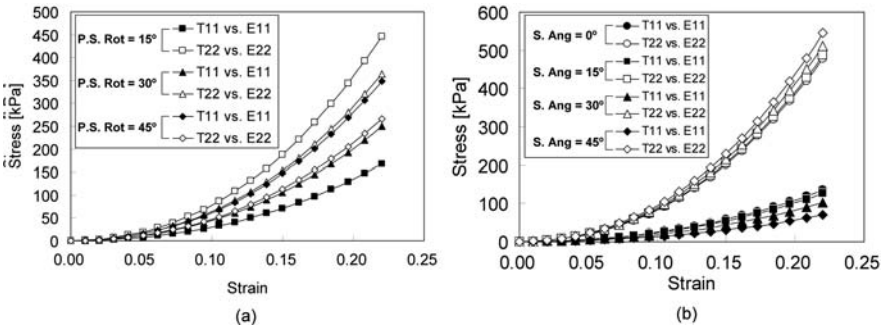

Fig. 13.8 (**a**) The constitutive curves associated with the primary/secondary fabric orientation of the Acorn CSD. P.S. Rot is the primary/secondary fabric rotation, T11 and T22 and E11 and E22 are the Cauchy stresses and Green strains in the primary and secondary directions, respectively. As the orientation of the primary/secondary fabric populations expand, the stiffness in the primary fabric direction is decreased but the stiffness in the secondary fabric direction is increased. Note that, at rotation of 45° for the primary/secondary fabric populations, the stiffness in the secondary fabric direction becomes greater than that of the primary fabric direction. The stress/strain curves for a rotation of 30° and 45° are close to each other, except for the transposed stiffness between the primary and the secondary fabric populations. (**b**) The constitutive curves associated with the secondary fabric orientation of the Acorn CSD. S. Ang is the secondary fabric angle. As the secondary fabric population approaches the primary fabric orientation, it slightly increases the stiffness in the primary fabric direction but decreases the stiffness in the secondary fabric direction

obtain the diastolic material constants of the CSD fabric (*C, bf, bt, bfs*), which were subsequently used as inputs to a 3-D FE model (Table 13.2).

Our results showed that variation in fabric orientation did not alter the amount of reduction in the end-diastolic muscle fiber stress and the pump function as compared to the case of the initial fabric structure of the Acorn CSD (Fig. 13.9 and 13.10). In conclusion, any alteration of structural anisotropy of the Acorn CSD fabric induced by the fabric reorientation during implantation has little or no impact on end-diastolic myofiber stress distributions and pump function.

Table 13.2 The material properties associated with the primary/secondary fabric orientation and the secondary fabric orientation of the Acorn CSD (C = material stiffness parameter in unit of kPa)

Material properties	C	b_f	b_t	b_{fs}	RMS
Prim./Sec. Rot = 15°	38.59	2.69	7.16	0.50	12.58
Prim./Sec. Rot = 30°	36.39	4.34	6.31	0.50	11.81
Prim./Sec. Rot = 45°	33.18	6.73	5.16	0.50	12.01
Sec. Ang = 0°	39.64	2.12	7.44	0.42	13.07
Sec. Ang = 15°	39.83	1.97	7.52	0.50	13.22
Sec. Ang = 30°	40.55	1.56	7.72	0.50	13.65
Sec. Ang = 45°	41.47	1.03	7.99	0.50	14.31

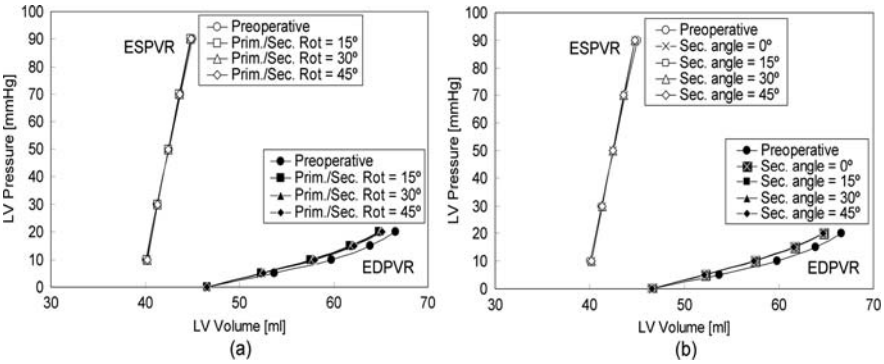

Fig. 13.9 (**a**) The end-diastolic (EDPVR) and end-systolic (ESPVR) pressure–volume relationships associated with the primary/secondary fabric orientation. No notable change in systolic elastance, E_{ES}, and ventricular volume intercept, V_0, associated with the fabric orientation for both (**a**) the primary/secondary and (**b**) the secondary fabric populations were found. The alteration of the diastolic compliance was also negligible

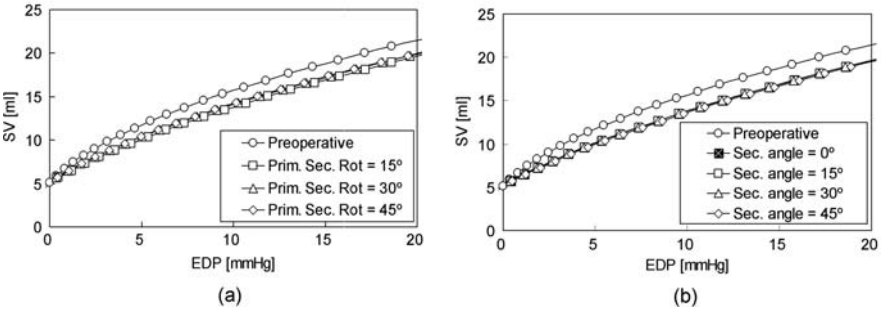

Fig. 13.10 The Starling relationships associated with (**a**) the primary/secondary fabric orientation, and (**b**) the secondary fabric orientation of the Acorn CSD. At any structural anisotropy, there were no significant differences in the ventricular pump function by either the primary/secondary or the secondary fabric. The stroke volume at the same given physiological pre-load (i.e., 17 mmHg) for the primary/secondary fabric orientations was 18.16 ± 0.018 ml. The stroke volume for the secondary fabric orientations was 18.12 ± 0.006 ml. This represents the depression of the pump function by ~20% at the time of implantation and this amount of depression is nearly identical to the case of the initial fabric structure

13.4 Adjustable Passive Constraint on the Failing Left Ventricle

There has been concern about the effect of passive constraint on diastolic LV chamber stiffness and pump function. To quantify this effect, Ghanta and associates placed a fluid-filled balloon around the LV [21]. In that study, a balloon pressure of 3 mmHg caused no acute change in mean aortic pressure but reduced the tension time index and pressure–volume area by 12% and 20%, respectively, and caused a chronic 30% reduction in LV EDV in sheep that had remodeled after occlusion

of left anterior, descending diagonal, coronary arteries 1 and 2 [21]. However, it should be noted that there was an acute 10% reduction in cardiac output [17].

By using a realistic 3-D FE model, the effect of the adjustable passive constraint on a failing canine heart was quantified. In addition to confirming the findings by Ghanta et al. [21], this study determines the relationship between the ventricular constraint, diastolic wall stress, diastolic chamber stiffness, and pump function by Starling's Law. We tested the hypothesis that passive constraint at 3 mmHg reduces diastolic wall stress without a change in pump function.

After creating a FE model of the globally dilated canine LV, ESP of 90 mmHg and EDP of 17 mmHg were applied outwards at the inner endocardial wall. EDV and ESV with no constraint were set to 65 ml and 45 ml. The levels of passive constraint, 3 mmHg, 5 mmHg, 7 mmHg, then 9 mmHg, were implemented by applying inward pressure on the epicardium. The material constants in Eq. (3.2) in Chapter 3 b_f, b_t, and b_{fs} were chosen as 49.25, 19.25, and 17.44, respectively. A material constant, C, was selected to be 0.33 kPa, enabling us to obtain the prescribed EDV. Active material parameters in Eq. (3.3 and 3.4) in Chapter 3 were selected to the following values: $Ca_0 = 4.35$ μmol/l, $(Ca_0)\max = 4.35$ μmol/l, $m = 1.0489$ s/μm, $b = -1.429$ s, $B = 4.75$ μm^{-1}, and $l0 = 1.58$. To achieve the prescribed ESV, we chose $T_{\max}$ to be 128 kPa.

It was found that if the reduction in cardiac output is to be less than 10%, passive constraint should not exceed 3.63 mmHg. At that amount of constraint, end-diastolic fiber stress was between 35.3% (mid-wall) and 48.8% (outer wall) of stress without constraint (Fig. 13.11). The compliance curves shift to the left as the level of constraint increases. Passive constraint on the Starling relationship causes progressive tapering of stroke volume at the same end-diastolic pressure. Both stress and cardiac

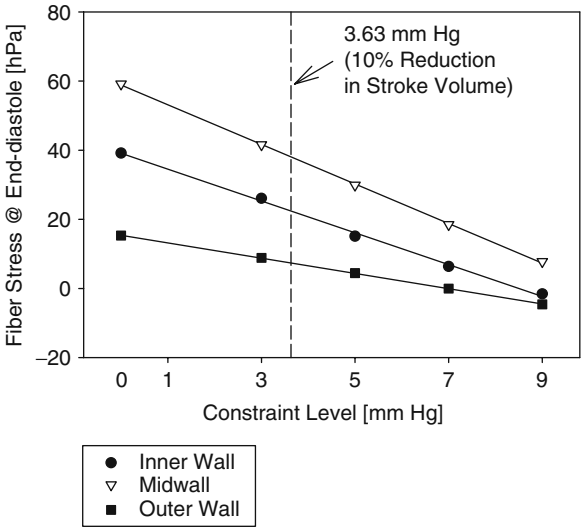

Fig. 13.11 End-diastolic fiber stress; as the level of passive constraint increases, ED-fiber stress is reduced. Fiber stress at end-diastole was reduced by 48.8% at the outer wall, 35.3% at the mid-wall, and 42.7% at the inner wall at 3.63 mmHg of constraint (*y*-axis label cut-off)

output decrease in a linear fashion as the amount of passive constraint is increased. In summary, if the reduction in cardiac output is to be less than 10% (Fig. 13.12), passive constraint should not exceed 3.63 mmHg, which appears sufficient to reverse eccentric hypertrophy after myocardial infarction.

13.5 Myosplint Decreases Wall Stress Without Depressing Function in the Failing Heart

Regional wall stress cannot be measured in the intact heart and LV function after surgical remodeling is often confounded by inotropic agents and mitral repair. We used a realistic mathematical (FE) model of the dilated human LV to test the hypothesis that Myosplint decreased regional ventricular fiber stress and improved LV function. A FE model was used to simulate the effects of the Myosplint on the LV stroke volume/EDP (Starling) relationship, and regional distributions of stress in the local muscle fiber direction (fiber stress) for a wide range of diastolic and end-systolic material properties. The nonlinear stress–strain relationship for the diastolic myocardium was anisotropic with respect to the local muscle fiber direction. An elastance model (Eq. (3.3)) for active fiber stress was incorporated in an axisymmetric geometric model of the globally dilated LV wall. Both diastolic compliance and end-systolic elastance shifted to the left on the pressure–volume diagram. LV EDV and EDV were reduced by 7.6% then 8.6% (Fig. 13.13). Mean end-diastolic and end-systolic fiber stress was decreased by 24% and 16%, respectively (Fig. 13.14). Although the effect of the Myosplint on the Starling relationship was not significant, there were trends toward an improvement in this relationship at low diastolic stiffness, C, high peak intracellular calcium concentration, Ca_0, and high arterial elastance, E_A. Of note, the effect of C was twice that of Ca_0 and E_A (Fig. 13.15).

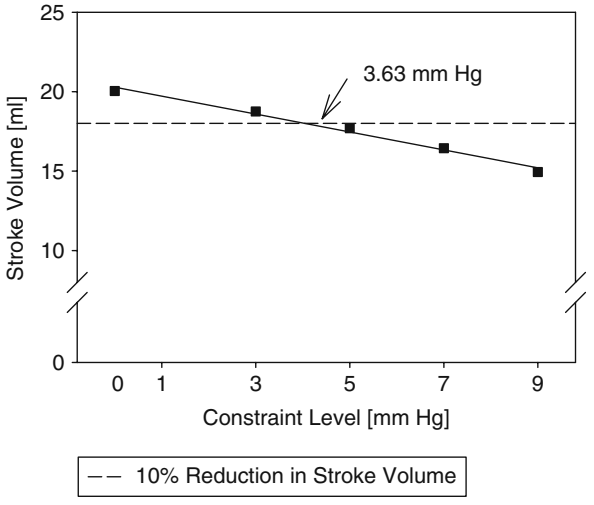

Fig. 13.12 Relationship between stroke volumes at initial end-diastolic pressure (17 mmHg.). Note that any amount of constraint is associated with a reduction in stroke volume. An arbitrary cut of 10% reduction in stroke volume occurs at 3.63 mmHg (y-axis label cutoff)

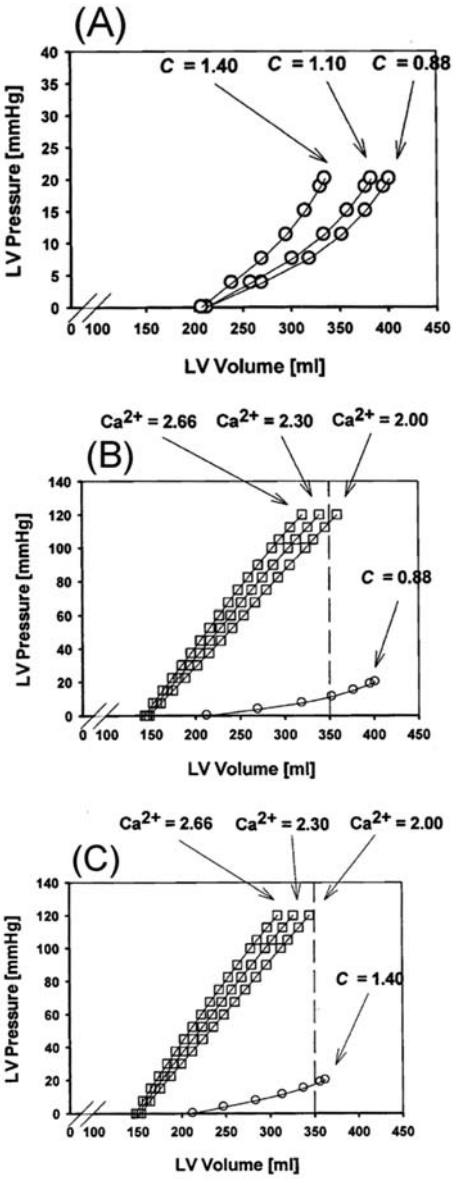

Fig. 13.13 Baseline (preoperative) diastolic (**a**) and end-systolic (**b** and **c**) pressure–volume relationships. (**a**) Diastolic compliance associated with C of 0.88 kPa, 1.10 kPa, and 1.40 kPa, respectively. (**b**) End-systolic elastance curves associated with $Ca_0 =$ 266 μmol/L, 2.30 μmol/L, and 2.00 μmol/L, respectively, and $C =$ 0.88 kPa. (**c**) Similar to (**b**) but with $C = 1.4$ kPa. Note that the elastance is dependent on both the diastolic stiffness variable and peak intracellular calcium concentration

Diastolic function would, therefore, be expected to be the prime determinant of success with Myosplint. The Myosplint reduces fiber stress without a decrement in the Starling relationship. The Myosplint should be much more effective than partial ventriculectomy as a surgical therapy for patients with dilated cardiomyopathy and end-stage congestive heart failure. Unfortunately, the Myosplint, CorCap CSD, and HealthNet VSS are all rather difficult to implant.

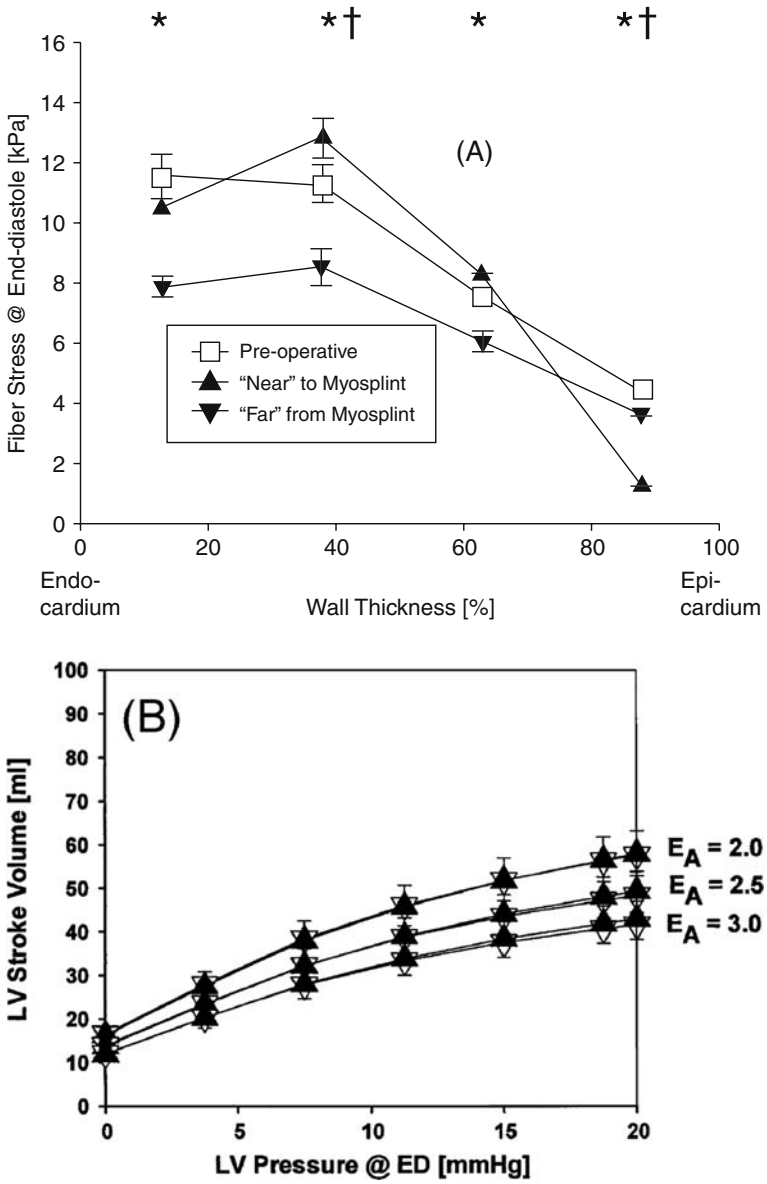

Fig. 13.14 (**a**) The effect of a 25% reduction in end-diastolic diameter (Myosplint) on the transmural distribution of (**a**) end-diastolic. (**b**) End-systolic fiber stress. Note the significant reduction in fiber stress in areas "far" from the Myosplint ($*$ = comparison between preoperative and "near;" † = comparison between preoperative and "far;" $p < 0.05$ by two-way ANOVA with Bonferroni correction)

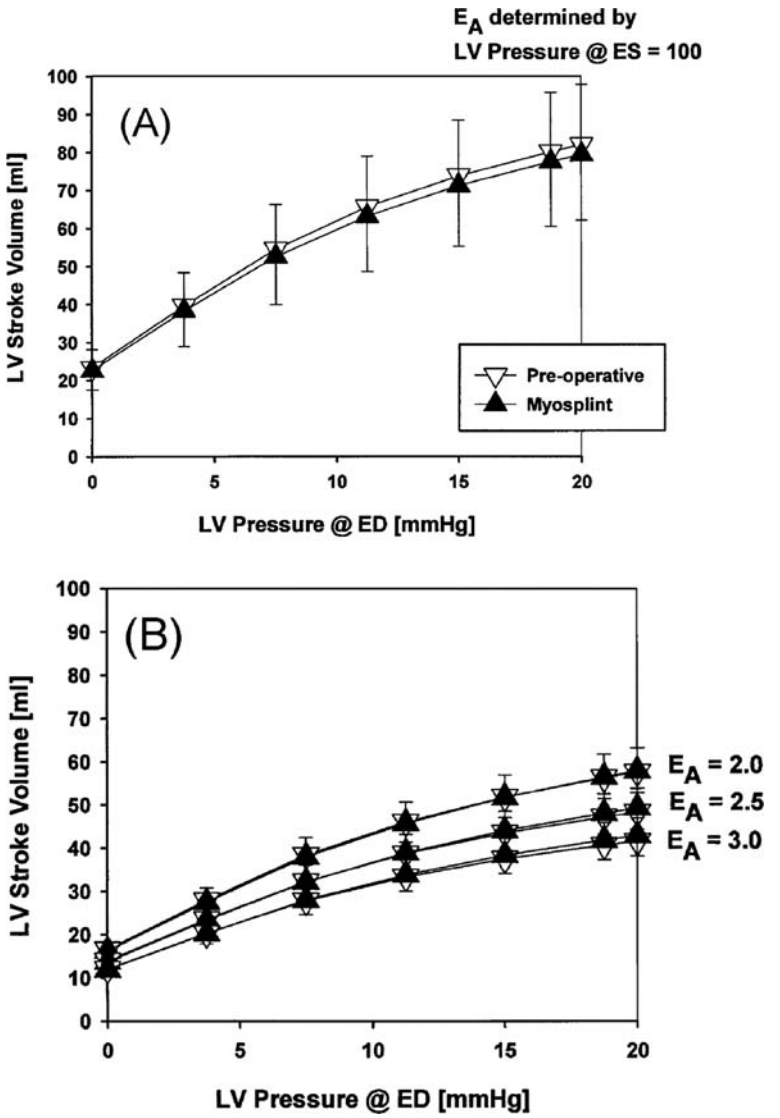

Fig. 13.15 The effect of a 25% reduction in end-diastolic diameter on the Starling relationship. (**a**) Preoperative E_A is calculated by fixing LV pressure at 100 mmHg. (**b**) Preoperative E_A is fixed at 2, 2.5, or 3. In all cases preoperative E_A = Myosplint E_A. Although changes were not significantly different, (all cases) there is a trend toward an improvement in the Starling relationship at high E_A. Note the change in scale in panel **B**

13.6 Conclusion

Passive mechanical constraint devices are potentially viable alternative surgical therapies for heart failure. However, comprehensive evaluations of the devices are

imperative for effective treatment. In this chapter, we looked at the functional properties of several of the passive constraint devices, Acorn, Fluid Filled Balloon, and Myosplint, using FE analysis, to determine their impact on ventricular function. Our studies provide the insight into the functionality of passive constraint devices on the ventricular function and mechanics.

Acknowledgments This research was supported by National Institutes of Health grant 5R01 HL077921 (Dr. Guccione) and 5R01 HL063348 (Dr. Ratcliffe). We thank Ms. Kimberly S. Yan, a technical writing expert for proof-reading of this chapter.

References

1. Hammermeister KE, DeRouen TA, Dodge HT. Variables predictive of survival in patients with coronary disease. Selection by univariate and multivariate analyses from the clinical, electrocardiographic, exercise, arteriographic, and quantitative angiographic evaluations. *Circulation*. 1979;59:421–30.
2. Kostuk WJ, Kazamias TM, Gander MP, Simon AL, Ross J Jr. Left ventricular size after acute myocardial infarction. Serial changes and their prognostic significance. *Circulation*. 1973;47:1174–9.
3. Shanoff HM, Little JA, Csima A, Yano R. Heart size and ten-year survival after uncomplicated myocardial infarction. *Am Heart J*. 1969;78:608–14.
4. White HD, Norris RM, Brown MA, Brandt PW, Whitlock RM, Wild CJ. Left ventricular end-systolic volume as the major determinant of survival after recovery from myocardial infarction. *Circulation*. 1987;76:44–51.
5. Douglas PS, Morrow R, Ioli A, Reichek N. Left ventricular shape, afterload and survival in idiopathic dilated cardiomyopathy. *J Am Coll Cardiol*. 1989;13:311–5.
6. Grossman W, Jones D, McLaurin LP. Wall stress and patterns of hypertrophy in the human left ventricle. *J Clin Invest*. 1975;56:56–64.
7. Hagege AA, Desnos M, Fernandez F, Besse B, Mirochnik N, Castaldo M, Chachques JC, Carpentier A, Guerot C. Clinical study of the effects of latissimus dorsi muscle flap stimulation after cardiomyoplasty. *Circulation*. 1995;92:II210–5.
8. Kass DA, Baughman KL, Pak PH, Cho PW, Levin HR, Gardner TJ, Halperin HR, Tsitlik JE, Acker MA. Reverse remodeling from cardiomyoplasty in human heart failure. External constraint versus active assist. *Circulation*. 1995;91:2314–8.
9. Nakajima H, Niinami H, Hooper TL, Hammond RL, Nakajima HO, Lu H, Ruggiero R, Thomas GA, Mocek FW, Fietsam R Jr, et al. Cardiomyoplasty: probable mechanism of effectiveness using the pressure–volume relationship. *Ann Thorac Surg*. 1994;57: 407–15.
10. 10. Blom AS, Mukherjee R, Pilla JJ, Lowry AS, Yarbrough WM, Mingoia JT, Hendrick JW, Stroud RE, McLean JE, Affuso J, Gorman RC, Gorman JH 3rd, Acker MA, Spinale FG. Cardiac support device modifies left ventricular geometry and myocardial structure after myocardial infarction. *Circulation.* 2005;112(9):1274–1283.
11. Cheng A, Nguyen TC, Malinowski M, Langer F, Liang D, Daughters GT, Ingels NB Jr, Miller DC. Passive ventricular constraint prevents transmural shear strain progression in left ventricle remodeling. *Circulation*. 2006;114:I79–86.
12. Pilla JJ, Blom AS, Brockman DJ, Bowen F, Yuan Q, Giammarco J, Ferrari VA, Gorman JH 3rd, Gorman RC, Acker MA. Ventricular constraint using the acorn cardiac support device reduces myocardial akinetic area in an ovine model of acute infarction. *Circulation*. 2002;106:I207–11.
13. Chaudhry PA, Mishima T, Sharov VG, Hawkins J, Alferness C, Paone G, Sabbah HN. Passive epicardial containment prevents ventricular remodeling in heart failure. *Ann Thorac Surg*. 2000;70:1275–80.

14. Starling RC, Jessup M, Oh JK, Sabbah HN, Acker MA, Mann DL, Kubo SH. Sustained benefits of the CorCap Cardiac Support Device on left ventricular remodeling: three year follow-up results from the Acorn clinical trial. *Ann Thorac Surg*. 2007;84(4):1236–1242.
15. Mann DL, Acker MA, Jessup M, Sabbah HN, Starling RC, Kubo SH. Clinical evaluation of the CorCap Cardiac Support Device in patients with dilated cardiomyopathy. *Ann Thorac Surg*. 2007;84(4):1226–1235.
16. Pelton A. Nitinol medical devices. *Adv Mater Processes*. 2005;163:S13(3).
17. Magovern JA. Experimental and clinical studies with the Paracor cardiac restraint device. *Semin Thorac Cardiovasc Surg*. 2005:17, 364–8.
18. Magovern JA, Teekell-Taylor L, Mankad S, Dasika U, McGregor W, Biederman RW, Yamrozik J, Trumble DR. Effect of a flexible ventricular restraint device on cardiac remodeling after acute myocardial infarction. *Asaio J*. 2006;52(2):196–200.
19. Cheng Y, Yi G, Hay I, Qin S, He K, Yue K, Li X, Tao Y, Wang J. A novel left ventricular passive support device alters the natural history of chronic heart failure in awake dogs. New Orleans, LA: AHA Scientific Sessions, 2004.
20. McCarthy PM, Takagaki M, Ochiai Y, Young JB, Tabata T, Shiota T, Qin JX, Thomas JD, Mortier TJ, Schroeder RF, Schweich CJ Jr, Fukamachi K. Device-based change in left ventricular shape: a new concept for the treatment of dilated cardiomyopathy. *J Thorac Cardiovasc Surg*. 2001;122:482–90.
21. Ghanta RK, Rangaraj A, Umakanthan R, Lee L, Laurence RG, Fox JA, Bolman RM 3rd, Cohn LH, Chen FY. Adjustable, physiological ventricular restraint improves left ventricular mechanics and reduces dilatation in an ovine model of chronic heart failure. *Circulation*. 2007;115:1201–10.
22. Humphrey JD. Cardiovascular solid mechanics: cells, tissues, and organs. New York: Springer, 2002, p. 757, pp. xvi.
23. Guccione JM, Costa KD, McCulloch AD. Finite element stress analysis of left ventricular mechanics in the beating dog heart. *J Biomech*. 1995;28:1167–77.
24. Guccione, JM, Salahieh A, Moonly SM, Kortsmit J, Wallace AW, Ratcliffe MB. Myosplint decreases wall stress without depressing function in the failing heart: a finite element model study. *Ann Thorac Surg*. 2003;76:1171–80.
25. Walker JC, Ratcliffe MB, Zhang P, Wallace AW, Fata B, Hsu EW, Saloner D, Guccione JM. MRI-based finite-element analysis of left ventricular aneurysm. *American journal of physiology*. 2005;289(2):H692–700.
26. Oz MC, Konertz WF, Kleber FX, Mohr FW, Gummert JF, Ostermeyer J, Lass M, Raman J, Acker MA, Smedira N. Global surgical experience with the Acorn cardiac support device. *J Thorac Cardiovasc Surg*. 2003;126:983–91.
27. Walsh RG. Design and features of the Acorn CorCap Cardiac Support Device: the concept of passive mechanical diastolic support. *Heart Fail Rev*. 2005;10:101–7.

Chapter 14
Left Ventricular Implantation of Biomaterials

Samuel T. Wall, Jonathan F. Wenk, Choon-Sik Jhun, and Julius M. Guccione

Abstract In recent years, there has been a significant effort to restore heart function by the addition of stem cells directly into the myocardium. These cells are normally carried in a synthetic extracellular matrix and implanted into the injured heart. While there has been little demonstration of actual tissue regeneration using such methods, there has been long-term improvement from these techniques, and surprisingly, from the implantation of biomaterials alone, without any included cells. This has in fact led to therapies that directly add passive materials into the ventricle to help prevent heart failure. Therefore, theoretically evaluating the addition of passive material volumes into the myocardium is of clinical importance to understand the mechanisms for the improvement of ventricular mechanics and for optimizing such treatments. In this chapter we discuss the role of finite element studies in investigating the direct addition of non-contractile materials into the myocardium.

14.1 Introduction

With an estimated associated cost of $34.8 billion in 2008 [1] in the US alone, heart failure (HF) continues to present a significant and growing medical and economic burden throughout the developed world. While there are numerous mechanisms for the development of HF, one central hypothesized cause for the progression of the condition is an elevation of left ventricular (LV) muscle fiber (myofiber) stress and strain that results from progressive LV enlargement and maladaptive shape changes. This hypothesis has led to research on novel treatments, such as the direct injection of non-contractile material [2, 3] into the myocardium to reduce elevated myofiber stress during the cardiac cycle and to retard the progression of HF. One of the limitations in clinical testing, with regards to implanting passive materials into the

J.M. Guccione (✉)
Department of Surgery, University of California at San Francisco and San Francisco VA Medical Center, San Francisco, CA, USA
e-mail: guccionej@surgery.ucsf.edu

J.M. Guccione, et al. (eds.), *Computational Cardiovascular Mechanics*,
DOI 10.1007/978-1-4419-0730-1_14,

myocardium for the reduction of wall stress, is that there have been no successful methods developed to measure forces or stresses in the intact LV wall – primarily because of its large deformations and the tissue injury caused by implanted transducers. Thus, determining whether wall stresses have been reduced requires alternative methods, such as the use of finite element (FE) simulations.

14.2 FE Studies of Non-contractile Material Addition to the Infarct-Injured Ventricle

Acute myocardial infarctions (AMIs) are a significant source of HF. One of the actively pursued approaches to treating CHF associated with AMI is cellular transplantation into the infarct or border zone region to improve regional and global pump function. Many types of cells have been injected into the injured myocardium, and in addition to cells alone, studies have also included ECM materials with or without the cells. FE studies on a ventricle with non-contractile regions have investigated how adding new contractile elements should improve systolic function [4], demonstrating global changes to ventricle function. However, it has recently been confirmed that adding cells to the myocardium creates little functional regeneration but still alters ventricular function. Therefore, the current study investigates the acute ventricular mechanical effects assuming the implanted materials, such as synthetic ECMs, act only as passive materials [5]. We tested the hypothesis that even small fractional changes in LV wall volume can significantly alter cardiac mechanics when properly located.

Development of models to accurately reflect the addition of non-contractile material requires careful mesh changes to best simulate the desired effect. We used a previously developed and validated FE model of an ovine LV suffering from an antero-apical, transmural, dyskinetic infarct [6]. Injection of material into the anterior wall of the infarct border zone was simulated by changing the transmural coordinates of epicardial and endocardial mesh nodes to create local bulging in the apical anterior wall. In the first set of simulations, the resulting deformation in the three chosen elements and surrounding nine elements was varied to achieve a total wall volume increase of 0.5–1.5 mL. To simulate the addition of non-contractile volume, contractility of these elements, as defined by the active contraction $T_{\max}$ parameter [7], was reduced to an extent proportional to the change in volume. In addition, to investigate the role that stiffness of the injected material contributes to changes in cardiac mechanics, the passive material parameters of the strain energy constitutive equation, described in Chapter 3, of the combined material/myocardium elements were modified to model added material with the use of a volume-mixing rule.

A second simulation tested the global effect of injected material as a potential therapy, with a total of 4.4 mL ($\sim$4.5% of total wall volume) added in multiple locations in the infarct border zone. In this simulation, a total of 12 border zone elements in 4 surgically accessible locations (in the anterior, posterior, and septal walls) were

modified. A third set of simulations determined the effect of adding material directly to the non-contractile infarct region. In these simulations, two regions of the apical infarct mesh were modified by transmural modifications to the epicardial nodes to model the geometry of material added to the infarct wall.

Midwall end-systolic fiber stresses in the local injection area were calculated at an LV pressure of 10.24 kPa for a range of injected volumes (0.5–1.5 mL) and a range of material properties (1–200% of normal diastolic stiffness). There are 12 elements in the volume-altered anterior region of these simulations, 6 of which are infarct elements and 6 of which are remote and border zone. Mean volume-weighted stress of each of these two groups of elements shows a linear decrease with increasing added volume. Material properties also appear to have an effect, with the higher stiffness materials bearing more of the load in the softer remote and border zone regions than the stiffer infarct, therefore resulting in a greater reduction in remote and border zone stresses. The small fractional volumes used in this single-injection simulation have no significant effect on ejection fraction (EF) or global function.

In the simulation, to investigate the effect of a potential treatment of multiple implantations throughout the peri-infarct border zone, results indicate that the addition of ~4.5% of the total wall volume to the border zone can bring mean volume-weighted end-systolic fiber stress in the border zone back down to near-normal levels in the remote myocardium (Fig. 14.1a). However, cross-fiber stresses

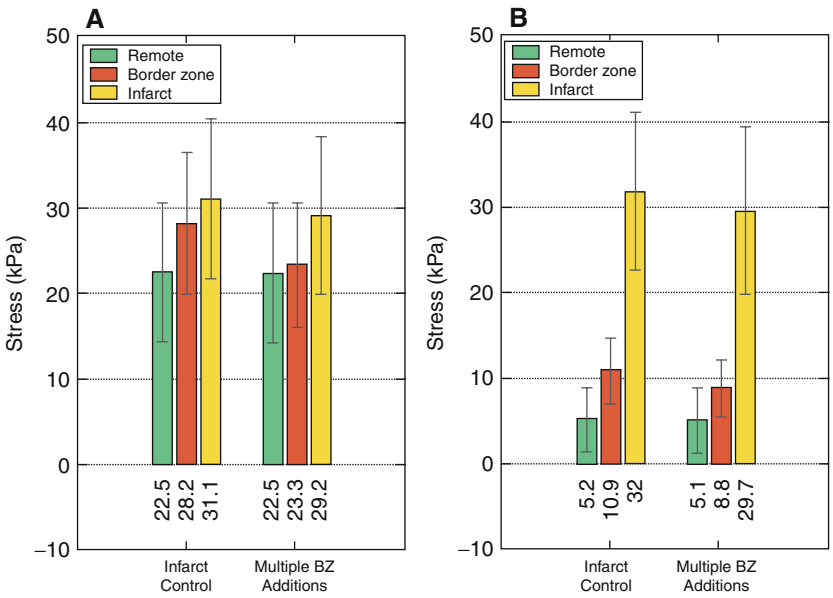

Fig. 14.1 Changes in average fiber (**a**) and cross-fiber (**b**) end-systolic stress as a function of the simulated injection of a total of 4.4 mL of material to the infarct border zone region in multiple injection sites [5]

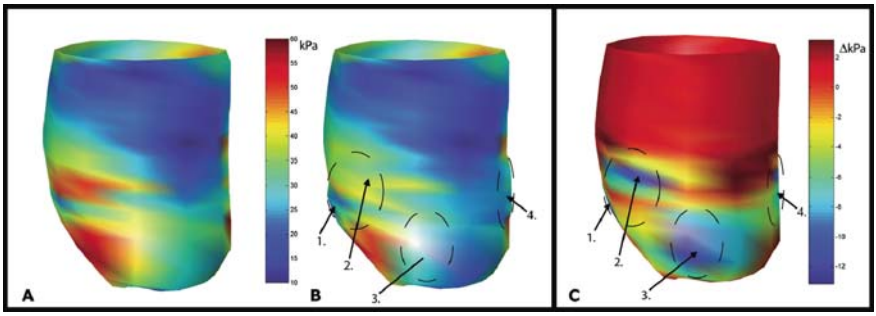

Fig. 14.2 Depiction of midwall end-systolic stress fields in the infarct-injured ventricle, both before (**a**) and after (**b**) the theoretical addition of ∼4 mL of non-contractile material to the infarct border zone. Differences in stress are localized in the areas of simulated addition (**c**) [5]

are not dramatically decreased (Fig. 14.1b), and the other four stress components are not changed significantly (data not shown). Figure 14.2 shows a three-dimensional color representation of mean end-systolic fiber stress before (Fig. 14.2a) and after (Fig. 14.2b) the injection of material to the ventricle wall, with yellow-red indicating areas of elevated fiber stress compared with the rest of the ventricle. Figure 14.2c shows the difference between the two states, with blue regions indicating localized areas of decreased stress in the regions of injection.

In addition, material added to the border zone in this simulation caused slight shifts to both the end-systolic and end-diastolic pressure–volume relationships, EDPVR and ESPVR, respectively [5]. Meanwhile, global heart function as estimated by the Starling relationship was not significantly altered by the model changes, with the multiple injections providing no change over the control simulation. The relationship between stroke volume and volume at end-diastole (SV/V_{ED}), as well as EF, see Fig. 14.3a, were only slightly altered.

Results of the third simulation show that direct injection of material to the infarct region can alter the EDPVR and ESPVR proportionally to the amount added, moving the EDPVR and ESPVR leftward, with a slight upward change to the slope of the ESPVR [5]. These changes result as a combination of two factors, the increased elastance of the ventricle from added material and the changes to ventricular volume. Although not significantly altering the Starling relationship, these geometric changes can lead to observed differences in SV/V_{ED} relationships and the often-reported metric EF, seen in Fig. 14.3b. A modest fractional increase in volume of the infarct (5.3 mL compared with 97 mL total wall volume) is capable of increasing the EF by ∼2 percentage points over the infarct control (24 versus 22), which is a 10% change in magnitude.

Our studies indicate that a small fractional change (0.5–5%) in myocardium wall volume can alter cardiac mechanics, decreasing wall stresses, affecting ESPVR and EDPVR, and increasing EF and SV/V_{ED} without improving the Starling

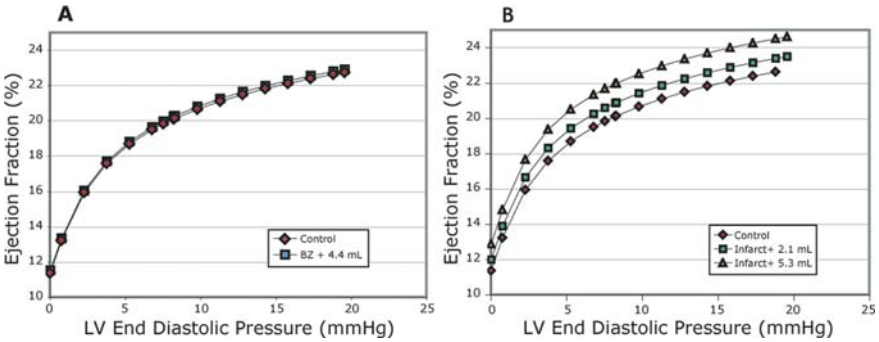

Fig. 14.3 EF as a function of end-diastolic pressure for the simulated injection of non-contractile volume to the border zone (**a**) and infarct (**b**) regions. Little observed difference is seen in the border zone injection, but in the infarct a 2% increase in wall volume produces a 1 percentage point increase in EF over control simulations, whereas a 5% increase in wall volume creates a 2 percentage point increase in EF [5]

relationship. These short-term mechanical effects are dependent on the location of the injection, the fractional volume of material added, and its relative stiffness to the local myocardium. Although simulating the long-term effect of these changes is beyond the scope of this FE study, the short-term calculated effects have direct relevance to ongoing clinical research that involves injecting cells and materials into the ventricle to treat the after effects of AMIs. These simulations have demonstrated that changes to global function can result from the addition of purely passive materials into the myocardium and that care needs to be taken when making claims of regeneration occurring due to cells being added to the myocardium, when in fact the changes may result directly from mechanical aspects of adding material to the border zone or infarct.

14.3 FE Studies of Non-contractile Material Addition to a Globally Failing Ventricle

While the infarct-injured ventricle presents one target for FE studies, many people suffer from a globally failing heart without an infarct. In this case, the ventricle can become substantially enlarged, and have poor contractile function, with increased wall stresses compared to a healthy heart. An FE model was developed to realistically simulate the mechanics of the globally failing canine LV [8]. An axisymmetric mesh was made to match end-diastolic and end-systolic metrics from dogs with coronary microembolization-induced HF [9]. These ventricles were enlarged, had thinner walls, and poor contractility. The baseline FE model, depicted in Fig. 14.4a with a cutaway view in Fig. 14.4b, was constructed in a prolate spherical coordinate system and consisted of 16 × 5 × 1 (longitudinal × transmural × circumferential) cubic hermite elements. Myofiber angles were assigned at the

nodes, and rotated from the circumferential direction by 60° at the endocardium and –60° at the epicardium, as previously described [10]. The non-linear, anisotropic stress–strain properties, as well as the time-varying elastance model of active contraction, have been previously described with the strain energy relation given in Chapter 3.

In order to simulate the weakly contracting ventricle of the failing heart, the active force at end-systole was reduced by changing the Ca_0 parameter, which governs the myofiber force–length curve, and can be loosely interpreted as a reduction in calcium handling in the heart. This parameter was varied to produce a final EF of approximately 30%, indicative of a weakly contracting, failing, ventricle and comparable to the in vivo measurements.

The baseline model of the failing heart was then modified to evaluate the effects of adding axisymmetric bands of non-contractile material into the ventricle. The bands were placed at one location in the ventricle midwall (Fig. 14.4c), as well as four bands along the longitudinal direction of the ventricle (Fig. 14.4d). For these simulations, the selected elements in the middle of the heart wall had contractility eliminated and the material properties modified, while the endocardial wall of the LV was deformed so that the total myocardial active wall volume remained constant after the mesh changes. Simulations were run with the total added volume ranging from 1 mL to 6 mL for the single band, and 0–8 mL for the four-band model. In addition to placement and volume studies, this type of analysis was also used to examine the role that the stiffness of added material has on the LV stress field.

Addition of passive material alters the predicted geometry at end-diastole and end-systole. Small changes in diastolic expansion (Fig. 14.5) are seen with volumes of even low stiffness, and changes in base-to-apex lengthening are observed at both end-diastole and end-systole. Mean stress is reduced in the ventricle, at both end-diastole and end-systole. By modeling the non-contractile material as discrete elements, this allows one to separate out the decrease in stress in the myocardial elements alone versus the entire mesh (Fig. 14.6). This is important, as decreases in myocardial stress are the desired effect of the implantation. It can be seen that the mean myofiber stress decreases as the volume of non-contractile material increases. The addition of multiple bands also result in a decrease in mean myofiber stress, but produce a much more complex stress field in the region around the non-contractile material.

The main purpose of this work was to quantify the effect of added material on end-diastolic and end-systolic myofiber stress distributions. Such models are useful as they allow better control over the addition of material compared to those in the previous section. With discrete elements of added material, individual mechanical properties can be assigned, and stress can be output for only the myocardium elements, instead of the lumped approach that does not differentiate between myocardium and added material. Simulation output indicates that addition of polymeric material into myocardium can acutely reduce myofiber stress in the failing LV. Thus, therapeutic use of such materials to reduce myofiber stress may be a beneficial strategy for treatment of advanced HF.

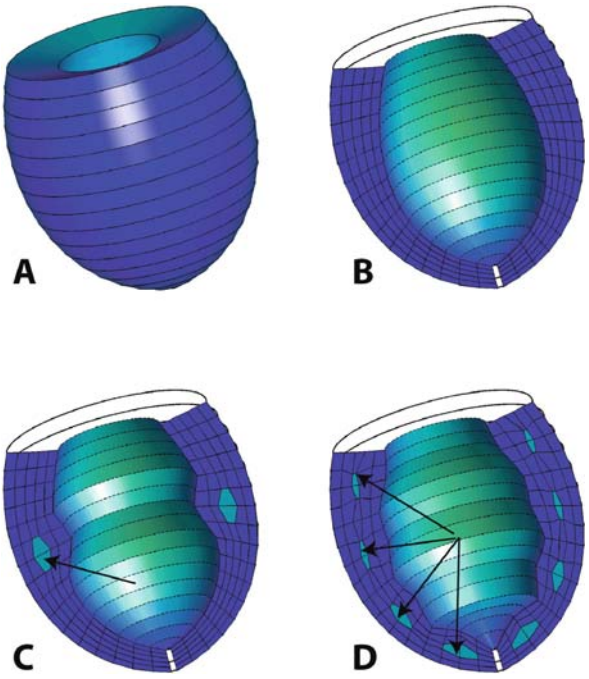

Fig. 14.4 Depiction of a simple axisymmetric FE model of the failing heart (**a,b**) with the addition of non-contractile material in one (**c**) and four (**d**) discrete axisymmetric bands

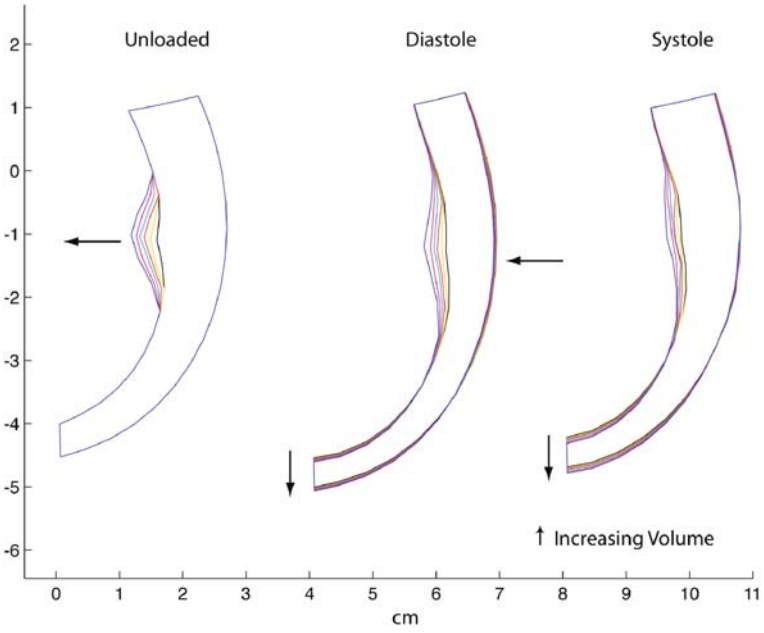

Fig. 14.5 Changes in ventricle motion with the addition of non-contractile material in a single midventricular band. Increasing added volume decreases the midventricular inflation during diastole, and increases apical lengthening during both diastole and systole

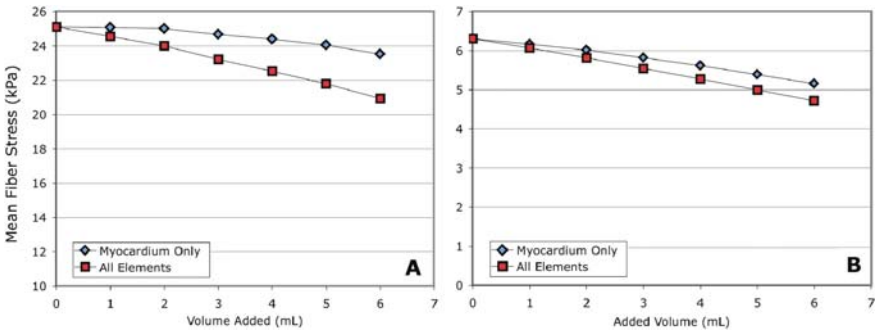

Fig. 14.6 Changes in LV midwall myofiber stress, (**a**) end-systole and (**b**) end-diastole, as a function of added volume for a single band of added material. Mean volume-weighted stress is plotted for both the entire FEM mesh, as well as for only myocardial elements

14.4 A Method for Automatically Optimizing the Pattern of Injected Non-contractile Material for Treating Heart Failure

Novel treatments involving the injection of polymeric materials into the myocardium of the failing LV are currently being developed which may reduce elevated myofiber stresses during the cardiac cycle and retard the progression of HF [5]. The objective of the present study is to develop an FE simulation-based optimization that can automatically determine the most effective injection pattern of the polymeric "inclusions". Moreover, this automatic optimization method should be applicable to the design of any novel medical device for treating HF [11].

The FE models used in the optimization were generated using the scheme described in Chapter 1. In this case, the injections are modeled as discrete spherical inclusions with a fixed volume of roughly 0.18 mL, rather than bands like the previous section. The number of inclusions in the longitudinal and circumferential directions was chosen as the design parameter in the trial run of the optimization. The number of inclusions in the longitudinal direction varied between 1 and 3, whereas the number of inclusions in the circumferential direction varied between 1 and 10. No inclusions were placed in the septal region of the LV. Nearly incompressible, transversely isotropic, hyperelastic, constitutive laws for passive and active myocardium were modeled in a user-defined material subroutine in the FE solver, LS-DYNA (Livermore Software Technology Corporation, Livermore, CA). The material response is described in detail in Chapter 3. The commercial optimization software, LS-OPT (Livermore Software Technology Corporation, Livermore, CA), uses a systematic search methodology to automatically explore the parameter space and find an optimum design. LS-OPT is based on the successive response surface method (SRSM). For further details on the optimization scheme see [11, 12].

The focus of this work is to generate a robust, simulation-based, optimization scheme for determining the injection pattern that minimizes the mean end-diastolic

and end-systolic myofiber stress throughout the LV myocardium, as well as maximizes LV stroke volume (difference between end-diastolic and end-systolic volume). It should be noted that the stress and volume are normalized, such that each term in the objective function has the same magnitude. The influence of each term in the objective function is controlled by adjusting the respective weight factors described below.

The initial optimization only examined the effects of minimizing mean myofiber stress (with $w_{SV} = 0$, weight factor for stroke volume). The results corresponding to several of the simulated patterns, shown in Fig. 14.7, are given in Table 14.1. The optimal pattern was found to contain the maximum number of inclusions, which are three in the longitudinal direction and ten in the circumferential (3 by 10), as shown in Fig. 14.7c. For the optimal pattern the predicted mean end-diastolic stress is 2.80 kPa and the end-systolic stress is 21.43 kPa. The difference between the predicted stress from the optimization and the stress computed from the FE simulation is less than 1% for the 3 by 10 pattern.

In the case of no inclusions in the myocardium, the mean myofiber stress at end-diastole is 3.28 kPa and at end-systole is 22.5 kPa. Thus, the optimal pattern reduces the mean stress by 0.491 kPa (15%) and 1.11 kPa (5%) for end-diastole and end-systole, respectively. The decrease in stress occurs locally near the inclusions, but

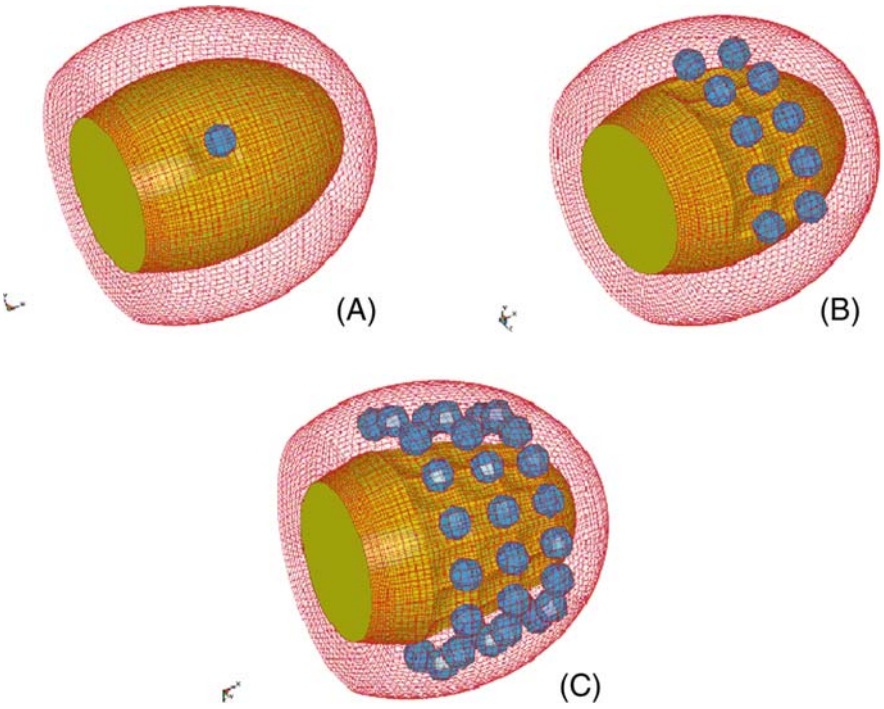

Fig. 14.7 Sampling of designs used for optimization, with injection patterns for the (**a**) 1 by 1 model, (**b**) 2 by 5 model, and (**c**) 3 by 10 model

Table 14.1 Mean myofiber stress for tree sample designs computed from FE simulations used in the optimization

Design point	Number of longitudinal	Number of circumferential	Mean end-diastolic stress (kPa)	Mean end-systolic stress (kPa)
A	1	1	3.275	22.481
B	2	5	3.117	22.088
C	**3**	**10**	**2.785**	**21.380**

Minimum myofiber stress is shown in bold

this leads to a reduction in the global mean stress in the myocardium. Cross-sections of the myofiber stress distribution for the pattern of 2 by 5 are shown in Fig. 14.8. It can be seen that the stress at the endocardium, near the inclusions, is reduced relative to the surrounding wall. This is due to the thickening effect that is produced by the inclusions. The reduction in stress that is caused by a single inclusion is amplified when more are added.

The overall influence of varying the two design parameters, in the initial optimization, is outlined in [11]. It was observed that as the number of inclusions increases, the mean myofiber stress in the LV decreases. This trend occurs at both end-diastole and end-systole. Additionally, the reduction in mean myofiber stress is greater when the maximum number of inclusions is used in the circumferential direction, rather than the longitudinal. This is because there is more space in the LV wall to add inclusions in the circumferential direction.

While the result of the initial optimization is an intuitive one (i.e., the largest number of inclusions represents the minimal mean myofiber stress), this verifies that the optimization scheme is functional. Such a method is valuable for quantifying the precise amount of stress reduction per inclusion. However, it is preferable to reduce stress without negatively impacting the pump function of the LV. Thus, a second optimization was conducted with $w_{ED} = w_{ES} = 0.25$ (weight factors for end-diastolic and end-systolic stress) and $w_{SV} = 0.5$ as a specific compromise between maximizing reductions in end-diastolic and end-systolic mean myofiber stress while minimizing a reduction in stroke volume. The second optimization resulted in a pattern of 2 by 1 as an optimal pattern, which is not an intuitive result at all. To confirm that changes in the weighting factors produce unintuitive relative results, a third optimization was conducted with $w_{ED} = w_{ES} = 0.285$ and $w_{SV} = 0.43$. The result was an optimal pattern with more inclusions, which was 3 by 1. These results imply that the optimal pattern produced by the optimization is sensitive to the influence of the selected weight factors. In addition, assessing the influence of stress and stroke volume together produces a result that deviates from the maximum or minimum number of inclusions.

Ongoing and future studies will add more design parameters to the optimization problem, with emphasis placed on the shape and size of the inclusions. In addition, the effects of the inclusions on the contractility of the myocardium will be explored

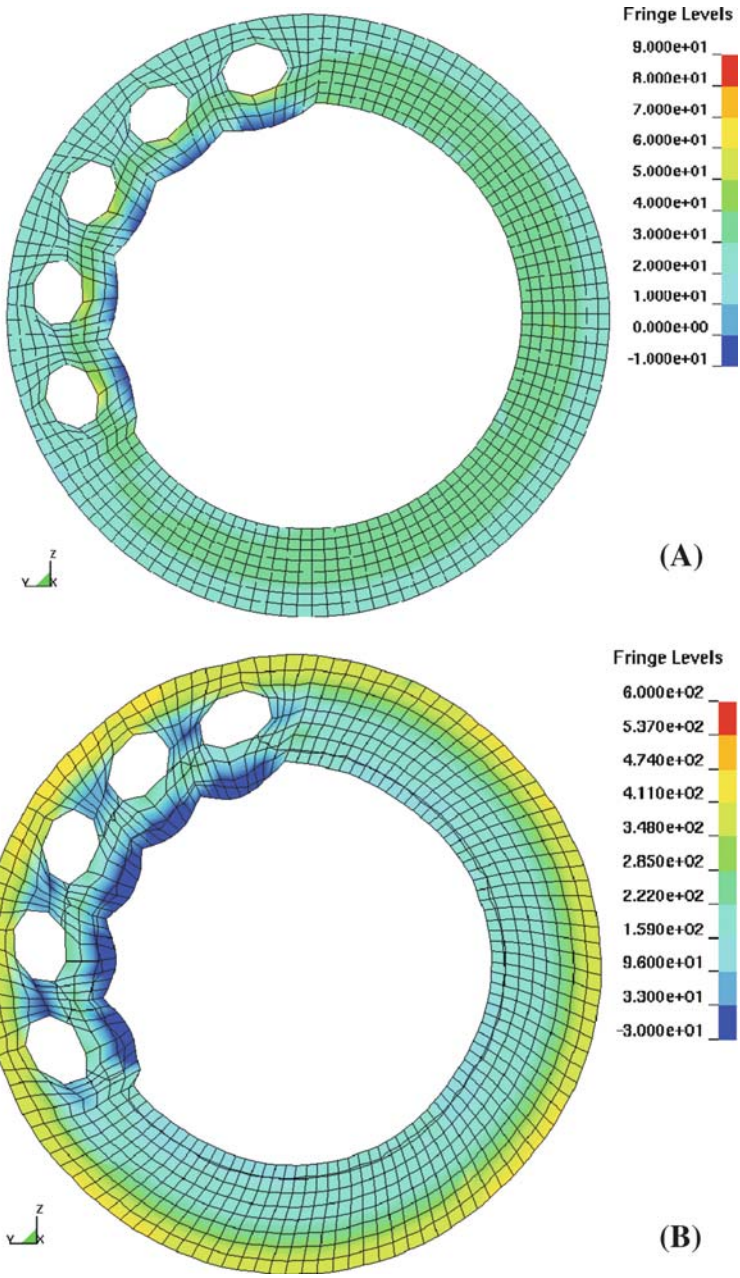

Fig. 14.8 Myofiber stress distribution at midventricle with an injection pattern of 2 by 5: (**a**) end-diastolic myofiber stress, and (**b**) end-systolic myofiber stress

by locally altering the material properties around the inclusions. MRI tagging of beating hearts before and after injection would help determine if myocardial material properties are affected by this treatment. This data can then be used to help determine the proper weight factors.

Acknowledgments The initial research was supported by National Institutes of Health grant 5R01 HL077921 (Dr. Guccione). We want to thank CardioPolymers, Inc. for providing additional funding for this research (Drs. Guccione, Wall and Wenk).

References

1. American Heart Association. Heart and Stroke Statistical Update, 2008
2. Yu J, Christman KL, Chin E, Sievers RE, Saeed M, Lee RJ. Restoration of left ventricular geometry and improvement of left ventricular function in a rodent model of chronic ischemic cardiomyopathy. *J Thorac Cardiovasc Surg*. 2009 Jan;137(1):180–7.
3. Kofidis T, Lebl DR, Martinez EC, Hoyt G, Tanaka M, Robbins RC. Novel injectable bioartificial tissue facilitates targeted, less invasive, large-scale tissue restoration on the beating heart after myocardial injury. *Circulation*. 2005;112:I173.
4. Quarterman RL, Moonly S, Wallace AW, Guccione J, Ratcliffe MB. A finite element model of left ventricular cellular transplantation in dilated cardiomyopathy. *ASAIO J*. 2002 Sep–Oct;48(5):508–13.
5. Wall ST, Walker JC, Healy KE, Ratcliffe MB, Guccione JM. Theoretical impact of the injection of material into the myocardium: a finite element model simulation. *Circulation*. 2006 Dec 12;114(24):2627–35. E-pub 2006 Nov 27.
6. Walker JC, Ratcliffe MB, Zhang P, Wallace AW, Fata B, Hsu EW, Saloner D, Guccione JM. MRI-based finite-element analysis of left ventricular aneurysm. *Am J Physiol Heart Circ Physiol*. 2005;289:H692.
7. Guccione JM, Costa KD, McCulloch AD. Finite element stress analysis of left ventricular mechanics in the beating dog heart. *J Biomech*. 1995 Oct;28(10):1167–77.
8. Wall ST, Wenk JF, Peterson RC, Helgerson SL, Sabah HN, Ratcliffe MB, Guccione JM. Implantation of polymeric material into the globally failing left ventricle reduces pathologic myofiber stress – a finite element model simulation. *Ann Biomed Eng*. (submitted).
9. Sabbah HN, Shimoyama H, Kono T, Gupta RC, Sharov VG, Scicli G, Levine TB, Goldstein S. Effects of long-term monotherapy with enalapril, metoprolol, and digoxin on the progression of left ventricular dysfunction and dilation in dogs with reduced ejection fraction. *Circulation*. 1994;89(6), 2852–9.
10. Streeter DD Jr, Spotnitz HM, Patel DP, Ross J Jr, Sonnenblick EH. Fiber orientation in the canine left ventricle during diastole and systole. *Circ Res*. 1969 Mar;24(3):339–47.
11. Wenk JF, Wall ST, Peterson RC, Helgerson SL, Sabah HN, Burger M, Stander N, Ratcliffe MB, Guccione JM. A method for automatically optimizing medical devices for treating heart failure: designing polymeric injection patterns. *J. Biomech. Eng*. accepted manuscript, doi:10.1115/1.4000165
12. Stander N, Roux W, Eggleston T, Craig K. LS-OPT user's manual version 3.2. Livermore, CA: Livermore Software Technology Corporation, 2007.

Chapter 15
Computational Modeling of Heart Failure with Application to Cardiac Resynchronization Therapy

Roy C.P. Kerckhoffs and Lawrence J. Mulligan

Abstract In recent years, cardiac resynchronization therapy (CRT) has become an effective and popular approach to the treatment of heart failure with a conduction disturbance, but it is unclear why 30% of patients do not respond. With improvements in computer power, diagnostic and therapeutic medical technologies, it is increasingly feasible to apply patient-specific modeling to guide and predict the response to CRT. In this chapter we discuss strategies as to how computational modeling of CRT could be used to try to predict the outcome of this therapy patient-specifically.

15.1 Introduction

The heart has a strong ability to adapt its cardiac output to a change in demand of blood. In the short term – within seconds – the heart can quickly increase its beating rate and strength of contraction as a response to exercise, thus increasing its output. It can do this because of signals it receives from the brainstem and sensing an increase in certain hormones circulating in the blood stream. In the long term – days to months – the heart can increase its left and right cavity volumes and thicken its walls when a more chronic increase in demand is needed (as in the athlete's heart). However, the normal functioning of the heart can be disturbed by, for example, an infarct – when a part of the wall does not receive enough oxygen due to a coronary occlusion – or by conduction disorders, such as left bundle branch block (LBBB). During the latter disturbance, the septal and lateral walls contract out of phase. In addition, the right ventricle and left ventricle also contract out of phase. The development of the dyssynchronous contraction creates a stimulus for several maladaptive events to begin.

R.C.P. Kerckhoffs (✉)
Department of Bioengineering, University of California San Diego, La Jolla, CA, USA
e-mail: roy@bioeng.ucsd.edu

J.M. Guccione, et al. (eds.), *Computational Cardiovascular Mechanics*,
DOI 10.1007/978-1-4419-0730-1_15,

15.1.1 Heart Failure

Heart failure (HF) is a condition when the heart fails to keep up with the amount of blood that is demanded by the body. Additional abnormalities – on top of the disorder that caused failure – may worsen cardiac function. In dilated cardiomyopathy, the ventricular walls become thinner, cavities enlarge, and venous pressures increase. At the cellular level, the cardiac action potential is prolonged, the transient outward and inward rectifier potassium currents are downregulated, and responsiveness to β-adrenergic stimulation is decreased [1]. Magnitude and relaxation of calcium transients are reduced and prolonged, respectively, resulting in altered contractile function, such as reduced myofiber peak force and prolonged relaxation [2, 3]. If left untreated, premature myocardial cell death may occur.

15.1.2 Dyssynchronous Heart Failure

Patients with HF and dyssynchronous mechanical contraction have among the worst overall prognosis and left ventricular (LV) dysfunction of all HF patients [4]). These patients can often see significant clinical and functional improvement following cardiac resynchronization therapy (CRT). CRT requires that a pacing lead is placed in the LV venous anatomy along with leads in the right ventricle and right atrium. This form of ventricular pacing is used to restore a more synchronous mechanical activation pattern. Currently, patients indicated for CRT have severe HF (New York Heart Association functional Class III or IV) and a QRS duration of more than 120 ms. Indeed, CRT acutely enhances cardiac function [5] and, in the longer term, can result in beneficial smaller cavity volumes and thicker walls (referred to as reverse ventricular remodeling) in responders [6–8]. CRT has also been seen in studies to increase quality of life and reduce mortality [9, 10].

However, 30% of patients receiving a CRT system do not respond. There appears to be an enhanced lack of response to those with post-infarct myocardial scar. The relationship between electrical and mechanical activation – which does not appear to be one-to-one [11] – may be complicated by the presence of scar. Clinically it has been shown that QRS widening is not a reliable predictor of mechanical dyssynchrony and LV dysfunction [12, 13], but that there exists a strong correlation between mechanical synchrony and global LV function [13]. In the longer term, it has been shown that synchronicity of contraction is an accurate independent predictor of reverse remodeling [14], even in the presence of transmural scar [15]. A large clinical trial is required to understand how scar impacts short- and long-term clinical and functional outcomes.

Moreover, there are no well-defined criteria for predicting outcomes or selecting pacing sites and protocols. These criteria include improvements in the distance walked in 6 min, in the peak oxygen utilization during exercise, and a decrease in LV end-systolic volume. Although these factors make it difficult to optimally select patients for CRT, this remains of paramount importance to reduce unnecessary implants, procedural risks, and healthcare expenses.

15.1.3 Patient-Specific Modeling

A new approach to CRT – and to medicine in general – might arise from the maturation of computational biology. During the last 5–10 years, improvements in diagnostic medical technologies such as multi-slice cardiac CT imaging and 3D electroanatomic mapping, combined with more powerful computing and more accurate predictive models, [17] have made it increasingly feasible to begin developing multi-scale patient-specific models that may help inform diagnosis, guide therapy or surgery, and predict outcomes, at least acutely. Indeed, in recent years there have been notable successes in patient-specific modeling in areas such as musculoskeletal [18, 19] and vascular [20] surgery. Such models will also provide pathophysiologic insights from cell to tissue to organ system, and therefore help to understand why specific interventions succeed or fail.

Therefore, this chapter focuses on computational modeling of cardiac electromechanics, applied to patient-specific CRT.

15.2 Computational Modeling of Cardiac Electromechanics

The patient-specific heart model should generate output that will predict successfully the outcome of CRT, and thus aid the cardiologist in his/her decision-making. This means that the model should contain key components that will influence model output. An important factor in predicting the outcome of CRT, in patients with HF and wide QRS, is mechanical synchrony of contraction in the ventricular walls (see Section 15.1). Logically, the model would include ventricular geometry and fiber architecture. The latter is important because of the distinct orientation of fibers in the heart, which affects both impulse conduction and mechanical contraction. Secondly, because ventricular pacing changes the electrical activation pattern, another important component is an impulse conduction model, in which conservation of current needs to be satisfied. Thirdly, to calculate synchrony of mechanical contraction, the model needs passive mechanical and myofiber contractile properties. And finally, because the heart pumps blood, a model of the closed circulation is needed. The coupling of a circulation model with a model of the ventricles allows for the quantification of pump function through stroke volumes, rate of change of LV pressure, and end-diastolic pressures and volumes.

15.2.1 Ventricular Anatomy and Fiber Architecture

Patient-specific ventricular anatomy can be obtained with computed tomography (CT, Fig. 15.1), preferably with cardiac contrast, or with magnetic resonance imaging (MRI, Fig. 15.2). Ventricular endocardial and epicardial surfaces (Figs. 15.3 and 15.4) can be mapped onto the nearest point on the surfaces of ellipsoidal finite

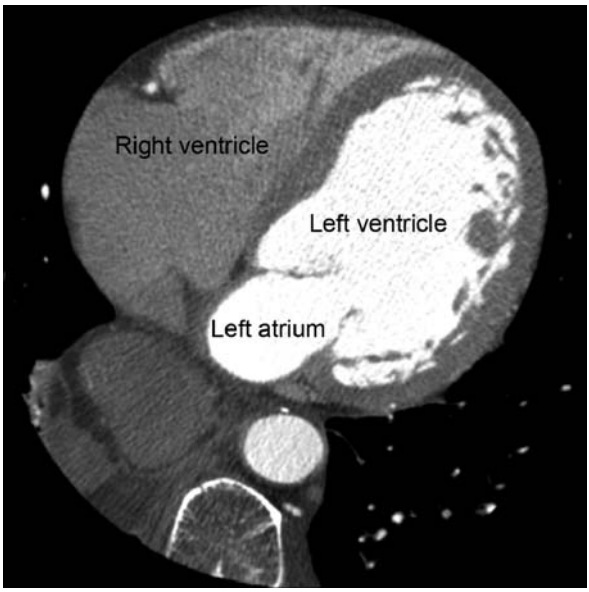

Fig. 15.1 CT image of a patient's heart (taken at the Veterans Affairs Medical Center, San Diego, California) with ischemic and dilated cardiomyopathy and left bundle branch block, showing the left ventricle (with contrast), right ventricle, and left atrium

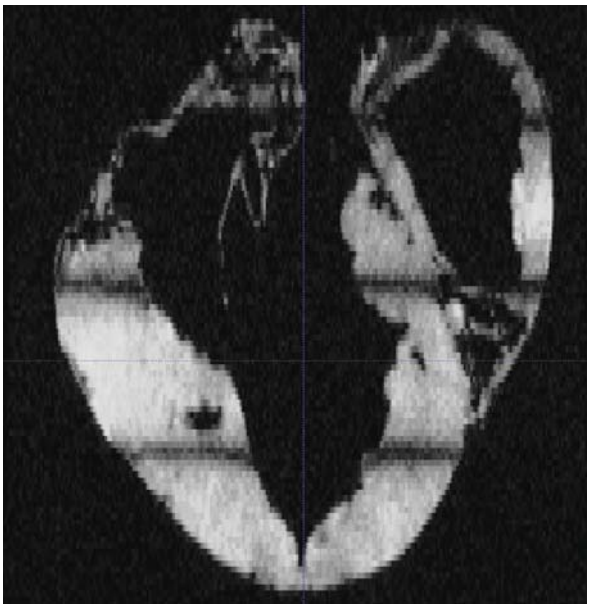

Fig. 15.2 Magnetic resonance image of a longitudinal cross-section of a dog's heart

element meshes and fitted using finite element least squares methods [21] with root mean square error lower than 1 mm. The meshes thus generated will serve as the

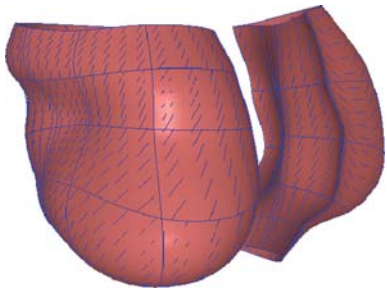

Fig. 15.3 Left and right ventricular endocardial surfaces of a patient with HF, fitted to a CT data set (Fig. 15.1). A fiber data set has been mapped to the mesh surfaces

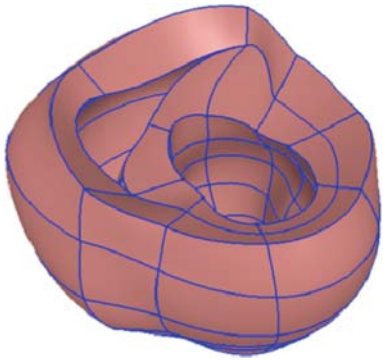

Fig. 15.4 Higher-order finite element mesh of a normal dog heart, fitted to a MRI data set (Fig. 15.2)

domain to solve for impulse conduction in the model of electrophysiology and force equilibrium in the model of cardiac mechanics.

Not all data can be obtained patient-specifically, such as fiber architecture. Fortunately, this seems to be fairly highly conserved across individuals and species, at least when geometric variations are accounted for [22]. Fiber architecture can only be obtained accurately post-mortem with diffusion tensor MRI (DTMRI) or histologically. Therefore, cardiac fiber angles can be taken from existing databases (for example, the Johns Hopkins University public database http://www.ccbm.jhu.edu/research/dSets.php) of a human heart measured with DTMRI. The fiber architecture will be morphed into the already obtained patient-specific ventricular geometry [23]. Fiber architecture defines material reference axes for anisotropic electrical conductivities and mechanical properties in the models of impulse conduction and biomechanics, respectively.

15.2.2 Impulse Conduction

There are several ways of obtaining information on a patient's ventricular electrical activation pattern. The easiest, but least accurate, would be to use the electrocardiogram (ECG). The ECG contains global information on activation patterns (for

example LBBB or RBBB) and total ventricular activation time. Conductivities and origin of impulse conduction can be adjusted in the model (i.e., for models of impulse conduction see [24–27]) such that modeled and measured QRS complex match. This is a crude approach since little is known about regional activation.

A better approach is to measure endocardial electrical activation in both ventricles, obtained using clinical electroanatomic mapping tools. Electroanatomic mapping [28] has proven utility for this purpose in subjects with HF. With this technique, the cardiologist digitizes several hundred locations and activation times on the endocardium using a catheter. The disadvantage is the invasive nature. From these maps, earliest activated regions serve as external stimuli in the model, and conductivities are adjusted to minimize errors between mapped and predicted endocardial activation patterns. The model will "fill in" the activation of the remaining myocardium.

A third approach is to solve inversely for epicardial activation from body surface potentials measurements [29]. Electrocardiographic imaging (ECGI) is a modality for noninvasive epicardial mapping [30] using body surface potentials and CT measurements of torso and heart geometry. This means that also a model of the torso is necessary in order to inversely calculate potentials on the ventricular epicardium (inverse model). Then, in the ventricular model of impulse conduction (forward model), stimuli locations and conductivities need to be estimated that will minimize the differences between the calculated epicardial potentials from the inverse and forward models.

The activation patterns thus obtained are then used to activate fibers in the cardiac mechanics model.

15.2.3 Cardiac Mechanics

For most biological tissue, there exists a large variety in values of material properties. This also applies to normal (non-failing) hearts, but is accentuated in the failing heart where a large variety of alterations in (mechanical and geometric) cellular properties have been demonstrated in which active properties such as peak force is reduced, force–frequency relation is depressed, and relaxation prolonged [2, 31, 32]. Increase in passive mechanics has also been reported due to alterations of the cytoskeleton [33, 34]. Therefore, material properties for passive and active mechanics also need to be determined patient-specifically, for these properties are continuously changing with HF stage [33].

In the model, passive mechanics can be described by an exponential anisotropic strain-energy function. This strain-energy function contains parameters for scaling the magnitude of the stress, (in)compressibility, and several parameters for handling the anisotropy of the tissue. Cardiac anisotropy can be modeled to be transversely isotropic or orthotropic [35]. Active stress can be described with, for example, a time-varying stiffness model which is dependent on time, sarcomere length, and intracellular calcium concentration (Fig. 15.5) [36] or in more detail with a model of excitation-contraction coupling [1, 37].

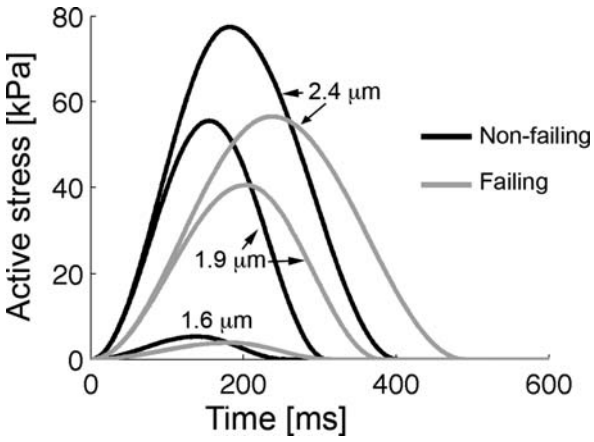

Fig. 15.5 Isometric fiber active stress as a function of time at three sarcomere lengths (1.6 μm, 1.9 μm and 2.4 μm) from a dog model with a non-failing (*black*) and failing (*gray*) heart [52]. The properties for the failing heart were based on force measurements on human trabeculae [63]

An estimation of (regional) material properties can be obtained from global measurements of ventricular volumes and pressures or from regional measurements such as MRI tagging.

15.2.3.1 Estimation of Properties from Global Measurements

Cardiac 2D ultrasound and LV pressure recordings provide dynamic ventricular pseudo-volumes and pressures, respectively. From the 2D echo images LV volumes can be calculated [38]. Accuracy of cavity volumes estimation from 2D echo images will be enhanced, because LV cavity volume is known from the 3D CT or MRI data, necessary for ventricular geometry. From these measurements, pressure–volume loops can be constructed. End-diastolic pressures and volumes are used to determine the diastolic relation between LV volumes and pressures (EDPVR) [39]. Volume-normalized EDPVRs, by appropriate scaling of LV volumes, have a common shape, despite different etiology and species (tested on human, canine, and rat hearts). For this technique, the root mean square error in pressure between measured and predicted EDPVRs over the range of 0–40 mmHg was 3 mmHg of measured EDPVR in all settings. This allows the entire end-diastolic pressure–volume curve to be predicted from only a few measurements.

For end-systole a similar approach has been developed, obtaining the end-systolic pressure and volume relation (ESPVR) [40]. It has been shown that single-beat estimations of the ESPVR is only reasonably accurate [41]. However, a more accurate ESPVR can be obtained from different end-systolic pressures and volumes by inducing a premature ventricular contraction, which is a common clinical approach to change ventricular preload, by means of altering the program of the pacemaker.

Having obtained the diastolic and systolic LV pressure–volume relation, passive and active mechanical material properties can be estimated as follows. The mechanical parameter estimation procedure has been published before, applied to a model of sheep cardiac mechanics [42]. Initial mechanical parameters are available

in the literature [43]. Next, the model of cardiac mechanics, in which 3D geometry is patient-specific, will be inflated passively and when it is fully active. This will yield the EDPVR and ESPVR for the model. The passive stress-scaling factor, passive exponential shape coefficient, and active stress-scaling factor in the model are then iteratively adjusted until the sum-of-squared differences between the clinically obtained pressure–volume relations and those from the model are smaller than a predetermined value.

15.2.3.2 Estimation of Properties from Regional Measurements

In cardiac MRI tagging, the heart is "tagged" with a spatially alternating pattern of magnetic saturation, visibly on MR images as alternating light and dark lines or checkerboard pattern [44]. From these tagged images, strains can be calculated [45–47], providing information on regional deformation of the tissue [48]. Walker and coworkers [42] have used a combination of MRI tagging and finite element modeling to determine sheep active material properties, in the presence of a myocardial scar. Cardiac circumferential, longitudinal, and radial strains in the LV midwall were calculated using the 4D spline method [46].

Meshes of the left ventricle were fitted to the geometry at end-isovolumic relaxation. Passive and active material properties were estimated specifically for each sheep, using an iterative approach, such that measured and calculated ventricular volumes and strains matched. First, the passive and active stress scaling coefficients were estimated such that end-diastolic and end-systolic volumes, respectively, were reproduced in the model for a given end-diastolic and end-systolic pressure. Next, the remaining coefficients in the passive strain-energy law that determine anisotropy were estimated such that the error between model and MR tagging strains was minimized.

15.2.4 Scar Tissue

A part of the cardiac wall becomes ischemic when a coronary artery that normally perfuses this region, becomes occluded. If left untreated, cardiac cells die and are replaced by collagen fibers, forming scar tissue. The infarct expands, thins, and over time, dead tissue is continuously resorbed and replaced with scar tissue [49]. Because of the increase in collagen density, the passive stiffness increases in that region, and since remodeling is an ongoing process, so does the passive stiffness change over time. Because myocardial cells are – mostly – absent in the scarred region, the generation of active stress is zero or almost zero (Fig. 15.6) and impulse propagation is much slower. Thus, the mechanical and electrical properties of scarred tissue are important determinants of regional (Fig. 15.7) and global cardiac function.

More than 50% of patients eligible for CRT show some degree of scar formation as a result of a prior myocardial infarct [50]. The location of scar tissue [51] or the degree of mechanical synchronization that can be obtained due to the location of the

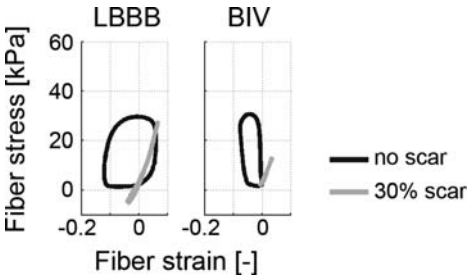

Fig. 15.6 Fiber stress–strain loops in the anterior LV free wall obtained from a canine model of failing cardiac electromechanics [52] with (*black*) and without scar (*gray*). Note the larger area of the *black* loop during left bundle branch block (LBBB, *left*) due to later activation than during biventricular pacing (BIV, *right*). In the simulation with the scar, the scar extended into this region. Therefore, the fibers in this region were passively stretched (*gray*), causing the disappearance of the loop

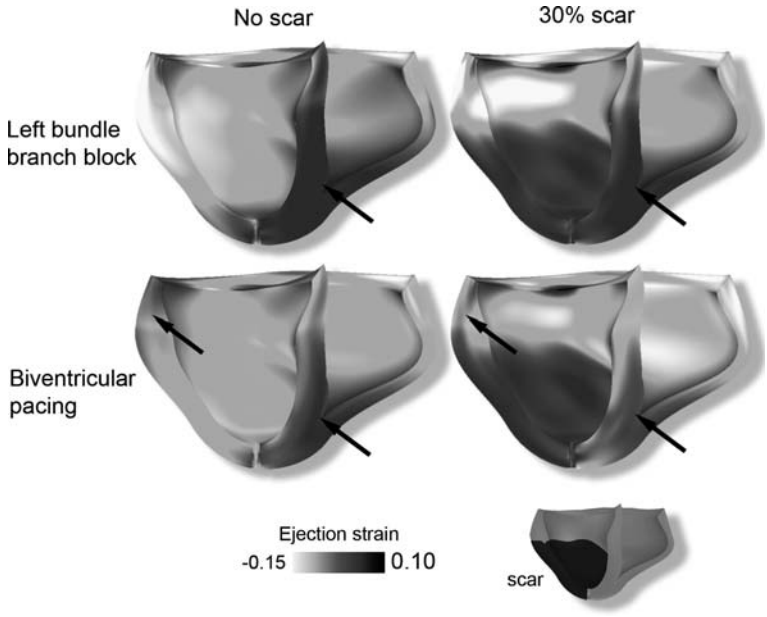

Fig. 15.7 Fiber strain during the ejection phase in a longitudinal cross-section (view is from posterior to anterior) of a canine model of electromechanics [52] without (*left*) and with (*right*) scarred tissue during left bundle branch block (*top*) and biventricular pacing (*middle*). *Arrows* denote the origin of stimulus. Note the more uniform strains during biventricular pacing without scar compared with LBBB without scar. In the hearts with scar, ejection strain is slightly positive in the scarred region. The strain pattern is less non-uniform in the LV with biventricular pacing compared with the LV with LBBB

pacing site with respect to the scar [15, 52] might be important determinants for the success or failure of CRT.

Therefore it is also important to obtain information on location, size, and electrical and mechanical properties of scar tissue and include these in the patient-specific model. Location and size can be determined from gadolinium-enhanced MRI or endocardial electroanatomical mapping. For the latter, scar will manifest itself as reduced magnitudes of measured potentials. This will also provide information on how, if at all, the impulse conducts through scar. Passive, and possibly active, mechanical properties can be estimated from MRI tagging [42].

15.2.5 Hemodynamics

Embedding the finite element model of the heart in a closed circulation allows for more realistic hemodynamic boundary conditions and for investigating steady-state conditions [53]. In order to save calculation time, lumped parameter systems models are preferred, of which several have been published in literature [54, 55]. One of these models is the "CircAdapt" model of the circulation [56]. This a model of the circulation that makes use of adaptation rules of the blood vessels in order to estimate resistance and compliance parameter values throughout the circulation patient-specifically. These calculations are not compute-intensive but have been shown to give good parameter estimates for a variety of clinical indications. In these adaptation rules, a locally sensed signal results in a local action of the tissue. The applied rules include dilation of the vessel wall due to flow shear stress (affecting resistance and compliance), whereas tensile stress thickens the wall (affecting compliance). This technique reduces the number of model parameters that need to be determined [57].

15.3 Model Prediction of CRT

The models need to be designed according to the native, dyssynchronous state of the patient's heart. The models can be validated by comparing the ventricular pacing results of the model with those obtained from the patient's measurements when the pacemaker was turned on – if available. Thus, the patient-specific models are tested by their ability to predict the observed short-term functional improvements seen in the recruited patients following CRT, whether clinically successful or not.

Long-term results can be predicted from the strong correlation that has been shown to exist between synchronicity of contraction and reverse remodeling [14]. The models provide contraction patterns throughout the cardiac walls, from which outputs of regional function can be calculated, just as in the clinic [58, 6, 14]. Among others, these outputs can include synchronicity of mechanical contraction [14], the CURE index [59], and variance of fiber strain [60]. These indices have been used before in models to assess regional function [57, 61, 52].

Although acute parameters may accurately predict long-term outcome, another useful application to enhance the predictive capabilities of patient-specific models after an intervention is the implementation of adaptation algorithms [62]. Developmental processes involve the growth, change of material properties (remodeling), and shape changes (morphogenesis) of tissues, which are controlled by biochemical signals. However, relatively few theoretical models have been published for adaptation of the heart, most of all because current modeling efforts suffer from a lack of experimental data required for adequate testing. Until such data become available, most models of adaptation can be only speculative. For an overview of these types of models see Taber [62].

Whenever possible, long-term model predictions should be validated by comparison against clinical follow-up. If model predictions and clinical follow-up are not congruent, components of the patient-specific model may be oversimplified. If so, these inadequate components should be replaced with more detailed models that may require additional measurements.

Acknowledgments This research was supported in part by Medtronic, UC Discovery Grant ITL06-10159, and the National Biomedical Computation Resource (NIH grant P41 RR08605). This investigation was conducted in part using a facility constructed with support from Research Facilities Improvement Program Grant Number C06 RR-017588-01 from the National Center for Research Resources, National Institutes of Health. We thank Drs. Sanjiv Narayan, MD and David Krummen, MD for providing the CT images.

References

1. O'Rourke B, Kass DA, Tomaselli GF, Kääb S, Tunin R, Marbán E. Mechanisms of altered excitation–contraction coupling in canine tachycardia-induced heart failure, I: experimental studies. *Circ Res*. 1999;84:562–70.
2. del Monte F, O'Gara P, Poole-Wilson PA, Yacoub M, Harding SE. Cell geometry and contractile abnormalities of myocytes from failing human left ventricle. *Cardiovasc Res*. 1995;30:281–90.
3. Pieske B, Kretschmann B, Meyer M, Holubarsch C, Weirich J, Posival H, Minami K, Just H, Hasenfuss G. Alterations in intracellular calcium handling associated with the inverse force–frequency relation in human dilated cardiomyopathy. *Circulation*. 1995;92:1169–78.
4. Kass DA. Cardiac resynchronization therapy. *J Cardiovasc Electrophysiol*. 2005;16:S35–41.
5. Kass DA, Chen CH, Curry C, Talbot M, Berger R, Fetics B, Nevo E. Improved left ventricular mechanics from acute VDD pacing in patients with dilated cardiomyopathy and ventricular conduction delay. *Circulation*. 1999;99:1567–73.
6. Bax JJ, Abraham T, Barold SS, Breithardt OA, Fung JWH, Garrigue S, Gorcsan J, Hayes DL, Kass DA, Knuuti J, Leclercq C, Linde C, Mark DB, Monaghan MJ, Nihoyannopoulos P, Schalij MJ, Stellbrink C, Yu C-M. Cardiac resynchronization therapy. Part 1 – issues before device implantation. *J Am Coll Cardiol*. 2005;46:2153–67.
7. Saxon LA, De Marco T, Schafer J, Chatterjee K, Kumar UN, Foster E. Effects of long-term biventricular stimulation for resynchronization on echocardiographic measures of remodeling. *Circulation*. 2002;105:1304–10.
8. Stellbrink C, Breithardt OA, Franke A, Sack S, Bakker P, Auricchio A, Pochet T, Salo R, Kramer A, Spinelli J. Impact of cardiac resynchronization therapy using hemodynamically optimized pacing on left ventricular remodeling in patients with congestive heart failure and ventricular conduction disturbances. *J Am Coll Cardiol*. 2001;38:1957–65.

9. Bristow MR, Saxon LA, Boehmer J, Krueger S, Kass DA, De Marco T, Carson P, DiCarlo L, DeMets D, White BG, DeVries DW, Feldman AM. Cardiac-resynchronization therapy with or without an implantable defibrillator in advanced chronic heart failure. *New Eng J Med*. 2004;350:2140–50.
10. Cleland JGF, Daubert J, Erdmann E, Freemantle N, Gras D, Kappenberger L, Tavazzi L, Daubert JC, Klein W, Poole-Wilson PA, Ryden L, Wedel H, Wellens HJJ, Uretsky B, Thygesen K, Bocker D, Marijianowski MMH, Calvert MJ, Christ G, Fruhwald F, Hofmann R, Krypta A, Leisch F, Pacher R, Rauscha F, Tavernier R, Thomsen PEB, Boesgaard S, Eiskjaer H, Esperen GT, Haarbo J, Hagemann A, Korup E, Moller M, Mortensen P, Sogaard P, Vesterlund T, Huikuri H, Niemela KI, Toivonen L, Bauer F, Cohen-Solal A, Crocq C, Djiane P, Dubois-Rande JL, de Groote P, Juilliere Y, Kirkorian G, Komajda M, Laperche T, Le Marec H, Leclercq C, Tribouilloy C, Er F, Fleck E, Hoppe UC, Kleber FX, Maisch B, Neuzner J, Reithmann C, Remp T, Schmitt C, Stahl C, Strasser RH, Albanese MC, Bartoloni A, Bocchiardo M, Capucci A, Carboni A, Circo A, Disertori M, del Medico R, Forzani T, Frigerio M, Gavazzi A, Landolina M, Lunati M, Mangiameli S, Piacenti M, Piti A, Ravazzi PA, Raviele A, Santini M, Serio A, Trevi GP, Volterrani M, Zardini M, Bracke F, de Cock CC, Meijer A, Tukkie R, Mediavilla JC, Concha M, Delgado JF, Gonzalez-Garcia A, Munoz-Aguilera R, Ferrer JM, Ridocci F, Andren B, Brandt J, et al. The effect of cardiac resynchronization on morbidity and mortality in heart failure. *New Engl J Med*. 2005;352:1539–49.
11. Usyk TP, McCulloch AD. Relationship between regional shortening and asynchronous electrical activation in a three-dimensional model of ventricular electromechanics. *J Cardiovasc Electrophysiol*. 2003;14:S196–202.
12. Bleeker GB, Schalij MJ, Molhoek SG, Verwey HF, Holman ER, Boersma E, Steendijk P, Van der Wall EE, Bax JJ. Relationship between QRS duration and left ventricular dyssynchrony in patients with end-stage heart failure. *J Cardiovasc Electrophysiol*. 2004;15:544–9, doi:10.1046/j.1540-8167.2004.03604.x
13. Leclercq C, Faris O, Tunin R, Johnson J, Kato R, Evans F, Spinelli J, Halperin H, McVeigh E, Kass DA. Systolic improvement and mechanical resynchronization does not require electrical synchrony in the dilated failing heart with left bundle-branch block. *Circulation*. 2002;106:1760–3.
14. Yu C-M, Fung W-H, Lin H, Zhang Q, Sanderson JE, Lau C-P. Predictors of left ventricular reverse remodeling after cardiac resynchronization therapy for heart failure secondary to idiopathic dilated or ischemic cardiomyopathy. *Am J Cardiol*. 2002;91:684–8.
15. Jansen AHM, Bracke F, van Dantzig JM, Peels KH, Post JC, van den Bosch HCM, van Gelder B, Meijer A, Korsten HHM, de Vries J, van Hemel NM. The influence of myocardial scar and dyssynchrony on reverse remodeling in cardiac resynchronization therapy. *Eur J Echocardiogr*. 2008;9:483–8.
16. Bleeker GB, Holman ER, Steendijk P, Boersma E, van der Wall EE, Schalij MJ, Bax JJ. Cardiac resynchronization therapy in patients with a narrow QRS complex. *J Am Coll Cardiol*. 2006;48:2243–50, 10.1016/j.jacc.200607.067.
17. Kerckhoffs RCP, Narayan SM, Omens JH, Mulligan LJ, McCulloch AD. Computational modeling for bedside application. *Heart Fail Clin*. 2008;4:371–8.
18. Delp SL, Anderson FC, Arnold AS, Loan P, Habib A, John CT, Guendelman E, Thelen DG. OpenSim: open-source software to create and analyze dynamic simulations of movement. *IEEE Trans Biomed Eng*. 2007;54:1940–50.
19. Reinbolt JA, Haftka RT, Chmielewski TL, Fregly BJ. A computational framework to predict post-treatment outcome for gait-related disorders. *Med Eng Phys*. 2008;30:434–43.
20. Wilson NM, Arko FR, Taylor CA. Predicting changes in blood flow in patient-specific operative plans for treating aortoiliac occlusive disease. *Comput Aided Surg*. 2005;10:257–77.
21. Vetter FJ, McCulloch AD. Three-dimensional analysis of regional cardiac function: a model of rabbit ventricular anatomy. *Prog Biophys Mol Biol*. 1998;69:157–83.
22. Helm PA, Younes L, Beg MF, Ennis DB, Leclercq C, Faris OP, McVeigh ER, Kass DA, Miller MI, Winslow RL. Evidence of structural remodeling in the dyssynchronous failing heart. *Circ Res*. 2006;98:125–132.

23. Fernandez J, Hunter P. An anatomically based patient-specific finite element model of patella articulation: towards a diagnostic tool. *Biomech Model Mechanobiol*. 2005;4:20–38.
24. Henriquez CS. Simulating the electrical behavior of cardiac tissue using the bidomain model. *Crit Rev Biomed Eng*. 1993;21:1–77.
25. Rogers JM, McCulloch AD. A collocation-Galerkin finite-element model of cardiac action-potential propagation. *IEEE Trans Biomed Eng*. 1994;41:743–57.
26. Trayanova N. Discrete versus syncytial tissue behavior in a model of cardiac stimulation .1. Mathematical formulation. *IEEE Trans Biomed Eng*. 1996;43:1129–40.
27. Trew M, Le Grice I, Smaill B, Pullan A. A finite volume method for modeling discontinuous electrical activation in cardiac tissue. *Ann Biomed Eng*. 2005;33:590–602.
28. Yue AM, Franz MR, Roberts PR, Morgan JM. Global endocardial electrical restitution in human right and left ventricles determined by noncontact mapping. *J Am Coll Cardiol*. 2005;46:1067–75.
29. Jia P, Ramanathan C, Ghanem RN, Ryu K, Varma N, Rudy Y. Electrocardiographic imaging of cardiac resynchronization therapy in heart failure: observation of variable electrophysiologic responses. *Heart Rhythm*. 2006;3:296–310.
30. Ramanathan C, Ghanem RN, Jia P, Ryu K, Rudy Y. Noninvasive electrocardiographic imaging for cardiac electrophysiology and arrhythmia. *Nat Med*. 2004;10:422–8.
31. Phillips PJ, Gwathmey JK, Feldman MD, Schoen FJ, Grossman W, Morgan JP. Post-extrasystolic potentiation and the force–frequency relationship: differential augmentation of myocardial contractility in working myocardium from patients with end-stage heart failure. *J Mol Cell Cardiol*. 1999;22:99–110.
32. Pieske B, Hasenfuss G, Holubarsch C, Schwinger R, Bohm M, Just H. Alterations of the force–frequency relationship in the failing human heart depend on the underlying cardiac disease. *Basic Res Cardiol*. 1992;87:213–21.
33. Costandi PN, Frank LR, McCulloch AD, Omens JH. Role of diastolic properties in the transition to failure in a mouse model of the cardiac dilatation. *Am J Physiol Heart Circ Physiol*. 2006;291:H2971–9.
34. Omens JH, Usyk TP, Li Z, McCulloch AD. Muscle LIM protein deficiency leads to alterations in passive ventricular mechanics. *Am J Physiol Heart Circ Physiol*. 2002;282:H680–7.
35. Costa KD, Holmes JW, McCulloch AD. Modelling cardiac mechanical properties in three dimensions. *Philos Trans R Soc Lond Ser A Math Phys Eng Sci*. 2001;359:1233–50.
36. Guccione JM, Costa KD, McCulloch AD. Finite-element stress-analysis of left-ventricular mechanics in the beating dog heart. *J Biomech*. 1995;28:1167–77.
37. Rice JJ, Wang F, Bers DM, de Tombe PP. Approximate model of cooperative activation and crossbridge cycling in cardiac muscle using ordinary differential equations. *Biophys J*. 2009;95:2368–2390.
38. Malm S, Frigstad S, Sagberg E, Larsson H, Skjaerpe T. Accurate and reproducible measurement of left ventricular volume and ejection fraction by contrast echocardiography: a comparison with magnetic resonance imaging. *J Am Coll Cardiol*. 2004;44:1030–5, 10.1016/j.jacc.2004.05.068.
39. Klotz S, Hay I, Dickstein ML, Yi G-H, Wang J, Maurer M, Kass DA, Burkhoff D. Single beat estimation of the end-diastolic pressure–volume relationship: a novel method with the potential for noninvasive application. *Am J Physiol Heart Circ Physiol*. 2006;291:H403–H412.
40. Chen C-H, Fetics B, Nevo E, Rochitte CE, Chiou K-R, Ding, P-A, Kawaguchi M, Kass DA. Noninvasive single-beat determination of left ventricular end-systolic elastance in humans. *J Am Coll Cardiol*. 2001;38:2028–34.
41. Kjorstad KE, Korvald C, Myrmel T. Pressure-volume-based single-beat estimations cannot predict left ventricular contractility in vivo. *Am J Physiol Heart Circ Physiol*. 2002;282:H1739–50.
42. Walker JC, Ratcliffe MB, Zhang P, Wallace AW, Fata B, Hsu EW, Saloner D, Guccione JM. MRI-based finite-element analysis of left ventricular aneurysm. *Am J Physiol Heart Circ Physiol*. 2005;289:H692–700.

43. Watanabe H, Sugiura S, Kafuku H, Hisada T. Multiphysics simulation of left ventricular filling dynamics using fluid–structure interaction finite element method. *Biophys J*. 2004;87: 2074–85.
44. McVeigh ER, Prinzen FW, Wyman BT, Tsitlik JE, Halperin HR, Hunter WC. Imaging asynchronous mechanical activation of the paced heart with tagged MRI. *Magn Reson Med*. 1998;39:507–13.
45. Osman NF, Prince JL. Visualizing myocardial function using HARP MRI. *Phys Med Biol*. 2000;45:1665–82.
46. Ozturk C, McVeigh ER. Four-dimensional B-spline based motion analysis of tagged MR images: introduction and in vivo validation. *Phys Med Biol*. 2000;45:1683–702.
47. Van der Toorn A, Barenbrug P, Snoep G, Van der Veen FH, Delhaas T, Prinzen FW, Maessen J, Arts T. Transmural gradients of cardiac myofiber shortening in aortic valve stenosis patients using MRI tagging. *Am J Physiol Heart Circ Physiol*. 2002;283:H1609–15.
48. Wyman BT, Hunter WC, Prinzen FW, McVeigh E. Mapping propagation of mechanical activation in the paced heart with MRI tagging. *Am J Physiol Heart Circ Physiol*. 1999;276:H881–91.
49. Gupta KB, Ratcliffe MB, Fallert MA, Edmunds LH Jr, Bogen DK. Changes in passive mechanical stiffness of myocardial tissue with aneurysm formation. *Circulation*. 1994;89:2315–26.
50. Ypenburg C, Roes SD, Bleeker GB, Kaandorp TAM, de Roos A, Schalij MJ, van der Wall EE, Bax JJ. Effect of total scar burden on contrast-enhanced magnetic resonance imaging on response to cardiac resynchronization therapy. *Am J Cardiol*. 2007;99:657–60.
51. Ypenburg C, Schalij MJ, Bleeker GB, Steendijk P, Boersma E, Dibbets-Schneider P, Stokkel MPM, van der Wall EE, Bax JJ. Impact of viability and scar tissue on response to cardiac resynchronization therapy in ischaemic heart failure patients. *Eur Heart J*. 2007;28:33–41, 10.1093/eurheartj/ehl379.
52. Kerckhoffs RCP, McCulloch AD, Omens JH, Mulligan LJ. Effects of biventricular pacing and scar size in a computational model of the failing heart with left bundle branch block. *Med Image Anal*. 2009;13:362–369.
53. Kerckhoffs RCP, Neal M, Gu Q, Bassingthwaighte JB, Omens JH, McCulloch AD. Coupling of a 3D finite element model of cardiac ventricular mechanics to lumped systems models of the systemic and pulmonic circulation. *Ann Biomed Eng*. 2007;35:1–18.
54. Lu K, Clark JW, Ghorbel FH, Ware DL, Bidani A. A human cardiopulmonary system model applied to the analysis of the Valsalva maneuver. *Am J Physiol Heart Circ Physiol*. 2001;281:H2661–79.
55. Olansen JB, Clark JW, Khoury D, Ghorbel F, Bidani A. A closed-loop model of the canine cardiovascular system that includes ventricular interaction. *Comput Biomed Res*. 2000;33:260–95.
56. Arts T, Delhaas T, Bovendeerd P, Verbeek X, Prinzen FW. Adaptation to mechanical load determines shape and properties of heart and circulation: the CircAdapt model. *Am J Physiol Heart Circ Physiol*. 2005;288, H1943–54.
57. Kerckhoffs RCP, Lumens J, Vernooy K, Omens JH, Mulligan LJ, Delhaas T, Arts T, McCulloch AD, Prinzen FW. Cardiac Resynchronization: insight from experimental and computational models. *Prog Biophys Mol Biol*. 2008;97:543–61.
58. Bax JJ, Abraham T, Barold SS, Breithardt OA, Fung JWH, Garrigue S, Gorcsan J III, Hayes DL, Kass DA, Knuuti J, Leclercq C, Linde C, Mark DB, Monaghan MJ, Nihoyannopoulos P, Schalij MJ, Stellbrink C, Yu C-M. Cardiac resynchronization therapy: Part 2 – issues during and after device implantation and unresolved questions. *J Am Coll Cardiol*. 2005;46:2168–82.
59. Helm RH, Byrne M, Helm PA, Daya SK, Osman NF, Tunin R, Halperin HR, Berger RD, Kass DA, Lardo AC. Three-dimensional mapping of optimal left ventricular pacing site for cardiac resynchronization. *Circulation*. 2007;115:953–61.
60. Helm RH, Leclercq C, Faris OP, Ozturk C, McVeigh E, Lardo AC, Kass DA. Cardiac dyssynchrony analysis using circumferential versus longitudinal strain – Implications for assessing cardiac resynchronization. *Circulation*. 2005;111:2760–7.

61. Kerckhoffs RCP, McCulloch AD, Omens JH, Mulligan LJ. Effect of pacing site and infarct location on regional mechanics and global hemodynamics in a model based study of heart failure. *Lect Notes Comput Sci*. 2007;4466:350–60.
62. Taber LA. Biomechanics of cardiovascular development. *Annu Rev Biomed Eng*. 2001;3:1–25.
63. Pieske B, Sütterlin M, Schmidt-Schweda S, Minami K, Meyer M, Olschewski M, Holubarsch C, Just H, Hasenfuss G. Diminished post-rest potentiation of contractile force in human dilated cardiomyopathy. *J Clin Invest*. 1996;88:765–76.

Chapter 16
Computational Modeling of Aortic Heart Valve Mechanics Across Multiple Scales

Laura R. Croft and Mohammad R. Kaazempur Mofrad

Abstract Computational modeling is an excellent tool with which to investigate the mechanics of the aortic heart valve. The setting of the heart valve presents complex dynamics and mechanical behavior in which solid structures interact with a fluid domain. There currently exists no standard approach; a variety of strategies have been used to address the different aspects of modeling the heart valve. Simplifications reduce computational costs, but could compromise accuracy. As advancements in modeling techniques are made and utilized, more physiologically relevant models are possible. Computational studies of the aortic valve have contributed to an improved understanding of the mechanics of the normal valve, and insights into the progression of diseased valves.

16.1 Introduction

The aortic heart valve poses a complex mechanical problem both for the physicians repairing the valve and for the engineers seeking to design replacements for the living valve. Approximately 26,000 people die annually in the United States with an aortic valve disorder as a contributing cause [1], and it is predicted that by the year 2020, nearly 800,000 people worldwide will require heart valve replacements annually [2]. Like other cardiovascular diseases, the number of people affected by heart valve disease will continue to rise as the average age of the world's population increases.

Many aspects of the mechanical environment of the heart valve have been studied in recent decades (see review by Sacks and Yoganathan [3]). In vitro studies have been performed investigating the mechanics of the valvular components on the

M.R.K. Mofrad (✉)
Department of Bioengineering, University of California, Berkeley, CA, USA
e-mail: mofrad@berkeley.edu

J.M. Guccione, et al. (eds.), *Computational Cardiovascular Mechanics*,
DOI 10.1007/978-1-4419-0730-1_16,

cellular level [4] and the tissue level [5]. The dynamic function, including hemodynamic data, of physiological and replacement valves has been examined using in vitro methods such as laser Doppler anemometry [6] and using in vivo imaging such as magnetic resonance imaging [7]. All of those experimental methods have limitations in fully characterizing mechanical behavior of the assembled physiological valve, particularly data such as spatially and temporally detailed stresses.

Computational modeling of the valve provides a robust means of investigation that can quantify many types of data and can simulate a variety of pathophysiological situations. As is the case when modeling any biological situation, simplifications and assumptions must be defined. A variety of approaches have been developed to tackle the difficulties associated with simulating complex biological material, recreating the large deformation of a solid structure within a fluid domain, and other aspects of the aortic valve which are not trivial to capture numerically. Using these computational methods, researchers have been able to provide a better illustration of the functioning biomechanics of the valve. Studies have examined specific aspects of the valve, and how changes in the valve environment, such as developing disease conditions, can perpetuate abnormal changes to the valve through the communication of deviant mechanical conditions. The insight gained through computational studies on the aortic valve can aid in the prevention and repair of valvular disease.

16.2 Background on Modeling the Aortic Valve

The aortic valve and its dynamic function present an interesting interplay of solid and fluid mechanics. This valve is responsible for the regulation of blood flow exiting the left ventricle into the aorta, presenting the gateway for the oxygenated blood which is being pumped from the heart to the peripheral circulation. In order to create a computational model of a complicated biological system like the aortic valve, simplifications and assumptions must be imposed on the geometrical and material properties. However, complexities are added at the cost of increased computation time and resources. The advent of fluid–structure interaction (FSI) capabilities has expanded the field of study to include the fluid mechanics associated with the problem, enabling a more physiologically relevant model. Throughout the cardiac cycle, the valve undergoes varied dynamic and mechanical changes, which can be simulated and examined using computational techniques to better understand this aspect of cardiac biomechanics.

The aortic valve is situated within the supporting aortic root between the left ventricle of the heart and the aorta. Like the pulmonary valve, which also controls blood flow exiting a ventricle, the aortic valve is a semilunar valve and has three cusps: the right coronary, left coronary, and noncoronary cusps. The cusps are attached to the wall of the aortic root at the crown-shaped annulus, circling the perimeter of the root. Each cusp is connected to its neighboring cusps at sites known as the commissures, which are the peaks of the crown-shaped annulus. Each cusp also has a corresponding sinus, which is a bulbous portion of the root. The sinus is defined

at one end by the cusp attachment and by the sinotubular junction at the end nearest the aorta. The left and right coronary sinuses have coronary ostia which supply blood to the heart muscle itself. For more information on the valvular structure see Thubrikar [8] and Misfeld and Sievers [9]. There exist two approaches most commonly used for recreating valve anatomy. One method is to construct an idealized geometry based on experimentally measured parameters (basic protocol described by Thubrikar [8]) based on the assumption that the three cusps and sinuses are identical. An example is shown in Fig. 16.1. Some studies have expanded this approach to include the coronary ostia [10] or variations in cusp thickness within a single cusp [11, 12]. To create a more realistic but computationally demanding geometry, magnetic resonance imaging data, generally of ex vivo specimens, can be used to create a geometry which accounts for differences between the left coronary, right coronary, and noncoronary cusps and sinuses such as areas, perimeters, thicknesses, and the presence of the coronary ostia in the left and right coronary sinuses [13, 14]. Additionally, variations in thickness within each cusp and within the root in the axial direction are included in the geometry.

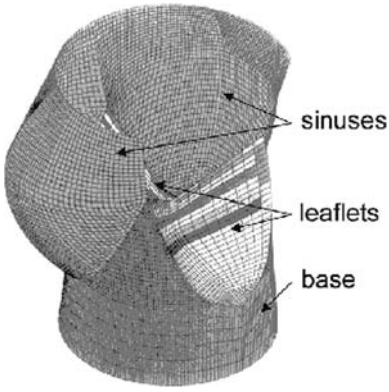

Fig. 16.1 Example of the computational mesh of the valve using geometry based on idealized parameters [11]

The cusp tissue is outwardly covered by a layer of endothelial cells, and beyond that is composed of fibrous extracellular matrix. Valvular interstitial cells, which have characteristics of both smooth muscle cells and fibroblasts, exist throughout the matrix. As displayed in Fig. 16.2, there are three main layers of the cusp: the ventricularis, the spongiosa, and the fibrosa, in order of inflow surface to outflow surface. The ventricularis is the thinnest layer and contains collagen and elastin fibers, the elastin being mainly radially oriented. This arrangement permits large radial strains of the cusp tissue. The spongiosa is gel-like, comprised primarily of glycosoaminoglycans, and likely acts as a shock and shear absorber. The layer nearest the outflow, the fibrosa, is predominantly composed of collagen fibers oriented circumferentially and strongly contributes to enduring the heavy loads experienced by the closed cusps [15]. The fibrosa has corrugations in the unstressed state which unfold as the valve opens, aiding the cusp in its ability to undergo considerable stretch. The differing constituents and characteristics of these layers integrate to compose cusps that are

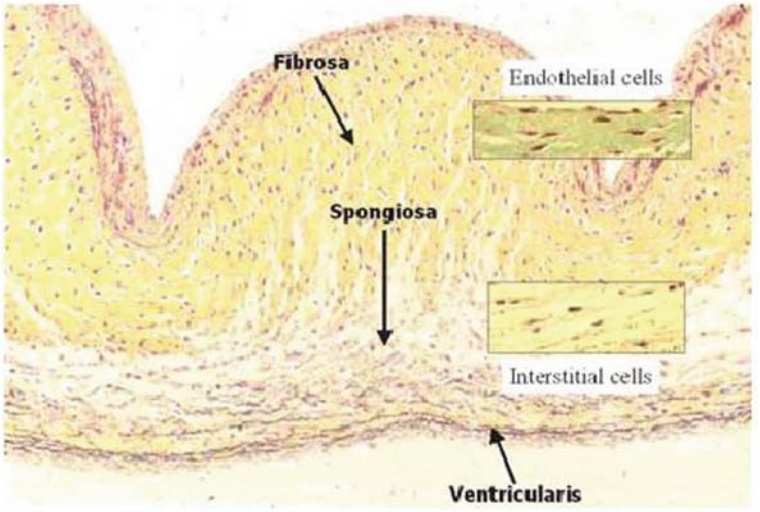

Fig. 16.2 Histology of cusp tissue and its three tissue layers [15]

capable of withstanding the heavy and varied mechanical demands of the valve function. Few computational studies have attempted to separately characterize the layers of the cusp [16, 12].

In reference to the designation of material properties of the cusp, this tissue is most accurately described as a nonlinear, pseudoelastic, incompressible, and anisotropic material. The fibrous layers, the fibrosa and ventricularis, contain collagen fibers oriented mainly in the circumferential direction and elastin fibers oriented mainly in the radial direction. This arrangement, illustrated in Fig. 16.3, causes the elastic modulus to be significantly greater in the circumferential direction than in

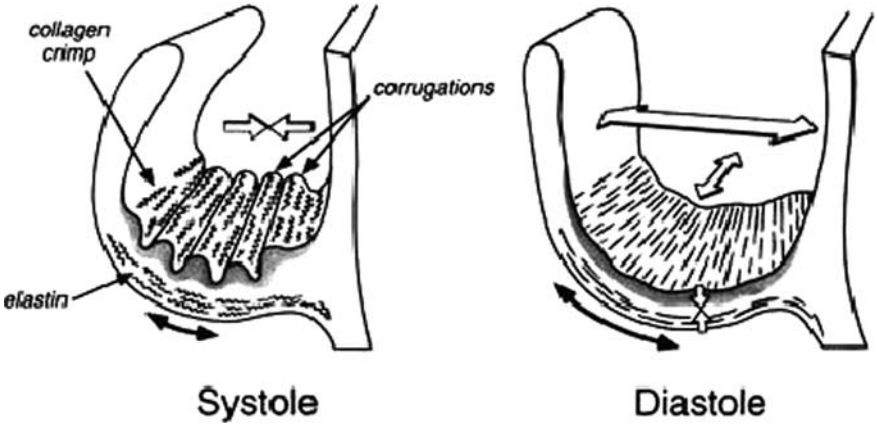

Fig. 16.3 Elastin and collagen arrangement during valve motion [15]

the radial direction, producing strong anisotropic behavior. A low elastic modulus is associated with systole when fiber crimping is present, which reduces flexion stresses on the cusps. When the cusps are closed during diastole, the tissue transitions to a much greater elastic modulus as the waviness of the fibers straighten, enabling the tissue to withstand the great pressure load without bulging or prolapse [17]. The stress–strain relationships of collagen and elastin are displayed in Fig. 16.4. This fiber crimping and two elastic modulus transition phases contribute to the nonlinear property of the cusp tissue. Many computational models have made the simplifications of isotropy [18, 11], linear elastic behavior [13, 14], or both [19, 20]. In the past, many of the commercial finite element modeling software packages were not capable of assigning both nonlinear and anisotropic material properties to the same structure. Studies have shown that the consideration of nonlinear elastic properties [21, 22] and anisotropy [23, 24] can significantly influence the results and accuracy of aortic valve simulations.

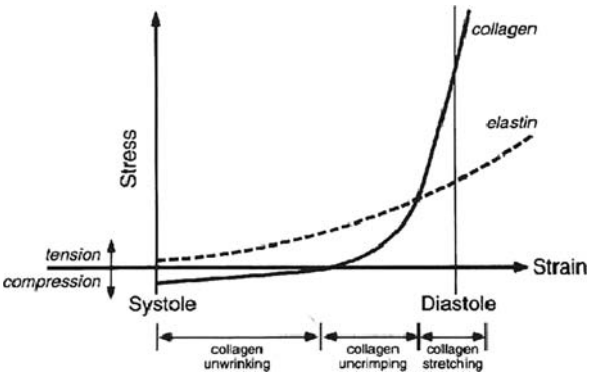

Fig. 16.4 Stress–strain relationship of elastin and collagen throughout cardiac cycle [15]

The aortic valve is mainly a passive structure, in which the cusps open and close based on the pressure difference across the valve, which varies with the cardiac cycle. This cycle has two main periods, systole and diastole. During the beginning of systole, pressure is high in the contracting left ventricle, forcing the valve open and propelling blood from the ventricle. As the pressure in the ventricle is relieved and the aortic pressure rises, the valve closes. During diastole, the left ventricle relaxes and is refilled via the mitral valve and left atrium, and the closed cusps of the aortic valve experience a mounting pressure load as the cycle approaches the start of systole once more. The valve and its surrounding structures of the sinuses and aortic root undergo dynamic local contractions and relaxations throughout the cardiac cycle (see review by Cheng et al. [25]). Computational studies have focused on both specific portions of the cycle and the entire cycle. Static models have focused on the stresses and strains experienced due to the increasing or maximum pressure load experienced after valve closure during diastole [26, 13, 22]. Dynamic models have broadened the scope of study to the deformations and stresses that occur throughout

the cardiac cycle as the valve opens and closes [19, 11]. FSI has enhanced the abilities of the dynamic valve study by incorporating the movement of both the solid and fluid [18, 16, 14, 10, 12]. In addition to measures of the solid deformations, hemodynamic data become available with which one can examine the fluid mechanics of the valve setting. Whether static or dynamic, solely structural or with FSI, the load imposed on the valve model is generally a spatially uniform pressure difference across the valve, which reasonably replicates the primary driving force of the physiological valve environment as supported by the study by Carmody et al. [18].

As advancements in computational modeling techniques have been achieved, more accurate and informative models of the aortic valve have been developed. Complex valve geometries and material properties can be included in these models; simplifications of the aortic valve setting are selected depending on the scope and aim of the study to maintain computational costs to an acceptable level. FSI studies have demonstrated how blood flow through the valve is altered by the anatomical structures present, and how correspondingly the movement of blood instigates and participates in the opening and closing of the valve cusps. Computational studies on the aortic valve are excellent tools to investigate the mechanical environment of the valve and to characterize how various factors can substantially alter this mechanical environment.

16.3 Regional Differences in the Aortic Valve

Organ-scale models of the aortic valve have provided information on the native state of the undiseased valve. These studies have demonstrated that computational modeling can be a very expedient tool for investigating the mechanics of the native aortic valve and can quantify values such as stress which are difficult to obtain in an in vitro or in vivo setting. These simulations have shown how the three cusps and three sinuses function together in a complex manner to distribute the heavy pressure load of diastole and to be capable of the high flexion required during systole.

Grande et al. [13] used commercial software to model the aortic valve and the aortic root to investigate regional variations in stress and strain. The valve geometry was obtained from MRI images of ex vivo specimens and also accounted for local variations in cusp and root thickness. Many FEM studies assume cusp symmetry, uniform thickness, and that all three cusps and corresponding sinuses are identical; in contrast, this study had a very complex geometry by which to more accurately characterize and compare local stress and strain magnitudes. The study was a static simulation of end systole to the end of left ventricular isovolumetric relaxation, focusing on the stresses generated as the pressure across the valve reaches a maximum during diastole (the coupling of fluid was not included in this model). The results showed that the asymmetrical and nonuniform nature of the simulated geometry led to asymmetrical and nonuniform distributions of stress and strain values in both the cusps and sinuses. The noncoronary cusp was shown to have the highest values of peak principal stress, which the authors conjectured to be partially due to

the fact that it is the cusp with the greatest area, perimeter, and thickness as well as radius of curvature which could cause higher values of stress. Peak principal stresses in cusps were seen in the free margin and in the belly near regions of coaptation, and stresses in the sinuses were higher near the annulus of the valve as opposed to near the sinotubular junction. Of the sinuses, the right coronary sinus and the non-coronary sinus had the greater values of stress. These results correspond well with clinical results which show that these two sinuses more commonly develop dilatation or an aneurysm [27]. This study showed that the regional anatomical differences of the aortic valve and root do have influences on the stresses and strains imposed during diastole, which could provide further information on which localized areas are more susceptible to disease or require special consideration during repair.

Grande et al.'s work sheds light on the differences in stress experienced by the three different cusps and sinuses, essential information on understanding the local variation within the valve. A thorough understanding of the condition of the physiological undiseased state provides a basis with which to compare the mechanics of pathological, repair, and replacement settings. A severe deviation from the native conditions could indicate a potential site for a pathological response. Grande-Allen extended her earlier work to incorporate a pathological model of Marfan's syndrome, a genetic disorder shown to have an adverse effect on elastic fibers. As these fibers become fragmented and disorganized, the aortic root can begin to stretch and stiffen. Grande-Allen et al. [28] investigated the mechanical effects which this abnormal aortic root could have on the cusps of the valve. Using a similar computational model to that discussed previously [13], the three aortic cusps and sinuses were modeled based on normal human specimens. The geometry of the model was altered to recreate four levels of aortic root dilation, 5%, 15%, 30%, and 50%, which subsequently moved the cusps radially outward. The elastic modulus of the root for the four models of Marfan syndrome was doubled to simulate the stiffened aortic root. A static analysis of diastolic loading was investigated. Regional stresses and strains of the cusps were significantly increased by root dilation and stiffening as compared to the undiseased model, particularly near the attachment to the root and the coaptation area (stress distributions are shown in Fig. 16.5). At 50% dilation, increases in stresses ranged from 77% to 357%, and increases in strain ranged from 57% to 195%. For the 30% and 50% dilation models, cusp coaptation decreased. For the 5% and 15% dilation models, increases in stress and strain were present without loss of coaptation, a scenario which could also be representative of cusp calcification. This study illustrated that the abnormal aortic root which develops in patients with Marfan syndrome can significantly alter the natural stresses and strains on the aortic valve cusps and can decrease coaptation, evidence which supports the instances of cusp thickening and regurgitation often seen in such cases. Information on the resulting cusp conditions including coaptation area, regional stresses, and regional strains can better inform surgeons on the most effective surgical repair or replacement to proceed with for patients with a dilated and stiffened aortic root such as that associated with Marfan syndrome.

Computational modeling can provide detailed information on how deviant conditions in the aortic valve and root may have a significant impact on the mechanics of

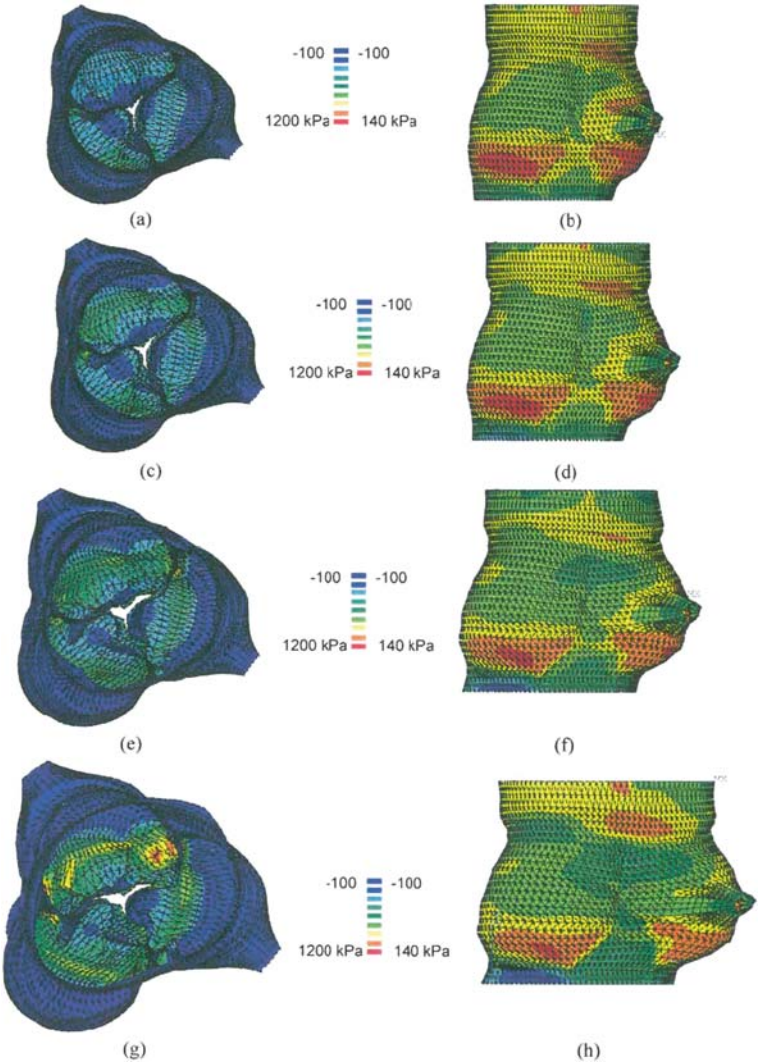

Fig. 16.5 Stress distributions in aortic valve models of Marfan syndrome: 5% dilation model (**a**,**b**), 15% dilation model (**c**,**d**), 30% dilation model (**e**,**f**), 50% dilation model (**g**,**h**) [28]

the valve. These subsequent changes have the potential to further precipitate abnormal biological responses. As more information on the effects of diseased conditions becomes available using this modality, clinicians can obtain a better understanding of the implications of these valvular pathologies. These types of studies also enable physicians to make a more informed decision on the course of treatment or surgical procedure, keeping in mind the mechanics which play a vital role in maintaining valve function.

16.4 Examining Aortic Root Compliance

One factor which has been studied extensively using computational methods is the compliancy of the aortic root, which has been demonstrated to have a significant impact on the cusps of the valve as well as the root itself. In a dynamic study by Gnyaneshwar et al. [19], the aortic root was seen to dilate at the level of the commissures before the cusps began to open. When the pressure load on the cusps was removed in the simulation, the cusps still opened up to 20% in response to the aortic root dilation alone, demonstrating the important relationship between the cusps of the valve and the aortic root. A healthy aortic root is elastic and able to expand and contract during the cardiac cycle. The loss of the ability of the aortic root to dilate and function alongside the cusps could be a factor in diseased conditions and could be important to maintain or recreate during repair or replacement. Sripathi et al. [20], Howard et al. [11], and De Hart et al. [16] studied the effects of aortic root stiffening on the cusps of the valve. The increasing rigidity of the aortic root and sinuses is associated with several conditions including aortic root disease as well as the loss of elastic fibers due to aging. The models by Sripathi and Howard were of a dynamic simulation, did not incorporate FSI, and had idealized geometry, whereas the model by De Hart differed by advancements in the inclusion of FSI and fiber-reinforced cusp properties.

The cusps of the compliant root model of the model by Sripathi opened smoothly into a symmetrical orifice, whereas the cusps of the rigid root had asymmetries and wrinkling of the cusps. Folding of the cusps also occurred in the rigid root model in Howard's study, particularly at the free edges of the cusps. Howard suggests that this abnormal folding would lead to increased bending at the free edge as well as increased compressive stresses within the cusps. De Hart's study did report increased bending at the free edges of the cusps of the rigid root model and that a flexible root reduces compressive stresses by 68% as compared to a rigid root model. Sripathi also compared the stresses of the two root models. No significant increase in maximum principal (tensile) stress was observed due to the wrinkling present in the stiffened root model; however, increased values of minimum principle (compressive) stress did exist and in increased area. It has been speculated in a study with similar findings that the cusp wrinkling and associated abnormal stresses caused by a stiffened aortic root may lead to cusp calcification [29]. These aberrant stresses may be damaging to biological tissue such as that of the cusp and could lead to a further decline in cardiac health.

The dilation of the aortic root which precedes and presumably aids cusp opening was seen in the compliant root model by Sripathi as seen in Gnyaneshwar et al. [19], and the root was able to increase effective valve orifice area as increases in root pressure and transvalvular gradient were imposed. In the stiffened root model, the root was no longer capable of these actions. The root was unable to adapt to changing conditions or to expand to facilitate cusp opening, and the opening of the cusps was delayed. The results from Howard's model were similar to that of Sripathi; the compliant aortic root facilitated cusp opening, allowing opening to occur sooner and at lower pressures than compared to the rigid root. In a stiffened

root the orifice area was reduced [11] and due to the folding of the cusps the orifice became triangular as opposed to circular [20]. Fig. 16.6 illustrates how orifice area and commissure displacement were affected.

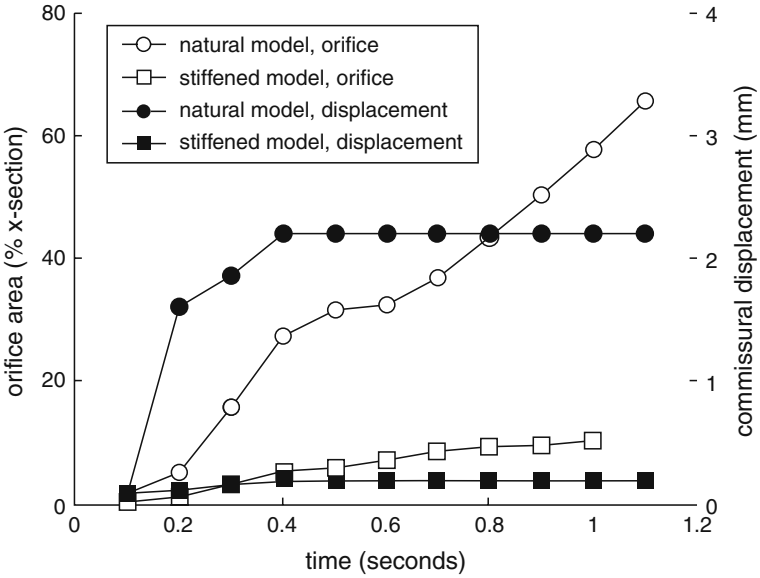

Fig. 16.6 Comparison of compliant and stiffened aortic root models: orifice area expressed as a percentage of cross-sectional area and displacement of the commissures [11]

As described earlier, the loss of elasticity of the aortic root does likely have adverse effects on the root's ability to dynamically aid valve function. Related studies on repair and replacement draw similar conclusions. Grande-Allen et al [30] used computational modeling to ascertain which synthetic material for an aortic root replacement graft best minimized deviations from the normal stress distribution of both the aortic root and cusps. Of the three materials simulated, the most compliant material was found to best preserve normal stress values throughout the cusps and root. Studies on artificial heart valves have examined whether a rigid or a flexible stent promotes an optimal stress distribution; the stent structure supports the artificial cusps and is in interface between these cusps and the natural root. These computational studies have also shown that the devices which do not hinder the ability of the root to dilate and contract minimize cusp stresses [31–33]. Aortic root contraction and expansion of the commissures aids valve opening and is an important component of the complex valvular stress-sharing and dynamics.

16.5 The Importance of the Sinuses of Valsalva

With the advent of FSI it became possible to study the role of the aortic valve sinuses using computational modeling. In the numerical study by De Hart et al. [16] it was illustrated that back flow along the aortic wall generates flow into the sinus, creating

a large vortex in the sinus cavity (shown in Fig. 16.7). This recirculation in the sinus region serves to promote valve closure as the flow through the valve begins to decelerate. The existence of vortices in the sinus cavity and their influence on valve closure has been discussed since the work of Leonardo da Vinci [34]. Computational modeling can further reveal the importance of the aortic sinuses, and much of this work has been done with the motivation of studying repair techniques.

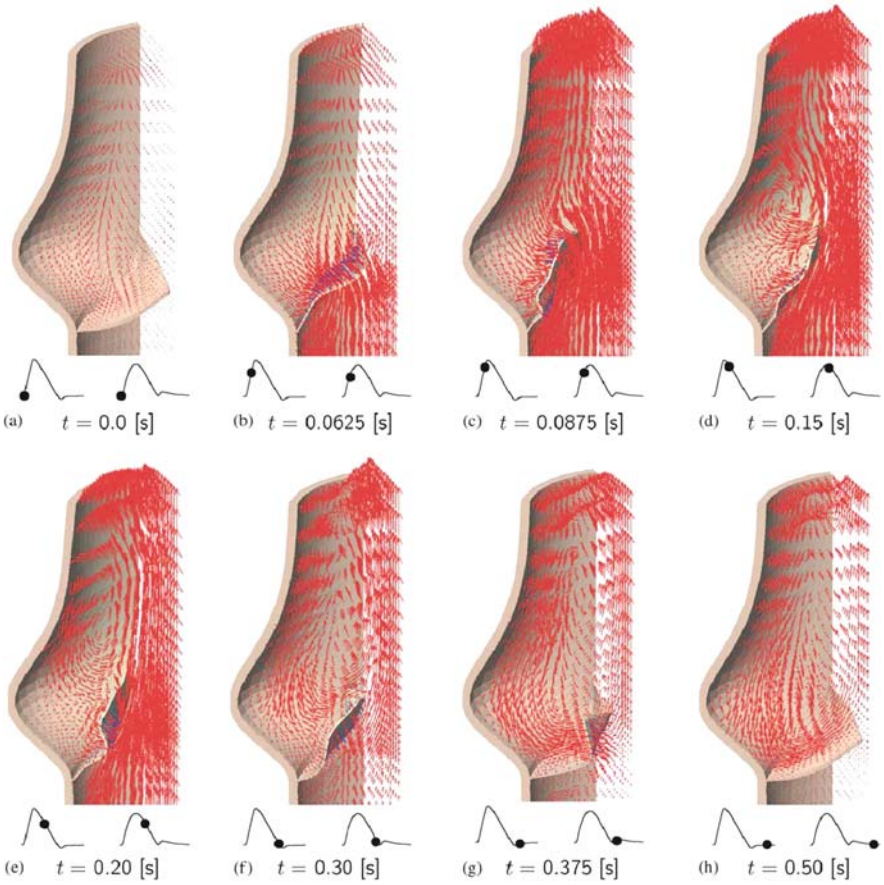

Fig. 16.7 Vortex formation in the sinus cavity during systole. At the *bottom* of each frame, the *left curve* represents the applied velocity curve and the *right curve* represents the applied pressure curve. [16]

For patients with a dilated aortic root, the common repair is to replace the aortic root with a synthetic graft while preserving the natural valve cusps. The optimal design of these grafts should be determined to provide the most restorative and durable repair, and a common debate is the necessity of restoring the sinus shape to the root as opposed to a simple cylindrical graft shape. Computational studies have been performed examining the two graft root shapes and the resulting comparative

stress and strain values present in the cusps. Grande-Allen et al. [30] and Ranga et al. [10] have both performed computational studies comparing roots with and without sinuses. Grande-Allen used a static computational model based on MRI data that simulated the load experienced during diastole whereas the model used by Ranga was a dynamic model with idealized geometry which incorporated FSI of the full cardiac cycle.

Grande-Allen observed that for both graft shapes the stresses in the root region were increased and strains were decreased. The stresses near the cusp attachment area were lower than those of other regions such as near the sinotubular junction, creating an altered stress distribution from that of the natural aortic root. Both graft shapes increased cusp coaptation as compared to the normal valve, but the percent increase for the cylindrical graft shape was double that of the pseudosinus graft, and directional strains implied that the valve may be displaced into the left ventricular outflow. The cylindrical grafts also produced severely altered stress and strain patterns and magnitudes in the cusps; the graft models which recreated the sinus regions had comparable values to that of normal valves. Ranga also observed that the cylindrical graft significantly altered the distribution of stress in the cusps, and compressive stresses were increased as compared to that of the normal valve, whereas the results of the graft with sinuses were relatively similar to the native condition. Another computational study by Beck et al. [35], which compared a cylindrical graft to the native root, also found that the tubular graft increased deformation and stress, particularly along the cusp attachment region, which was also the site where Grande-Allen observed the greatest increases in stress and strain in the cusps. The normal allocation of load between the root/graft and cusps was disturbed, causing atypical stress and strain distributions in the aortic root and cusps in the case of the cylindrical graft in which there is a lack of sinus region.

Although these results all imply that reimplantation with a cylindrical graft is not a durable repair, clinical results indicate otherwise. Long-term results by David et al. [36] showed that 94% of patients with a cylindrical graft were free from moderate or severe aortic insufficiency after 10 years and 96% did not require reoperation. The long-term clinical results of a remodeling procedure, which tailored the graft to the patient's valve and more physiologically recreated the sinuses and normal valve motion, were also examined. In this case, only 75% of patients were free from returning aortic insufficiency after 10 years. While computational studies can characterize the stresses and strains present under very controlled conditions, the studies did not consider the biological processes which may ensue after surgery. In many cases, annular dilation will continue or return depending on the pathology, and a more rigid constraining repair may better prevent future remodeling and the reoccurrence of aortic insufficiency. Further development of grafts which reproduce the sinuses is being pursued; while these clinical results are still not as positive as those of the standard cylindrical graft, they are promising [37].

The cylindrical conduit also affected the normal function and dynamics of the valve as seen in Ranga's simulation of the complete cardiac cycle. These results indicated loss of expansion of the commissures during opening, decreased opening and

closing times, and the introduction of abnormal folding of the cusps. Grande-Allen also concluded that the cusps within the cylindrical graft may experience folding as a consequence of increased coaptation and increased cusp strains in the attachment and belly regions. The fluid component of Ranga's study provided further information on the implications of the absence of the sinuses. Peak velocities were increased in the cylindrical graft model (those of the pseudosinus graft were similar to normal values), and without the sinuses the vortices which aid in closing were no longer present. The lack of sinuses was disadvantageous to maintaining normal hemodynamics as well as normal deformations and stress distributions of the solid structures. The aortic valve sinuses appear to play a role in maintaining an optimal stress distribution in the cusps and, through an influence on fluid mechanics, aid in valve closure.

16.6 Fiber-Reinforcement of Aortic Cusps

As previously mentioned, the aortic cusp tissue contains collagen fibers, which bear the bulk of the load on the cusps. These fibers are oriented primarily in the circumferential direction, causing the tissue to be less extensible circumferentially as opposed to radially. Although these fibers are integral components of the valve's structure, most computational studies do not consider them in the material definition of the cusp tissue. A few studies have specifically focused on these fibers and how their arrangement is related to the mechanics of the valve.

Experimental work has demonstrated that collagen fiber alignment changes in response to the mechanical environment; throughout the cusp, collagen fiber direction changes and becomes highly aligned as transvalvular pressure increases from zero to 4 mmHg [3]. Computational work by Driessen seeks to imitate this adaptive response and thereby better understand this process. This valve model is a purely structural static model of idealized geometry of the fibrosa layer. In earlier work, Driessen assumed that fiber direction aligns with principal stretch directions [38]. The final computed fiber directions resembled those of experimental work by Sacks (displayed in Fig. 16.8), with the fibers running from commissure to commissure in the circumferential direction. However, this model also predicted a secondary population of fibers which were oriented in the radial direction, which is not physically realistic. In a later study, Driessen revised his model so that in areas of biaxial loading, such as the belly region of the cusp, the preferred fiber direction was assumed to be located between the principal stretch directions [26]. Regions such as that near the free edge which are loaded primarily uniaxially were still assumed to have preferred fiber directions which coincide with the principal stretch direction. The final computed fiber alignments of the cusp agreed with experimental data. The areas of tissue near the free edge and commissures had circumferential fiber alignment similar to the previous study, whereas the fibers in the belly region had a more branched architecture.

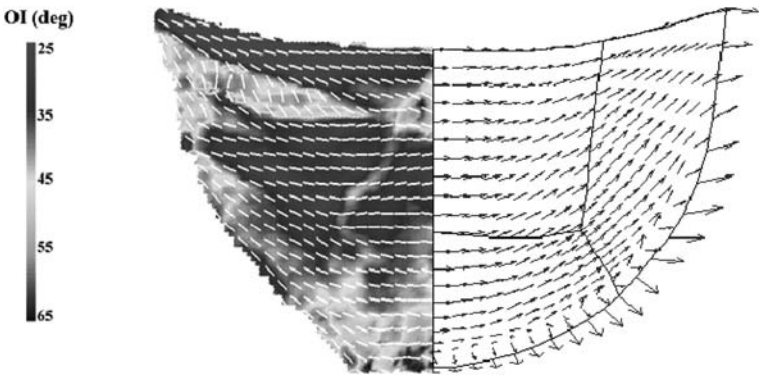

Fig. 16.8 Computed preferred fiber direction (*right*) compared to experimental results (*left*). Orientation index (OI) scale denotes degree of alignment; low OI values indicate highly aligned networks, and high OI values represent randomly oriented networks [38]

For implementation into the construction of synthetic artificial heart valves, De Hart has explored the use of fiber-reinforcements within the cusp material, recreating the network of collagen fibers of the native valve and simulating proposed fiber-reinforcements for synthetic valve design. The computational models are dynamic models of idealized geometry which include FSI. For the simulations of the native valve, two fibrous layers of the cusp are simulated: one with radially aligned fibers and one with those oriented circumferentially. The use of fiber-reinforcement (imitating that of the native valve) compared to a non-reinforced valve stabilized the cusps in the open configuration and eliminated high bending deformations during closure. Fiber-reinforcement also decreased maximum tensile stresses by 31% and reduced maximum compressive stresses by 33% [16]. Cauchy stresses and opening configurations are comparatively depicted in Fig. 16.9. In studies examining various arrangements of fibers, the number and orientation of the fibers were seen to have an effect on stress distribution and magnitudes [39]. These studies have shown the strong mechanical impact of the presence and alignment of fibers embedded within the valve tissue. This data demonstrates the importance of including fiber families in computational models to accurately recreate the cusp tissue, and shows the importance of fiber-reinforcement design in synthetic valves so as to maintain a favorable stress distribution across the cusp tissue to enhance artificial valve durability.

These studies strive to elucidate the development and role of the collagen fiber network within the cusp tissue. By testing hypotheses on what determines fiber alignment, one can find a way to recreate their network structure and gain insight on why these networks form as they do. Models comparing fiber-reinforced and non-reinforced valves demonstrate how collagen fibers serve to alleviate stress from the cusps while also aiding in opening and closing stability. This organization of sturdy fibers is crucial to valve function and durability, and through computational techniques a better comprehension of them can be gained.

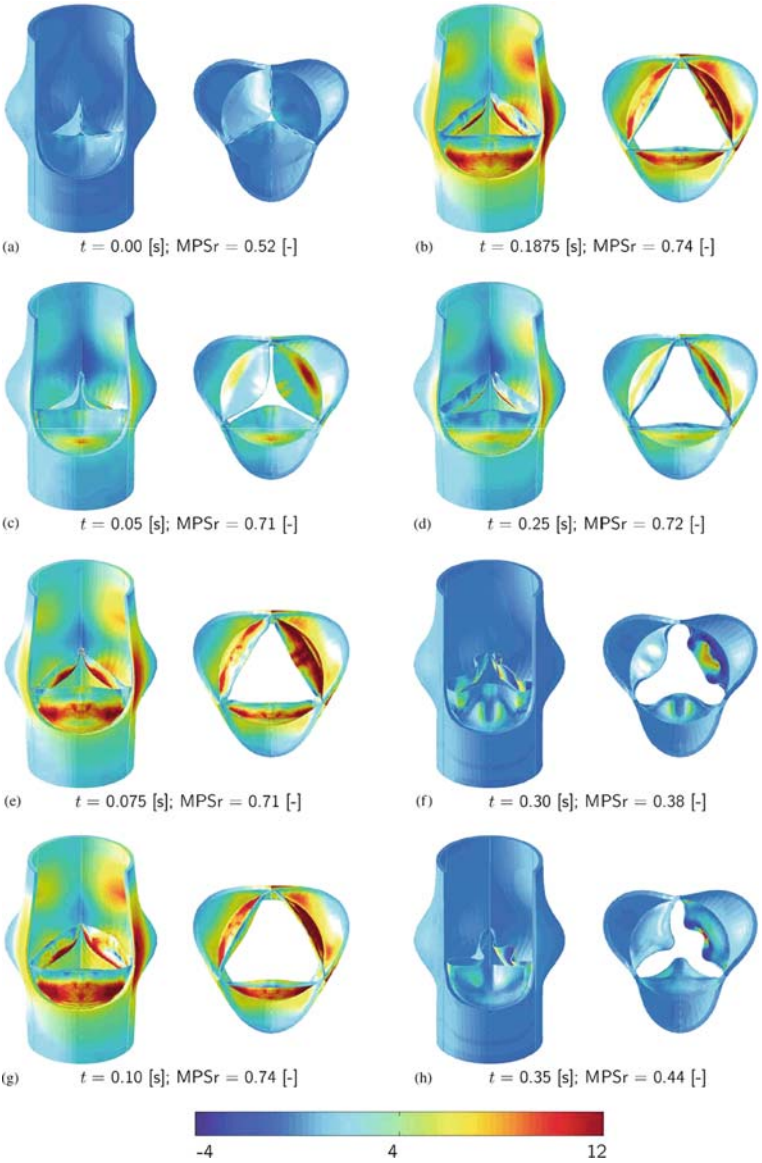

Fig. 16.9 Maximum principle Cauchy stresses during systole. *Upper right* cusp is from the non-reinforced model in comparison to the fiber-reinforced model (*left* and *bottom* cusps). MPSr is the ratio of maximum principle stress of the fiber-reinforced and non-reinforced models. Stress scale is in kPa. [16]

16.7 Multiscale Studies

In a model developed by Weinberg and Mofrad [12], not only are the individual layers of the valvular tissue described using nonlinear anisotropic designations and simulated within a fluid domain, but the model is capable of simulations at the organ, tissue, and cell levels of the system as well. This multiscale approach makes it possible to analyze a problem from the organ level which includes the complex multi-structure and fluid interplay to the cellular level where cellular deformation could indicate a biological response. Multiscale methods have also been employed in other areas of research [40, 41].

In Weinberg and Mofrad [12], a set of reference configurations were defined to describe the state of the tissue from the individual layers to a loaded assembled valve and are derived from those created by Stella and Sacks [5]. In the first configuration $\Omega_{0,}$ the fibrosa and ventricularis are separate and free from stress; the layers are then combined with the appropriate corrugations and arrangement to construct configuration Ω_1. Next the tissue is assembled into the valve structure, pressure-free Ω_2. For the next configuration Ω_3, a pressure is applied to the valve to create a physiological initial state. Finally Ω_t represents the functioning valve as it varies with time. Radial and circumferential extensibilities were assigned to the tissue in each configuration; these values were based on published experimental studies. These reference configurations were used as the framework for the multiscale simulations. Simulations were first performed in the organ scale and the resulting element strains were then used as boundary conditions imposed on the tissue-scale model. Similarly, the strains from the tissue-scale model were then used as boundary conditions for the cell scale model. In this manner, simulations are executed with data passing down from the largest to smallest scale.

The organ-scale simulations included FSI and used an idealized geometry. A constitutive model was used for the material in which discrete isotropic solid elements had embedded one-dimensional cable elements on their top and bottom perimeters. Time-varying physiological pressures were applied as boundary conditions to the fluid inlet and outlet sources, and the motion created by ventricular contraction was also included in the model by applying experimentally-derived radial displacements to the base of the valve. For continuation to the tissue-scale model, the element deformations at three points throughout the radius of the cusp were tracked to be transferred to the tissue-scale model. The three individual tissue layers were included in the tissue-level simulation. The ventricularis and fibrosa were modeled as isotropic exponential materials with embedded exponential fibers [42] which traversed in the circumferential direction to simulate collagen fibers, whereas the spongiosa was modeled as a nonlinear isotropic material. The constants for these functions were adapted from published experimental data with respect to configurations Ω_0 and Ω_1. A radial stretch was then applied to modify the tissue from Ω_1 to Ω_2, and the element deformations from the organ-scale model were imposed for configurations Ω_2 to Ω_t. The deformations of a selected element of either fibrosa or ventricularis were tracked to use as boundary conditions for the cell-scale model. The model for

the cell scale was comprised of a single cell surrounded by matrix. The same constitutive models as the tissue-scale model were utilized for that of the cell level, and the matrix could represent either the fibrosa or the ventricularis. The element deformations from the tissue-scale model were applied as boundary conditions to the outer faces of the matrix, and simulations began from reference configuration Ω_2. The results obtained from this level of simulation were cell aspect ratio (CAR) data.

Like the preceding computational models of the aortic valve, this model can demonstrate the deformation occurring during the opening and closing of the valve, and the stress and strain distributions which result. With its FSI facilities, the mutual effects of the solid and fluid domains are included in the analysis, and fluid flow data can be acquired in addition to that of the solid structures. However, unlike previously developed models of the valve, the capabilities of this model extend beyond the organ scale (see Fig. 16.10). The mechanical response of the individual layers of the tissue can be investigated, examining the distributions of stress and strain throughout the layers, accounting for the unique corrugated nature of the fibrous layers. Most interesting is the information available on cellular deformation at key points in the tissue assembly, to better ascertain which conditions are truly sensed on the cellular level and therefore capable of eliciting a biological change. This utile model shows great promise as a tool to investigate pathologies such as aortic calcification which are triggered by the interstitial cells of the cusp tissue in response to abnormal mechanical stimuli.

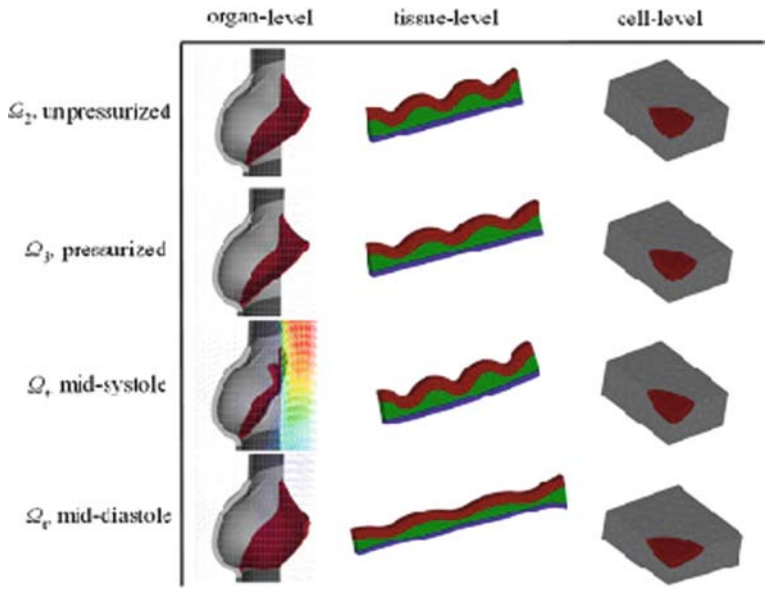

Fig. 16.10 Deformations experienced at each of the three levels of the multiscale model [12]

This multiscale model has been used to investigate the congenital disease condition of a bicuspid aortic valve. Whereas the normal aortic valve has three cusps and three sinuses, 1–2% of the population is born with only two cusps and two corresponding sinuses. These patients are more likely to develop valvular diseases such as calcific aortic stenosis and generally present symptoms at an earlier age. Weinberg and Mofrad [43] utilized the multiscale model described [12] to investigate the mechanical effects of this cusp geometry on the organ, tissue, and cellular levels. The two different valve geometries are shown in Fig. 16.11. At the organ level, the bicuspid valve did not open as fully, creating a jet formation differing from that seen in the fluid phase of the tricuspid valve. Higher levels of flexure were observed for the bicuspid valve in both the coaptation area and the region near the cusp attachment to the root wall, and the cusps opened with visible wrinkling. Cellular deformation values were computed for the regions of high flexure on the aortic surface of the cusp (the surface where calcification develops) for both the bicuspid and tricuspid valves and compared. Although the bicuspid had aberrant deformation on the organ level, cellular deformations were similar for both models, and therefore no significant difference may be detected on the cellular level. Since calcific aortic stenosis is thought to be regulated at the cellular level, this study concluded that the higher occurrence of calcification in bicuspid valves is not necessarily caused solely by the geometric difference of the reduced number of cusps. Bicuspid valves may be more susceptible to disease due to other genetic differences such as abnormal matrix components. Further information outside the capabilities of computational modeling is needed to identify the reason bicuspid valves are vulnerable to disease; however, computational modeling was successful in providing evidence against the simple assumption that the geometric difference of two cusps was fully responsible for diseases such as calcification and demonstrates that further investigation is warranted.

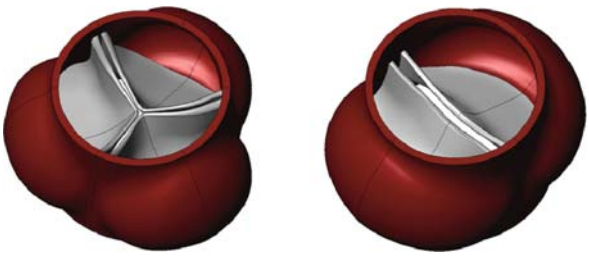

Fig. 16.11 Trileaflet (*left*) and bileaflet (*right*) geometries used in Weinberg and Mofrad [43]

16.8 Conclusion

Computer simulations of the aortic valve have provided mechanical information on the valve which may have otherwise been unattainable. Heart valve diseases are a widespread problem and in many cases are linked to mechanical factors and

abnormalities. Modeling studies have presented a platform to elucidate the mechanical environment of the healthy valve and have provided insight into the progression of pathological conditions. Continuing improvements in numerical simulations are eliminating past modeling limitations so that new models can more closely replicate the physiological problem. This field shows great promise in continuing to supply vital information to improve heart valve healthcare.

References

1. Rosamund W, Flegal K, Friday G, Furie K, Go A, Greenlund K, Haase N, Ho M, Howard V, Kissela B, Kittner S, Lloyd-Jones D, McDermott M, Meigs J, Moy C, Nichol G, O'Donnell CJ, Roger V, Rumsfeld J, Sorlie P, Steinberger J, Thom T, Wasserthiel-Smoller S, Hong Y. Heart disease and stroke statistics – 2007 update. *Circulation*. 2007;115:e69–e171.
2. Yacoub MH, Takkenberg JJ. Will heart valve tissue engineering change the world? *Nat Clin Pract Cardiovasc Med*. 2005;2:60–1.
3. Sacks MS, Yoganathan AP. Heart valve function: a biomechanical perspective. *Phil Trans R Soc B*. 2007;362:1369–91.
4. Butcher JT, Nerem RM. Valvular endothelial cells and the mechanoregulation of valvular pathology. *Phil Trans R Soc B*. 2007;362:1445–57.
5. Stella JA, Sacks MS. On the biaxial mechanical properties of the layers of the aortic valve leaflet. *J Biomech Eng*. 2007;129:757–66.
6. Yoganathan AP, Woo YR, Sung HW, Jones M. Advances in prosthetic heart valves: fluid mechanics of aortic valve designs. *J Biomater Appl*. 1988;2:579–614.
7. Yang G, Merrifield R, Masood S, Kilner PJ. Flow and myocardial interaction: an imaging perspective. *Phil Trans R Soc B*. 2007;362:1329–41.
8. Thubrikar MJ. Geometry of the aortic valve. In: *The Aortic Valve*. Boca Raton, FL: CRC Press, 1990.
9. Misfeld M, Sievers HH. Heart valve macro- and microstructure. *Phil Trans R Soc B*. 2007;362:1421–36.
10. Ranga A, Bouchot O, Mongrain R, Ugolini P, Cartier R. Computational simulations of the aortic valve validated by imaging data: evaluation of valve-sparing techniques. *Interact Cardiovasc Thorac Surg*. 2006;5:373–8.
11. Howard IC, Patterson EA, Yoxall A. On the opening mechanism of the aortic valve: some observations from simulations. *J Med Eng Technol*. 2003;27:259–66.
12. Weinberg EJ, Mofrad MRK. Transient, three-dimensional, multiscale simulations of the human aortic valve. *Cardiovasc Eng*. 2007;7:140–55
13. Grande KJ, Cochran RP, Reinhall PG, Kunzelman KS. Stress variations in the human aortic root and valve: the role of anatomic asymmetry. *Ann Biomed Eng*. 1998;26:534–545.
14. Nicosia MA, Cochran RP, Einstein DR, Rutland CJ, Kunzelman KS. A coupled fluid-structure finite element model of the aortic valve and root. *J Heart Valve Dis*. 2003;12:781–9.
15. Mendelson K, Schoen FJ. Heart valve tissue engineering: concepts, approaches, progress, and challenges. *Ann Biomed Eng*. 2006;34:1799–819.
16. De Hart J, Baaijens FP, Peters GW, Schreurs PJ. A computational fluid-structure interaction analysis of a fiber-reinforced stentless aortic valve. *J Biomech*. 2003;36:699–712.
17. Thubrikar M, Piepgrass WC, Bosher LP, Nolan SP. The elastic modulus of canine aortic valve leaflets in vivo and in vitro. *Circ Res*. 1980;47:792–800.
18. Carmody CJ, Burriesci G, Howard IC, Patterson EA. An approach to the simulation of fluid-structure interaction in the aortic valve. *J Biomech*. 2006;39:158–69.
19. Gnyaneshwar R, Kumar RK, Balakrishnan KR. Dynamic analysis of the aortic valve using a finite element model. *Ann Thorac Surg*. 2002;73:1122–9.

20. Sripathi VC, Kumar RK, Balakrishnan KR. Further insights into normal aortic valve function: role of a compliant aortic root on leaflet opening and valve orifice area. *Ann Thorac Surg*. 2004;77:844–51.
21. Patterson EA, Howard IC, Thornton MA. A comparative study of linear and nonlinear simulations of the leaflets in a bioprosthetic heart valve during the cardiac cycle. *J Med Eng Technol*. 1996;20:95–108.
22. Ranga A, Mongrain R, Mendes Galaz R, Biadillah Y, Cartier R. Large-displacement 3D structural analysis of an aortic valve model with nonlinear material properties. *J Med Eng Technol*. 2004;28:95–103.
23. Burriesci G, Howard IC, Patterson EA. Influence of anisotropy on the mechanical behaviour of bioprosthetic heart valves. *J Med Eng Technol*. 1999;23:203–15.
24. Li J, Luo XY, Kuang ZB. A nonlinear anisotropic model for porcine aortic heart valves. *J Biomech*. 2001;34:1279–89.
25. Cheng A, Dagum P, Miller DC. Aortic root dynamics and surgery: from craft to science. *Phil Trans R Soc B*. 2007;362:1407–19.
26. Driessen NJ, Bouten CV, Baaijens FP. Improved prediction of the collagen fiber architecture in the aortic heart valve. *J Biomech Eng*. 2005;127:329–36.
27. David TE, Feindel CM, Bos J. Repair of the aortic valve in patients with aortic insufficiency and aortic root aneurysm. *J Thorac Cardiovasc Surg*. 1995;109:345–51.
28. Grande-Allen KJ, Cochran RP, Reinhall PG, Kunzelman KS. Mechanisms of aortic valve incompetence: finite-element modeling of Marfan syndrome. *J Thorac Cardiovasc Surg*. 2001;122:946–54.
29. Robicsek F, Thubrikar MJ, Fokin AA. Cause of degenerative disease of the trileaflet aortic valve: review of subject and presentation of a new theory. *Ann Thorac Surg*. 2002;73:1346–54.
30. Grande-Allen KJ, Cochran RP, Reinhall PG, Kunzelman KS. Finite-element analysis of aortic valve-sparing: influence of graft shape and stiffness. *IEEE Trans Biomed Eng*. 2001;48:647–59.
31. Cacciola G, Peters GW, Schreurs PJ. A three-dimensional mechanical analysis of a stentless fibre-reinforced aortic valve prosthesis. *J Biomech*. 2000;33:521–30.
32. Chandran KB, Kim SH, Han G. Stress distribution on the cusps of a polyurethane trileaflet heart valve prosthesis in the closed position. *J Biomech*. 1991;24:385–95.
33. Krucinski S, Vesely I, Dokainish MA, Campbell G. Numerical simulation of bioprosthetic valves mounted on rigid and expansile stents. *J Biomech*. 1993;26:929–43.
34. Robicsek F. Leonardo da Vinci and the sinuses of Valsalva. *Ann Thorac Surg*. 1991;52:328–35.
35. Beck A, Thubrikar MJ, Robicsek F. Stress analysis of the aortic valve with and without the sinuses of Valsalva. *J Heart Valve Dis*. 2001;10:1–11.
36. David TE, Feindel CM, Webb GD, Colman JM, Armstrong S, Maganti M. Long-term results of aortic valve-sparing operations for aortic root aneurysm. *J Thorac Cardiovasc Surg*. 2006;132:347–54.
37. Pacini D, Settepani F, De Paulis R, Loforte A, Nardella S, Ornaghi D, Gallotti R, Chiariello L, Di Bartolomeo R. Early results of valve-sparing reimplantation procedure using the Valsalva conduit: a multicenter study. *Ann Thorac Surg*. 2006;82:865–71.
38. Driessen NJ, Boerboom RA, Huyghe JM, Bouten CV, Baaijen FP. Computational analyses of mechanically induced collagen fiber remodeling in the aortic heart valve. *J Biomech Eng*. 2003;125:549–57.
39. De Hart J, Cacciola G, Schreurs PJ, Peters GW. A three-dimensional analysis of a fibre-reinforced aortic valve prosthesis. *J Biomech*. 1998;31:629–38.
40. Chandran PL, Barocas VH. Deterministic material-based averaging theory model of collagen gel micromechanics. *J Biomech Eng*. 2007;129:137–47.

41. Migliavacca F, Balossino R, Pennati G, Dubini G, Hsia TY, de Level MR, Bove EL. Multiscale modeling in biofluidynamics: application to reconstructive paediatric cardiac surgery. *J Biomech*. 2006;39:1010–20.
42. Holzapfel GA, Gasser TC, Ogden RW. A new constitutive framework for arterial wall mechanics and a comparative study of material models. *J Elast*. 2000;61:1–48.
43. Weinberg EJ, Mofrad MRK. A multiscale computational comparison of the bicuspid and tricuspid aortic valves in relation to calcific aortic stenosis. *J Biomech*. 2008;41:3482–7.

Chapter 17
Blood Flow in an Out-of-Plane Aorto-left Coronary Sequential Bypass Graft

Meena Sankaranarayanan, Dhanjoo N. Ghista, Leok Poh Chua, Tan Yong Seng, Kannan Sundaravadivelu, and Ghassan S. Kassab

Abstract Coronary artery bypass graft (CABG) is a major therapy for ischemic heart disease which if left untreated can progress to failure of the heart. Restenosis, a leading cause of CABG, can be correlated with the geometric configuration and the hemodynamics of the graft. In this chapter we use computational fluid dynamics (CFD) to investigate the hemodynamics in a 3D out-of-plane sequential bypass graft model. Using a finite volume approach, quasi-steady flow simulations are performed at mid-ejection and at mid-diastole. Plots of velocity vectors, wall shear stress (WSS), and spatial WSS gradient (WSSG) distribution are presented in the aorto-left coronary bypass graft domain. Simulation results reveal a more uniform WSS and spatial WSSG distribution in the side-to-side (sequential graft) anastomosis configuration over the end-to-side (multiple graft) anastomosis. Results for the multiple bypass graft model show the peak magnitudes of the spatial WSSG are higher compared to the sequential bypass graft model. These findings suggest that sequential bypass grafting may be preferable over multiple bypass grafting to avoid non-uniformities of WSS.

17.1 Introduction

The sequential coronary artery bypass grafting (CABG) technique, as described in early years [1, 2], is a technique in which two or more coronary artery anastomoses are made with a single graft, usually the saphenous vein. The distal anastomosis is constructed in an end-to-side fashion, while the proximal anastomosis is constructed in a side-to-side fashion. The advantages of this technique over the single graft technique include fewer anastomoses and higher graft flow [3, 4]. Higher patency rates have also been observed through post angiograms in the proximal side-to-side

M. Sankaranarayanan (✉)
Mathematics, Department of Science and Humanities, Hindustan University, Padur, Kelambakkam, Chennai, India
e-mail: meenasankaranarayanan@rediffmail.com

J.M. Guccione, et al. (eds.), *Computational Cardiovascular Mechanics*,
DOI 10.1007/978-1-4419-0730-1_17,

anastomoses as compared to the distal (end-to-side) anastomoses. Similar results were reported by O'Neill et al. [5], who confirmed that the proximal segment of the sequential graft has a higher velocity than that seen in a single bypass graft. Kerem et al. [6] found that higher patency rates are achieved by using sequential grafts in bypass surgeries that involve coronary arteries with small diameter (around 1.5 mm) or with a poor run-off.

Despite the apparent advantages of sequential bypass grafting, this technique has been criticized because revascularization depends on a single proximal anastomosis [7]. A comparison of the results of single venous grafts with those of patients with sequential grafts revealed that the latter have the same 10-year outcome as single venous grafts [8].

Earlier works reported that formation of intimal hyperplasia plays a vital role in bypass graft failure [9, 10]. Several factors contribute to anastomotic intimal hyperplasia, including boundary layer separation [11], compliance mismatch [12], and other hemodynamic factors [13]. A wealth of literature on both experimental and computational fluid dynamics (CFD) studies in CABG have been cited in a recent publication [14] to investigate the role of various issues including the 3D aspects of the flow.

Previous works on CABG have been confined to limited segments of total CABG blood flow field. The present chapter expands the CFD study of blood flow in the entire flow field domain in a complete sequential bypass graft model as compared to multiple grafts. The objective is to investigate the flow patterns, velocity distributions, wall shear stress (WSS) distributions and their spatial gradients (WSSG) in two different anastomotic configurations, namely the side-to-side anastomosis and an end-to-side anastomosis of the out-of-plane aorto-left coronary sequential bypass graft. Although there are experimental studies on the hemodynamics of sequential bypass grafts [15, 16], this chapter presents the first CFD simulation of a sequential bypass.

17.2 CFD Analysis

17.2.1 Geometry

The sequential CABG model to simulate the flow field in the anastomoses of the aorto-left coronary bypass graft is constructed using dimensions based on surgical observations from patients (Fig. 17.1.). The 3D geometry of the aorto-coronary bypass graft model is constructed using the commercial fluid dynamic software *GAMBIT.*

As indicated in Fig. 17.1, the saphenous vein originates from the aorta at point A and is anastomosed to the 90% proximally occluded obtuse marginal OM1 branch at point B in a side-to-side anastomosis. It is then anastomosed in an end-to-side fashion with the 80% proximally occluded obtuse marginal (OM2) branch at C. The intersection between the graft and the OM1 results in a diamond-shape anastomosis

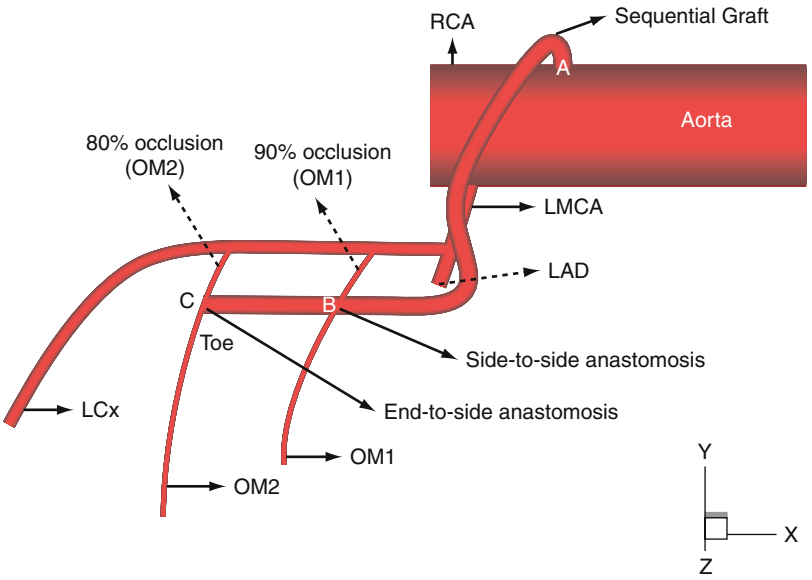

Fig. 17.1 A schematic of out-of-plane aorto-left coronary sequential bypass graft model (model I) includes the ascending aorta, the right coronary artery inlet (RCA), the left main coronary artery (LMCA) and its branches LCx and LAD. The proximal portion of the branches of the LCx artery namely the obtuse marginals OM1 and OM2 are 90% and 80% occluded respectively; B and C denote proximal and distal anastomoses

geometry, while that between the graft and the OM2 artery has an elliptical shape. The latter is caused by the deformation of the larger diameter graft sutured to the smaller LAD vessel as observed in surgery.

In order to avoid competition of flow between the obtuse marginal branches, the OM1 artery is assumed to be more severely occluded (90%) than the OM2 artery (80%). From a clinical point of view, it is desirable to have both branches well perfused in a sequential graft.

17.2.2 Material Properties and Flow Conditions

Blood is assumed to be an incompressible, Newtonian fluid with a dynamic viscosity (μ) of 0.00408 Pa s. The density (ρ) of blood is taken as 1050 kg/m^3. The inlet Reynolds numbers are 421, 128, 40, and 106 for the aorta, the LCx, and the branches OM1 and OM2. The vessels are considered as rigid conduits and the no-slip conditions are applied at the walls. For a 3D flow, the conservation of mass and linear momentum are expressed by the equations of continuity and Navier–Stokes, respectively, as

$$\nabla . q = 0, \tag{17.1}$$

$$\rho\left(\frac{\partial q}{\partial t} + q.\nabla q\right) = -\nabla p + \mu\nabla^2 q, \tag{17.2}$$

where p denotes the pressure and$q$denotes the velocity vector in 3D space. The flow dynamics were analyzed at mid-ejection and mid-diastole. A quasi-steady flow analysis is carried out by taking into account the cardiac cycle data on blood flow-rate waveforms at the entrances to the aorta, LAD, LCx, and RCA. The velocity distribution is obtained by solving Equations (17.1) and (17.2), subject to the input boundary conditions given below.

The input conditions to the model are the measured time-varying flow-rate waveforms at the aorta entrance, LAD entrance, RCA entrance, and the LCx

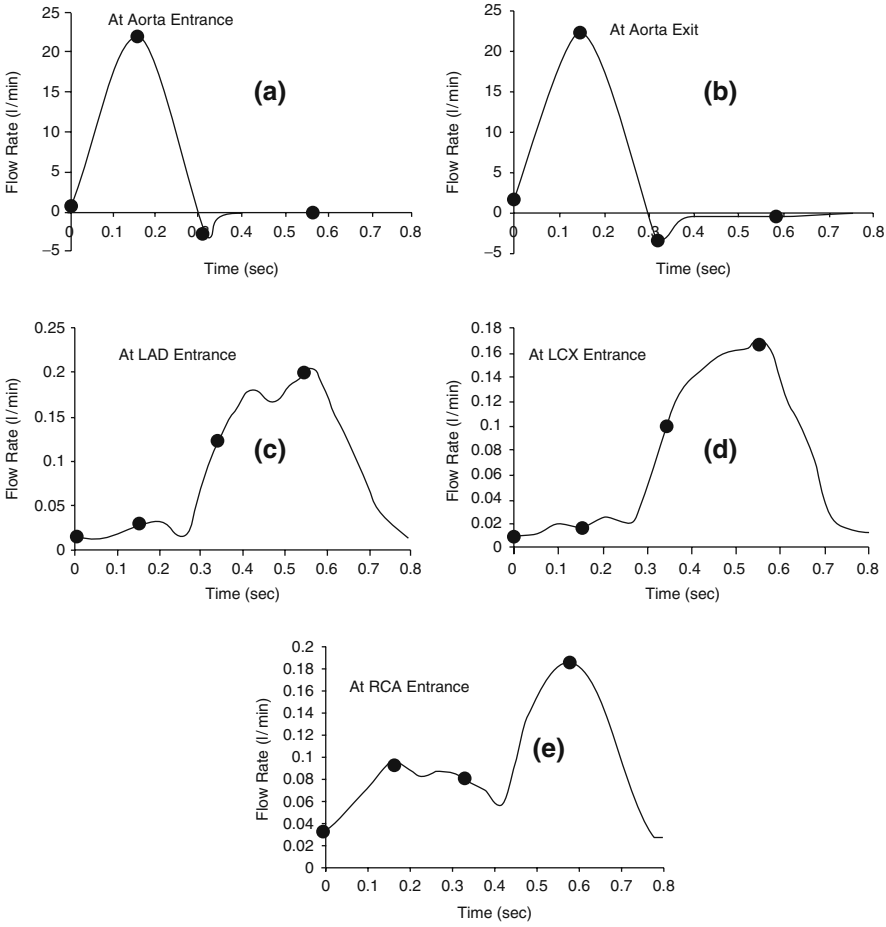

Fig. 17.2 (**a**) Flow-rate waveform at the inlet of the aorta. (**b**) Flow-rate waveform at the ascending aorta exit. (**c**) Flow-rate waveform at the entrance of the LAD artery. (**d**) Flow-rate waveform at the entrance of the LCx artery. (**e**) Flow-rate waveform at the entrance of the RCA

(Fig. 17.2 a–e). A detailed explanation of the input flow conditions are reported in an earlier work [14].

The flow discharges were set proportional to the third power of the branching vessel diameter according to Murray's law [17]. Throughout the analysis, the flow discharge values (as a percentage of the LCA inlet flow) fixed at the various outlet branches of the LCA tree (namely, LCx, OM1, OM2, and LAD) were set to 22.4, 5.82, 15.4, and 56.3, respectively.

17.2.3 Computational Setup

The CFD simulations were performed using a control volume-based technique, implemented in the CFD code Fluent (Fluent User's Guide, Fluent, Lebanon, NH). In the Fluent solution algorithm, the governing equations (conservation of mass and linear momentum) are solved sequentially. As the equations are non-linear (and coupled), several iterations of the solution loop are needed before a convergent solution obtained. Using this approach, the resultant algebraic equations for the dependent variables (namely the velocities) in each control volume are solved sequentially, by a point implicit (Gauss-Seidel) linear equation solver in conjunction with an algebraic multi-grid method.

In order to carry out a mesh sensitivity test, numerical simulations were performed by varying the number of grid cells in the computational domain. The mesh sensitivity on the flow variables (namely the velocity and WSS) are tested by varying the number of grid cells. It is found that the computational domain of 146,825 cells was sufficient for convergence. The simulation results did not show any difference when the convergence criterion set was changed from 10^{-5} to 10^{-6}. Hence, the study was carried out with the convergence criteria of 10^{-5}.

17.3 Simulation Results

17.3.1 Sequential Bypass Graft

The flow characteristics are analyzed at two instances of the cardiac cycle: (1) during mid-ejection (t=0.15 s) when there is maximum flow entering the aorta, and (2) during mid-diastole (t=0.57 s) when the aortic valve is fully closed and there is maximum perfusion in the coronary arteries.

To study the influence of the geometry on the flow field, the velocity distribution of the entire flow field is computed. Due to the complex out-of-plane geometry, the computed velocity vectors are illustrated in the respective plane of symmetry of the conduits. The WSS distributions are also likewise illustrated for the respective instances of the cardiac cycle along with the WSSG in the bypassed regions.

At mid-ejection, the majority of LV flow enters the ascending aorta with very little blood entering the coronaries, as noted in Fig. 17.3. The flow in the aorta is

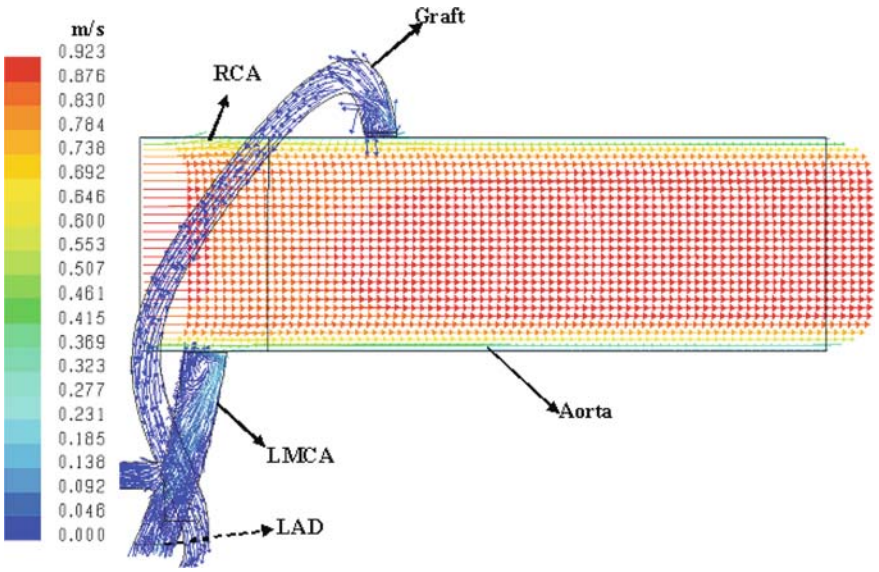

Fig. 17.3 At the mid-ejection phase t=0.15 s, the velocity vectors are displayed in the center plane of the aorta. Flow enters the aorta with a higher uniform velocity. Regions of recirculation are observed at the graft entrance and at the entrance of the LMCA

nearly uniform with a very high velocity. Due to the high pressure gradient, strong regions of recirculation are seen at both the entrance of the graft and at the LMCA branch.

The recirculation regions observed at the entrances of the graft and the LMCA reduces the amount of blood flow from entering into other branches (LCx, OM1, and OM2). Due to the large variation in the magnitude of velocity, the velocity vectors around the side-to-side anastomosis (B) region and the end-to-side anastomosis (C) region are shown separately (Figs. 17.4 and 17.5). The 90% stenotic region in the proximal portion of OM1 allows negligible flow into the distal end of OM1. The majority of the flow in the distal branch of OM1, however, comes from the graft (Fig. 17.4). The flow profile of LCx is skewed due to the curvature of the vessel. Blood flow from the graft impinges on the bed of OM2. The majority of the flow issuing out of the graft progresses into the distal end of OM2 (Fig. 17.5), while a small amount passing through the proximal portion of the constricted OM2 vessel enters the LCx.

Despite the flow patterns remaining qualitatively similar at the start of ejection (not shown), the slight increase in graft flow (0.0074 l/min) compared to the start of ejection contributes to a small increase in the magnitude of velocity in OM1 and OM2 vessels. The respective flow rates in the distal ends of OM1 and OM2 are 0.0021 l/min and 0.0057 l/min. The magnitude of mean velocities at the different vessels, namely, the aorta, graft, LCx, OM1, and OM2 are 0.738 m/s, 0.01 m/s, 0.08 m/s, 0.018 m/s, and 0.068 m/s respectively.

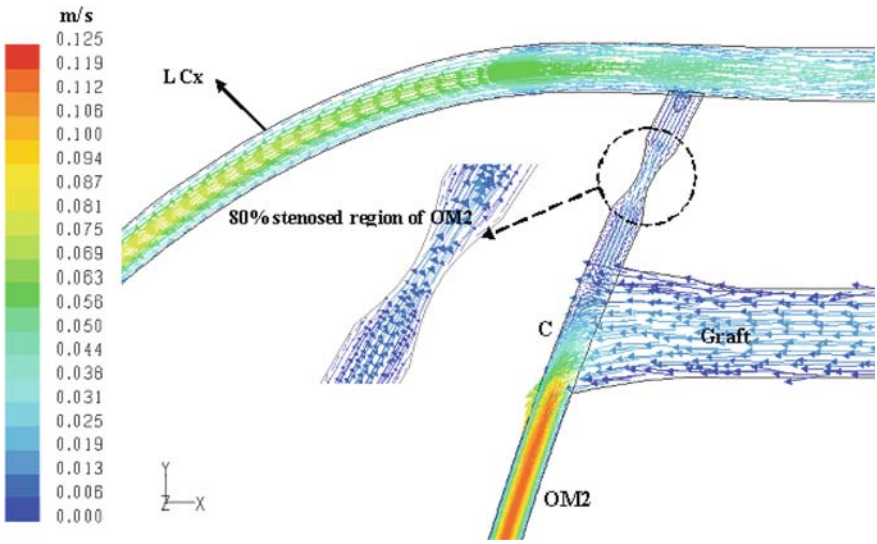

Fig. 17.4 The velocity vectors (m/s) in the side-to-side anastomosis region at t=0.15 s. The regions of recirculation (at the entrance of the graft and LMCA) do not allow much blood to enter the left coronary artery and its branches

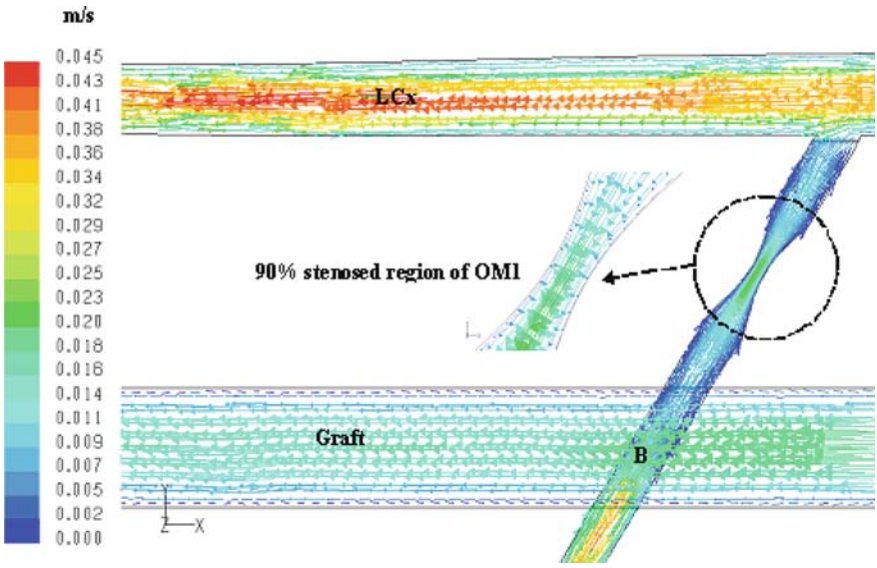

Fig. 17.5 The velocity vectors (m/s) in the end-to-side anastomosis region at t=0.15 s. Skewing of blood flow profile is predominant in the LCx artery, reflecting the influence of the curvature of the vessel wall

At mid-ejection, it is observed (Fig. 17.6) that the peak WSS is increased by a factor of 4 compared to that observed at the start of ejection phase due to the increase in magnitude of velocity entering the aorta from the LV.

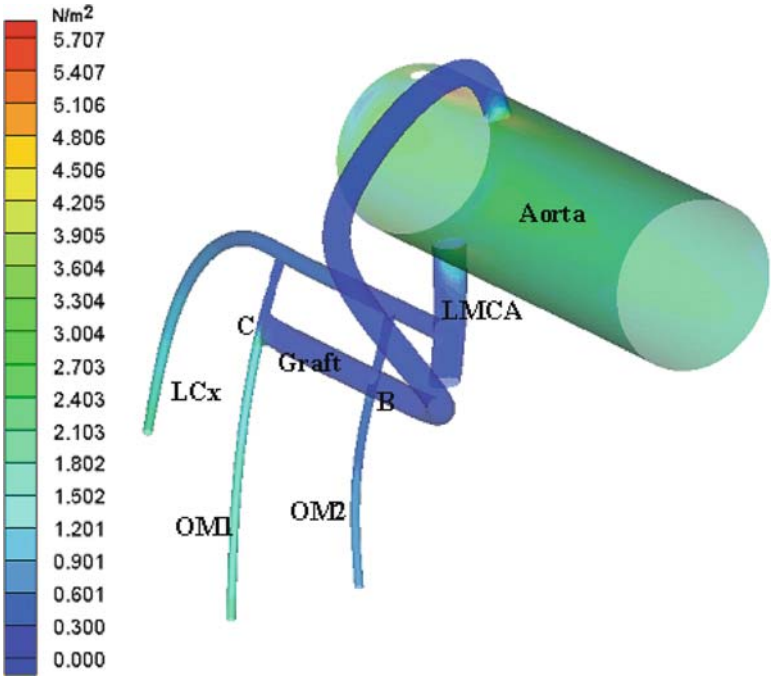

Fig. 17.6 The WSS at mid-ejection t=0.15 s. Maximum WSS of around 5.7 N/m^2 observed around the entrance of the RCA and at the graft entrance. Within the aortic domain, the WSS distribution is relatively uniform (around 2.29 N/m^2), reflecting the smooth flow pattern

The maximum WSS (∼5.7 N/m^2) is observed around the RCA region with a WSS distribution in the range of 2.29 N/m^2 in the aortic domain and the distal regions of the branches of the LCA. This may be attributed to the steep velocity gradients seen in those regions.

The peak WSS at the side-to-side anastomosis region B is much smaller than the peak WSS that is observed at the toe of the end-to-side anastomosis C (Fig. 17.7).

There is a low WSSG in the side-to-side anastomosis region, and sharp gradients at the toe of the end-to-side anastomosis, reflecting the non-uniform distribution of WSS (Fig. 17.8).

At mid-diastole (t=0.57 s), the aortic valve is fully closed and the blood perfuses the coronary vessels from the ascending aorta (inlet flow rate of 0.0937 l/min). At the graft entrance, strong skewing of blood toward the outer wall of the graft is observed which gradually changes its path due to the curvature of the graft vessel (Fig. 17.9). The flow field pattern remains qualitatively the same as compared to the start of diastole (t=0.32 s), except with a rise in the magnitude of velocity observed in the LCx and its branches OM1 and OM2 (not shown). The increase

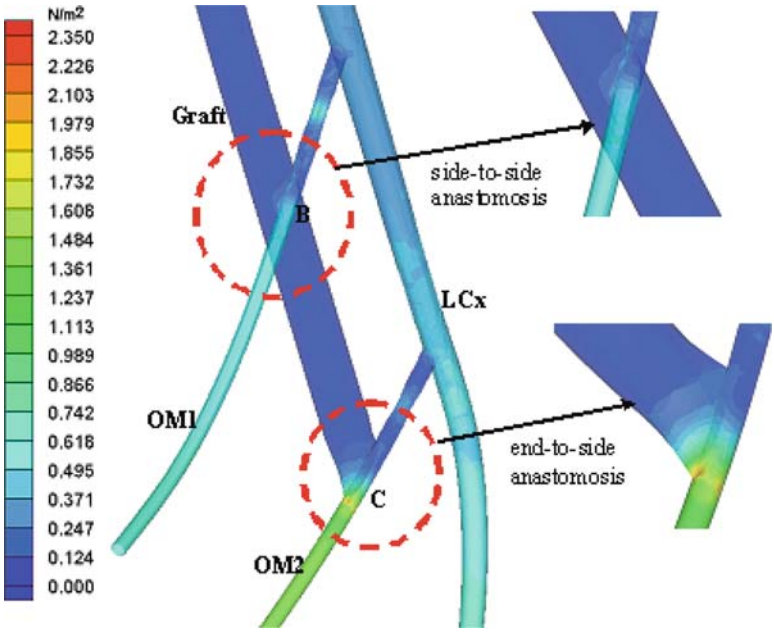

Fig. 17.7 WSS distribution seen around the side-to-side anastomosis is very small (of magnitude 0.75 Pa) compared to the high WSS (2.3 N/m^2) seen at the toe of the end-to-side anastomosis. However, an increase in WSS is observed in the distal end of the branches compared to the proximal portions (that may be attributed to the complexity of the vessel geometry)

in flow rate to the graft during mid-diastole results in good perfusion of the OM1 artery (0.0217 l/min), Fig. 17.10. Prominent skewing of flow profile is seen in the LCx branch, resulting in good perfusion of the distal portion of the LCx. The high graft flow impinges on the floor of the OM2 artery with a large force, thus allowing a significant amount of blood to enter the 80% constricted region, with the majority of blood flow (0.0628 l/min) proceeding toward the distal end of the OM2 artery (Fig. 17.11). A significant rise in the mean velocities during mid-diastole phase is observed.

The maximum WSS observed at the distal end of the LCx vessel wall reflects the prominent skewing of the flow field. As observed earlier, the WSS in the aortic domain is negligible (Fig. 17.12). The proximal portion of OM1, where the flow is almost stagnant, results in very low WSS. The region close to the side-to-side anastomosis and further downstream has a nearly uniform WSS (around 4 N/m^2). In contrast, there is a large spatial variation in WSS distribution (ranging from 0 N/m^2 to 48 N/m^2) in the OM2 branch of LCx, due to the strong impingement of blood on the floor of the artery and the complex geometry of the end-to-side anastomosis (Fig. 17.13).

The WSSG distribution is qualitatively similar to t=0.32 s, except for an increase in magnitude of the WSSG to around 25.9 N/m^3 seen at the toe of the end-to-side anastomosis (Fig. 17.14).

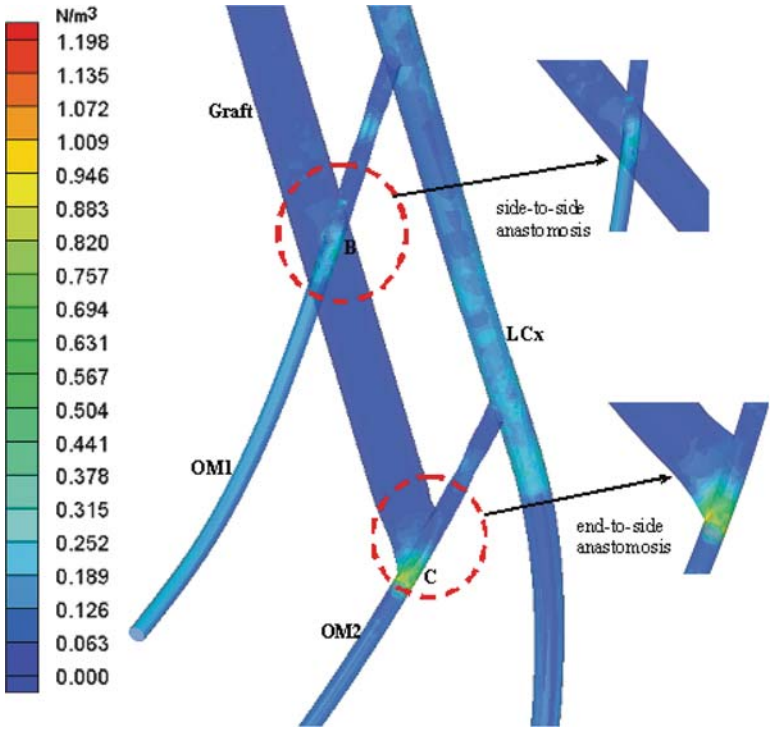

Fig. 17.8 The spatial distribution of the wall shear stress gradients at t=0.15 s

17.3.2 Comparison of Sequential and Multiple Bypass Graft

In order to have a clearer comparison of sequential bypass graft and multiple bypass grafts, the WSS and WSSG are also computed at the same instances of the cardiac cycle in a multiple bypass grafts model for the same input conditions of flow discharges. For convenience, we refer to the sequential CABG model (shown in Fig. 17.1) as model I and the multiple bypass graft model as model II (Fig. 17.15).

Since the main focus is to understand how the hemodynamics varies in the anastomosis regions of the two models, the WSSG plots pertaining to the anastomosis regions are shown which reflect distinct differences. Except for the toe region of model I (Fig. 17.8) which experiences a steep gradient (about 1.15 N/m^3), all other regions show a relatively small variation in WSSG. In model II, however, the spatial gradients are steeper (with maximum gradient seen at the toe) and the variation along the bed of the artery is more pronounced (Fig. 17.16).

During mid-diastole phase, t=0.57 s, the spatial WSSG is qualitatively similar to that observed during mid-ejection. The peak WSSG is higher in model II (around 28 N/m^3) as seen in Fig. 17.17, compared to the sequential bypass grafts model I (around 26 N/m^3), Fig. 17.14.

For both instances of the cardiac cycle, the multiple bypass graft model generally experiences a higher WSSG compared to the sequential bypass graft model.

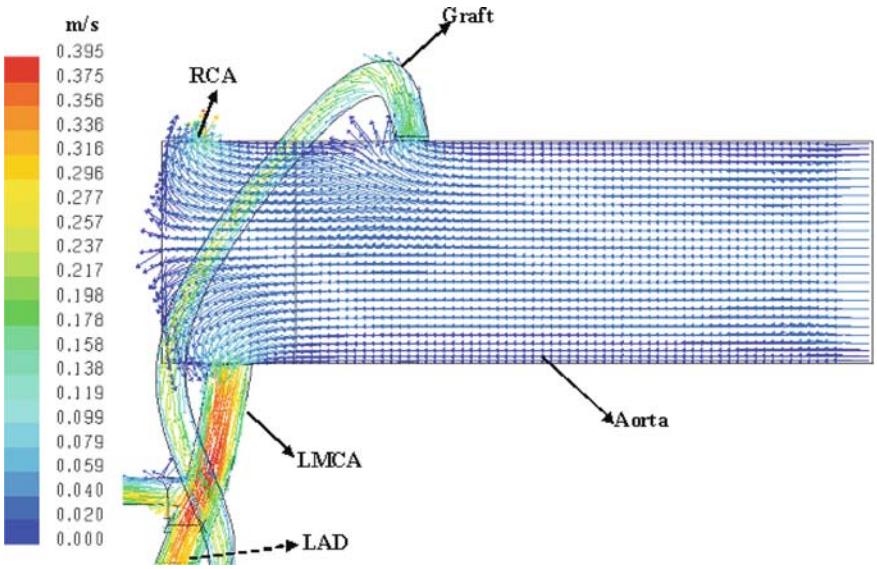

Fig. 17.9 At the mid-diastole t=0.57 s, the velocity vectors (m/s) are displayed in the center plane of the aorta. Blood from the ascending aorta perfuses the coronary vessels

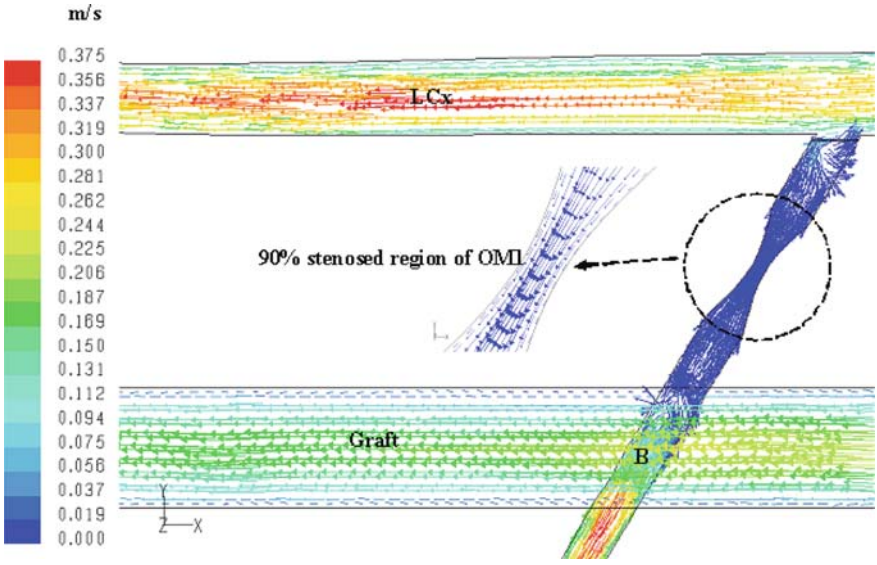

Fig. 17.10 The velocity vectors (m/s) in the side-to-side anastomosis region at mid-diastole, t=0.57 s. Maximum perfusion of the stenosed vessels occur during mid-diastole phase, with a maximum velocity of 0.375 m/s. A small recirculation region is observed at the entrance of the OM1 artery

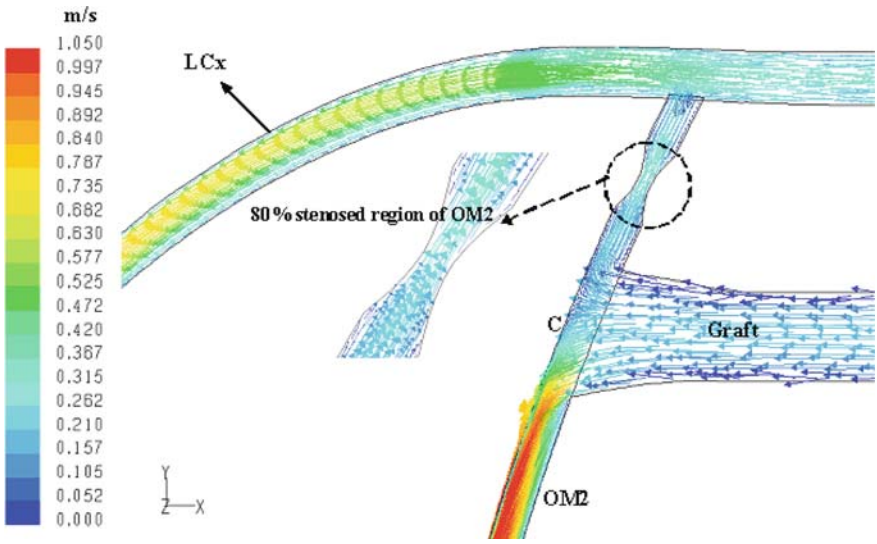

Fig. 17.11 The velocity vectors (m/s) in the end-to-side anastomosis region at t=0.57 s. Maximum perfusion of distal OM2 occurs during mid-diastole phase, with a maximum velocity of 1.05 m/s. Significant skewing of the velocity profile is seen in the LCx artery toward the outer wall as a result of the high flow rate and the vessel curvature

The reason for lower WSSG in the sequential bypass graft model may be attributed to the flow splitting caused by the side-to-side anastomosis. In the case of sequential bypass grafting, the flow splitting in the graft causes the parabolic graft flow profile to change to a flat profile thus resulting in a plug flow and consequential reduction of the velocity gradient. Hence the influence of the side-to-side anastomosis B on the end-to-side anastomosis C contributes to better WSSG environment which is in agreement with other reports [18]. These findings are also in agreement with Pietrabissa et al. [19] who also showed that sequential bypasses exhibited better hemodynamics (velocity, WSS, and spatial WSSG) in the graft segments upstream from the first anastomosis (side-to-side anastomosis). In addition to this, angiographic studies have also shown that a sequential bypass grafting may result in better patency than the conventional bypass grafting [6].

It is well known that fluid shear stresses have a definite bearing on endothelial cell shape and function. It has been shown that, in lesion-prone regions, the endothelial cells are polygon shaped, whereas in non-atherosclerotic regions they are elongated and aligned in the flow direction [20]. Lei et al. [21] have shown that in disturbed flow regions the elongation and alignment of endothelial cells are difficult to achieve because of high WSS gradients. Another numerical study on flow in two-way bypass grafts [18] reported that spatial WSSG could best relate to the initiation of disease formation, and the decrease of spatial WSSG may contribute to the improved hemodynamic condition. From this, we may infer that the toe and the floor of the end-to-side anastomosis region (in the sequential grafting) are more

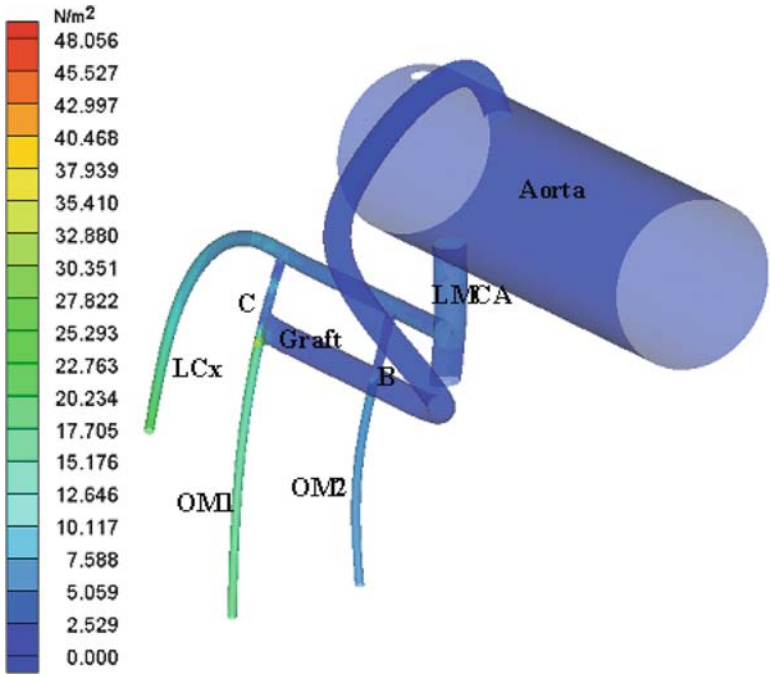

Fig. 17.12 The wall shear stress distribution (WSS) at the mid-diastole instant t=0.57 s indicates that magnitude of WSS increases from the proximal to the distal part of the LCx and its branches

prone to lesion development as these are regions that experience a high WSSG. This may be a reason for considering sequential bypass over multiple single grafts.

17.3.3 Critique of Simulation

Firstly, the elasticity of the vessel walls has not been considered since earlier work by Friedman [22] has suggested that wall elasticity is of lesser importance (than geometry) as far as the gross features of the flow is concerned. Steinmann and Ethier [23] have reported that the effects of wall distensibility were less pronounced than those of arterial geometry and flow conditions. Despite the fact that the coronary arteries move considerably throughout the cardiac cycle, Zeng et al. [24] have shown that pulsatility is the main characterizing factor of WSS distributions. Another study by Santamarina et al. [25] has revealed that the movement of coronary arteries has little effect on the velocity.

The model also does not take into account the non-Newtonian rheology of blood. This is because it is observed that there is variation of less than 6% observed in the peak WSS magnitude between the Newtonian model and the non-Newtonian Carreau model (data not shown).

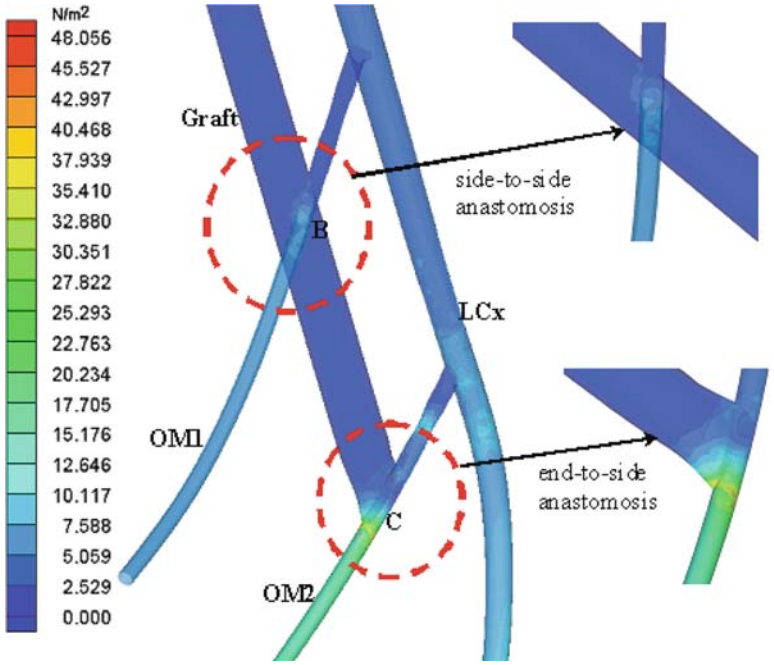

Fig. 17.13 WSS distribution seen around the side-to-side anastomosis is relatively high (around 10 N/m^2) while the toe of the end-to-side anastomosis and the floor of the OM2 artery experiences a very high WSS (around 48 N/m^2)

Models by Myers et al. [26] have shown that non-Newtonian nature of blood did not affect the inlet velocity profiles. Numerical simulations of non-Newtonian flow in a 2D end-to-side anastomosis investigated by Ballyk et al. [27] under pulsatile conditions have also shown only minor effects on WSS distributions.

17.4 Implications and Limitations of Simulations

17.4.1 Patency of CABG Procedures

Clinical studies [3, 28] have demonstrated that sequential vein bypass grafts retain their patency longer than single vein grafts. McNamara et al. [29], however, concludes that there is no significant difference between single graft and multiple grafts. This is in agreement with a recent work [30] that predicted similar patency of both single and sequential types of bypass. Al-Ruzzeh et al. [31] have shown that the combination of sequential bypass grafting and off-pump techniques was safe, and provided good early clinical and angiographic outcomes.

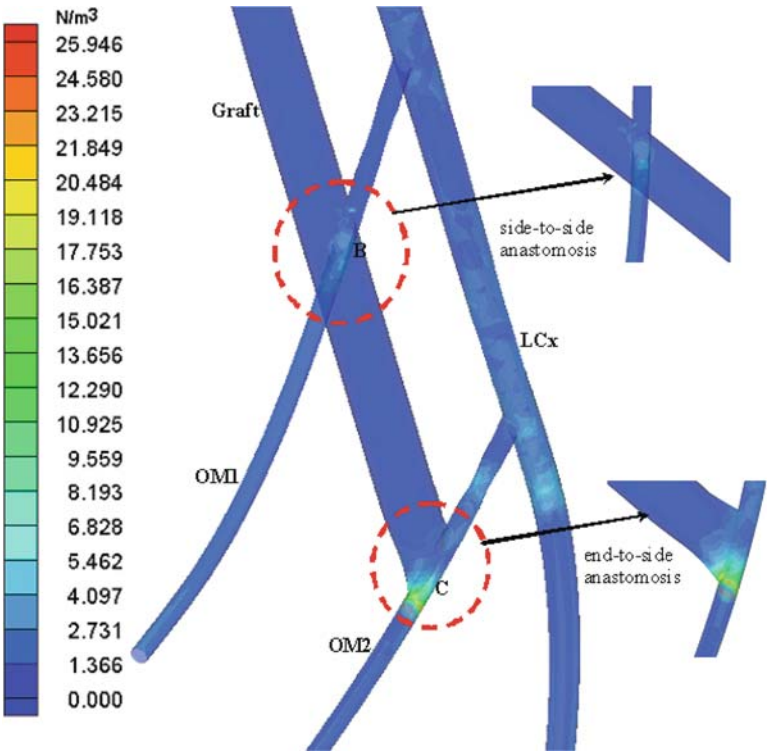

Fig.17.14 The spatial distribution of the wall shear stress gradients (WSSG) at t=0.57 s. Peak WSSG of magnitude 25.95 N/m^3 is seen at the toe of the end-to-side anastomosis. The region just after the toe experiences negligible WSSG

17.4.2 WSS, Spatial WSSG, and Atherosclerosis

Although the mechanism for the initiation and progression of atherosclerosis is not completely understood, studies have shown that local flow dynamics play a major role in the localization of atherogenesis [32, 33]. The major reason for this predisposition is the WSS and its temporal and spatial gradients. Numerous studies have shown that local blood flow characteristics and WSS distribution are strongly influenced by vessel geometry and by the anastomosis configuration (see review in Meena et al. [14]). When blood flow is disturbed, the frictional force exerted by the flowing blood on the endothelial surface (WSS) plays an important role in the pathogenesis of atherosclerotic plaque. Significant departure from uniformity of laminar flow imparts changes in endothelial cell behavior, which alters the biology of the monolayer and subsequently the susceptibility of conduit vessels to atherosclerotic disease. When the flow is uniform, however, the distribution of WSS is also uniform and thus results in low spatial WSSG. It is the low WSSG that results in a uniform hemodynamic environment that may contribute to better graft patency.

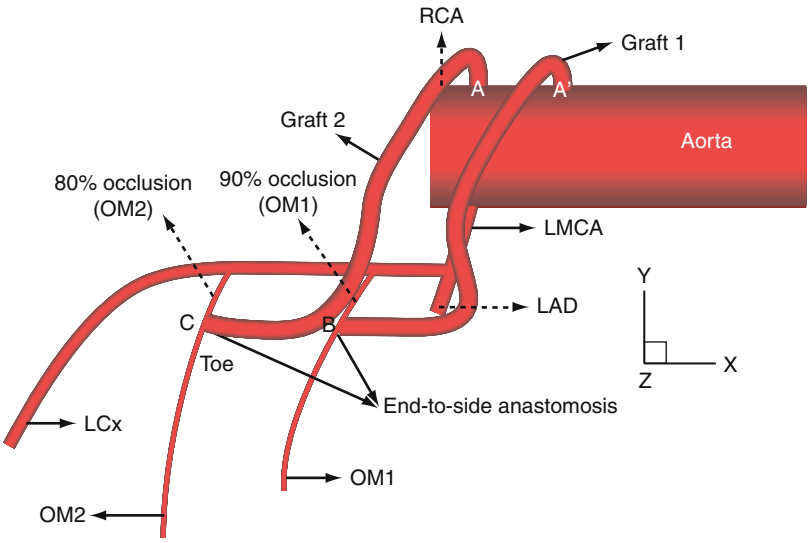

Fig. 17.15 Geometry of the multiple bypass graft model (model II). The dimensions of the vessels are the same as that of model I. Both the grafts are of uniform diameter, 4 mm

Both in vivo and CFD studies have shown that in unbranched arterial portions, the normal range of WSS that forces the endothelial cells to generate molecules that

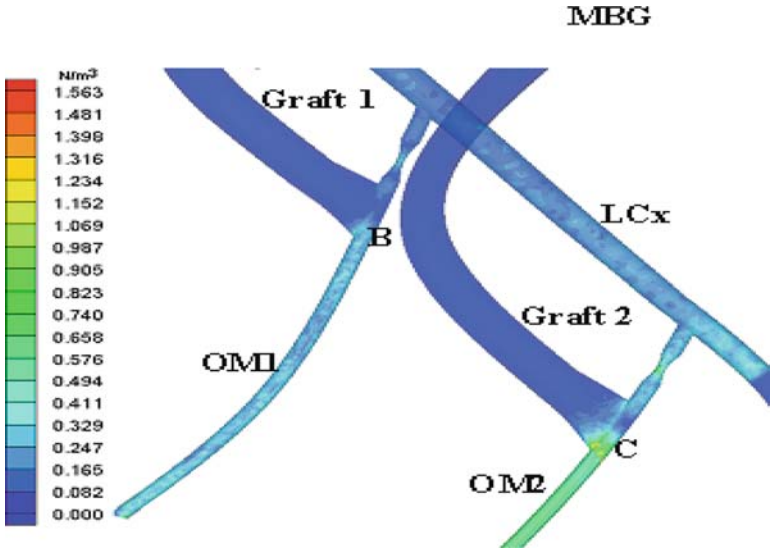

Fig. 17.16 Spatial WSSG (N/m^3) distribution in the anastomosis regions in model II at mid-ejection, t=0.15 s

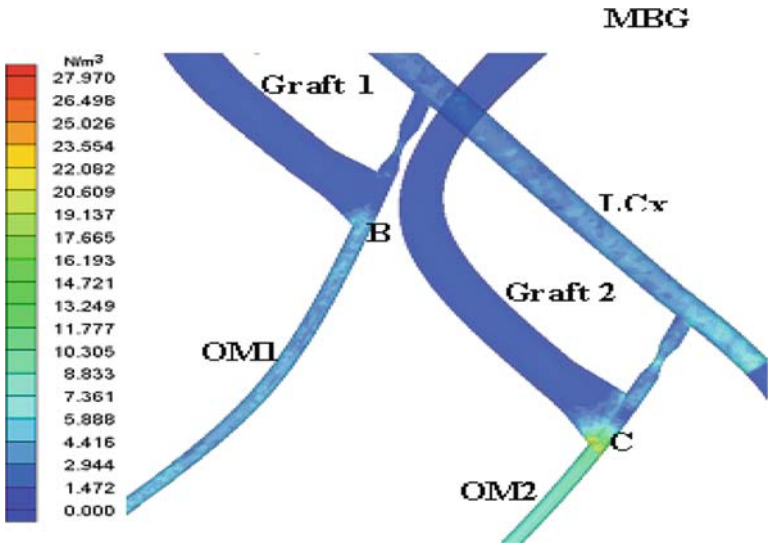

Fig. 17.17 Spatial WSSG (N/m^3) distribution in the anastomosis regions in model II at mid-ejection, t=0.57 s

promote a vasodilatory, anti-coagulant, anti-inflammatory, and growth-inhibitory surface is around 1.0–7.0 N/m^2 [34, 35]. On the other hand, a recent experimental study [36] revealed that at branches, bifurcations, and inner curvatures where disturbed flow occurs, abnormal WSS of less than 1.0 N/m^2 stimulates mechanosensors located on endothelial cells. This results in gene alterations which in turn causes structural changes of the endothelial cells. A detailed study [37] on flow in carotid arteries has determined some of the important hemodynamic factors (WSS, WSSG) by combining medical images (obtained using magnetic MRI and 3D ultrasound) with CFD simulations. Their results were closely in agreement with those of Malek et al. [38], who showed that values of WSS below 0.4 N/m^2 are known to stimulate proatherogenic endothelial phenotype while WSS > 1.5 N/m^2 is found to induce endothelial quiescence. Endothelial regions with WSS > 10 N/m^2 are prone to denudation.

The simulations reveal that there is a large variation in WSS in the distal anastomotic region owing to the non-uniform flow patterns resulting from the impingement of blood flow from the graft into the artery. This flow behavior results in non-uniform WSS distribution in the CABG, resulting in the possibility of intimal hyperplasia. In particular, peak WSS is seen at the toe of the end-to-side anastomosis which may be due to the sharp anastomotic geometry. Other regions that experience high WSS are the distal ends of the LCx and its branches. This may be attributed to the tapering of the vessels and the lack of consideration of smaller branches.

17.5 Summary and Conclusions

To our knowledge, this is the first CFD analysis of a sequential CABG in a fully integrated model that accounts for factors such as a realistic geometry and physiological inlet flow conditions. The analysis demonstrates the utility of CFD models to compare various CABG procedures. The simulation results suggest advantages of sequential grafting over multiple grafts. These findings call attention to further experimental and clinical studies to improve the long-term outcome of CABG.

Acknowledgments This research was supported in part by the National Institute of Health-National Heart, Lung, and Blood Institute Grant HL086400 and HL084529.

References

1. Flemma RJ, Johnson WD, Lepley D Jr. Triple aorto-coronary vein bypass as treatment for coronary insufficiency. *Arch Surg*. 1971;103:82–3.
2. Bartley TD, Bigelow JC, Page US. Aortocoronary bypass grafting with multiple sequential anastomoses to a single vein. *Arch Surg*. 1972;105:915–7.
3. Grondin CM, Limet R. Sequential anastomoses in coronary artery grafting: technical aspects and early and late angiographic results. *Ann Thorac Surg*. 1977;23:1–8.
4. Minale C, Bourg NP, Bardos P, Messmer BJ. Flow characteristics in single and sequential aorto-coronary bypass grafts. *J Cardiovasc Surg*. 1984;25:12–5.
5. O'Neill MJ Jr, Wolf PD, O'Neill TK, Montesano RM, Waldhausen JA. A rationale for the use of sequential coronary artery bypass grafts. *J Thorac Cardiovasc Surg*. 1981;81:686–90.
6. Kerem M, Sener E, Tasdemir O. Long-term patency of sequential and individual saphenous vein coronary bypass grafts. *Eur J Cardiovasc Surg*. 2001;19:140–4.
7. Kieser TM, FitzGibbon M, Keon WJ. Sequential coronary bypass grafts. long-term follow up. *J Thorac Cardiovasc Surg*. 1986;91:767–72.
8. Meeter K, Veldkamp R, Tijssen JG, Van Herwerden LL, Bos E. Clinical outcome of single versus sequential grafts in coronary bypass operations at ten years' follow-up. *J Thorac Cardiovasc Surg*. 1991;101:1076–81.
9. Clowes AW. Pathologic intimal hyperplasia as a response to vascular injury and reconstruction. In: Rutherford RB (Ed.) Vascular surgery, 4th edn. Philadelphia: WB Saunders, 1995:285–95.
10. Imparato AM, Bracco A, Kim GFE, Zeff RZ. Intimal and neointimal fibrous proliferation causing failure of arterial reconstruction. *Surgery*. 1972;72:1007–17.
11. Lo Gerfo FW, Soncrant T, Teel T, Dewey CF Jr. Boundary layer separation in models of side-to-end arterial anastomoses. *Arch Surg*. 1979;114:1369–73.
12. Clark RE, Apostolou S, Kardos JL. Mismatch of mechanical properties as a cause of arterial prosthesis thrombosis. *Surg Forum*. 1976;27:208–10.
13. Kassab GS, Navia JA. Biomechanical considerations in the design of graft: the homeostasis hypothesis. *Annu Rev Biomed Eng*. 2006;8:499–535.
14. Meena S, Ghista DN, Chua LP, Tan YS, Kassab GS. Analysis of blood flow in an out-of-plane CABG model. *Am J Physiol Heart Circ Physiol*. 2006;291:H283–95.
15. Hadcock MM, Ubatuba J, Littooy FN, Baker WH. Hemodynamics of sequential grafts. *Am J Surg*. 1983;146:170–3.
16. Ochi M, Yamada K, Ishii Y et al. Impact of sequential grafting of the internal thoracic or right gastroepiploic arteries on multiple coronary revascularization. *Cardiovasc Surg*. 2000;8(5):386–92.
17. Murray CD. The physiological principle of minimum work I. The vascular system and the cost of blood volume. *Proc Natl Acad Sci*. 1926;12:207–14.

18. Qiao A, Liu Y, Li S, Zhao H. Numerical simulation of physiological blood flow in 2-way coronary artery bypass grafts. *J Bio Phys*. 2005;31:161–82.
19. Pietrabissa R, Mantero S, Marotta T, Menicanti L. A lumped parameter model to evaluate the fluid dynamics of different coronary bypasses. *Med Eng Phy*. 1996;18(6):477–84.
20. Nerem RM. Vascular fluid mechanics and the arterial wall, and atherosclerosis. *J Biomech Eng*. 1992;114:274–82.
21. Lei M, Kleinstreuer C, Truskey G. Numerical investigation and prediction of atherogenic sites in branching arteries. *J Biomech Eng*. 1995;11:350–7.
22. Friedman MH. Arteriosclerosis research using vascular flow models: from 2-D branches to compliant replicas. ASME J Biomech Eng. 1993;115:595–601.
23. Steinmann DA, Ethier CR. The effect of wall distensibility on flow in a two-dimensional end-to-side anastomosis. *J Biomech Eng*. 1994;116:294–301.
24. Zeng DH, Ding ZH, Friedman MH, Ethier CR. Effects of cardiac motion on right coronary artery hemodynamics. *Ann Biomed Eng*. 2003;31:420–9.
25. Santamarina A, Weydahl E, Siegel JM Jr, Moore JE Jr. Computational analysis of flow in curved tube model of the coronary arteries: effects of time varying curvature. *Ann Biomed Eng*. 1998;26(6):944–54.
26. Myers JG, Moore JA, Ojha M, Johnston KW, Ethier CR. Factors influencing blood flow patterns in the human right coronary artery. *Ann Biomed Eng*. 2001;29:109–20.
27. Ballyk PD, Stienmann DA, Ethier CR. A simulation of non-Newtonian blood in an end-to-side anastomosis. *Biorheology*. 1994;31:565–86.
28. Meurala H, Valle M, Hekali P, Somer K, Frick MH, Harjola PT. Patency of sequential versus single vein grafts in coronary bypass surgery. *Thorac Cardiovasc Surg*. 1982;30:147–51.
29. McNamara JJ, Berke HS, Chung GKT, Dang CR. Blood flow in sequential vein grafts. *Circulation*. 1979;60:33–8.
30. Gwozdziewicz M, Nemec P, Simek M, Hajek R, Troubil M. Sequential bypass grafting on beating heart: blood flow characteristics. *Ann Thorac Surg*. 2006;82:620–3.
31. Al-Ruzzeh S, George S, Bustami M, Nakamura K, Khan S, Amrani M. The early clinical and angiographic outcome of sequential coronary artery bypass grafting with the off-pump technique. *J Thorac Cardiovasc Surg*. 2002;123:525–30.
32. Berthier B, Bouzerar R, Legallais C. Blood flow patterns in an anatomically realistic coronary vessel: influence of three different reconstruction methods. *J Biomech*. 2002;35:1347–56.
33. Perktold K, Peter R. Numerical 3D-simulation of pulsatile wall shear stress in an arterial T-bifurcation model. *J Biomed Eng*. 1990;12:2–12.
34. Stone PH, Coskun AU, Yeghiazarians Y, Al-Ruzzeh S, George S et al. Prediction of sites of coronary atherosclerosis progression: in vivo profiling of endothelial shear stress, lumen, and outer vessel wall characteristics to predict vascular behaviour. *Curr Opin Cardiol*. 2003;18:458–70.
35. Giannoglou GD, Soulis JV, Farmakis TM, Farmakis DM, Louridas GE. Hemodynamic factors and the important role of local low static pressure in coronary wall thickening. *Int J Cardiol*. 2002;86:27–40.
36. Cunningham KS, Gotlieb AI. The role of shear stress in the pathogenesis of atherosclerosis. *Lab Investig*. 2005;85:9–23.
37. Glor FP, Ariff B, Hughes AD et al. WImage-based carotid flow reconstruction: a comparison between MRI and ultrasound. *Physiol Meas*. 2004;25:1495–509.
38. Malek AM, Alper SL, Izumo S. Hemodynamic stress and its role in atherosclerosis. *J Am Med Assoc*. 1999;282:2035–42.

Chapter 18
Computational Fluid Dynamics Models of Ventricular Assist Devices

Karen May-Newman

Abstract A ventricular assist device (VAD) is a pump surgically connected to the heart and aorta in order to boost systemic blood flow in heart failure patients. The design of these devices has evolved over the past 30 years, with improvements and innovations enabled through the synergistic use of experimental research, clinical studies, and computational models. The application of computational fluid dynamics models has allowed the design of VADs to shift from large, bulky devices designed for patients with severe cardiac failure to a variety of smaller devices designed for a range of patients and cardiovascular conditions.

18.1 Introduction

Heart failure is a debilitating condition in which patients have enlarged hearts and decreased pumping function [1]. Therapy to improve function includes pharmacological treatment and, if the condition does not stabilize or improve, eventual transplant. Unfortunately, each year only 2300 of the 100,000 Americans with CHF receive heart transplants, while 300,000 CHF patients die [2]. Patients unable to survive until transplant have been aided by mechanical circulatory support as a "bridge" to transplantation (BTT) and even as a long-term therapy. Support devices have been researched and developed for decades and include both total artificial heart and ventricular assist devices (VADs). The total artificial heart aims to completely replace the native heart with a positive displacement pump that functions much like the native heart. VADs assist the native ventricle to pump blood through the body thereby reducing its workload [3].

K. May-Newman (✉)
Bioengineering Program, Department of Mechanical Engineering, San Diego State University, San Diego, CA, USA
e-mail: kmn@kahuna.sdsu.edu

J.M. Guccione, et al. (eds.), *Computational Cardiovascular Mechanics*,
DOI 10.1007/978-1-4419-0730-1_18,

18.2 Clinical Impact

VADs augment hemodynamic function by increasing systemic blood flow. A long wait for a donor heart is faced by many patients eligible for cardiac transplantation, and a VAD can provide a BTT for up to several years [4]. Patients who are ineligible for transplant receive a VAD as destination therapy (DT), which provides chronic support [5]. For other patients unable to wean from cardiopulmonary bypass, VADs can provide support during the post-cardiotomy recovery period and, for patients in acute hemodynamic compromise, give time for long-term treatment decisions to be made [6].

The documented benefits of mechanical circulatory support include the restoration of cardiac output and blood flow, resumption of daily living with a significant reduction of heart failure symptoms, improved end-organ function, and molecular and cellular improvements in the myocardium. Mechanical circulatory support has facilitated a consistent improvement in NYHA functional class from Class IV to Class I or II for most patients [7–9]. Under some circumstances, patients' hearts recover sufficiently to be weaned off the device, and the recovered heart is able to sustain them without additional support, known as bridge-to-recovery (BTR) [10–15]. In many cases, however, the patients remain on the device for several years.

18.3 History of VAD Use

The first VADs were developed in the wake of the artificial heart program at NIH in the 1960s and 1970s. Originally, VADs were designed as positive displacement pumps that mimic the native heart, filling during the diastolic phase of the cycle and ejecting during the systolic phase. These pulsatile VADs (PF-VADs) use valves on the inflow and outflow sides to ensure unidirectional flow. They have been used since 1970 to improve the cardiac output of cardiac failure patients, as demonstrated in the REMATCH trial [7], and have been implanted in over 10,000 patients. Implantable PF-VADs have been successful as a BTT device in thousands of patients since 1980. The most popular PF-VAD has been the Thoratec HeartMate XVE, received by over 4500 patients worldwide [16]. The results of clinical studies demonstrated an 81% improvement in 2-year survival among patients receiving HeartMate XVE versus optimal medical management [7]. A DT study following the REMATCH trial demonstrated an additional 17% improvement (61% vs. 52%) in 1-year survival of patients receiving the HeartMate XVE [17, 18]. The WorldHeart Novacor LVAS device has been implanted in over 1700 patients, with a BTT success rate similar to the HeartMate XVE [19]. Because the design of these PF-VADs resembles the native heart, they are large and bulky devices with noisy pumping and poor reliability due to bearing wear.

The PF-VAD is surgically connected to the apex of the left ventricle (inflow conduit) and the aorta (outflow conduit), as shown in Fig. 18.1. Blood entering the left ventricle exits through the PF-VAD inflow conduit as well as through the native

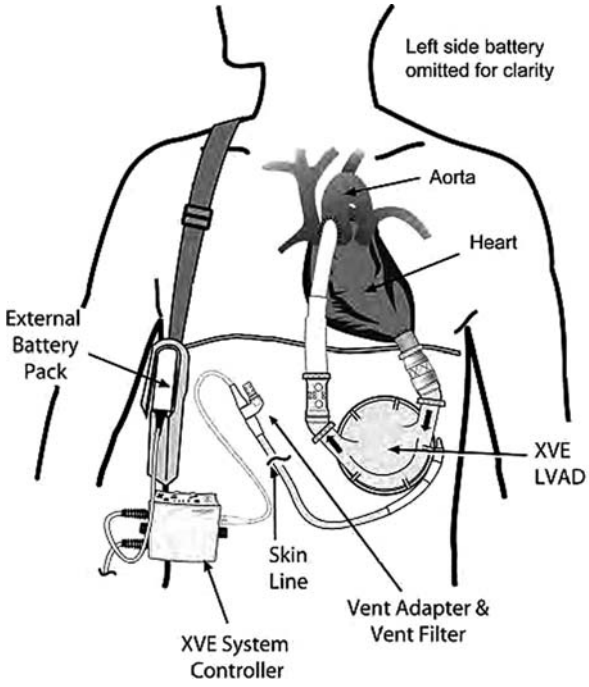

Fig. 18.1 Schematic of the HeartMate XVE PF-VAD placement in the human body. From Thoratec Corporation [22]

aortic valve. In many patients, especially in the early weeks following PF-VAD implantation, flow through the aortic valve is minimal, and the pump is said to be operating *in series* with the heart (see Fig. 18.2). In this case, flow into the aortic sinus and the coronary vessels occurs via retrograde flow from the pump. In some patients, the heart begins to recover function and contributes to the cardiac output by pumping blood through the native valve, at which time it is operating *in parallel* with the PF-VAD. This native flow merges with the PF-VAD flow at the junction of the aortic outflow conduit. The fluid mechanics of the circulation is thus significantly altered with the addition of the PF-VAD, which gives rise to a variety of concerns in these patients.

The design of most PF-VADs are similar, using flexible membranes or pusher plates and valves to ensure unidirectional flow. An example is the HeartMate XVE pump design, shown in Fig. 18.3, in which the housing is fabricated from sintered titanium and contains a flexible, textured polyurethane diaphragm bonded to a rigid pusher plate which is actuated by an electromechanical motor. A percutaneous line is required for energy transfer and an air vent to equalize pressure in the motor chamber [20]. Porcine bioprosthetic valves are positioned in the inlet and outlet conduits, which are made of a Dacron vascular graft material. Power is provided by an external console or battery packs. The blood-contacting surfaces are porous to encourage formation and adherence of a pseudoneointima to optimize biocompatibility and

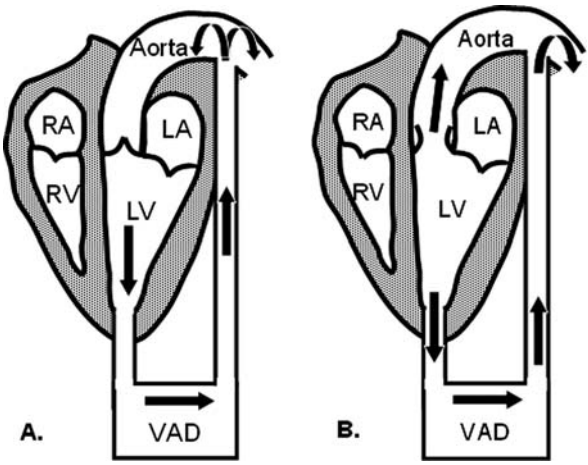

Fig. 18.2 **a**. When the aortic valve does not open, the left ventricle (LV) functions in series with the VAD. **b**. If the heart pumps strongly enough to open the valve, the LV is operating in parallel with the VAD

minimize thrombosis [21]. Once this tissue layer has formed, anticoagulant therapy can be greatly reduced or eliminated.

PF-VADs are often referred to as first-generation pumps. Blood flows into these devices during the filling phase, when the pusher plate is down and the chamber volume is at maximum (top of Fig. 18.3b). As the pusher plate moves up, pressure is generated within the chamber until the level exceeds the afterload of the aortic pressure in the outflow conduit. At this point, the valve opens and the chamber empties while the pusher plate advances until the end of the stroke is reached (bottom of Fig. 18.3b). As the pressure falls in the PF-VAD chamber, the outflow valve closes and the pusher plate moves down, filling the chamber through the open inflow valve. The time course of pressure and volume in the HeartMate XVE VAD is shown in Fig. 18.6a [22].

The second, third, and fourth generation of VADs have all been designed with a rotating element that provides continuous flow (CF-VADs). These CF-VADs are valveless and are sensitive to the pressure gradient across the pump. There are a wide variety of CF-VAD designs that are generally classified as either axial or centrifugal flow pumps. The axial-flow blood pump functions as an Archimedes screw, which can be successfully miniaturized to provide support for small or pediatric patients. The impeller of the axial-flow pump typically rotates at approximately 10 krpm and is designed following the principles of turbomachinery. The centrifugal pump uses a spinning top inside the chamber to move blood through the pump. Its impeller typically rotates at one-third to one-fifth of the rate of the axial pump, at approximately 2000–3000 rpm. Because of this lower rotational speed, the bearing life is expected to be longer than an axial pump and its endurance life greater than 2 years. Centrifugal blood pumps have been widely used for short-term support during cardiopulmonary bypass for many years and are relatively atraumatic to the blood in that application.

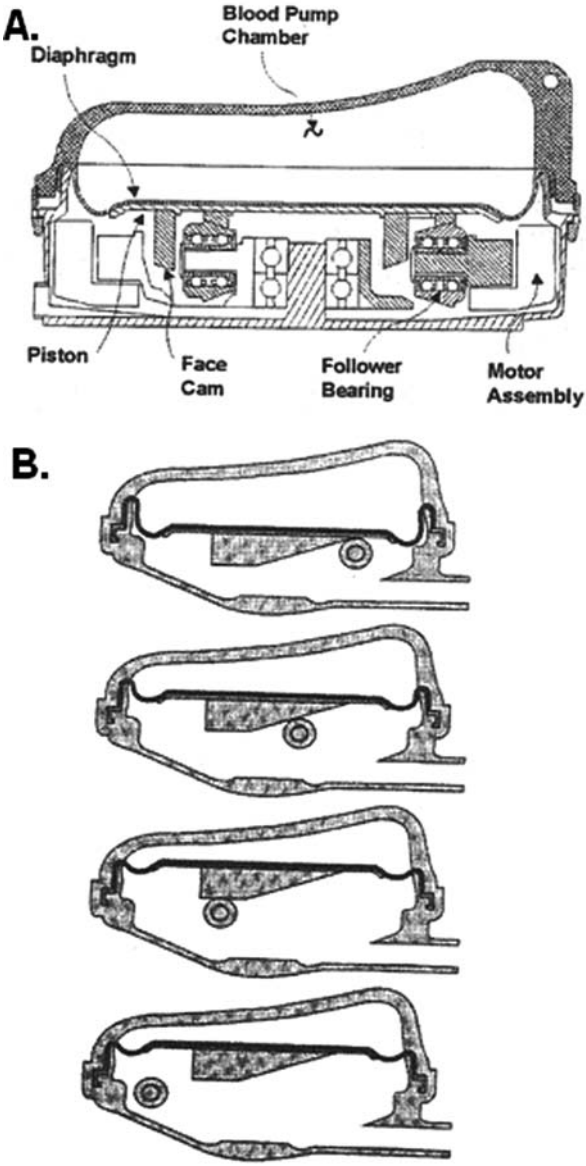

Fig. 18.3 **a**. Cross-section of the Thoratec HeartMate XVE pump. **b**. Sequence of movement of bearings and diaphragm of HeartMate XVE pump. The diaphragm is filled in the *top* image and emptied in the *bottom* image. From Nose and Motomura [20]

The second-generation devices are axial-flow devices that use a magnetic coupling between the housing and the rotating element positioned with blood-washed bearings. These CF-VADs include the Berlin Heart Incor VAD, the Thoratec HeartMate II, and the Micromed Debakey VAD. Many of these devices have received CE certification, but only one of these has been approved by the FDA, the

HeartMate II by Thoratec. This CF-VAD has been implanted in over 1000 patients, with very good results. Seventy-nine percent of the BTT patients were successfully bridged to transplant, demonstrating a 10% improvement over PF-VAD results. Over 200 patients have received this CF-VAD for DT as part of an ongoing clinical trial [16]. Another device, the Micromed Debakey VAD, has been used in over 400 patients, and the Jarvik 2000 Flowmaker in over 200 patients. Updated information on the clinical results of approved devices can be found at the INTERMACS registry website (www.intermacs.org).

A cross-sectional view of an axial-flow pump, the Micromed Debakey VAD, is shown in Fig. 18.4. In this CF-VAD, a rigid inflow cannula is inserted into the apex of the left ventricle. The housing around the inflow tube has a brushless motor stator which provides a rotating magnetic field. The inducer, impeller, and diffuser are mounted close together. The flow straightener is mounted foremost to maintain a laminar fluid stream and acts as a suspension for the front shaft bearing; the impeller blades contain permanent magnets and act as a rotor. Behind the impeller is the diffuser, which converts tangentially directed fluid into axial flow, as well as supporting the rear bearing of the impeller shaft [20]. The fluid dynamics of

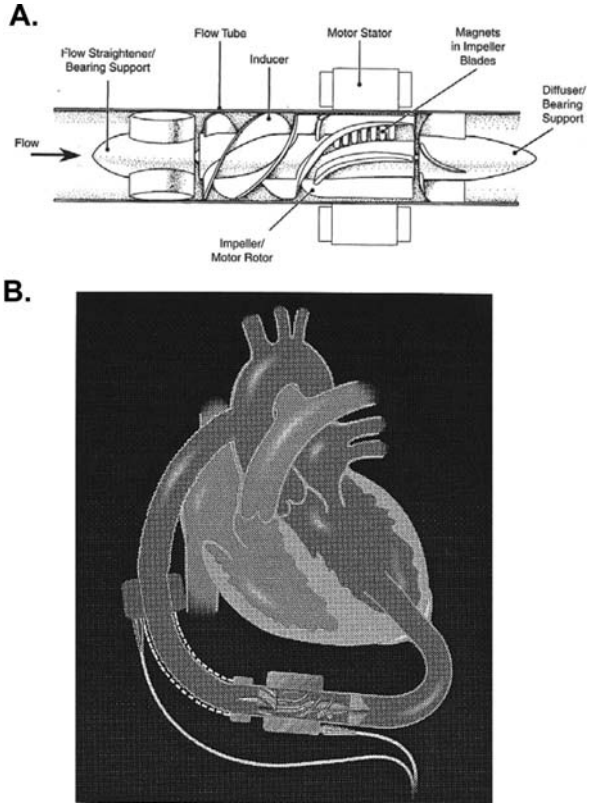

Fig. 18.4 **a**. Cross-section of the Micromed Debakey axial-flow pump (from Debakey, *Ann Thorac Surg.* 1999;68:637–40). **b**. Configuration of the VAD placement in the cardiovascular circuit. From Nose and Motomura [20]

these pumps resemble typically turbomachinery performance. They are sensitive to the pressure gradient decreasing their flow with increasing pressure at a constant rotational speed, as shown in Fig. 18.6b. They are designed to pump 5–6 L/min at 100 mmHg pressure.

The third generation are CF-VADs that eliminate all mechanical contacts between the impeller and drive mechanism. This improvement gets rid of mechanical wear and heat production at the impeller-housing contact points. These designs gave way to the fourth-generation pumps, which include both axial and centrifugal designs and have magnetically suspended impellers. Pumps in this category are still in clinical trials, and include the Levacor, DuraHeart, and VentrAssist pumps. Magnetically levitating impellers have replaced coupled systems that require bearings and have greater reliability.

In centrifugal pumps, the fluid enters through the inlet tube into the center of the pump, where an impeller that resembles a spinning top moves the fluid towards the outside of the pump, where it is collected and expelled through the outflow tube (see Fig. 18.5). Hydraulic levitation of the impeller occurs at a certain rotational speed, usually 1500–2000 rpm, and can achieve a wide range of flow rates at a fairly constant pressure. Impeller position, shape, and size are very important, as they affect the magnitude of the vortex force on the blood. Eliminating stagnant areas, typically at the bottom of the impeller, is important for reducing thrombogenicity and is sometimes accomplished with secondary channels [20].

Fig. 18.5 Cross-section of the HeartMate III centrifugal pump. From Thoratec Corporation [16]

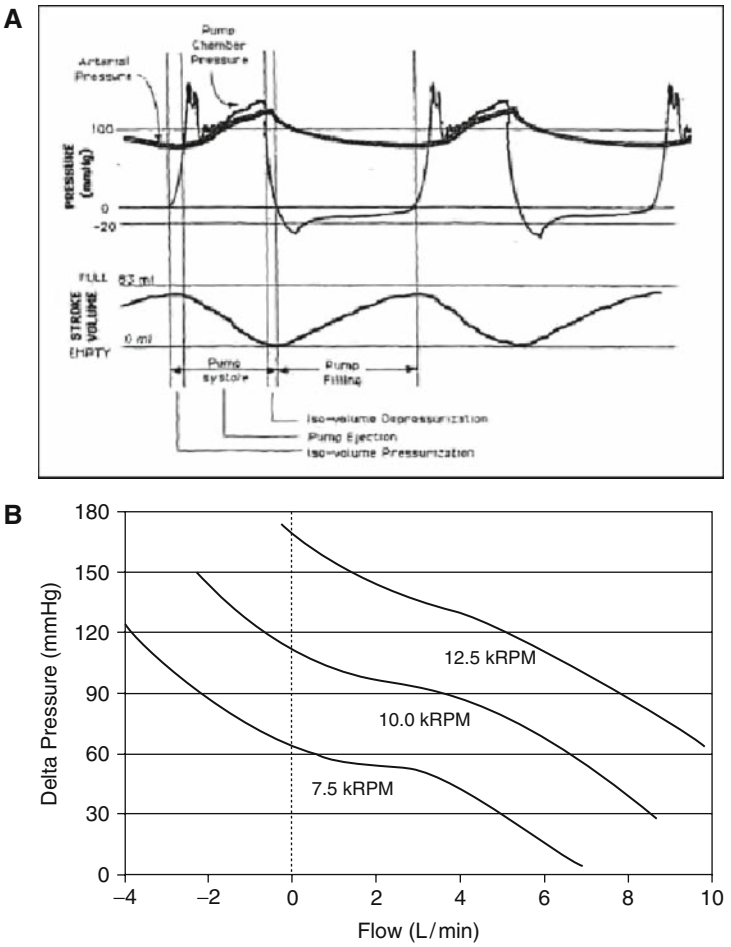

Fig. 18.6 **a**. Performance of the Thoratec HeartMate XVE LVAS (from Operating Manual). **b**. Hydraulic performance curve of the MicroMed DeBakey VAD. From Nose and Motomura [20]

18.4 Design Concerns with VADs

Compatibility of a device with blood is difficult to predict with any standardized test, in vitro or animal [23]. The goal, therefore, of design research for a blood-contacting device is to minimize undesirable blood reactions, which is unfortunately rather vague. Clotting can occur at the surface of the device or the tissue, forming a thrombus. Some devices can also exhibit regions of stasis, where disturbed or stagnant flow could lead to the formation of whole blood clots. In either case, circulating clots (emboli) can enter the brain circulation and cause stroke. Techniques for reducing thrombogenicity in a device vary widely, from coating surfaces with anticoagulant to engineering the flow pattern to minimize abnormalities.

In general, integrating a blood-contacting device with the human body increases the risk of thrombus formation and stroke. This is particularly true with VADs, as they often attach to the aorta proximal to the arteries that supply blood to the brain [24, 25]. Although it is well known that abnormalities in flow and shear patterns can lead to platelet activation and clot formation, the mechanisms involved are not well understood. In general, regions of flow stagnation are correlated with clotting [26–28], and reversing or recirculating flow can produce shear gradients that make blood "hypercoagulable" or even lead to red blood cell damage and hemolysis [29, 30].

18.4.1 Blood Damage Models

Changes in the blood flow profile can lead to damage to the blood, specifically the red blood cells. Mechanical shear stress is seen as the major cause of this type of damage with current medical devices [31]. With enough damage the cells burst, termed hemolysis. This is quantified experimentally by looking at the increase in plasma-free hemoglobin over the hemoglobin concentration [32]. However, shear-induced alterations to the cells are produced that affect function, termed sub-lethal blood damage. Exposure to shear can induce a stiffening of the cell membrane, causing more difficulty in deforming while passing through capillaries [33, 34]. In reality, many of the red blood cells in VAD patients have been chronically exposed to the high-shear environment of the pump, which has been shown to shorten their normal lifetime [33].

Hemolysis can be estimated from the flow field with one of the many models that have been developed. The first and widely adopted was the Giersiepen model [35] in which the percentage of hemoglobin released from red blood cells is a function of the magnitude of shear stress (τ) and the exposure time (t)

$$\frac{\Delta \mathrm{Hb}}{\mathrm{Hb}}(\%) = 3.62 \times 10^{-5} \bullet \tau^{2.416} \bullet t^{0.785} \tag{18.1}$$

This is usually calculated from particle tracking a large number of cells through the flow field. Cumulative damage to red cells can be calculated with an integral approach evaluating the blood damage index, D, which reflects the percentage of red cells damaged [36].

$$D = \sum_{\text{inlet}}^{\text{outlet}} 1.8 \times 10^{-6} \tau^{1.991} \Delta t^{0.765} \tag{18.2}$$

The shear stress term was modified to include viscous and turbulent contributions [37]. The Normalized Index of Hemolysis (NIH) gives the amount of free hemoglobin (g/100 mL):

$$\mathrm{NIH} = (\mathrm{Hb}) D(t,\tau) \tag{18.3}$$

where Hb is the hemoglobin concentration (g/dL) [38]. All of these methods have had good correlation with experimental measurements under specific experimental conditions.

Thrombosis, rather than hemolysis, is the major clinical problem associated with blood-contacting medical devices [39]. The primary cause of thromboembolism in blood-contacting devices is platelet activation, which can occur by contact with foreign surfaces and by nonphysiological flow patterns or their combination. Generally speaking, blood needs to be in constant motion to avoid clotting and thrombosis. Platelets are very sensitive to the flow conditions and respond to shear stresses by initiating procoagulant activity in several ways. The ideal flow path through the pump should be smooth and nonobstructive in order to maintain a continuous wash over all surfaces and to avoid recirculation or stagnant flow regions that would encourage platelet deposition [40]. A smooth flow path and laminar flow patterns near surfaces can reduce potential deposition and activation of the coagulation cascade. Recent studies demonstrate that device thrombogenicity is due primarily to the nonphysiological flow patterns and stresses that activate and support the aggregation of platelets, increasing the risk of thromboembolism and stroke [39].

18.5 CFD Modeling of VADs

Computational fluid dynamics can provide a simple and cost-effective way to study multiple boundary conditions for a fluid mechanics problem. The time and resources necessary to run a computational model are much less than those needed for a physical model. Computational methods often provide a greater level of detail, provided they are formulated correctly.

Most of the recent CFD studies in VADs have focused on the design of CF-VADs. In fact, CFD is considered an important design tool not only for assessing performance, but for design optimization [41]. When based on parameterized designs combined with automated grid generators, a matrix of parameter combinations can be solved to optimize performance that provides a cost-effective and timely way to make good design decisions. CFD models of VADs have been used to detect vortex and stagnation points in the flow fields, to predict blood damage induced by high shear stresses, and to calculate hydraulic parameters such as fluid forces, moments, torque, and efficiency.

The flow inside the blood pump is usually turbulent due to highly disturbed flow caused by the moving impeller. The choice of turbulence models is an important factor for the CFD simulation of VADs. Several turbulence models are available, but include assumptions that must be valid for the specific flow conditions of the pump. Another issue is the small gap for fluid flow and the relatively low absolute speed of the blood, which makes wall effects influence the flow field more strongly. The treatment of near-wall regions, their constraint for grid distribution, and their compatibility with turbulence models are critical for the accuracy and feasibility of CFD prediction [42]. Finally, the clinical performance of VADs is evaluated by

connecting the fluid dynamics with blood damage and thromboembolism, which is influenced by a variety of both patient and device-specific factors.

18.5.1 Turbulence Models

The majority of VAD CFD models incorporating turbulence have adopted the *k-e* scheme, where *k* and *e* denote the turbulent kinetic energy and turbulent dissipation rate, respectively [37, 43]. The *k-e* model utilizes the eddy viscosity assumption to relate the Reynolds stress and turbulent terms to the mean flow variables [42]. An alternative to the *k-e* model is the *k-w* description, which uses a two-layer approach. An analytical expression for *w*, turbulent frequency, is obtained for the viscous sublayer, enabling an automated switch to a different near-wall calculation scheme. This feature makes the grid design in *k-w* model more flexible and robust. [42]

18.5.2 Validation With Experimental Data

CFD predictions cannot be used without validating with experimental measurements of flow, pressure, and blood damage under matched conditions. PIV is the most common technique for validating flow fields, but requires transparent models for flow visualization. For many pumps, transparent housings are used for flow visualization models, but it is impossible to make the electromagnetic components with any other materials. Thus, experimental data are compared to predictions for performance and flow, and if there is good correlation, the model predictions for conditions and locations that cannot be experimentally measured are presumed valid.

18.6 CFD Model Results

There are considerably fewer reports of the use of CFD for the design of PF-VADs than for CF-VADs. One group has used CFD models to redesign a PF-VAD to decrease pump size and blood damage. In these studies, transient and turbulent blood flow through the PF-VAD were performed using solid models built in CAD/CAM software. Fluid dynamics analysis using Ansys-Flotran was used to evaluate the effect of a seamless polyurethane blood sac, showing that this design eliminated an area of stasis and reduced the level of blood damage using the NIH model given above [44]. Another study by this group used an index of pump geometry, IPG, to optimize the positions and angles of the inflow and outflow conduits, selecting the pump design with the lowest IPG that produced a spiral flow around the housing which reduces thrombus formation [45]. A novel approach to simulating the dynamics of PF-VAD pusher plate and valve motion by Medvitz [46] showed good agreement with experimental measurements during transient simulations of pulsatile flow (Fig. 18.7). Valve closure was simulated with a sharp increase in fluid

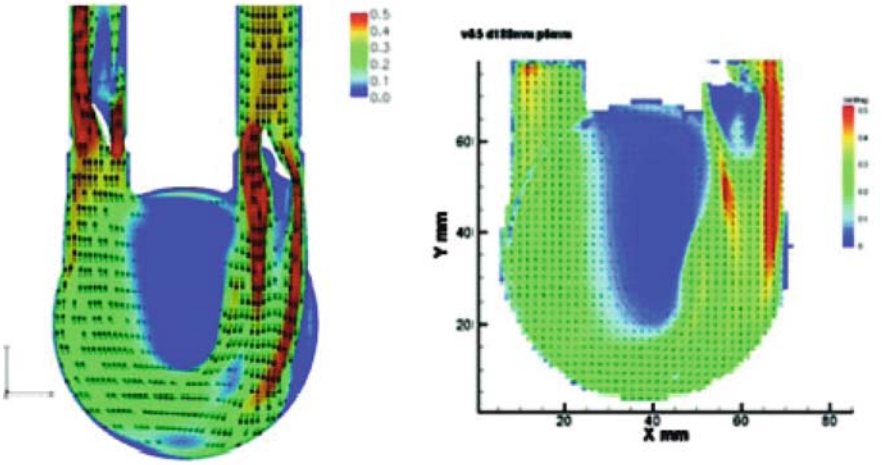

Fig. 18.7 **a**. A comparison of computational (*left*) and experimental (*right*) velocity fields in the 50-cc Penn State PF-VAD showing good agreement. From Medvitz et al. [46]

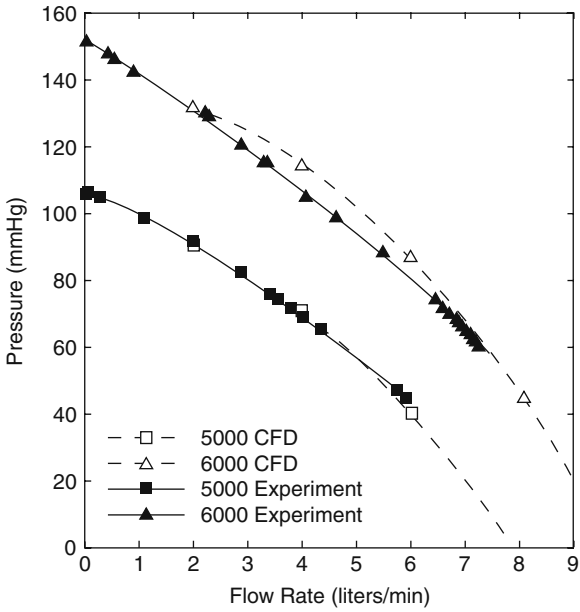

Fig. 18.8 Comparison of CFD and experimental performance curves for an axial pump. From Untaroiu et al. [47]

viscosity at that boundary, and pusher plate motion approximated with a boundary with a changing velocity during the cardiac cycle.

CFD has been used in several CF-VAD pump designs, including both long- and short-term devices. For axial-flow pumps, the design goal is to produce a streamlined, nonobstructive flow path that minimizes shear stress to the blood and areas

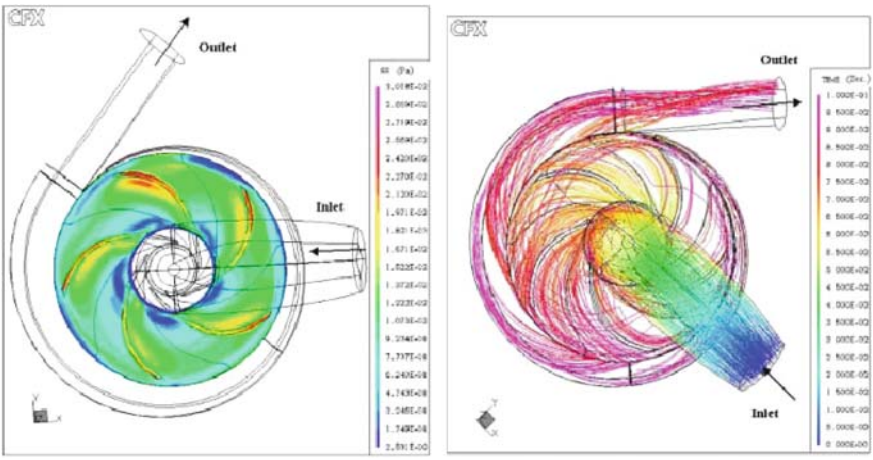

Fig. 18.9 CFD results for a centrifugal pump. From Song et al. [49]

of stasis that may lead to thrombus formation. The pump should develop a pressure rise of 100 mmHg at a flow rate of 6 L/min [40]. Axial pumps are designed on the principles of turbomachinery, in which energy is transferred from the motor to the fluid using a rotating impeller.

Additional design considerations include minimizing high fluid forces and controlling the position of the impeller in the flow stream. CFD simulations have been valuable in enabling these design considerations in a systematic fashion when optimizing a new pump. Recent studies of the LEV-VAD, a collaborative effort between the Virginia Artificial Heart Institute and the Utah Artificial Heart Institute, have used CFD for a series of prototype pumps for Heartquest [40]. A suite of software by ANSYS was used, including Bladegen, GridPro, and TascFlow. Bladegen, designed especially for turbomachinery, can automatically generate different geometries for the inducer, impeller, and diffuser. GridPro is used to generate a mesh of the fluid region based on rules defined by the user. TascFlow is then used to simulate the flow through the device. A *k-e* turbulence model is used and *H-Q* curves, axial fluid forces, and hydraulic efficiencies are calculated over a range of flow rates. In general, there was good agreement but the CFD model consistently overpredicted pump performance and fluid forces by 10–18% (Fig. 18.8) [47].

Probably the most extensive use of CFD has been for optimizing centrifugal blood pump design. CFD has been an invaluable tool for developing the design of short-term extracorporeal blood pumps based on centrifugal designs [38, 43]. This design for CF-VADs has become more popular than axial pumps due to the lower rotational speeds of the impeller. The Virginia-Utah collaboration has applied CFD to a series of prototype designs for the Heartquest magnetically levitated centrifugal VAD. The ANSYS software suite was used to optimize impeller design by systematically varying blade height, angle, and sweep. Pressure head, efficiency, and net fluid force was used to evaluate fluid flow and blood damage [36]. The optimized design

demonstrated improved fluid characteristics and reduced blood damage when compared with earlier prototypes (Fig. 18.9) [48, 49]. Transient behavior in these models can predict different peak values than steady-state condition and must be considered during simulations [50]. A study of the HeartMate III using the Fluent software package found good agreement with experimental measurements of flow fields in the pump inlet, outlet, and volute, although there analysis was for a laminar flow field, which may not adequately represent the behavior at higher speeds [51]. A concern in the design of rotary pumps is regions where reverse flow can occur against a positive pressure gradient. Reverse flow generally occurs in the impeller blade channels, particularly near the exit. High shear stresses are found in this region, as well as at the cutwater, which are associated with high blood trauma [52]. The magnetically levitated impeller design for a centrifugal VAD generates a secondary blood flow path through the clearances between the pump housing and the rotating impeller [49]. This secondary flow path may create possibilities of flow stagnation and high shear stresses, which could lead to hemolysis and possible thrombosis. In contrast to centrifugal VADs, the magnetically levitated impeller design for an axial-flow pump does not include a secondary blood flow path. Furthermore, axial pumps have better anatomic fit because of their compact sizes and tubular configurations. As a result, axial-flow pumps require less time to implant, thereby decreasing the cost and invasiveness of the procedure. [53, 54].

18.6.1 Pediatric VADs

Over the last few years, substantial progress has been made in pediatric mechanical support. VADs are being used more often in children with cardiac failure as a long-term BTR or BTT [55]. The importance of CFD for pump design becomes critical when miniaturizing CF-VADs for pediatric patients. The design of both short-term and long-term devices is optimized by reducing high shear stress, stasis, and blood damage in these smaller pumps. Simply shrinking the design of adult-size blood pumps does not adequately address these considerations. An axial-flow pump design for pediatric patients described in a paper by Throckmorton, et al. produces a pressure rise 75 mmHg at a flow rate of 1.5 L/min that has good flow characteristics such as minimal blood damage and good control of impeller position [37], and demonstrates the successful use of CFD in the design of a CF-VAD.

A study of the Levitronix Maglev pediatric centrifugal pump used Fluent to optimize impeller design and select the most optimal configuration that improved pressure rise without sacrificing hemocompatibility [55]. An extensive CFD optimization effort by Wu et al. found that secondary blades along the back or sides of the impeller can minimize reverse flow in the clearance gap, which was confirmed by experimental measurements [41]. Smooth operation of centrifugal pumps for pediatric patients relies on minimizing flow perturbations by balancing forces on the suspended impeller. A study by Throckmorton and coworkers

developed a CFD methodology for estimating these forces, which compared favorably to experimental results and contributed to the design of an improved pump [56].

The pump operational speed is inversely proportional to the pump's size, a smaller pump corresponds to a higher rotational speed of the rotor. Unfortunately, a higher rotor speed implies a higher value of shear stress, which could have a traumatic effect on blood. Therefore, the second important constraint becomes the rotor rotational speed and the clearance gaps between the rotor and the stationary housing. The larger the clearance gaps, the smaller the shear stress value under a given rotational speed. However, wider clearance gaps create more challenges to the CF-VAD designs [3].

18.6.2 Host–VAD Interaction

The fluid mechanics of specific VAD designs have been thoroughly studied, but without a direct link to the interaction with the host tissue. Therefore many long-term physiological effects have not been evaluated despite recommendations that VADs be used as DT [7, 21].

As the duration of support with implantable VADs lengthens, longer term issues such as device durability and cardiac remodeling have emerged. Previous studies of the host–VAD interaction have focused on the geometry of the interface between the native aorta and the VAD outflow conduit. The geometry of this junction is likely to have a significant effect on the specific flow patterns that arise, which may be correlated with both short- and long-term consequences. Both the angle of attachment of the outflow conduit and its location along the aorta can be varied. The outflow conduit of a VAD is usually attached to the ascending portion of the aorta, a few centimeters away from the aortic valve. However, in some cases, previous sternotomy has resulted in excessive fibrosis in the patient's chest, and the VAD is connected instead to the descending aorta, which is anatomically more accessible. Unfortunately, this has led to reports of extensive aortic thrombosis, even with pulsatile VADs [57]. The convergent branched flow of the aorta and VAD outflow conduit is a simple geometry that has not been studied much in medicine, compared with its cousin, the divergent branched flow such as seen in vessel bifurcations. Studies in classical fluid dynamics, however, have shown that the angle of insertion of a jet into a slower flow affects vortex formation in the distal vessel [58], indicating that this factor may have an important influence on the flow dynamics of the VAD–aorta system.

CFD models were developed to investigate the altered fluid dynamics of the native aorta in VAD patients. The effect of VAD aortic outflow conduit (AOC) anastomosis geometry on the flow in the native aorta was evaluated using software package CFD-RC (ESI, Inc. France). Results demonstrate that the flow patterns are significantly affected by the angle of insertion of the AOC into the native aorta, both during series and parallel flow conditions. Zones of flow recirculation and

high shear stress on the aortic wall can be observed at the highest angle, gradually decreasing in size until disappearing at the lowest angle of 30°. The highest velocity and shear stress values were associated with series flow. The results suggest that connecting the VAD outflow conduit to the proximal aorta at a shallower angle produces fewer secondary flow patterns in the native cardiovascular system [59]. The fluid mechanics of three different anastomoses geometries ((P) proximal, (D) distal, and (IP) in-plane) were studied and the implications for short- and long-term medical consequences explored by evaluating the flow fields, wall shear, and hemolysis (Fig. 18.10). The greatest disruptions in the normal aortic flow pattern occurred with series flow conditions, when flow through the aortic valve was minimal. Under series conditions, circulation in the proximal aorta is retrograde, originating from the VAD outflow conduit. The (P) geometry provided the most blood washout of

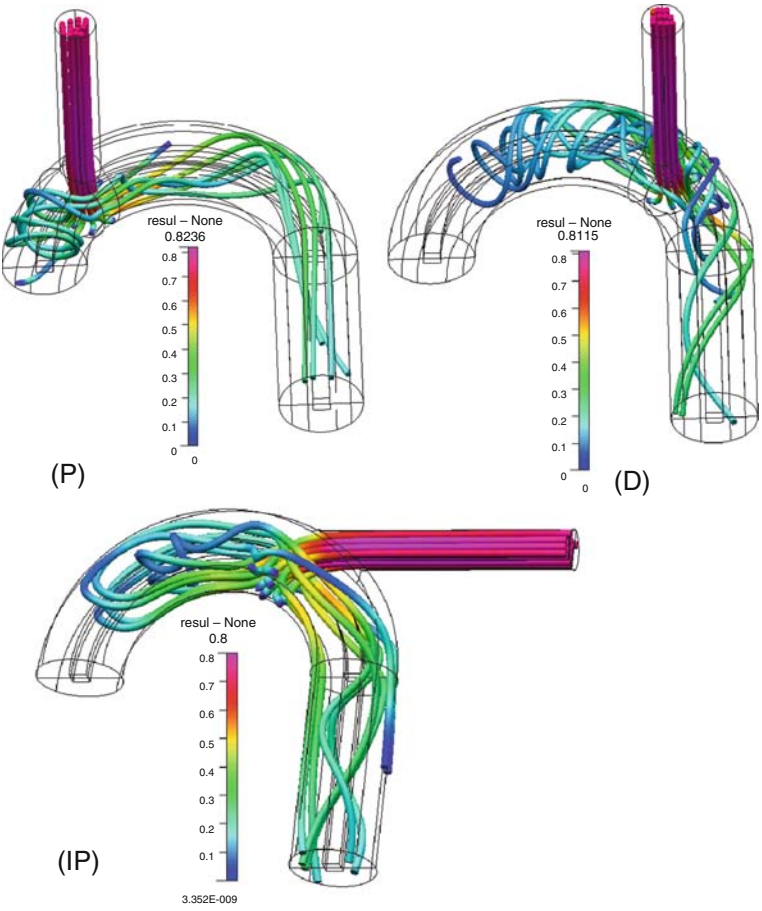

Fig. 18.10 A CFD study of flow in the aorta of a CF-VAD user shows that circulation of blood is limited during series flow unless the VAD conduit is placed in the proximal (P) position. (D) for distal, (IP) for in-plane. From [60]

the proximal aorta, with a larger region of slow-moving flow observed in the (D) and (IP) models. Wall shear stress was reduced for the (IP) geometry, which lacks the direct flow impingement present in the (P) and (D) models. Clinically, the (D) and (IP) geometries require less traumatic surgeries and are likely better tolerated by the patient. In this situation, the (IP) geometry suggests improvement in both increased flow to the proximal aorta and decreased shear stress compared with (D). However, the (D) and (IP) configurations are not recommended for patients with low or no flow from the heart, due to the lack of blood washout near the aortic valve and therefore possible thrombus formation in that area [60].

More recent studies evaluating the host–VAD interaction have begun using fluid–structure interaction (FSI) theory to understand longer-term responses to the abnormal biomechanics introduced by the VAD. In particular, the aortic valve is the cardiovascular structure most affected by these abnormal biomechanics, which can induce structural remodeling, potentially causing aortic valve dysfunction over time ([61], submitted). These host responses will continue to play an important role in evaluating the long-term success of VADs.

18.7 Conclusions

VADs have been shown to improve patient health and quality of life, and dramatically reduce the mortality of patients with severe cardiac failure. PF-VADs provided the first implantable mechanical circulatory assistance over 30 years ago with large, noisy pulsatile devices that functioned as a BTT but were unreliable for long-term usage. These older designs have been superseded by continuous flow devices, which are smaller, quieter, and designed for DT. The designs of these CF-VADs have been optimized by the use of CFD, which provides details of fluid flow through the devices. Predicting clinically relevant flow results depends on using appropriate models, which should include turbulence as well as blood damage. A continued effort is underway to develop better models for predicting thrombus formation in VADs as well as other blood-contacting devices, as this affects the potential for neurological damage. The interaction of the VADs with the native cardiovascular system can produce abnormal flow patterns in the aorta and ventricle which may lead to thrombus formation or soft tissue remodeling, as VADs greatly alter the host biomechanics. VADs hold great promise and their continued improvement will enable their use in patients with a wider variety of cardiovascular conditions, addressing an unmet need in the treatment of heart failure.

References

1. Goldstein S, Ali AS, Samuels LE. Ventricular remodeling: mechanisms and prevention. *Cardiol Clin*. 1998;16:623–32.
2. American Heart Association. Heart disease and stroke statistics – 2009 update. Dallas, TX: American Heart Association, 2009.

3. Song X, Untariou A, Wood HG, Allaire PE, Throckmorton AL, Day SW, Olsen DB. Design and transient computational fluid dynamics study of a continuous flow ventricular assist device. *ASAIO J*. 2004;50:215–24.
4. Miller L. Use of a continuous-flow device in patients awaiting heart transplantation. *NEJM*. 2007;357:885–96.
5. Park SJ, Tector A, Piccioni W, Raines E, Gelijns A, Moskowitz A, Rose E, Holman W, Furukawa S, Frazier OH, Dembitsky W. Left ventricular assist devices as destination therapy: a new look at survival. *J Thorac Cardiovasc Surg*. 2005;129(1):9–17. Erratum in: *J Thorac Cardiovasc Surg*. 2005;129(6):1464.
6. Westaby S. Elective transfer from cardiopulmonary bypass to centrifugal blood pump support in very high-risk cardiac surgery. *J Thorac Cardiovasc Surg*. 2007;133:577–8.
7. Rose EA, Gelijns AC, Moskowitz AJ, Heitjan DF, Stevenson LW, Dembitsky W, Long JW, Ascheim DD, Tierney AR, Levitan RG, Watson JT, Meier P, Ronan NS, Shapiro PA, Lazar RM, Miller LW, Gupta L, Frazier OH, Desvigne-Nickens P, Oz MC, Poirier VL. Long-term mechanical left ventricular assistance for end-stage heart failure. *N Engl J Med*. 2001;345:1435–43.
8. Frazier OH, Rose EA, Oz MC. Multi-center clinical evaluation of the HeartMate vented electric left ventricular assist system in patients awaiting heart transplantation. *J Thorac Cardiovasc Surg*. 2009;122:1186–95.
9. Russell SD, Miller LW, Pagani FD. Advanced heart failure: a call to action. *Congest Heart Fail*. 2008;14:316–21.
10. Farrar DJ, Holman WR, McBride LR, Kormos RL, Icenogle TB, Hendry P J, Moore CH, Loisance, DY, El Banayosy A, Frazier H. Long-term follow-up of Thoratec ventricular assist device bridge-to- recovery patients successfully removed from support after recovery of ventricular function. *J Heart Lung Transplant*. 2002;21:516–21.
11. Hetzer R, Muller JH, Weng Y, Meyer R, Dandel M. Bridging-to-recovery. *Ann Thorac Surg*. 2001;71:S109–13.
12. Kumpati GS, McCarthy PM, Hoercher KJ. Left ventricular assist device bridge to recovery: a review of the current status. *Ann Thorac Surg*. 2001;71:S103–8.
13. Mancini DM, Beniaminovitz A, Levin H, Catanese K, Flannery M, DiTullio M, Savin S, Cordisco ME, Rose E, Oz M. Low incidence of myocardial recovery after left ventricular assist device implantation in patients with chronic heart failure. *Circulation*. 1998;98: 2383–9.
14. Young JB. Healing the heart with ventricular assist device therapy: mechanisms of cardiac recovery. *Ann Thorac Surg*. 2001;71:S210–9.
15. Mueller J, Wallukat G, Weng Y, Dandel M, Ellinghaus P, Huetter J, Hetzer R. Predictive factors for weaning from a cardiac assist device. An analysis of clinical, gene expression and protein data. *J Heart Lung Transplant*. 2001;20:202.
16. Thoratec Corporation. Heartmate XVE Clinical Outcomes website. http://www.thoratec.com/vad-trials-outcomes/clinical-outcomes/heartmate-xve-lvad.aspx.
17. Lietz K, Long JW, Kfoury AG, Slaughter MS, Silver MA, Milano CA, Rogers JG, Naka Y, Mancini D, Miller LW. Outcomes of left ventricular assist device implantation as destination therapy in the post-REMATCH era: implications for patient selection. *Circulation*. 2007;116:497–505.
18. Long JW, Kfoury AG, Slaughter MS, Silver M, Milano C, Rogers J, Delgado R, Frazier OH. Long-term destination therapy with the HeartMate XVE left ventricular assist device: improved outcomes since the REMATCH study. *Congest Heart Fail*. 2005;11: 133–8.
19. Worldheart Corporation. Worldheart corporation company. Website, 2009.
20. Nose Y, Motomura T. Cardiac prosthesis: artificial heart and assist circulation: past, present and future. Houston, TX: ICMT Publishers, 2003.
21. Nose Y, Yoshikawa M, Murabayashi S, Takano T. Development of rotary blood pump technology: past, present, and future. *Artif Organs*. 2000;24:412–20.

22. Thoratec Corporation. HEARTMATE® XVE LVAS EXtended Lead vented electric left ventricular assist system operating manual. Pleasanton, CA: Thoratec Corporation, 2008.
23. Hanson S, Ratner BD. Testing of blood–materials interactions. In: Ratner, BD, Hoffman AS, Schoen FJ, Lemons JE. (Eds.), Biomaterials science: an introduction to materials in medicine. San Diego, CA: Academic Press, 1996, pp. 228–38.
24. Snyder TA, Watach MJ, Litwak KN, Wagner WR. Platelet activation, aggregation, and life span in calves implanted with axial flow ventricular assist devices. *Ann Thorac Surg*. 2002;73:1933–8.
25. Gross DR. Concerning thromboembolism associated with left ventricular assist devices. *Cardiovasc Res*. 1999;42:45–7.
26. Folie BJ, McIntire LV. Mathematical analysis of mural thrombogenesis: concentration profiles of platelet-activating agents and effects of viscous shear flow. *Biophys J*. 1989;56:1121–41.
27. Karino T, Goldsmith HL, Motomiya M, Mabuchi S, Sohara Y. Flow patterns in vessels of simple and complex geometries. In: Leonard EF, Turitto VT, Vroman L. (Eds.), Contact with natural and artificial surfaces. New York: New York Academy of Sciences, 1987, pp. 422–41.
28. Muraki N. Ultrasonic studies of the abdominal aorta with special reference to hemodynamic considerations on thrombus formation in the abdominal aortic aneurysm. *J Jpn Coll Angiol*. 1983;23:401–13.
29. Apel J, Paul R, Klaus S, Siess T, Reul H. Assessment of hemolysis related quantities in a microaxial blood pump by computational fluid dynamics. *Artif Organs*. 2001;25:341–7.
30. Bluestein D, Niu L, Schoephoerster RT, Dewanjee MK. Steady flow in an aneurysm model: correlation between fluid dynamics and blood platelet deposition. *J Biomech Eng*. 1996;118:280–6.
31. De Wachter D, Verdonck P. Numerical calculation of hemolysis levels in peripheral hemodialysis cannulas. *Artif Organs*. 2002;26:576–82.
32. Yano T, Sekine K, Mitoh A, Mitamura Y, Okamoto E, Kim D, Nishimura I, Murabayashi S, Yozu R. An estimation method of hemolysis within an axial flow blood pump by computational fluid dynamics analysis. *Artif Organs*. 2003;27:920–5.
33. Kameneva M, Burgreen GW, Kono K, Repko B, Antaki JF, Umezu M. Effects of turbulent stresses upon mechanical hemolysis: experimental and computational analysis. *ASAIO J*. 2004;50:418–23.
34. Kameneva M, Marad PF, Brugger JM, Repko B, Wang JH, Moran J, Borovetz HS. In vitro evaluation of hemolysis and sublethal blood trauma in a novel subcutaneous vascular access system for hemodialysis. *ASAIO J*. 2002;48:34–8.
35. Giersiepen M, Wurzinger LJ, Opitz R, Reul H. Estimation of shear stress-related blood damage in heart valve prostheses – in vitro comparison of 25 aortic valves. *Int J Artif Organs*. 1990;13:300–6.
36. Song X, Throckmorton AL, Wood HG, Antaki JF, Olsen DB. Computational fluid dynamics prediction of blood damage in a centrifugal pump. *Artif Organs*. 2003;27:938–41.
37. Throckmorton AL, Lim DS, McCulloch MA, Jiang W, Song X, Allaire PE, Wood HG, Olsen DB. Computational design and experimental performance testing of an axial-flow pediatric ventricular assist device. *ASAIO J*. 2005;51:629–35.
38. Zhang J, Gellman B, Koert A, Dasse KA, Gilbert RJ, Griffith BP, Wu ZJ. Computational and experimental evaluation of the fluid dynamics and hemocompatibility of the CentriMag blood pump. *Artif Organs*. 2006;30:168–77.
39. Bluestein D. Research approaches for studying flow-induced thromboembolic complications in blood recirculating devices. *Expert Rev Med Devices*. 2004 Sep;1(1):65–80. Review.
40. Song X, Untaroiu A, Wood HG, Allaire PE, Throckmorton AL, Day SW, Olsen DB. Design and transient computational fluid dynamics study of a continuous axial flow ventricular assist device. *ASAIO J*. 2004;50:215–24.
41. Wu J, Antaki JF, Wagner WR, Snyder TA, Paden BE, Borovetz HS. Elimination of adverse leakage flow in a miniature pediatric centrifugal blood pump by computational fluid dynamics-based design optimization. *ASAIO J*. 2005;51:636–43.

42. Song X, Wood HG, Day SW, Olsen DB. Studies of turbulence models in a computational fluid dynamics model of a blood pump. *Artif Organs*. 2003;27:935–7.
43. Legendre D, Antunes P, Bock E, Andrade A, Biscegli JF, Ortiz JP. Computational fluid dynamics investigation of a centrifugal blood pump. *Artif Organs*. 2008;32:342–8.
44. Okamoto E, Hashimoto T, Inoue T, Mitamura Y. Blood compatible design of a pulsatile blood pump using computational fluid dynamics and computer-aided design and manufacturing technology. *Artif Organs*. 2003;27:61–7.
45. Okamoto E, Hashimoto T, Mitamura Y. Design of a miniature implantable left ventricular assist device using CAD/CAM technology. *J Artif Organs*. 2003;6:162–7.
46. Medvitz RB, Kreider JW, Manning KB, Fontaine AA, Deutsch S, Paterson EG. Development and validation of a computational fluid dynamics methodology for simulation of pulsatile left ventricular assist devices. *ASAIO J*. 2007;53:122–31.
47. Untaroiu A, Wood HG, Allaire PE, Throckmorton AL, Day S, Patel SM, Ellman P, Tribble C, Olsen DB. Computational design and experimental testing of a novel axial flow LVAD. *ASAIO J*. 2005;51:702–10.
48. Curtas AR, Wood HG, Allaire PE, McDaniel JC, Day SW, Olsen DB. Computational fluid dynamics modeling of impeller designs for the HeartQuest left ventricular assist device. *ASAIO J*. 2002;48:552–61.
49. Song X, Wood HG, Olsen D. Computational Fluid Dynamics (CFD) study of the 4th generation prototype of a continuous flow ventricular assist device (VAD). *J Biomech Eng*. 2004;126:180–7.
50. Song X, Throckmorton AL, Wood HG, Allaire PE, Olsen DB. Transient and quasi-steady computational fluid dynamics study of a left ventricular assist device. *ASAIO J*. 2004;50: 410–7.
51. Burgreen GW, Loree HM, Bourque K, Dague C, Poirier VL, Farrar D, Hampton E, Wu ZJ, Gempp TM, Schob R. Computational fluid dynamics analysis of a Maglev centrifugal left ventricular assist device. *Artif Organs*. 2004;28:874–80.
52. Chua LP, Song G, Lim TM, Zhou T. Numerical analysis of the inner flow field of a biocentrifugal blood pump. *Artif Organs*. 2006;30:467–77.
53. Ashton RC, Goldstein DJ, Rose EA, Weinberg AD. Duration of left ventricular assist device support affects transplant survival. *J Heart Lung Transplant*. 1996;15:1151–6.
54. Song X, Throckmorton AL, Untaroiu A, Patel S, Allaire PE, Wood HG, Olsen DB. Axial flow blood pumps. *ASAIO J*. 2003;49:355–64.
55. Zhang J, Koert A, Gellman B, Gempp TM, Dasse KA, Gilbert RJ, Griffith BP, Wu ZJ. Optimization of a miniature Maglev ventricular assist device for pediatric circulatory support. *ASAIO J*. 2007;53:23–31.
56. Throckmorton AL, Untaroiu A, Allaire PE, Wood HG, Lim DS, McCulloch MA, Olsen DB. Numerical design and experimental hydraulic testing of an axial flow ventricular assist device for infants and children. *ASAIO J*. 2007;53:754–61.
57. Kar B, Delgado RM 3rd, Frazier OH, Gregoric ID, Harting MT, Wadia Y, Myers TJ, Moser RD, Freund J. The effect of LVAD aortic outflow-graft placement on hemodynamics and flow: Implantation technique and computer flow modeling. *Tex Heart Inst J*. 2005;32(3):294–8.
58. Carr RT, Kotha SL. Separation surfaces for laminar flow in branching tubes – effect of Reynolds number and geometry. *J Biomech Eng*. 1995;117:442–7.
59. May-Newman K, Hillen BK, Sironda CS, Dembitsky W. Effect of LVAD outflow conduit insertion angle on flow through the native aorta. *J Med Engin Technol*. 2004;28:105–9.
60. May-Newman K, Hillen BK, Dembitsky W. The effect of LVAD outflow conduit anastomosis location on flow patterns in the native aorta. *ASAIO J*. 2006;52:132–9.
61. May-Newman K, Abulon DJ, Joshi M, Dembitsky W. (submitted). Morphology and tissue characterization of fusion in aortic heart valves excised from LVAD patients.

Index

J.M. Guccione, et al. (eds.), *Computational Cardiovascular Mechanics*,
DOI 10.1007/978-1-4419-0730-1,